Data
Models
Inventories

PARIS

Process Attribution of Regional Emissions

GA 101081430, RIA

Draft annex to National Inventory Report (NIR) for each focus country – first update

Deliverable 2.3	
Delivery due date Annex I	PM 34 | 31/10/2025
Actual date of submission	31/10/2025
Lead beneficiary: [acronym]	Work package: 2 Nature: Report Dissemination level: PU
Responsible scientist	A. Manning, UK Met Office
Contributors	A. Ganesan, H. de Longueville, A. Danjou, B. Murphy (University of Bristol) S. Henne, D. Brito Melo (Empa) A. Ramsden, A. Redington, P. Andrews (UK Met Office)
Internal reviewers	A. Ganesan, University of Bristol, co-coordinator, A. Manning, UK Met Office, WP2 lead
Version: 0.1	

Horizon Europe Cluster 5: Climate, energy and mobility
"This project has received funding from the European Union's Horizon Europe Research and Innovation programme under HORIZON-CL5-2022-D1-02 Grant Agreement No 101081430 - PARIS".

Table of content

1. CHANGES WITH RESPECT TO THE DOA (DESCRIPTION OF THE ACTION) 4

2. DISSEMINATION AND UPTAKE 4

3. SHORT SUMMARY OF RESULTS 4

4. EVIDENCE OF ACCOMPLISHMENT 4

4.1 INTRODUCTION | BACKGROUND OF THE DELIVERABLE | MILESTONE 5
4.2 SCOPE OF THE DELIVERABLE | MILESTONE 5
4.3 CONTENT OF THE DELIVERABLE | MILESTONE 6
4.4 CONCLUSION AND POSSIBLE IMPACT 7
4.5 REFERENCES 7

5. HISTORY OF THE DOCUMENT 8

ANNEX
MODEL DESCRIPTION
DRAFT NIR ANNEX – GERMANY
DRAFT NIR ANNEX – HUNGARY
DRAFT NIR ANNEX – ITALY
DRAFT NIR ANNEX – NETHERLANDS
DRAFT NIR ANNEX – NORWAY
DRAFT NIR ANNEX – SWITZERLAND
DRAFT NIR ANNEX – UNITED KINGDOM
DRAFT NIR ANNEX – IRELAND

1. Changes with respect to the DoA (Description of the Action)

This deliverable is included in the 2nd amendment and reintroduced as an iterative update to D2.1. The content has been reviewed and updated accordingly.

2. Dissemination and uptake

These draft Annexes to the National Inventory Documents (NIDs) are provided to the national inventory compilers of the eight focus countries of the project (UK, Netherlands, Ireland, Italy, Switzerland, Germany, Norway, Hungary). The Annexes provide a comparison between the emissions reported annually in NIDs versus those that are derived from atmospheric measurements ("top-down").

The Annexes provide an assessment of 1) gases or processes for which there are significant discrepancies between the NID and top-down, 2) gases that show consistency between the NID and top-down, 3) regions that are not currently constrained by the observational network and are "blind" to the top-down estimates, and 4) gases for which large uncertainties exist due to complex emissions characteristics (e.g., episodic release).

The national inventory compilers may choose to include the Annexes directly or use the results presented in the Annexes in their national submissions, as was the case in the Netherlands NID Annex in 2025.

3. Short Summary of results

Inversion-derived emissions are presented for Europe with a focus on eight countries (UK, Netherlands, Ireland, Italy, Switzerland, Germany, Norway, Hungary) for the period 2017-2024.

Three inverse systems and two atmospheric transport models were used, resulting in a total of six inversions, to assess modelling uncertainty. National emissions and spatial distributions are presented and tabulated for methane, nitrous oxide and reported F-gases and are compared to the values reported by the countries to UNFCCC.

The specific gases estimated for each country varied depending on the available observational constraint in the measurement networks. In addition, Northern and Southern Hemisphere background concentration trends of these gases are given to provide a global context.

An evaluation of the current state of fossil fuel CO_2 estimation is provided as a separate section in the Annex to describe the main challenges in comparing inversion and inventory reported CO_2 values and future work in this area.

4. Evidence of accomplishment

The eight draft Annexes are available as individual reports. All associated inverse modelling results (grid-distributed and country-aggregated fluxes) are provided as netcdf files.

4.1 Introduction | Background of the deliverable | milestone

There are only a few countries worldwide, and only two in Europe (the UK and Switzerland), who currently routinely report their emissions using bottom-up (inventory) and top-down (atmospheric data-based) methods together.

The central aim of this project is to significantly increase the uptake of this joint approach to emissions evaluation. For each of the eight focus countries, national emissions were derived using atmospheric data from the European measurement networks. These results and comparisons to the National Inventory Documents (NID) are documented in draft Annexes to the NID for each focus country. Each draft Annex contains an Introduction section that describes the background to the document.

In this document, global concentration trends and national emissions estimates derived from atmospheric observations ("inverse estimates") are presented for each reported gas. Comparing the emissions submitted in national inventories with those calculated using atmospheric observations allows for emissions to be assessed using two fundamentally different approaches. Substantial differences can highlight areas that could warrant further investigation.

4.2 Scope of the deliverable | milestone

National emissions estimates for methane, nitrous oxide, HFC-134a, HFC-143a, HFC-125, HFC-32, HFC-227ea, HFC-245fa, HFC-23, HFC-365mfc, HFC-152a, HFC-43-10-mee, PFC-14, PFC-116, PFC-218, PFC-318, NF_3 and SF_6 over 2017-2024 using three inverse methods and two atmospheric transport models (six inversions) for the eight focus countries. Not all gases were estimated for each country, due to limitations in the observational network.

An assessment of the current progress toward estimating fossil fuel CO_2 emissions from atmospheric observations is also included.

Major changes since the 2024 submitted Draft Annex Reports (D2.1):

- Comprehensive documentation of PARIS inversion methodologies (included as separate document)
- Inclusion of an additional transport model (FLEXPART) by all inverse methods, increasing the number of individual inversions from three to six for all gases (except SF_6 where results from RHIME inversion system were not included)
- Extended common inversion period across the six inverse systems to: 2017-2024
- Extended inversion results to additional gases, now including NF3 and HFC-236fa
- Inclusion of the German Weather Service (DWD) ITMS-Demonstrator inversion estimate for German CH_4 emissions
- Extended list of observation stations used for CH_4, N_2O inversions improving the European-wide spatial coverage (e.g., Lampedusa, south of Italy, Puy de Dome and Roc'h Trédudon, central and north-western France)
- Extended list of observations used for HFCs/PFCs including observations carried out as part of PARIS
- Extended list of observations used for SF_6 including observations carried out as part of PARIS and ICOS flask sampling
- Sensitivity tests that assess the impact of new (PARIS) observations, included in reports to Italy and Hungary

- Progress report assessing the current capability to estimate fossil CO_2 emissions from atmospheric observations
- Re-visited inversion setups to test the impact of model assumptions
- Improved tables and figures through the use of the fluxy tool (https://github.com/openghg/fluxy)

4.3 Content of the deliverable | milestone

The eight Draft Annexes are available as individual reports. All associated inverse modelling results (grid-distributed and country-aggregated fluxes) are provided as netcdf files in a common format and available on the ICOS fileshare. A DOI on the ICOS Carbon Portal will replace this link in due course. A comprehensive description of the methodologies of the three inverse models used for PARIS is also provided in a separate document.

An overview of the methodology, the work carried out, and results are described within the Annex reports. For ease, the introductory text from the Annexes is reproduced here. Data files containing the emissions estimates will be uploaded to the ICOS portal.

In this document, global concentration trends and national emissions estimates derived from atmospheric observations ("inverse estimates") are presented for most reported gases. Comparing the emissions submitted in national inventories with those calculated using atmospheric observations allows for emissions to be assessed using two fundamentally different approaches. Substantial differences can highlight areas that could warrant further investigation.

Global concentration trends for each gas are first shown using annual average concentrations from Mace Head, Ireland (Northern Hemisphere) and Kennaook/Cape Grim, Tasmania, Australia (Southern Hemisphere). Data from these stations were selected to exclude regionally-polluted air masses and therefore represents northern and southern hemispheric concentration trends. Mace Head observations were sup- ported by the National Aeronautics and Space Administration (NASA) and the UK Department of Energy, Security and Net Zero (DESNZ), and Kennaook/Cape Grim observations by NASA and the Australian Bureau of Meteorology.

Observations of European concentrations of greenhouse gases used to derive national inverse emission estimates were collected from many different networks and providers. Methane and nitrous oxide concentrations originated from the European ICOS (Integrated Carbon Observation System) network, the UK DECC (Deriving Emissions related to Climate Change) network and other national or individual initiatives. F-gas observations were made by affiliates of the AGAGE (Advanced Global Atmospheric Gases Experiment) network. Observations from additional stations across Europe were supported by the Horizon-EU PARIS (Process Attribution of Regional Emissions) project. The observation stations used to derive emissions for each gas are shown in the corresponding sections of this document.

An atmospheric transport model provides the link between surface fluxes and concentrations measured at the observing stations. If not otherwise mentioned, inversion-based emissions estimates were derived using two atmospheric transport models combined with three inverse models, yielding a total of six sensitivity inversions. This ensemble of six inversions allows us to better quantify the uncertainties associated with inverse modelling.

The two atmospheric transport models used are the Numerical Atmospheric dispersion Modelling Environment (NAME, Jones et al., 2007), and the FLEXible PARTicle dispersion model (FLEXPART, Stohl et al., 2005). Both models are backwards-running Lagrangian Particle Dispersion Models (LPDMs) that simulate the recent transport of air to each observing station. The two LPDMs have been widely used in the estimation of x greenhouse gas emissions (Ganesan et al., 2015; Rigby et al., 2019; Manning et al., 2021; Henne et al., 2016).

The three inverse methods used are InTEM (Inversion Technique for Emission Modelling, Manning et al., 2021), ELRIS (Empa Lagrangian Regional Inversion System, Henne et al., 2016; Katharopoulos et al., 2023), and RHIME (Regional Hierarchical Inverse Modelling Environment, Ganesan et al., 2014). All three inverse methods estimate emissions within Europe along with boundary conditions that account for the concentration of the air entering Europe. All three systems started from the same set of a priori emissions that were either derived from the global EDGAR emission inventory (version 8, European Commission: Joint Research et al., 2023) or a uniform land-based emission, depending on the gas. A natural emission component, from the WETCHARTS product, was included in the methane prior. The same observational dataset was used by each inverse model, but data selection (i.e., filtering datasets for specific conditions) and treatment of uncertainties were chosen separately and hence differ. The three methods also differ in their statistical approaches for estimating emissions.

Emission estimates are presented for the period 2008-2024. Emissions for the full 2008-2024 period were derived with the InTEM-NAME inversion only, while emissions from 2017-2024 are presented as the mean of the six inversions (denoted the "PARIS mean"). The uncertainty shown is the minimum/maximum of the uncertainties in the ensemble.

All inversions employed a resolution of one month for CH_4 and N_2O and 1-year for the fluorinated gases. The inversion results used to compare with the inventories are a one-year calendar average for CH_4 and N_2O and the yearly value derived from a 3-year moving average for the fluorinated gases. For the 2008- 2024 InTEM-NAME results, a 3-year moving average was also applied to CH_4 and N_2O due to lack of observational coverage in the earlier years.

4.4 Conclusion and possible impact

These Draft Annexes are used to guide discussions with the national inventory compilers of the focus countries and to build collaboration between inventory and atmospheric modelling teams. Tailored country-specific analyses are also provided to address specific country circumstances. The national inventory compilers may choose to use the information provided in the Draft Annexes to guide where further work is needed to reconcile large uncertainties or discrepancies. The countries can also choose to include the Draft Annexes or the results from PARIS in their submitted NIDs. Additional analysis of the inversion results is provided using the visualisation and analysis package 'fluxy' which can be either used directly by the inventory teams on the provided netcdf results or interactively during the PARIS consultations with the inventory teams.

The results of PARIS inversions were included by the Netherlands in their 2025 NID. PARIS results are also being used to support the German ITMS project.

4.5 References

European Commission: Joint Research Centre et al. (2023). GHG emissions of all world countries – 2023. Publications Office of the European Union. doi: 10.2760/953322.

Ganesan, A. L. et al. (2014). "Characterization of uncertainties in atmospheric trace gas inversions using hierarchical Bayesian methods". In: Atmospheric Chemistry and Physics 14.8, pp. 3855–3864. doi:10.5194/acp-14-3855-2014.

Ganesan, A. L. et al. (2015). "Quantifying methane and nitrous oxide emissions from the UK and Ireland using a national-scale monitoring network". In: Atmos. Chem. Phys. 15.11, pp. 6393–6406. doi: 10.5194/acp- 15- 6393- 2015.

Henne, S. et al. (2016). "Validation of the Swiss methane emission inventory by atmospheric observations and inverse modelling". In: Atmospheric Chemistry and Physics 16.6, pp. 3683–3710. doi: 10.5194/acp-16-3683-2016.

Jones, A.R. et al. (2007). "The U.K. Met Office's next-generation atmospheric dispersion model, NAMEIII, in Borrego C. and Norman A.-L. (Eds)". In: Air Pollution Modeling and its Application XVII (Proceedings of the 27th NATO/CCMS International Technical Meeting on Air Pollution Modelling and its Application), Springer, pp. 580–589.

Katharopoulos, I. et al. (2023). "Impact of transport model resolution and a priori assumptions on inverse modeling of Swiss F-gas emissions". In: Atmos. Chem. Phys. 23.22, pp. 14159–14186. doi: 10.5194/acp-23-14159-2023.

Manning, A. J. et al. (2021). "Evidence of a recent decline in UK emissions of hydrofluorocarbons determined by the InTEM inverse model and atmospheric measurements". In: Atmospheric Chemistry and Physics 21.16, pp. 12739–12755. doi: 10 . 5194/acp - 21 - 12739 - 2021.

Rigby, M. et al. (2019). "Increase in CFC-11 emissions from eastern China based on atmospheric observations". In: Nature 569, pp. 546–550. doi: 10.1038/s41586-019-1193-4. url: https://doi.org/10.1038/s41586-019-1193-4.

5. History of the document

Version	Author(s)	Date	Changes
0.1	A. Manning, A. Ganesan, S. Henne, D. Brito Melo, A. Ramsden, H. De Longueville, A. Danjou, B. Murphy, P. Andrews	24/10/2025	

Inverse modelling of greenhouse gas surface fluxes with ELRIS, InTEM and RHIME: general methodology and model settings

Daniela Brito Melo[1], Brendan Murphy[2], Peter Andrews[3], Joseph Pitt[2], Alison Redington[3], Alice Ramsden[3], Hélène De Longueville[2], Alexandre Danjou[2], Alistair Manning[3], Stephan Henne[1], and Anita Ganesan[4]

[1]Empa, Laboratory for Air Pollution / Environmental Technology, Dübendorf, Switzerland
[2]School of Chemistry, University of Bristol, Bristol, UK
[3]Met Office Hadley Centre, Exeter, UK
[4]School of Geographical Sciences, University of Bristol, Bristol, UK

October 2025

1 Introduction

The quantification of greenhouse gas (GHG) surface fluxes is a global effort supported by the United Nations Framework Convention on Climate Change (UNFCCC). The UNFCCC reporting process follows the tiered methods described in the 2006 Intergovernmental Panel on Climate Change (IPCC) Guidelines for National Greenhouse Gas Inventories (IPCC, 2006), the 2013 Wetlands Supplement (IPCC, 2014), and the respective 2019 refinements (IPCC, 2019). We refer to these methods as "bottom-up" as they are based on upscaling activity data and emission factors of individual processes to total fluxes. Alternatively, atmospheric observations and inverse modelling can be used to estimate total GHG surface fluxes, which include both anthropogenic and natural sources. It is an independent approach, which can complement and support national inventory compilers. We refer to inverse modelling as "top-down" because surface fluxes are inferred from atmospheric observations, rather than being directly measured.

The UNFCCC requests countries to report surface fluxes of carbon dioxide (CO_2), methane (CH_4), nitrous oxide (N_2O), and fluorinated gases (F-gases). CO_2 fluxes from anthropogenic sources are the largest contributor and are relatively well known and well quantified with the bottom-up method in most European countries. Biogenic surface fluxes of CO_2 are more complex to assess with bottom-up methods. Separating biogenic and anthropogenic sources/sinks of CO_2 from top-down methods at a scale relevant for policy makers is an ongoing area of research. Non-CO_2 GHG emissions (CH_4, N_2O and F-gases) are more challenging to quantify with bottom-up methods due to uncertainties in emission factors and more complex emission processes, such as CH_4 and N_2O from agriculture.

Therefore, top-down estimates of these surface fluxes might be of particular interest for national inventory compilers.

The Horizon Europe research project Process Attribution of Regional Emissions (PARIS) focuses on using top-down methods to estimate European emissions of non-CO_2 GHGs, as well as improving the attribution of CO_2, CH_4 and N_2O surface fluxes to particular sources and sinks. Although further studies are needed to attribute surface fluxes to specific processes, European emissions of all major non-CO_2 GHGs were estimated using three regional inverse models in 2024 and 2025. These modelling systems are the Empa Lagrangian Regional Inversion System (ELRIS, Henne et al., 2016), the Inversion Technique for Emission Modelling (InTEM, Manning et al., 2021) and the Regional Hierarchical Inverse Modelling Environment (RHIME, Ganesan et al., 2014). In light of pre-established collaborations between the PARIS consortium and national GHG inventory compilers of the UK, Ireland, Norway, Netherlands, Germany, Italy, Switzerland and Hungary, reports in the form of Draft Annexes to the National Inventory Document (NID) were produced for these eight European countries (Manning et al., 2024). The 2024 emission estimates over the Netherlands were subsequently incorporated into the 2025 Dutch NID (RIVM, 2025).

Different versions of these inversion models have been used to estimate emissions of trace gases in various regions of the globe. ELRIS has been primarily used to estimate emissions of methane and F-gases from Switzerland (Henne et al., 2016; Rust et al., 2022; Katharopoulos et al., 2023), while InTEM and RHIME tend to focus on United Kingdom (UK) emissions of methane, nitrous oxide and F-gases (Manning et al., 2011, 2021; Ganesan et al., 2015; Lunt et al., 2021; Ramsden et al., 2022; Saboya et al., 2024). More broadly, these models have been used to assess F-gas emissions over Europe (Keller et al., 2011; Schoenenberger et al., 2018; Simmonds et al., 2020), East Asia (Arnold et al., 2018; An et al., 2024a,b), and beyond (Ganesan et al., 2014; Kuyper et al., 2019). Other studies have focused on methane emissions in multiple parts of the globe (e.g., Ganesan et al., 2017; Fraser et al., 2020; France et al., 2022).

Emission estimates from these models have been intercompared in the past, for instance concerning emissions of F-gases over Europe (Brunner et al., 2017), and ozone-depleting substances over Europe (Redington et al., 2023) and East Asia (Lunt et al., 2018; Rigby et al., 2019; Park et al., 2021). Moreover, since 2003 and 2016, top-down assessments based on InTEM and ELRIS, respectively, have been combined with bottom-up methods to support the annual reporting of UK and Swiss emissions to the UNFCCC (Say et al., 2016; FOEN, 2025).

Detailed descriptions of the inversion systems ELRIS, InTEM and RHIME can be found separately in previous studies (see, respectively, Henne et al., 2016; Manning et al., 2021; Ganesan et al., 2014). In order to complement the existing literature, this document summarizes common features and individual characteristics of the modelling techniques, describes new model developments that were not previously documented, and presents the model settings used in the 2025 Draft Annexes to the NID produced during the PARIS project. Even though an attempt is made to keep the text accessible to non-experts, readers looking for an introduction to GHG emission monitoring are referred to the World Meteorological Organization (WMO) IG3IS guidelines (WMO-GAW, 2025), which is tailored

for a wider audience. Moreover, a more formal introduction to inverse modelling can be found in Brasseur and Jacob (2017).

Section 2 is a general description of the modelling framework, common to ELRIS, InTEM and RHIME. Section 3 introduces the different statistical methods that comprise the optimization algorithms of each of these models. Section 4 describes the main sources of uncertainty, which will help the reader develop a critical view on inverse modelling estimates. Sections 5, 6 and 7 are specific to ELRIS, InTEM and RHIME, respectively. A detailed description of the modelling choices can be found in these sections, which are mainly addressed to readers well acquainted with the inverse modelling technique. Finally, summary tables with the main model settings can be found in Section 8.

2 Model framework

In this section, we describe the model framework common to ELRIS, InTEM and RHIME. The model description is focused on the PARIS setup, which targets non-CO_2 GHG surface fluxes in Europe. An overview of the different modelling options implemented to date in ELRIS, InTEM and RHIME can be obtained by looking at previous publications (see Katharopoulos et al., 2023; Manning et al., 2021; Ganesan et al., 2015, and references therein).

2.1 General description

The chemical composition of the atmosphere varies in time and space according to the sources, atmospheric transport, chemical conversion, and sinks of various compounds (*species*). For long-lived greenhouse gases (with atmospheric lifetimes of the order of years), chemical production and destruction in the atmosphere is negligible on short timescales, and sources and sinks are largely limited to surface fluxes. For all major GHGs except CO_2, surface fluxes are mainly positive, that is, they correspond to emissions into the atmosphere, $\mathbf{e}$, from surface sources.

For a given long-lived species, atmospheric transport models simulate the atmospheric mole fraction that results from a given flux distribution and the dilution of those fluxes in the atmosphere. Regional transport models also rely on the state of the atmosphere at the boundaries of the computational domain, in particular the mole fraction of the species being simulated, $\boldsymbol{\chi}_{\mathbf{bc}}$ (*boundary conditions*). This is exemplified in Figure 2.1, which illustrates the impact of both surface fluxes and boundary conditions on the *simulated mole fraction*, $\boldsymbol{\chi}$, at a given time and location. The simulated mole fraction is therefore the sum of two components: the *regional mole fraction*, $\boldsymbol{\chi}_{\mathbf{p}}$, related to surface fluxes, and the *baseline mole fraction*, $\boldsymbol{\chi}_{\mathbf{b}}$, associated with boundary conditions,

$$\boldsymbol{\chi} = \boldsymbol{\chi}_{\mathbf{p}} + \boldsymbol{\chi}_{\mathbf{b}}. \tag{1}$$

Inverse models make use of the atmospheric dynamics given by atmospheric transport models, atmospheric observations, and a first estimate of surface fluxes (*prior fluxes*) to infer an updated estimate of surface fluxes (*posterior fluxes*). Atmospheric observations, $\boldsymbol{\chi}_{\mathbf{o}}$, are typically the dry-air

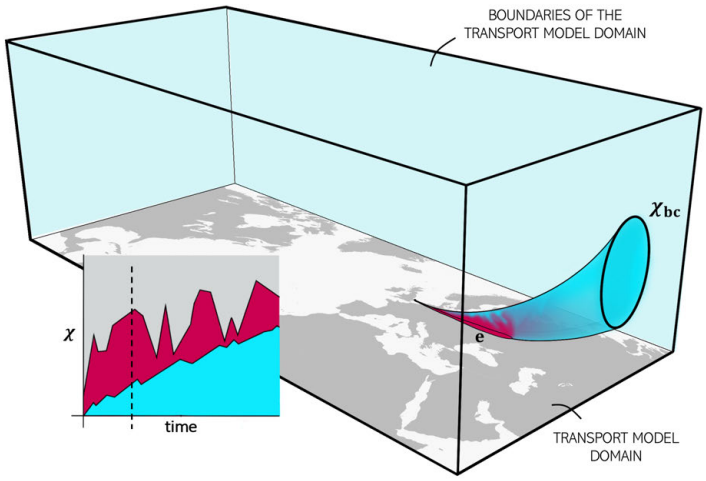

Figure 2.1: Illustration of the transport model domain and its boundaries. An air plume arriving in the UK originated from the Eastern boundary of the transport model domain. The plume carries the chemical composition of the Eastern boundary (represented in blue) enriched with contributions from surface fluxes (shown in red). These two contributions to the simulated mole fraction are illustrated in the time series in blue and red, respectively. (Design by Julian Gisler).

mole fraction at ground-based measurement stations. Alternatively, remote sensing techniques based on satellites or aircraft can be used, which measure the total dry-air mole fraction of the respective species along a vertical column of air. Prior fluxes are normally from national inventories or global gridded datasets. The core of an inversion system is an optimization algorithm that adjusts the surface fluxes to statistically balance the mismatch between observed and simulated atmospheric mole fractions and between prior and posterior fluxes. Boundary conditions can also be adjusted as part of the optimization.

To define the inversion problem, one must select atmospheric observations and derive the relationship between the simulated mole fraction, $\boldsymbol{\chi} = \boldsymbol{\chi}_\mathbf{p} + \boldsymbol{\chi}_\mathbf{b}$, and the surface fluxes and boundary conditions. This is explained in the following sub-sections.

2.2 Atmospheric observations

In the inversion problem, simulated mole fractions, $\boldsymbol{\chi}$, are estimated at multiple locations and time instances, where and when atmospheric observations exist. In the current framework, these locations are measurement sites with continuous or semi-continuous on-site observations, as well as sites where air samples are collected in flasks and measured in a laboratory. The collection of these stations is referred to as the *measurement network*.

The extent of the measurement network varies according to the compound of interest, the time window and target geographical region. For instance, over the last decade, mole fractions of fluorinated gases in Europe were continuously measured at only 2-5 stations (Prinn et al., 2018), whereas mole fractions of CH_4 and N_2O were continuously measured at 25-45 stations (Heiskanen et al., 2022). The measurement network of CH_4 and the hydrofluorocarbon HFC-134a considered in the PARIS

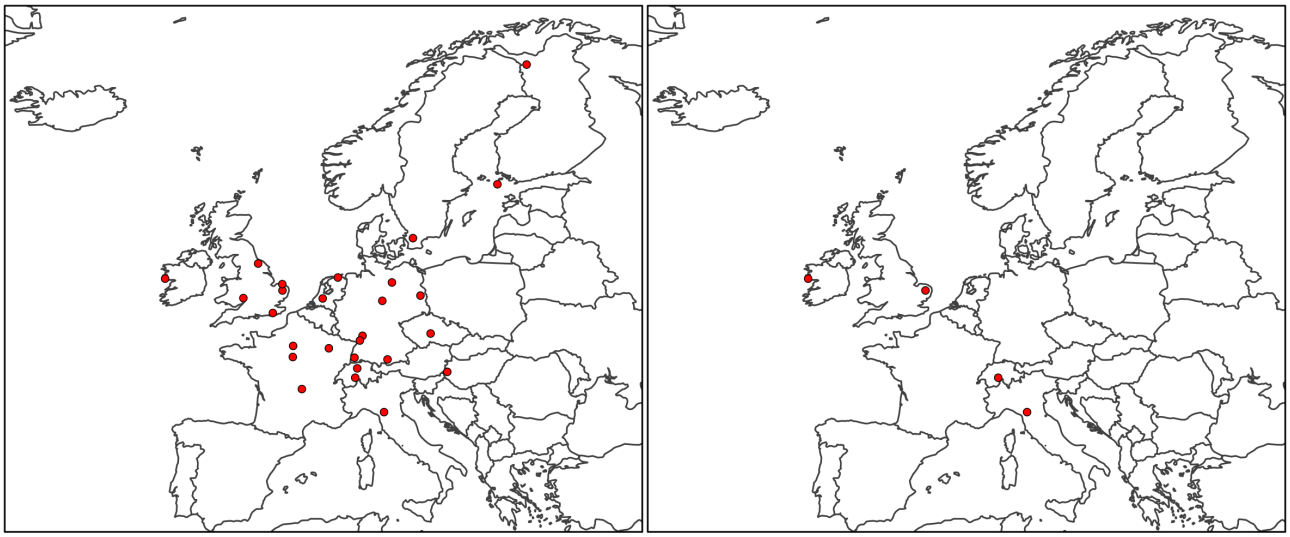

a) CH_4 b) HFC-134a

Figure 2.2: European measurement network for CH_4 and HFC-134a considered in the 2018 inversions.

inversions for 2018 is depicted in Figure 2.2 as an example.

Atmospheric mole fraction observations that are not sufficiently separated in time or space cannot be regarded as fully independent, as they were impacted by largely the same surface fluxes prior to their analysis. The same can be said about the mismatch between observed and simulated mole fractions. The respective correlations are challenging to characterize (e.g., Steiner et al., 2024) and subjective methods are typically employed. This complexity is frequently minimized by averaging the mole fraction measurements over a given time interval (*aggregation interval*). The aggregation of atmospheric observations can also reduce the size of the inverse problem without significant loss of information. Potential errors associated to a temporal misalignment between observed and simulated meteorological events characterized by time scales difficult to resolve by atmospheric transport models are also minimized with this approach. Aggregation intervals of 1 to 12 hours are typically considered.

Furthermore, selection of observations, according to time of day or meteorological variables, is common in regional inversions. This strategy allows us to focus on observations characterized by the meteorological conditions best represented by atmospheric transport models (e.g., afternoon observations characterized by well-mixed boundary layers). As a result, $\boldsymbol{\chi}_\mathbf{o}$ and $\boldsymbol{\chi}$ are vectors of length L, given by the total number of selected aggregated mole fraction measurements in the measurement network and time window of interest.

The measurement network considered in the 2025 Draft Annexes to the NID are listed in Table 8.4. An aggregation interval of 4 hours was considered and the criteria applied in ELRIS, InTEM and RHIME for observation selection are described in Sections 5, 6 and 7, respectively.

2.3 Regional mole fraction

The regional mole fraction, $\boldsymbol{\chi}_\mathbf{p}$, refers to mole fraction enhancements above the baseline value, related to recent emission fluxes (referred to as pollution events). One way to calculate the functional

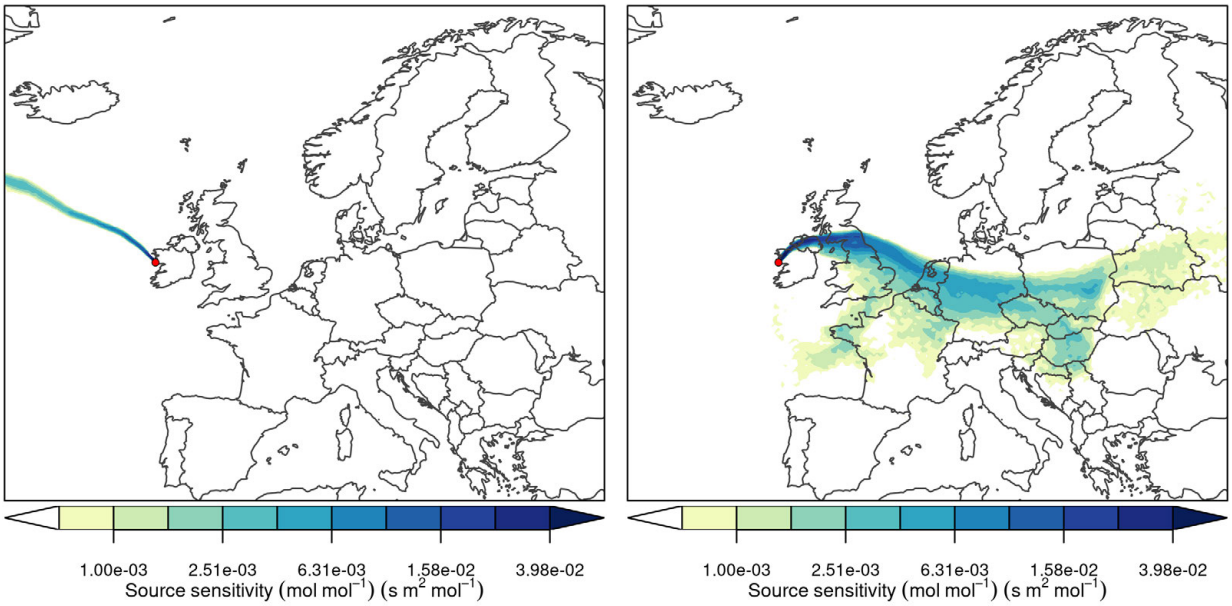

a) 13 February 2018 (00h00-01h00)

b) 5 March 2018 (00h00-01h00)

Figure 2.3: Source sensitivity at MHD at two time instances. Results obtained with the NAME LPDM.

relationship between surface fluxes and the associated changes in mole fraction at various locations is the application of Lagrangian Particle Dispersion Models (LPDM). These models make use of meteorological fields, for example estimated by Numerical Weather Prediction (NWP) models and data assimilation, to compute advection, and turbulent and convective mixing of chemical species in the atmosphere. In the context of greenhouse gas inversions, they are used to compute the trajectories of a multitude of air parcels backwards in time, from a given measurement time (and location) to typically 4-50 days into the past (Vojta et al., 2022). From these simulations, one obtains the recent history of the air masses arriving at each measurement station. The quantity of interest is the residence time of these air parcels between the surface and a given height (e.g., 40-100 m above ground level or some fraction of the boundary layer height). The sensitivity of an air parcel composition to surface mass fluxes of a given chemical compound is proportional to the residence time. This sensitivity is frequently denoted source sensitivity, source-receptor relationship, or concentration footprint. In PARIS, two LPDMs are used: the Numerical Atmospheric dispersion Modelling Environment (NAME, Jones et al., 2007) and the FLEXible PARTicle dispersion model (FLEXPART, Stohl et al., 2005). More details on these models and their setup are given in Appendix A.

In Figure 2.3, the source sensitivities at Mace Head, Ireland (MHD), at two time instances are presented as an example. While on 13 February 2018, air masses arriving at MHD were sensitive to surface fluxes from the North Atlantic, on 5 March 2018, they were mainly sensitive to surface fluxes from Northwest (NW) Europe.

The relationship between recent emission fluxes within the transport model domain and the associated increase in mole fraction above the baseline value is therefore given by

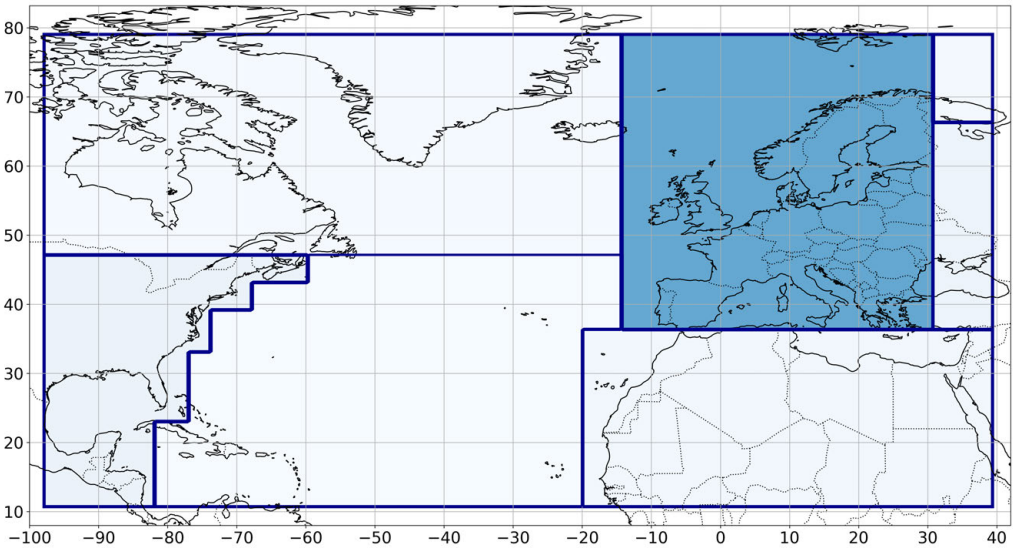

Figure 2.4: Geographical area of interest (highlighted in darker blue) and the six outer regions considered in InTEM. The former is further discretized as described in Section 6.2.

$$\boldsymbol{\chi}_{\mathbf{p}} = \mathbf{M}_{\mathbf{E}}\mathbf{e}, \tag{2}$$

where $\mathbf{M}_{\mathbf{E}}$ is the source sensitivity matrix and $\mathbf{e}$ is the emission flux at various surface points. In order to reduce the problem size and avoid overfitting in areas of low source sensitivity, the inversion problem is not resolved at the resolution of the transport model, but over a coarser and irregular grid. The transport model domain is discretized into K areas where emission fluxes are estimated (inversion grid cells). A higher resolution is specified in the geographical area of interest (*inner inversion grid*) and a much lower resolution is considered outside the geographical area of interest (*outer regions*). In Figure 2.4, the geographical area of interest and outer regions defined in InTEM are shown as an example. As a result, $\mathbf{e}$ is a vector of length K and $\mathbf{M}_{\mathbf{E}}$ is a matrix of size $L \times K$. In ELRIS and InTEM, the native source sensitivities at transport model resolution are averaged over those K inversion grid cells. Therefore, each row of $\mathbf{M}_{\mathbf{E}}$ is comprised of K source sensitivities computed from a single LPDM backwards simulation starting at a specific time/location. A different approach is followed by RHIME, which also considers a coarser and irregular inversion grid defined by K inversion grid cells, but makes use of the source sensitivities at the transport model resolution. This approach is explained in greater detail in Section 7.

The inversion problem is resolved over a given time window (*inversion period*) and the emission fluxes are assumed to be invariant in time during this period. Therefore, Equation (2) relates the regional mole fraction at all times/sites used in the inversion to a single emission flux at each inversion grid cell. The inversion period must therefore be chosen according to the expected emission flux temporal variability of the compound under study. For instance, a time window of several weeks to months is frequently used if the emission fluxes are expected to exhibit significant variability (e.g., seasonal due to environmental drivers) (Steiner et al., 2024), and a time window of 1-3 years might

be appropriate for compounds with relatively constant emissions (e.g., emitted by anthropogenic processes that are not significantly impacted by environmental drivers, such as industrial production) (Manning et al., 2021). In practice however, this resolution can be further constrained by the density of the measurement network and the consequent overall sensitivity to surface fluxes. Hence, in the PARIS inversions, an inversion period of 1 month is used when simulating CH_4 and N_2O surface fluxes, which have sufficient spatial coverage of measurement data. For fluorinated compounds, despite some studies having shown that, for instance, HFC-134a emissions exhibit seasonal variability (Hu et al., 2015; Katharopoulos et al., 2023), an inversion period of 1 year is used for all F-gases. This choice was found to be appropriate for quantifying total annual emissions of fluorinated gases (Katharopoulos et al., 2023).

2.4 Baseline mole fraction

In regional inversions, the baseline mole fraction, $\boldsymbol{\chi}_\mathbf{b}$, must encompass all the temporal and spatial variability of $\boldsymbol{\chi}$ that is not simulated by the LPDM and, consequently, is not represented in $\boldsymbol{\chi}_\mathbf{p}$. $\boldsymbol{\chi}_\mathbf{b}$ includes not only the time-varying globally-averaged atmospheric composition (due to the sources and sinks of chemical compounds at the global scale), but also the temporal and spatial variability associated with the inhomogeneous composition of the air masses entering the transport model domain along its boundaries (far-field contributions).

Different methods can be used to characterize the spatial and temporal variability of $\boldsymbol{\chi}_\mathbf{b}$. For instance, by assessing the observed atmospheric mole fractions which were not recently affected by pollution events (Henne et al., 2016; Manning et al., 2021). Moreover, the LPDM can be used to retrieve the origin of the air masses arriving at each measurement site at various moments in time (Ganesan et al., 2015; Arnold et al., 2018; Manning et al., 2021). This is given by the location at which the backwards-tracked air parcels, released at a particular time/location, exit the transport model domain along its boundaries (or enter, in a time forward sense). This information is used by ELRIS, InTEM and RHIME to constrain $\boldsymbol{\chi}_\mathbf{b}$.

By discretizing the boundaries of the transport model domain in P grid cells (*boundary interfaces*), the baseline mole fraction at each time/location can be computed by weighting the boundary conditions according to the fraction of air parcels reaching the measurement site from each boundary interface (see example discretization in Figure 2.5). The respective weights are denoted baseline sensitivities. In this way,

$$\boldsymbol{\chi}_\mathbf{b} = \mathbf{M}_\mathbf{B}\boldsymbol{\chi}_\mathbf{bc}, \tag{3}$$

where $\mathbf{M}_\mathbf{B}$ is the baseline sensitivity matrix and $\boldsymbol{\chi}_\mathbf{bc}$ is the vector of boundary conditions. If the boundary conditions are estimated at T time instances within the inversion period, $\boldsymbol{\chi}_\mathbf{bc}$ is a vector of length $N = P \times T$. Thus, $\mathbf{M}_\mathbf{B}$ is a matrix of size $L \times N$, composed of weighting coefficients given by the baseline sensitivities and temporal interpolation factors. This is the approach followed by ELRIS, described in Section 5.

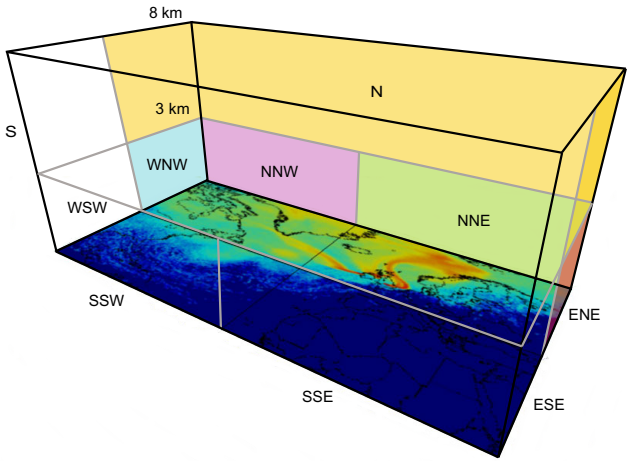

Figure 2.5: Boundary interfaces considered by ELRIS and InTEM: eight interfaces in the lowest 3 km, two interfaces between 3-8 km height, and a single interface above 8 km height independent of direction (not represented). The five Northern interfaces are highlighted with different colours for clarity. (Adapted from Figure 2 in Ganesan et al., 2015).

Alternatively, the right-hand side of Equation (3) can be written as the product of a matrix of mole fraction contributions (size $L \times N$) and a vector of mole fraction scaling factors (length N). This is the approach followed by InTEM and RHIME, explained in greater detail in Sections 6 and 7, respectively. For InTEM, this allows the model to define boundary conditions at a higher temporal resolution, while for RHIME, this approach enables the model to make use of the baseline sensitivities at a higher spatial resolution.

2.5 Simulated vs observed mole fraction

From Equations (1) to (3), $\boldsymbol{\chi}$ is described as a linear model:

$$\boldsymbol{\chi} = \begin{bmatrix} \mathbf{M_E} & \mathbf{M_B} \end{bmatrix} \begin{bmatrix} \mathbf{e} \\ \boldsymbol{\chi}_{\mathbf{bc}} \end{bmatrix} = \mathbf{Mx}, \tag{4}$$

where $\mathbf{M}$ is the sensitivity matrix of size $L \times (K + N)$, given by the horizontal concatenation of $\mathbf{M_E}$ and $\mathbf{M_B}$; and $\mathbf{x}$ is the state vector of length $K + N$, which results from the vertical concatenation of $\mathbf{e}$ and $\boldsymbol{\chi}_{\mathbf{bc}}$. The elements of $\mathbf{x}$ are the variables to be estimated in the inversion problem.

Equation (4) establishes a linear relationship between atmospheric mole fractions and emission fluxes, as provided by the transport model and the representation of the baseline mole fraction. However, even if $\mathbf{e}$ equals the true emission fluxes and $\boldsymbol{\chi}_{\mathbf{bc}}$ equals the true mole fractions at the boundary interfaces, $\boldsymbol{\chi}$ may differ from the observed mole fractions, $\boldsymbol{\chi}_{\mathbf{o}}$, for two main reasons: i) there are errors in the measured mole fractions (instrument error); ii) there are errors in the transport model and, consequently, in the computed sensitivities (model error). Other modelling choices, such as the option to solve the inversion problem at a coarser resolution than the transport model (aggregation error), will also contribute to discrepancies. If we denote the sum of these different errors by $\boldsymbol{\varepsilon}_{\mathbf{o}}$

(*observational error*, also denoted *model-data mismatch error*), the simulated and measured mole fractions are related by

$$\boldsymbol{\chi}_{\mathbf{o}} = \boldsymbol{\chi} + \boldsymbol{\varepsilon}_{\mathbf{o}} = \mathbf{M}\mathbf{x} + \boldsymbol{\varepsilon}_{\mathbf{o}}, \tag{5}$$

where $\boldsymbol{\varepsilon}_{\mathbf{o}}$ is a vector of length L. The elements of $\boldsymbol{\varepsilon}_{\mathbf{o}}$ are unknown and challenging to estimate. In the current framework, they are described in a probabilistic way: $\boldsymbol{\varepsilon}_{\mathbf{o}}$ is defined as a vector of random variables characterized by a probability density function (PDF). As a result, the sum $\mathbf{M}\mathbf{x} + \boldsymbol{\varepsilon}_{\mathbf{o}}$ is not deterministic and the state vector must be computed using statistical methods.

3 Statistical methods for inversion of surface fluxes

One commonly applied statistical method for the inversion of greenhouse gas surface fluxes uses Bayes' theorem to estimate $\mathbf{x}$ by taking into account atmospheric mole fraction observations and prior fluxes (e.g., Tarantola, 2005),

$$\rho(\mathbf{x} \mid \boldsymbol{\chi}_{\mathbf{o}}) = \frac{\rho(\boldsymbol{\chi}_{\mathbf{o}} \mid \mathbf{x})\rho(\mathbf{x})}{\rho(\boldsymbol{\chi}_{\mathbf{o}})} \propto \rho(\boldsymbol{\chi}_{\mathbf{o}} \mid \mathbf{x})\rho(\mathbf{x}). \tag{6}$$

On the right-hand side, $\rho(\boldsymbol{\chi}_{\mathbf{o}} \mid \mathbf{x})$ is the PDF of atmospheric mole fractions taking into account a hypothesized state vector. It is given by the PDF of the sum $\mathbf{M}\mathbf{x} + \boldsymbol{\varepsilon}_{\mathbf{o}}$, as described by Equation (5), where $\boldsymbol{\varepsilon}_{\mathbf{o}}$ is a vector of random variables as previously discussed. The second factor on the right-hand side, $\rho(\mathbf{x})$, is the PDF of the state vector when no knowledge of atmospheric mole fraction observations exists (*prior* distribution). The denominator, $\rho(\boldsymbol{\chi}_{\mathbf{o}})$, is the PDF of atmospheric mole fractions. It only serves as a normalizing factor and can be omitted for simplicity when optimizing $\mathbf{x}$. On the left-hand side, $\rho(\mathbf{x} \mid \boldsymbol{\chi}_{\mathbf{o}})$ is the PDF of the state vector taking into account atmospheric mole fraction observations (*posterior* distribution).

The goal of a statistical inversion is to find the posterior distribution of the state vector, while the prior distribution is a first guess which helps constrain the posterior distribution within reasonable bounds. Two methods to compute the posterior distribution of the state vector are described in the next sub-sections: the analytical solution to Bayes' theorem, which assumes Gaussian PDFs, considered in ELRIS and InTEM (Katharopoulos et al., 2023; Manning et al., 2021), and the hierarchical Bayesian inversion approach employing Markov Chain Monte Carlo sampling used in RHIME (Ganesan et al., 2014, 2015).

3.1 Bayesian analytical inversion

Under the assumptions of normally distributed and unbiased errors, the posterior distribution can be computed analytically. More formally, if $\boldsymbol{\varepsilon}_{\mathbf{o}}$ is unbiased (mean zero) and normally distributed with covariance matrix $\mathbf{R}$, then given $\mathbf{x}$, Equation (5) implies that $\boldsymbol{\chi}_{\mathbf{o}}$ is normally distributed with mean $\mathbf{M}\mathbf{x}$ and covariance $\mathbf{R}$. Hence the PDF of $\boldsymbol{\chi}_{\mathbf{o}}$ given $\mathbf{x}$ is

$$\rho(\boldsymbol{\chi}_\mathbf{o} \mid \mathbf{x}) \propto \exp\left(-\frac{1}{2}(\boldsymbol{\chi}_\mathbf{o} - \mathbf{M}\mathbf{x})^T \mathbf{R}^{-1}(\boldsymbol{\chi}_\mathbf{o} - \mathbf{M}\mathbf{x})\right). \tag{7}$$

For simplicity, we have omitted the normalizing constant that makes the right-hand side of the previous equation a true PDF. This un-normalized quantity is sometimes called the *likelihood* of $\boldsymbol{\chi}_\mathbf{o}$ given $\mathbf{x}$. The matrix $\mathbf{R}$ is a symmetric square matrix (of dimension L), which we call the *observational error* covariance matrix (or *model-data mismatch error* covariance matrix).

Writing the state vector as $\mathbf{x} = \mathbf{x_a} + \boldsymbol{\varepsilon}_\mathbf{a}$, where $\mathbf{x_a}$ is a first estimate of the state vector (*prior state vector*) and $\boldsymbol{\varepsilon}_\mathbf{a}$ is the vector of prior errors, allows a similar formulation for the prior distribution. If $\boldsymbol{\varepsilon}_\mathbf{a}$ is unbiased and normally distributed with covariance matrix $\mathbf{B}$, then the prior distribution of the state vector has the form

$$\rho(\mathbf{x}) \propto \exp\left(-\frac{1}{2}(\mathbf{x} - \mathbf{x_a})^T \mathbf{B}^{-1}(\mathbf{x} - \mathbf{x_a})\right). \tag{8}$$

We call the symmetric square matrix $\mathbf{B}$ (of dimension $K + N$) the *prior error* covariance matrix. The diagonal elements of $\mathbf{R}$ and $\mathbf{B}$ are given by the variances of the observational and prior error distributions, $\sigma^2_{\mathrm{o}_l}$ and $\sigma^2_{\mathrm{a}_k}$, respectively ($l = 1, ..., L$; $k = 1, ..., K + N$). The non-diagonal elements are generally estimated by assuming a given spatial and temporal correlation between the K emission fluxes, the N boundary conditions, and the L atmospheric mole fractions. The approach followed by ELRIS and InTEM to determine the covariance matrices $\mathbf{R}$ and $\mathbf{B}$ is detailed in Sections 5 and 6.

Inserting these distributions into Bayes' theorem (Equation 6) yields the following expression for the posterior distribution of the state vector

$$\rho(\mathbf{x} \mid \boldsymbol{\chi}_\mathbf{o}) \propto \exp\left(-\frac{1}{2}(\mathbf{x} - \mathbf{x_a})^T \mathbf{B}^{-1}(\mathbf{x} - \mathbf{x_a}) - \frac{1}{2}(\boldsymbol{\chi}_\mathbf{o} - \mathbf{M}\mathbf{x})^T \mathbf{R}^{-1}(\boldsymbol{\chi}_\mathbf{o} - \mathbf{M}\mathbf{x})\right). \tag{9}$$

From Equation (9), it can be shown that $\rho(\mathbf{x} \mid \boldsymbol{\chi}_\mathbf{o})$ is normally distributed (Rodgers, 2000, page 25), which means that the normalizing factor that is implicit in (9) can be found. Thus, when assuming normally distributed and unbiased errors, one obtains an exact description of the posterior distribution.

The state vector at the maximum of $\rho(\mathbf{x} \mid \boldsymbol{\chi}_\mathbf{o})$ when $\boldsymbol{\chi}_\mathbf{o}$ equals the atmospheric mole fraction measurements is the main variable of interest and is called the *posterior state vector*. Finding the maximum of Equation 9 is equivalent to the minimization of the cost function (Tarantola, 2005)

$$J(\mathbf{x}) = \frac{1}{2}(\mathbf{x} - \mathbf{x_a})^T \mathbf{B}^{-1}(\mathbf{x} - \mathbf{x_a}) + \frac{1}{2}(\boldsymbol{\chi}_\mathbf{o} - \mathbf{M}\mathbf{x})^T \mathbf{R}^{-1}(\boldsymbol{\chi}_\mathbf{o} - \mathbf{M}\mathbf{x}). \tag{10}$$

Therefore, the posterior state vector is the value of $\mathbf{x}$ in Equation (10) that minimizes the weighted differences between the observed and simulated mole fractions as well as between the posterior and prior state vectors. An analytical expression for the *posterior error* covariance matrix is also obtained with this methodology. Please refer to Manning et al. (2021) and Katharopoulos et al. (2023) for the complete mathematical descriptions of InTEM and ELRIS, respectively.

3.2 Hierarchical Bayesian inversion

Parameters for the prior and likelihood distributions, such as the covariance matrices $\mathbf{R}$ and $\mathbf{B}$, are typically elicited by "expert judgement", rendering selection of these values to be subjective. For such uncertain terms, *hierarchical Bayesian inference* allows additional levels of parameters and importantly, their uncertainties to be propagated through Bayes' theorem (Gelman et al., 2013).

More formally, if θ is a parameter (or a vector of parameters) that influences the prior distribution and likelihood, then Bayes' theorem gives us a rule for inferring $\mathbf{x}$ and θ from $\boldsymbol{\mathcal{X}}_\mathbf{o}$:

$$\rho(\mathbf{x}, \theta \mid \boldsymbol{\mathcal{X}}_\mathbf{o}) \propto \rho(\boldsymbol{\mathcal{X}}_\mathbf{o} \mid \mathbf{x}, \theta)\rho(\mathbf{x}, \theta).$$

Using the definition of a conditional distribution, we may factor the joint distribution $\rho(\mathbf{x}, \theta)$ as $\rho(\mathbf{x} \mid \theta)\rho(\theta)$ yielding

$$\rho(\mathbf{x}, \theta \mid \boldsymbol{\mathcal{X}}_\mathbf{o}) \propto \rho(\boldsymbol{\mathcal{X}}_\mathbf{o} \mid \mathbf{x}, \theta)\rho(\mathbf{x} \mid \theta)\rho(\theta). \tag{11}$$

The parameter θ is called a *hyper-parameter*, and its distribution is called a *hyper-prior*. (Note that θ can be a vector, and for clarity it may be written in terms of components.) For each fixed value of θ, the right-hand side of (11) has the form $\rho(\boldsymbol{\mathcal{X}}_\mathbf{o} \mid \mathbf{x}, \theta)\rho(\mathbf{x} \mid \theta)$, which is the same form as the right-hand side of (6), but with distributions conditional on θ. Thus, Equation (11) gives us a consistent way to incorporate unknown parameters in our model configuration.

Hierarchical Bayesian models often do not have analytical solutions for the posterior distribution (left-hand side of (11)), so the posterior must be simulated using sampling methods like Markov Chain Monte Carlo (MCMC). The simulated posterior comprises thousands of samples for each parameter; this "chain" or "trace" of samples can be used to compute descriptive statistics such as the mean, the median, or confidence regions. RHIME uses a variation of *Hamiltonian Monte Carlo* (HMC) (Neal, 2011; Duane et al., 1987) called the *No-U-Turn Sampler* (NUTS) (Hoffman and Gelman, 2011), which is an extremely efficient form of MCMC. See Appendix B for further details.

Using MCMC has another benefit: the distributions used for the priors and likelihood do not need to be Gaussian. This allows us to select PDFs most appropriate to the flux characteristics, such as PDFs defined only on the positive axis for gases that do not have negative fluxes.

4 Sources of uncertainty

The quality of greenhouse gas emission estimates using inverse modelling depends on a variety of factors, including: i) the spatial coverage of the measurement network; ii) the frequency, precision and accuracy of atmospheric observations; iii) the accuracy and uncertainty of the transport model; iv) the representativeness of modelling choices, such as, the discretization of the inversion grid/boundary interfaces or the inversion period; as well as v) the accuracy and uncertainty of the prior emissions. These elements impact the posterior fluxes in different ways depending on the compound under study and the meteorological conditions during the inversion period. These elements are discussed in the following sub-sections with a particular focus on the PARIS setup.

Some factors, such as the spatial coverage of the measurement network and the measurement frequency, impose hard constraints on the inversion problem. Other factors, such as the accuracy of atmospheric observations and transport models, can only be partially corrected for. This can be achieved by optimizing a measurement bias per site and by disregarding atmospheric observations characterized by meteorological conditions that are challenging to simulate (Section 2.2). The precision of atmospheric observations and the uncertainty of the transport model/prior emissions can be accounted for in the inversion problem in the form of error covariance matrices (Section 3). Therefore, an effort is made to correctly quantify the observational (or model-data mismatch) and prior uncertainties, which are used to construct these matrices. The former is mainly a function of the instrument and model uncertainties.

4.1 Atmospheric observations: spatial coverage, frequency, precision and accuracy

The spatial coverage of the measurement network determines the geographical region over which emission fluxes can be inferred from atmospheric observations. The meteorological conditions during the inversion period also play a role. For instance, depending on the wind patterns, the same measurement network might detect pollution events from a wider area in a given year and from a narrower area in a different year. The cumulative source sensitivity over the inversion period provides a qualitative indication of the regions that are well or poorly constrained by atmospheric observations. Example cumulative source sensitivity distributions for 2024 are presented in Figure 4.1 for CH_4 and HFC-134a.

The frequency and precision of mole fraction measurements depend on the species and the respective measurement system. Within the PARIS project, we use CH_4 and N_2O ambient mole fraction measurements provided by the Integrated Carbon Observation System (ICOS) (Yver-Kwok et al., 2021), in addition to measurements from other national and international networks, for example the Deriving Emissions linked to Climate Change (DECC) network (Stanley et al., 2018) and the Advanced Global Atmospheric Gases Experiment (AGAGE) network (Prinn et al., 2018). These gases are measured using various optical and gas chromatography (GC) based techniques with different sampling frequencies. For optical instruments, the measurement data correspond to 1-minute averages of higher frequency measurements (usually 1 second) reported as hourly averages. The sub-hourly sampling frequency guarantees that the reported values are a good representation of the average atmospheric conditions during each 1-hour time period. GC-based observations are provided as hourly averages of two measurements only.

A measure of *repeatability*, σ_{rept}, is provided together with the 1-hour averaged mole fractions. It corresponds to the standard deviation of multiple mole fraction measurements of a target gas (working standard) during a relatively short time period (for instance, 3 days) (Yver Kwok et al., 2015). For optical instruments, a measure of *variability*, σ_{var}, is also provided. It is the standard deviation of the high-frequency measurements within each 1-hour averaging period. In inverse modelling of greenhouse gas emissions, the reported repeatability is generally used as a measure of instrument uncertainty. The variability, σ_{var}, that characterizes the 1-hour averaged mole fractions are a measure of the unsteady nature of the meteorological conditions/emission patterns during each 1-hour period. Since highly

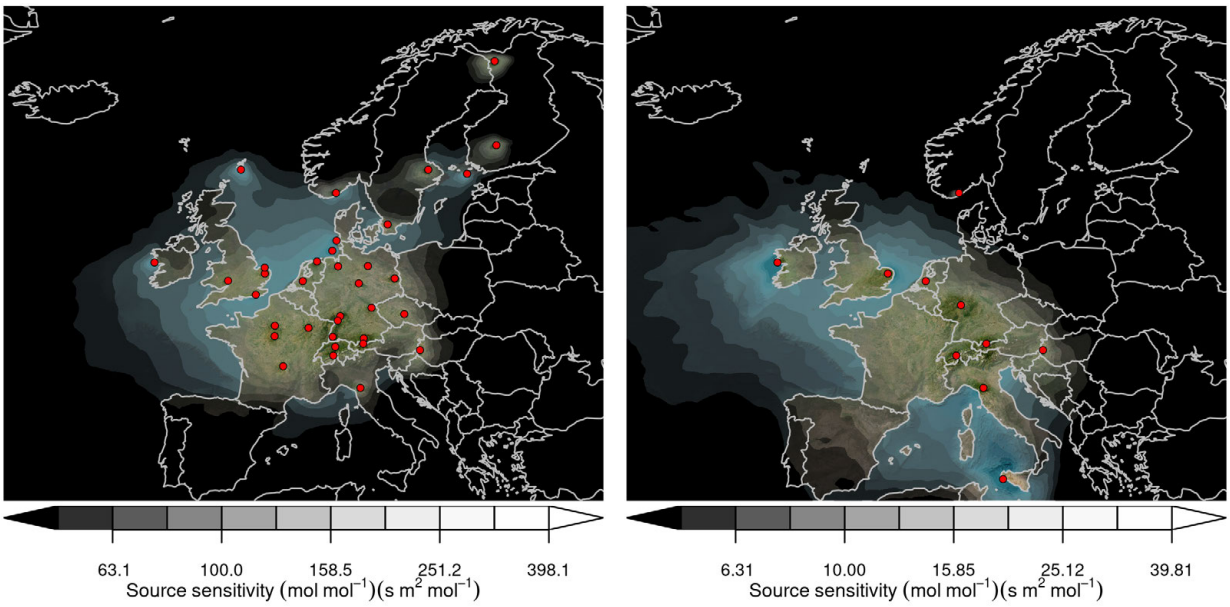

a) CH_4

b) HFC-134a

Figure 4.1: Cumulative source sensitivity to CH_4 and HFC-134a surface fluxes in 2024. Darker areas represent regions that are poorly constrained by the measurement network (note the one order of magnitude difference in the colour scales). The measurement sites are represented by red circles. The expansion of the measurement network is visible in comparison to 2018, illustrated in Figure 2.2.

variable meteorological conditions are more challenging to reproduce by atmospheric models, σ_{var} is taken into account in ELRIS, InTEM and RHIME when quantifying the observational uncertainty.

Continuous measurements of ambient mole fractions of fluorinated gases are mainly provided by AGAGE (Prinn et al., 2018). Measurements are performed either with the Medusa Gas Chromatography Mass Spectrometry (GC-MS) instrument (Miller et al., 2008), or its predecessor, Adsorption-Desorption System (ADS) GC-MS. To this dataset, we add mole fraction observations from Zugspitze, Germany (ZSF), provided by the German Environmental Agency (Umweltbundesamt, UBA). The concentration of F-gases in the atmosphere is 3-6 orders of magnitude lower than the concentration of CH_4 and N_2O. Therefore, pre-concentration of the air samples is necessary prior to the measurements themselves. Air sampling takes 20 minutes (40 minutes for the ADS) and the overall measurement procedure takes approximately 1 hour. In addition, each measurement of ambient air is preceded and succeeded by measurements of a target gas, resulting in gaps of 2 hours or more between atmospheric air samples. Therefore, in comparison to CH_4 and N_2O observations, F-gas mole fraction measurements are characterized by a longer raw sampling period (20 minutes vs. 1 s) and a lower frequency (approximately 1 measurement every 2 hours vs. 1 measurement per second). As a consequence, they capture the atmospheric dynamics at a lower temporal scale. The AGAGE F-gas mole fraction measurements are also accompanied by a measure of repeatability, σ_{rept}, derived from the standard

deviation of target gas measurements preceding and succeeding each ambient air observation[1].

Additional measurements of F-gas mole fractions are carried out during the PARIS project based on either continuous (Capo Granitola, Italy) or flask sampling (Cabauw, Netherlands; Birkenes, Norway; Hegyhátsál, Hungary), using various GC-based devices. Moreover, flask measurements of sulphur hexafluoride (SF_6) are carried out at ICOS Class 1 atmospheric stations. The raw sampling period of flask measurements is comparable with continuous observations (from 1 minute to 1 hour), but the measurement frequency is much lower (1 measurement every other day or per week). These measurements expand the geographical region where emission fluxes can be inferred from atmospheric observations. However, they are unable to capture hourly/daily variations in the atmospheric composition. The repeatability of flask measurements is calculated in different ways depending on the data source. For ICOS flasks, it is the standard deviation of replicate measurements from the same flask. For the remaining sites, it is the standard deviation of target gas measurements.

The accuracy of mole fraction measurements depends on the proper calibration of the measurement devices (e.g., Prinn et al., 2018). Similar calibration scales are normally used, or corrections are applied to the measurements to compensate for deviations. Uncorrected biases between measurement devices can potentially be corrected in the inversion via the optimization of a site bias.

4.2 Transport model

Transport models and the driving meteorology offer an imperfect description of the geophysical system. This is due to limitations of the physical model (for instance, the usage of simplifying assumptions or parameterizations), and its discretization in both space and time. In the context of greenhouse gas inversions, these errors influence both the selection of observations (recall Section 2.2) and the formulation of the model error.

The wind field is one of the most important parameters when estimating the transport of greenhouse gases. Wind speed and direction are measured at multiple automatic weather stations (AWS) and this information is generally assimilated by NWP models and/or used for validation. Nevertheless, some errors remain or get amplified when these data are applied to atmospheric transport in LPDMs due to the use of a coarser resolution in space and time than in the original NWP.

Another key parameter in estimating the atmospheric mixing of trace compounds in LPDMs is the *planetary boundary layer* (PBL) height (Maryon et al., 1991; Ryall and Maryon, 1998; Lopez-Coto et al., 2020). In NAME and FLEXPART, the PBL height is estimated taking into account the wind and temperature fields provided by the NWP and a simplified conceptualization of the PBL. In both models, PBL heights are used to generate vertical profiles of turbulence parameters and turbulent mixing is largely confined to the PBL. Hence, errors in the estimated PBL height have a strong effect on source sensitivities computed by LPDMs, and comprise a major component of model error (Gerbig

[1]For ZSF, σ_{rept} of sulphur hexafluoride (SF_6) is given by the daily standard deviation of target gas measurements. For the remaining gases, the standard deviation of all target gas measurements of the latest tank is used instead (working standard GUF-44 from 25 July 2024 to 11 February 2025).

et al., 2008). For instance, large errors can occur if the PBL height is incorrectly placed above or below the inlet height of a measurement site, h_{i}, as pollutant concentrations tend to be much lower in the free atmosphere (that is, above the PBL) (Stull, 1988). Moreover, when the measurement site is within the PBL, overestimation of the PBL height overestimates turbulent mixing and, consequently, underestimates mole fraction concentrations related to local sources.

For low to medium elevation sites, two problems arise when the PBL height is low. First, as mentioned above, it is possible that PBL height is wrongly placed above or below the inlet height, causing large errors. Second, when the PBL height is low, the air within the PBL is stably stratified, which increases the influence of vertical mixing errors and local (sub-grid scale) sources. These issues often pose a problem for using night-time and early morning observations as stable PBLs usually form during the night and break-up in the morning. These processes are challenging to capture correctly with NWP models with limited vertical resolution and simple turbulence parameterizations.

Mountain sites, such as Jungfraujoch, Switzerland (JFJ) and Monte Cimone, Italy (CMN), present special challenges for transport models. For instance, JFJ mainly receives air from the free atmosphere, but the surrounding complex topography may cause boundary layer air to be injected into the free atmosphere before reaching the site (Henne et al., 2004, 2010). These effects are difficult to simulate. In fact, at the spatial resolution of input data used by the two employed LPDMs ($\sim$10 km, see Appendix A), the Alpine topography is smoothed to the degree that it is not clear at what height to release particles in the LPDM, and the choice of release height can induce significant error (Brunner et al., 2012). Despite this, JFJ and CMN provide useful signal for constraining emissions on the European scale (Stohl et al., 2009).

4.3 Spatial and temporal aggregation

Next to the limited spatial resolution of the transport model, spatial and temporal aggregation of the state vector poses another source of uncertainty. As mentioned in Section 2.3, the inversion problem is typically resolved at a coarser spatial resolution than the transport model and over a monthly/yearly time window, which is assumed to correctly capture the temporal variability of surface fluxes. The spatial/temporal aggregation introduces an error denoted aggregation error (e.g., Engelen et al., 2002). Nevertheless, the spatial aggregation can be beneficial to the inversion problem when the measurement network is sparse and the prior information has considerable uncertainties.

4.4 Prior emissions

The prior emissions are particularly important in inversion problems with a reduced measurement network or when the emission sources are inhomogeneous in space/time. Sensitivity tests can be made to assess the effect of prior emissions on the final solution. In addition, the correct quantification of the uncertainty of the prior emissions allows us to make the best use of the prior information. However, this value is rarely provided by bottom-up compilers or is itself very uncertain. Consequently, high uncertainty values are typically assumed in the inversion problem.

5 Empa Lagrangian Regional Inversion System (ELRIS)

The Empa Lagrangian Regional Inversion System (ELRIS) follows the general framework described in Section 2 and is based on the Bayesian analytical method introduced in Section 3.1. The system is implemented in the R programming language and has been continuously developed since 2009 (Vollmer et al., 2009; Henne et al., 2016; Katharopoulos et al., 2023). In this section, we present the main modelling choices regarding the filtering of observations, discretization of the inversion grid and boundary conditions, and the construction of covariance matrices. We revisit some of the modelling features described in previous publications (Henne et al., 2016; Katharopoulos et al., 2023) and present new model developments.

5.1 Filtering of mole fraction observations

As discussed in Section 4.2, inaccurate source sensitivities would be obtained if the LPDM wrongly predicts the PBL height to be below or above the measurement inlet height. For low to medium elevation sites, this problem will mainly occur when the transport model predicts low PBL heights at the measurement site. Therefore, time instances for which the simulated PBL height is lower than 200 m a.g.l. (above ground level) or less than 50 m above the inlet height (for tall tower observations) are flagged. The respective mole fraction observations are excluded from the inversion problem.

For high elevations sites, such as Jungfraujoch and Monte Cimone, no filtering of observations is currently applied and the total number of aggregated mole fraction observations is used in the inversions. These sites are frequently above the PBL. However, during specific atmospheric conditions (summer, fair-weather) PBL air can reach up to the altitude of these measurement stations. This atmospheric condition might not be correctly captured by the models. Consequently, an additional filter for mountain site observations may be reconsidered in the future.

5.2 Inversion grid

The inner inversion grid, which encompasses the geographical area of interest, is discretized in K_{I} areas of various sizes according to the average source sensitivity. Similarly to Henne et al. (2016), finer (coarser) grid cells are defined in areas with larger (smaller) source sensitivities. The inner inversion grid is discretized in 700-1000 grid cells with this methodology.

The region outside the inner inversion grid (outer region) is divided in $K_{\mathrm{O}} = 4$ areas. The discretization follows the cardinal directions, defined at the centre of the transport model domain. The inversion grid is therefore comprised of $K = K_{\mathrm{I}} + K_{\mathrm{O}}$ grid cells.

5.3 Discretization of boundary conditions and respective prior values

Following Manning et al. (2021), the boundaries of the transport model domain are discretized in $P = 11$ boundary interfaces: between 0-3 km height, the vertical borders are discretized in 8 interfaces following the cardinal and inter-cardinal directions; between 3-8 km height, the vertical borders are discretized in 2 interfaces following the E-W direction; and above 8 km height, only a single interface

is considered, independent of direction (Figure 2.5). The mole fraction at the borders of the transport model domain (boundary conditions) are therefore defined at these 11 interfaces.

In order to capture the temporal variability of the boundary conditions, these are defined at multiple time instances T within the inversion period. When the inversion period is of the order of months, the boundary conditions are defined once a week; when the inversion period is of the order of years, they are defined once a month (e.g., $T = 12$ for a 1-year inversion). As a result, $\boldsymbol{\chi}_{\mathbf{bc}}$ is a vector of length $N = P \times T$.

The boundary conditions at all time instances with aggregated mole fraction observations, L, are linearly interpolated from these T time instances. Therefore, each row of $\mathbf{M_B}$ with index $l = 1, ..., L$ is comprised of N weighting coefficients given by the product of the baseline sensitivities of air masses released at time/location l and time interpolation factors.

The prior boundary conditions at these N points in time/space are given by a first estimate of the baseline mole fraction at MHD. MHD is located on the west coast of Ireland and the collected air samples are frequently unaffected by recent pollution events (see Figure 2.3a). As detailed in Henne et al. (2016), the Robust Estimation of Baseline Signal (REBS) method (Ruckstuhl et al., 2012) is used to estimate the baseline mole fraction by iteratively fitting a non-parametric local regression curve to the observations. The uncertainty of the fit is also estimated by the REBS method and used as prior uncertainty of the baseline elements of the state vector (see Sections 5.5 and 5.6).

5.4 Mole fraction bias correction

In order to correct for potential biases in the mole fraction measurements (for example, due to calibration offsets in the measurement devices), one bias term per site is added to the baseline mole fraction and is optimized in the inversion problem. If the measurement network is composed of S observation sites, the state vector $\mathbf{x}$ is expanded to include these S additional terms that constitute vector $\boldsymbol{\chi}_{\mathbf{s}}$. The sensitivity matrix, $\mathbf{M}$, is adapted accordingly so that Equation (4) becomes

$$\boldsymbol{\chi} = \begin{bmatrix} \mathbf{M_E} & \mathbf{M_B} & \mathbf{M_S} \end{bmatrix} \begin{bmatrix} \mathbf{e} \\ \boldsymbol{\chi}_{\mathbf{bc}} \\ \boldsymbol{\chi}_{\mathbf{s}} \end{bmatrix} = \mathbf{Mx}, \tag{12}$$

where $\mathbf{M_S}$ is a matrix composed of only zeros and ones (size $L \times S$). The elements of each row are equal to 1 at the column of the respective mole fraction measurement site and equal to 0 otherwise. The prior error covariance matrix, $\mathbf{B}$, is also expanded to include the prior uncertainty of $\boldsymbol{\chi}_{\mathbf{s}}$. This is described in Section 5.6.

5.5 Observational error covariance matrix

The diagonal elements of the observational error covariance matrix, $\sigma^2_{\mathrm{o}_l}$ $(l = 1, ..., L)$, are the squared sum of the instrument and model uncertainties. As in Henne et al. (2016), the instrument uncertainty is given by the value of repeatability, σ_{rept}, reported by the data providers (see Section 4.1). An

average value of repeatability is computed for each aggregated mole fraction measurement following the ISO 11222:2002 (ISO, 2025).

In previous works, the model uncertainty was estimated considering two contributions: a constant value, σ_{min}, and a term proportional to the prior regional mole fraction, $\chi^{\mathrm{a}}_{\mathrm{p}_l}$, with proportionality constant σ_{srr} (see Henne et al., 2016). As a result, the diagonal elements of the observational error covariance matrix (observational error variances) were computed by

$$\sigma^2_{\mathrm{o}_l} = \sigma^2_{\mathrm{rept}_l} + \sigma^2_{\mathrm{min}} + \sigma^2_{\mathrm{srr}} \left(\chi^{\mathrm{a}}_{\mathrm{p}_l}\right)^2, \tag{13}$$

where σ_{min} and σ_{srr} were determined separately for each site used in the inversion through an iterative procedure relating model/observation residuals and prior regional mole fractions.

The above approach may underestimate the model uncertainty when events characterized by high mole fraction measurements cannot be reproduced by the LPDM. This can be due to the misrepresentation of the diffusion situation (e.g., stable PBL) or the incorrect timing of frontal passages or intermittent plumes originating from dominant point-like sources. In these cases, it is beneficial to consider additional contributions to the observational uncertainty, such as the variability of the mole fraction observations, σ_{var}. For CH_4 and N_2O, σ_{var} is reported by the data providers. Similarly to σ_{rept}, an average value is computed for each aggregated mole fraction measurement. For F-gases and GC-based measurements of CH_4 and N_2O, a measure of σ_{var} is not provided and the observed standard deviation within the aggregation interval is used as a proxy. For typical aggregation intervals of 4 hours, only very few observations (2-8) are available. Therefore, we use the observations unbiased standard deviation over the same time window as an estimator of σ_{var}. If there are less than 7 observations in the aggregation interval, an extended time interval of 12 hours centered around the 4-hour time window of interest is considered instead to compute the unbiased standard deviation. If there is only one observation in this extended time interval, the variability of the respective observation is approximated by the annual median of σ_{var}. For flask measurements, there is typically a single sample every two days or once a week. In this case, variability is estimated from the observed unbiased standard deviation over the entire year. Thus, it reflects only a relative weighting between more and less polluted sites and cannot resolve temporal changes in variability. The observational error variance is therefore given by

$$\sigma^2_{\mathrm{o}_l} = \sigma^2_{\mathrm{rept}_l} + \sigma^2_{\mathrm{min}} + \sigma^2_{\mathrm{srr}} \left(\chi^{\mathrm{a}}_{\mathrm{p}_l}\right)^2 + \sigma^2_{\mathrm{var}_l}. \tag{14}$$

For F-gases only, we add the contribution of the prior baseline mole fraction uncertainty, σ_{b}, to the total model uncertainty. This term is estimated from the REBS method, introduced in Section 5.3, applied to MHD observations. The estimated REBS uncertainty is applied to all sites and time instances. The quantity $\sigma^2_{\mathrm{b}_l}$ is therefore added to Equation (14).

The off-diagonal elements of the observational error covariance matrix are computed by assuming a temporal covariance of the observational error, described by an exponential decay in time with a temporal correlation length of 0.2 days. This value is shorter than in previous studies (Henne et al., 2016), but more generally fits observed auto-correlation structures in model residuals. Even though the

temporal correlation length is expected to vary in time, a constant value is assumed in the inversion. This avoids observational error covariance matrices with complicated structures, which may result in singular matrices. No observational uncertainty correlation is considered between mole fractions from different sites.

In order to avoid over- or under-fitting of the inverse problem, we scale the observational uncertainty such that the posterior cost function follows the statistics of a Chi-squared distribution. This is achieved within the same iteration in which σ_{min} and σ_{srr} are determined, and using the Chi-squared index (Berchet et al., 2013) of the previous iteration as a scaling factor on σ_{min} and σ_{srr}. Note that in most cases σ_{min} and σ_{srr} dominate the uncertainty budget and, hence, a Chi-squared index close to 1 can be achieved within 3-4 iterations.

5.6 Prior error covariance matrix

The prior error covariance matrix, $\mathbf{B}$, comprises the uncertainty of the prior state vector as well as the temporal and spatial correlation between its elements. It is a block diagonal matrix of size $K_{\text{I}} + K_{\text{O}} + N + S$ composed of four symmetric square matrices: $\mathbf{B_I}$ (size K_{I}), $\mathbf{B_O}$ (size K_{O}), $\mathbf{B_B}$ (size N), and $\mathbf{B_S}$ (size S). They correspond to the prior error covariance matrix of, respectively, the emissions in the inner inversion grid, the emissions in the outer region, the boundary conditions, and the mole fraction bias per site. The calculation of each of these matrices is described in the following sub-sections.

5.6.1 Error covariance matrix $\mathbf{B_I}$

The calculation of $\mathbf{B_I}$ follows closely what is described in Henne et al. (2016) and Katharopoulos et al. (2023). The uncertainty of the prior emissions at each inversion grid cell is assumed proportional to the respective emissions, $\sigma_{\text{a}_i} = f e_{\text{a}_i},\ i = 1, ..., K_{\text{I}}$, where f is the proportionality factor. The uncertainty of the prior emissions squared populate the diagonal of $\mathbf{B_I}$: $b_{ii} = \sigma^2_{\text{a}_i},\ i = 1, ..., K_{\text{I}}$.

The prior emissions along the inner inversion grid are assumed to be spatially correlated. The correlation between the emissions from two grid cells is assumed to decrease exponentially with the distance between them (Henne et al., 2016). Therefore, the off-diagonal elements of $\mathbf{B_I}$ are given by

$$b_{ij} = \exp(-d_{ij}/D)\sqrt{b_{ii}}\sqrt{b_{jj}}, \quad i, j = 1, ..., K_{\text{I}}, \tag{15}$$

where d_{ij} is the distance between two grid cell centres and D is the correlation length. D is set to 100 km for gases with localized sources (such as HFC-23, SF_6 and all perfluorocarbons investigated) and to 500 km for gases with widely distributed emission sources.

The proportionality constant, f, is calculated so that the total uncertainty along the inner inversion grid is proportional to the total prior emissions,

$$\sqrt{\sum_{i,j=1}^{K_{\text{I}}} b_{ij}} = f_{\text{total}} \sum_{i=1}^{K_{\text{I}}} e_{\text{a}_i}, \tag{16}$$

where f_{total} is the proportionality factor applied to the total prior emissions. Differently from previous works, f_{total} is set to 1 for F-gases, which corresponds to a total uncertainty of 100%, and to 0.25 for CH_4 and N_2O (total uncertainty of 25%).

5.6.2 Error covariance matrix $\mathbf{B_O}$

In order to prevent a strong optimization of the emissions in the outer regions, a lower uncertainty of 20% is specified at each grid cell. Moreover, no spatial correlation is considered between the emissions. $\mathbf{B_O}$ is therefore a diagonal matrix with elements $b_{ii} = (0.2e_{\text{a}_i})^2\ ,\ i = 1, ..., K_{\text{O}}$. For simplicity, symbol b is used to denote the elements of $\mathbf{B_I}$, $\mathbf{B_O}$, $\mathbf{B_B}$, and $\mathbf{B_S}$ alike.

5.6.3 Error covariance matrix $\mathbf{B_B}$

The calculation of $\mathbf{B_B}$ follows closely the approach described in Henne et al. (2016) and Katharopoulos et al. (2023). As described in Section 5.3, the uncertainty of the prior boundary conditions is given by the REBS method (Ruckstuhl et al., 2012). The uncertainty of the MHD baseline fit is used as a proxy for the uncertainty of the boundary conditions at the P boundary interfaces and T time instances. The diagonal elements of $\mathbf{B_B}$ are therefore given by $b_{ii} = \sigma_{\text{b}}^2,\ i = 1, ..., N$.

For each border region, a temporal correlation is assumed between the T boundary conditions, following an exponential decay. The off-diagonal elements of $\mathbf{B_B}$ are therefore given by

$$b_{ij} = \exp(-\Delta t_{ij}/\tau)\sqrt{b_{ii}}\sqrt{b_{jj}}, \quad i, j = 1, ..., N, \tag{17}$$

where Δt_{ij} is the time difference between two boundary conditions and τ the temporal correlation. The latter is set to 60 days for all inversions performed.

5.6.4 Error covariance matrix $\mathbf{B_S}$

The uncertainty of the mole fraction bias per site is assumed equal to the uncertainty of the boundary conditions. Therefore, the same value computed with the REBS method is considered. No correlation is assumed between the sites. $\mathbf{B_S}$ is therefore a diagonal matrix with elements $b_{ii} = \sigma_{\text{b}}^2,\ i = 1, ..., S$.

5.7 Temporally varying emissions

As discussed in Section 2.3, in the current inversion framework, the emission fluxes are assumed constant over the inversion period. The inversion period is frequently chosen according to the expected emission flux temporal variability, but might be limited by the extent of the measurement network and the respective overall sensitivity to surface fluxes. In this context, an inversion period of 1 month is considered when simulating CH_4 and N_2O surface fluxes, while an inversion period of 1 year is chosen for fluorinated compounds.

These monthly/yearly emission fluxes are estimated from independent inversions, which make use of atmospheric observations of the respective month/year only. However, for monthly inversions, this

setup has the caveat of neglecting the correlation between emissions and atmospheric observations of a given month and the respective values of the preceding and succeeding months.

In order to resolve CH_4 and N_2O emission fluxes monthly while taking into account longer temporal correlations, we have considered temporally-varying emissions and boundary conditions in the state vector. Specifically, a longer inversion period of 3 months is employed (comprising the month of interest and the preceding and succeeding months) and the state vector is expanded to include one set of emission fluxes and boundary conditions per month. Therefore, Equation (4) takes the form

$$\boldsymbol{\chi} = \begin{bmatrix} \mathbf{M}_0 & \mathbf{M}_1 & \mathbf{M}_2 \end{bmatrix} \begin{bmatrix} \mathbf{x}_0 \\ \mathbf{x}_1 \\ \mathbf{x}_2 \end{bmatrix}, \tag{18}$$

where index 1 indicates the sensitivity matrix and state vector of the month of interest, and indexes 0 and 2 indicate the respective quantities for the preceding and succeeding months.

The covariance matrices $\mathbf{R}$ and $\mathbf{B}$ are expanded in an analogous way, which allows us to account for temporal correlations beyond the month we are interested in. In particular for $\mathbf{B_I}$, we now account for an exponentially decaying temporal correlation with a correlation time of 14 days. After optimization, we conserve the posterior distribution of the state vector $\mathbf{x}_1$ only, while $\mathbf{x}_0$ and $\mathbf{x}_2$ are discarded. The posterior covariance matrix is also divided and partly discarded in an equivalent manner.

6 Inversion Technique for Emission Modelling (InTEM)

InTEM (Inversion Technique for Emission Modelling) follows the framework laid out in Section 2; using the Bayesian analytical method in Section 3.1. The current evolution of the model has been developed in Fortran 90 since 2011 (Manning et al., 2011; Arnold et al., 2018). In this section, we discuss observation selection techniques, the creation of the inversion grid and boundary conditions, and the covariance matrices.

6.1 Filtering of mole fraction observations

As explained in Section 4.2, the height of the planetary boundary layer (PBL) is important for accurate prediction of source sensitivities with LPDMs. For sites not considered to be mountainous, the observations are filtered out when the meteorology predicts low PBL heights. This prevents observations that are biased towards local air being included. When the boundary layer is low, the atmosphere is very stable, and the air received at the station will be from very close by. The PBL lower limit is defined as 200 m when using NAME and 300 m when using FLEXPART. Some stations have specific limits, owing to local pollution sources, as seen in Table 6.1. In addition, times when the model atmosphere is very stable, characterised using the modelled vertical profile of potential temperature at the station, and times when the contribution from the 9 model grid boxes centred on the station is high are also excluded irrespective of the PBL height.

Station	Lower PBL limit [m]	Upper PBL limit [m]
Zeppelin, Norway (ZEP)	0	N/A
Jungfraujoch, Switzerland (JFJ)	900	1100
Monte Cimone, Italy (CMN)	400	600

Table 6.1: Station-specific filtering criteria.

At high-altitude sites, observations recorded when the PBL height is close to the particle release height (within 100 m) are excluded. The particle release height is the height at which the LPDM model particles are released. This does not always match the inlet height at the station in areas of complex topography.

6.2 Inversion grid

The inversion grid is split into two sections, a high-resolution grid covering the area of interest, and a coarsely resolved set of outer regions (see Figure 2.4). The inner inversion grid is initially divided into geographical regions of interest, largely following the borders of Exclusive Economic Zones (EEZs). Other undefined regions covering large areas of sea are subdivided to prevent them being too large. There are also some EEZs which are further divided based on size (e.g. France becomes North and South France), or being an area of significant interest (the UK is split into Devolved Governments: Scotland, Wales, England and Northern Ireland).

These regions are systematically subdivided during the inversion, as described in Manning et al. (2021), resulting in K_{I} grid cells of differing sizes. Unlike in ELRIS, InTEM splits these cells based on both the current posterior emissions (the number of iterations cannot exceed 16) and the overall inversion sensitivity. The coarse outer regions, of which there are $K_{\mathrm{O}} = 6$, cannot be split and are also described in Manning et al. (2021). Thus, the inversion grid consists of $K = K_{\mathrm{I}} + K_{\mathrm{O}}$ grid cells.

6.3 Discretization of boundary conditions

The InTEM boundary conditions are discretized in the manner described in Manning et al. (2021), and laid out in Section 5.3, that is, with eight interfaces along cardinal and inter-cardinal directions up to 3 km, two interfaces along the E-W direction between 3 km and 8 km, and a single interface above this.

The boundary conditions are initially calculated in the manner described in Manning et al. (2021) based on LPDM footprints. The eleven boundary values ($P = 11$) are assumed to be time invariant across the entire inversion period, as opposed to ELRIS, which defines them at multiple times T within the inversion period. Therefore, the state vector accounts for $N = P = 11$ boundary condition elements to be optimized.

6.4 Calculation of baseline mole fraction

The prior baseline mole fractions for all stations, except JFJ, CMN, and Zeppelin, Norway (ZEP), are calculated from the Mace Head baseline observations. For JFJ, CMN and ZEP the prior baseline is calculated from each station's own baseline observations. Baseline observations are those where the air arriving at the station has not passed over any regional pollution sources, and is assumed to be representative of the background hemisphere mole fraction. Mace Head is generally used for this because, as it sits on the west coast of Ireland, it frequently receives air from the Atlantic, which is assumed to have no pollution sources (recall Figure 2.3a).

An observation defined as baseline still has a degree of noise within it, for example from unexpected emissions from shipping or issues with modelling atmospheric transport or meteorology. To deal with these events, a daily baseline value is calculated as the mean of all baseline observations in that day. These daily baseline values are further evaluated by fitting a fourth order polynomial through them in an 180-day window. The uncertainty of the baseline is the root mean square error (RMSE) of this fit. The window moves in one day steps, so each day is fitted 180 times, and has 180 estimated baseline values. The final daily baseline value for a day is estimated as the average of the 31 values when the centre of the 180-day window is within 15 days of the current day. The baseline uncertainty, σ_{b}, for this day is calculated by taking the mean of the 31 RMSE values for these estimates.

At each aggregation interval in an inversion period, the ratio of air coming from each of the eleven boundary interfaces (baseline sensitivities) is R_{lp}. These ratios are multiplied by the prior baseline mole fraction at that time, $\chi^{\mathrm{a}}_{\mathrm{b}_l}$, and $P = 11$ baseline scaling factors, f_p. Thus, the baseline at each station/time, l, is calculated as

$$\chi_{\mathrm{b}_l} = \chi^{\mathrm{a}}_{\mathrm{b}_l} \sum_{p=1}^{P} R_{lp} f_p, \quad l = 1, ..., L, \tag{19}$$

where R_{lp} is different at each location/time l, but always sums over p to 1. If all $f_p = 1$, the baseline at all stations are unchanged. For each station there is additionally a solved-for station bias, which is applied as a positive or negative systematic change. The eleven prior f_p are estimated as described in Manning et al. (2021).

6.5 Observational error covariance matrix

6.5.1 Repeatability and variability of observed mole fractions

InTEM uses an aggregation interval of 4 hours, see Section 2.2. Each observation has a standard deviation associated with it. These are processed in InTEM into an uncertainty for each aggregation interval formed of two parts

$$\sigma^2 = \sigma^2_{\mathrm{rept}} + \sigma^2_{\mathrm{var}}. \tag{20}$$

The observational repeatability, σ_{rept}, is the average of the observational precision in the observation window, as obtained from the data provider. For CH_4 and N_2O the data are often provided as 1-minute

or 1-hour averages (data provider's time window), with an associated standard deviation and number of observations. For other observations, the data provided are single values. The process of calculating σ_{var} depends on the number of observations present within the aggregation interval. When there are at least six observations available, the following equation is used

$$\sigma_{\text{var}}^2 = \frac{\sum_i n_i(s_i^2 + m_i^2)}{N} - \mu^2, \tag{21}$$

where,

- n_i is the number of observations in the data provider's time window,
- m_i is the mean of the observations in the data provider's time window,
- s_i is the standard deviation of the observations in the data provider's time window,
- $N = \sum_i n_i$ is the total number of observations in the aggregation interval,
- μ is the mean of the observations in the aggregation interval.

If there are fewer than six observations in the aggregation interval, the two adjacent aggregation intervals are considered as well. If there are more than three observations across this extended interval, the same process as above is used. If there are only two observations, the difference between them is taken as the variance. In the case that only one observation is present in the extended interval, the variance is set to an average, either the average over the year if there are more than fifty calculated variances, or the average observed at Tacolneston, UK (TAC), for this gas if there are insufficient data.

6.5.2 Model uncertainty

Through analysis of the CH_4 measurements at observation sites in the UK DECC network with two or more inlet heights, it is clear that no single meteorological variable describes the model uncertainty well (Manning et al., 2017). It is assumed that the level of model uncertainty is directly linked to the difference in the observations measured at different heights within each aggregation interval. When the difference is small, it implies the atmosphere is well mixed and can be well modelled, conversely when the difference is large, it implies the atmosphere has strong vertical gradients that are unlikely to be well modelled. The best descriptor of the difference between the two/three heights was found to be the size of the pollution event at any given time. The average linear gradient across all years at all stations with multiple inlet heights was found to be 0.1 of the size of the pollution event. In addition, a minimum uncertainty is applied, defined as the median pollution event over the year. This is used to define the model uncertainty, σ_{mod}, that is applied to each selected aggregation interval.

6.5.3 Observational uncertainty

The total uncertainty applied to observations is the $\mathbf{R}$ matrix (see Equation (9)). In InTEM, this is a symmetric matrix, with the main diagonal populated with variances

$$\sigma_{\mathrm{o}_l}^2 = (\sigma_{\mathrm{rept}})_l^2 + (\sigma_{\mathrm{var}})_l^2 + (\sigma_{\mathrm{mod}})_l^2 + (\sigma_{\mathrm{b}})_l^2, \quad l = 1, ..., L \tag{22}$$

where σ_{b} is the baseline uncertainty; and σ_{rept}, σ_{var} and σ_{mod} are defined as before.

The off-diagonals of $\mathbf{R}$ are populated with cross-correlation terms, providing time and spatial correlation. Each aggregation interval is assumed to be correlated to those on either side of it, so an error in one is likely to be felt in both preceding and following periods. This correlation is assumed to exponentially decay with a time correlation of 12 hours. In the same vein, observation stations that are close to one another cannot be assumed to provide entirely independent information. Thus, an exponentially decaying, geographical distance correlation of 100 km is also applied. So the $\mathbf{R}$ off-diagonal elements, r_{ij}, are populated as such:

$$r_{ij} = \sigma_{\mathrm{o}_i}\sigma_{\mathrm{o}_j} \exp\left(\frac{-\Delta t_{ij}}{12}\right) \exp\left(\frac{-d_{ij}}{100}\right), \tag{23}$$

where i and j are the row and column respectively, relating to two different observations; Δt is the time difference in hours between the observations and d is the horizontal distance in km between the observation stations.

6.6 Prior error covariance matrix

In InTEM, the prior error covariance matrix $\mathbf{B}$ is assumed to have no spatial covariance, so there are no off-diagonal elements. It comprises 4 block diagonal matrices associated with the inner inversion grid, the baseline, the outer regions, and the bias terms. The diagonal elements for the inner inversion grid are defined by species and lead to overall prior uncertainties in NW Europe of between 10-200%. The baseline uncertainty is discussed above. The bias uncertainties are species dependent. The prior uncertainties prescribed for the outer regions are set to be 100%.

7 Regional Hierarchical Inverse Modelling Environment (RHIME)

We now describe the specifics of the RHIME inversion set-up. The hierarchical Bayesian model used by RHIME was introduced by Ganesan et al. (2014). The current version of RHIME is simplified in some ways, omitting hyper-parameters on the prior uncertainties, but with a more sophisticated model of observational uncertainty. The source code from RHIME is available on GitHub[2] and the most recent release is tagged with a DOI[3].

7.1 Resampling of observations and source sensitivities

Observations are resampled over a 4-hour aggregation interval, and source sensitivities from the transport model are resampled to match. The method of resampling observations depends on what quan-

[2]https://github.com/openghg/openghg_inversions
[3]https://doi.org/10.5281/zenodo.10650595

tities are present in the data. For high-frequency in situ measurements, available for CH_4 and N_2O, the mole fraction is resampled as a mean weighted by the number of observations associated with each time point, and the variability of the mole fraction is resampled using these weights as well. This method produces the same values that would result if the raw data was resampled to our chosen frequency (for instance, 4 hours). The formulas used by RHIME are the same as Equation (21).

For fluorinated gases, we resample the mole fraction by taking the mean and use the standard deviation of the mole fraction as a measurement of variability. Fluorinated gas observations have a measurement of repeatability, which is resampled as if it was the standard deviation of a sequence of uncorrelated variables, using the formula for the variance of a mean of uncorrelated variables: if $\sigma_{\text{rept},1}, \ldots, \sigma_{\text{rept},n}$ are the values of repeatability in a single aggregation interval, they are resampled as

$$\sigma_{\text{rept}}^2 = \frac{1}{n^2} \sum_{i=1}^{n} \sigma_{\text{rept},i}^2. \tag{24}$$

7.2 Filtering of mole fraction observations

Observations at a site are discarded when either

1. the planetary boundary layer is below 200 m, or
2. the planetary boundary layer is within 50 m of the inlet height.

As explained in Section 4.2, we consider the transport model to be unreliable under these conditions. No filtering is applied to the mountain sites Jungfraujoch, Monte Cimone, and Zugspitze.

7.3 Inversion grid

The transport model domain is aggregated into groups of grid cells, called *basis regions* (or *basis functions*) so that:

1. the product of the average source sensitivity (over all sites) and the prior value of the emissions flux, summed over each basis region, is bounded above by a certain threshold, and
2. optionally, that each basis region contains only land or only sea grid cells.

The threshold in condition 1 is optimized to produce a target number of basis regions. This aggregation is only applied to the inner inversion grid, and the outer grid consists of six fixed basis regions, as used by InTEM (see Figure 2.4).

7.4 Calculation of regional mole fraction

We do not solve for the posterior distributions of the flux and boundary conditions directly. Rather, we solve for a scaling of the prior flux and boundary conditions.

Suppose $\mathbf{M}_0$ is the source sensitivity matrix at the transport model resolution. Let L and K_0 denote the number of rows and columns of $\mathbf{M}_0$, respectively. Let $\mathbf{e}_{0,\mathrm{a}}$ denote the prior value of the emissions flux at the transport model resolution.

To get the source sensitivity matrix $\mathbf{M_E}$ on the K basis regions, first we multiply the columns of $\mathbf{M}_0$ by $\mathbf{e}_{0,\mathrm{a}}$. Recall that each column of $\mathbf{M}_0$ corresponds to sensitivities for a grid cell at the transport model resolution; thus the columns of this product are the contributions to the simulated mole fractions for a single grid cell. Next, we group the columns of this product by the basis region they belong to, and then sum over each group. This reduces the number of columns to K, the resulting matrix is $\mathbf{M_E}$. See Appendix C for further details.

With this definition of $\mathbf{M_E}$, the regional mole fractions satisfy

$$\boldsymbol{\chi}_\mathbf{p} = \mathbf{M_E}\mathbf{1}, \tag{25}$$

where $\mathbf{1} = (1, \ldots, 1)^T$ is the vector of 1's of length K. This means that the vector of 1's plays the role of the prior value of $\mathbf{e}$ for RHIME, and information about the flux is incorporated into the sensitivity matrix $\mathbf{M_E}$. This is advantageous if the prior flux is accurate, but it also means that RHIME cannot remove any inaccuracies in the spatial variability of prior emissions within basis regions.

Further, Equation (25) means that the prior for $\mathbf{e}$ (which is part of the prior for the state vector $\mathbf{x}$) should have a central value of 1 to avoid introducing a bias. (More specifically, we choose the mean to be 1, to avoid a bias in our country totals[4].)

7.5 Discretization of boundary conditions

RHIME uses one boundary interface for each cardinal direction (NESW), so P equals 4. For all inversions in the 2025 Draft Annexes to NID, separate boundary condition scaling factors are solved for each month, so the number T of time periods solved for is 1 for monthly inversions and 12 for yearly inversions.

7.6 Calculation of baseline mole fraction

The baseline mole fraction $\boldsymbol{\chi}_\mathbf{b}$ is computed by taking a weighted average of boundary condition mole fractions, where the weights are the proportion of LPDM particles that exited through the corresponding boundary interface. To describe this formally, let I_t denote the set of measurement times/locations corresponding to month t of the inversion, and define a $L \times T$ "dummy" matrix by

$$D_{lt} = \begin{cases} 1 & l \in I_t \\ 0 & \text{otherwise} \end{cases} \tag{26}$$

[4]Since the components of RHIME's flux prior are independent, the Central Limit Theorem implies that the total flux in countries that contain many basis regions will be approximately normal; thus the mean, mode, and median of the country totals will be approximately equal, and the mean of the country total will be the sum of the means of the flux totals for the basis regions within that country. Hence any choice of central value for country totals in this case will be influenced by biases in the mean of the flux

Let W_p denote the grid cells contained on boundary interface p and let R_{lw} denote the fraction of air reaching the grid cell w on a boundary interface at time/location $l = 1, ..., L$, so that for all l,

$$\sum_{p=1}^{P} \sum_{w \in W_p} R_{lw} = 1. \tag{27}$$

Recall that χ_{b_l} is the lth component of $\boldsymbol{\chi}_{\mathbf{b}}$. Let $\chi^{\mathrm{a}}_{\mathrm{b}_w}$ denote the prior value of the boundary conditions at a grid cell w on one of the boundary interfaces. Let H_{pl} denote the fraction-weighted prior value of the boundary conditions for border region p, and let f_{pt} be a scaling factor for border region p and time t.

Then,

$$H_{pl} = \sum_{w \in W_p} R_{lw} \chi^{\mathrm{a}}_{\mathrm{b}_w}, \tag{28}$$

and

$$\chi_{\mathrm{b}_l} = \sum_{p=1}^{P} \sum_{t=1}^{T} H_{pl} D_{lt} f_{pt}$$

In matrix notation (matching equation (3)), this is

$$\boldsymbol{\chi}_{\mathbf{b}} = \mathbf{M}_{\mathbf{B}} \boldsymbol{\chi}_{\mathbf{bc}}, \tag{29}$$

where (before flattening the indices p and t)

$$(M_B)_{lpt} = H_{pl} D_{lt} \tag{30}$$

and component pt of $\boldsymbol{\chi}_{\mathbf{bc}}$ is f_{pt}. Note that because D_{lt} is a binary matrix, there is no interpolation between boundary conditions across different values of t.

7.7 Prior boundary conditions

For methane (Bergamaschi et al., 2013) and nitrous oxide (Thompson et al., 2014), the prior value of the boundary conditions are computed using the CAMS global inversion-optimised greenhouse gas fluxes (CAMS) by taking slices of their 3D mole fraction fields along the boundaries of the transport model domain. For 2023 and 2024, CAMS data was not available when inversions were made. For those years, the boundary conditions of year n are taken as the boundary conditions of year $n-1$ with an offset added (derived as the mean of the boundary conditions of year $n-1$ minus the mean of the boundary conditions of year $n-2$).

For F-gases, CAMS global fluxes are unavailable, so we use "uniform" prior boundary conditions, where the mole fractions for all boundary curtains are set to a single value. The value used is typically calculated as a mean of observed values at sites where meteorological conditions suggest the air measured has not been subject to recent pollution events. For inversions targeting NW Europe, we calculate the prior boundary condition mole fraction as the monthly mean of observations at Mace Head when the wind is between 180 and 300 degrees, when air is arriving from over the Atlantic.

7.8 Mole fraction bias correction

RHIME has an option for adding a scalar bias for each station, which is solved for over the entire inversion period. This bias can account for small instrumental differences between measurement sites. Recent N_2O inversions using RHIME (Saboya et al., 2024) included a bias, however a bias is not used by default. The SF_6 inversions performed by RHIME for the 2025 Draft Annexes to NID used a bias term due to systematic errors in some of the observations.

7.9 Observational error specification

RHIME uses a hierarchical Bayesian model to help calibrate uncertainties using the data, rather than expert judgement. However, this technique is not a magic bullet, and modelling uncertainties is still very difficult. Observational uncertainty is particularly influential; the balance between observational and prior uncertainty affects model flexibility and bias (generally, less observational uncertainty than prior uncertainty will make the model more flexible, risking overfitting). This is further complicated by the extremely heteroscedastic nature of the observational error: as noted in Section 6.5.2 the model error appears to scale with pollution event size, meaning the uncertainty during large pollution events can be orders of magnitude greater than at baseline conditions.

RHIME uses a likelihood based on a Gaussian distribution whose (diagonal) covariance matrix $\mathbf{R}$ depends on a hyper-parameter σ:

$$\rho(\boldsymbol{\chi}_\mathbf{o} \mid \mathbf{x}, \sigma) = \frac{1}{\sqrt{(2\pi)^L |\det(\mathbf{R}(\sigma))|}} \exp\left(-\frac{1}{2}(\boldsymbol{\chi}_\mathbf{o} - \mathbf{M}\mathbf{x})^T \mathbf{R}(\sigma)^{-1} (\boldsymbol{\chi}_\mathbf{o} - \mathbf{M}\mathbf{x})\right) \tag{31}$$

The hyper-parameter[5] σ has a dimension for the measurement site and a temporal dimension, with different values optimised for each month in the inversion period. For example, for an inversion with four sites and a one year inversion period, if the "sigma frequency" is monthly, then σ will have 48 components, which are forward filled in time to align with the observed and simulated mole fraction vectors.

The purpose of σ is to scale a factor R_{PE} that estimates the size of "pollution events": we hypothesize that the transport model is less accurate when the regional mole fraction is large (meaning that the observed mole fraction is much larger than the baseline mole fraction), and so we increase the model error at these times. The hyper-parameter σ represents our uncertainty in the relationship between pollution event size and model error, and, in this work, is given by a hyper-prior that is uniform from 0.1 to 1.

Pollution events are measured as a power of the absolute difference between the observations and the simulated baseline:

$$R_{PE} = (\boldsymbol{\chi}_\mathbf{o} - \boldsymbol{\chi}_\mathbf{b})^p, \tag{32}$$

where $p < 2$. The pollution events vector R_{PE} has length L. In this work, we set $p = 1.99$, though it could be given a prior and treated as a hyper-parameter. We will discuss the power p in Appendix D.

[5]Some definitions of "hierarchical" require that hyper-parameters do not explicitly appear in the likelihood.

At times when pollution events are small, we still believe there is some model error, and we use a fixed minimum threshold σ_{min} (or *minimum model error*) to represent this. The minimum model error σ_{min} has a separate value for each site, and is based on percentiles of the observations: for each month in the inversion period, the 5th percentile of $\boldsymbol{\chi}_{\mathbf{o}}$ is subtracted from the median of $\boldsymbol{\chi}_{\mathbf{o}}$, and the mean of these differences are used for σ_{min}.

Instrument error, σ_{rept}, and the standard deviation of the observations over the resampling period (variability), σ_{var}, are added to the model error, giving the complete expression for the observational error used by RHIME[6]:

$$\mathbf{R}(\sigma) = \text{diag}(\max(\sigma_{\text{rept}}^2 + \sigma_{\text{var}}^2 + \sigma^2 R_{PE}, \sigma_{\text{min}}^2)). \tag{33}$$

7.10 Prior distributions for flux and boundary conditions scaling factors

For the flux scaling factors, we need a prior distribution that:

- only takes non-negative values,
- has a mean of 1,
- can have a specified variance, given the previous constraints.

These criteria are satisfied by the log-normal and gamma distributions, and are approximately satisfied by a truncated normal distribution with (non-truncated) mean of 1, small standard deviation, and a lower cut-off at 0 (the truncation increases the mean beyond the value set for the non-truncated normal). Because we use scaling factors and priors with a mean of 1, the standard deviation of these priors represent uncertainty as a proportion of the mean.

In this work, RHIME is used with a log-normal distribution, with a standard deviation of 8 (800% uncertainty) for the prior of the flux scaling factors, and a truncated normal distribution with small standard deviation for the prior of the boundary conditions scaling factor. In this work, the flux and boundary conditions scaling factors have no spatial or temporal correlation.

A variable is log-normally distributed if its logarithm is normally distributed. In one dimension, the PDF for a log-normally distributed variable t is

$$\rho(t) = \frac{1}{t\sigma\sqrt{2\pi}} \exp\left(-\frac{(\log(t) - \mu)^2}{2\sigma^2}\right). \tag{34}$$

It is important to note that μ and σ are the mean and standard deviation of $\log t$, not of t. However, it is possible to solve algebraically for values of μ and σ so that t has a specified mean and standard deviation. For instance, $\mu = -2.087$ and $\sigma = 2.043$ yields a log-normal variable with mean approximately equal to 1 and standard deviation approximately equal to 8.

[6]The instrument error, σ_{rept}, and variability, σ_{var}, should be added to the minimum model error σ_{min} as well, but due to an oversight in the code for RHIME, it was not; Equation (33) is an accurate description of the model used in this work.

8 Inversion settings

This section includes summary tables with the inversion settings used in the 2025 Draft Annexes to the NID produced during the PARIS project.

Table 8.1: Common LPDM settings used in NAME and FLEXPART. Refer to Appendix A for further details.

LPDM domain	-97.9°to 39.7°E, 10.7°to 79.3°N
LPDM resolution	0.352°E, 0.234°N
Time interval between LPDM simulations	1 hour
Number of released air parcels	20000 parcels/hour
Duration of LPDM backwards trajectory	30 days
Surface layer height	40 m

Table 8.2: Common inversion settings.

Aggregation interval	4 hours
Country masks	Exclusive Economic Zones (EEZ)

Table 8.3: Common inversion settings per species.

	CH_4	N_2O	F-gases
Inversion period	1 month	1 month	1 year
Prior emissions	EDGAR(1)+WetCHARTs(2)	EDGAR(1)	EDGAR/Uniform per country(3)

(1) Emissions Database for Global Atmospheric Research (Crippa et al., 2023).

(2) Global Wetland Methane Emissions and Uncertainty (Bloom et al., 2021).

(3) The first entry refers to HFC-125, HFC-134a, HFC-143a and HFC-32, and the second to all remaining gases. For the second group, 2019 EDGAR values are used in the outer inversion grid.

Table 8.4: Measurement stations used in the inversions.

Station code	Location	CH_4	N_2O	SF_6	F-gases (except SF_6)
BIR	Birkenes Observatory, Norway	×		×	×
BRM	Beromunster, Swizterland	×	×		
BSD	Bilsdale, UK	×	×	×	
CBW	Cabauw Tower, Netherlands	×	×	×	×
CGR	Capo Granitola station, Italy				×
CMN	Monte Cimone, Italy	×	×	×	×

Continued on following page

Table 8.4, continued.

Station code	Location	CH_4	N_2O	SF_6	F-gases (except SF_6)
GAT	Gartow, Germany	×	×	×	
HEI	Heidelberg, Germany	×	×		
HEL	Helgoland, Germany	×	×		
HFD	Heathfield, UK	×	×	×	
HPB	Hohenpeissenberg, Germany	×	×	×	
HTM	Hyltemossa, Sweden	×		×	
HUN	Hegyhátsál, Hungary	×	×	×	×
JFJ	Jungfraujoch, Switzerland	×	×	×	×
KIT	Karlsruhe, Germany	×	×	×	
KRE	Kresin u Pacova, Czech Republic	×	×	×	
LIN	Lindenberg, Germany	×	×	×	
LMP	Lampedusa, Italy	×			
LUT	Lutjewad, Netherlands	×	×		
MHD	Mace Head, Ireland	×	×	×	×
MLH	Malin Head, Ireland	×			
NOR	Norunda, Sweden	×		×	
OPE	Observatoire Perenne de l'Environnement, France	×	×	×	
OXK	Ochsenkopf, Germany	×	×	×	
PAL	Pallas, Finland	×	×	×	
PUY	Puy de Dome, France	×	×		
RGL	Ridge Hill, UK	×	×	×	
ROC	Roc'h Trédudon, France	×			
SAC	Saclay, France	×	×	×	
SIS	Shetland Islands, UK	×			
SMR	Hyytiala, Finland	×			
SSL	Schauinsland, Germany	×	×		
STE	Steinkimmen, Germany	×	×	×	
TAC	Tacolneston Tower, UK	×	×	×	×
TOB	Taunus, Germany			×	×
TOH	Torfhaus, Germany	×	×		
TRN	Trainou, France	×	×	×	
TTA	Angus Tower, UK	×			
UTO	Uto, Finland	×			
WAO	Weybourne, UK	×	×		
WES	Westerland, Germany	×			
ZEP	Ny-Alesund, Svalbard, Norway and Sweden	×		×	×
ZSF	Zugspitze Schneefernerhaus, Germany	×	×	×	×
	Total number of stations	44	29	26	11

Table 8.5: Summary of ELRIS-specific settings.

Filtering of observations	
Filtering criteria	(PBLH < 200 m a.g.l.) or (PBLH < $h_i + 50$)
Non-filtered sites	Mountain sites (BRM, BSD, CMN, HPB, JFJ, OXK, PAL, SSL, TOB[(1)], TOH, TTA, ZEP, ZSF, PUY, ROC, PRS)
[(1)] Filtering omitted from TOB observations when optimizing all F-gas emissions except SF_6.	
Discretization	
Number of cells in inner inversion grid (IIG), K_I	700 F-gases, 1000 $CH_4$and N_2O(target value)
Number of cells in outer inversion grid (OIG), K_O	4
Number of border regions, P	11
Temporal discretization of BC, T	
- yearly inversions	12 (once a month)
- monthly inversions	4 or 5 (once a week)
Prior state vector	
Prior emissions	Species specific (see Table 8.3)
Prior BC	From REBS method based on MHD observations
Prior bias per site	0 ppt
Prior covariance matrix	
Total uncertainty of prior emissions (IIG)	100 % for F-gases, 25 % for $CH_4$and N_2O
Prior uncertainty of prior emissions per cell (OIG)	20 %
Prior uncertainty of BC	From REBS method based on MHD observations
Prior uncertainty of bias per site	From REBS method based on MHD observations
Spatial correlation of prior emissions (IIG)	
- HFC-23, SF_6 and all PFCs	100 km
- All other species	500 km
Temporal correlation of prior emissions (IIG)	
- When solving temporally varying emissions	14 days
Temporal correlation of BC	60 days
Observational covariance matrix	
Temporal correlation of observations	0.2 days

Table 8.6: Summary of InTEM-specific settings.

Filtering of observations	
Filtering criteria	(PBLH $< X$ m a.g.l.) or (Potential Temperature Gradient > 1.5) or (Local Concentration > 20) X = 200 m (NAME) and X=300 m (FLEXPART)
Mountain sites	($h_\mathrm{i} - 100 <$ PBLH $< h_\mathrm{i} + 100$)
Discretization	
Number of gridding iterations	up to 16
Cell splitting concentration limit	20
Events at concentration limit required	32
Number of cells in outer inversion grid (OIG), K_O	6
Number of border regions, P	11
Temporal discretization of BC, T	
- yearly inversions	1 (once a year)
- monthly inversions	1 (once a month)
Prior state vector	
Prior emissions	Gas specific (see Table 8.3)
Prior BC	based on MHD and RPB[(1)] observations
Prior bias per site	0 ppt
[(1)] Ragged Point Barbados	
Prior covariance matrix	
Total uncertainty of prior emissions	Gas dependent
Prior uncertainty of BC	Gas and direction dependent
Prior uncertainty of bias per site	Gas dependent
Observational covariance matrix	
Temporal correlation of observations	0.5 days
Spatial correlation of observations	100 km

Table 8.7: Summary of RHIME-specific settings.

Filtering of observations	
Filtering criteria	(PBLH $<$ 200 m a.s.l.) or (PBLH $< h_{\mathrm{i}} + 50$)
Non-filtered sites	Mountain sites (CMN, JFJ, PUY[(1)], ZSF)
[(1)] Filtering omitted from PUY observations when optimizing CH_4 emissions.	
Discretization	
Number of cells in inner inversion grid (IIG), K_{I}	250 (target value)
Number of cells in outer inversion grid (OIG), K_{O}	6
Number of border regions, P	4
Temporal discretization of BC, T	
- yearly inversions	12 (once a month)
- monthly inversions	1 (once a month)
Prior state vector	
Prior emissions	Species specific (see Table 8.3)
Prior BC	
- CH_4 and N_2O	Derived from CAMS global mole fraction field.
- F-gases	Mean of MHD observations when air is from N. Atlantic.
Prior bias per site	0 ppt (bias only for SF_6)
Prior distributions	
Total uncertainty of prior emissions	800%
Flux prior distribution	Log normal with mean 1 and standard deviation 8
Prior uncertainty of BC	$\approx 10\%$
BC prior distribution	Normal distribution with mean 1 and standard deviation 0.1, truncated at 0.
Prior uncertainty of bias per site	1 ppt (SF_6 only)
Observational uncertainty	
Pollution event scaling distribution	uniform on $[0.1, 1]$

References

An, M., Prinn, R. G., Western, L. M., Yao, B., Zhao, X., Kim, J., Mühle, J., Chi, W., Harth, C. M., Hu, J., Ganesan, A. L., and Rigby, M. Substantial increase in perfluorocarbons CF4 (PFC-14) and c2f6 (PFC-116) emissions in china. 121(30):e2400168121, 2024a. doi: 10.1073/pnas.2400168121.

An, M., Prinn, R. G., Western, L. M., Zhao, X., Yao, B., Hu, J., Ganesan, A. L., Mühle, J., Weiss, R. F., Krummel, P. B., O'Doherty, S., Young, D., and Rigby, M. Sustained growth of sulfur hexafluoride emissions in china inferred from atmospheric observations. 15(1):1997, 2024b. doi: 10.1038/s41467-024-46084-3.

Arnold, T., Manning, A. J., Kim, J., Li, S., Webster, H., Thomson, D., Mühle, J., Weiss, R. F., Park, S., and O'Doherty, S. Inverse modelling of CF_4 and NF_3 emissions in East Asia. *Atmospheric Chemistry and Physics*, 18(18):13305–13320, 2018. doi: 10.5194/acp-18-13305-2018. URL `https://acp.copernicus.org/articles/18/13305/2018/`.

Berchet, A., Pison, I., Chevallier, F., Bousquet, P., Conil, S., Geever, M., Laurila, T., Lavrič, J., Lopez, M., Moncrieff, J., Necki, J., Ramonet, M., Schmidt, M., Steinbacher, M., and Tarniewicz, J. Towards better error statistics for atmospheric inversions of methane surface fluxes. *Atmospheric Chemistry and Physics*, 13(14): 7115–7132, 2013. doi: 10.5194/acp-13-7115-2013.

Bergamaschi, P., Houweling, S., Segers, A., Krol, M., Frankenberg, C., Scheepmaker, R. A., Dlugokencky, E., Wofsy, S. C., Kort, E. A., Sweeney, C., Schuck, T., Brenninkmeijer, C., Chen, H., Beck, V., and Gerbig, C. Atmospheric ch4 in the first decade of the 21st century: Inverse modeling analysis using sciamachy satellite retrievals and noaa surface measurements. *Journal of Geophysical Research: Atmospheres*, 118(13): 7350–7369, 2013.

Bingham, E., Chen, J. P., Jankowiak, M., Obermeyer, F., Pradhan, N., Karaletsos, T., Singh, R., Szerlip, P. A., Horsfall, P., and Goodman, N. D. Pyro: Deep universal probabilistic programming. *J. Mach. Learn. Res.*, 20:28:1–28:6, 2019.

Bloom, A., Bowman, K., Lee, M., Turner, A., Schroeder, R., Worden, J., Weidner, R., McDonald, K., and Jacob, D. Cms: Global 0.5-deg wetland methane emissions and uncertainty (wetcharts v1.3.1). Technical report, ORNL DAAC, Oak Ridge, Tennessee, USA, 2021.

Brasseur, G. P. and Jacob, D. J. Inverse Modeling for Atmospheric Chemistry. In *Modeling of Atmospheric Chemistry*, pages 487–537. Cambridge University Press, Cambridge, 2017. 9781107146969.

Brunner, D., Henne, S., Keller, C. A., Vollmer, M. K., Reimann, S., and Buchmann, B. *Estimating European Halocarbon Emissions Using Lagrangian Backward Transport Modeling and in Situ Measurements at the Jungfraujoch High-Alpine Site*, chapter 18, pages 207–222. American Geophysical Union (AGU), 2012.

Brunner, D., Arnold, T., Henne, S., Manning, A., Thompson, R. L., Maione, M., O'Doherty, S., and Reimann, S. Comparison of four inverse modelling systems applied to the estimation of HFC-125, HFC-134a, and SF_6 emissions over Europe. *Atmospheric Chemistry and Physics*, 17(17):10651–10674, 2017. doi: 10.5194/acp-17-10651-2017. URL `https://acp.copernicus.org/articles/17/10651/2017/acp-17-10651-2017.html`.

CAMS. Copernicus atmosphere monitoring service (2020): Cams global inversion-optimised greenhouse gas fluxes and concentrations. Copernicus Atmosphere Monitoring Service (CAMS) Atmosphere Data Store.

Crippa, M., Guizzardi, D., Pagani, F., Banja, M., Muntean, M., Schaaf E.and Becker, W., Monforti-Ferrario, F., Quadrelli, R., Risquez Martin, A., Taghavi-Moharamli, P., Köykkä, J., Grassi, G., Rossi, S., Brandao De Melo, J., Oom, D., Branco, A., San-Miguel, J., and Vignati, E. Ghg emissions of all world countries. *Publications Office of the European Union*, JRC134504, 2023. doi: 10.2760/953322.

Duane, S., Kennedy, A., Pendleton, B. J., and Roweth, D. Hybrid monte carlo. *Physics Letters B*, 195(2): 216–222, 1987.

Engelen, R. J., Denning, A. S., and Gurney, K. R. On error estimation in atmospheric CO2 inversions. *Journal of Geophysical Research: Atmospheres*, 107:ACL 10–1–ACL 10–13, 2002. doi: 10.1029/2002JD002195.

FOEN. Switzerland's Greenhouse Gas Inventory 1990–2023: National Inventory Document and reporting tables (CRT), 2025. URL `https://unfccc.int/documents/646407`.

France, J. L., Lunt, M. F., Andrade, M., Moreno, I., Ganesan, A. L., Lachlan-Cope, T., Fisher, R. E., Lowry, D., Parker, R. J., Nisbet, E. G., and Jones, A. E. Very large fluxes of methane measured above bolivian seasonal wetlands. 119(32):e2206345119, 2022. doi: 10.1073/pnas.2206345119.

Fraser, P. J., Dunse, B. L., Krummel, P. B., Steele, L. P., Derek, N., Mitrevski, B., Allison, C. E., Loh, Z., Manning, A. J., Redington, A., and Rigby, M. Australian chlorofluorocarbon (CFC) emissions: 1960–2017. 17(8):525–544, 2020. doi: 10.1071/EN19322.

Ganesan, A. L., Rigby, M., Zammit-Mangion, A., Manning, A. J., Prinn, R. G., Fraser, P. J., Harth, C. M., Kim, K. R., Krummel, P. B., Li, S., Mühle, J., O'Doherty, S. J., Park, S., Salameh, P. K., Steele, L. P., and Weiss, R. F. Characterization of uncertainties in atmospheric trace gas inversions using hierarchical Bayesian methods. *Atmospheric Chemistry and Physics*, 14(8):3855–3864, 2014. doi: 10.5194/acp-14-3855-2014. URL `http://www.atmos-chem-phys.net/14/3855/2014/`.

Ganesan, A. L., Manning, A. J., Grant, A., Young, D., Oram, D. E., Sturges, W. T., Moncrieff, J. B., and O'Doherty, S. Quantifying methane and nitrous oxide emissions from the UK and Ireland using a national-scale monitoring network. *Atmos. Chem. Phys.*, 15(11):6393–6406, 2015. doi: 10.5194/acp-15-6393-2015. URL `https://www.atmos-chem-phys.net/15/6393/2015/`.

Ganesan, A. L., Rigby, M., Lunt, M. F., Parker, R. J., Boesch, H., Goulding, N., Umezawa, T., Zahn, A., Chatterjee, A., Prinn, R. G., Tiwari, Y. K., van der Schoot, M., and Krummel, P. B. Atmospheric observations show accurate reporting and little growth in india's methane emissions. 8(1):836, 2017. doi: 10.1038/s41467-017-00994-7.

Gelman, A., Carlin, J., Stern, H., Dunson, D., Vehtari, A., and Rubin, D. *Bayesian Data Analysis*. Chapman and Hall/CRC, 3rd ed. edition, 2013.

Gerbig, C., Körner, S., and Lin, J. C. Vertical mixing in atmospheric tracer transport models: error characterization and propagation. *Atmospheric Chemistry and Physics*, 8(3):591–602, 2008.

Heiskanen, J., Brümmer, C., Buchmann, N., Calfapietra, C., Chen, H., Gielen, B., Gkritzalis, T., Hammer, S., Hartman, S., Herbst, M., Janssens, I. A., Jordan, A., Juurola, E., Karstens, U., Kasurinen, V., Kruijt, B., Lankreijer, H., Levin, I., Linderson, M.-L., Loustau, D., Merbold, L., Myhre, C. L., Papale, D., Pavelka,

M., Pilegaard, K., Ramonet, M., Rebmann, C., Rinne, J., Rivier, L., Saltikoff, E., Sanders, R., Steinbacher, M., Steinhoff, T., Watson, A., Vermeulen, A. T., Vesala, T., Vítková, G., and Kutsch, W. The Integrated Carbon Observation System in Europe. *Bulletin of the American Meteorological Society*, 103(3):E855–E872, 2022. doi: 10.1175/BAMS-D-19-0364.1. URL `https://journals.ametsoc.org/view/journals/bams/103/3/BAMS-D-19-0364.1.xml`.

Henne, S., Furger, M., Nyeki, S., Steinbacher, M., Neininger, B., de Wekker, S. F. J., Dommen, J., Spichtinger, N., Stohl, A., and Prévôt, A. S. H. Quantification of topographic venting of boundary layer air to the free troposphere. 4(2):497–509, 2004. doi: 10.5194/acp-4-497-2004.

Henne, S., Brunner, D., Folini, D., Solberg, S., Klausen, J., and Buchmann, B. Assessment of parameters describing representativeness of air quality in-situ measurement sites. 10(8):3561–3581, 2010. doi: 10.5194/acp-10-3561-2010.

Henne, S., Brunner, D., Oney, B., Leuenberger, M., Eugster, W., Bamberger, I., Meinhardt, F., Steinbacher, M., and Emmenegger, L. Validation of the Swiss methane emission inventory by atmospheric observations and inverse modelling. *Atmospheric Chemistry and Physics*, 16(6):3683–3710, 2016. doi: 10.5194/acp-16-3683-2016. URL `http://www.atmos-chem-phys.net/16/3683/2016/`.

Hoffman, M. D. and Gelman, A. The no-u-turn sampler: Adaptively setting path lengths in hamiltonian monte carlo. *arXiv*, 2011.

Hu, L., Montzka, S. A., Miller, J. B., Andrews, A. E., Lehman, S. J., Miller, B. R., Thoning, K., Sweeney, C., Chen, H., Godwin, D. S., Masarie, K., Bruhwiler, L., Fischer, M. L., Biraud, S. C., Torn, M. S., Mountain, M., Nehrkorn, T., Eluszkiewicz, J., Miller, S., Draxler, R. R., Stein, A. F., Hall, B. D., Elkins, J. W., and Tans, P. P. U.s. emissions of HFC-134a derived for 2008–2012 from an extensive flask-air sampling network. 120(2):801–825, 2015. doi: 10.1002/2014JD022617.

IPCC. *2006 IPCC Guidelines for National Greenhouse Gas Inventories*. IGES, Japan, 2006.

IPCC. *2013 Supplement to the 2006 IPCC Guidelines for National Greenhouse Gas Inventories: Wetlands*. IPCC, Switzerland, 2014.

IPCC. *2019 Refinement to the 2006 IPCC Guidelines for National Greenhouse Gas Inventories*. IPCC, Switzerland, 2019.

ISO. Air quality — Determination of the uncertainty of the time average of air quality measurements. Technical Report ISO 11222:2002, Edition 1 2002-07, International Organization for Standardization, 2025.

Jones, A., Thomson, D., Hort, M., and Devenish, B. The u.k. met office's next-generation atmospheric dispersion model, NAME III. In Borrego, C. and Norman, A.-L., editors, *Air Pollution Modeling and Its Application XVII*, pages 580–589. Springer US, 2007. doi: 10.1007/978-0-387-68854-1_62.

Katharopoulos, I., Rust, D., Vollmer, M. K., Brunner, D., Reimann, S., O'Doherty, S. J., Young, D., Stanley, K. M., Schuck, T., Arduini, J., Emmenegger, L., and Henne, S. Impact of transport model resolution and a priori assumptions on inverse modeling of Swiss F-gas emissions. *Atmos. Chem. Phys.*, 23(22):14159–14186, 2023. doi: 10.5194/acp-23-14159-2023. URL `https://acp.copernicus.org/articles/23/14159/2023/`.

Keller, C. A., Brunner, D., Henne, S., Vollmer, M. K., O'Doherty, S., and Reimann, S. Evidence for under-reported western European emissions of the potent greenhouse gas HFC-23. *Geophysical Research Letters*,

38(15), 2011. doi: 10.1029/2011GL047976. URL https://onlinelibrary.wiley.com/doi/abs/10.1029/2011GL047976.

Kuyper, B., Say, D., Labuschagne, C., Lesch, T., Joubert, W. R., Martin, D., Young, D., Khan, M. A. H., Rigby, M., Ganesan, A. L., Lunt, M. F., O'Dowd, C., Manning, A. J., O'Doherty, S., Davies-Coleman, M. T., and Shallcross, D. E. Atmospheric HCFC-22, HFC-125, and HFC-152a at cape point, south africa. 53(15): 8967–8975, 2019. doi: 10.1021/acs.est.9b01612.

Lopez-Coto, I., Hicks, M., Karion, A., Sakai, R. K., Demoz, B., Prasad, K., and Whetstone, J. Assessment of Planetary Boundary Layer parametrizations and urban heat island comparison: Impacts and implications for tracer transport. *Journal of Applied Meteorology and Climatology*, 59(10), 2020. doi: 10.1175/jamc-d-19-0168.1.

Lunt, M. F., Park, S., Li, S., Henne, S., Manning, A. J., Ganesan, A. L., Simpson, I. J., Blake, D. R., Liang, Q., O'Doherty, S., Harth, C. M., Mühle, J., Salameh, P. K., Weiss, R. F., Krummel, P. B., Fraser, P. J., Prinn, R. G., Reimann, S., and Rigby, M. Continued emissions of the ozone-depleting substance carbon tetrachloride from eastern asia. 45(20):11,423–11,430, 2018. doi: 10.1029/2018GL079500.

Lunt, M. F., Manning, A. J., Allen, G., Arnold, T., Bauguitte, S. J.-B., Boesch, H., Ganesan, A. L., Grant, A., Helfter, C., Nemitz, E., O'Doherty, S. J., Palmer, P. I., Pitt, J. R., Rennick, C., Say, D., Stanley, K. M., Stavert, A. R., Young, D., and Rigby, M. Atmospheric observations consistent with reported decline in the UK's methane emissions (2013–2020). 21(21):16257–16276, 2021. ISSN 1680-7316. doi: 10.5194/acp-21-16257-2021.

Manning, A., Ganesan, A., De Longueville, H., Danjou, A., Murphy, B., Henne, S., Melo, D. B., Ramsden, A., Redington, A., and Andrews, P. Draft Annexes to National Inventory Reports, 2024. URL https://horizoneurope-paris.eu/wp-content/uploads/sites/914/2025/02/PARIS-D2.1-Draft-Annexes-to-National-Inventory-Reports-all-final.pdf.

Manning, A. J., O'Doherty, S., Jones, A. R., Simmonds, P. G., and Derwent, R. G. Estimating uk methane and nitrous oxide emissions from 1990 to 2007 using an inversion modeling approach. *Journal of Geophysical Research: Atmospheres*, 116(D2), 2011. doi: https://doi.org/10.1029/2010JD014763. URL https://agupubs.onlinelibrary.wiley.com/doi/abs/10.1029/2010JD014763.

Manning, A. J., Stanley, K., Redington, A., O'Doherty, S., and Young, D. Methodology Report Verification of Emissions using Atmospheric Observations. Technical report, BEIS, 2017.

Manning, A. J., Redington, A. L., Say, D., O'Doherty, S., Young, D., Simmonds, P. G., Vollmer, M. K., Mühle, J., Arduini, J., Spain, G., Wisher, A., Maione, M., Schuck, T. J., Stanley, K., Reimann, S., Engel, A., Krummel, P. B., Fraser, P. J., Harth, C. M., Salameh, P. K., Weiss, R. F., Gluckman, R., Brown, P. N., Watterson, J. D., and Arnold, T. Evidence of a recent decline in uk emissions of hydrofluorocarbons determined by the intem inverse model and atmospheric measurements. *Atmospheric Chemistry and Physics*, 21(16):12739–12755, 2021. doi: 10.5194/acp-21-12739-2021. URL https://acp.copernicus.org/articles/21/12739/2021/.

Maryon, R. H., Smith, F. B., Conway, B. J., and Goddard, D. M. The u.k. nuclear accident model. *Progress in Nuclear Energy*, 26(2):85–104, 1991.

Miller, B. R., Weiss, R. F., Salameh, P. K., Tanhua, T., Greally, B. R., Mühle, J., and Simmonds, P. G. Medusa: A sample preconcentration and GC/MS detector system for in situ measurements of atmospheric

trace halocarbons, hydrocarbons, and sulfur compounds. *Analytical Chemistry*, 80(5):1536–1545, 2008. doi: 10.1021/ac702084k.

Neal, R. M. *Handbook of Markov Chain Monte Carlo*, chapter 5. MCMC Using Hamiltonian Dynamics. Chapman and Hall/CRC, 1 edition, 2011.

Park, S., Western, L. M., Saito, T., Redington, A. L., Henne, S., Fang, X., Prinn, R. G., Manning, A. J., Montzka, S. A., Fraser, P. J., Ganesan, A. L., Harth, C. M., Kim, J., Krummel, P. B., Liang, Q., Mühle, J., O'Doherty, S., Park, H., Park, M.-K., Reimann, S., Salameh, P. K., Weiss, R. F., and Rigby, M. A decline in emissions of CFC-11 and related chemicals from eastern China. *Nature*, 590(7846):433–437, 2021. doi: 10.1038/s41586-021-03277-w. URL `https://www.nature.com/articles/s41586-021-03277-w`.

Phan, D., Pradhan, N., and Jankowiak, M. Composable effects for flexible and accelerated probabilistic programming in numpyro. *arXiv preprint arXiv:1912.11554*, 2019.

Prinn, R. G., Weiss, R. F., Arduini, J., Arnold, T., DeWitt, H. L., Fraser, P. J., Ganesan, A. L., Gasore, J., Harth, C. M., Hermansen, O., Kim, J., Krummel, P. B., Li, S., Loh, Z. M., Lunder, C. R., Maione, M., Manning, A. J., Miller, B. R., Mitrevski, B., Mühle, J., O'Doherty, S., Park, S., Reimann, S., Rigby, M., Saito, T., Salameh, P. K., Schmidt, R., Simmonds, P. G., Steele, L. P., Vollmer, M. K., Wang, R. H., Yao, B., Yokouchi, Y., Young, D., and Zhou, L. History of chemically and radiatively important atmospheric gases from the Advanced Global Atmospheric Gases Experiment (AGAGE). *Earth System Science Data*, 10(2): 985–1018, 2018. doi: 10.5194/essd-10-985-2018.

Ramsden, A. E., Ganesan, A. L., Western, L. M., Rigby, M., Manning, A. J., Foulds, A., France, J. L., Barker, P., Levy, P., Say, D., Wisher, A., Arnold, T., Rennick, C., Stanley, K. M., Young, D., and O'Doherty, S. Quantifying fossil fuel methane emissions using observations of atmospheric ethane and an uncertain emission ratio. 22(6):3911–3929, 2022. doi: 10.5194/acp-22-3911-2022.

Redington, A. L., Manning, A. J., Henne, S., Graziosi, F., Western, L. M., Arduini, J., Ganesan, A. L., Harth, C. M., Maione, M., Mühle, J., O'Doherty, S., Pitt, J., Reimann, S., Rigby, M., Salameh, P. K., Simmonds, P. G., Spain, T. G., Stanley, K., Vollmer, M. K., Weiss, R. F., and Young, D. Western European emission estimates of CFC-11, CFC-12 and CCl_4 derived from atmospheric measurements from 2008 to 2021. *Atmospheric Chemistry and Physics*, 23(13):7383–7398, 2023. doi: 10.5194/acp-23-7383-2023. URL `https://acp.copernicus.org/articles/23/7383/2023/`.

Rigby, M., Park, S., Saito, T., Western, L. M., Redington, A. L., Fang, X., Henne, S., Manning, A. J., Prinn, R. G., Dutton, G. S., Fraser, P. J., Ganesan, A. L., Hall, B. D., Harth, C. M., Kim, J., Krummel, P. B., Lee, T., Li, S., Liang, Q., Lunt, M. F., Montzka, S. A., Mühle, J., O'Doherty, S., Park, M. K., Reiman, S., Salameh, P. K., Simmonds, P., Tunnicliffe, R. L., Weiss, Y., and Young, D. Increase in cfc-11 emissions from eastern china based on atmospheric observations. *Nature*, 569:546–550, 2019. doi: 10.1038/s41586-019-1193-4. URL `https://doi.org/10.1038/s41586-019-1193-4`.

RIVM. Greenhouse gas emissions in the Netherlands 1990-2023: National Inventory Document, 2025. URL `https://unfccc.int/documents/646509`.

Rodgers, C. D. *Inverse Methods for Atmospheric Sounding*. WORLD SCIENTIFIC, 2000.

Ruckstuhl, A. F., Henne, S., Reimann, S., Steinbacher, M., Vollmer, M. K., O'Doherty, S., Buchmann, B., and Hueglin, C. Robust extraction of baseline signal of atmospheric trace species using local regression. *Atmospheric Measurement Techniques*, 5(11):2613–2624, 2012. doi: 10.5194/amt-5-2613-2012.

Rust, D., Katharopoulos, I., Vollmer, M. K., Henne, S., O'Doherty, S., Say, D., Emmenegger, L., Zenobi, R., and Reimann, S. Swiss halocarbon emissions for 2019 to 2020 assessed from regional atmospheric observations. *Atmospheric Chemistry and Physics*, 22(4):2447–2466, 2022. doi: 10.5194/acp-22-2447-2022. URL `https://acp.copernicus.org/articles/22/2447/2022/`.

Ryall, D. B. and Maryon, R. H. Validation of the uk met. office's name model against the etex dataset. *Atmospheric Environment*, 32(24):4265–4276, 1998.

Saboya, E., Manning, A. J., Levy, P., Stanley, K. M., Pitt, J., Young, D., Say, D., Grant, A., Arnold, T., Rennick, C., Tomlinson, S. J., Carnell, E. J., Artioli, Y., Stavart, A., Spain, T. G., O'Doherty, S., Rigby, M., and Ganesan, A. L. Combining top-down and bottom-up approaches to evaluate recent trends and seasonal patterns in uk n2o emissions. *Journal of Geophysical Research: Atmospheres*, 129(14):e2024JD040785, 2024.

Say, D., Manning, A. J., O'Doherty, S., Rigby, M., Young, D., and Grant, A. Re-evaluation of the UK's HFC-134a emissions inventory based on atmospheric observations. 50(20):11129–11136, 2016. doi: 10.1021/acs.est.6b03630.

Schoenenberger, F., Henne, S., Hill, M., Vollmer, M. K., Kouvarakis, G., Mihalopoulos, N., O'Doherty, S., Maione, M., Emmenegger, L., Peter, T., and Reimann, S. Abundance and sources of atmospheric halocarbons in the Eastern Mediterranean. *Atmospheric Chemistry and Physics*, 18(6):4069–4092, 2018. doi: 10.5194/acp-18-4069-2018. URL `https://acp.copernicus.org/articles/18/4069/2018/`.

Simmonds, P. G., Rigby, M., Manning, A. J., Park, S., Stanley, K. M., McCulloch, A., Henne, S., Graziosi, F., Maione, M., Arduini, J., Reimann, S., Vollmer, M. K., Mühle, J., O'Doherty, S., Young, D., Krummel, P. B., Fraser, P. J., Weiss, R. F., Salameh, P. K., Harth, C. M., Park, M.-K., Park, H., Arnold, T., Rennick, C., Steele, L. P., Mitrevski, B., Wang, R. H. J., and Prinn, R. G. The increasing atmospheric burden of the greenhouse gas sulfur hexafluoride (SF_6). *Atmospheric Chemistry and Physics*, 20(12):7271–7290, 2020. doi: 10.5194/acp-20-7271-2020. URL `https://acp.copernicus.org/articles/20/7271/2020/`.

Stanley, K. M., Grant, A., O'Doherty, S., Young, D., Manning, A. J., Stavert, A. R., Spain, T. G., Salameh, P. K., Harth, C. M., Simmonds, P. G., Sturges, W. T., Oram, D. E., and Derwent, R. G. Greenhouse gas measurements from a UK network of tall towers: technical description and first results. 11(3):1437–1458, 2018. doi: 10.5194/amt-11-1437-2018.

Steiner, M., Peters, W., Luijkx, I., Henne, S., Chen, H., Hammer, S., and Brunner, D. European CH_4 inversions with ICON-ART coupled to the CarbonTracker Data Assimilation Shell. *Atmospheric Chemistry and Physics*, 24(4):2759–2782, 2024. doi: 10.5194/acp-24-2759-2024. URL `https://acp.copernicus.org/articles/24/2759/2024/`.

Stohl, A., Forster, C., Frank, A., Seibert, P., and Wotawa, G. Technical note: The lagrangian particle dispersion model FLEXPART version 6.2. 5(9):2461–2474, 2005. doi: 10.5194/acp-5-2461-2005.

Stohl, A., Seibert, P., Arduini, J., Eckhardt, S., Fraser, P., Greally, B. R., Lunder, C., Maione, M., Mühle, J., O'Doherty, S., Prinn, R. G., Reimann, S., Saito, T., Schmidbauer, N., Simmonds, P. G., Vollmer, M. K., Weiss, R. F., and Yokouchi, Y. An analytical inversion method for determining regional and global emissions of greenhouse gases: Sensitivity studies and application to halocarbons. *Atmospheric Chemistry and Physics*, 9(5):1597–1620, 2009. doi: 10.5194/acp-9-1597-2009. URL `https://acp.copernicus.org/articles/9/1597/2009/acp-9-1597-2009.html`.

Stull, R. B. *An Introduction to Boundary Layer Meteorlogy.* Atmospheric and Oceanographic Sciences Library. Springer Dordrecht, 1 edition, 1988.

Tarantola, A. *Inverse Problem Theory and Methods for Model Parameter Estimation.* SIAM, Philadelphia, PA, 2005.

Thompson, R. L., Chevallier, F., Crotwell, A. M., Dutton, G., Langenfelds, R. L., Prinn, R. G., Weiss, R. F., Tohjima, Y., Nakazawa, T., Krummel, P. B., Steele, L. P., Fraser, P., O'Doherty, S., Ishijima, K., and Aoki, S. Nitrous oxide emissions 1999 to 2009 from a global atmospheric inversion. *Atmospheric Chemistry and Physics*, 14(4):1801–1817, 2014.

Thomson, D. J. Criteria for the Selection of Stochastic-Models of Particle Trajectories in Turbulent Flows. *Journal of Fluid Mechanics*, 180:529–556, 1987. URL `<GotoISI>://A1987J458000025`.

Tipka, A., Haimberger, L., and Seibert, P. Flex_extract v7.1.2 – a software package to retrieve and prepare ECMWF data for use in FLEXPART. *Geosci. Model Dev.*, 13(11):5277–5310, 2020. doi: 10.5194/gmd-13-5277-2020. URL `https://gmd.copernicus.org/articles/13/5277/2020/https://gmd.copernicus.org/articles/13/5277/2020/gmd-13-5277-2020.pdf`.

Vojta, M., Plach, A., Thompson, R. L., and Stohl, A. A comprehensive evaluation of the use of lagrangian particle dispersion models for inverse modeling of greenhouse gas emissions. 15(22):8295–8323, 2022. doi: 10.5194/gmd-15-8295-2022.

Vollmer, M. K., Zhou, L. X., Greally, B. R., Henne, S., Yao, B., Reimann, S., Stordal, F., Cunnold, D. M., Zhang, X. C., Maione, M., Zhang, F., Huang, J., and Simmonds, P. G. Emissions of ozone-depleting halocarbons from China. *Geophysical Research Letters*, 36(15), 2009. doi: 10.1029/2009GL038659. URL `https://onlinelibrary.wiley.com/doi/abs/10.1029/2009GL038659`.

WMO-GAW. IG3IS National Scale Greenhouse Gas Emission Observation and Monitoring Good Practice Guidance. Technical report, World Meteorological Organization - Global Atmosphere Watch, 2025.

Yver Kwok, C., Laurent, O., Guemri, A., Philippon, C., Wastine, B., Rella, C. W., Vuillemin, C., Truong, F., Delmotte, M., Kazan, V., Darding, M., Lebègue, B., Kaiser, C., Xueref-Rémy, I., and Ramonet, M. Comprehensive laboratory and field testing of cavity ring-down spectroscopy analyzers measuring h_2o, CO_2, CH_4 and CO. *Atmospheric Measurement Techniques*, 8(9):3867–3892, 2015. doi: 10.5194/amt-8-3867-2015.

Yver-Kwok, C., Philippon, C., Bergamaschi, P., Biermann, T., Calzolari, F., Chen, H., Conil, S., Cristofanelli, P., Delmotte, M., Hatakka, J., Heliasz, M., Hermansen, O., Komínková, K., Kubistin, D., Kumps, N., Laurent, O., Laurila, T., Lehner, I., Levula, J., Lindauer, M., Lopez, M., Mammarella, I., Manca, G., Marklund, P., Metzger, J.-M., Mölder, M., Platt, S. M., Ramonet, M., Rivier, L., Scheeren, B., Sha, M. K., Smith, P., Steinbacher, M., Vítková, G., and Wyss, S. Evaluation and optimization of ICOS atmosphere station data as part of the labeling process. 14(1):89–116, 2021. doi: 10.5194/amt-14-89-2021.

A The atmospheric transport models NAME and FLEXPART: general features and PARIS-specific setup

We use two Lagrangian Particle Dispersion Models (LPDMs) to describe the atmospheric transport and diffusion of trace compounds: NAME (Numerical Atmospheric dispersion Modelling Environment Jones et al., 2007) and FLEXPART (FLEXible PARTicle dispersion model Stohl et al., 2005). LPDMs simulate this transport by calculating the trajectories of a multitude of model particles (or air parcels). These trajectories are determined deterministically by the mean atmospheric flow as obtained from a NWP model and stochastically for the representation of atmospheric turbulence and deep convection (if not resolved by the NWP). The stochastic description of turbulence relies on the simulation of the particles' turbulent velocities by a Markov process based on the Langevin equation (Thomson, 1987). The latter requires the calculation of turbulence intensities and Lagrangian timescales at the location of each particle, which in the case of NAME and FLEXPART is achieved through the use of similarity profiles taking surface momentum and heat flux and boundary layer heights into account (Stohl et al., 2005; Jones et al., 2007).

For all simulations performed for the PARIS project, a common setup for both LPDMs was agreed on. For each observational site 20,000 model particles were released per hour and tracked back for 30 days in the atmosphere or until they crossed the border of a domain extending from Europe across the North Atlantic and into America (98° W to 39° E, 11° N to 79° N). Source sensitivities were stored for the same domain with a spatial resolution of 0.352° by 0.234° (approximately 25 km x 25 km) and considering all model particles residing between the model surface and 40 m above ground. Next to these surface source sensitivities, the location of where particles left the output domain was converted to boundary sensitivities giving the fraction of particles leaving the domain through a certain interface with a given horizontal and vertical extend. The horizontal spacing was aligned with that of the surface sensitivities, whereas the vertical grid spacing of the boundary sensitivities was set to 500 m up to a maximum height of 20 km above ground. For FLEXPART, air parcels that remained inside the transport model domain after the end of the backward integration were assigned to the closest boundary interface. This corresponds to approximately 10 % of the particles. In NAME, these particles are ignored. Surface source and boundary sensitivities were stored in monthly files by observational site, using the same interchangeable format for output from NAME and FLEXPART. Table 8.1 summarizes the settings just described.

The NAME model was driven by 3-dimensional meteorological fields from the operational weather model operated by the UK Meteorological Office (Unified Model). The horizontal and vertical resolution of these fields varies over time with the development of the meteorological model (**?**, Table 1 therein). After 2010 the resolution was ∼25 km and increased over time to a resolution of ∼12 km from July 2017 onward. For sites in the UK and Ireland nested input at a resolution of ∼1 km was available from 2012 onwards. In NAME particles were released at a height above ground according to the inlet height of the observations. This approach was adjusted for the mountain sites Jungfraujoch, Monte Cimone, Schauinsland, and Zugspitze, where model particles were released at 500 m, 1000 m, 200 m, and 600 m above model ground, respectively, according to previous sensitivity tests.

FLEXPART was driven by 3-dimensional meteorological fields from the operational high resolution analysis/forecast (HRES) of the European Centre for Medium Range Weather Forecast (ECMWF). Since 2020 these fields were available hourly with 0.1° by 0.1° horizontal resolution for the European domain and with 0.5° by 0.5° resolution elsewhere. Before 2020 3-hourly inputs at 0.2° by 0.2° and 1° by 1° were used. These fields were extracted from ECMWF's archive using the flexextract tool (Tipka et al., 2020). In FLEXPART, particles were released at a height above model ground according to the inlet height of the observations for sites in flat terrain,

whereas for elevated sites a release height at the middle between model and real topography was chosen. The latter was additionally offset by the inlet height of the observation. Sites were categorised as elevated if their real height above sea level was at least 200 m higher than the model ground elevation at the same location.

B Markov Chain Monte Carlo

Markov Chain Monte Carlo (MCMC) is a method for producing a *chain* (or *trace*) of samples from a given distribution. The samples produced are not independent, but can be used to calculate statistics from the distribution.

The *Metropolis-Hastings* algorithm is a flexible MCMC algorithm for constructing a trace of samples. Suppose the distribution we wish to sample from is (proportional to) ρ and we have a function for producing *proposals* for new samples given a current sample. (For simplicity, we assume the proposal function is "symmetric".) Starting from a random initial point in the sample space, new samples are produced as follows:

- let X_n denote the current sample and let X' be a proposal for the next sample
- draw a value $0 \leq u \leq 1$ uniformly at random
- if $u \leq \min(1, \rho(X')/\rho(X_n))$, let $X_{n+1} = X'$ (accept the proposal)
- otherwise, let $X_n = X_{n+1}$ (reject the proposal).

RHIME uses *Hamiltonian Monte Carlo* (HMC) (Neal, 2011; Duane et al., 1987), which uses Hamiltonian Dynamics to produce proposals for the Metropolis-Hastings algorithm. The method works as follows: starting from a point in the sample space, randomly choose a momentum vector, and use Hamilton's equations to move around the state space, with $-\log \rho(x)$ acting as the potential energy. For the analytic model discussed above, the potential energy is the cost function J from Equation (10). This means that the rate of change of momentum is equal to the gradient of the log probability $\nabla_x \log \rho(x)$; this is the same quantity that is used to guide us to a minimum in optimisation methods like gradient descent, but here it is used to update position indirectly by updating momentum. The use of the gradient of the log probability also means that HMC can only be used with continuous distributions, but that is not a serious limitation for inverse problems.

There are many parameters to tune in HMC. Incorrect tuning can result in "divergences", where the numerically integrated paths in the state space fail to conserve the "Hamiltonian". The *No-U-Turn Sampler* (NUTS) algorithm (Hoffman and Gelman, 2011) is a modification of HMC that automatically tunes parameters, essentially by stopping the dynamics when the path starts to move back towards the initial point. RHIME uses the NUTS algorithms from PyMC and Numpyro (Bingham et al., 2019; Phan et al., 2019; PyM).

C Applying Basis Functions

Here we give a more precise derivation of the sensitivity matrix used by RHIME's forward model, then compare this with ELRIS and InTEM's method.

Suppose $\mathbf{M}_0$ is the source sensitivity matrix at the transport model resolution. Let L and K_0 denote the number of rows and columns of $\mathbf{M}_0$, respectively, and let $\mathbf{e}_{0,\mathrm{a}}$ denote the prior value of the emissions flux at the transport model resolution.

If $D = \mathrm{diag}(\mathbf{e}_{0,\mathrm{a}})$ is a diagonal matrix with the entries of $\mathbf{e}_{0,\mathrm{a}}$ on the diagonal, then multiplying the columns of $\mathbf{M}_0$ by $\mathbf{e}_{0,\mathrm{a}}$ yields the matrix $\mathbf{M}_0 D$. To describe the aggregation over the basis regions, we need a function that maps from the flux at the transport model resolution to the K basis regions used in the inversion. This

function is linear, and given by a $K \times K_0$ matrix A with entries a_{ij} such that $a_{ij} = 1$ if the jth grid cell (at transport model resolution) is in the ith basis region, and $a_{ij} = 0$ otherwise.

Multiplying $\mathbf{M}_0 D$ on the right by the transpose A^T accomplishes the aggregation described above, thus

$$\mathbf{M_E} = \mathbf{M}_0 D A^T. \tag{35}$$

The matrix DA^T is an *interpolation* matrix that maps values on the K basis regions to vectors at the transport grid resolution. If we multiply the interpolation matrix by the vector $\mathbf{1} = (1, \ldots, 1)^T$ of length K, then we recover the original prior flux value $\mathbf{e}_{0,\mathrm{a}}$, which establishes (25).

To compare this method, used by RHIME, to the method used by ELRIS and InTEM, we will look more closely at the *interpolation* and *projection* matrices used by RHIME. Define the interpolation map $\rho(\mathbf{e}) = DA^T\mathbf{e}$, which maps vectors $\mathbf{e}$ on the inversion grid to vectors $\mathbf{e}_0$ on the transport grid. The corresponding *projection* matrix that maps vectors $\mathbf{e}_0$ on the transport grid to vectors $\mathbf{e}$ on the inversion grid is given by

$$\pi(\mathbf{e}_0) = (AD^2A^T)^{-1}AD\mathbf{e}_0. \tag{36}$$

The matrix $(AD^2A^T)^{-1}$ is diagonal, and the ith entry on its diagonal is the sum of the squares of the values of $\mathbf{e}_{0,\mathrm{a}}$ in the ith basis region. So the projection map takes a sort of weighted average over the basis regions. The interpolation and projection matrices satisfy the relation $\pi(\rho(\mathbf{e})) = \mathbf{e}$:

$$\pi(\rho(\mathbf{e})) = (AD^2A^T)^{-1}AD(DA^T\mathbf{e}) = \mathbf{e}. \tag{37}$$

In practice, RHIME does not use the projection matrix π explicitly, and simply requires that the basis projection maps the prior flux value $\mathbf{e}_{0,\mathrm{a}}$ to the vector of 1's.

An alternative method used to project to basis regions, used by ELRIS and InTEM is as follows. Let A be as above and define the basis projection $\pi(\mathbf{e}_0) = A\mathbf{e}_0$, where $\mathbf{e}_0$ is a vector at the transport model resolution. The ith component of $\mathbf{e} = A\mathbf{e}_0$ is the sum of all components in $\mathbf{e}_0$ corresponding to grid cells within the ith basis region.

The corresponding interpolation map, which maps vectors on the inversion grid to vectors on the transport grid, is $\rho(\mathbf{e}) = A^T(AA^T)^{-1}$. If n_i is the number of grid cells in the ith basis region, then $(AA^T)^{-1} = \mathrm{diag}(1/n_1, \ldots, 1/n_K)$, so the source sensitivity matrix at the inversion grid resolution

$$\mathbf{M_E} = \mathbf{M}_0 A^T(AA^T)^{-1} \tag{38}$$

is obtained by averaging the columns of $\mathbf{M}_0$ over the basis regions.

As with RHIME's method, for any vector on the inversion grid $\mathbf{e}$, we have

$$\pi(\rho(\mathbf{e})) = A(A^T(AA^T)^{-1})\mathbf{e} = \mathbf{e}. \tag{39}$$

Comparing the method used by RHIME to the method used by ELRIS and InTEM, there are two differences:

1. The projection map used by RHIME maps the prior flux value $\mathbf{e}_{0,\mathrm{a}}$ to the vector of 1's; this is accomplished by adding the matrix $D = \mathrm{diag}(\mathbf{e}_{0,\mathrm{a}})$ to the interpolation matrix.
2. RHIME puts the "averaging" factor $(AD^2A^T)^{-1}$ in the projection map, while ELRIS and InTEM put the averaging factor $(AA^T)^{-1}$ in the interpolation map.

In other words, RHIME takes a (weighted) sum of the columns of the sensitivity matrix and a (weighted) average of the flux values over the basis regions, while ELRIS and InTEM take an average of the columns of the sensitivity matrix, and sum the flux values over basis regions. In general terms, the method employed by all models is to specify either the interpolation or projection matrix, and then define the other matrix as its *pseudoinverse*, which essentially means that $\mathbf{e}_0 = \rho(\mathbf{e})$ is the least-squares solution to the linear equation $\pi(\mathbf{e}_0) = \mathbf{e}$.

D RHIME Pollution Event Size

The uncertainty in the likelihood used by RHIME depends on the observations $\boldsymbol{\chi}_\mathbf{o}$ through the pollution event term R_{PE} defined in (32). This means that the likelihood is *not Gaussian.* Further, choosing $p < 2$ is necessary for the likelihood to be a proper probability distribution.

Since $\mathbf{R}$ is diagonal, we can see the influence of p by looking at a single observation. If $\boldsymbol{\chi}_\mathbf{o}$ is large enough that $\mathbf{R}(\sigma) \approx \sigma^2 R_{PE}$, the (31) becomes

$$\rho(\boldsymbol{\chi}_\mathbf{o} \mid \mathbf{x}, \sigma) \approx \frac{1}{\sigma\sqrt{R_{PE}}} \exp\left(-\frac{(\boldsymbol{\chi}_\mathbf{o} - \mathbf{M}\mathbf{x})^2}{2\sigma^2 R_{PE}}\right). \tag{40}$$

Using (32) and $\mathbf{M}\mathbf{x} = \boldsymbol{\chi}_\mathbf{p} + \boldsymbol{\chi}_\mathbf{b}$, we have

$$\rho(\boldsymbol{\chi}_\mathbf{o} \mid \mathbf{x}, \sigma) \approx \frac{1}{\sigma(\boldsymbol{\chi}_\mathbf{o} - \boldsymbol{\chi}_\mathbf{b})^{p/2}} \exp\left(-\frac{(\boldsymbol{\chi}_\mathbf{o} - \boldsymbol{\chi}_\mathbf{p} - \boldsymbol{\chi}_\mathbf{b})^2}{2\sigma^2(\boldsymbol{\chi}_\mathbf{o} - \boldsymbol{\chi}_\mathbf{b})^p}\right). \tag{41}$$

If $p = 2$, then for large $\boldsymbol{\chi}_\mathbf{o}$, the exponential term in (41) tends to the constant value $\exp(-1/2\sigma^2)$, while the normalising factor in front is only decaying at a rate of roughly $1/\boldsymbol{\chi}_\mathbf{o}$; this rate of decay is too slow for the area under the curve defined by $\rho(\boldsymbol{\chi}_\mathbf{o} \mid \mathbf{x}, \sigma)$ to be finite. However, if $p < 2$, then there is still exponential decay, and the likelihood can be normalised to be a probability distribution.

Through experiment, we have found that if a hyper-prior is placed on p, say uniform from 1.01 to 1.99, the posterior of p is heavily concentrated at the maximum possible value. Thus we set $p = 1.99$ for simplicity. While technically incorrect, in practice we see no difference when using $p = 2$ in place of $p = 1.99$. If p is allowed to vary by site and over fixed time periods, like the parameter σ, then some posterior values for p may be smaller than the maximum allowed by the prior, but in limited experiments, this had a negligible impact on posterior country totals.

The parameter p influences the effect of large pollution events on the model: larger values of p increase robustness against large observations (or in terms of a cost function, penalize discrepancies between observations and modelled observations *less* when the observations greatly exceed the baseline). Setting p close to 2 makes the model conservative: we accept bias in modelled observations at large pollution events to try to avoid systematic bias.

Draft Inventory Annex
Germany 2025

30th October, 2025

1 Introduction

In this document, global concentration trends and national emissions estimates derived from atmospheric observations ("inverse estimates") are presented for most reported gases. Comparing the emissions submitted in national inventories with those calculated using atmospheric observations allows for emissions to be assessed using two fundamentally different approaches. Substantial differences can highlight areas that could warrant further investigation.

Global concentration trends for each gas are first shown using annual average concentrations from Mace Head, Ireland (Northern Hemisphere) and Kennaook/Cape Grim, Tasmania, Australia (Southern Hemisphere). Data from these stations were selected to exclude regionally-polluted air masses and therefore represents northern and southern hemispheric concentration trends. Mace Head observations were supported by the National Aeronautics and Space Administration (NASA) and the UK Department of Energy, Security and Net Zero (DESNZ), and Kennaook/Cape Grim observations by NASA and the Australian Bureau of Meteorology.

Observations of European concentrations of greenhouse gases used to derive national inverse emission estimates were collected from many different networks and providers. Methane and nitrous oxide concentrations originated from the European ICOS (Integrated Carbon Observation System) network, the UK DECC (Deriving Emissions related to Climate Change) network and other national or individual initiatives. F-gas observations were made by affiliates of the AGAGE (Advanced Global Atmospheric Gases Experiment) network. Observations from additional stations across Europe were supported by the Horizon-EU PARIS (Process Attribution of Regional Emissions) project. The observation stations used to derive emissions for each gas are shown in the corresponding sections of this document.

An atmospheric transport model provides the link between surface fluxes and concentrations measured at the observing stations. If not otherwise mentioned, inversion-based emissions estimates were derived using two atmospheric transport models combined with three inverse models, yielding a total of six inversions. This ensemble of six inversions allows us to better quantify the uncertainties associated with inverse modelling.

The two atmospheric transport models used are the Numerical Atmospheric dispersion Modelling Environment (NAME, Jones et al., 2007), and the FLEXible PARTicle dispersion model (FLEXPART, Stohl et al., 2005). Both models are backwards-running Lagrangian Particle Dispersion Models (LPDMs) that simulate the recent transport of air to each observing station. The two LPDMs have been widely used in the estimation of greenhouse gas emissions (Ganesan et al., 2015; Rigby et al., 2019; Manning et al., 2021; Henne et al., 2016).

The three inverse methods used are InTEM (Inversion Technique for Emission Modelling, Manning et al., 2021), ELRIS (Empa Lagrangian Regional Inversion System, Henne et al., 2016; Katharopoulos et al., 2023), and RHIME (Regional Hierarchical Inverse Modelling Environment, Ganesan et al., 2014). All three inverse methods estimate emissions within Europe along with boundary conditions that account for the concentration of the air entering Europe. All three systems started from the same set of a priori emissions that were either derived from the global EDGAR emission inventory (version 8, European Commission: Joint Research et al., 2023) or a uniform land-based emission, depending on the gas. A natural emission component, from the WETCHARTS product, was included in the methane prior. The same observational dataset was used by each inverse model, but data selection (i.e., filtering datasets for specific conditions) and treatment of uncertainties were chosen separately and hence differ. The three methods also differ in their statistical approaches for estimating emissions.

Emission estimates are presented for the period 2008-2024. Emissions for the full 2008-2024 period were derived with the InTEM-NAME inversion only, while emissions from 2017-2024 are presented as the mean of the six inversions (denoted the "PARIS mean"). The uncertainty shown is the minimum/maximum of the uncertainties in the ensemble.

All inversions employed a resolution of one month for CH_4 and N_2O and 1-year for the fluorinated gases. The inversion results used to compare with the inventories are a one-year calendar average for CH_4 and N_2O and the yearly value derived from a 3-year moving average for the fluorinated gases. For the 2008-2024

InTEM-NAME results, a 3-year moving average was also applied to the annualised CH_4 and N_2O results due to lack of observational coverage in the earlier years.

In the case of CH_4, one additional inverse modelling system was included in the ensemble of inversions. The ICON-ART synthesis inversion system (Bruch et al., 2025), the so-called ITMS-Demonstrator (ITMS-D), was developed by the German Weather Service (DWD) and jointly with the German Integrated Greenhouse Gas Monitoring System (ITMS) initiative. In contrast to the transport and inversion models described above, ITMS-D uses fundamentally different model approaches. First, the transport is carried out online by a Eulerian numerical weather prediction model with support for tracer transport (ICON-ART), relying on daily updated meteorology fields from the ICON-DREAM reanalysis and CAMS concentrations at the boundary of the limited area model. Within the domain, emissions provided by CAMS are used, except for Germany, where this is substituted by the National Inventory emissions from UBA which were spatially distributed with the GRETA tool by UBA. This approach allows calculating different tracers for different sectors and geographic areas of origin. Second, the inversion method optimises emissions by sector and from different geographic areas with a focus on Germany. Third, the a priori assumptions and use of observational data are largely independent of the three inversion systems described above.

2 Global Concentration Trends

2.1 Methane (CH_4)

Figure 2.1.1: Background Northern Hemisphere monthly concentrations of CH_4 estimated from MHD, Ireland observations are shown in red, and background Southern Hemisphere monthly concentrations from CGO, Tasmania are shown in blue. Grey shading represents provisional data.

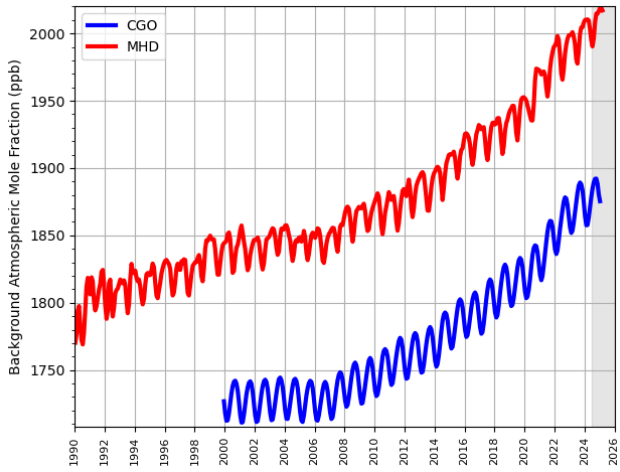

2.2 Nitrous Oxide (N_2O)

Figure 2.2.1: Background Northern Hemisphere monthly concentrations of N_2O estimated from MHD, Ireland observations are shown in red, and background Southern Hemisphere monthly concentrations from CGO, Tasmania are shown in blue. Grey shading represents provisional data.

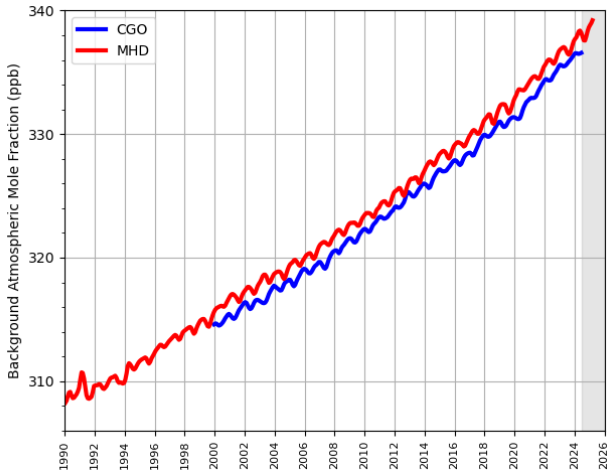

2.3 Hydrofluorocarbons (HFCs)

Figure 2.3.1: Background Northern Hemisphere monthly concentrations of six HFCs estimated from MHD, Ireland observations are shown in red, and background Southern Hemisphere monthly concentrations from CGO, Tasmania are shown in blue. Grey shading represents provisional data.

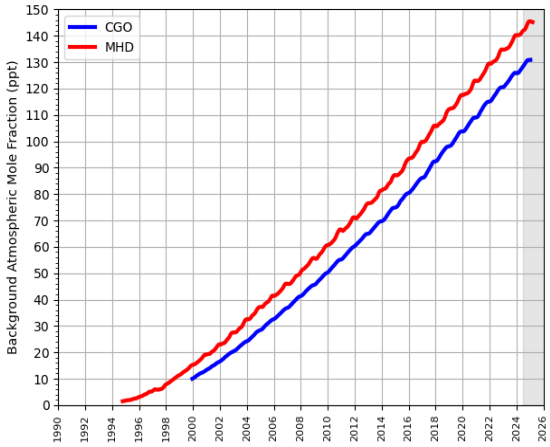

(a) HFC-134a

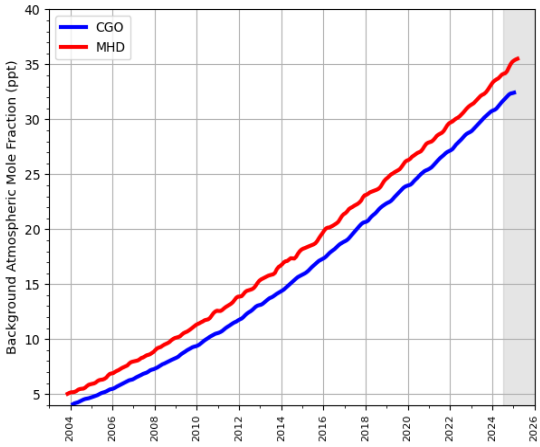

(b) HFC-143a

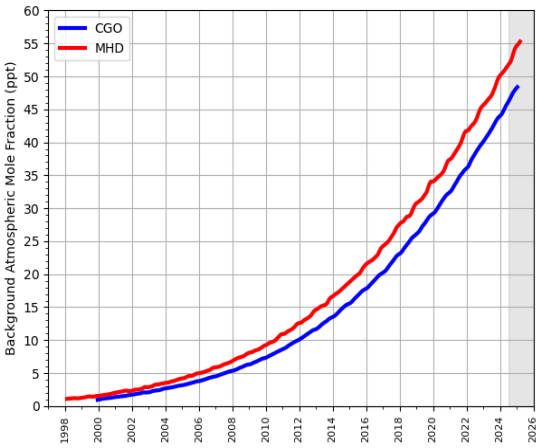

(c) HFC-125

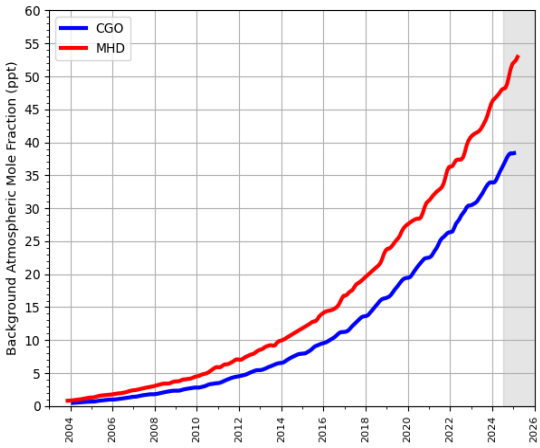

(d) HFC-32

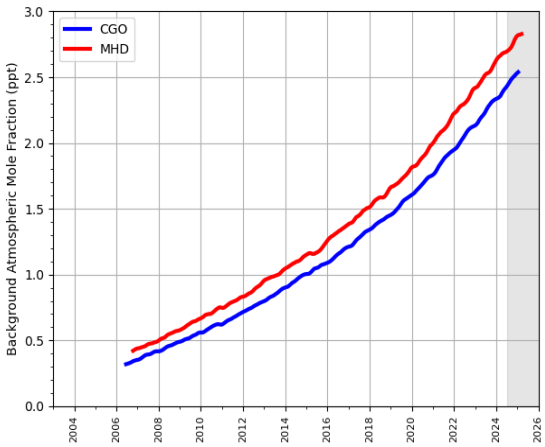

(e) HFC-227ea

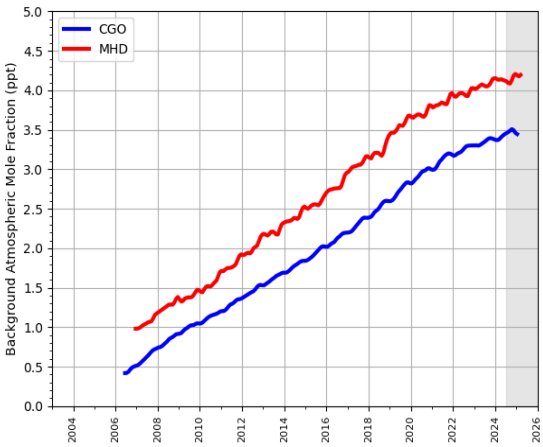

(f) HFC-245fa

Figure 2.3.2: Background Northern Hemisphere monthly concentrations of four HFCs estimated from MHD, Ireland observations are shown in red, and background Southern Hemisphere monthly concentrations from CGO, Tasmania are shown in blue. Grey shading represents provisional data.

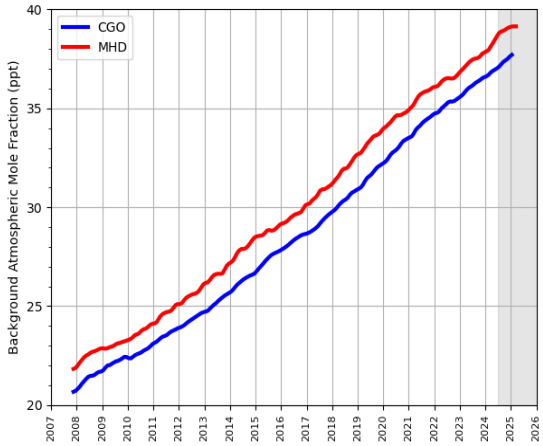

(a) HFC-23

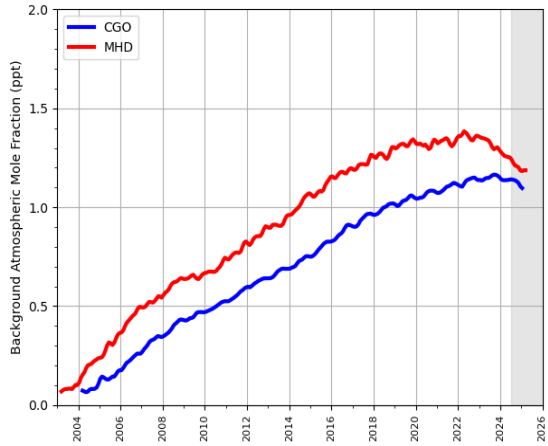

(b) HFC-365mfc

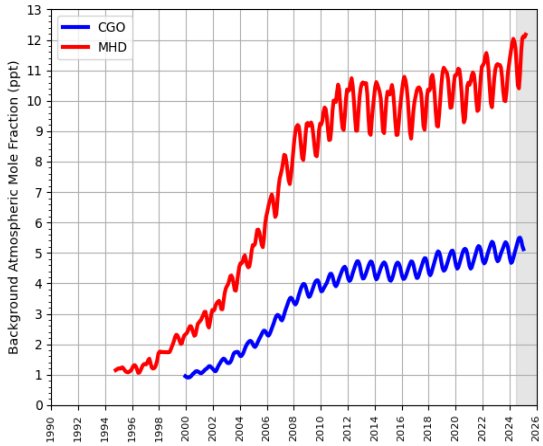

(c) HFC-152a

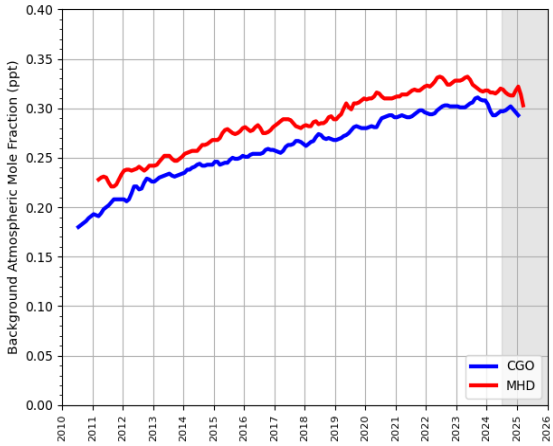

(d) HFC-43-10-mee

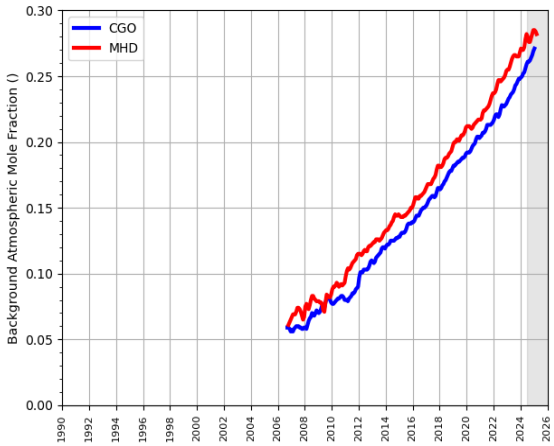

(e) HFC-236fa

2.4 Perfluorocarbons (PFCs)

Figure 2.4.1: Background Northern Hemisphere monthly concentrations of four PFCs estimated from MHD, Ireland observations are shown in red, and background Southern Hemisphere monthly concentrations from CGO, Tasmania are shown in blue. Grey shading represents provisional data.

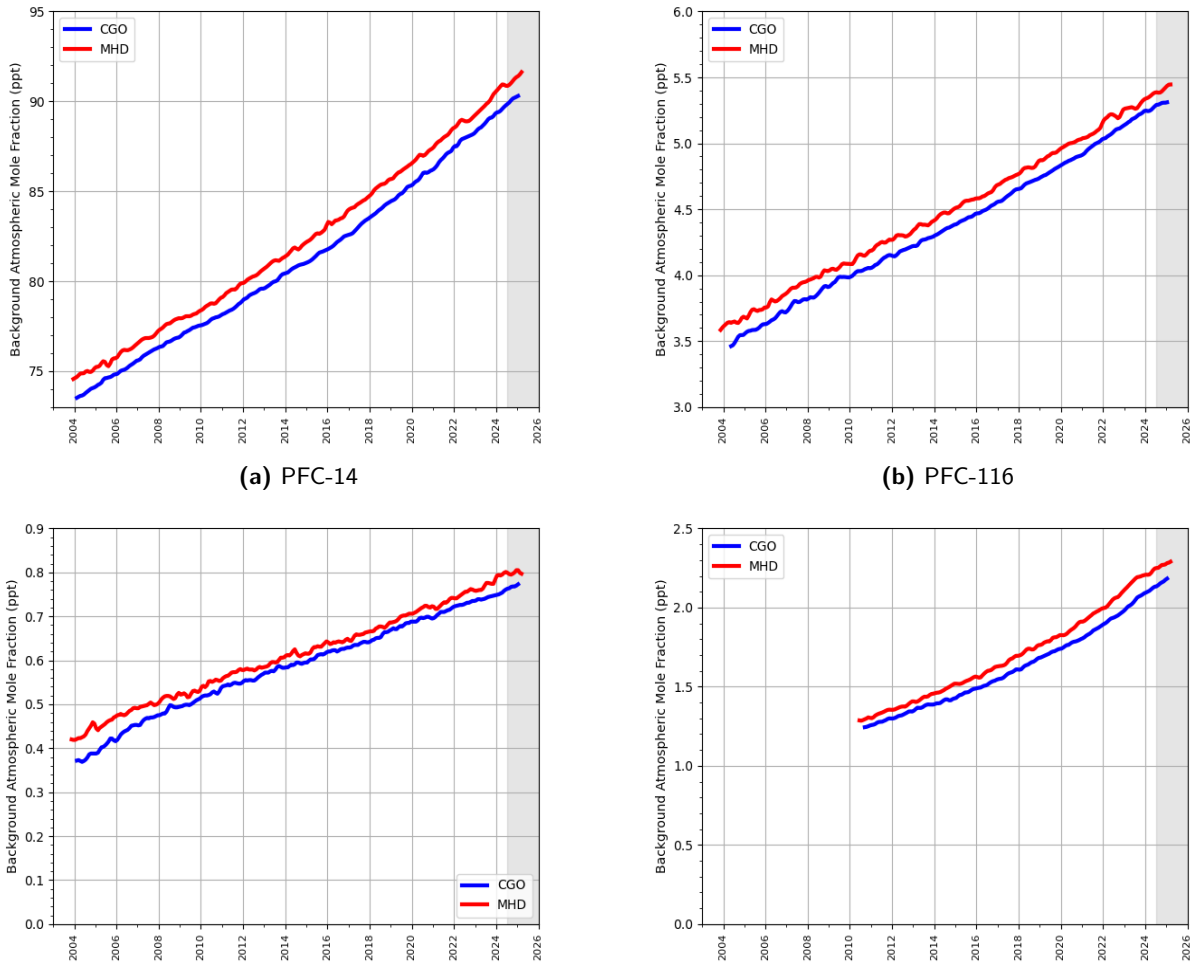

(a) PFC-14 **(b)** PFC-116 **(c)** PFC-218 **(d)** PFC-318

2.5 Sulphur Hexafluoride (SF_6) and Nitrogen Trifluoride (NF_3)

Figure 2.5.1: Background Northern Hemisphere monthly concentrations of SF_6 and NF_3 estimated from MHD, Ireland observations are shown in red, and background Southern Hemisphere monthly concentrations from CGO, Tasmania are shown in blue. Grey shading represents provisional data.

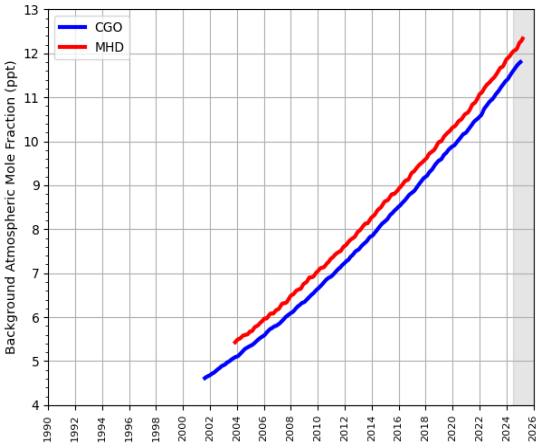

(a) SF_6

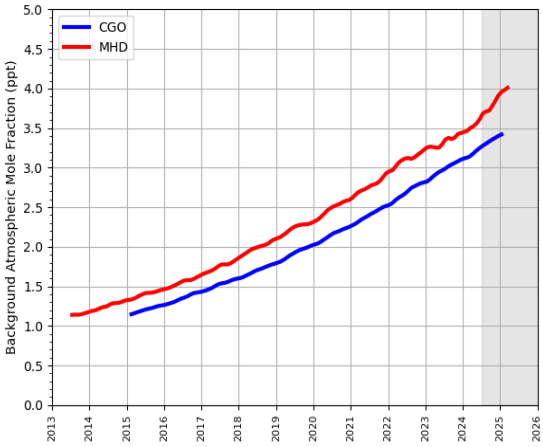

(b) NF_3

2.6 Carbon Dioxide (CO_2)

Figure 2.6.1: Background Northern Hemisphere monthly concentrations of CO_2 estimated from MHD, Ireland observations are shown in red, and background Southern Hemisphere monthly concentrations from CGO, Tasmania are shown in blue. Grey shading represents provisional data.

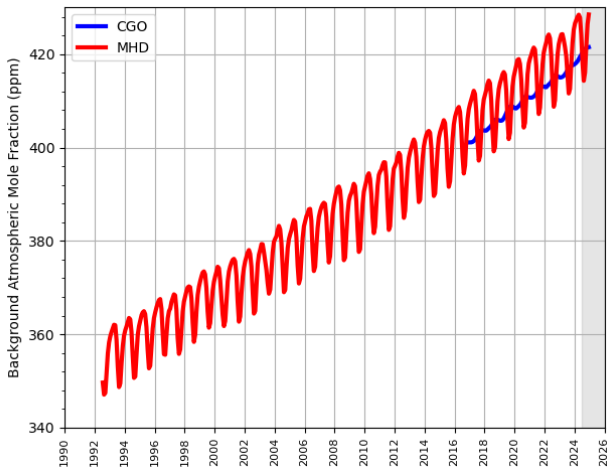

3 Key findings

- Methane (CH_4): Overall, inverse models estimate higher emissions than the inventory (Figure 4.0.2). Between 2017 and 2023, the mean over the six standard inversions is 10-20 % higher than the inventory. The decreasing trend reported in the inventory is captured by the inversion results only during 2015-2020, with growing discrepancy afterwards. For annual emission totals, relatively good agreement between the inversion systems is reached. Inverse estimates by the more independent ITMS-D inversion system are at the upper end of the inversion ensemble (almost 30 % larger than the inventory). CH_4 emissions are maximum in the north-west of the country, which is largely dominated by intense agriculture (Figure 4.0.5). High emissions are also obtained in the neighbouring countries, which makes it challenging to fully differentiate the German emissions from those from the Benelux region. For most inversions, higher emissions are obtained during the autumn and winter months (Figures 4.0.4 and 4.0.6). However, the seasonality is not uniform in all sensitivity inversions, but somewhat depends on the employed atmospheric transport model, with NAME and ICON-ART based inversions favouring a pronounced winter/autumn peak, whereas FLEXPART based inversions tend towards reduced seasonality. Overall, the seasonality is attributed to areas with intensive agriculture and large livestock density (north-western and south-eastern Germany), but stretches into neighbouring countries as well (Benelux and France).

- Nitrous oxide (N_2O): The inverse results show a stronger year-to-year variability than the inventory (Figure 5.0.2). Between 2020 and 2023, the mean over the six inverse estimates is in good agreement with the inventory ($\sim$10 % higher). N_2O emissions are maximum in the north-west of the country, with secondary maxima in Bavaria, Thuringia, and Saxony (Figure 5.0.5). Higher emissions are obtained during the summer months (Figures 5.0.4 and 5.0.6). The strongest seasonality is seen in the north-west of the country, Bavaria and all of eastern Germany, again indicating a seasonality in agricultural emissions.

- Hydrofluorocarbons (HFCs): The European measurement network for HFCs and PFCs is significantly smaller than for methane and nitrous oxide (Figure 6.0.1). This increases the uncertainty of the model predictions especially before 2021. Compared to last year's report, observations from additional measurement sites were included in the inverse modelling, most importantly data from Taunus Observatory and Zugspitze added to the coverage of German emissions. Overall, very similar emissions are obtained from the inverse models as given in the inventory when looking at the sum of all HFCs (Figure 6.7.1). Also for individual HFCs, the inventory values are mostly within the estimated model uncertainty. Most important aspects for individual gases are the increasing trend of HFC-32 (Figure 6.6.1) and the decreasing trend of HFC-125 (Figure 6.1.1), HFC-134a (Figure 6.2.1), and HFC-152a (Figure 6.4.1) that is visible in both reporting and inverse modelling.

- Perfluorocarbons (PFCs): PFC emissions in Germany are small in comparison to the remaining greenhouse gases investigated. The sporadic nature of the emissions and the sparse measurement network result in high model uncertainties. Generally, PFC emissions in the inversions are a factor of two to four larger than in the inventory (Figure 7.1.1), which could indicate insufficient exhaust gas treatment by industries. Relatively high emissions of all PFCs are seen around the Rhur region (Figures 7.1.2, 7.2.2, 7.3.2, and 7.4.2).

- Sulphur hexafluoride (SF_6): A reasonable agreement is obtained between the inverse results and the inventory (Figure 8.0.2). High emissions are obtained in the south-west of the country (Figure 8.0.3), where a factory of SF_6 is known to exist. Note that all inverse models assumed uniform emissions of SF_6 over Germany as their prior spatial distribution. Nevertheless, they all pick up the emission hot spot solely based on the atmospheric observations. In comparison to last years report additional observations were included in the inversion, namely continuous observations from Taunus observatory and Zugspitze, as well as flask sampling from German ICOS stations. For SF_6 no inversion results were obtained with RHIME due to technical difficulties.

Table 1: Emissions estimation for the main greenhouse gases of focus according to the National Inventory Document (NID) 2025 and the inversions done in the PARIS project. For the PARIS estimation, the mean of all models is displayed, along with a range of uncertainty estimated via the half distance between the maximum and minimum uncertainties of the different models. For SF_6, the PARIS mean is the average of all InTEM and ELRIS inversions only.

		2020	2021	2022	2023	2024
CH_4	NID 2025	54.4	54.1	52.1	52.7	
$(\mathrm{TgCO_2\text{-}eq \cdot yr^{-1}})$	PARIS mean	59.9 ± 8.5	61.4 ± 10.1	64.1 ± 7.1	65.3 ± 8.1	68.9 ± 10.4
N_2O	NID 2025	27.4	26.7	26.4	24.9	
$(\mathrm{TgCO_2\text{-}eq \cdot yr^{-1}})$	PARIS mean	29.9 ± 5.4	33.3 ± 5.3	24.9 ± 3.5	28.9 ± 3.4	32.5 ± 4.3
Total HFC	NID 2025	8.0	7.8	7.5	7.3	
$(\mathrm{TgCO_2\text{-}eq \cdot yr^{-1}})$	PARIS mean	8.7 ± 2.3	8.2 ± 1.9	7.2 ± 1.5	6.7 ± 1.2	6.5 ± 1.1
SF_6	NID 2025	3.1	2.7	2.0	1.8	
$(\mathrm{TgCO_2\text{-}eq \cdot yr^{-1}})$	PARIS mean	2.5 ± 0.7	2.3 ± 0.5	2.1 ± 0.4	1.9 ± 0.3	1.8 ± 0.3
Total PFC	NID 2025	0.19	0.19	0.16	0.15	
$(\mathrm{TgCO_2\text{-}eq \cdot yr^{-1}})$	PARIS mean	0.44 ± 0.37	0.40 ± 0.36	0.45 ± 0.40	0.45 ± 0.38	0.48 ± 0.35

4 Methane (CH_4)

Figure 4.0.1: Average monthly total source sensitivity of CH_4 observing sites as calculated by the FLEXPART transport model for the year 2018 (left) and 2024 (right) and used in the inversions. Observing stations active in each year are marked with red dots. Areas with visible land surface represent regions for which emissions can be observed well from the network. Shaded or dark areas represent regions for which limited emission information can be obtained from the network.

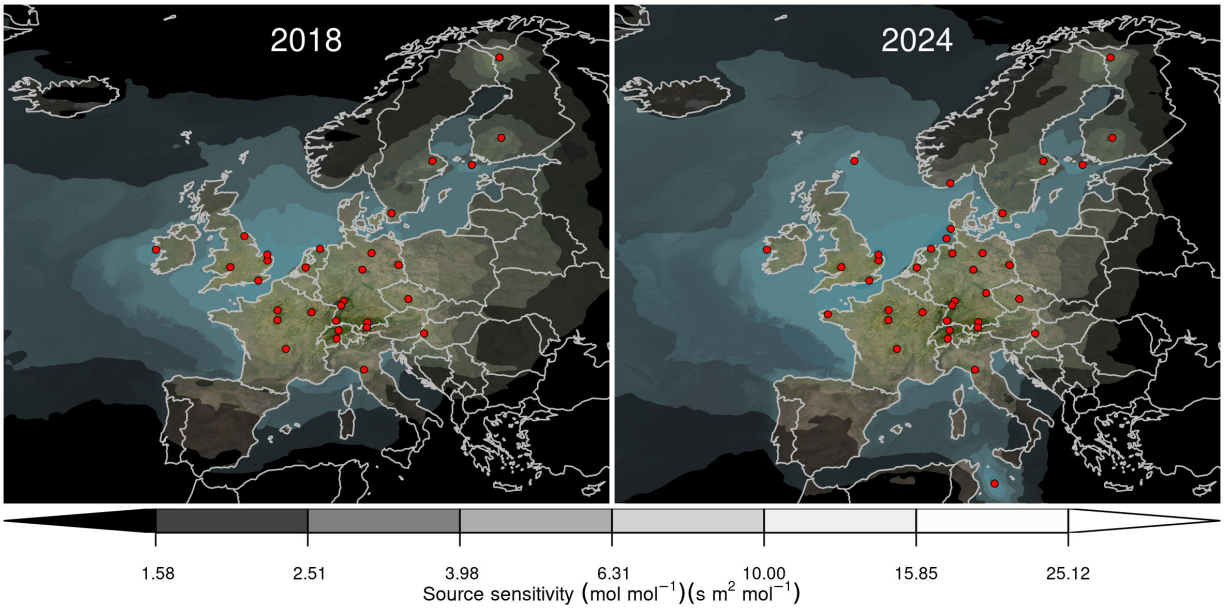

Figure 4.0.2: Verification of the German emissions inventory estimates for CH_4. Modelled annual emissions are given as the mean from all InTEM, ELRIS and RHIME inversions (black line) and the individual results from InTEM-NAME (blue line) and ITMS-D (orange line). The shaded blue and orange areas are the 68 % confidence interval (CI) of InTEM-NAME and ITMS-D, respectively, and the shaded grey area encompasses the 68 % CI from all InTEM, ELRIS and RHIME inversions. National inventory annual totals from 2024 and 2025 are given as grey and black bars, respectively.

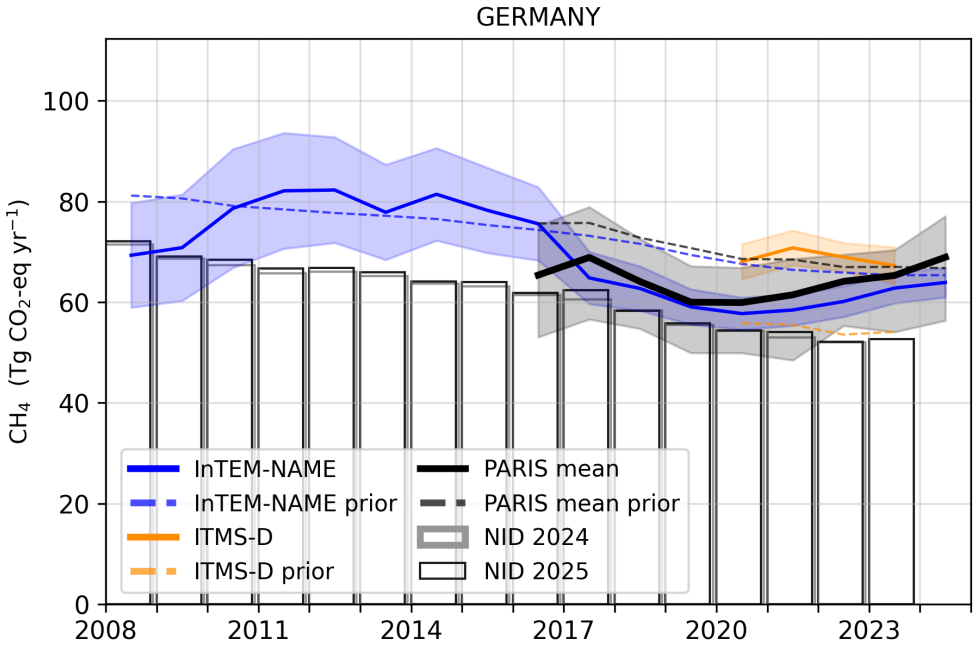

Figure 4.0.3: Verification of the German emissions inventory estimates for CH_4 (zoom in to 2018-2024). Modelled annual emissions are given as the mean from all InTEM, ELRIS and RHIME inversions (black line) and the individual results from InTEM-NAME (blue line) and ITMS-D (orange line). The shaded blue and orange areas are the 68 % confidence interval (CI) of InTEM-NAME and ITMS-D, respectively, and the shaded grey area encompasses the 68 % CI from all InTEM, ELRIS and RHIME inversions. National inventory annual totals from 2024 and 2025 are given as grey and black bars, respectively.

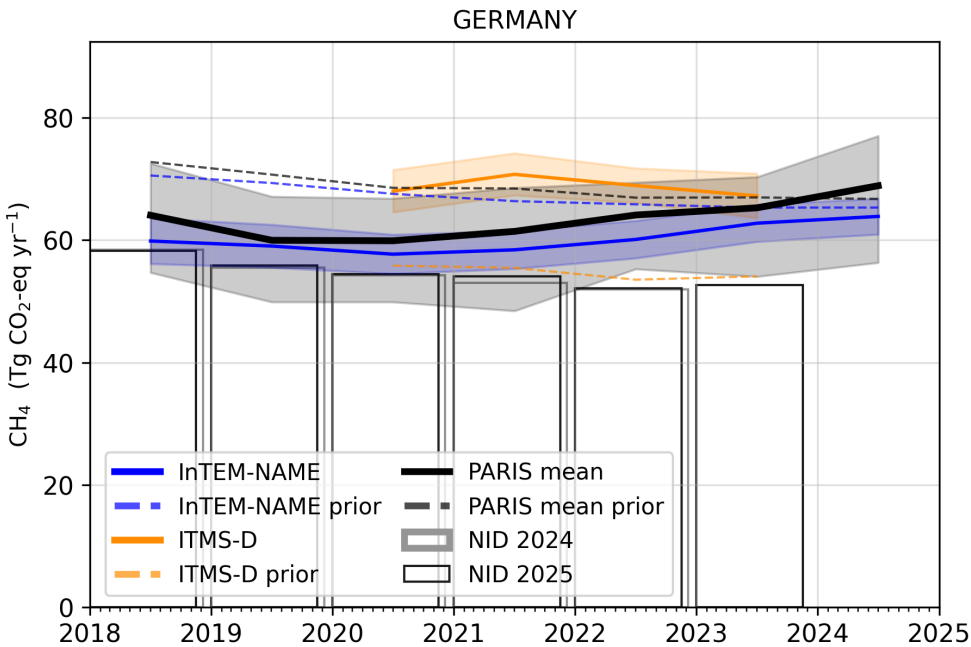

Figure 4.0.4: Verification of the German emissions inventory estimates for CH_4 (zoom in to 2018-2024). Modelled monthly emissions are given as the mean from all InTEM, ELRIS and RHIME inversions (black line) and the individual results from InTEM-NAME (blue line) and ITMS-D (orange line). The shaded blue and orange areas are the 68 % confidence interval (CI) of InTEM-NAME and ITMS-D, respectively, and the shaded grey area encompasses the 68 % CI from all InTEM, ELRIS and RHIME inversions. National inventory annual totals from 2024 and 2025 are given as grey and black bars, respectively.

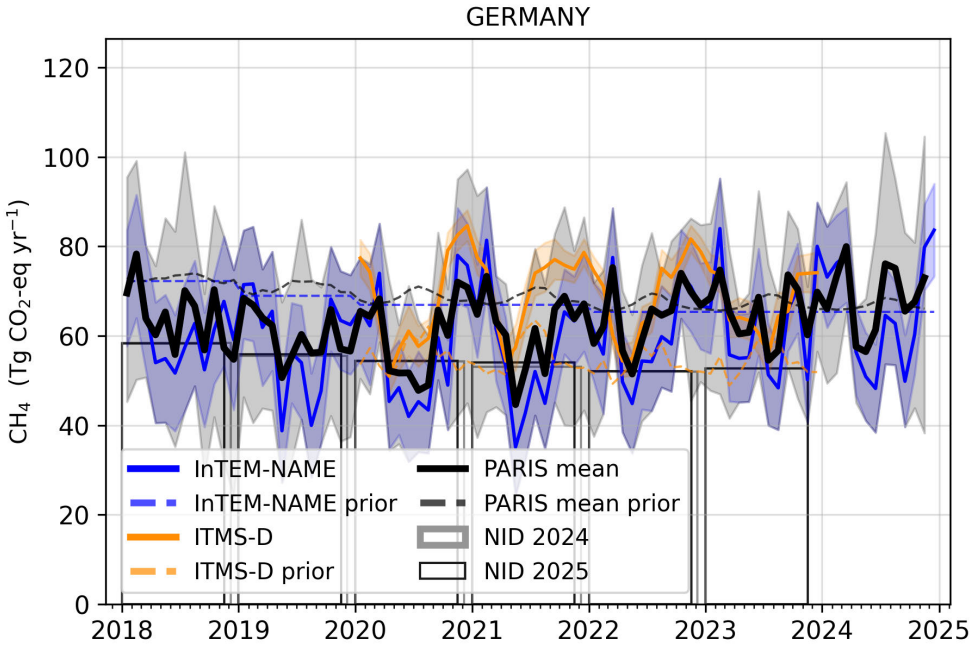

Figure 4.0.5: Spatial distribution of the German average modelled emissions of CH_4 during the period of 2020-2023. Comparison between a) mean from all InTEM, ELRIS and RHIME inversions and b) mean from ITMS-D inversions. Observing stations are marked with red circles and highly-populated cities are marked with red triangles.

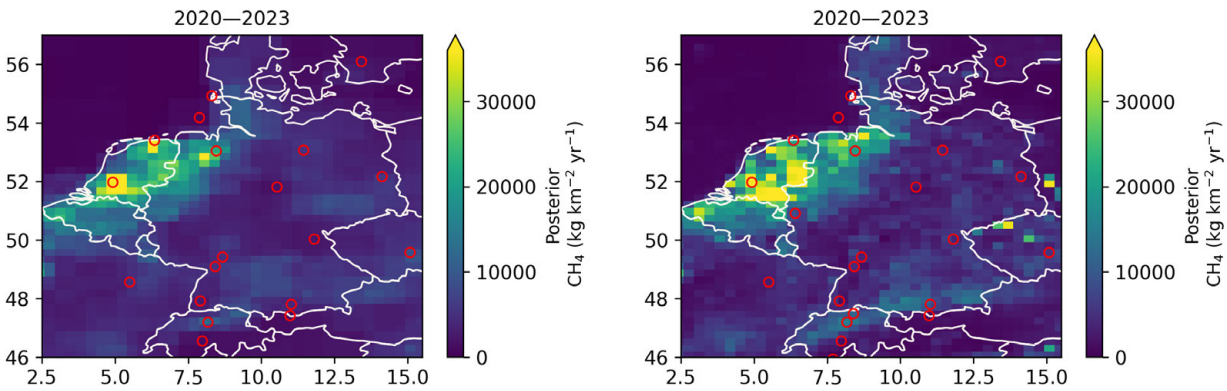

(a) InTEM, ELRIS and RHIME **(b) ITMS-D**

Figure 4.0.6: Spatial distribution of the seasonal deviation from the mean. The deviation is defined as the modelled German seasonally averaged CH_4 emissions over 2020-2023 minus the average over the whole period. Comparison between a) mean from all InTEM, ELRIS and RHIME inversions and b) mean from ITMS-D inversions. Observing stations are marked with black circles and highly-populated cities are marked with black triangles.

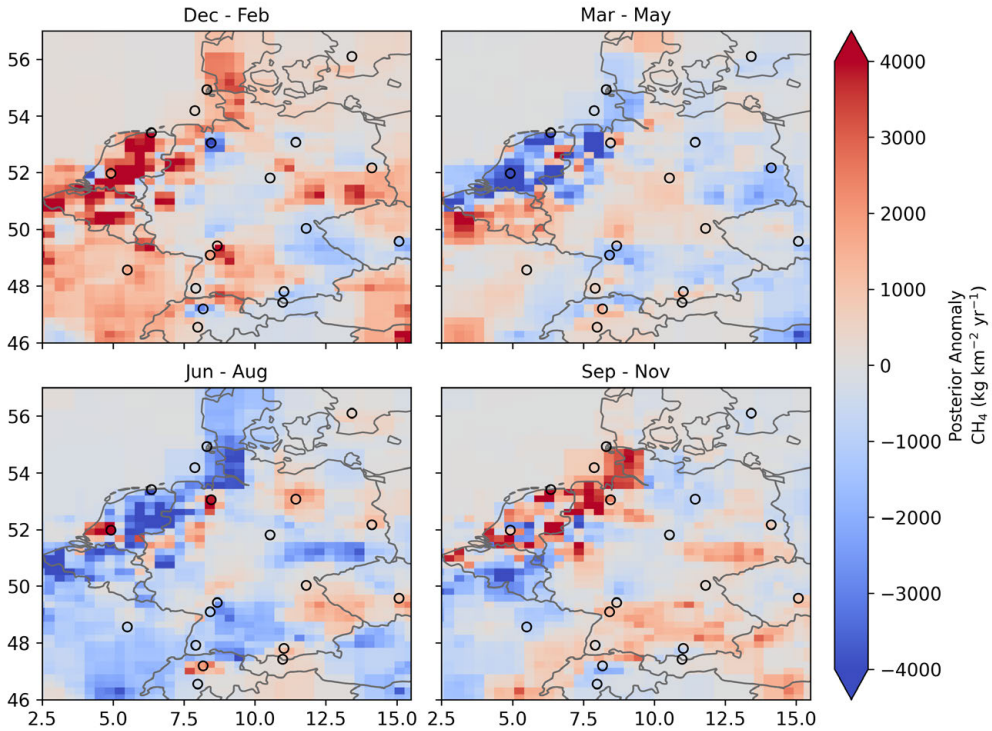

(a) InTEM, ELRIS and RHIME

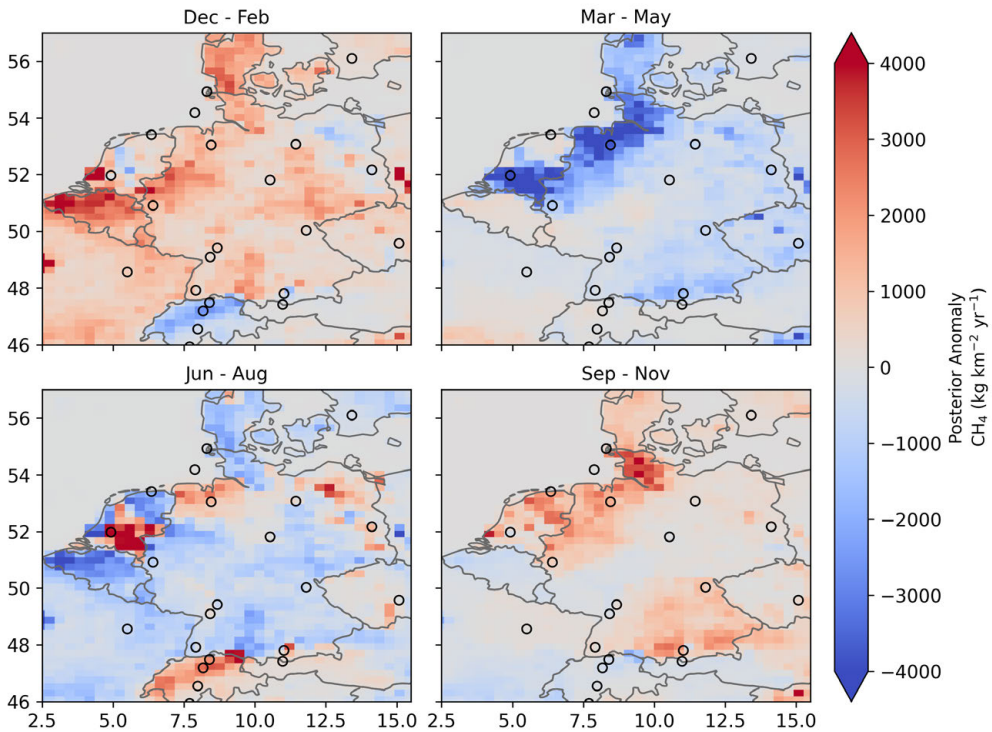

(b) ITMS-D

5 Nitrous Oxide (N_2O)

Figure 5.0.1: Average monthly total source sensitivity of N_2O observing sites as calculated by the FLEXPART transport model for the year 2018 (left) and 2024 (right) and used in the inversions. Observing stations active in each year are marked with red dots. Areas with visible land surface represent regions for which emissions can be observed well from the network. Shaded or dark areas represent regions for which limited emission information can be obtained from the network.

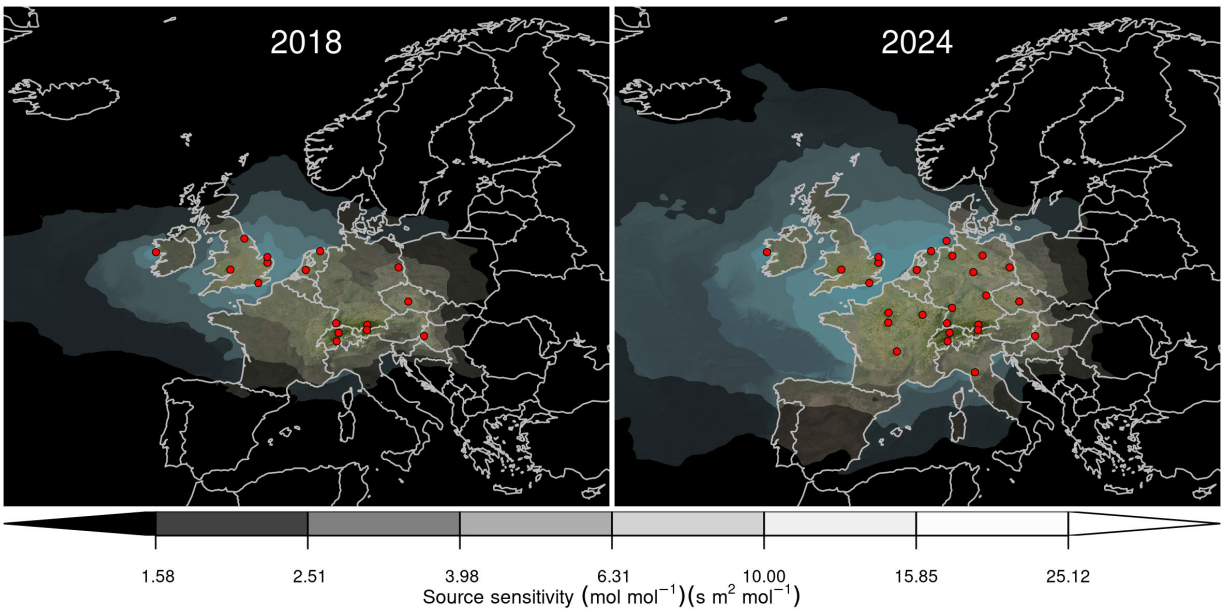

Figure 5.0.2: Verification of the German emissions inventory estimates for N_2O. Modelled annual emissions are given as the mean from all models (black line) and the individual result from InTEM-NAME (blue line). The shaded blue area is the 68 % confidence interval (CI) of InTEM-NAME and the shaded grey area encompasses the 68 % CI from all models. National inventory annual totals from 2024 and 2025 are given as grey and black bars, respectively.

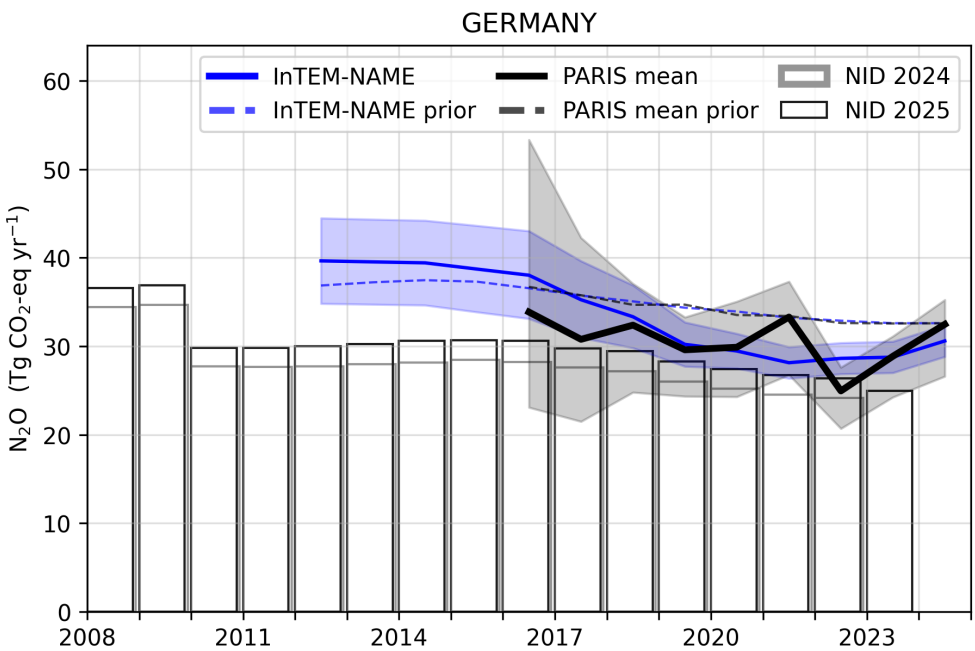

Figure 5.0.3: Verification of the German emissions inventory estimates for N_2O (zoom in to 2018-2024). Modelled annual emissions are given as the mean from all models (black line) and the individual result from InTEM-NAME (blue line). The shaded blue area is the 68 % confidence interval (CI) of InTEM-NAME and the shaded grey area encompasses the 68 % CI from all models. National inventory annual totals from 2024 and 2025 are given as grey and black bars, respectively.

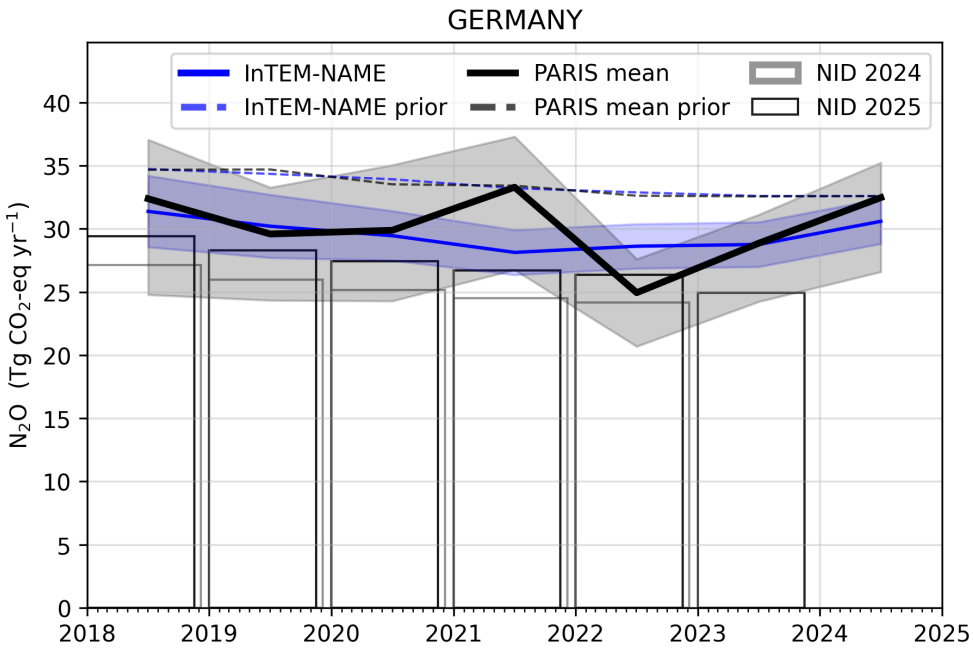

Figure 5.0.4: Verification of the German emissions inventory estimates for N_2O (zoom in to 2018-2024). Modelled monthly emissions are given as the mean from all models (black line) and the individual result from InTEM-NAME (blue line). The shaded blue area is the 68 % confidence interval (CI) of InTEM-NAME and the shaded grey area encompasses the 68 % CI from all models. National inventory annual totals from 2024 and 2025 are given as grey and black bars, respectively.

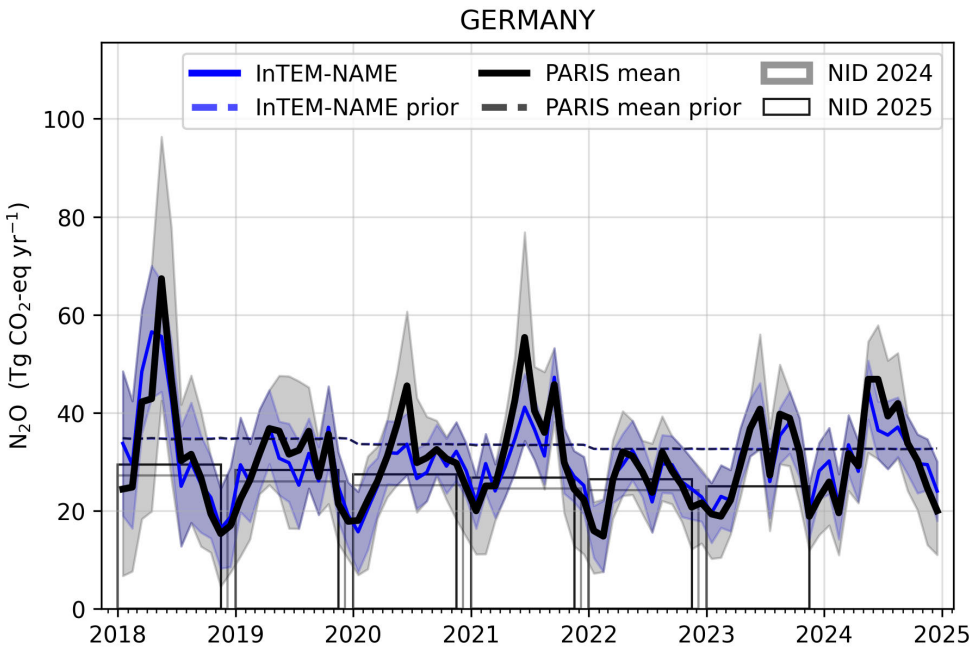

Figure 5.0.5: Spatial distribution of the German average modelled emissions of N_2O during the period of 2020-2024 (mean from all models). Observing stations are marked with red circles and highly-populated cities are marked with red triangles.

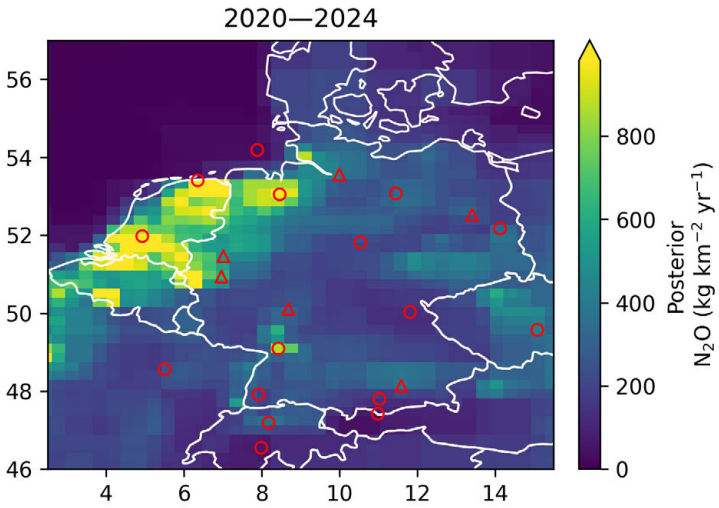

Figure 5.0.6: Spatial distribution of the seasonal deviation from the mean. The deviation is defined as the modelled German seasonally averaged N_2O emissions over 2020-2024 minus the average over the whole period. The mean across all models is shown. Observing stations are marked with black circles and highly-populated cities are marked with black triangles.

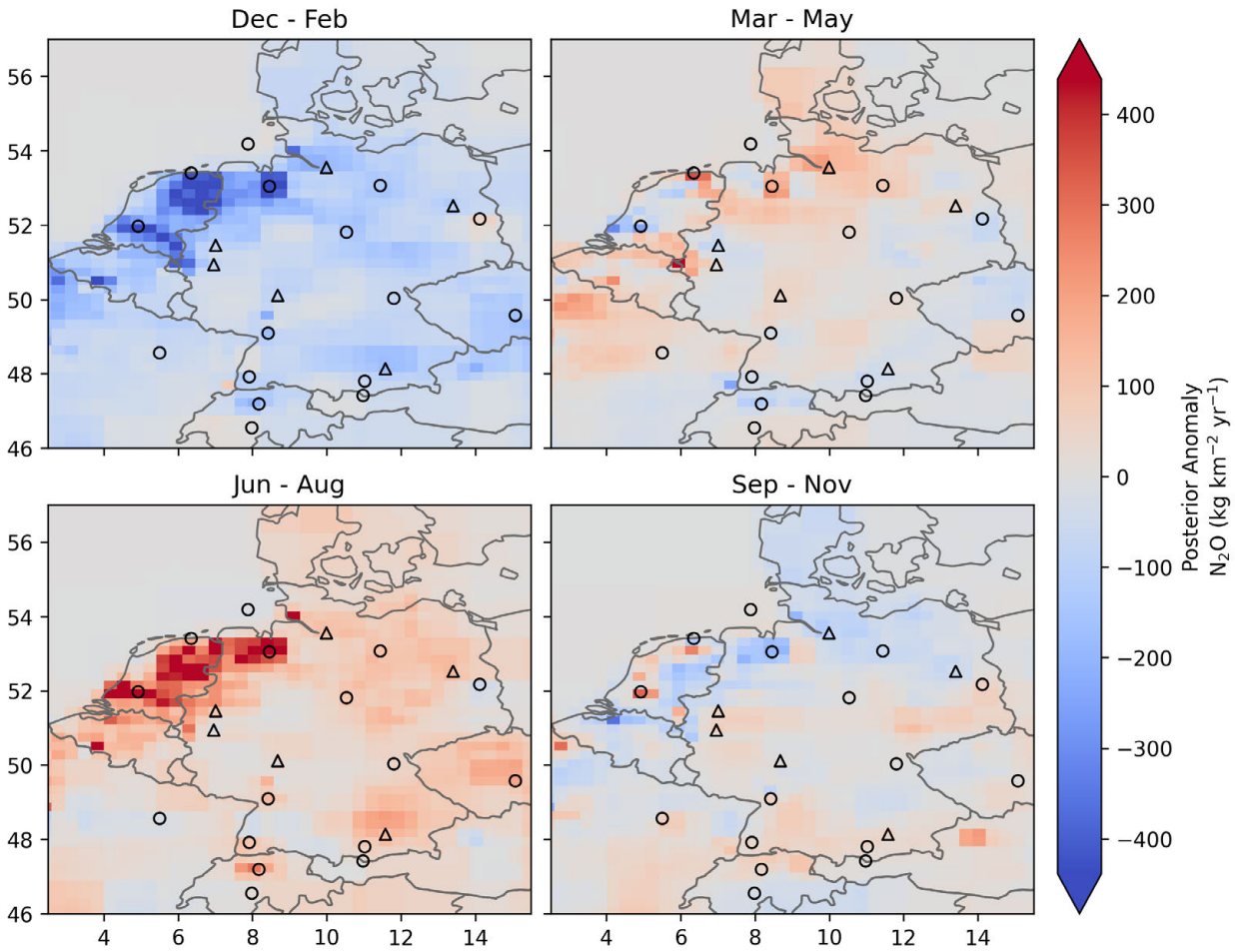

6 Hydrofluorocarbons (HFCs)

Figure 6.0.1: Total source sensitivity of HFCs/PFCs observing sites as calculated by the FLEXPART transport model for the year 2018 (left) and 2024 (right) and used in the inversions. Observing stations active in each year are marked with red dots. Areas with visible land surface represent regions for which emissions can be observed well from the network. Shaded or dark areas represent regions for which limited emission information can be obtained from the network.

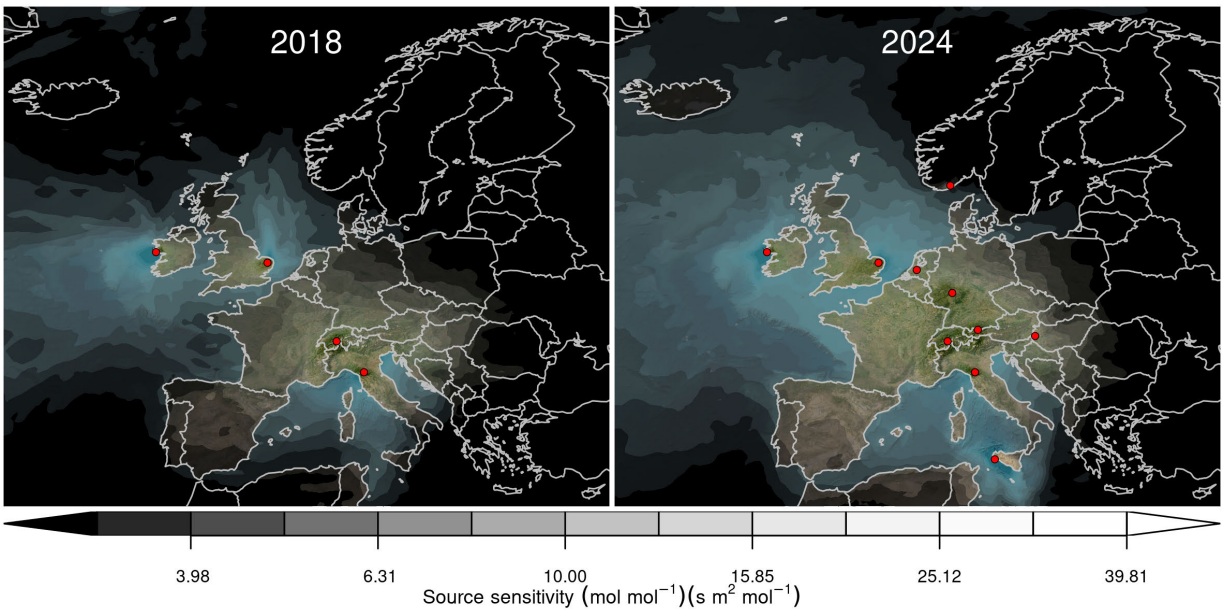

6.1 HFC-125

Figure 6.1.1: Verification of the German emissions inventory estimates for HFC-125. Modelled annual emissions are given as the mean from all models (black line) and the individual result from InTEM-NAME (blue line). The shaded blue area is the 68 % confidence interval (CI) of InTEM-NAME and the shaded grey area encompasses the 68 % CI from all models. National inventory annual totals from 2024 and 2025 are given as grey and black bars, respectively.

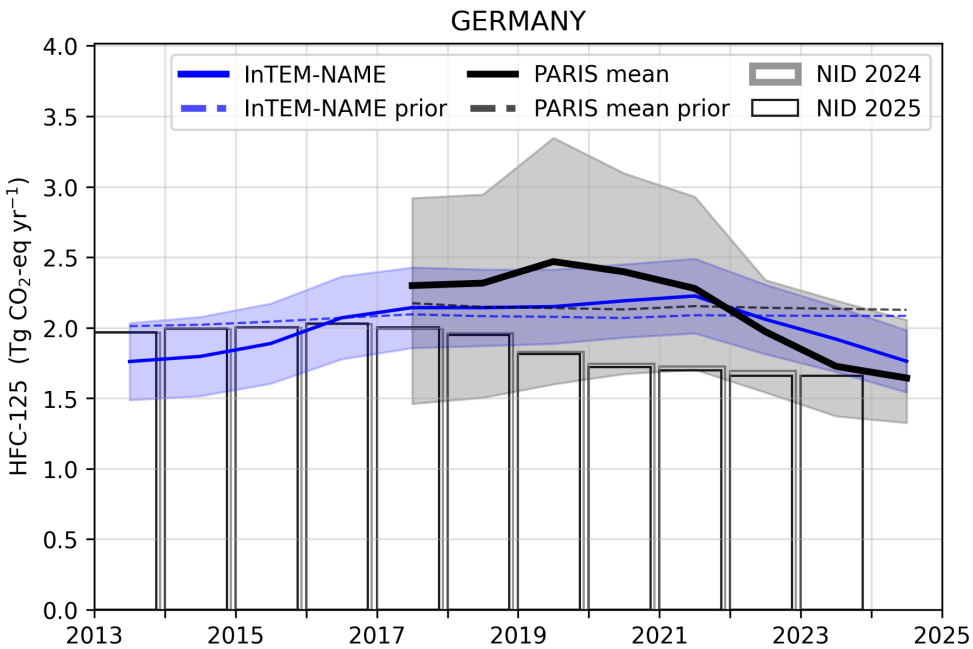

Figure 6.1.2: Spatial distribution of the German average modelled emissions of HFC-125 during the period of 2020-2024 (mean from all models). Observing stations are marked with red circles and highly-populated cities are marked with red triangles.

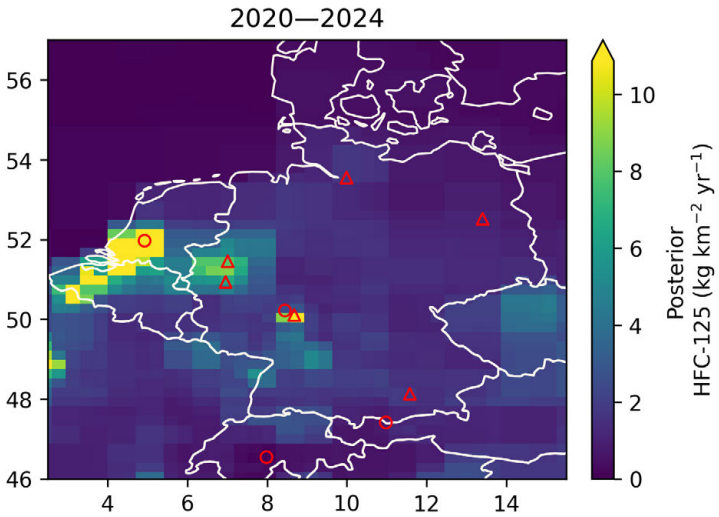

6.2 HFC-134a

Figure 6.2.1: Verification of the German emissions inventory estimates for HFC-134a. Modelled annual emissions are given as the mean from all models (black line) and the individual result from InTEM-NAME (blue line). The shaded blue area is the 68 % confidence interval (CI) of InTEM-NAME and the shaded grey area encompasses the 68 % CI from all models. National inventory annual totals from 2024 and 2025 are given as grey and black bars, respectively.

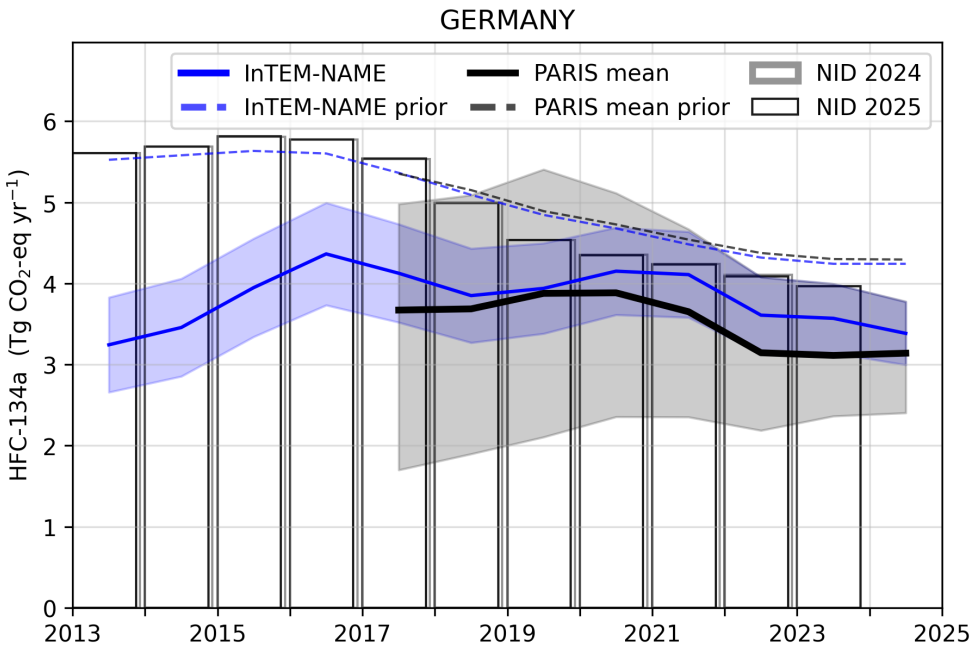

Figure 6.2.2: Spatial distribution of the German average modelled emissions of HFC-134a during the period of 2020-2024 (mean from all models). Observing stations are marked with red circles and highly-populated cities are marked with red triangles.

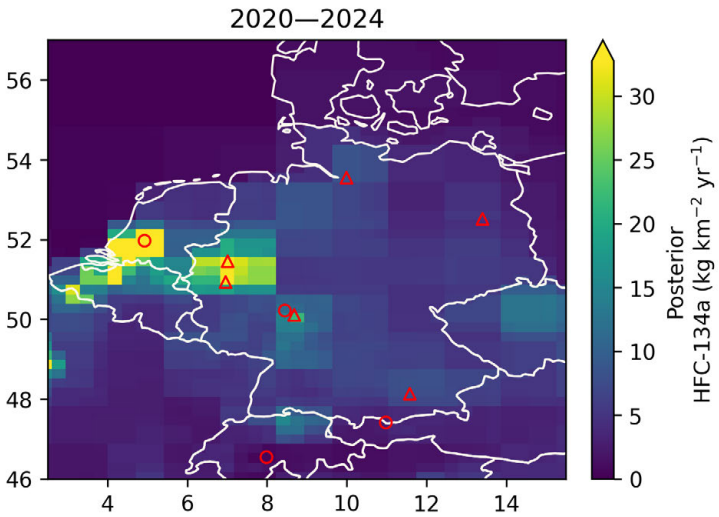

6.3 HFC-143a

Figure 6.3.1: Verification of the German emissions inventory estimates for HFC-143a. Modelled annual emissions are given as the mean from all models (black line) and the individual result from InTEM-NAME (blue line). The shaded blue area is the 68 % confidence interval (CI) of InTEM-NAME and the shaded grey area encompasses the 68 % CI from all models. National inventory annual totals from 2024 and 2025 are given as grey and black bars, respectively.

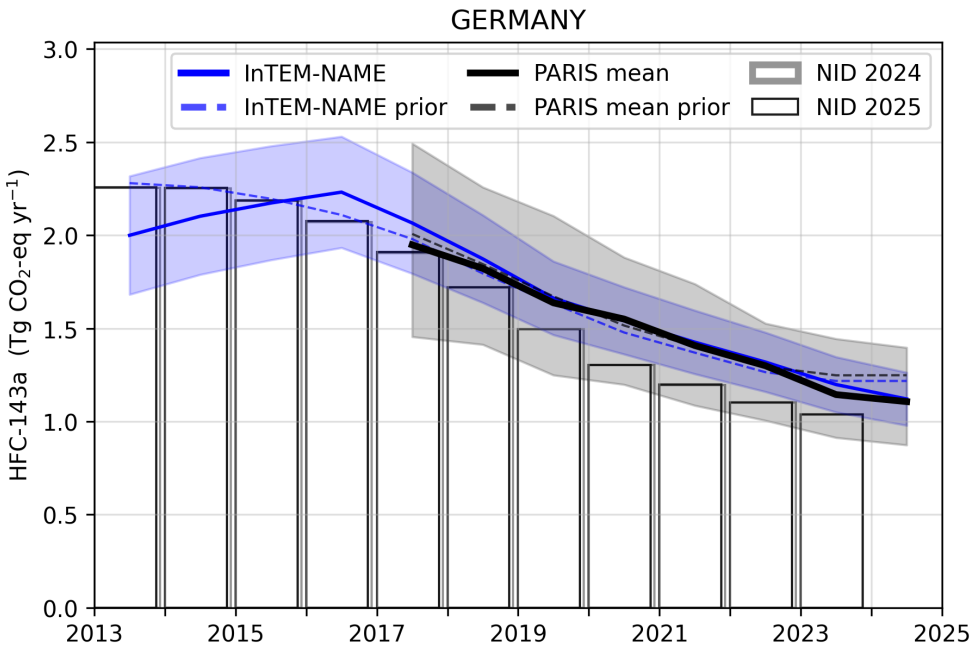

Figure 6.3.2: Spatial distribution of the German average modelled emissions of HFC-143a during the period of 2020-2024 (mean from all models). Observing stations are marked with red circles and highly-populated cities are marked with red triangles.

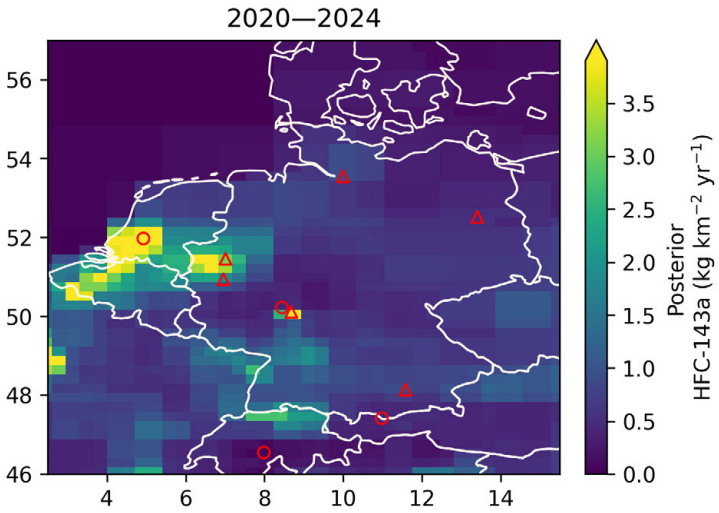

6.4 HFC-152a

Figure 6.4.1: Verification of the German emissions inventory estimates for HFC-152a. Modelled annual emissions are given as the mean from all models (black line) and the individual result from InTEM-NAME (blue line). The shaded blue area is the 68 % confidence interval (CI) of InTEM-NAME and the shaded grey area encompasses the 68 % CI from all models. National inventory annual totals from 2024 and 2025 are given as grey and black bars, respectively.

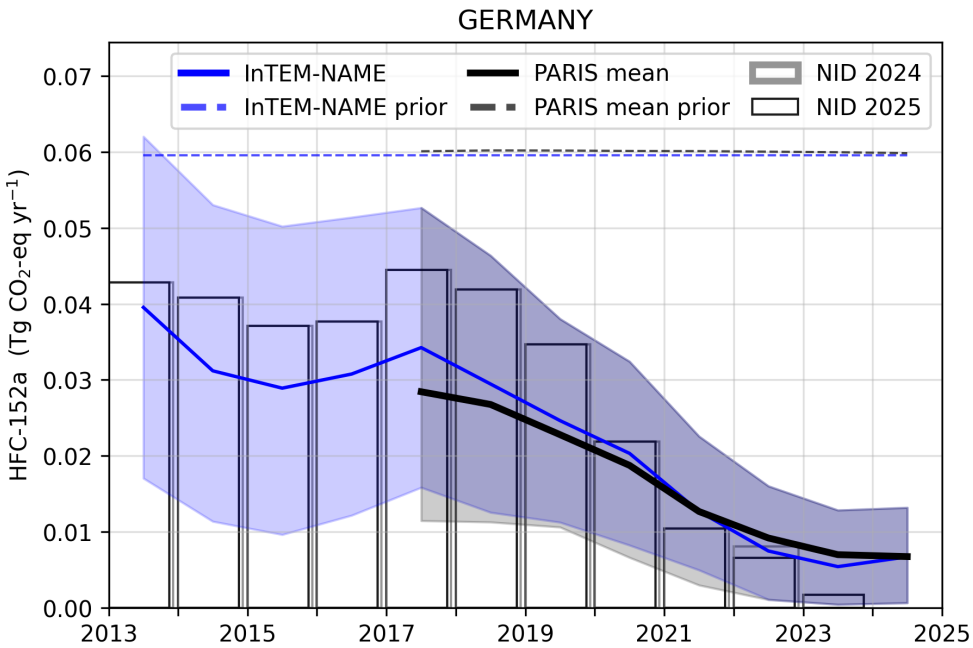

Figure 6.4.2: Spatial distribution of the German average modelled emissions of HFC-152a during the period of 2020-2024 (mean from all models). Observing stations are marked with red circles and highly-populated cities are marked with red triangles.

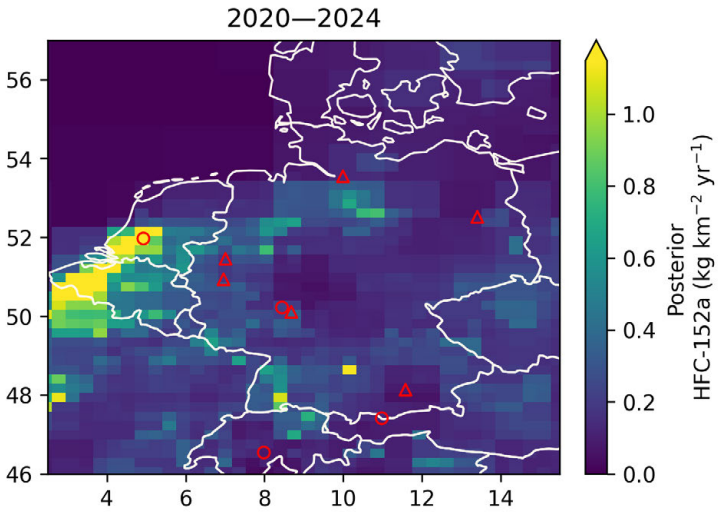

6.5 HFC-227ea

Figure 6.5.1: Verification of the German emissions inventory estimates for HFC-227ea. Modelled annual emissions are given as the mean from all models (black line) and the individual result from InTEM-NAME (blue line). The shaded blue area is the 68 % confidence interval (CI) of InTEM-NAME and the shaded grey area encompasses the 68 % CI from all models. National inventory annual totals from 2024 and 2025 are given as grey and black bars, respectively.

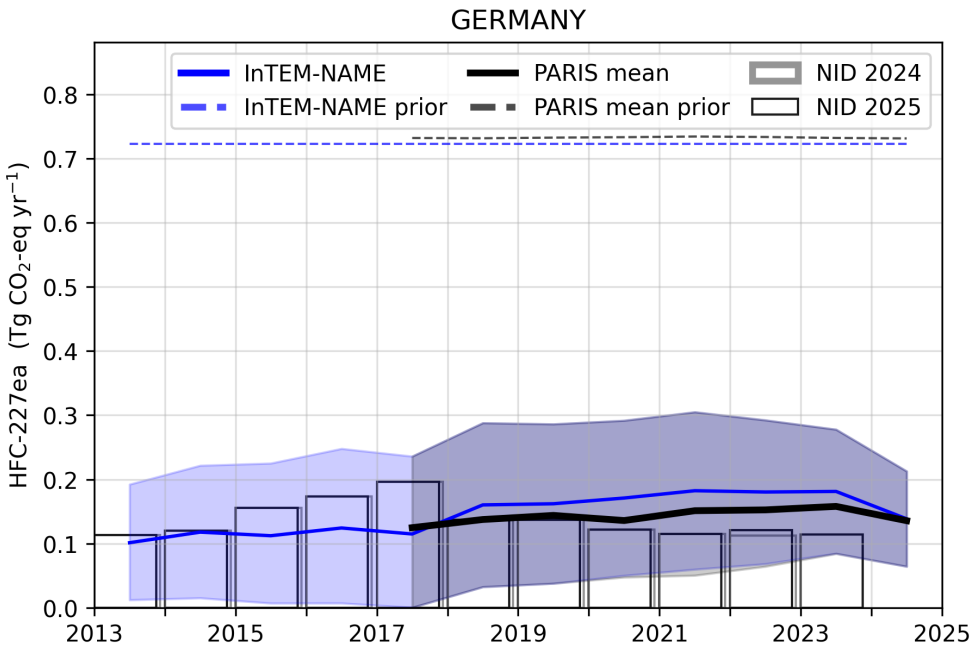

Figure 6.5.2: Spatial distribution of the German average modelled emissions of HFC-227ea during the period of 2020-2024 (mean from all models). Observing stations are marked with red circles and highly-populated cities are marked with red triangles.

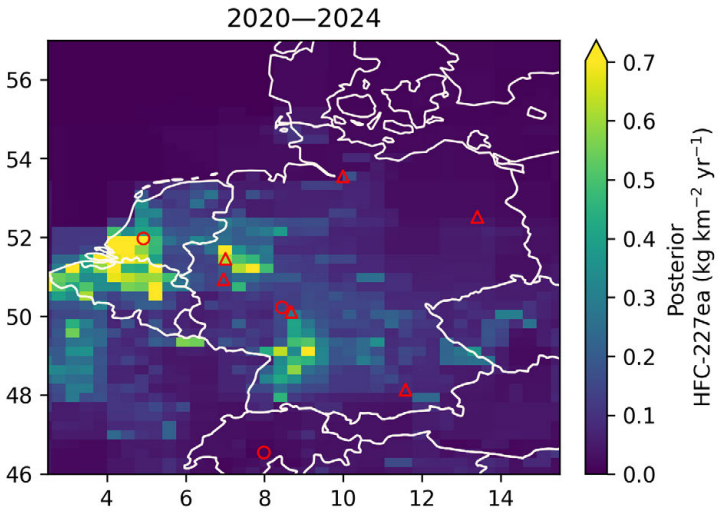

6.6 HFC-32

Figure 6.6.1: Verification of the German emissions inventory estimates for HFC-32. Modelled annual emissions are given as the mean from all models (black line) and the individual result from InTEM-NAME (blue line). The shaded blue area is the 68 % confidence interval (CI) of InTEM-NAME and the shaded grey area encompasses the 68 % CI from all models. National inventory annual totals from 2024 and 2025 are given as grey and black bars, respectively.

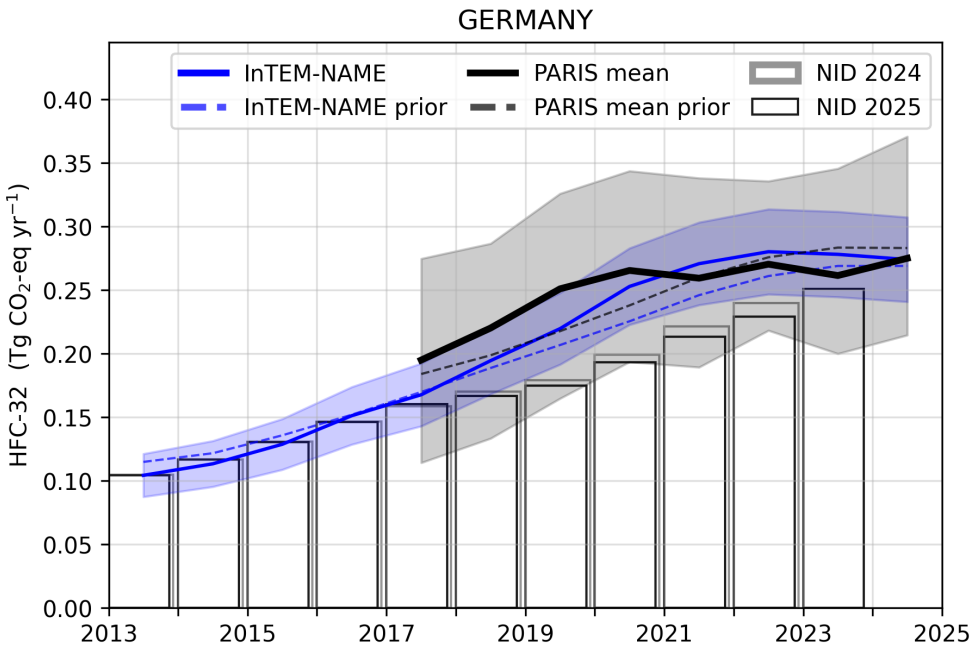

Figure 6.6.2: Spatial distribution of the German average modelled emissions of HFC-32 during the period of 2020-2024 (mean from all models). Observing stations are marked with red circles and highly-populated cities are marked with red triangles.

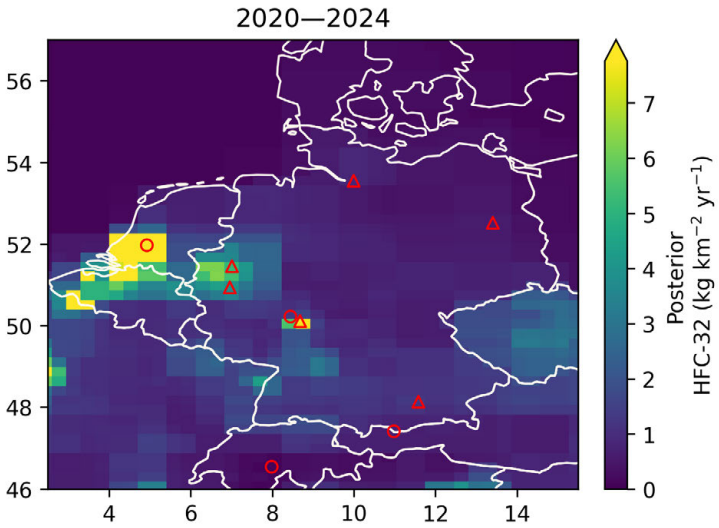

6.7 Total HFCs

Figure 6.7.1: Verification of the German emissions inventory estimates for total HFCs. Modelled annual emissions are given as the mean from all models (black line) and the individual result from InTEM-NAME (blue line). The shaded blue area is the 68 % confidence interval (CI) of InTEM-NAME and the shaded grey area encompasses the 68 % CI from all models. National inventory annual totals from 2024 and 2025 are given as grey and black bars, respectively.

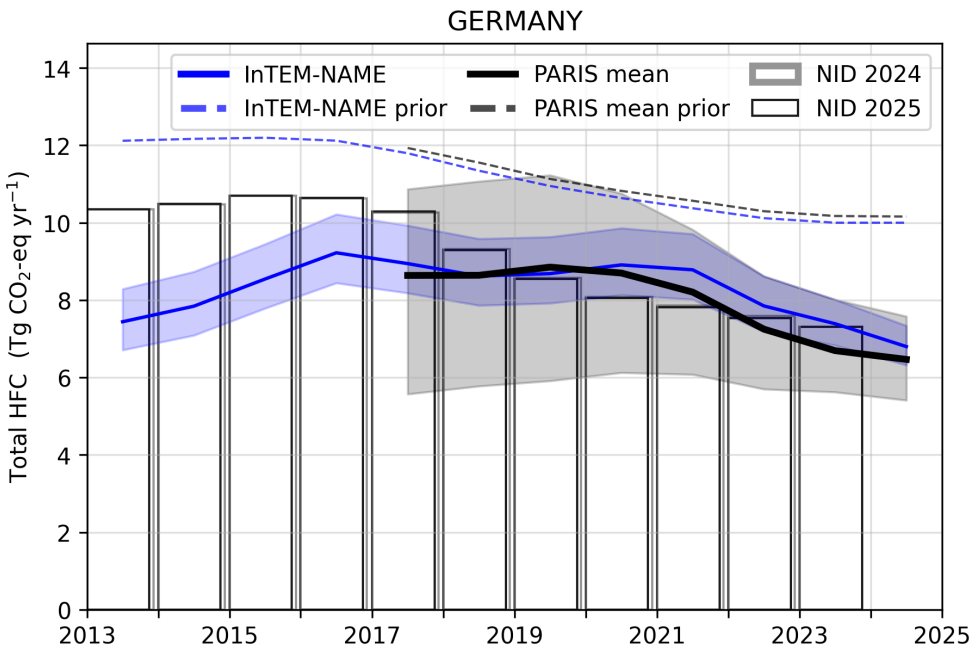

Table 2: Emissions estimation for HFCs according to the National Inventory Document (NID) 2025 and the inversions done in the PARIS project. For the PARIS estimation, the mean of all models is displayed, along with a range of uncertainty estimated via the half distance between the maximum and minimum uncertainties of the different models.

		2020	2021	2022	2023	2024
HFC-134a	NID 2025	4.3	4.2	4.1	4.0	
$(\mathrm{TgCO_2\text{-}eq \cdot yr^{-1}})$	PARIS mean	3.9 ± 1.4	3.7 ± 1.2	3.1 ± 0.9	3.1 ± 0.8	3.1 ± 0.7
HFC-125	NID 2025	1.7	1.7	1.7	1.7	
$(\mathrm{TgCO_2\text{-}eq \cdot yr^{-1}})$	PARIS mean	2.4 ± 0.7	2.3 ± 0.6	2.0 ± 0.4	1.7 ± 0.4	1.6 ± 0.4
HFC-143a	NID 2025	1.3	1.2	1.1	1.0	
$(\mathrm{TgCO_2\text{-}eq \cdot yr^{-1}})$	PARIS mean	1.6 ± 0.3	1.4 ± 0.3	1.3 ± 0.3	1.1 ± 0.3	1.1 ± 0.3
HFC-32	NID 2025	0.19	0.21	0.23	0.25	
$(\mathrm{TgCO_2\text{-}eq \cdot yr^{-1}})$	PARIS mean	0.27 ± 0.08	0.26 ± 0.07	0.27 ± 0.06	0.26 ± 0.07	0.28 ± 0.08
HFC-23	NID 2025	0.06	0.08	0.05	0.05	
$(\mathrm{TgCO_2\text{-}eq \cdot yr^{-1}})$	PARIS mean	0.31 ± 0.57	0.32 ± 0.55	0.31 ± 0.40	0.21 ± 0.25	0.10 ± 0.15
HFC-227ea	NID 2025	0.12	0.11	0.12	0.11	
$(\mathrm{TgCO_2\text{-}eq \cdot yr^{-1}})$	PARIS mean	0.14 ± 0.12	0.15 ± 0.13	0.15 ± 0.11	0.16 ± 0.10	0.14 ± 0.07
HFC-365mfc	NID 2025	91	84	85	23	
$(\mathrm{GgCO_2\text{-}eq \cdot yr^{-1}})$	PARIS mean	85 ± 58	72 ± 44	44 ± 34	29 ± 25	17 ± 15
HFC-245fa	NID 2025	0.18	0.19	0.19	0.20	
$(\mathrm{TgCO_2\text{-}eq \cdot yr^{-1}})$	PARIS mean	0.03 ± 0.03	0.03 ± 0.03	0.02 ± 0.03	0.02 ± 0.02	0.02 ± 0.02
HFC-236fa	NID 2025	37	37	38	37	
$(\mathrm{GgCO_2\text{-}eq \cdot yr^{-1}})$	PARIS mean	18 ± 33	21 ± 36	14 ± 24	16 ± 23	13 ± 16
HFC-152a	NID 2025	22	10	7	2	
$(\mathrm{GgCO_2\text{-}eq \cdot yr^{-1}})$	PARIS mean	19 ± 13	13 ± 10	9 ± 7	7 ± 6	7 ± 6
HFC-4310mee	NID 2025	0.0	0.0	0.0	0.0	
$(\mathrm{GgCO_2\text{-}eq \cdot yr^{-1}})$	PARIS mean	7.2 ± 11.4	5.0 ± 9.1	6.7 ± 12.1	8.0 ± 12.6	9.0 ± 13.4

7 Perfluorocarbons (PFCs)

7.1 PFC-14

Figure 7.1.1: Verification of the German emissions inventory estimates for PFC-14. Modelled annual emissions are given as the mean from all models (black line) and the individual result from InTEM-NAME (blue line). The shaded blue area is the 68 % confidence interval (CI) of InTEM-NAME and the shaded grey area encompasses the 68 % CI from all models. National inventory annual totals from 2024 and 2025 are given as grey and black bars, respectively.

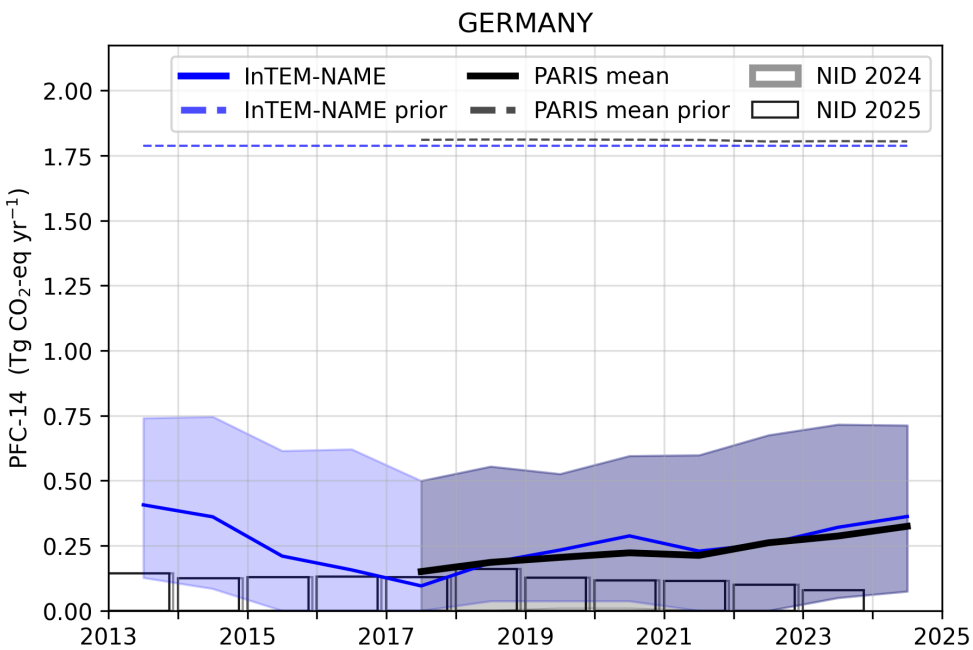

Figure 7.1.2: Spatial distribution of the German average modelled emissions of PFC-14 during the period of 2020-2024 (mean from all models). Observing stations are marked with red circles and highly-populated cities are marked with red triangles.

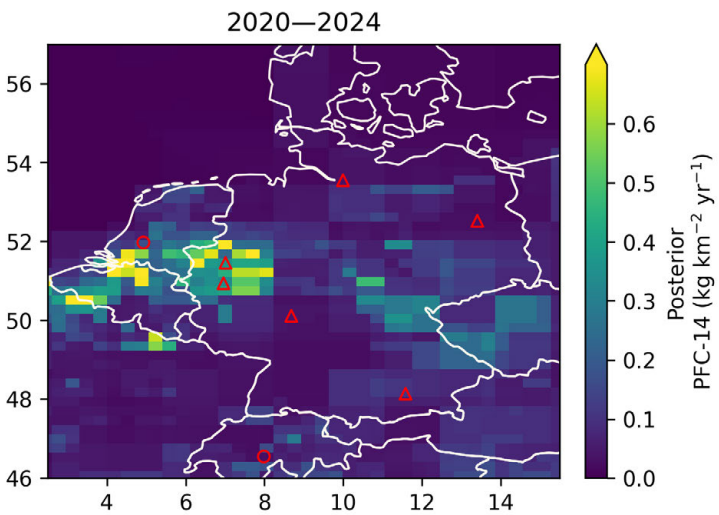

7.2 PFC-116

Figure 7.2.1: Verification of the German emissions inventory estimates for PFC-116. Modelled annual emissions are given as the mean from all models (black line) and the individual result from InTEM-NAME (blue line). The shaded blue area is the 68 % confidence interval (CI) of InTEM-NAME and the shaded grey area encompasses the 68 % CI from all models. National inventory annual totals from 2024 and 2025 are given as grey and black bars, respectively.

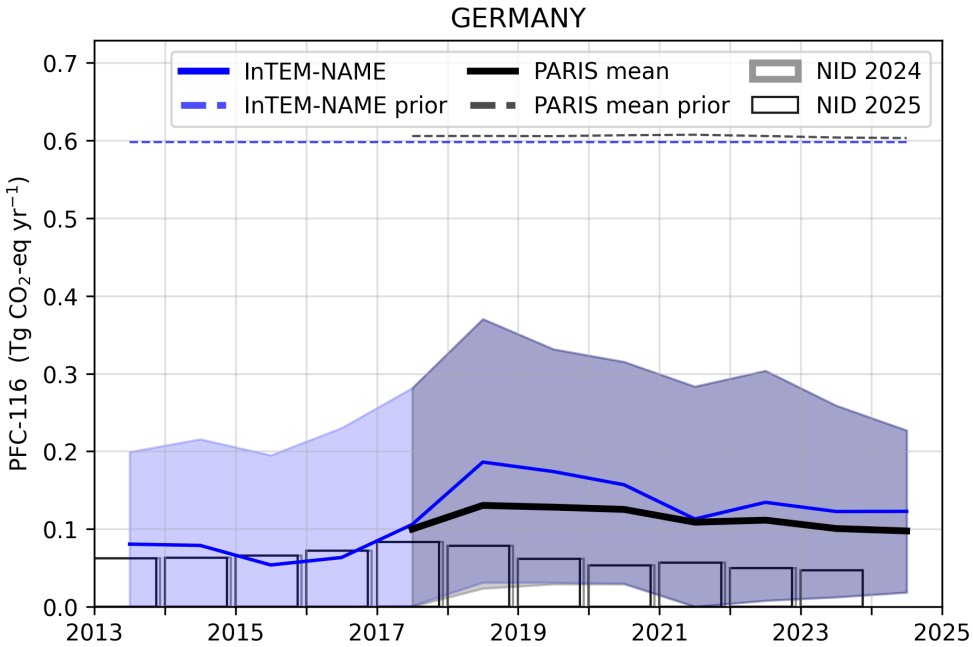

Figure 7.2.2: Spatial distribution of the German average modelled emissions of PFC-116 during the period of 2020-2024 (mean from all models). Observing stations are marked with red circles and highly-populated cities are marked with red triangles.

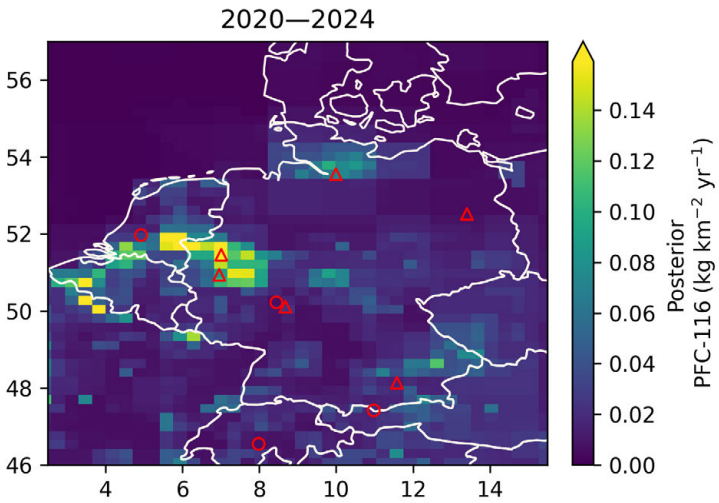

7.3 PFC-218

Figure 7.3.1: Verification of the German emissions inventory estimates for PFC-218. Modelled annual emissions are given as the mean from all models (black line) and the individual result from InTEM-NAME (blue line). The shaded blue area is the 68 % confidence interval (CI) of InTEM-NAME and the shaded grey area encompasses the 68 % CI from all models. National inventory annual totals from 2024 and 2025 are given as grey and black bars, respectively.

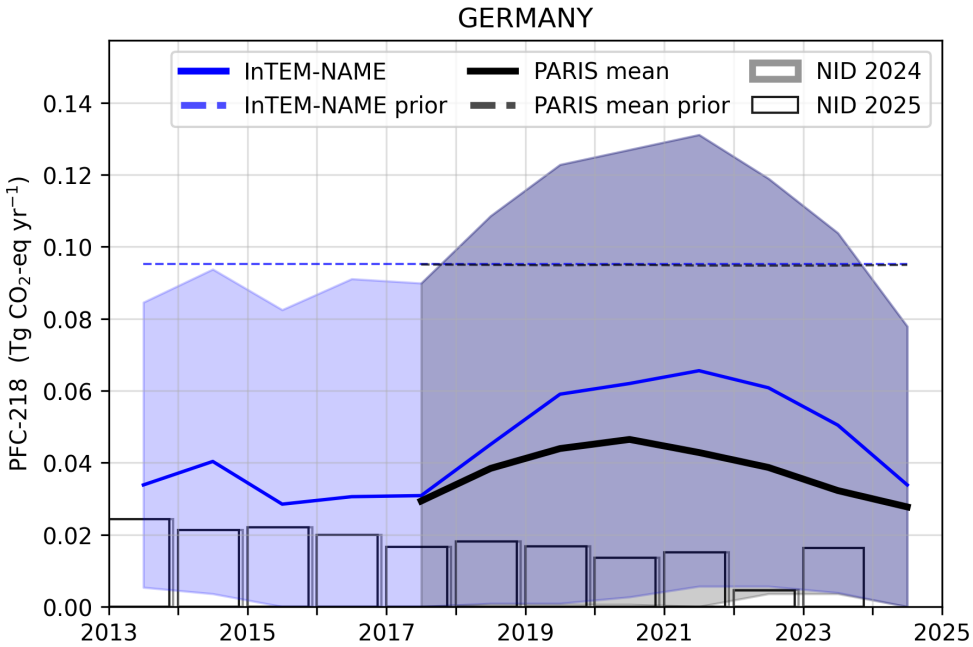

Figure 7.3.2: Spatial distribution of the German average modelled emissions of PFC-218 during the period of 2020-2024 (mean from all models). Observing stations are marked with red circles and highly-populated cities are marked with red triangles.

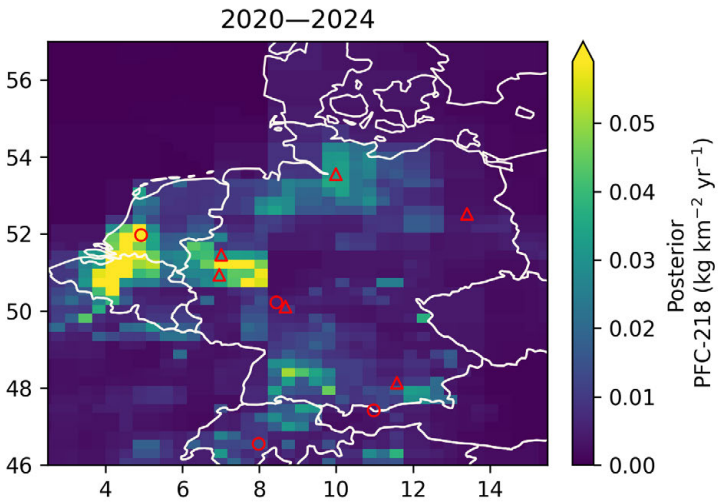

7.4 PFC-318

Figure 7.4.1: Verification of the German emissions inventory estimates for PFC-318. Modelled annual emissions are given as the mean from all models (black line) and the individual result from InTEM-NAME (blue line). The shaded blue area is the 68 % confidence interval (CI) of InTEM-NAME and the shaded grey area encompasses the 68 % CI from all models. National inventory annual totals from 2024 and 2025 are given as grey and black bars, respectively.

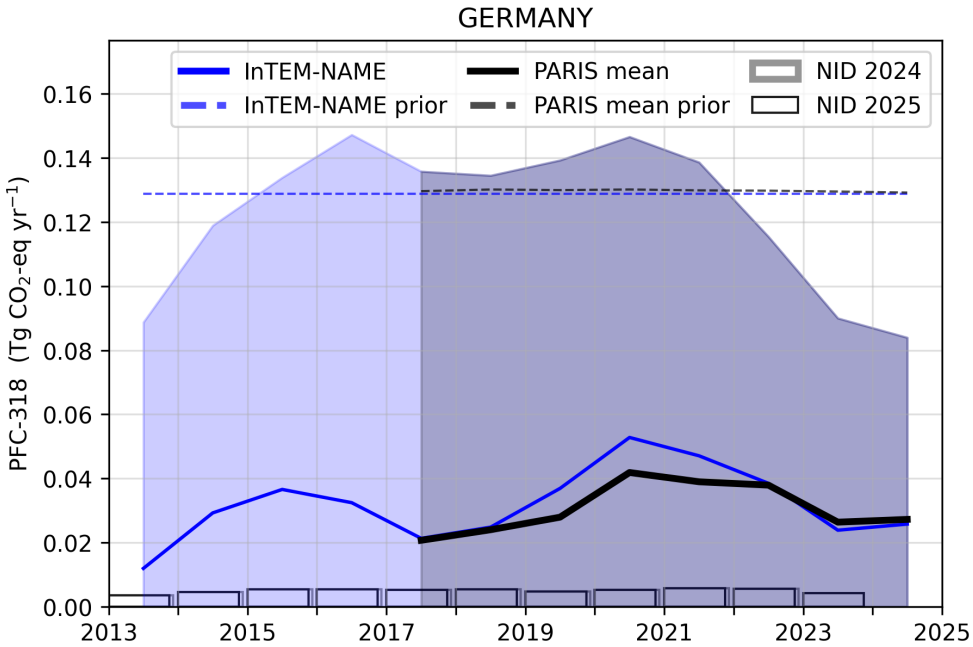

Figure 7.4.2: Spatial distribution of the German average modelled emissions of PFC-318 during the period of 2020-2024 (mean from all models). Observing stations are marked with red circles and highly-populated cities are marked with red triangles.

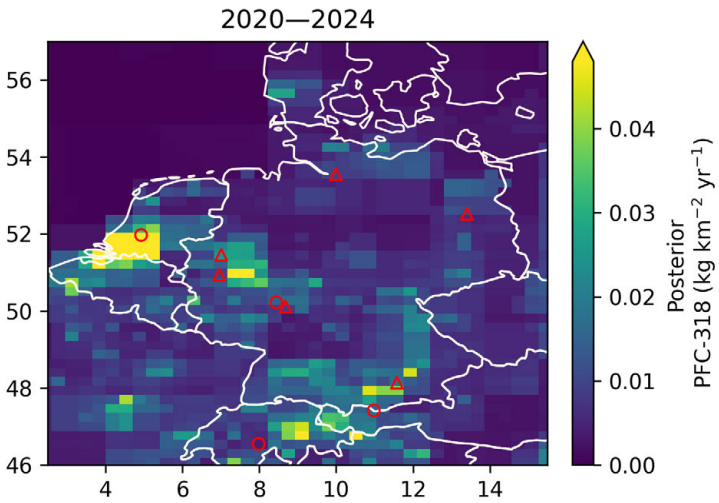

7.5 Total PFCs

Figure 7.5.1: Verification of the German emissions inventory estimates for total PFCs. Modelled annual emissions are given as the mean from all models (black line) and the individual result from InTEM-NAME (blue line). The shaded blue area is the 68 % confidence interval (CI) of InTEM-NAME and the shaded grey area encompasses the 68 % CI from all models. National inventory annual totals from 2024 and 2025 are given as grey and black bars, respectively.

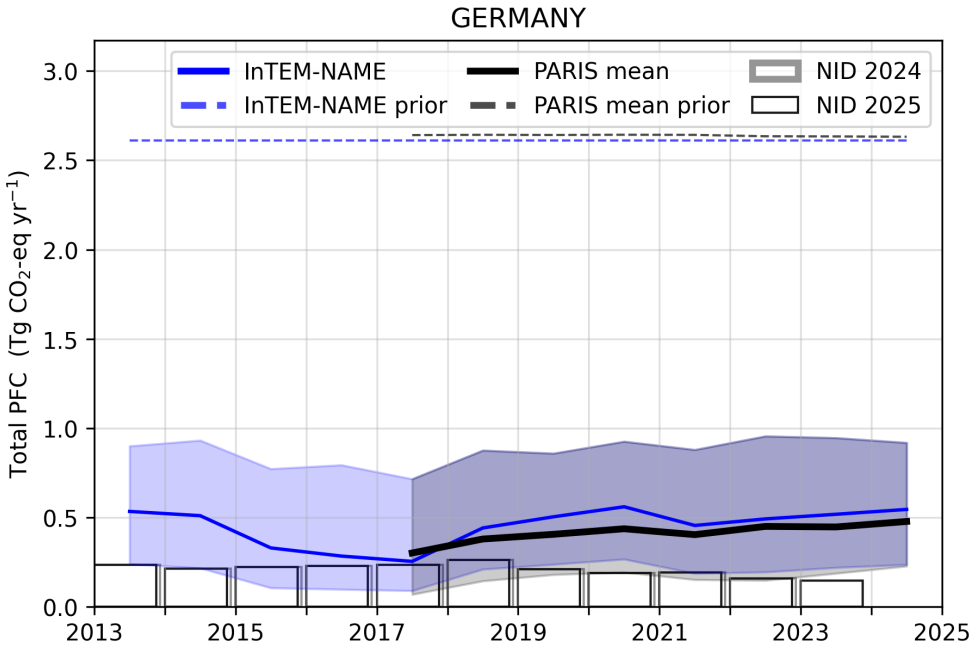

Table 3: Emissions estimation for PFCs according to the National Inventory Document (NID) 2025 and the inversions done in the PARIS project. For the PARIS estimation, the mean of all models is displayed, along with a range of uncertainty estimated via the half distance between the maximum and minimum uncertainties of the different models.

		2020	2021	2022	2023	2024
PFC-14	NID 2025	0.12	0.11	0.10	0.08	
$(\mathrm{TgCO_2\text{-}eq \cdot yr^{-1}})$	PARIS mean	0.22 ± 0.29	0.21 ± 0.30	0.26 ± 0.34	0.29 ± 0.33	0.32 ± 0.32
PFC-116	NID 2025	0.05	0.06	0.05	0.05	
$(\mathrm{TgCO_2\text{-}eq \cdot yr^{-1}})$	PARIS mean	0.13 ± 0.14	0.11 ± 0.14	0.11 ± 0.15	0.10 ± 0.12	0.10 ± 0.10
PFC-218	NID 2025	14	15	5	16	
$(\mathrm{GgCO_2\text{-}eq \cdot yr^{-1}})$	PARIS mean	46 ± 63	43 ± 66	39 ± 58	32 ± 50	28 ± 39
PFC-318	NID 2025	5	6	6	4	
$(\mathrm{GgCO_2\text{-}eq \cdot yr^{-1}})$	PARIS mean	42 ± 73	39 ± 69	38 ± 58	26 ± 45	27 ± 42

8 Sulphur hexafluoride (SF_6)

Figure 8.0.1: Total source sensitivity of SF_6 observing sites as calculated by the FLEXPART transport model for the year 2018 (left) and 2024 (right) and used in the inversions. Observing stations active in each year are marked with red dots. Areas with visible land surface represent regions for which emissions can be observed well from the network. Shaded or dark areas represent regions for which limited emission information can be obtained from the network.

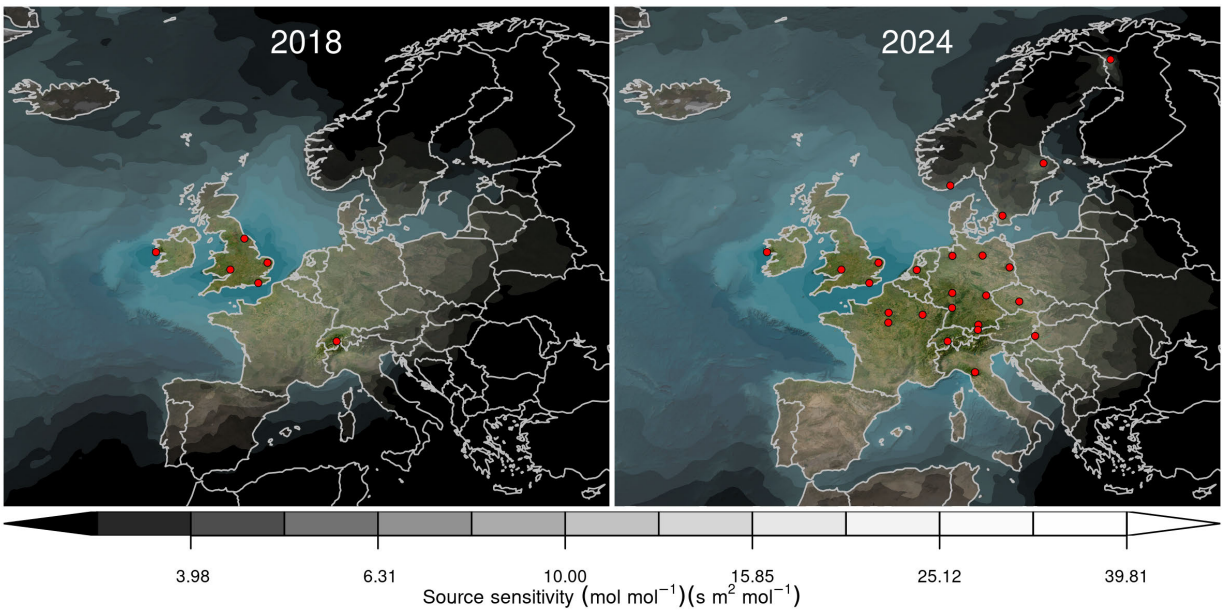

Figure 8.0.2: Verification of the German emissions inventory estimates for SF_6. Modelled annual emissions are given as the mean from all InTEM and ELRIS inversions (black line) and the individual result from InTEM-NAME (blue line). The shaded blue area is the 68 % confidence interval (CI) of InTEM-NAME and the shaded grey area encompasses the 68 % CI from all models. National inventory annual totals from 2024 and 2025 are given as grey and black bars, respectively.

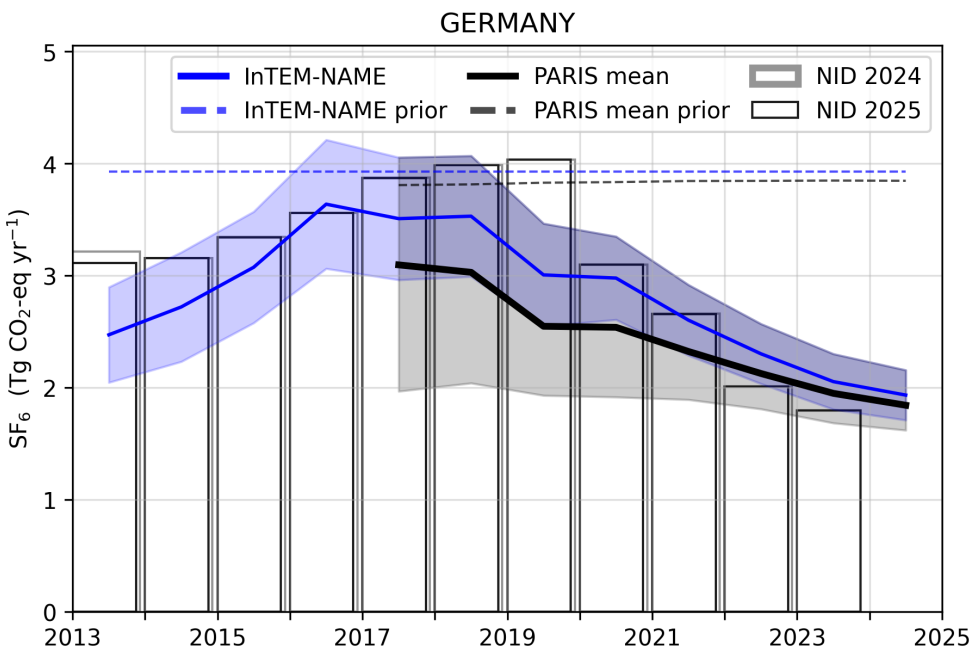

Figure 8.0.3: Spatial distribution of the German average modelled emissions of SF_6 during the period of 2020-2024 (mean from all InTEM and ELRIS inversions). Observing stations are marked with red circles and highly-populated cities are marked with red triangles.

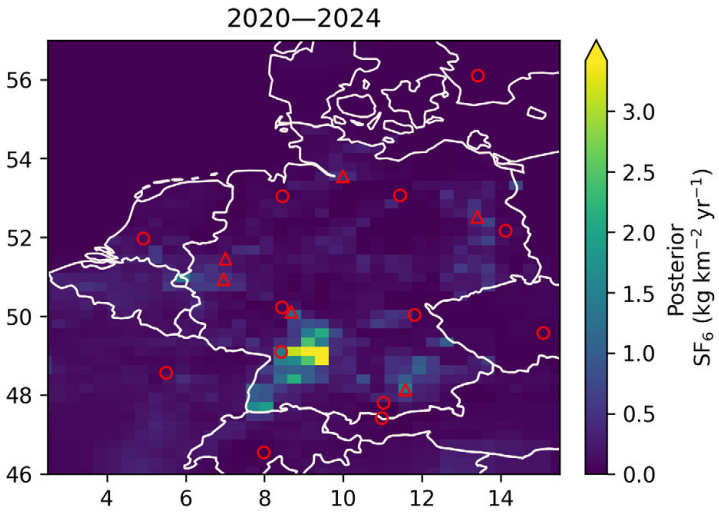

9 Carbon Dioxide (CO_2)

Measurements of CO_2 at ICOS sites and related observatories are influenced by a complex combination of sources and sinks. Fossil fuel combustion for transport, heating, energy generation, and other applications produce CO_2, along with other anthropogenic activities such as cement production. The terrestrial and oceanic biosphere produces CO_2 through animal and plant respiration and takes up CO_2 through photosynthesis. Furthermore, CO_2 is exchanged with the ocean through physical and chemical processes.

When considering high-frequency (∼hourly) CO_2 mole fraction deviations from baseline values—used to infer national emissions in regional inverse modelling studies—the influence of biospheric fluxes can be comparable to, or larger than, those of anthropogenic sources (e.g. White et al., 2019). Therefore, research is under way to develop new tracers that can determine fossil fuel CO_2 fluxes independent of biosphere sources and sinks.

Ongoing Horizon Europe projects PARIS and CORSO are examining methods for estimating fossil fuel CO_2 fluxes based on simultaneous measurements of CO_2 and O_2 (Figure 9.0.1). The method relies on the fact that CO_2 and O_2 are inter-converted during combustion and terrestrial biosphere exchange, but with different ratios for the two processes. A quantity can be constructed from these measurements, known as Atmospheric Potential Oxygen (APO), which is insensitive to biosphere fluxes, and may therefore be useful for isolating fossil fuel signals (Pickers et al., 2022).

High-frequency (∼hourly) timeseries of APO are available from Weybourne (WAO, 2010 – present) and Heathfield (HFD, 2021 - present) in the UK (Figure 9.0.1; Pickers, Adcock, and Manning, 2024), and new sites are being established at Cabauw and Zweth in the Netherlands. Preliminary analyses of the WAO data have revealed regional APO trends consistent with the drop in fossil fuel CO_2 emissions during the COVID lockdowns in the UK (Pickers et al., 2022). However, quantification of absolute regional fossil fuel CO_2 emissions remains an area of active research. Recent studies have derived fossil fuel CO_2 emissions for the UK that are highly uncertain (Rigby et al., 2025). Potential confounding factors were identified in Chawner et al. (2024), such as highly uncertain APO fluxes from the ocean, and a poorly constrained regional APO background. These factors are the subject of ongoing research using atmospheric models and new APO measurements from PARIS, CORSO and ICOS.

An alternative method for top-down fossil fuel CO_2 emissions evaluation uses measurements of radiocarbon isotopologues ($^{14}CO_2$, compared to the dominant $^{12}CO_2$). Fossil fuels do not contain ^{14}C, and therefore, their combustion tends to decrease the atmospheric $^{14}CO_2/^{12}CO_2$ ratio. Currently, radiocarbon mea-

surements can only be made at low frequency using flask sampling. However, a relatively intensive flask sampling campaign was carried out across Europe during 2024 as part of CORSO, and the results of this study will be reported on soon.

Figure 9.0.1: Carbon dioxide (top, red) and oxygen (bottom, blue) measurements from Weybourne Atmospheric Observatory in the UK, available from the ICOS Carbon Portal (Adcock et al., 2024).

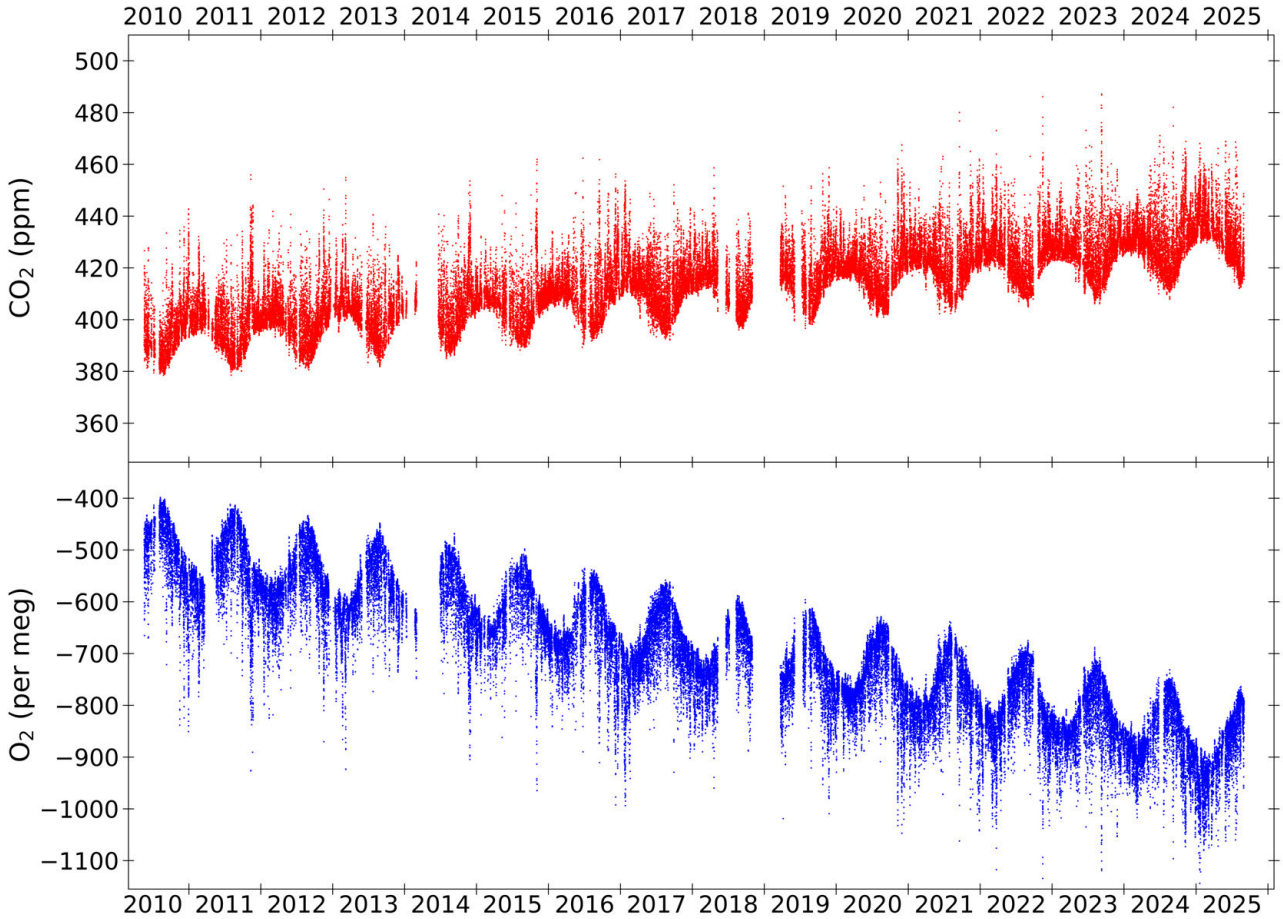

References

Adcock, Karina et al. (2024). *Atmospheric GHG data product (o2, o2_stdev, co2, co2_stdev) from Weybourne (10.0 m), 2010-05-19–2023-12-31*. URL: https://hdl.handle.net/11676/j4LzdHQiq3fPgfNeXHruC0Bb.

Bruch, V. et al. (2025). "German methane fluxes in 2021 estimated with an ensemble-enhanced scaling inversion based on the ICON–ART model". In: *EGUsphere* 2025, pp. 1–50. DOI: 10.5194/egusphere-2025-1464. URL: https://egusphere.copernicus.org/preprints/2025/egusphere-2025-1464/https://egusphere.copernicus.org/preprints/2025/egusphere-2025-1464/egusphere-2025-1464.pdf.

Chawner, Hannah et al. (Apr. 2024). "Atmospheric oxygen as a tracer for fossil fuel carbon dioxide: a sensitivity study in the UK". en. In: *Atmospheric Chemistry and Physics* 24.7, pp. 4231–4252. ISSN: 1680-7324. DOI: 10.5194/acp-24-4231-2024. URL: https://acp.copernicus.org/articles/24/4231/2024/ (visited on 04/10/2024).

European Commission: Joint Research, Centre et al. (2023). *GHG emissions of all world countries – 2023*. Publications Office of the European Union. DOI: 10.2760/953322.

Ganesan, A. L. et al. (2014). "Characterization of uncertainties in atmospheric trace gas inversions using hierarchical Bayesian methods". In: *Atmospheric Chemistry and Physics* 14.8, pp. 3855–3864. DOI: 10.5194/acp-14-3855-2014. URL: http://www.atmos-chem-phys.net/14/3855/2014/http://www.atmos-chem-phys.net/14/3855/2014/acp-14-3855-2014.pdf.

Ganesan, A. L. et al. (2015). "Quantifying methane and nitrous oxide emissions from the UK and Ireland using a national-scale monitoring network". In: *Atmos. Chem. Phys.* 15.11, pp. 6393–6406. DOI: 10.5194/acp-15-6393-2015. URL: https://www.atmos-chem-phys.net/15/6393/2015/https://www.atmos-chem-phys.net/15/6393/2015/acp-15-6393-2015.pdf.

Henne, S. et al. (2016). "Validation of the Swiss methane emission inventory by atmospheric observations and inverse modelling". In: *Atmospheric Chemistry and Physics* 16.6, pp. 3683–3710. DOI: 10.5194/acp-16-3683-2016. URL: http://www.atmos-chem-phys.net/16/3683/2016/.

Jones, A.R. et al. (2007). "The U.K. Met Office's next-generation atmospheric dispersion model, NAME III, in Borrego C. and Norman A.-L. (Eds)". In: *Air Pollution Modeling and its Application XVII (Proceedings of the 27th NATO/CCMS International Technical Meeting on Air Pollution Modelling and its Application), Springer*, pp. 580–589.

Katharopoulos, I. et al. (2023). "Impact of transport model resolution and a priori assumptions on inverse modeling of Swiss F-gas emissions". In: *Atmos. Chem. Phys.* 23.22, pp. 14159–14186. DOI: 10.5194/acp-23-14159-2023. URL: https://acp.copernicus.org/articles/23/14159/2023/.

Manning, A. J. et al. (2021). "Evidence of a recent decline in UK emissions of hydrofluorocarbons determined by the InTEM inverse model and atmospheric measurements". In: *Atmospheric Chemistry and Physics* 21.16, pp. 12739–12755. DOI: 10.5194/acp-21-12739-2021. URL: https://acp.copernicus.org/articles/21/12739/2021/.

Pickers, P., K. Adcock, and A. Manning (Feb. 2024). *Atmospheric oxygen and carbon dioxide observations from Weybourne Atmospheric Observatory, Norfolk, UK uploaded to public archives*. Tech. rep. Process Attribution of Regional Emissions (PARIS). URL: https://horizoneurope-paris.eu/wp-content/uploads/sites/914/2024/07/PARIS-deliverables-D6.1-High-frequency-APO-data-uploaded-final.pdf.

Pickers, Penelope A. et al. (Apr. 2022). "Novel quantification of regional fossil fuel CO2 reductions during COVID-19 lockdowns using atmospheric oxygen measurements". en. In: *Science Advances* 8.16, eabl9250. ISSN: 2375-2548. DOI: 10.1126/sciadv.abl9250. URL: https://www.science.org/doi/10.1126/sciadv.abl9250 (visited on 12/01/2023).

Rigby, M. et al. (2019). "Increase in CFC-11 emissions from eastern China based on atmospheric observations". In: *Nature* 569, pp. 546–550. DOI: 10.1038/s41586-019-1193-4. URL: https://doi.org/10.1038/s41586-019-1193-4.

Rigby, M. et al. (Apr. 2025). *Inverse estimates of fossil fuel CO2 emission*. Tech. rep. Process Attribution of Regional Emissions (PARIS). URL: https://horizoneurope-paris.eu/wp-content/uploads/sites/914/2025/01/PARIS-M24-Inverse-estimates-of-fossil-fuel-CO2-emissions-final.pdf.

Stohl, A. et al. (2005). "Technical note: The Lagrangian particle dispersion model FLEXPART version 6.2". In: *Atmospheric Chemistry and Physics* 5, pp. 2461–2474. DOI: 10.5194/acp-5-2461-2005. URL: <GotoISI>://000231983600002.

White, Emily D. et al. (Apr. 2019). "Quantifying the UK's carbon dioxide flux: an atmospheric inverse modelling approach using a regional measurement network". en. In: *Atmospheric Chemistry and Physics* 19.7, pp. 4345–4365. ISSN: 1680-7324. DOI: 10.5194/acp-19-4345-2019. URL: https://www.atmos-chem-phys.net/19/4345/2019/ (visited on 04/05/2019).

Draft Inventory Annex
Hungary 2025

30th October, 2025

1 Introduction

In this document, global concentration trends and national emissions estimates derived from atmospheric observations ("inverse estimates") are presented for most reported gases. Comparing the emissions submitted in national inventories with those calculated using atmospheric observations allows for emissions to be assessed using two fundamentally different approaches. Substantial differences can highlight areas that could warrant further investigation.

Global concentration trends for each gas are first shown using annual average concentrations from Mace Head, Ireland (Northern Hemisphere) and Kennaook/Cape Grim, Tasmania, Australia (Southern Hemisphere). Data from these stations were selected to exclude regionally-polluted air masses and therefore represents northern and southern hemispheric concentration trends. Mace Head observations were supported by the National Aeronautics and Space Administration (NASA) and the UK Department of Energy, Security and Net Zero (DESNZ), and Kennaook/Cape Grim observations by NASA and the Australian Bureau of Meteorology.

Observations of European concentrations of greenhouse gases used to derive national inverse emission estimates were collected from many different networks and providers. Methane and nitrous oxide concentrations originated from the European ICOS (Integrated Carbon Observation System) network, the UK DECC (Deriving Emissions related to Climate Change) network and other national or individual initiatives. F-gas observations were made by affiliates of the AGAGE (Advanced Global Atmospheric Gases Experiment) network. Observations from additional stations across Europe were supported by the Horizon-EU PARIS (Process Attribution of Regional Emissions) project. The observation stations used to derive emissions for each gas are shown in the corresponding sections of this document.

An atmospheric transport model provides the link between surface fluxes and concentrations measured at the observing stations. If not otherwise mentioned, inversion-based emissions estimates were derived using two atmospheric transport models combined with three inverse models, yielding a total of six inversions. This ensemble of six inversions allows us to better quantify the uncertainties associated with inverse modelling.

The two atmospheric transport models used are the Numerical Atmospheric dispersion Modelling Environment (NAME, Jones et al., 2007), and the FLEXible PARTicle dispersion model (FLEXPART, Stohl et al., 2005). Both models are backwards-running Lagrangian Particle Dispersion Models (LPDMs) that simulate the recent transport of air to each observing station. The two LPDMs have been widely used in the estimation of greenhouse gas emissions (Ganesan et al., 2015; Rigby et al., 2019; Manning et al., 2021; Henne et al., 2016).

The three inverse methods used are InTEM (Inversion Technique for Emission Modelling, Manning et al., 2021), ELRIS (Empa Lagrangian Regional Inversion System, Henne et al., 2016; Katharopoulos et al., 2023), and RHIME (Regional Hierarchical Inverse Modelling Environment, Ganesan et al., 2014). All three inverse methods estimate emissions within Europe along with boundary conditions that account for the concentration of the air entering Europe. All three systems started from the same set of a priori emissions that were either derived from the global EDGAR emission inventory (version 8, European Commission: Joint Research et al., 2023) or a uniform land-based emission, depending on the gas. A natural emission component, from the WETCHARTS product, was included in the methane prior. The same observational dataset was used by each inverse model, but data selection (i.e., filtering datasets for specific conditions) and treatment of uncertainties were chosen separately and hence differ. The three methods also differ in their statistical approaches for estimating emissions.

Emission estimates are presented for the period 2008-2024. Emissions for the full 2008-2024 period were derived with the InTEM-NAME inversion only, while emissions from 2017-2024 are presented as the mean of the six inversions (denoted the "PARIS mean"). The uncertainty shown is the minimum/maximum of the uncertainties in the ensemble.

All inversions employed a resolution of one month for CH_4 and N_2O and 1-year for the fluorinated gases. The inversion results used to compare with the inventories are a one-year calendar average for CH_4 and N_2O and the yearly value derived from a 3-year moving average for the fluorinated gases. For the 2008-2024

InTEM-NAME results, a 3-year moving average was also applied to the annualised CH_4 and N_2O results due to lack of observational coverage in the earlier years.

2 Global Concentration Trends

2.1 Methane (CH_4)

Figure 2.1.1: Background Northern Hemisphere monthly concentrations of CH_4 estimated from MHD, Ireland observations are shown in red, and background Southern Hemisphere monthly concentrations from CGO, Tasmania are shown in blue. Grey shading represents provisional data.

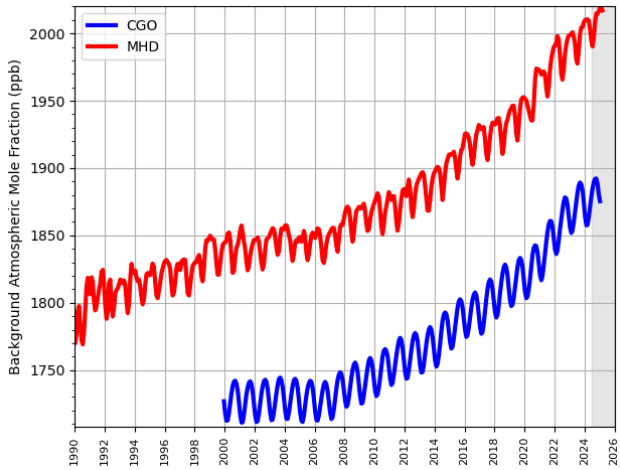

2.2 Nitrous Oxide (N_2O)

Figure 2.2.1: Background Northern Hemisphere monthly concentrations of N_2O estimated from MHD, Ireland observations are shown in red, and background Southern Hemisphere monthly concentrations from CGO, Tasmania are shown in blue. Grey shading represents provisional data.

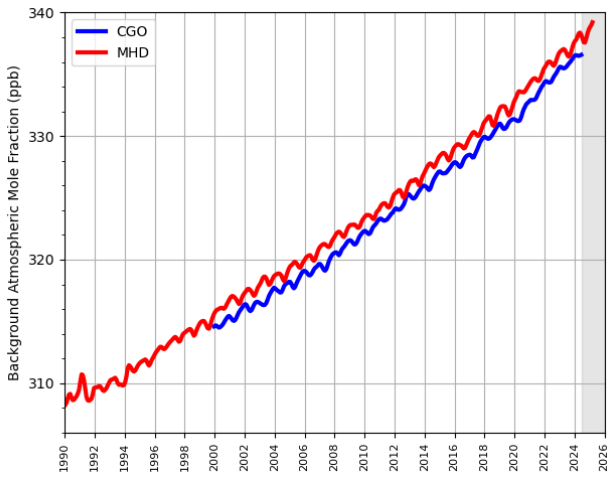

2.3 Hydrofluorocarbons (HFCs)

Figure 2.3.1: Background Northern Hemisphere monthly concentrations of six HFCs estimated from MHD, Ireland observations are shown in red, and background Southern Hemisphere monthly concentrations from CGO, Tasmania are shown in blue. Grey shading represents provisional data.

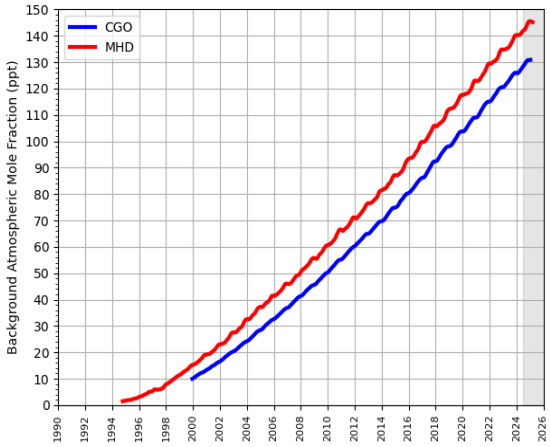

(a) HFC-134a

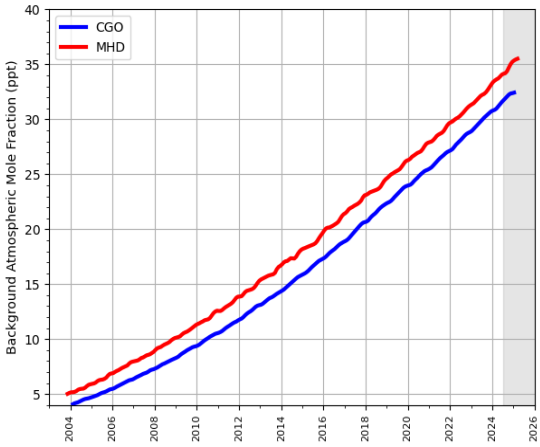

(b) HFC-143a

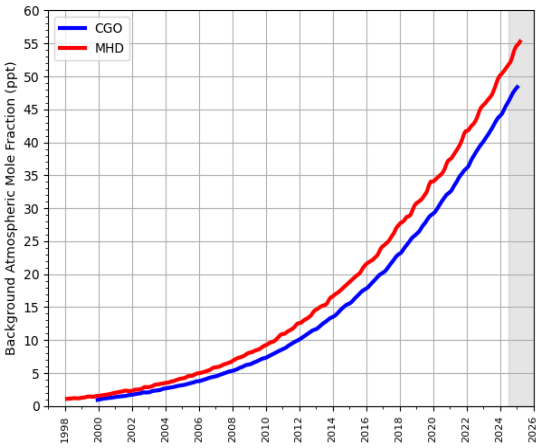

(c) HFC-125

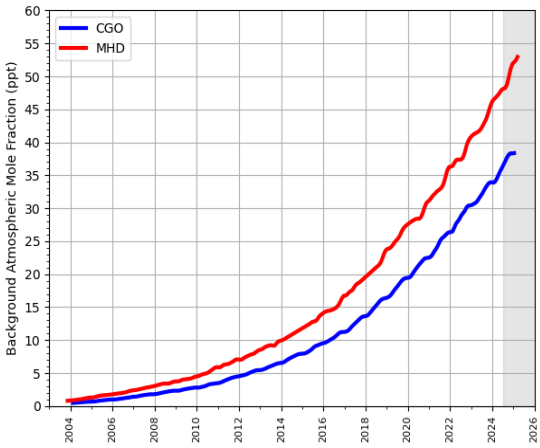

(d) HFC-32

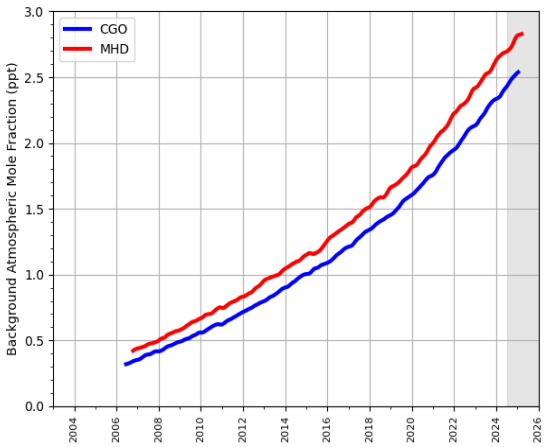

(e) HFC-227ea

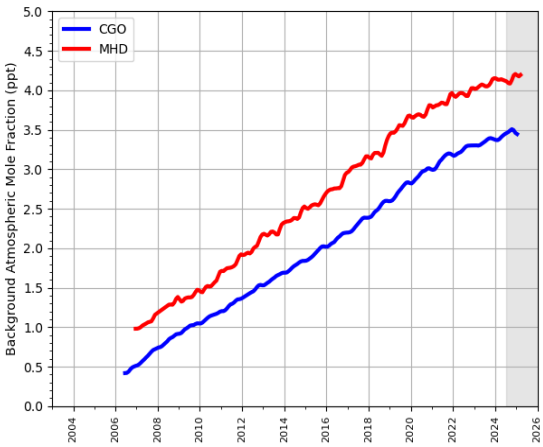

(f) HFC-245fa

Figure 2.3.2: Background Northern Hemisphere monthly concentrations of four HFCs estimated from MHD, Ireland observations are shown in red, and background Southern Hemisphere monthly concentrations from CGO, Tasmania are shown in blue. Grey shading represents provisional data.

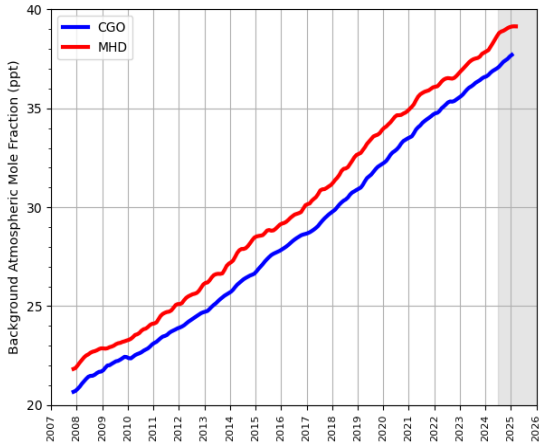

(a) HFC-23

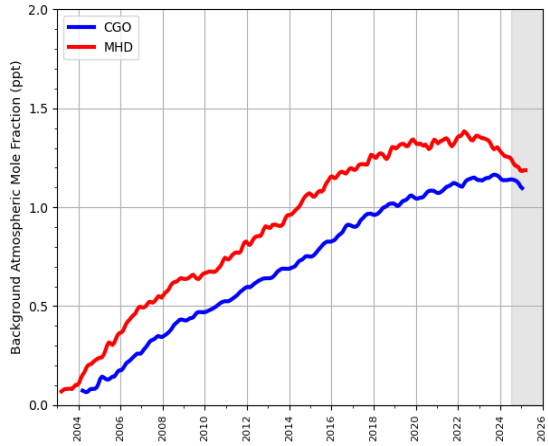

(b) HFC-365mfc

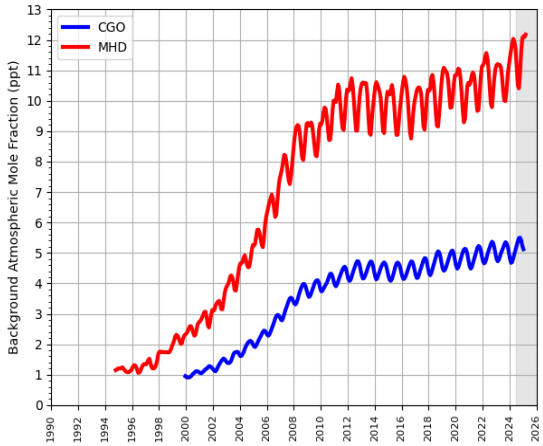

(c) HFC-152a

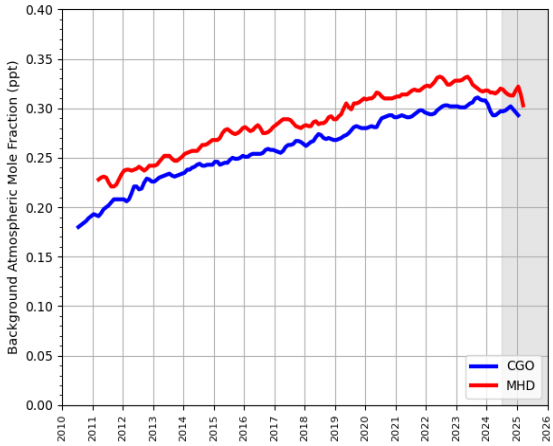

(d) HFC-43-10-mee

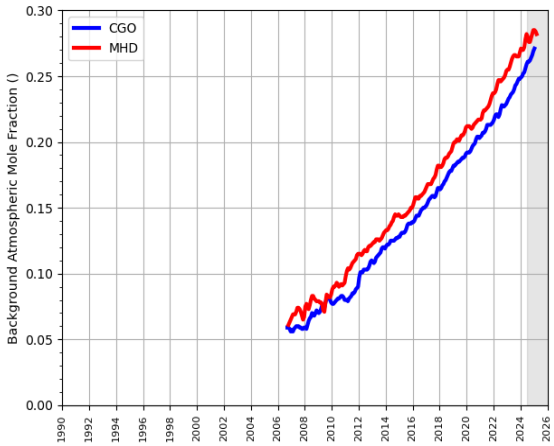

(e) HFC-236fa

2.4 Perfluorocarbons (PFCs)

Figure 2.4.1: Background Northern Hemisphere monthly concentrations of four PFCs estimated from MHD, Ireland observations are shown in red, and background Southern Hemisphere monthly concentrations from CGO, Tasmania are shown in blue. Grey shading represents provisional data.

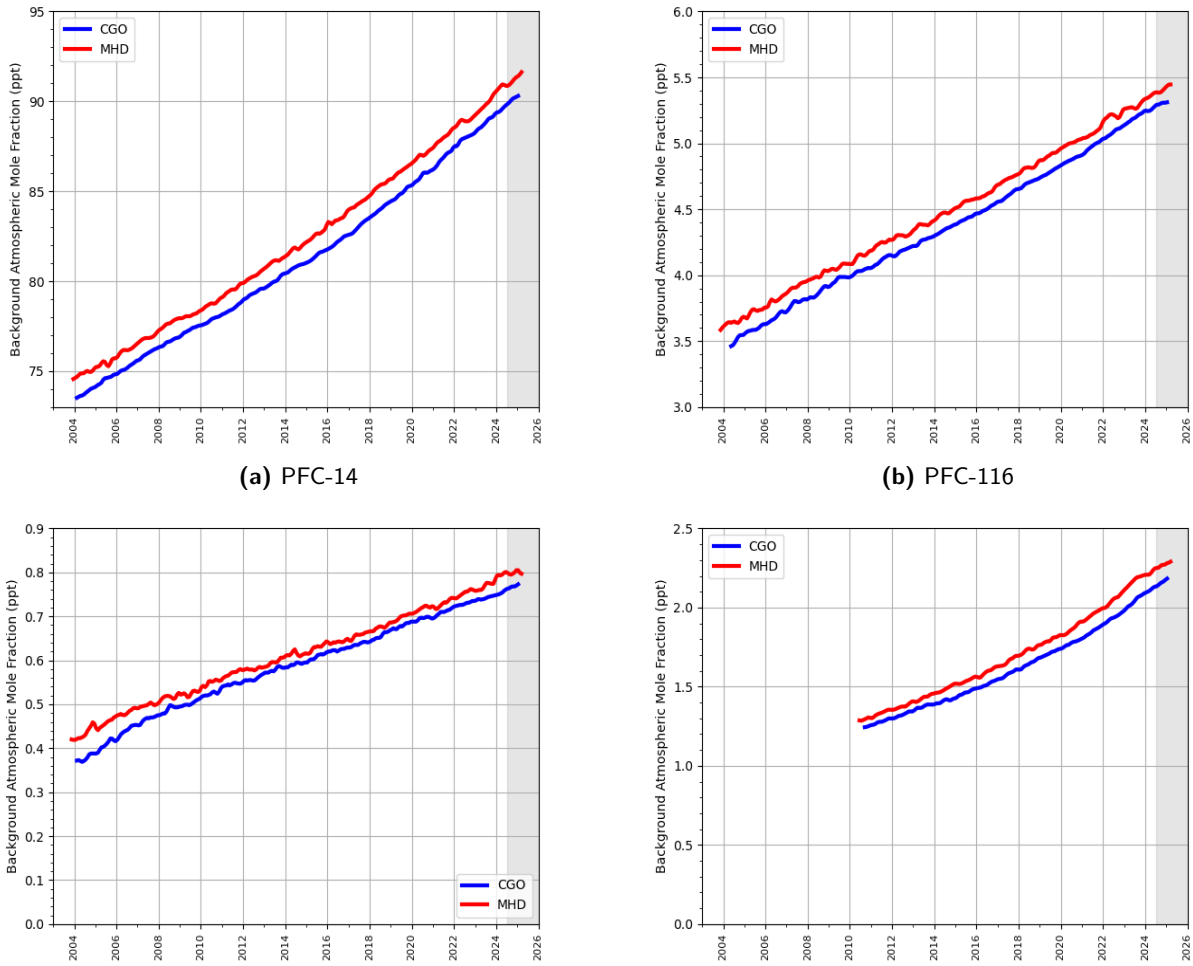

(a) PFC-14 **(b)** PFC-116 **(c)** PFC-218 **(d)** PFC-318

2.5 Sulphur Hexafluoride (SF_6) and Nitrogen Trifluoride (NF_3)

Figure 2.5.1: Background Northern Hemisphere monthly concentrations of SF_6 and NF_3 estimated from MHD, Ireland observations are shown in red, and background Southern Hemisphere monthly concentrations from CGO, Tasmania are shown in blue. Grey shading represents provisional data.

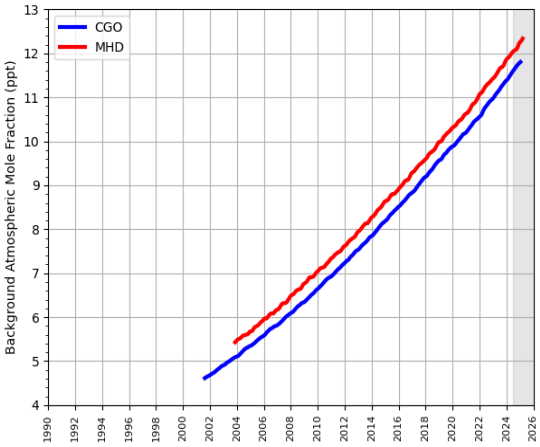

(a) SF_6

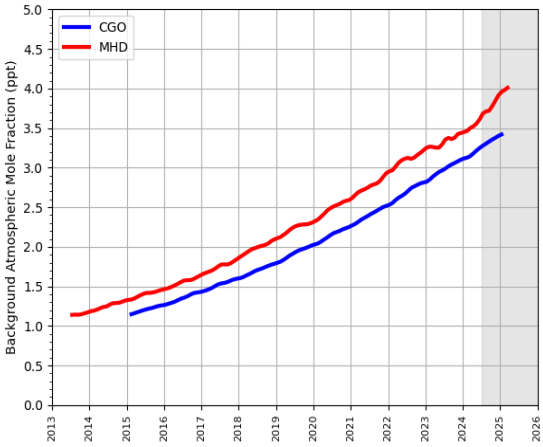

(b) NF_3

2.6 Carbon Dioxide (CO_2)

Figure 2.6.1: Background Northern Hemisphere monthly concentrations of CO_2 estimated from MHD, Ireland observations are shown in red, and background Southern Hemisphere monthly concentrations from CGO, Tasmania are shown in blue. Grey shading represents provisional data.

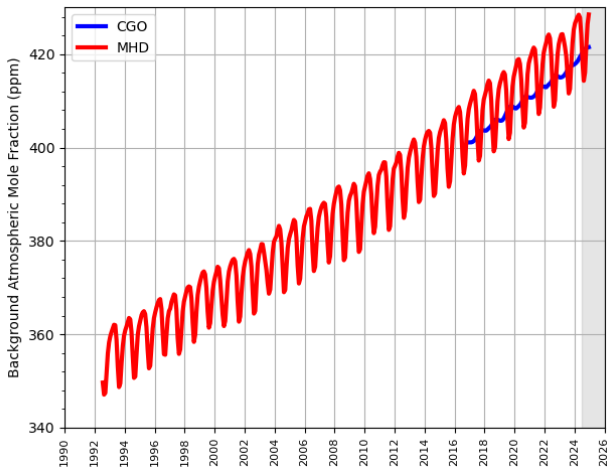

3 Key findings

- General note: The presented inverse modelling estimates of Hungarian emissions currently are limited by the sparsity of atmospheric observations in south-eastern Europe. For the inversion period 2018-2024, the only available observations within the Hungarian domain were those of CH_4 and N_2O from the Hungarian tall tower site Hegyhátsál close to the western border with Austria. Limited source sensitivity towards eastern Hungary results from the current observing network. As part of the PARIS project, flask sampling of halogenated species was initiated at Hegyhátsál in 2024 and about 150 samples from this location were included in the inverse modelling of F-gases for 2024. For earlier years, limited source sensitivities from observations at Jungfraujoch (Switzerland), Zugspitze (Germany) and Monte Cimone (Italy) are not sufficient to derive Hungarian F-gase emissions with any degree of certainty.
- Methane (CH_4): Inverse results are about 50 % larger than inventory estimates between 2018 and 2023 (Figure 4.0.2). However, inversion results show a relatively large a posteriori uncertainty, which even encompasses the reported emissions. No significant temporal trend is discernable in both data sets. Highest emissions are obtained for the western part of Hungary, potentially driven by the stronger observational constraint in this area (Figure 4.0.4). The inverse results indicate a pronounced seasonality in the methane emissions, broadly spread over the domain. The results suggest that CH_4 emissions are at maximum in winter (Figures 4.0.3 and 4.0.5).
- Nitrous oxide (N_2O): Inverse results are significantly larger, almost double, than inventory estimates between 2018 and 2023 (Figure 5.0.2). As for CH_4, highest emissions are obtained for the western part of the country (Figure 5.0.4). The inverse results indicate a considerable seasonality in the nitrous oxide emissions with a maximum in summer and autumn most likely related to emissions from agricultural soils. This feature is widespread in the Hungarian domain, with an exception in neighbouring Slovakia, where a larger point source seems to be present which may overshadow agricultural emissions (Figures 5.0.3 and 5.0.5).
- Hydrofluorocarbons (HFCs): The observational constraint for Hungarian HFC emissions remains relatively poor before 2024 as only observations from a few sites in Europe were available. In comparison to last year's PARIS inversions additional observations were added in this years iteration: Zugspitze and Taunus observatory (Germany) and, more importantly, flask observations from Hegyhátsál (HUN) starting in the year 2024 (Figure 6.0.1). For most HFCs, inversion-derived emission estimates stay relatively close to the a priori values (Figure 6.7.1), the latter being generally larger than the inventory and not showing a decrease in recent years. Incorporating the novel flask observations from (HUN) improves the inverse estimates of several HFCs in the western part of Hungary and neighbouring countries (see section 10). However, continued sampling at HUN will be necessary to establish a longer time series that will allow for a more robust long-term estimation of HFC emissions in the area. For some HFCs (e.g., HFC-23) no observations from HUN were available due to technical problems and their emission estimate remains uncertain.
- Perfluorocarbons (PFCs): The observational coverage for PFCs is similar to that of HFCs. Of the PFCs simulated in PARIS only PFC-318 was observed at HUN. Hence, very large uncertainties remain in the Hungarian PFC emissions estimates obtained from inverse modelling. These estimates are mostly smaller than their a priori values, but associated with uncertainties much larger than 100 % (Figure 7.5.1).
- Sulphur hexafluoride (SF_6): Similar to HFCs and PFCs, SF_6 samples from HUN were only available for 2024. However, additional flask observations from ICOS sites were added to this year's PARIS inversions. Despite the added observations, inverse emission estimates of SF_6 remain relatively uncertain ($\pm$100 %). The inverse estimates stay in close agreement with the a priori assumption, which for this gas is in line with the national inventory (Figure 8.0.2).

Table 1: Emissions estimation for the main greenhouse gases of focus according to the National Inventory Document (NID) 2025 and the inversions done in the PARIS project. For the PARIS estimation, the mean of all models is displayed, along with a range of uncertainty estimated via the half distance between the maximum and minimum uncertainties of the different models. For SF_6, the PARIS mean is the average of all InTEM and ELRIS inversions only.

		2020	2021	2022	2023	2024
CH_4	NID 2025	9.2	9.0	8.7	8.3	
$(\mathrm{TgCO_2\text{-}eq \cdot yr^{-1}})$	PARIS mean	14.1 ± 4.8	15.5 ± 7.6	11.7 ± 4.2	14.7 ± 5.7	15.6 ± 5.2
N_2O	NID 2025	4.71	4.74	3.96	3.86	
$(\mathrm{TgCO_2\text{-}eq \cdot yr^{-1}})$	PARIS mean	8.43 ± 2.85	8.43 ± 3.32	5.97 ± 2.36	7.42 ± 2.75	6.54 ± 1.72
Total HFC	NID 2025	1.9	1.8	1.8	1.7	
$(\mathrm{TgCO_2\text{-}eq \cdot yr^{-1}})$	PARIS mean	1.5 ± 1.0	1.4 ± 0.9	1.6 ± 1.0	1.7 ± 0.9	1.9 ± 0.8
SF_6	NID 2025	0.12	0.11	0.11	0.12	
$(\mathrm{TgCO_2\text{-}eq \cdot yr^{-1}})$	PARIS mean	0.05 ± 0.14	0.05 ± 0.14	0.08 ± 0.14	0.11 ± 0.15	0.14 ± 0.16
Total PFC	NID 2025	2	2	2	3	
$(\mathrm{GgCO_2\text{-}eq \cdot yr^{-1}})$	PARIS mean	31 ± 635	30 ± 590	47 ± 508	39 ± 286	47 ± 273

4 Methane (CH_4)

Figure 4.0.1: Average monthly total source sensitivity of CH_4 observing sites as calculated by the FLEXPART transport model for the year 2018 (left) and 2024 (right) and used in the inversions. Observing stations active in each year are marked with red dots. Areas with visible land surface represent regions for which emissions can be observed well from the network. Shaded or dark areas represent regions for which limited emission information can be obtained from the network.

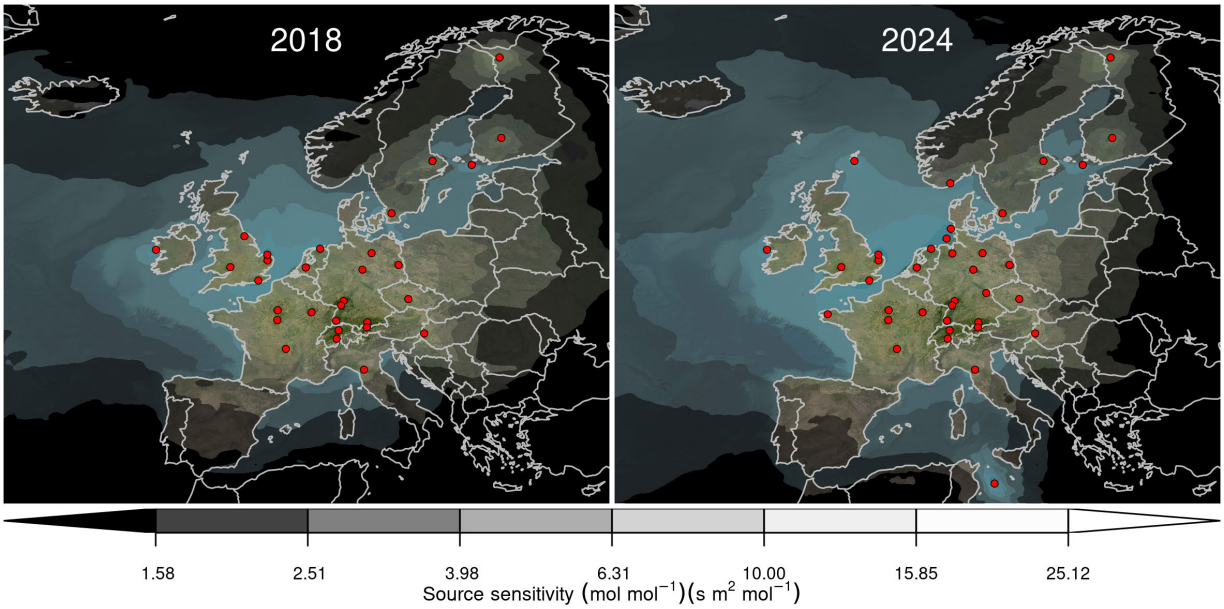

Figure 4.0.2: Verification of the Hungarian emissions inventory estimates for CH_4 (zoom in to 2018-2024). Modelled annual emissions are given as the mean from all models (black line) and the individual result from InTEM-NAME (blue line). The shaded blue area is the 68 % confidence interval (CI) of InTEM-NAME and the shaded grey area encompasses the 68 % CI from all models. National inventory annual totals from 2024 and 2025 are given as grey and black bars, respectively.

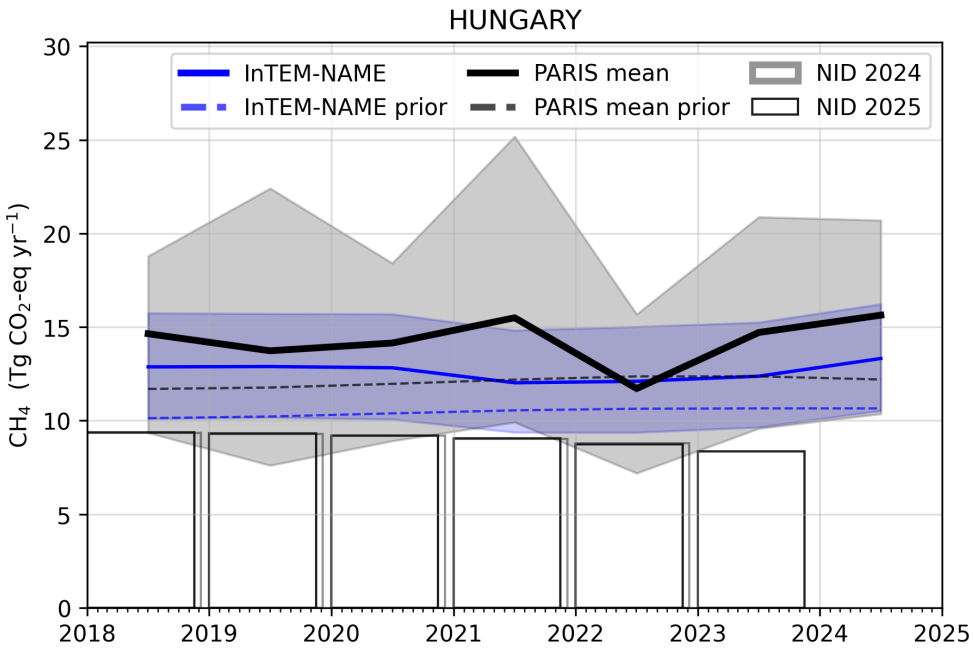

Figure 4.0.3: Verification of the Hungarian emissions inventory estimates for CH_4 (zoom in to 2018-2024). Modelled monthly emissions are given as the mean from all models (black line) and the individual result from InTEM-NAME (blue line). The shaded blue area is the 68 % confidence interval (CI) of InTEM-NAME and the shaded grey area encompasses the 68 % CI from all models. National inventory annual totals from 2024 and 2025 are given as grey and black bars, respectively.

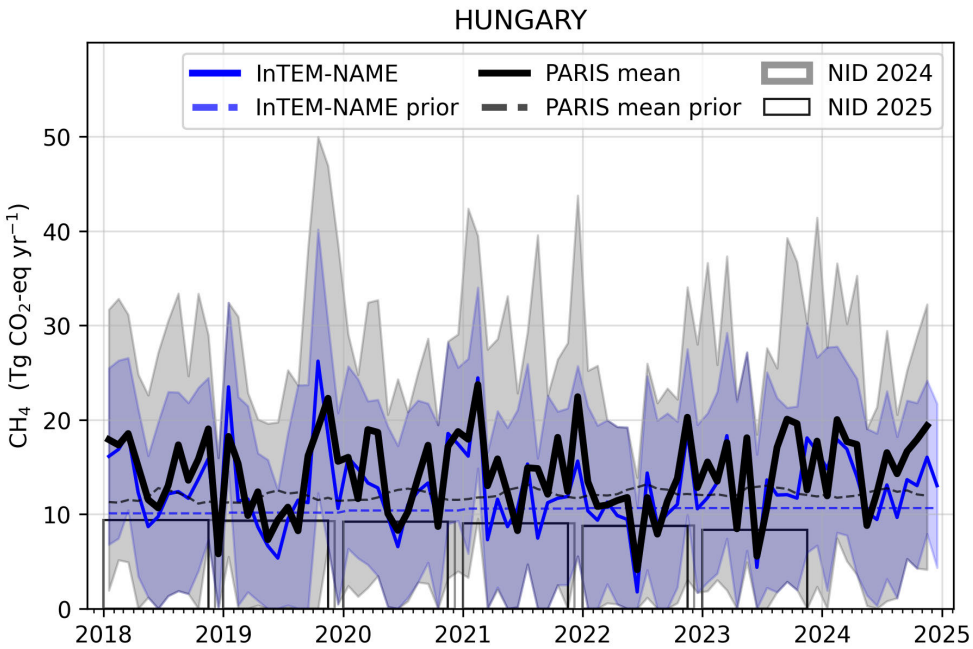

Figure 4.0.4: Spatial distribution of the Hungarian average modelled emissions of CH_4 during the period of 2020-2024 (mean from all models). Observing stations are marked with red circles and highly-populated cities are marked with red triangles.

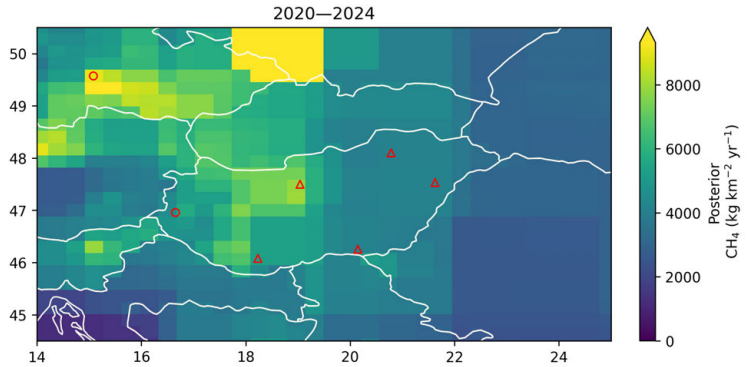

Figure 4.0.5: Spatial distribution of the seasonal deviation from the mean. The deviation is defined as the modelled Hungarian seasonally averaged CH_4 emissions over 2020-2024 minus the average over the whole period. The mean across all models is shown. Observing stations are marked with black circles and highly-populated cities are marked with black triangles.

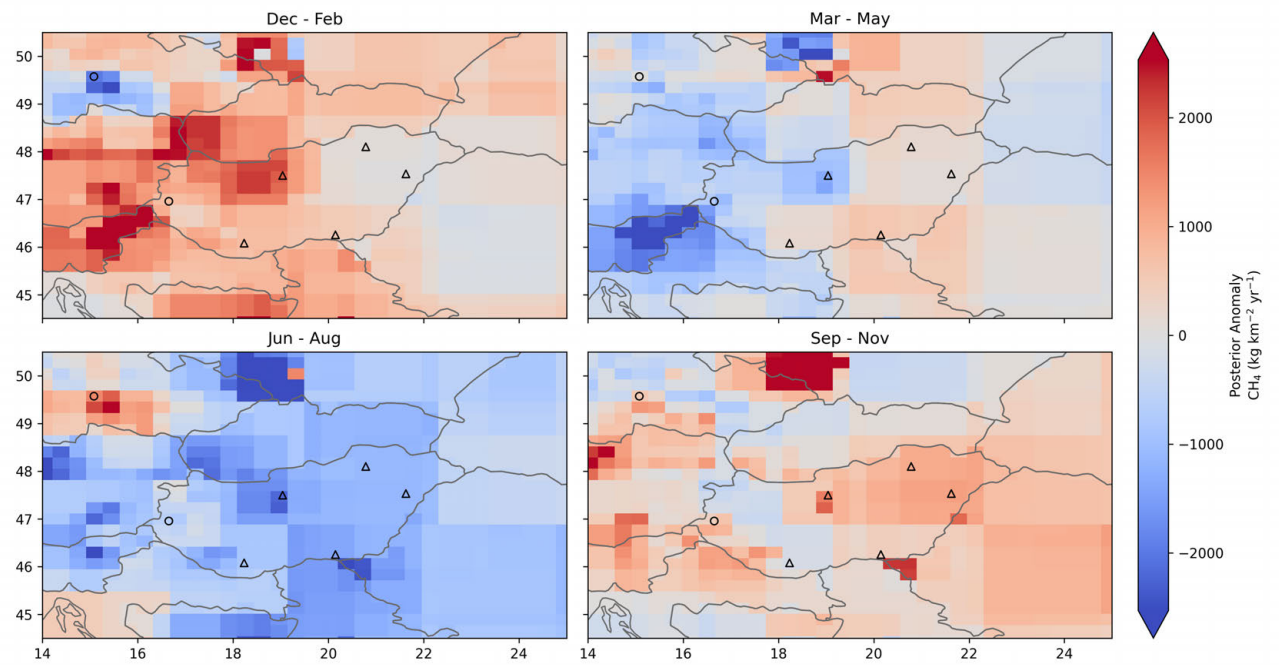

5 Nitrous Oxide (N_2O)

Figure 5.0.1: Average monthly total source sensitivity of N_2O observing sites as calculated by the FLEXPART transport model for the year 2018 (left) and 2024 (right) and used in the inversions. Observing stations active in each year are marked with red dots. Areas with visible land surface represent regions for which emissions can be observed well from the network. Shaded or dark areas represent regions for which limited emission information can be obtained from the network.

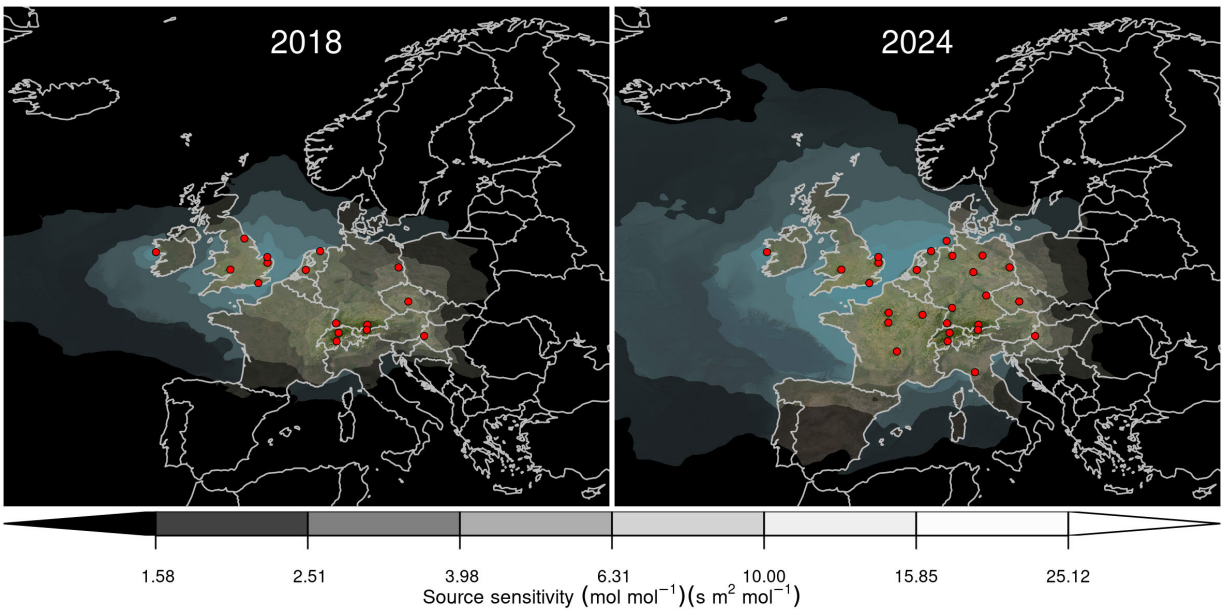

Figure 5.0.2: Verification of the Hungarian emissions inventory estimates for N_2O (zoom in to 2018-2024). Modelled annual emissions are given as the mean from all models (black line) and the individual result from InTEM-NAME (blue line). The shaded blue area is the 68 % confidence interval (CI) of InTEM-NAME and the shaded grey area encompasses the 68 % CI from all models. National inventory annual totals from 2024 and 2025 are given as grey and black bars, respectively.

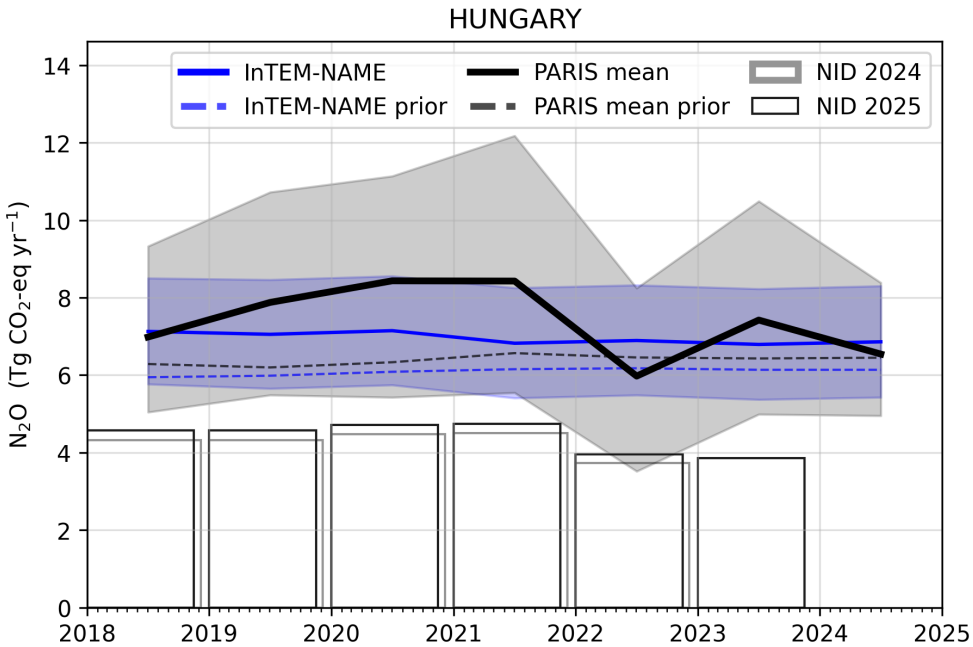

Figure 5.0.3: Verification of the Hungarian emissions inventory estimates for N_2O (zoom in to 2018-2024). Modelled monthly emissions are given as the mean from all models (black line) and the individual result from InTEM-NAME (blue line). The shaded blue area is the 68 % confidence interval (CI) of InTEM-NAME and the shaded grey area encompasses the 68 % CI from all models. National inventory annual totals from 2024 and 2025 are given as grey and black bars, respectively.

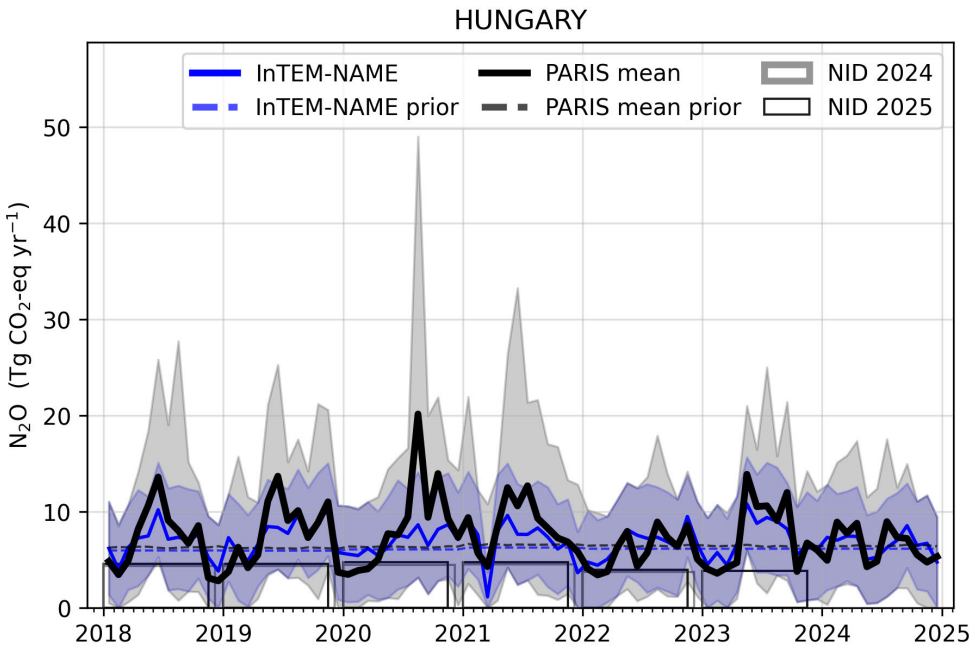

Figure 5.0.4: Spatial distribution of the Hungarian average modelled emissions of N_2O during the period of 2020-2024 (mean from all models). Observing stations are marked with red circles and highly-populated cities are marked with red triangles.

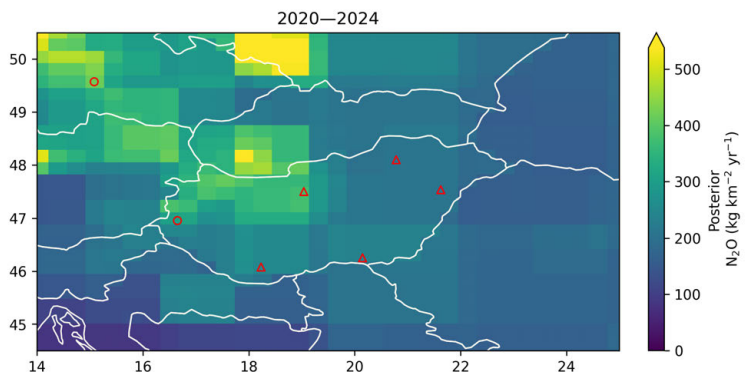

Figure 5.0.5: Spatial distribution of the seasonal deviation from the mean. The deviation is defined as the modelled Hungarian seasonally averaged N_2O emissions over 2020-2024 minus the average over the whole period. The mean across all models is shown. Observing stations are marked with black circles and highly-populated cities are marked with black triangles.

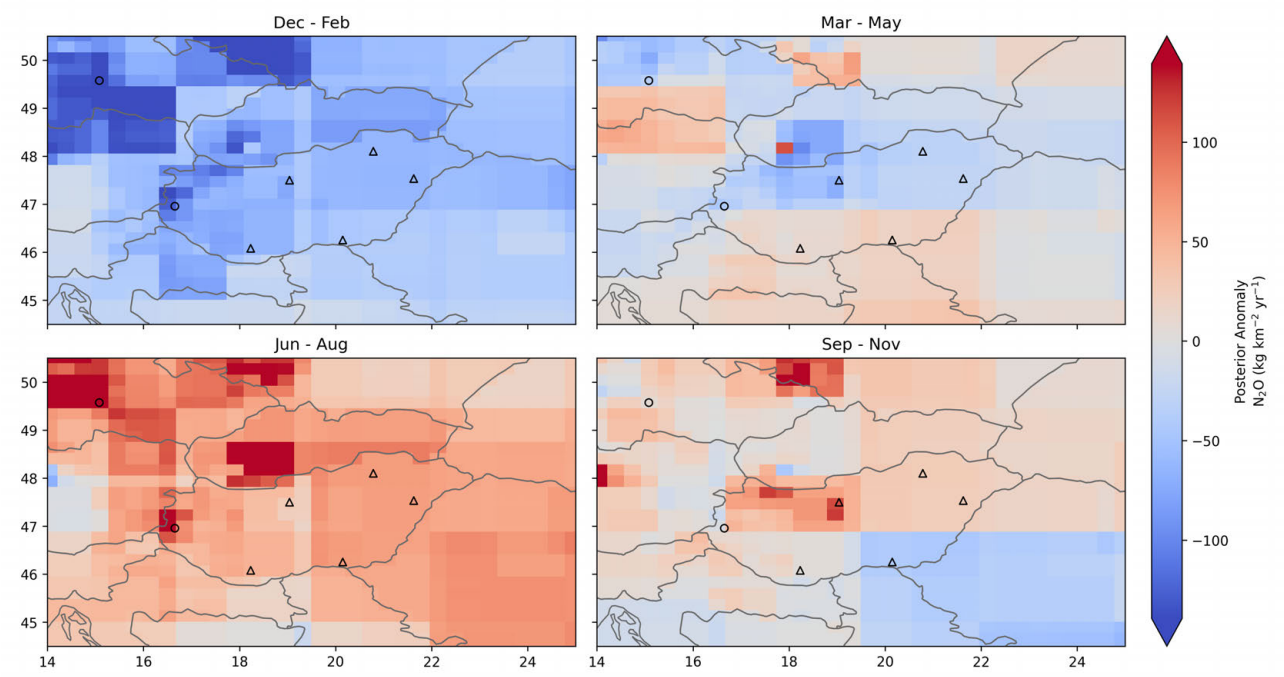

6 Hydrofluorocarbons (HFCs)

Figure 6.0.1: Total source sensitivity of HFCs/PFCs observing sites as calculated by the FLEXPART transport model for the year 2018 (left) and 2024 (right) and used in the inversions. Observing stations active in each year are marked with red dots. Areas with visible land surface represent regions for which emissions can be observed well from the network. Shaded or dark areas represent regions for which limited emission information can be obtained from the network.

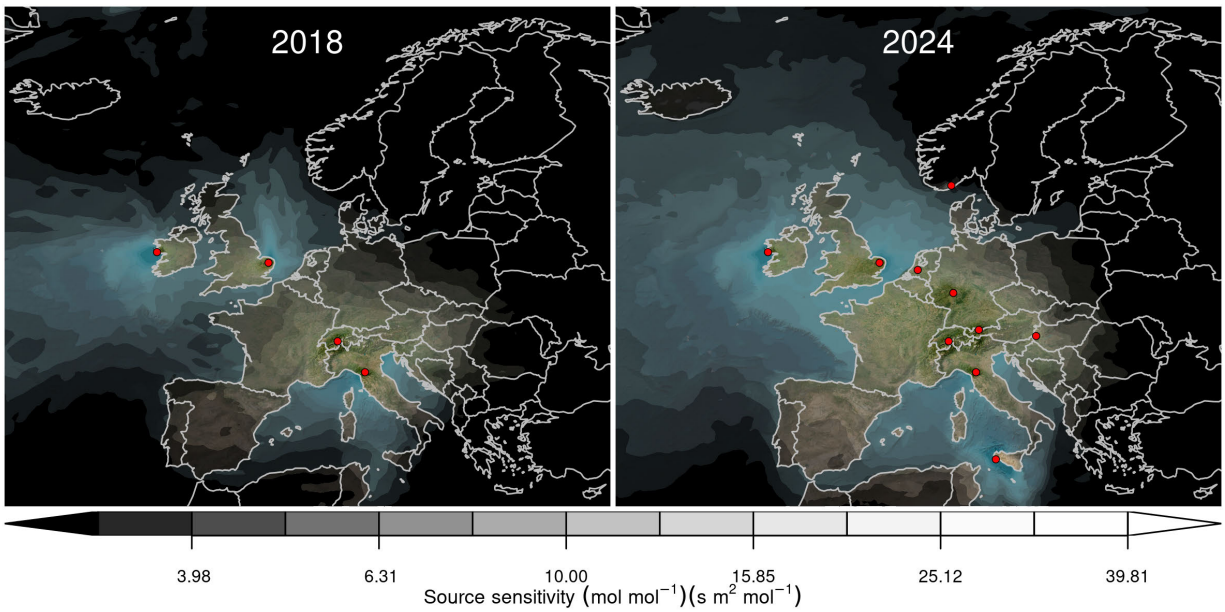

6.1 HFC-125

Figure 6.1.1: Verification of the Hungarian emissions inventory estimates for HFC-125. Modelled annual emissions are given as the mean from all models (black line) and the individual result from InTEM-NAME (blue line). The shaded blue area is the 68 % confidence interval (CI) of InTEM-NAME and the shaded grey area encompasses the 68 % CI from all models. National inventory annual totals from 2024 and 2025 are given as grey and black bars, respectively.

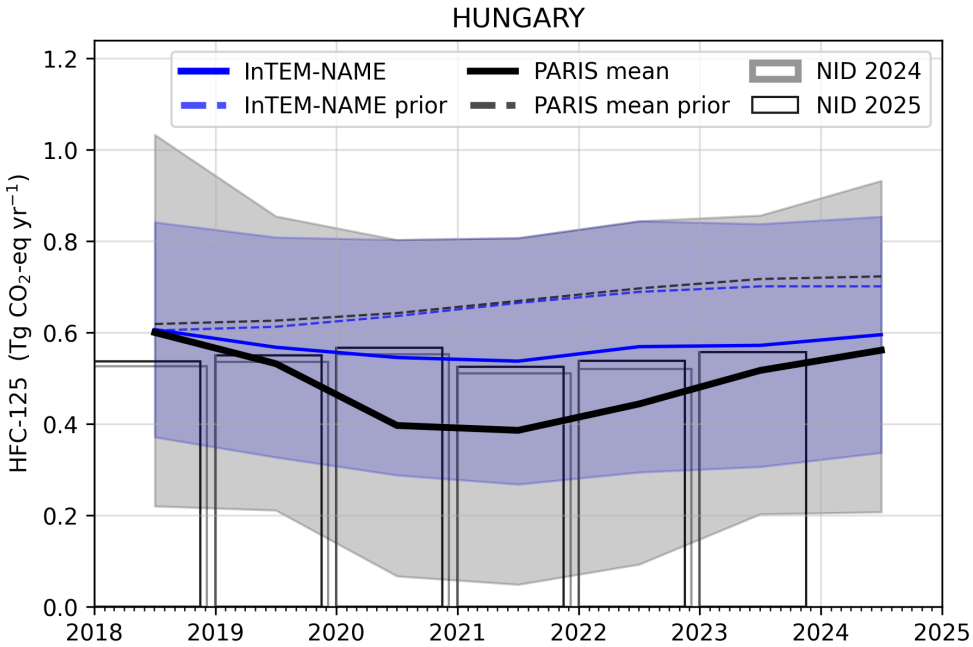

Figure 6.1.2: Spatial distribution of the Hungarian average modelled emissions of HFC-125 during the period of 2020-2024 (mean from all models). Observing stations are marked with red circles and highly-populated cities are marked with red triangles.

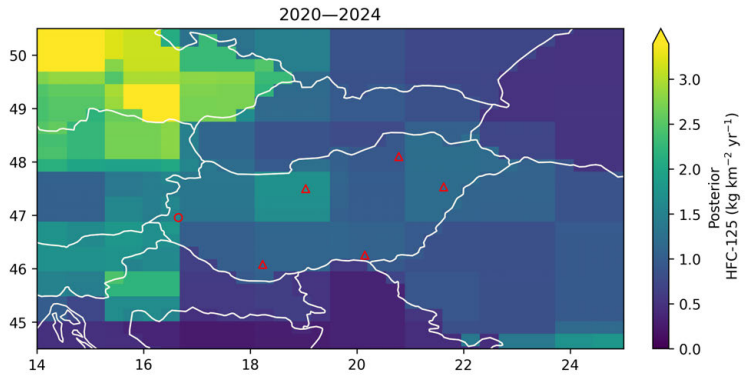

6.2 HFC-134a

Figure 6.2.1: Verification of the Hungarian emissions inventory estimates for HFC-134a. Modelled annual emissions are given as the mean from all models (black line) and the individual result from InTEM-NAME (blue line). The shaded blue area is the 68 % confidence interval (CI) of InTEM-NAME and the shaded grey area encompasses the 68 % CI from all models. National inventory annual totals from 2024 and 2025 are given as grey and black bars, respectively.

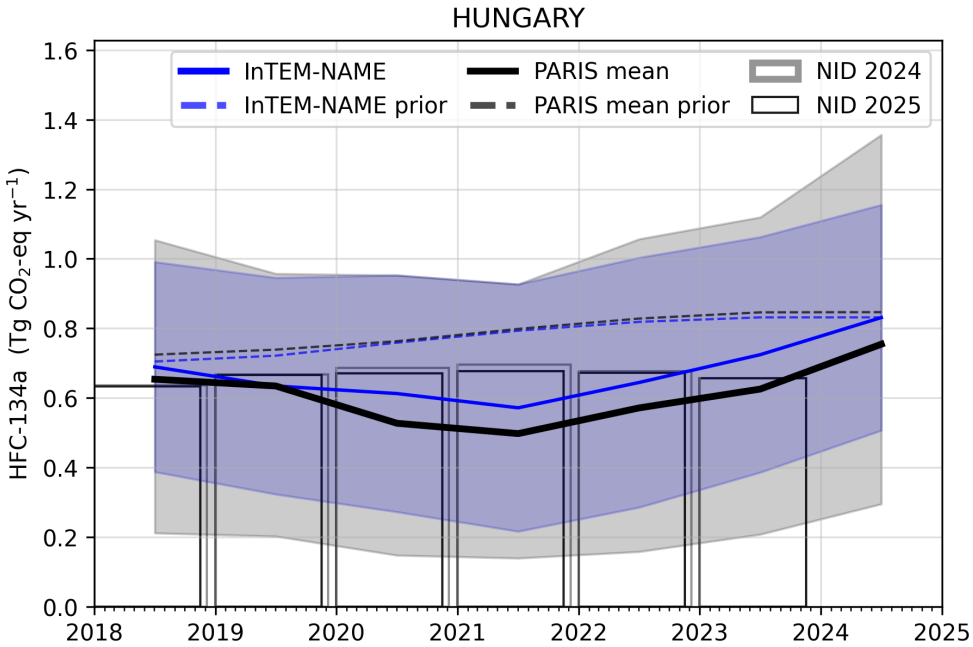

Figure 6.2.2: Spatial distribution of the Hungarian average modelled emissions of HFC-134a during the period of 2020-2024 (mean from all models). Observing stations are marked with red circles and highly-populated cities are marked with red triangles.

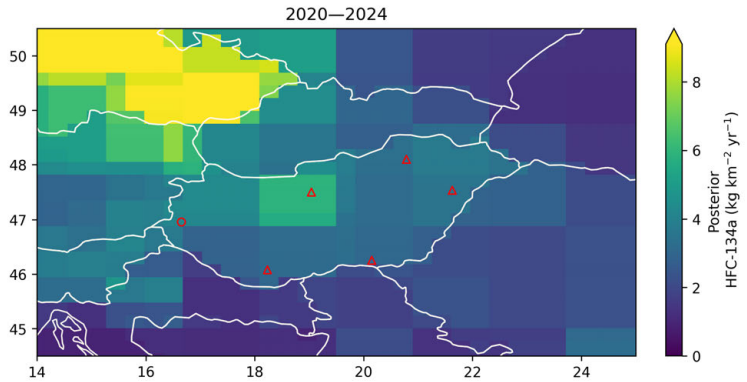

6.3 HFC-143a

Figure 6.3.1: Verification of the Hungarian emissions inventory estimates for HFC-143a. Modelled annual emissions are given as the mean from all models (black line) and the individual result from InTEM-NAME (blue line). The shaded blue area is the 68 % confidence interval (CI) of InTEM-NAME and the shaded grey area encompasses the 68 % CI from all models. National inventory annual totals from 2024 and 2025 are given as grey and black bars, respectively.

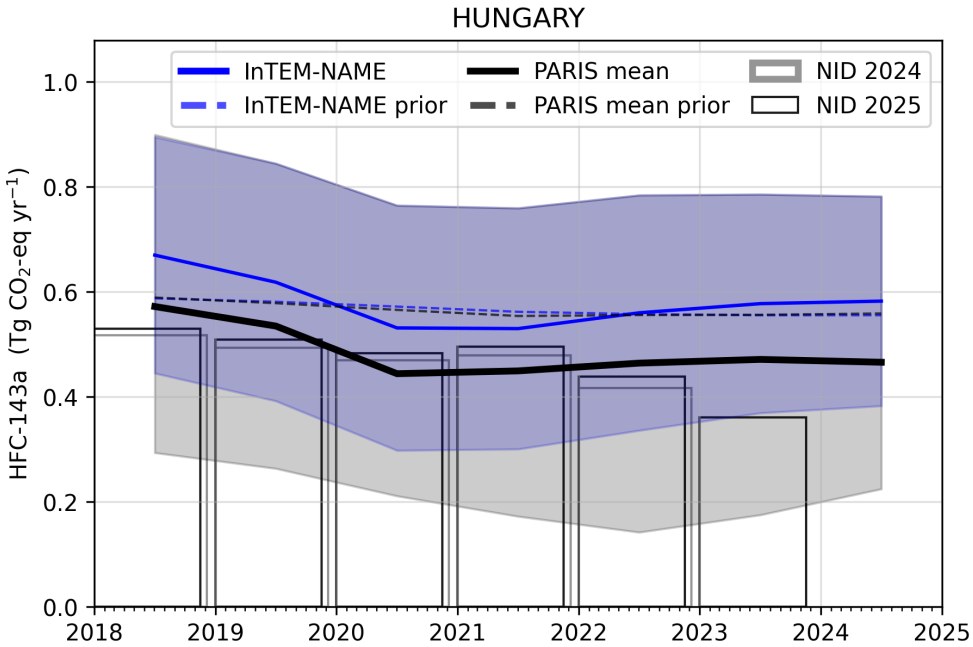

Figure 6.3.2: Spatial distribution of the Hungarian average modelled emissions of HFC-143a during the period of 2020-2024 (mean from all models). Observing stations are marked with red circles and highly-populated cities are marked with red triangles.

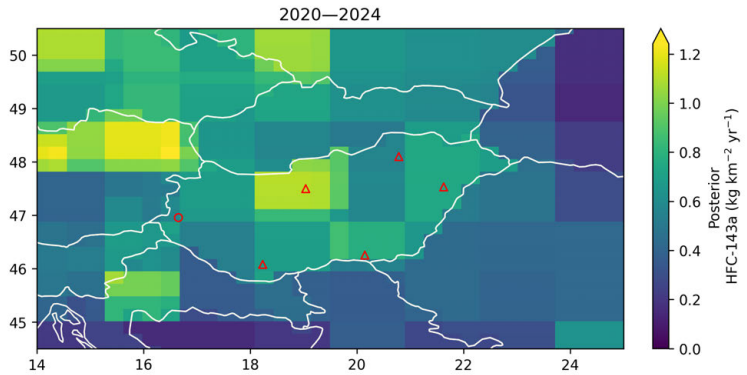

6.4 HFC-152a

Figure 6.4.1: Verification of the Hungarian emissions inventory estimates for HFC-152a. Modelled annual emissions are given as the mean from all models (black line) and the individual result from InTEM-NAME (blue line). The shaded blue area is the 68 % confidence interval (CI) of InTEM-NAME and the shaded grey area encompasses the 68 % CI from all models. National inventory annual totals from 2024 and 2025 are given as grey and black bars, respectively.

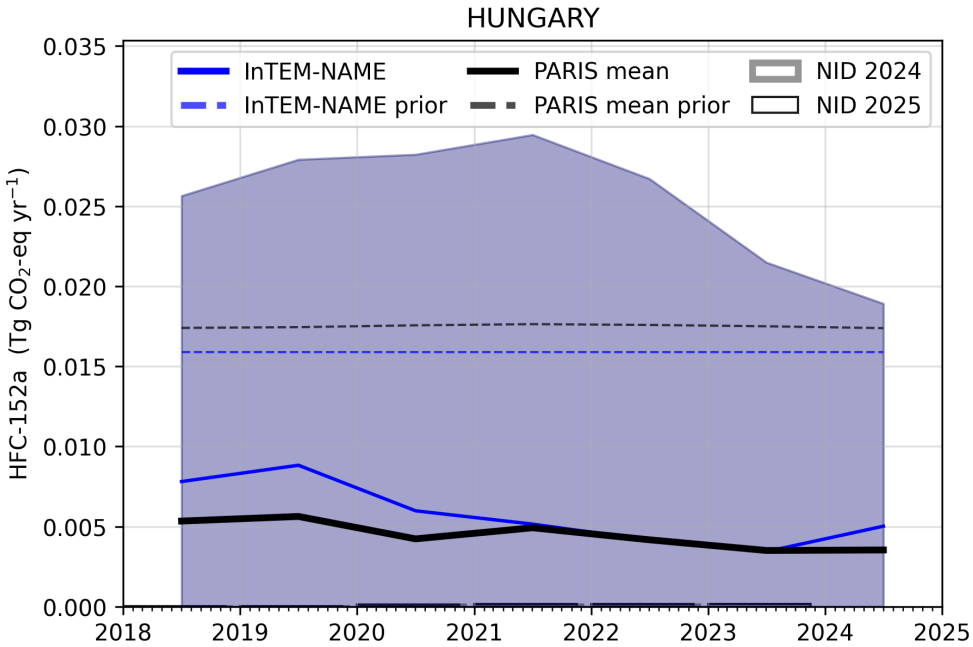

Figure 6.4.2: Spatial distribution of the Hungarian average modelled emissions of HFC-152a during the period of 2020-2024 (mean from all models). Observing stations are marked with red circles and highly-populated cities are marked with red triangles.

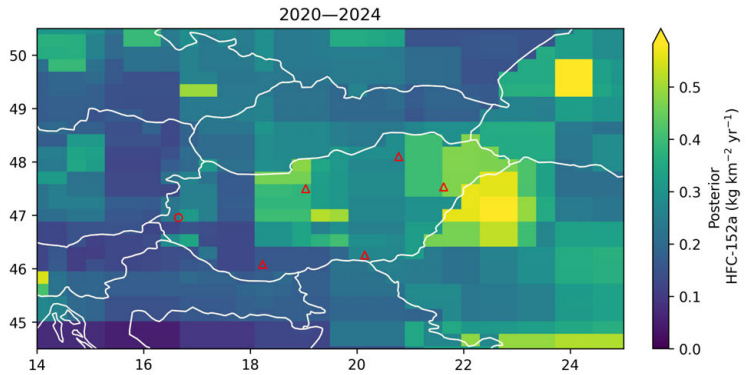

6.5 HFC-227ea

Figure 6.5.1: Verification of the Hungarian emissions inventory estimates for HFC-227ea. Modelled annual emissions are given as the mean from all models (black line) and the individual result from InTEM-NAME (blue line). The shaded blue area is the 68 % confidence interval (CI) of InTEM-NAME and the shaded grey area encompasses the 68 % CI from all models. National inventory annual totals from 2024 and 2025 are given as grey and black bars, respectively.

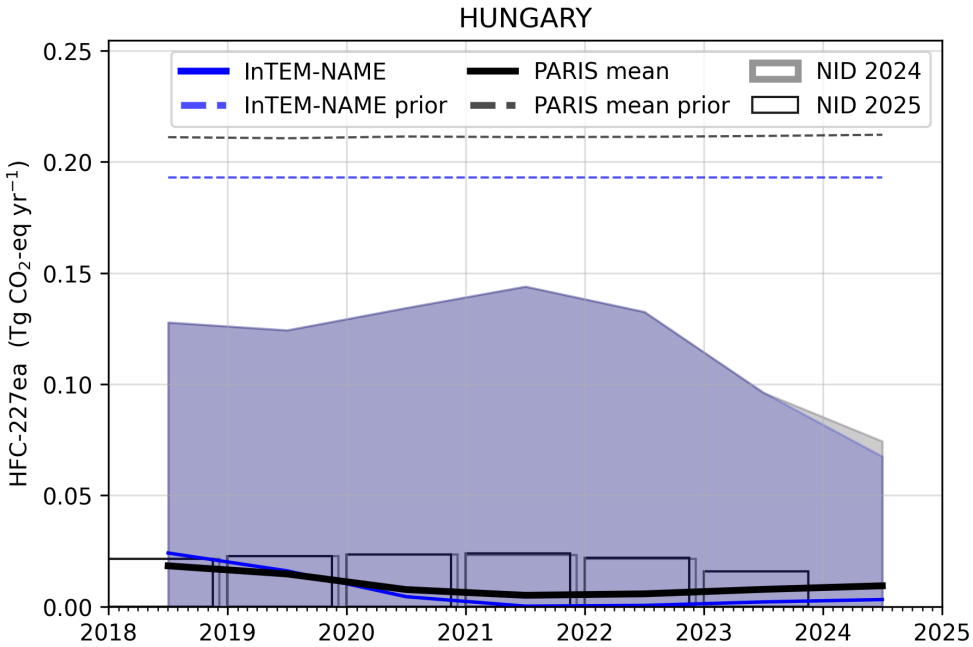

Figure 6.5.2: Spatial distribution of the Hungarian average modelled emissions of HFC-227ea during the period of 2020-2024 (mean from all models). Observing stations are marked with red circles and highly-populated cities are marked with red triangles.

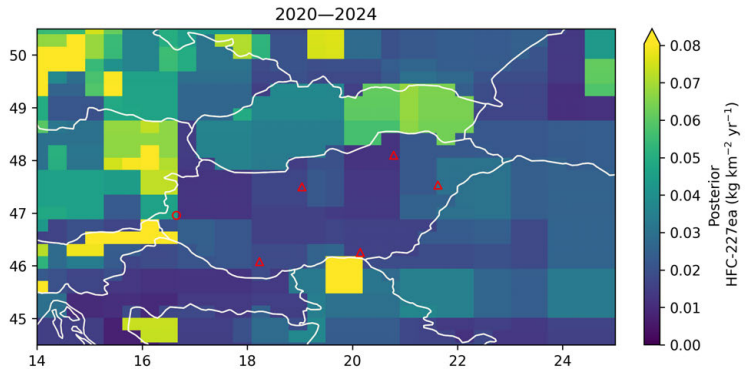

6.6 HFC-32

Figure 6.6.1: Verification of the Hungarian emissions inventory estimates for HFC-32. Modelled annual emissions are given as the mean from all models (black line) and the individual result from InTEM-NAME (blue line). The shaded blue area is the 68 % confidence interval (CI) of InTEM-NAME and the shaded grey area encompasses the 68 % CI from all models. National inventory annual totals from 2024 and 2025 are given as grey and black bars, respectively.

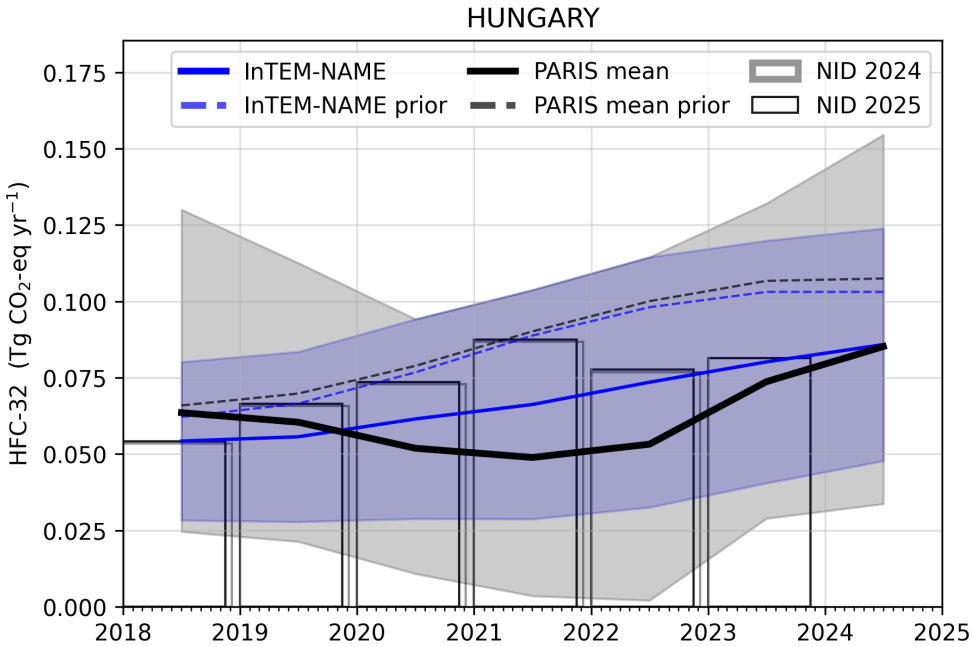

Figure 6.6.2: Spatial distribution of the Hungarian average modelled emissions of HFC-32 during the period of 2020-2024 (mean from all models). Observing stations are marked with red circles and highly-populated cities are marked with red triangles.

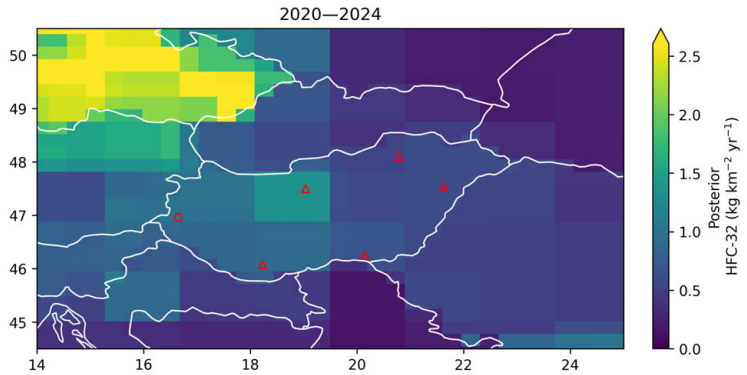

6.7 Total HFCs

Figure 6.7.1: Verification of the Hungarian emissions inventory estimates for total HFCs. Modelled annual emissions are given as the mean from all models (black line) and the individual result from InTEM-NAME (blue line). The shaded blue area is the 68 % confidence interval (CI) of InTEM-NAME and the shaded grey area encompasses the 68 % CI from all models. National inventory annual totals from 2024 and 2025 are given as grey and black bars, respectively.

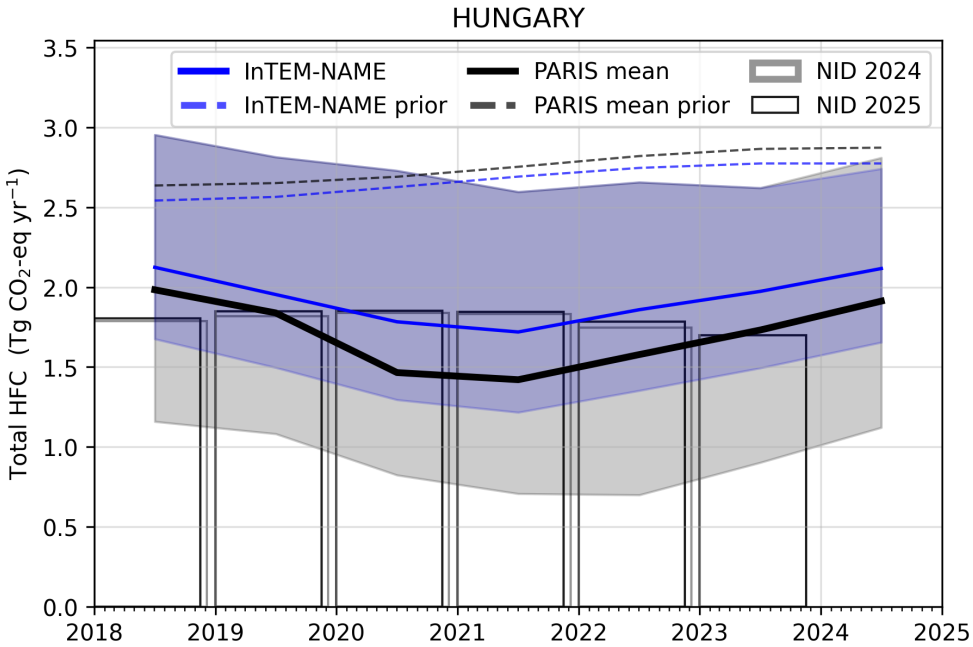

Table 2: Emissions estimation for HFCs according to the National Inventory Document (NID) 2025 and the inversions done in the PARIS project. For the PARIS estimation, the mean of all models is displayed, along with a range of uncertainty estimated via the half distance between the maximum and minimum uncertainties of the different models.

		2020	2021	2022	2023	2024
HFC-134a	NID 2025	0.67	0.68	0.67	0.66	
$(\mathrm{TgCO_2\text{-}eq} \cdot \mathrm{yr}^{-1})$	PARIS mean	0.53 ± 0.40	0.50 ± 0.39	0.57 ± 0.45	0.63 ± 0.46	0.75 ± 0.53
HFC-125	NID 2025	0.57	0.53	0.54	0.56	
$(\mathrm{TgCO_2\text{-}eq} \cdot \mathrm{yr}^{-1})$	PARIS mean	0.40 ± 0.37	0.39 ± 0.38	0.44 ± 0.38	0.52 ± 0.33	0.56 ± 0.36
HFC-143a	NID 2025	0.48	0.50	0.44	0.36	
$(\mathrm{TgCO_2\text{-}eq} \cdot \mathrm{yr}^{-1})$	PARIS mean	0.44 ± 0.28	0.45 ± 0.29	0.46 ± 0.32	0.47 ± 0.31	0.47 ± 0.28
HFC-32	NID 2025	74	87	78	81	
$(\mathrm{GgCO_2\text{-}eq} \cdot \mathrm{yr}^{-1})$	PARIS mean	52 ± 42	49 ± 50	53 ± 56	74 ± 52	85 ± 60
HFC-23	NID 2025	5	6	6	7	
$(\mathrm{GgCO_2\text{-}eq} \cdot \mathrm{yr}^{-1})$	PARIS mean	20 ± 405	18 ± 343	28 ± 293	24 ± 209	25 ± 207
HFC-227ea	NID 2025	23	24	22	16	
$(\mathrm{GgCO_2\text{-}eq} \cdot \mathrm{yr}^{-1})$	PARIS mean	8 ± 67	5 ± 72	6 ± 66	8 ± 48	9 ± 37
HFC-365mfc	NID 2025	31	32	29	20	
$(\mathrm{GgCO_2\text{-}eq} \cdot \mathrm{yr}^{-1})$	PARIS mean	9 ± 29	6 ± 29	4 ± 24	3 ± 20	4 ± 15
HFC-152a	NID 2025	0.1	0.1	0.2	0.2	
$(\mathrm{GgCO_2\text{-}eq} \cdot \mathrm{yr}^{-1})$	PARIS mean	4.2 ± 14.1	4.9 ± 14.7	4.2 ± 13.4	3.5 ± 10.7	3.5 ± 9.5
HFC-245fa	NID 2025	0.0	0.0	0.0	0.0	
$(\mathrm{GgCO_2\text{-}eq} \cdot \mathrm{yr}^{-1})$	PARIS mean	3.2 ± 29.9	3.2 ± 31.1	3.1 ± 25.2	3.7 ± 17.6	2.0 ± 10.9
HFC-236fa	NID 2025	0.0	0.0	0.0	0.0	
$(\mathrm{GgCO_2\text{-}eq} \cdot \mathrm{yr}^{-1})$	PARIS mean	1.7 ± 26.3	1.7 ± 26.9	1.5 ± 24.3	2.1 ± 18.9	2.6 ± 16.7
HFC-4310mee	NID 2025	0.00	0.00	0.00	0.00	
$(\mathrm{GgCO_2\text{-}eq} \cdot \mathrm{yr}^{-1})$	PARIS mean	0.66 ± 19.33	0.46 ± 17.11	0.34 ± 13.17	0.31 ± 8.69	0.32 ± 8.25

7 Perfluorocarbons (PFCs)

7.1 PFC-14

Figure 7.1.1: Verification of the Hungarian emissions inventory estimates for PFC-14. Modelled annual emissions are given as the mean from all models (black line) and the individual result from InTEM-NAME (blue line). The shaded blue area is the 68 % confidence interval (CI) of InTEM-NAME and the shaded grey area encompasses the 68 % CI from all models. National inventory annual totals from 2024 and 2025 are given as grey and black bars, respectively.

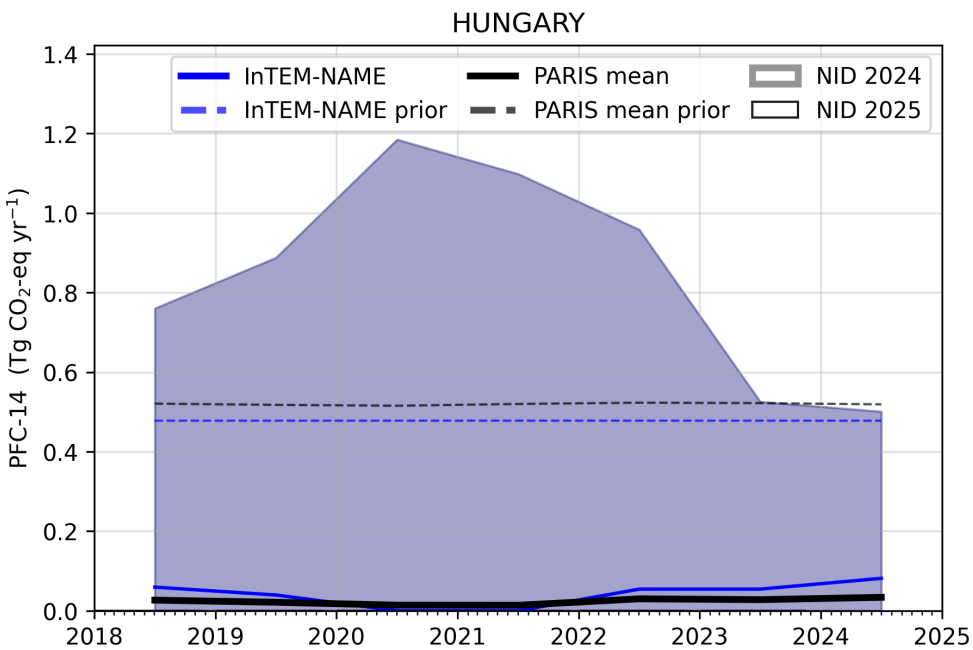

Figure 7.1.2: Spatial distribution of the Hungarian average modelled emissions of PFC-14 during the period of 2020-2024 (mean from all models). Observing stations are marked with red circles and highly-populated cities are marked with red triangles.

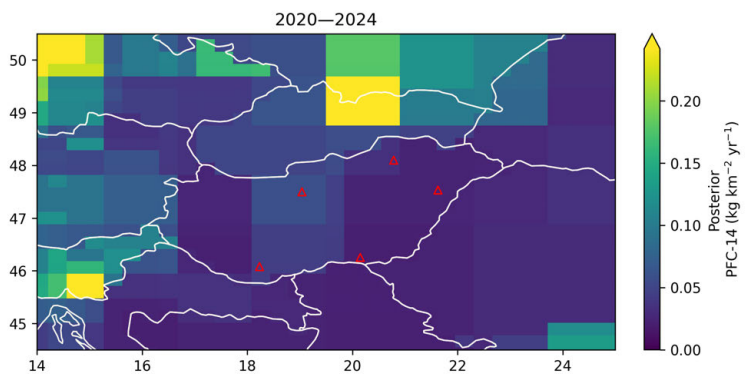

7.2 PFC-116

Figure 7.2.1: Verification of the Hungarian emissions inventory estimates for PFC-116. Modelled annual emissions are given as the mean from all models (black line) and the individual result from InTEM-NAME (blue line). The shaded blue area is the 68 % confidence interval (CI) of InTEM-NAME and the shaded grey area encompasses the 68 % CI from all models. National inventory annual totals from 2024 and 2025 are given as grey and black bars, respectively.

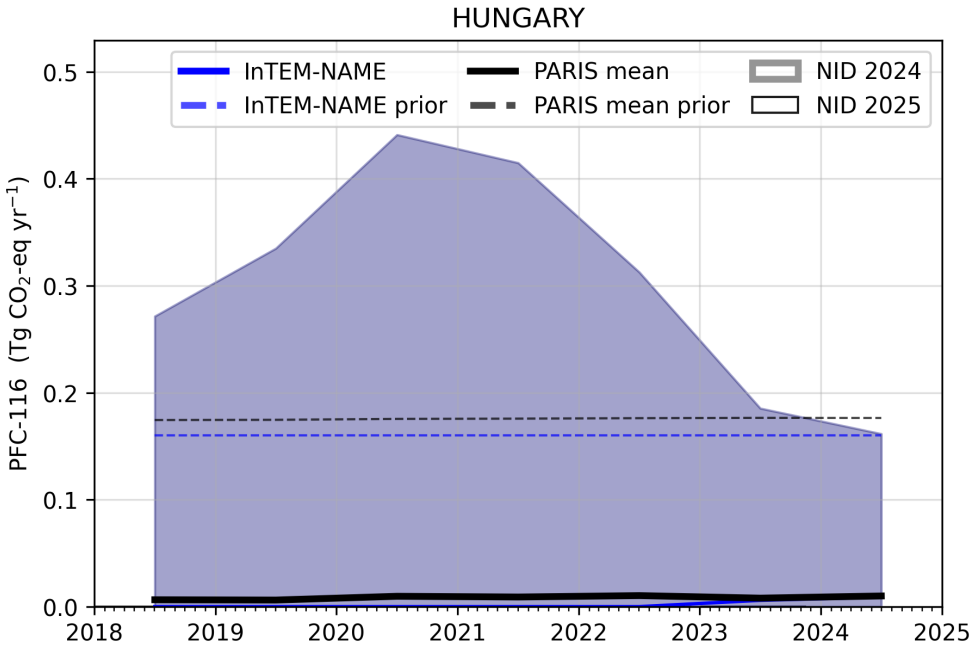

Figure 7.2.2: Spatial distribution of the Hungarian average modelled emissions of PFC-116 during the period of 2020-2024 (mean from all models). Observing stations are marked with red circles and highly-populated cities are marked with red triangles.

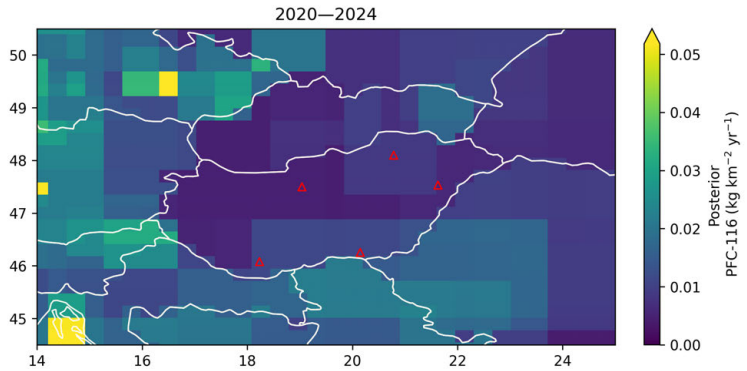

7.3 PFC-218

Figure 7.3.1: Verification of the Hungarian emissions inventory estimates for PFC-218. Modelled annual emissions are given as the mean from all models (black line) and the individual result from InTEM-NAME (blue line). The shaded blue area is the 68 % confidence interval (CI) of InTEM-NAME and the shaded grey area encompasses the 68 % CI from all models. National inventory annual totals from 2024 and 2025 are given as grey and black bars, respectively.

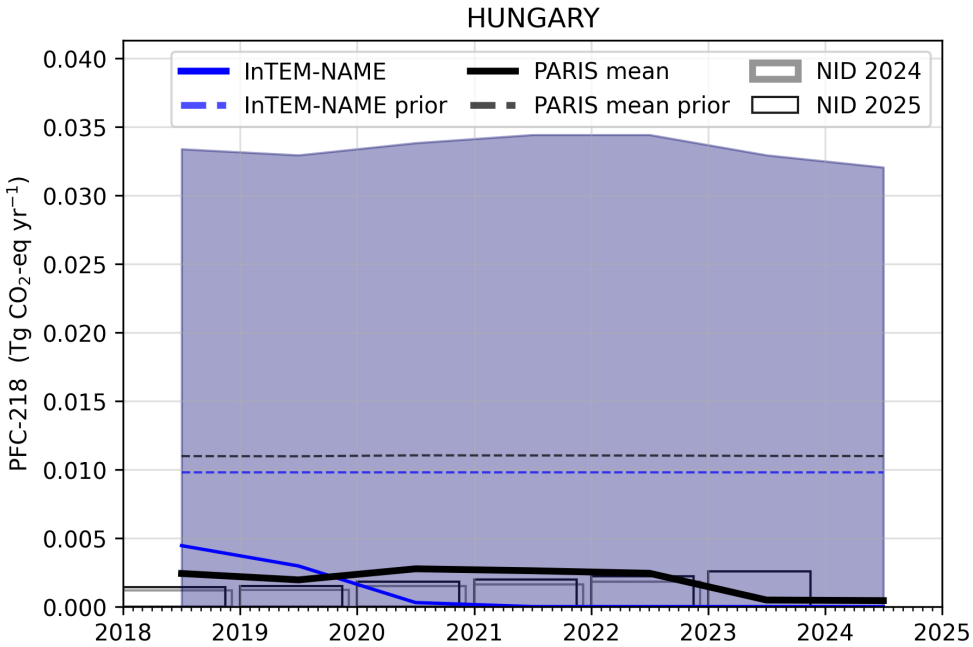

Figure 7.3.2: Spatial distribution of the Hungarian average modelled emissions of PFC-218 during the period of 2020-2024 (mean from all models). Observing stations are marked with red circles and highly-populated cities are marked with red triangles.

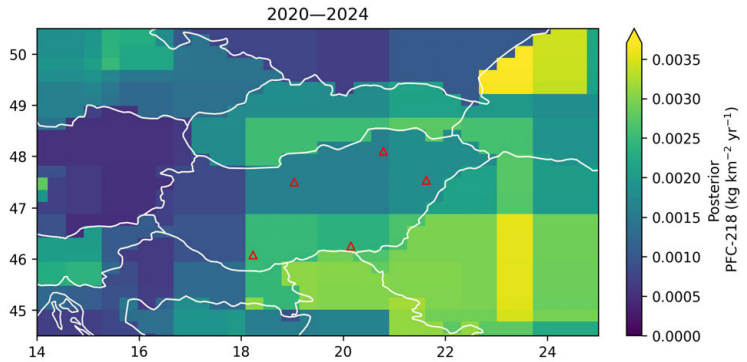

7.4 PFC-318

Figure 7.4.1: Verification of the Hungarian emissions inventory estimates for PFC-318. Modelled annual emissions are given as the mean from all models (black line) and the individual result from InTEM-NAME (blue line). The shaded blue area is the 68 % confidence interval (CI) of InTEM-NAME and the shaded grey area encompasses the 68 % CI from all models. National inventory annual totals from 2024 and 2025 are given as grey and black bars, respectively.

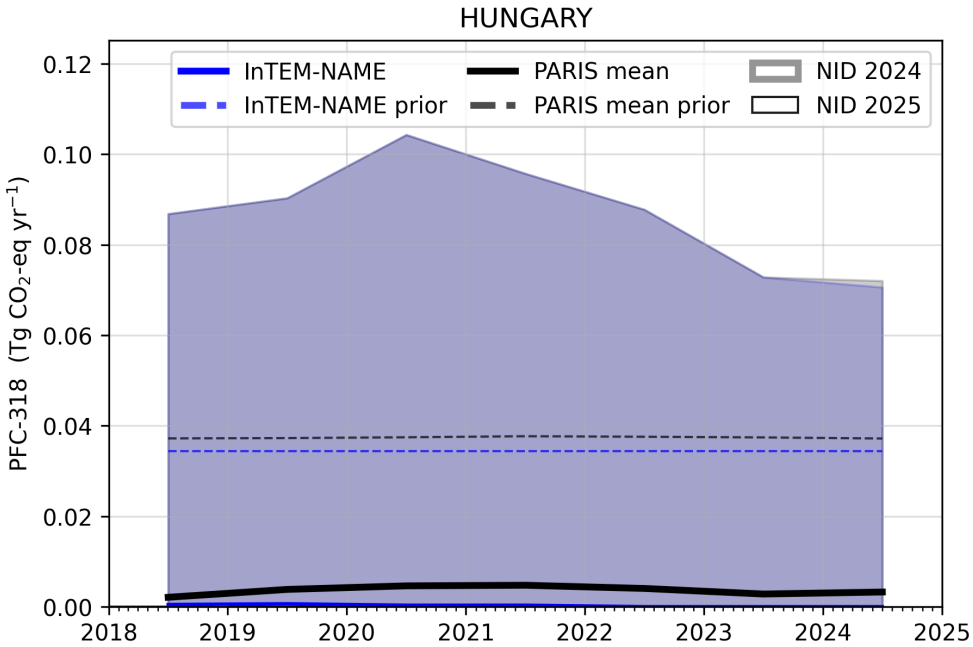

Figure 7.4.2: Spatial distribution of the Hungarian average modelled emissions of PFC-318 during the period of 2020-2024 (mean from all models). Observing stations are marked with red circles and highly-populated cities are marked with red triangles.

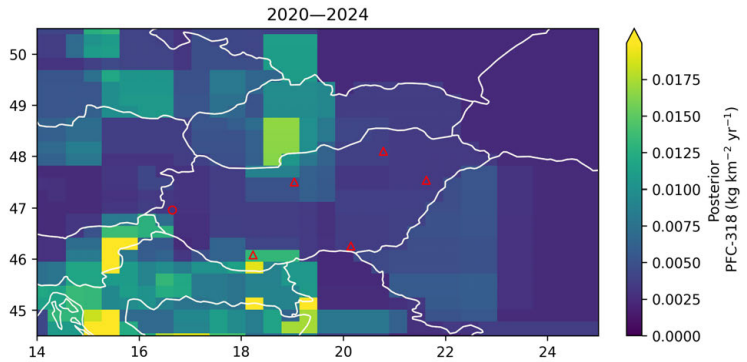

7.5 Total PFCs

Figure 7.5.1: Verification of the Hungarian emissions inventory estimates for total PFCs. Modelled annual emissions are given as the mean from all models (black line) and the individual result from InTEM-NAME (blue line). The shaded blue area is the 68 % confidence interval (CI) of InTEM-NAME and the shaded grey area encompasses the 68 % CI from all models. National inventory annual totals from 2024 and 2025 are given as grey and black bars, respectively.

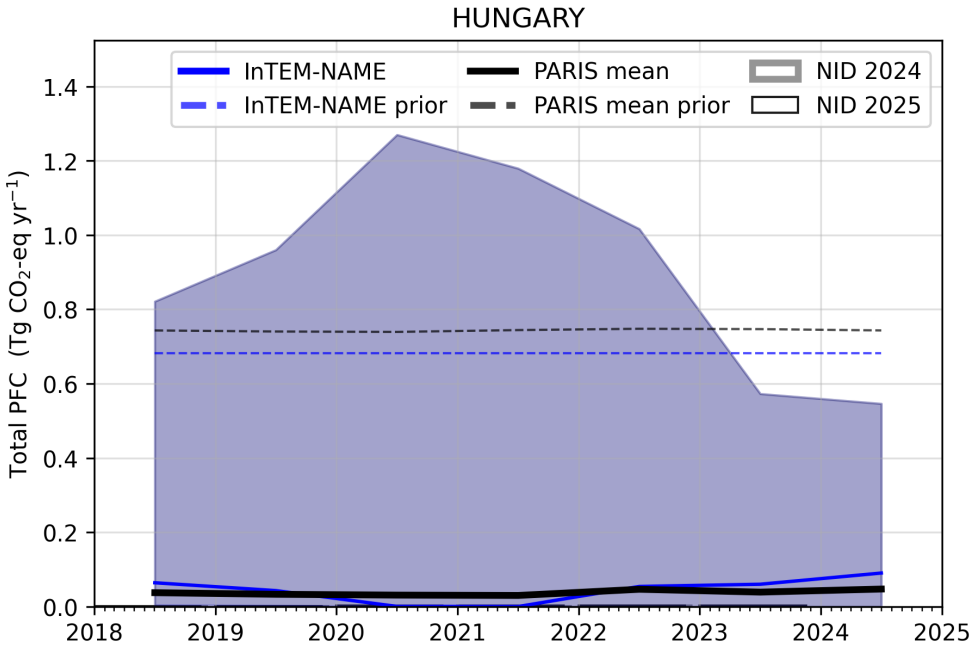

Table 3: Emissions estimation for PFCs according to the National Inventory Document (NID) 2025 and the inversions done in the PARIS project. For the PARIS estimation, the mean of all models is displayed, along with a range of uncertainty estimated via the half distance between the maximum and minimum uncertainties of the different models.

		2020	2021	2022	2023	2024
PFC-14	NID 2025	0	0	0	0	
$(\mathrm{GgCO_2\text{-}eq} \cdot \mathrm{yr}^{-1})$	PARIS mean	14 ± 592	14 ± 549	30 ± 479	28 ± 263	34 ± 250
PFC-116	NID 2025	0	0	0	0	
$(\mathrm{GgCO_2\text{-}eq} \cdot \mathrm{yr}^{-1})$	PARIS mean	10 ± 221	9 ± 207	10 ± 156	8 ± 93	10 ± 81
PFC-318	NID 2025	0.0	0.0	0.0	0.0	
$(\mathrm{GgCO_2\text{-}eq} \cdot \mathrm{yr}^{-1})$	PARIS mean	4.6 ± 52.2	4.7 ± 47.9	4.0 ± 43.9	2.8 ± 36.4	3.2 ± 36.0
PFC-218	NID 2025	1.8	2.0	2.2	2.6	
$(\mathrm{GgCO_2\text{-}eq} \cdot \mathrm{yr}^{-1})$	PARIS mean	2.8 ± 16.9	2.6 ± 17.2	2.4 ± 17.2	0.5 ± 16.5	0.4 ± 16.0

8 Sulphur hexafluoride (SF_6)

Figure 8.0.1: Total source sensitivity of SF_6 observing sites as calculated by the FLEXPART transport model for the year 2018 (left) and 2024 (right) and used in the inversions. Observing stations active in each year are marked with red dots. Areas with visible land surface represent regions for which emissions can be observed well from the network. Shaded or dark areas represent regions for which limited emission information can be obtained from the network.

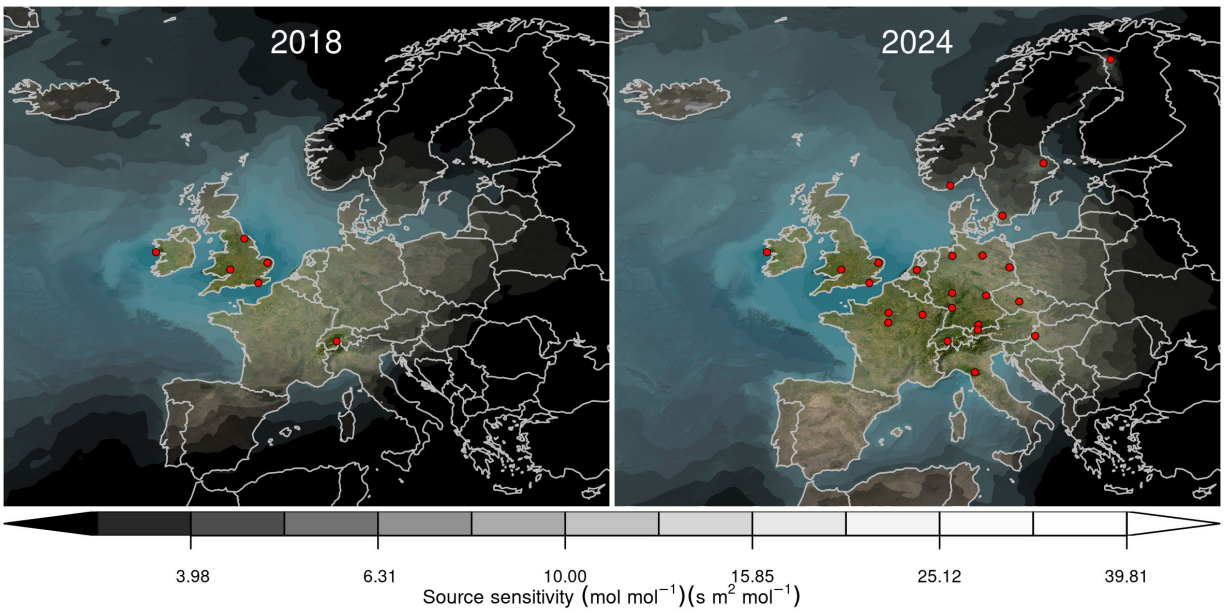

Figure 8.0.2: Verification of the Hungarian emissions inventory estimates for SF_6. Modelled annual emissions are given as the mean from all InTEM and ELRIS inversions (black line) and the individual result from InTEM-NAME (blue line). The shaded blue area is the 68 % confidence interval (CI) of InTEM-NAME and the shaded grey area encompasses the 68 % CI from all models. National inventory annual totals from 2024 and 2025 are given as grey and black bars, respectively.

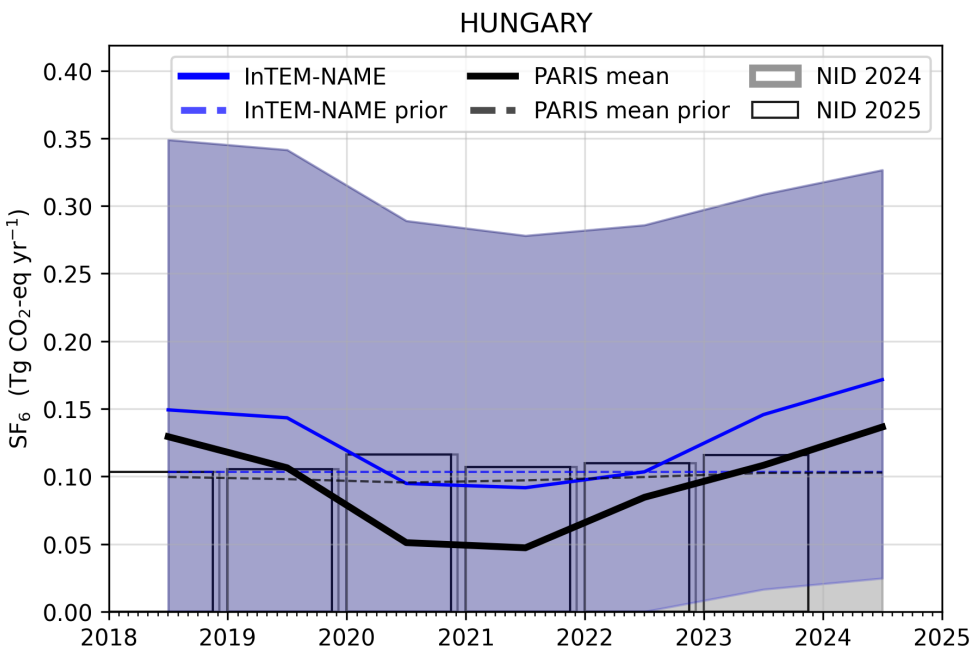

Figure 8.0.3: Spatial distribution of the Hungarian average modelled emissions of SF_6 during the period of 2020-2024 (mean from all InTEM and ELRIS inversions). Observing stations are marked with red circles and highly-populated cities are marked with red triangles.

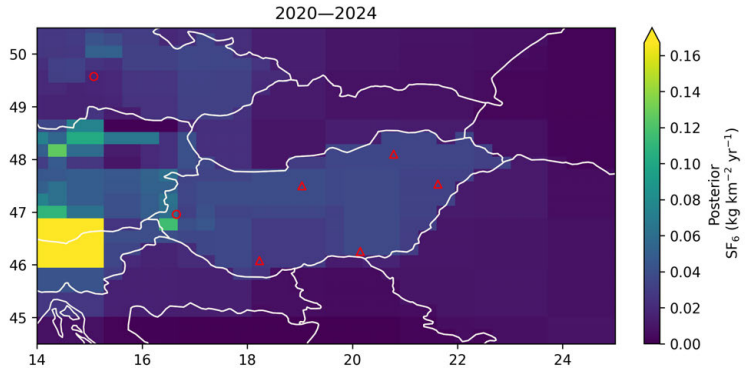

9 Carbon Dioxide (CO_2)

Measurements of CO_2 at ICOS sites and related observatories are influenced by a complex combination of sources and sinks. Fossil fuel combustion for transport, heating, energy generation, and other applications produce CO_2, along with other anthropogenic activities such as cement production. The terrestrial and oceanic biosphere produces CO_2 through animal and plant respiration and takes up CO_2 through photosynthesis. Furthermore, CO_2 is exchanged with the ocean through physical and chemical processes.

When considering high-frequency (∼hourly) CO_2 mole fraction deviations from baseline values—used to infer national emissions in regional inverse modelling studies—the influence of biospheric fluxes can be comparable to, or larger than, those of anthropogenic sources (e.g. White et al., 2019). Therefore, research is under way to develop new tracers that can determine fossil fuel CO_2 fluxes independent of biosphere sources and sinks.

Ongoing Horizon Europe projects PARIS and CORSO are examining methods for estimating fossil fuel CO_2 fluxes based on simultaneous measurements of CO_2 and O_2 (Figure 9.0.1). The method relies on the fact that CO_2 and O_2 are inter-converted during combustion and terrestrial biosphere exchange, but with different ratios for the two processes. A quantity can be constructed from these measurements, known as Atmospheric Potential Oxygen (APO), which is insensitive to biosphere fluxes, and may therefore be useful for isolating fossil fuel signals (Pickers et al., 2022).

High-frequency (∼hourly) timeseries of APO are available from Weybourne (WAO, 2010 – present) and Heathfield (HFD, 2021 - present) in the UK (Figure 9.0.1; Pickers, Adcock, and Manning, 2024), and new sites are being established at Cabauw and Zweth in the Netherlands. Preliminary analyses of the WAO data have revealed regional APO trends consistent with the drop in fossil fuel CO_2 emissions during the COVID lockdowns in the UK (Pickers et al., 2022). However, quantification of absolute regional fossil fuel CO_2 emissions remains an area of active research. Recent studies have derived fossil fuel CO_2 emissions for the UK that are highly uncertain (Rigby et al., 2025). Potential confounding factors were identified in Chawner et al. (2024), such as highly uncertain APO fluxes from the ocean, and a poorly constrained regional APO background. These factors are the subject of ongoing research using atmospheric models and new APO measurements from PARIS, CORSO and ICOS.

An alternative method for top-down fossil fuel CO_2 emissions evaluation uses measurements of radiocarbon isotopologues ($^{14}CO_2$, compared to the dominant $^{12}CO_2$). Fossil fuels do not contain ^{14}C, and therefore, their combustion tends to decrease the atmospheric $^{14}CO_2/^{12}CO_2$ ratio. Currently, radiocarbon measurements can only be made at low frequency using flask sampling. However, a relatively intensive flask sampling campaign was carried out across Europe during 2024 as part of CORSO, and the results of this study will be reported on soon.

Figure 9.0.1: Carbon dioxide (top, red) and oxygen (bottom, blue) measurements from Weybourne Atmospheric Observatory in the UK, available from the ICOS Carbon Portal (Adcock et al., 2024).

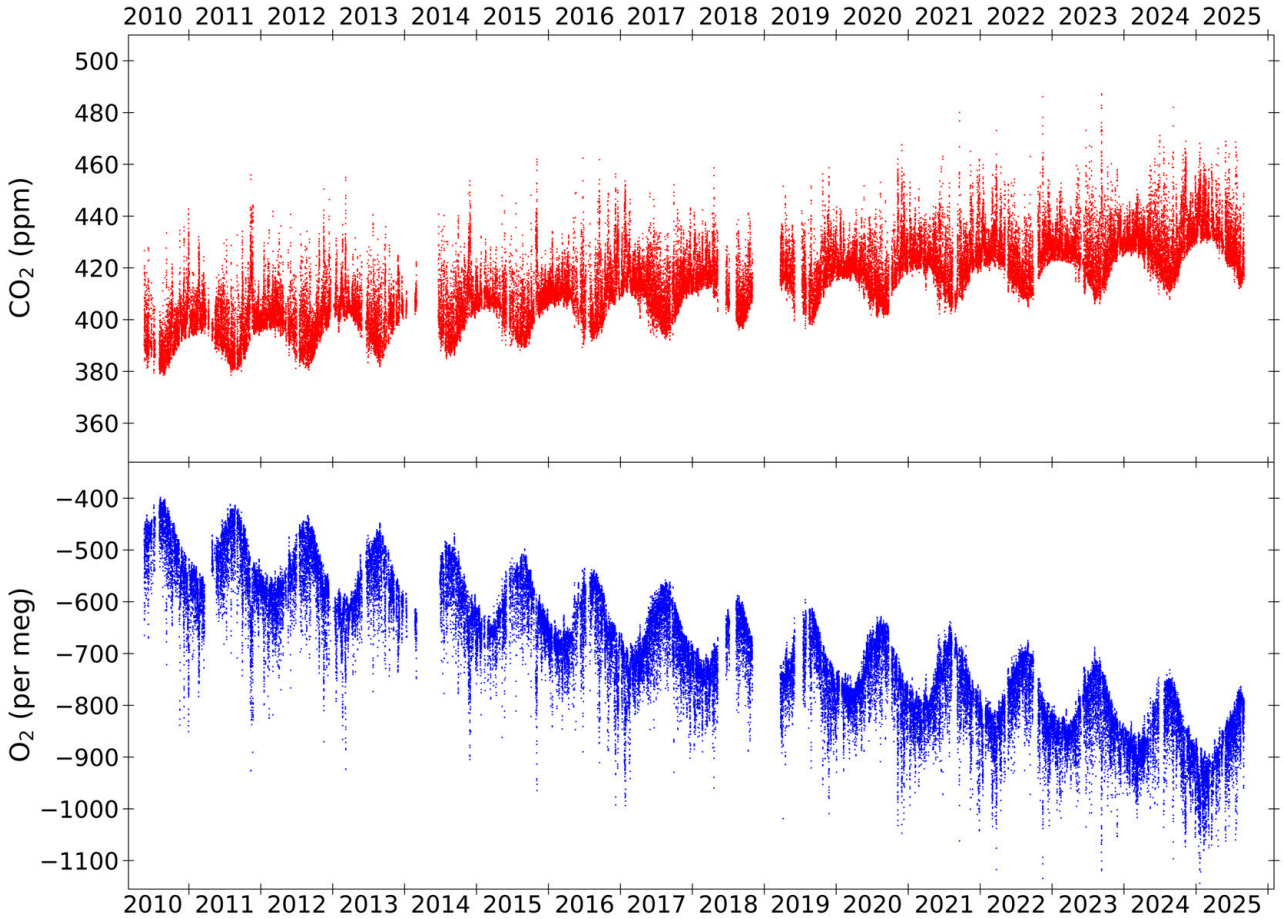

10 Impact of Hegyhátsál

The impact on derived HFC emissions of including observations from additional European stations, as developed partly within the PARIS project, can be assessed by running two sets of inversions, with (expanded network) and without (7-site network) these additional stations. Additional stations are Zugspitze, Germany (ZSF), Capo Granitola, Italy (CGR), Hegyhátsál, Hungary (HUN), Birkenes, Norway (BIR), whereas the seven core sites are Mace Head, Ireland (MHD), Tacolneston, UK (TAC), Jungfraujoch, Switzerland (JFJ), Monte Cimone, Italy (CMN), Zeppelin, Spitsbergen (ZEP), Taunus observatory, Germany (TOB), and Cabauw, Netherlands (CBW). Of special interest for estimating Hungarian emissions are the new samples taken at Hegyhátsál in 2024. These samples were taken as flask samples at the station and then shipped for analysis to the University of Frankfurt, Germany. Samples were taken every other day and a total of 150 analysed and validated samples were available in 2024 for the compounds HFC-125, HFC-134a, HFC-143a, HFC-152a, HFC-227ea, HFC-32.

For all six gases, observations from HUN help to constrain emissions in the western part of Hungary and the neighbouring countries as indicated by comparing sensitivity inversions with (expanded) and without (7-site) the use of observations from HUN. This is especially obvious for an improved localisation of emission to large cities (Vienna, Bratislava, Zagreb) when using the expanded network (e.g., Figure 10.0.1, 10.0.2, 10.0.3). For some gases emissions from Budapest become more discernable as well (e.g., Figure 10.0.2, 10.0.6). However, network sensitivity towards eastern Hungary remains low and large uncertainty in total Hungarian emission estimates remain without additional observing sites.

Figure 10.0.1: 2024 HFC-125 emissions derived using (left) an expanded network, (middle) the base network, and (left) their difference. Measurement stations are shown as red circles, major cities as red triangles.

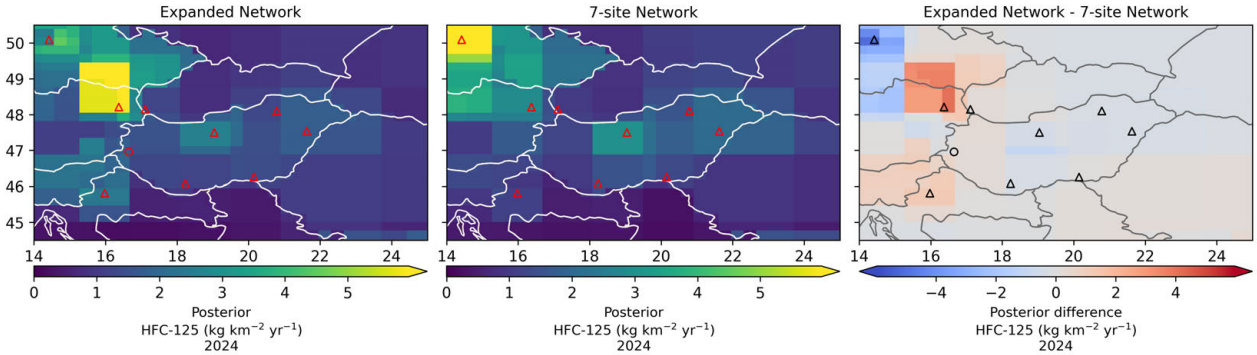

Figure 10.0.2: 2024 HFC-134a emissions derived using (left) an expanded network, (middle) the base network, and (left) their difference. Measurement stations are shown in circles, major cities as triangles.

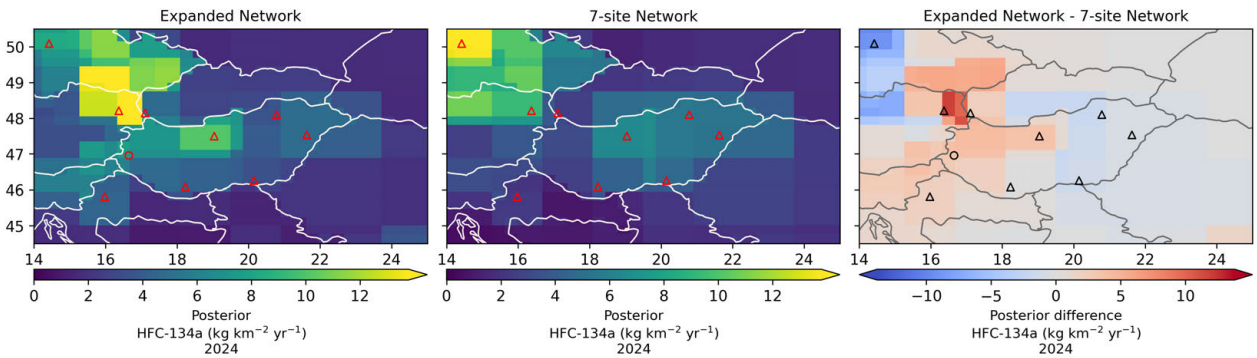

Figure 10.0.3: 2024 HFC-143a emissions derived using (left) an expanded network, (middle) the base network, and (left) their difference. Measurement stations are shown in circles, major cities as triangles.

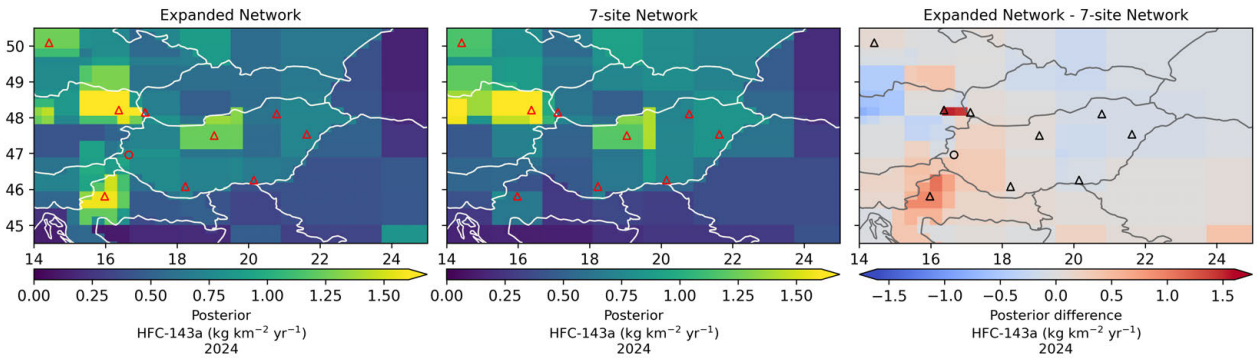

Figure 10.0.4: 2024 HFC-152a emissions derived using (left) an expanded network, (middle) the base network, and (left) their difference. Measurement stations are shown in circles, major cities as triangles.

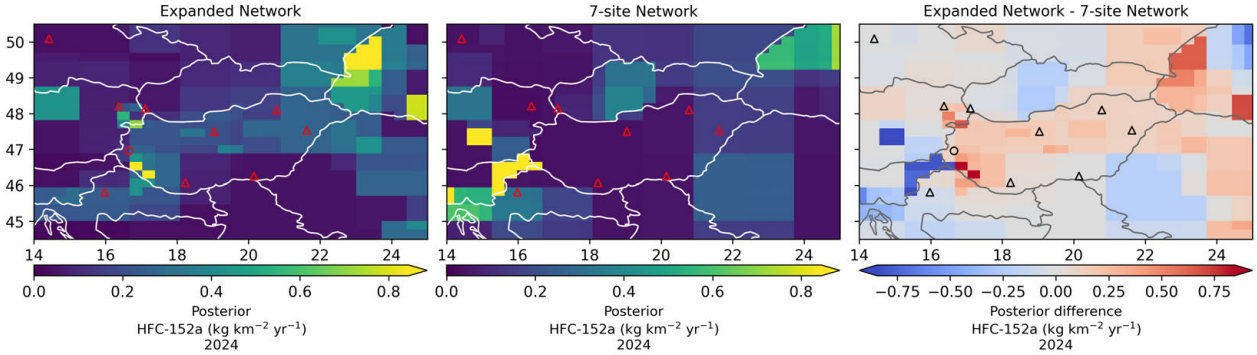

Figure 10.0.5: 2024 HFC-227ea emissions derived using (left) an expanded network, (middle) the base network, and (left) their difference. Measurement stations are shown in circles, major cities as triangles.

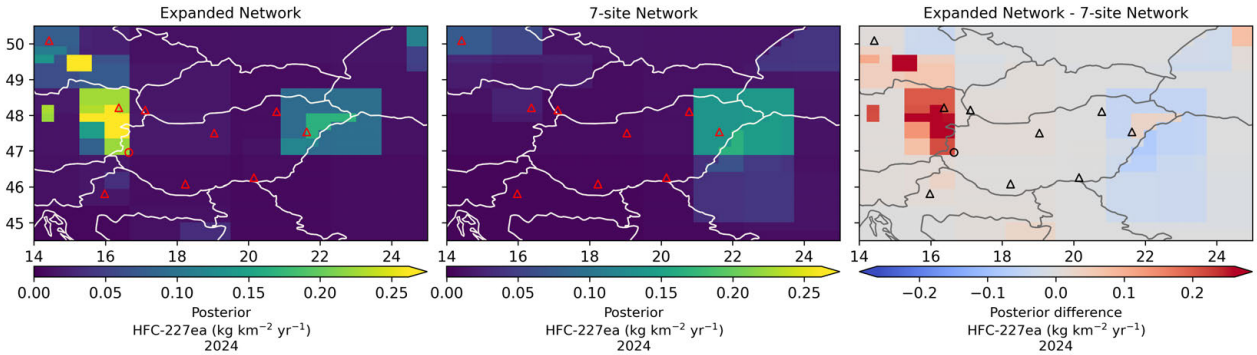

Figure 10.0.6: 2024 HFC-32 emissions derived using (left) an expanded network, (middle) the base network, and (left) their difference. Measurement stations are shown in circles, major cities as triangles.

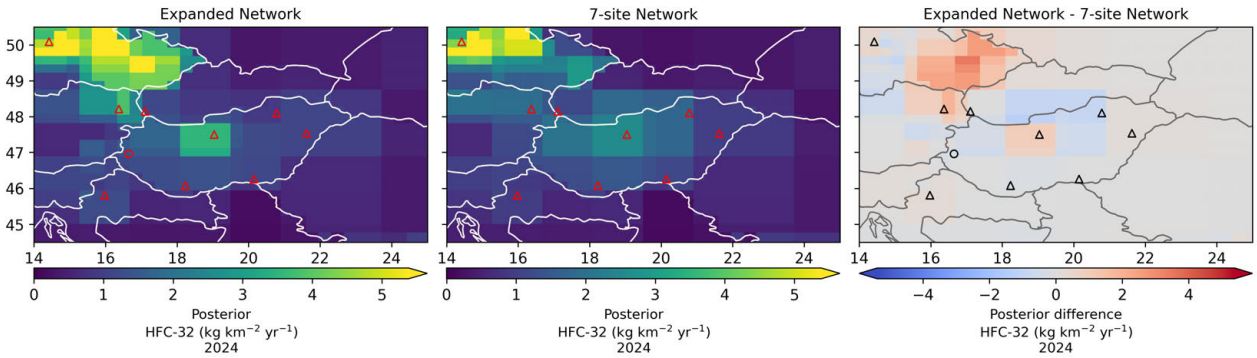

References

Adcock, Karina et al. (2024). *Atmospheric GHG data product (o2, o2_stdev, co2, co2_stdev) from Weybourne (10.0 m), 2010-05-19–2023-12-31*. URL: https://hdl.handle.net/11676/j4LzdHQiq3fPgfNeXHruC0Bb.

Chawner, Hannah et al. (Apr. 2024). "Atmospheric oxygen as a tracer for fossil fuel carbon dioxide: a sensitivity study in the UK". en. In: *Atmospheric Chemistry and Physics* 24.7, pp. 4231–4252. ISSN: 1680-7324. DOI: 10.5194/acp-24-4231-2024. URL: https://acp.copernicus.org/articles/24/4231/2024/ (visited on 04/10/2024).

European Commission: Joint Research, Centre et al. (2023). *GHG emissions of all world countries – 2023*. Publications Office of the European Union. DOI: 10.2760/953322.

Ganesan, A. L. et al. (2014). "Characterization of uncertainties in atmospheric trace gas inversions using hierarchical Bayesian methods". In: *Atmospheric Chemistry and Physics* 14.8, pp. 3855–3864. DOI: 10.5194/acp-14-3855-2014. URL: http://www.atmos-chem-phys.net/14/3855/2014/http://www.atmos-chem-phys.net/14/3855/2014/acp-14-3855-2014.pdf.

Ganesan, A. L. et al. (2015). "Quantifying methane and nitrous oxide emissions from the UK and Ireland using a national-scale monitoring network". In: *Atmos. Chem. Phys.* 15.11, pp. 6393–6406. DOI: 10.5194/acp-15-6393-2015. URL: https://www.atmos-chem-phys.net/15/6393/2015/https://www.atmos-chem-phys.net/15/6393/2015/acp-15-6393-2015.pdf.

Henne, S. et al. (2016). "Validation of the Swiss methane emission inventory by atmospheric observations and inverse modelling". In: *Atmospheric Chemistry and Physics* 16.6, pp. 3683–3710. DOI: 10.5194/acp-16-3683-2016. URL: http://www.atmos-chem-phys.net/16/3683/2016/.

Jones, A.R. et al. (2007). "The U.K. Met Office's next-generation atmospheric dispersion model, NAME III, in Borrego C. and Norman A.-L. (Eds)". In: *Air Pollution Modeling and its Application XVII (Proceedings of the 27th NATO/CCMS International Technical Meeting on Air Pollution Modelling and its Application), Springer*, pp. 580–589.

Katharopoulos, I. et al. (2023). "Impact of transport model resolution and a priori assumptions on inverse modeling of Swiss F-gas emissions". In: *Atmos. Chem. Phys.* 23.22, pp. 14159–14186. DOI: 10.5194/acp-23-14159-2023. URL: https://acp.copernicus.org/articles/23/14159/2023/.

Manning, A. J. et al. (2021). "Evidence of a recent decline in UK emissions of hydrofluorocarbons determined by the InTEM inverse model and atmospheric measurements". In: *Atmospheric Chemistry and Physics* 21.16, pp. 12739–12755. DOI: 10.5194/acp-21-12739-2021. URL: https://acp.copernicus.org/articles/21/12739/2021/.

Pickers, P., K. Adcock, and A. Manning (Feb. 2024). *Atmospheric oxygen and carbon dioxide observations from Weybourne Atmospheric Observatory, Norfolk, UK uploaded to public archives*. Tech. rep. Process Attribution of Regional Emissions (PARIS). URL: https://horizoneurope-paris.eu/wp-content/uploads/sites/914/2024/07/PARIS-deliverables-D6.1-High-frequency-APO-data-uploaded-final.pdf.

Pickers, Penelope A. et al. (Apr. 2022). "Novel quantification of regional fossil fuel CO2 reductions during COVID-19 lockdowns using atmospheric oxygen measurements". en. In: *Science Advances* 8.16, eabl9250. ISSN: 2375-2548. DOI: 10.1126/sciadv.abl9250. URL: https://www.science.org/doi/10.1126/sciadv.abl9250 (visited on 12/01/2023).

Rigby, M. et al. (2019). "Increase in CFC-11 emissions from eastern China based on atmospheric observations". In: *Nature* 569, pp. 546–550. DOI: 10.1038/s41586-019-1193-4. URL: https://doi.org/10.1038/s41586-019-1193-4.

Rigby, M. et al. (Apr. 2025). *Inverse estimates of fossil fuel CO2 emission*. Tech. rep. Process Attribution of Regional Emissions (PARIS). URL: https://horizoneurope-paris.eu/wp-content/uploads/sites/914/2025/01/PARIS-M24-Inverse-estimates-of-fossil-fuel-CO2-emissions-final.pdf.

Stohl, A. et al. (2005). "Technical note: The Lagrangian particle dispersion model FLEXPART version 6.2". In: *Atmospheric Chemistry and Physics* 5, pp. 2461–2474. DOI: 10.5194/acp-5-2461-2005. URL: <GotoISI>://000231983600002.

White, Emily D. et al. (Apr. 2019). "Quantifying the UK's carbon dioxide flux: an atmospheric inverse modelling approach using a regional measurement network". en. In: *Atmospheric Chemistry and Physics*

19.7, pp. 4345–4365. ISSN: 1680-7324. DOI: 10.5194/acp-19-4345-2019. URL: https://www.atmos-chem-phys.net/19/4345/2019/ (visited on 04/05/2019).

Draft Inventory Annex
Italy 2025

30th October, 2025

1 Introduction

In this document, global concentration trends and national emissions estimates derived from atmospheric observations ("inverse estimates") are presented for most reported gases. Comparing the emissions submitted in national inventories with those calculated using atmospheric observations allows for emissions to be assessed using two fundamentally different approaches. Substantial differences can highlight areas that could warrant further investigation.

Global concentration trends for each gas are first shown using annual average concentrations from Mace Head, Ireland (Northern Hemisphere) and Kennaook/Cape Grim, Tasmania, Australia (Southern Hemisphere). Data from these stations were selected to exclude regionally-polluted air masses and therefore represents northern and southern hemispheric concentration trends. Mace Head observations were supported by the National Aeronautics and Space Administration (NASA) and the UK Department of Energy, Security and Net Zero (DESNZ), and Kennaook/Cape Grim observations by NASA and the Australian Bureau of Meteorology.

Observations of European concentrations of greenhouse gases used to derive national inverse emission estimates were collected from many different networks and providers. Methane and nitrous oxide concentrations originated from the European ICOS (Integrated Carbon Observation System) network, the UK DECC (Deriving Emissions related to Climate Change) network and other national or individual initiatives. F-gas observations were made by affiliates of the AGAGE (Advanced Global Atmospheric Gases Experiment) network. Observations from additional stations across Europe were supported by the Horizon-EU PARIS (Process Attribution of Regional Emissions) project. The observation stations used to derive emissions for each gas are shown in the corresponding sections of this document.

An atmospheric transport model provides the link between surface fluxes and concentrations measured at the observing stations. If not otherwise mentioned, inversion-based emissions estimates were derived using two atmospheric transport models combined with three inverse models, yielding a total of six inversions. This ensemble of six inversions allows us to better quantify the uncertainties associated with inverse modelling.

The two atmospheric transport models used are the Numerical Atmospheric dispersion Modelling Environment (NAME, Jones et al., 2007), and the FLEXible PARTicle dispersion model (FLEXPART, Stohl et al., 2005). Both models are backwards-running Lagrangian Particle Dispersion Models (LPDMs) that simulate the recent transport of air to each observing station. The two LPDMs have been widely used in the estimation of greenhouse gas emissions (Ganesan et al., 2015; Rigby et al., 2019; Manning et al., 2021; Henne et al., 2016).

The three inverse methods used are InTEM (Inversion Technique for Emission Modelling, Manning et al., 2021), ELRIS (Empa Lagrangian Regional Inversion System, Henne et al., 2016; Katharopoulos et al., 2023), and RHIME (Regional Hierarchical Inverse Modelling Environment, Ganesan et al., 2014). All three inverse methods estimate emissions within Europe along with boundary conditions that account for the concentration of the air entering Europe. All three systems started from the same set of a priori emissions that were either derived from the global EDGAR emission inventory (version 8, European Commission: Joint Research et al., 2023) or a uniform land-based emission, depending on the gas. A natural emission component, from the WETCHARTS product, was included in the methane prior. The same observational dataset was used by each inverse model, but data selection (i.e., filtering datasets for specific conditions) and treatment of uncertainties were chosen separately and hence differ. The three methods also differ in their statistical approaches for estimating emissions.

Emission estimates are presented for the period 2008-2024. Emissions for the full 2008-2024 period were derived with the InTEM-NAME inversion only, while emissions from 2017-2024 are presented as the mean of the six inversions (denoted the "PARIS mean"). The uncertainty shown is the minimum/maximum of the uncertainties in the ensemble.

All inversions employed a resolution of one month for CH_4 and N_2O and 1-year for the fluorinated gases. The inversion results used to compare with the inventories are a one-year calendar average for CH_4 and N_2O and the yearly value derived from a 3-year moving average for the fluorinated gases. For the 2008-2024

InTEM-NAME results, a 3-year moving average was also applied to the annualised CH_4 and N_2O results due to lack of observational coverage in the earlier years.

2 Global Concentration Trends

2.1 Methane (CH_4)

Figure 2.1.1: Background Northern Hemisphere monthly concentrations of CH_4 estimated from MHD, Ireland observations are shown in red, and background Southern Hemisphere monthly concentrations from CGO, Tasmania are shown in blue. Grey shading represents provisional data.

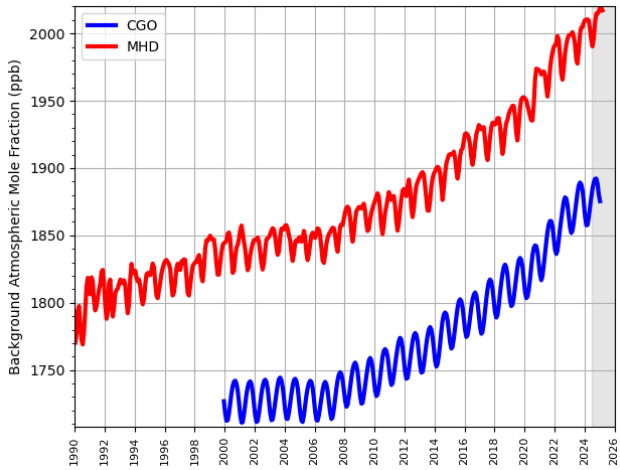

2.2 Nitrous Oxide (N_2O)

Figure 2.2.1: Background Northern Hemisphere monthly concentrations of N_2O estimated from MHD, Ireland observations are shown in red, and background Southern Hemisphere monthly concentrations from CGO, Tasmania are shown in blue. Grey shading represents provisional data.

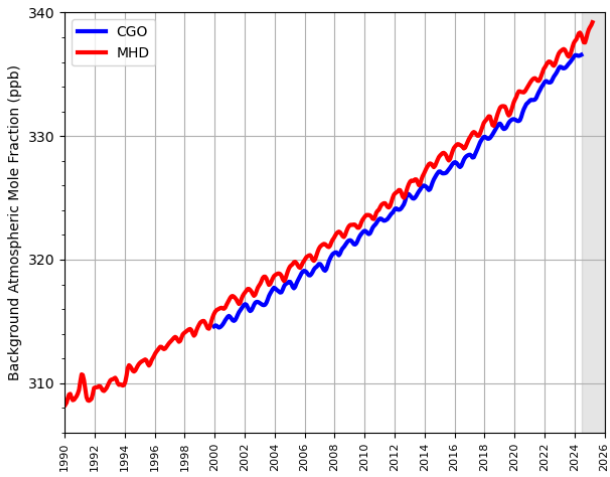

2.3 Hydrofluorocarbons (HFCs)

Figure 2.3.1: Background Northern Hemisphere monthly concentrations of six HFCs estimated from MHD, Ireland observations are shown in red, and background Southern Hemisphere monthly concentrations from CGO, Tasmania are shown in blue. Grey shading represents provisional data.

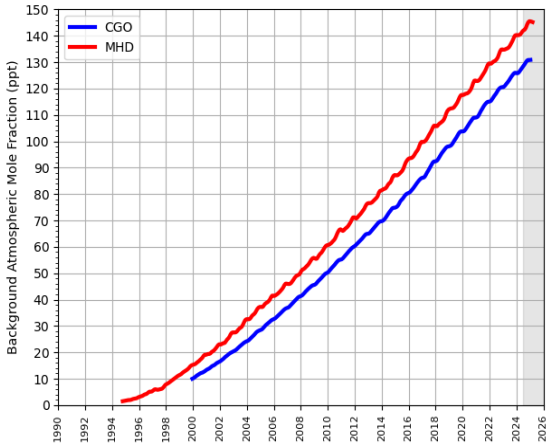

(a) HFC-134a

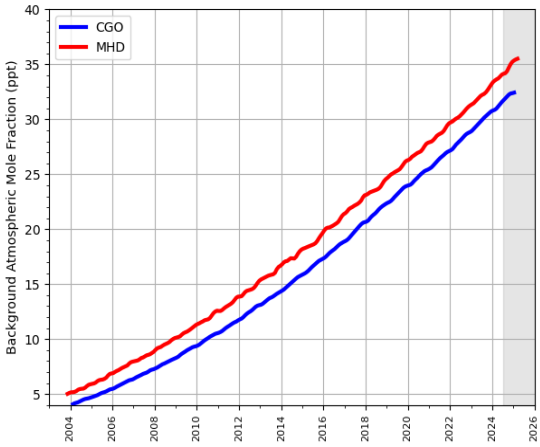

(b) HFC-143a

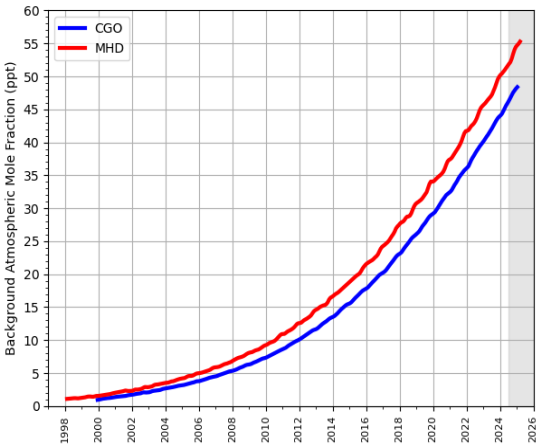

(c) HFC-125

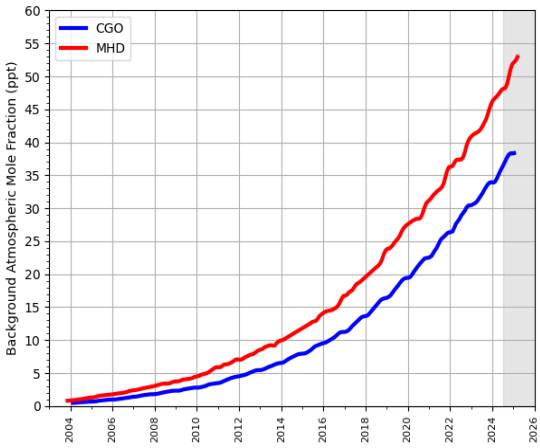

(d) HFC-32

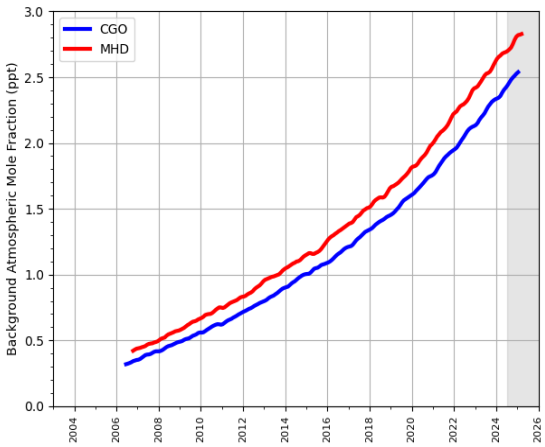

(e) HFC-227ea

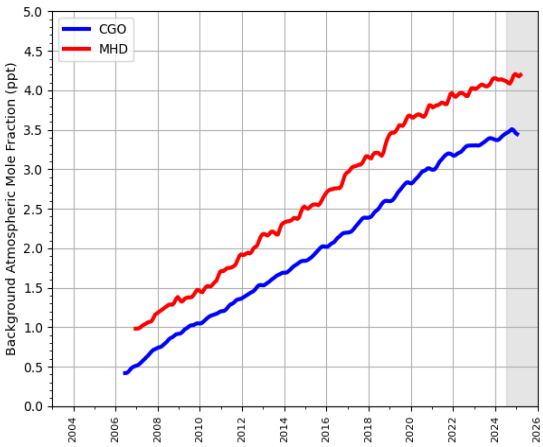

(f) HFC-245fa

Figure 2.3.2: Background Northern Hemisphere monthly concentrations of four HFCs estimated from MHD, Ireland observations are shown in red, and background Southern Hemisphere monthly concentrations from CGO, Tasmania are shown in blue. Grey shading represents provisional data.

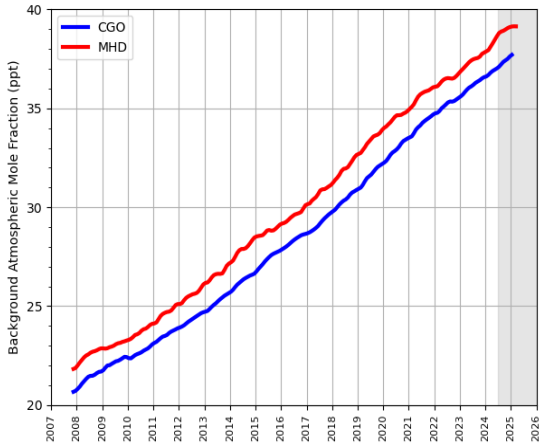

(a) HFC-23

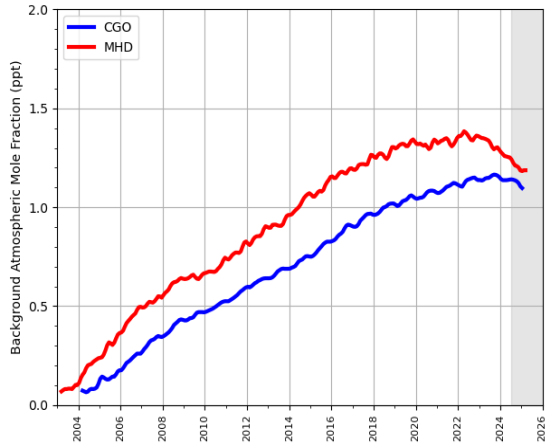

(b) HFC-365mfc

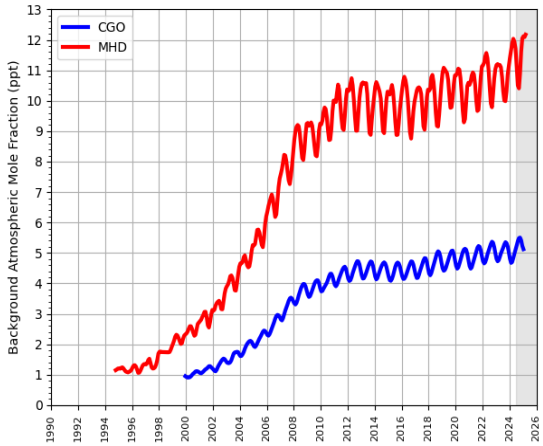

(c) HFC-152a

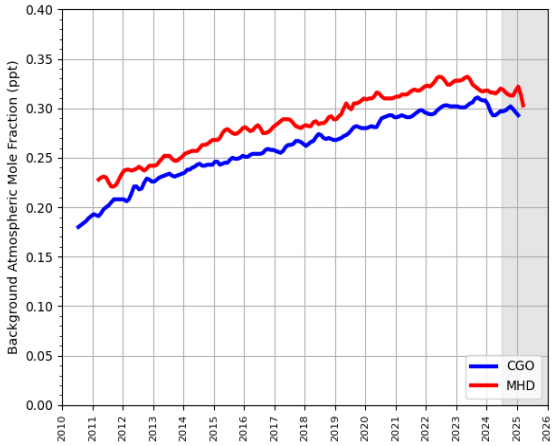

(d) HFC-43-10-mee

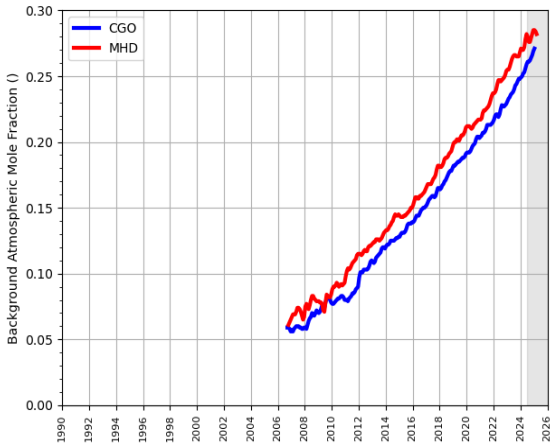

(e) HFC-236fa

2.4 Perfluorocarbons (PFCs)

Figure 2.4.1: Background Northern Hemisphere monthly concentrations of four PFCs estimated from MHD, Ireland observations are shown in red, and background Southern Hemisphere monthly concentrations from CGO, Tasmania are shown in blue. Grey shading represents provisional data.

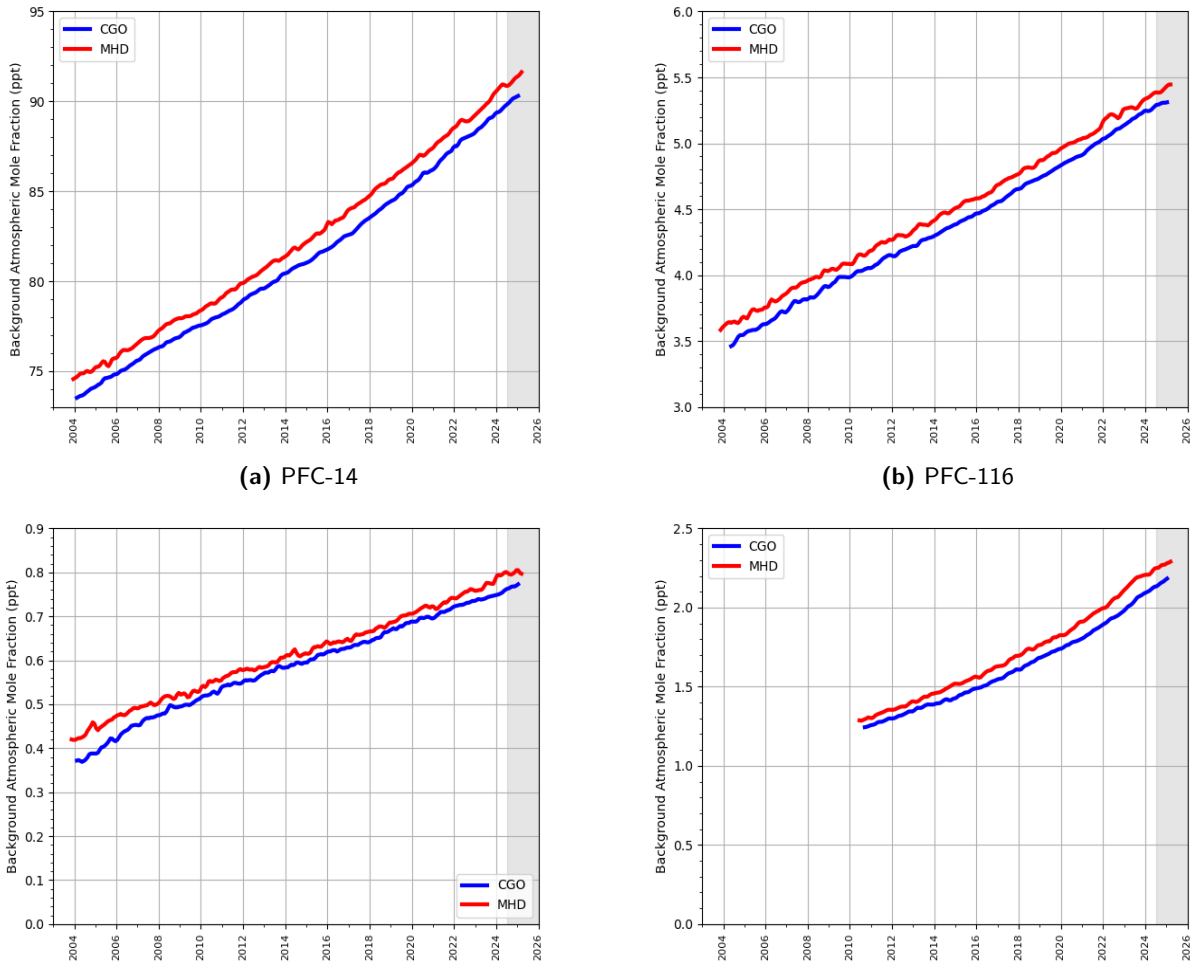

(a) PFC-14 **(b)** PFC-116 **(c)** PFC-218 **(d)** PFC-318

2.5 Sulphur Hexafluoride (SF_6) and Nitrogen Trifluoride (NF_3)

Figure 2.5.1: Background Northern Hemisphere monthly concentrations of SF_6 and NF_3 estimated from MHD, Ireland observations are shown in red, and background Southern Hemisphere monthly concentrations from CGO, Tasmania are shown in blue. Grey shading represents provisional data.

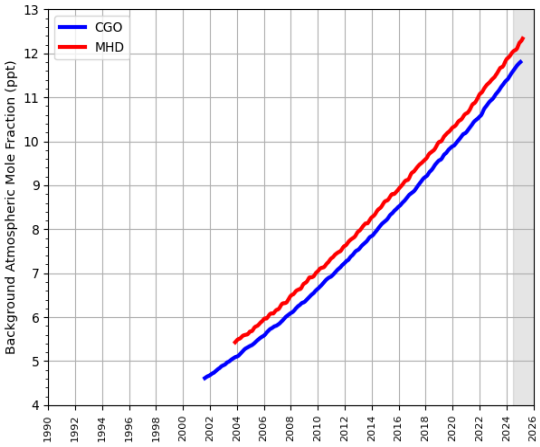

(a) SF_6

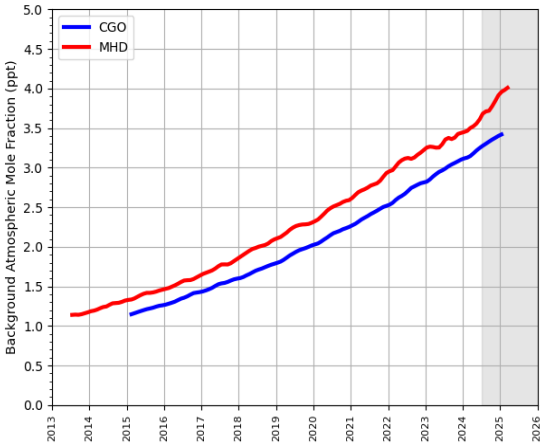

(b) NF_3

2.6 Carbon Dioxide (CO_2)

Figure 2.6.1: Background Northern Hemisphere monthly concentrations of CO_2 estimated from MHD, Ireland observations are shown in red, and background Southern Hemisphere monthly concentrations from CGO, Tasmania are shown in blue. Grey shading represents provisional data.

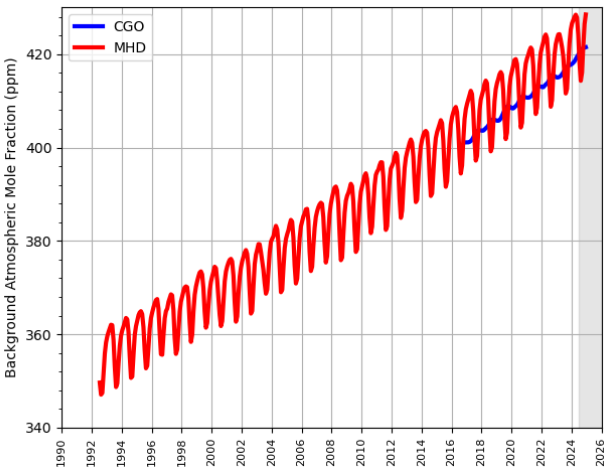

3 Key findings

- For methane and nitrous oxide, the observations used to derive the emissions presented in this report have limited sensitivity to central and southern Italy, resulting in larger uncertainties in these regions. Some measurement stations for methane have been excluded from this analysis: Ispra (ISP) due the complexities of modelling local emission sources in a complex terrain, Plateau Rosa (PRS) as model simulations were not available, and Potenza (POT), for which data is not yet available. The aggregation of inversion-derived emissions across the whole of Italy suggests that methane emissions are approximately half those of the inventory. However, without further spatial disaggregation of the inventory, it is not possible to compare the top-down and inventory estimates for northern Italy alone. Future analyses will include methane data from POT as they become available and this may help to better constrain emissions from central and southern Italy.
- Emissions derived with and without Lampedusa methane observations are consistent.
- A new station in Sicily (Capo Granitola) for halogenated gases started in 2024 measuring HFC-134a, HFC-143a, HFC-152a, HFC-23, HFC-227ea, HFC-236fa, HFC-245fa, HFC-365mfc, HFC-4310mee, PFC-218, and PFC-318. The analysis shows that this station is able to help constrain emissions for Sicily and the west coast of Southern Italy. Larger uncertainties still remain in central Italy.
- Emissions are likely present for PFC-14 and PFC-318 from northern Italy but large uncertainties remain in identifying the precise location of those emissions.
- There is a likely emissions source of HFC-23 in Northwestern Italy but large uncertainties remain in the magnitude of those emissions.

Table 1: Emissions estimation for the main greenhouse gases of focus according to the National Inventory Document (NID) 2025 and the inversions done in the PARIS project. For the PARIS estimation, the mean of all models is displayed, along with a range of uncertainty estimated via the half distance between the maximum and minimum uncertainties of the different models. For SF_6, the PARIS mean is the average of all InTEM and ELRIS inversions only.

		2020	2021	2022	2023	2024
CH_4	NID 2025	47.6	47.5	46.1	45.4	
$(\mathrm{TgCO_2\text{-}eq} \cdot \mathrm{yr}^{-1})$	PARIS mean	22.1 ± 8.8	21.3 ± 6.2	21.7 ± 9.8	21.2 ± 7.2	18.2 ± 5.6
N_2O	NID 2025	18.4	18.5	16.7	17.6	
$(\mathrm{TgCO_2\text{-}eq} \cdot \mathrm{yr}^{-1})$	PARIS mean	14.2 ± 4.5	15.1 ± 3.9	13.4 ± 5.5	15.9 ± 8.8	9.9 ± 2.5
Total HFC	NID 2025	10	10	9	9	
$(\mathrm{TgCO_2\text{-}eq} \cdot \mathrm{yr}^{-1})$	PARIS mean	6 ± 1	6 ± 1	6 ± 1	6 ± 1	6 ± 1
SF_6	NID 2025	0.3	0.3	0.4	0.4	
$(\mathrm{TgCO_2\text{-}eq} \cdot \mathrm{yr}^{-1})$	PARIS mean	1.1 ± 0.7	1.0 ± 0.7	0.9 ± 0.6	0.8 ± 0.5	0.7 ± 0.5
Total PFC	NID 2025	0.52	0.41	0.46	0.30	
$(\mathrm{TgCO_2\text{-}eq} \cdot \mathrm{yr}^{-1})$	PARIS mean	0.44 ± 0.81	0.42 ± 0.78	0.34 ± 0.57	0.30 ± 0.35	0.27 ± 0.34

4 Methane (CH_4)

While methane emissions aggregated across the whole of Italy are presented below, the observational network is mainly sensitive to northern Italy.

Figure 4.0.1: Average monthly total source sensitivity of CH_4 observing sites as calculated by the FLEXPART transport model for the year 2018 (left) and 2024 (right) and used in the inversions. Observing stations active in each year are marked with red dots. Areas with visible land surface represent regions for which emissions can be observed well from the network. Shaded or dark areas represent regions for which limited emission information can be obtained from the network.

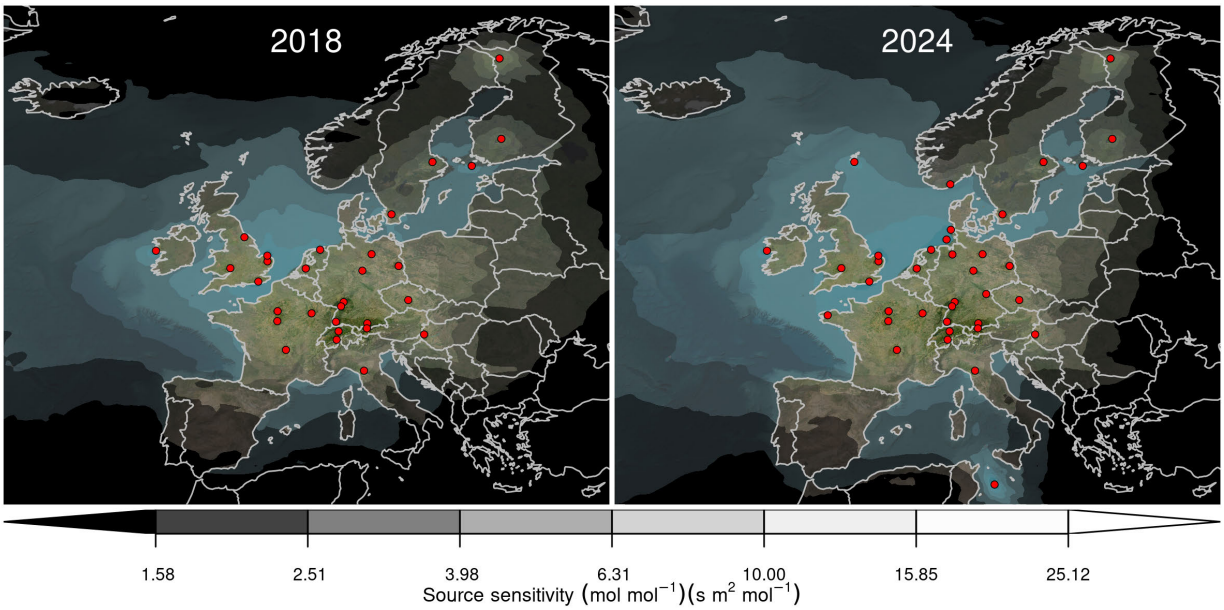

Figure 4.0.2: Verification of the Italian emissions inventory estimates for CH_4. Modelled annual emissions are given as the mean from all models (black line) and the individual result from InTEM-NAME (blue line). The shaded blue area is the 68 % confidence interval (CI) of InTEM-NAME and the shaded grey area encompasses the 68 % CI from all models. National inventory annual totals from 2024 and 2025 are given as grey and black bars, respectively.

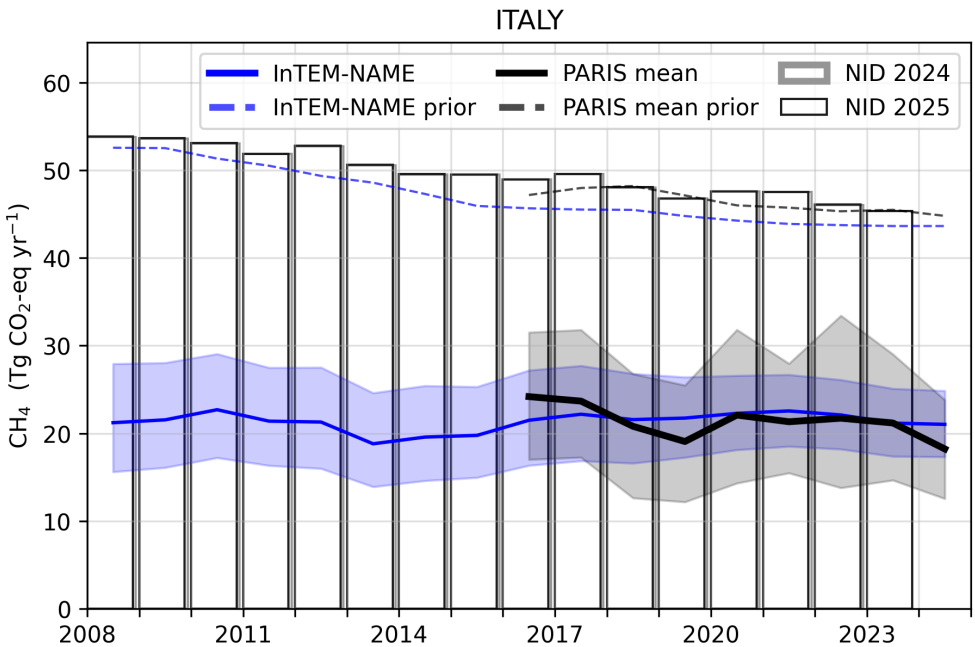

Figure 4.0.3: Verification of the Italian emissions inventory estimates for CH_4 (zoom in to 2018-2024). Modelled annual emissions are given as the mean from all models (black line) and the individual result from InTEM-NAME (blue line). The shaded blue area is the 68 % confidence interval (CI) of InTEM-NAME and the shaded grey area encompasses the 68 % CI from all models. National inventory annual totals from 2024 and 2025 are given as grey and black bars, respectively.

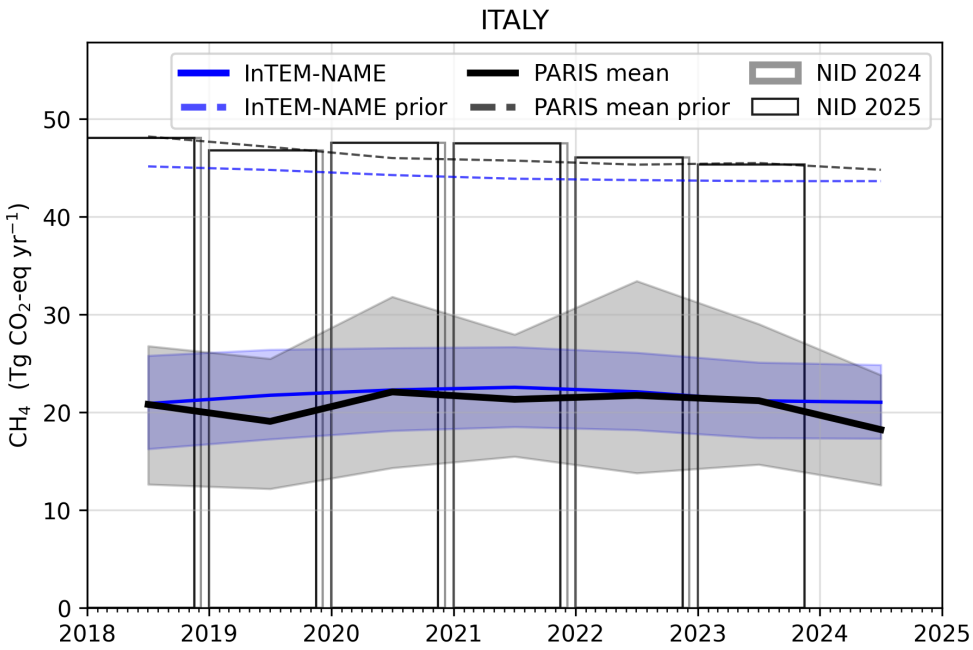

Figure 4.0.4: Verification of the Italian emissions inventory estimates for CH_4 (zoom in to 2018-2024). Modelled monthly emissions are given as the mean from all models (black line) and the individual result from InTEM-NAME (blue line). The shaded blue area is the 68 % confidence interval (CI) of InTEM-NAME and the shaded grey area encompasses the 68 % CI from all models. National inventory annual totals from 2024 and 2025 are given as grey and black bars, respectively.

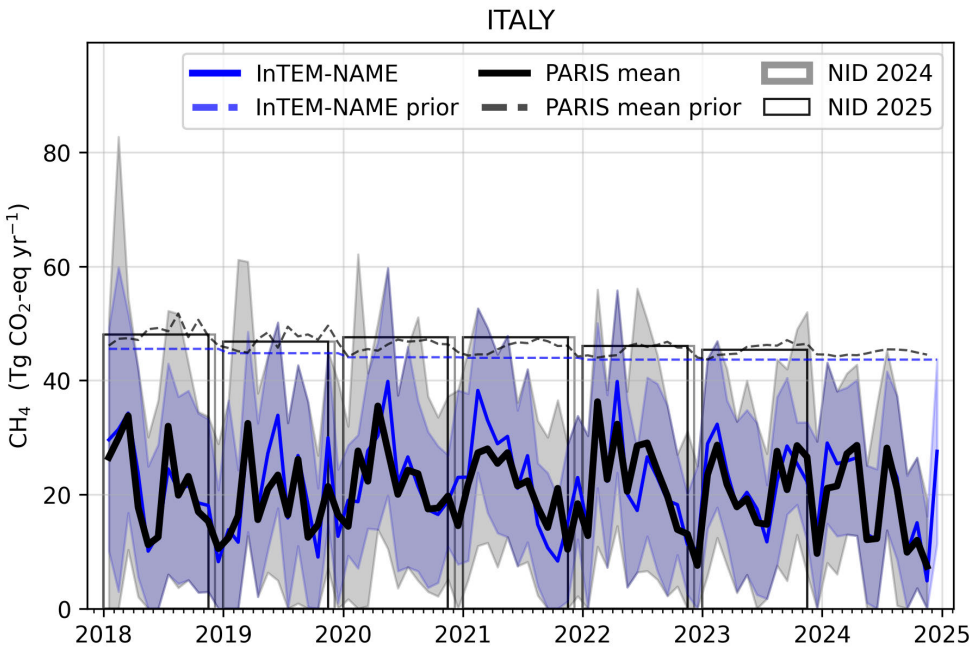

Figure 4.0.5: Spatial distribution of the Italian average modelled emissions of CH_4 during the period of 2020-2024 (mean from all models). Observing stations are marked with red circles and highly-populated cities are marked with red triangles.

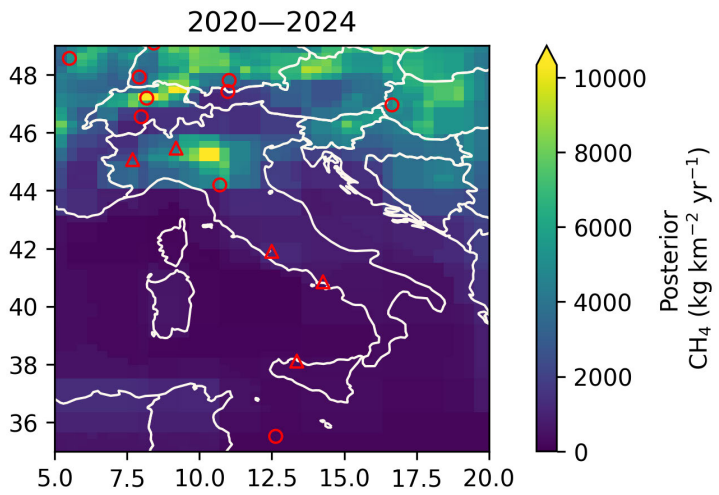

Figure 4.0.6: Spatial distribution of the seasonal deviation from the mean. The deviation is defined as the modelled Italian seasonally averaged CH_4 emissions over 2020-2024 minus the average over the whole period. The mean across all models is shown. Observing stations are marked with black circles and highly-populated cities are marked with black triangles.

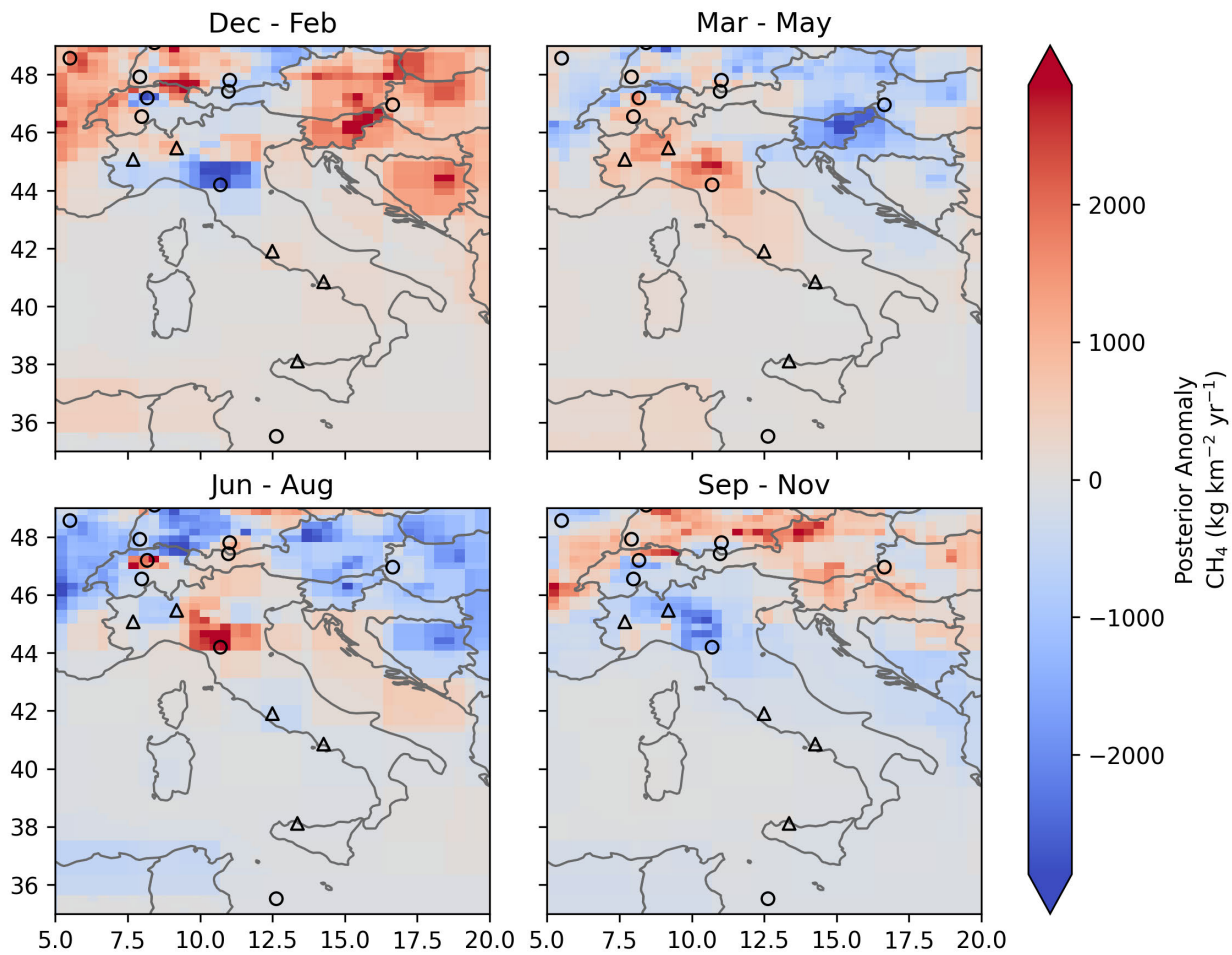

5 Nitrous Oxide (N_2O)

While nitrous emissions aggregated across the whole of Italy are presented below, the observational network is mainly sensitive to northern Italy.

Figure 5.0.1: Average monthly total source sensitivity of N_2O observing sites as calculated by the FLEXPART transport model for the year 2018 (left) and 2024 (right) and used in the inversions. Observing stations active in each year are marked with red dots. Areas with visible land surface represent regions for which emissions can be observed well from the network. Shaded or dark areas represent regions for which limited emission information can be obtained from the network.

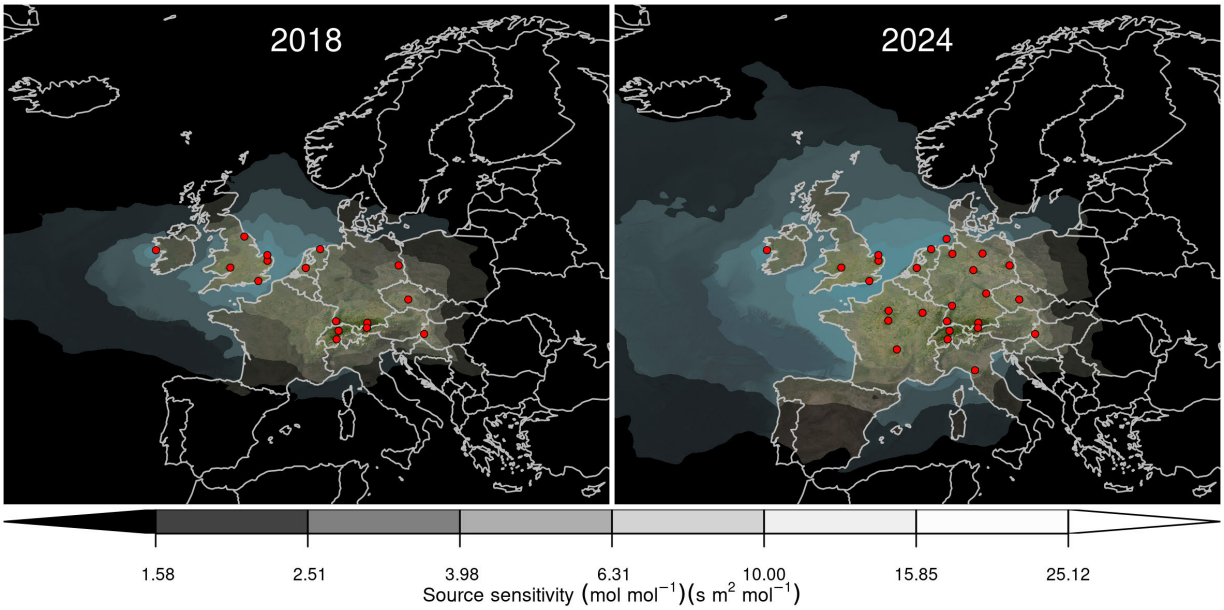

Figure 5.0.2: Verification of the Italian emissions inventory estimates for N_2O. Modelled annual emissions are given as the mean from all models (black line) and the individual result from InTEM-NAME (blue line). The shaded blue area is the 68 % confidence interval (CI) of InTEM-NAME and the shaded grey area encompasses the 68 % CI from all models. National inventory annual totals from 2024 and 2025 are given as grey and black bars, respectively.

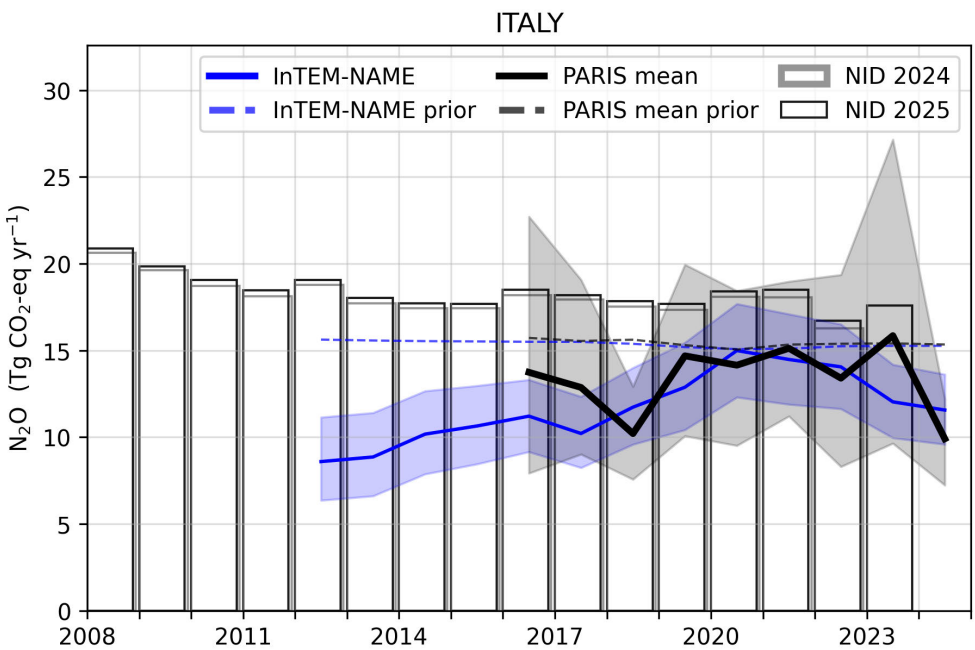

Figure 5.0.3: Verification of the Italian emissions inventory estimates for N_2O (zoom in to 2018-2024). Modelled annual emissions are given as the mean from all models (black line) and the individual result from InTEM-NAME (blue line). The shaded blue area is the 68 % confidence interval (CI) of InTEM-NAME and the shaded grey area encompasses the 68 % CI from all models. National inventory annual totals from 2024 and 2025 are given as grey and black bars, respectively.

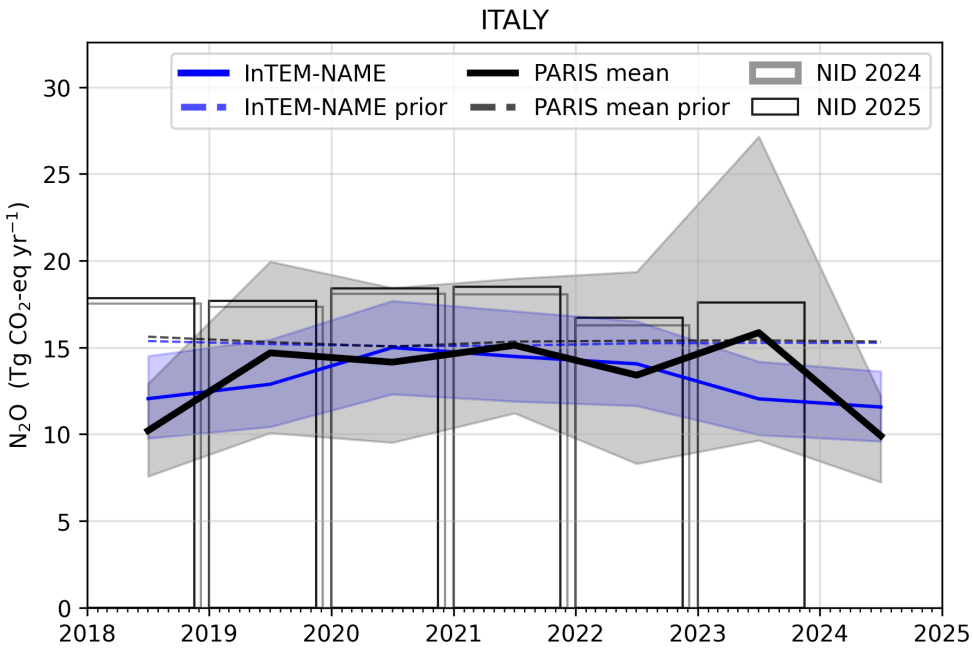

Figure 5.0.4: Verification of the Italian emissions inventory estimates for N_2O (zoom in to 2018-2024). Modelled monthly emissions are given as the mean from all models (black line) and the individual result from InTEM-NAME (blue line). The shaded blue area is the 68 % confidence interval (CI) of InTEM-NAME and the shaded grey area encompasses the 68 % CI from all models. National inventory annual totals from 2024 and 2025 are given as grey and black bars, respectively.

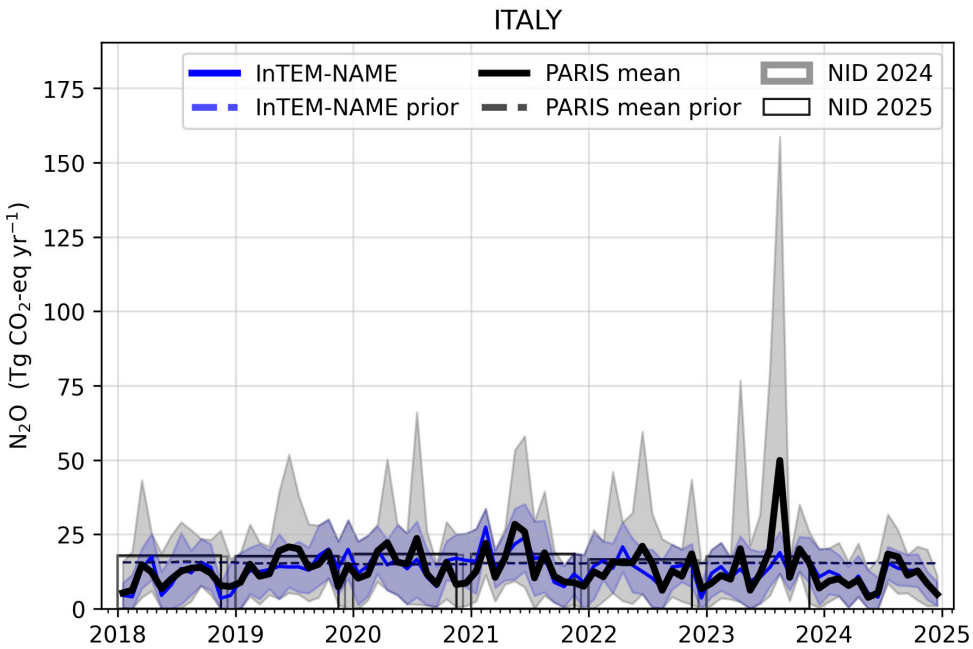

Figure 5.0.5: Spatial distribution of the Italian average modelled emissions of N_2O during the period of 2020-2024 (mean from all models). Observing stations are marked with red circles and highly-populated cities are marked with red triangles.

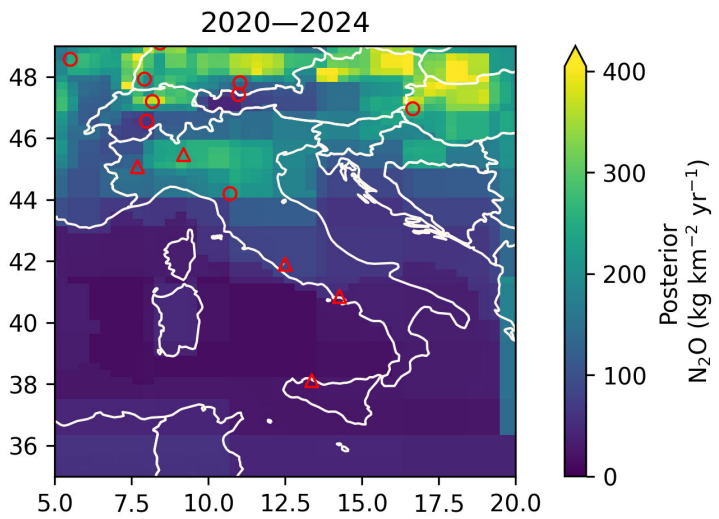

Figure 5.0.6: Spatial distribution of the seasonal deviation from the mean. The deviation is defined as the modelled Italian seasonally averaged N_2O emissions over 2020-2024 minus the average over the whole period. The mean across all models is shown. Observing stations are marked with black circles and highly-populated cities are marked with black triangles.

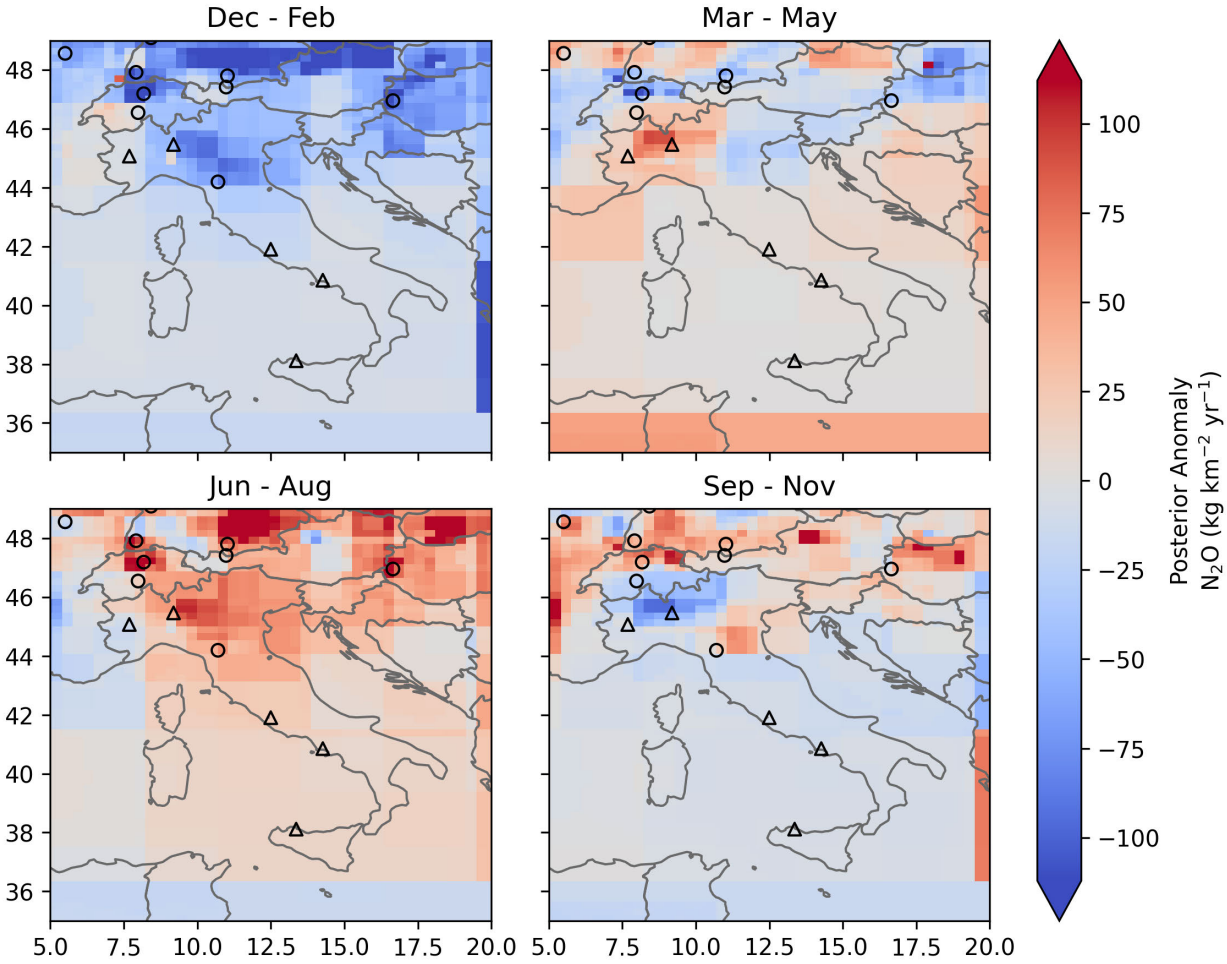

6 Hydrofluorocarbons (HFCs)

Figure 6.0.1: Total source sensitivity of HFCs/PFCs observing sites as calculated by the FLEXPART transport model for the year 2018 (left) and 2024 (right) and used in the inversions. Observing stations active in each year are marked with red dots. Areas with visible land surface represent regions for which emissions can be observed well from the network. Shaded or dark areas represent regions for which limited emission information can be obtained from the network.

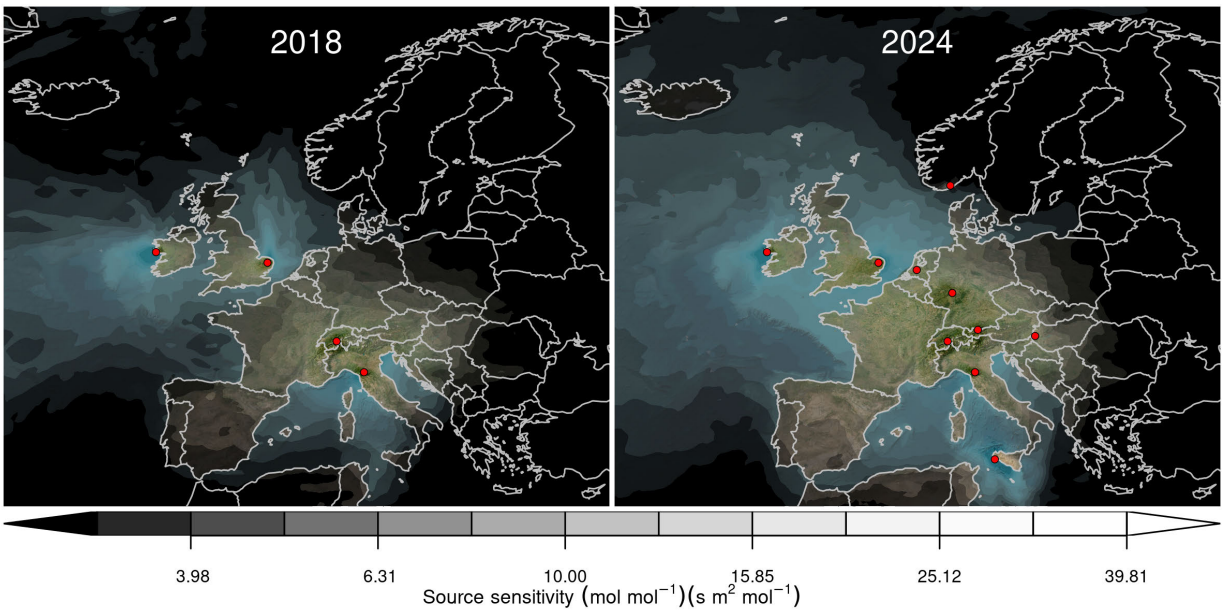

6.1 HFC-125

Figure 6.1.1: Verification of the Italian emissions inventory estimates for HFC-125. Modelled annual emissions are given as the mean from all models (black line) and the individual result from InTEM-NAME (blue line). The shaded blue area is the 68 % confidence interval (CI) of InTEM-NAME and the shaded grey area encompasses the 68 % CI from all models. National inventory annual totals from 2024 and 2025 are given as grey and black bars, respectively.

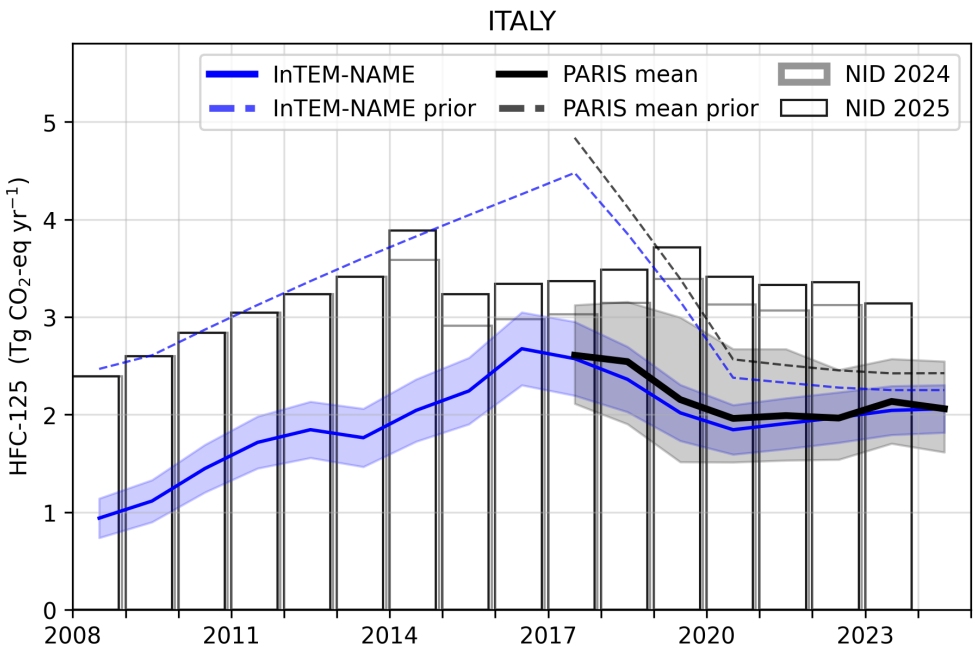

Figure 6.1.2: Spatial distribution of the Italian average modelled emissions of HFC-125 during the period of 2020-2024 (mean from all models). Observing stations are marked with red circles and highly-populated cities are marked with red triangles.

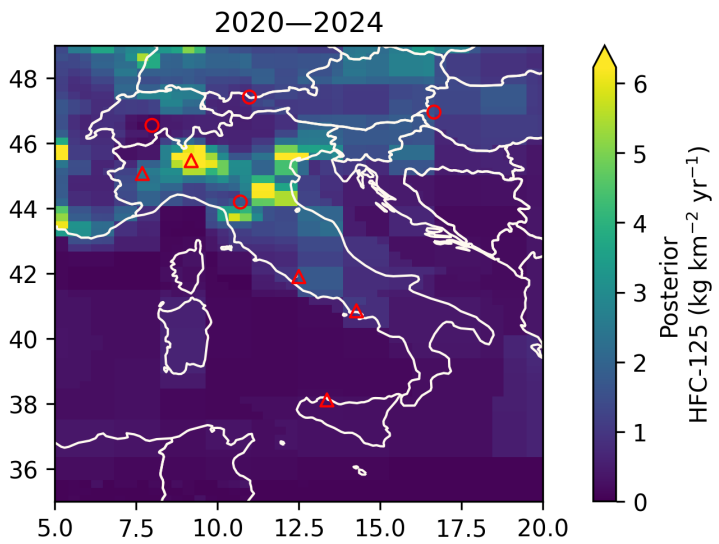

6.2 HFC-134a

Figure 6.2.1: Verification of the Italian emissions inventory estimates for HFC-134a. Modelled annual emissions are given as the mean from all models (black line) and the individual result from InTEM-NAME (blue line). The shaded blue area is the 68 % confidence interval (CI) of InTEM-NAME and the shaded grey area encompasses the 68 % CI from all models. National inventory annual totals from 2024 and 2025 are given as grey and black bars, respectively.

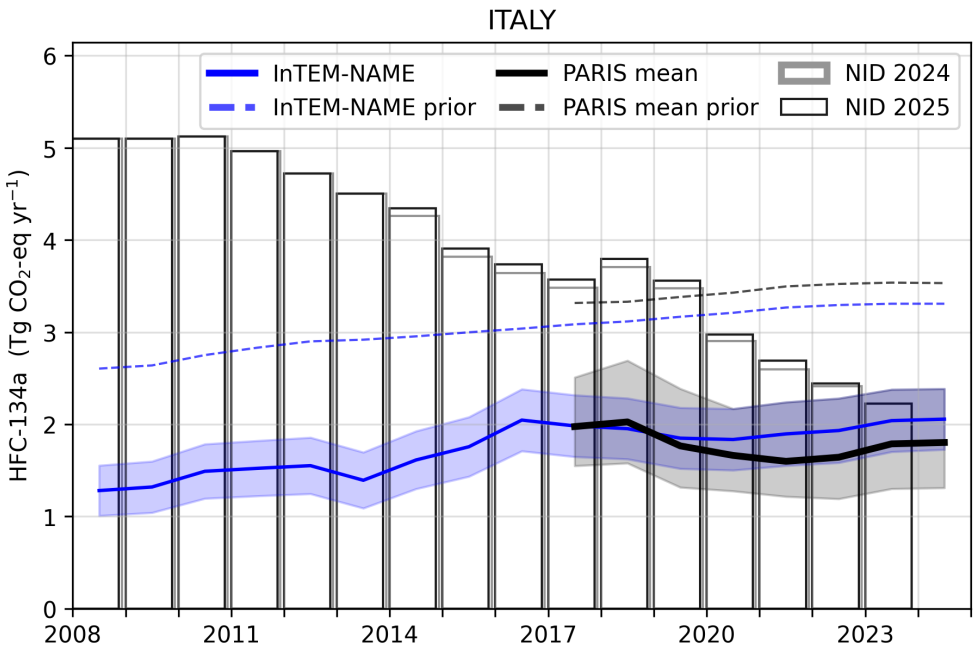

Figure 6.2.2: Spatial distribution of the Italian average modelled emissions of HFC-134a during the period of 2020-2024 (mean from all models). Observing stations are marked with red circles and highly-populated cities are marked with red triangles.

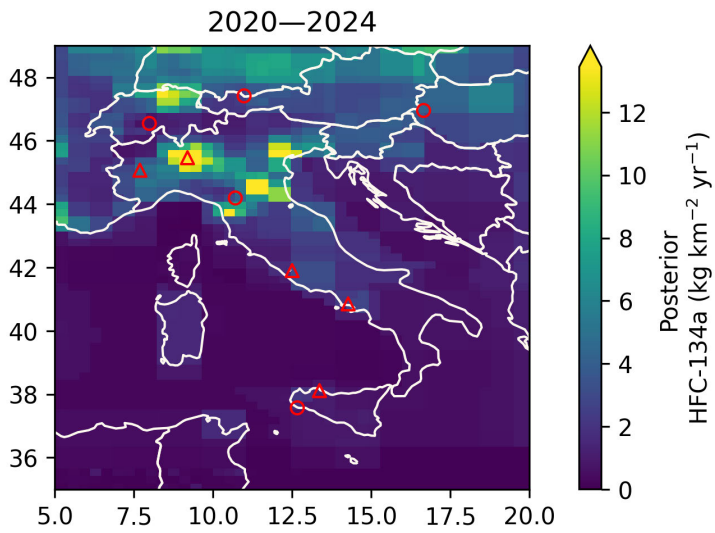

6.3 HFC-143a

Figure 6.3.1: Verification of the Italian emissions inventory estimates for HFC-143a. Modelled annual emissions are given as the mean from all models (black line) and the individual result from InTEM-NAME (blue line). The shaded blue area is the 68 % confidence interval (CI) of InTEM-NAME and the shaded grey area encompasses the 68 % CI from all models. National inventory annual totals from 2024 and 2025 are given as grey and black bars, respectively.

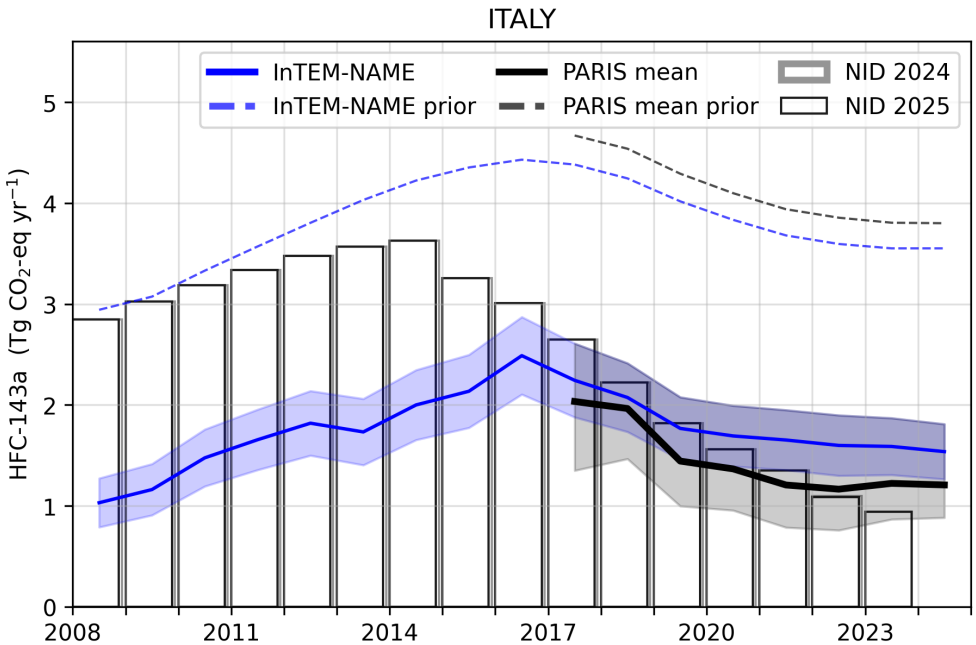

Figure 6.3.2: Spatial distribution of the Italian average modelled emissions of HFC-143a during the period of 2020-2024 (mean from all models). Observing stations are marked with red circles and highly-populated cities are marked with red triangles.

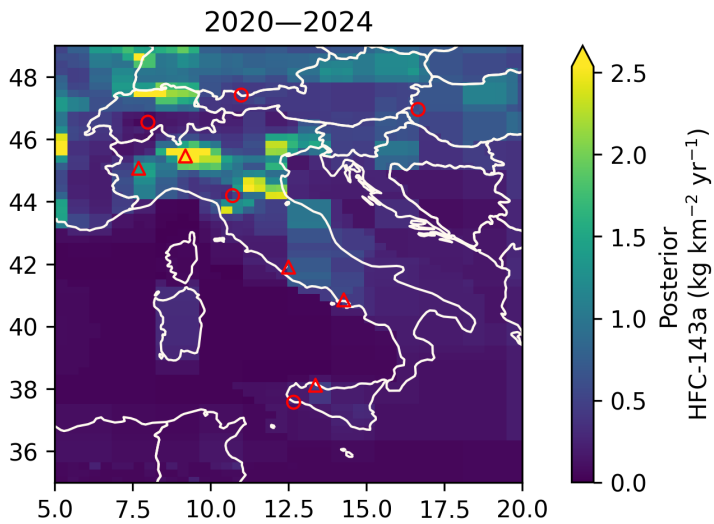

6.4 HFC-227ea

Figure 6.4.1: Verification of the Italian emissions inventory estimates for HFC-227ea. Modelled annual emissions are given as the mean from all models (black line) and the individual result from InTEM-NAME (blue line). The shaded blue area is the 68 % confidence interval (CI) of InTEM-NAME and the shaded grey area encompasses the 68 % CI from all models. National inventory annual totals from 2024 and 2025 are given as grey and black bars, respectively.

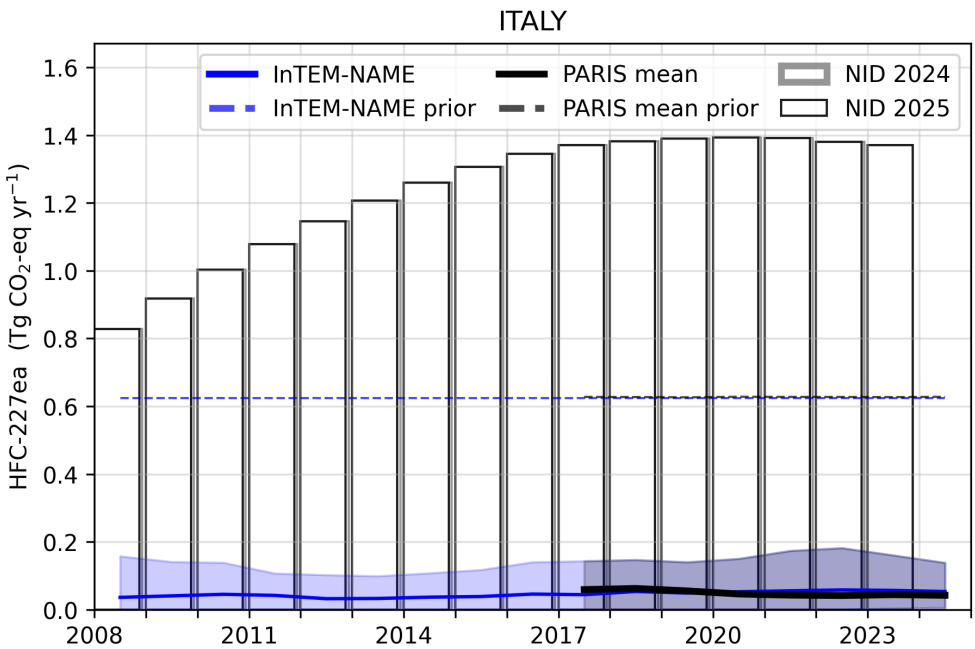

Figure 6.4.2: Spatial distribution of the Italian average modelled emissions of HFC-227ea during the period of 2020-2024 (mean from all models). Observing stations are marked with red circles and highly-populated cities are marked with red triangles.

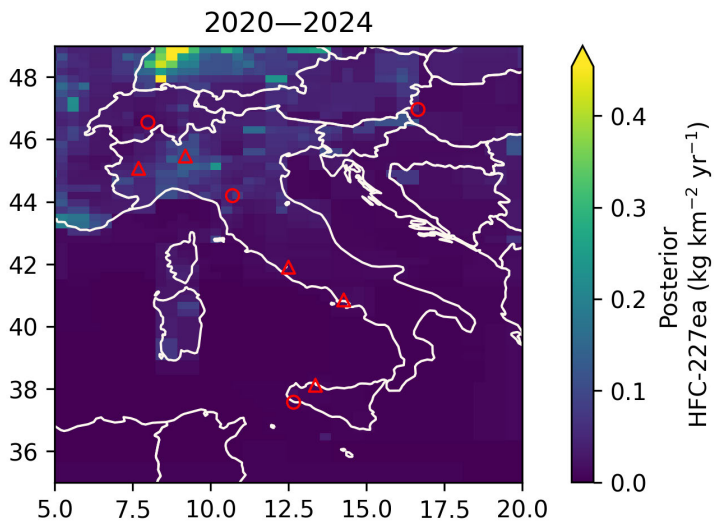

6.5 HFC-32

Figure 6.5.1: Verification of the Italian emissions inventory estimates for HFC-32. Modelled annual emissions are given as the mean from all models (black line) and the individual result from InTEM-NAME (blue line). The shaded blue area is the 68 % confidence interval (CI) of InTEM-NAME and the shaded grey area encompasses the 68 % CI from all models. National inventory annual totals from 2024 and 2025 are given as grey and black bars, respectively.

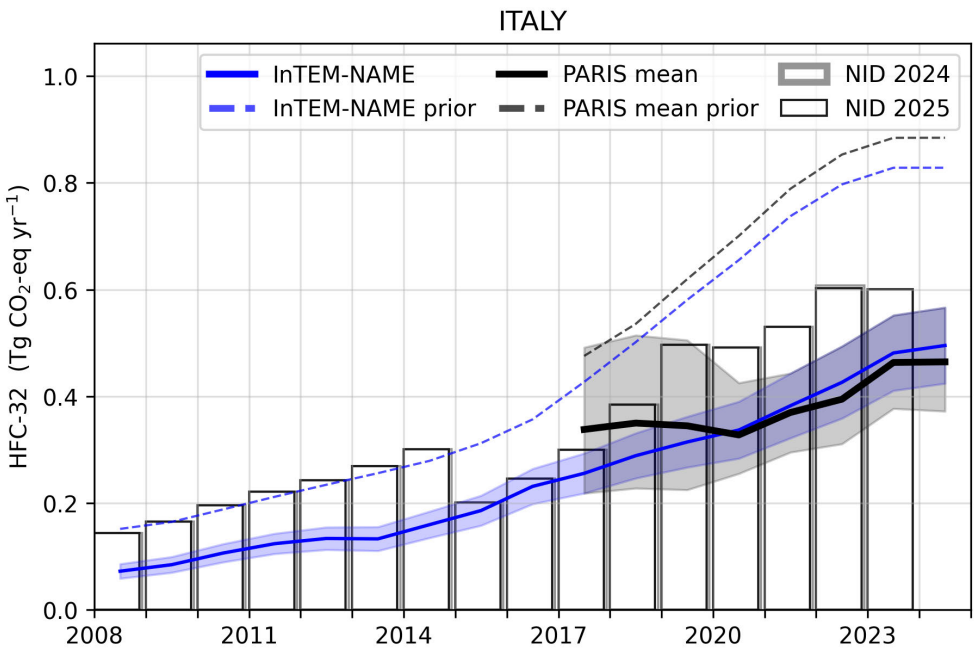

Figure 6.5.2: Spatial distribution of the Italian average modelled emissions of HFC-32 during the period of 2020-2024 (mean from all models). Observing stations are marked with red circles and highly-populated cities are marked with red triangles.

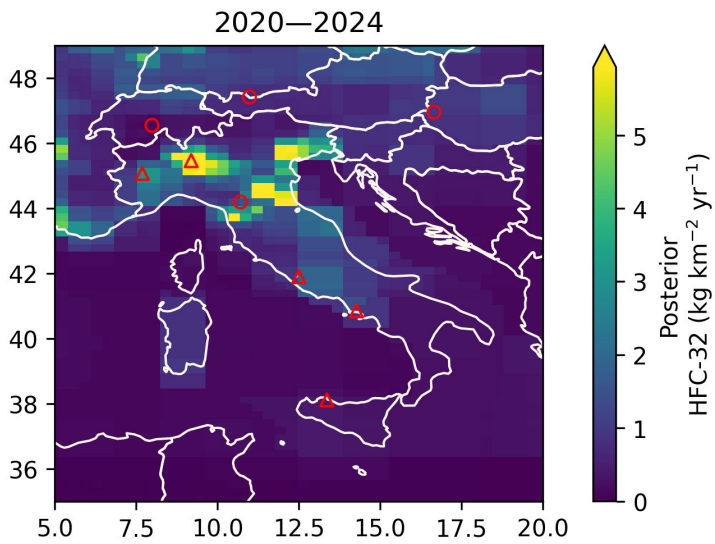

6.6 HFC-23

Figure 6.6.1: Verification of the Italian emissions inventory estimates for HFC-23. Modelled annual emissions are given as the mean from all models (black line) and the individual result from InTEM-NAME (blue line). The shaded blue area is the 68 % confidence interval (CI) of InTEM-NAME and the shaded grey area encompasses the 68 % CI from all models. National inventory annual totals from 2024 and 2025 are given as grey and black bars, respectively.

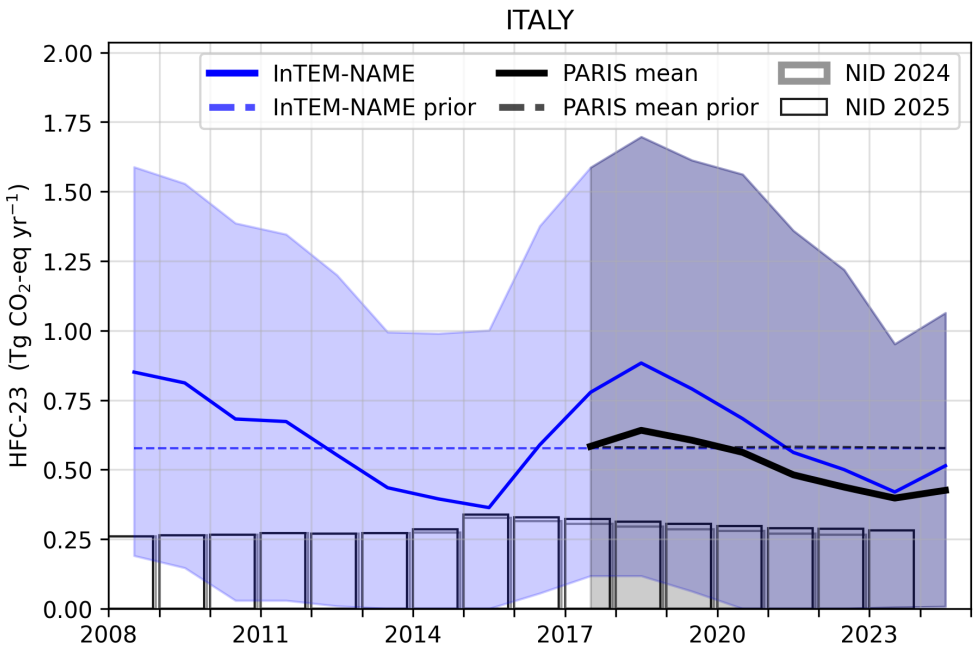

Figure 6.6.2: Spatial distribution of the Italian average modelled emissions of HFC-23 during the period of 2020-2024 (mean from all models). Observing stations are marked with red circles and highly-populated cities are marked with red triangles.

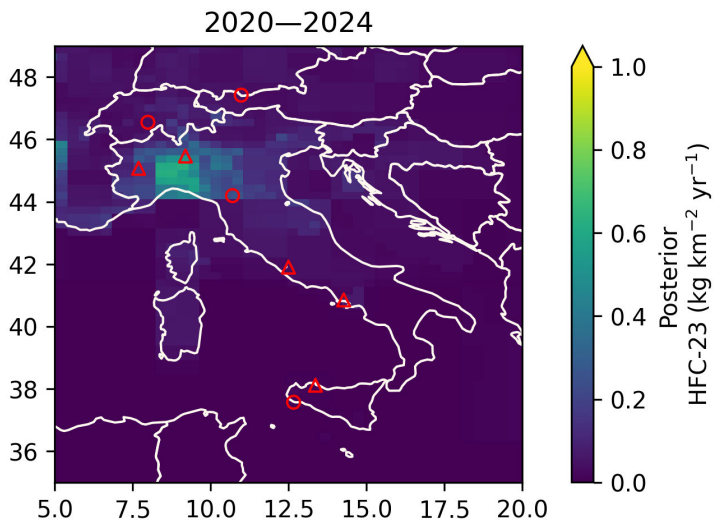

6.7 Total HFCs

Figure 6.7.1: Verification of the Italian emissions inventory estimates for total HFCs. Modelled annual emissions are given as the mean from all models (black line) and the individual result from InTEM-NAME (blue line). The shaded blue area is the 68 % confidence interval (CI) of InTEM-NAME and the shaded grey area encompasses the 68 % CI from all models. National inventory annual totals from 2024 and 2025 are given as grey and black bars, respectively.

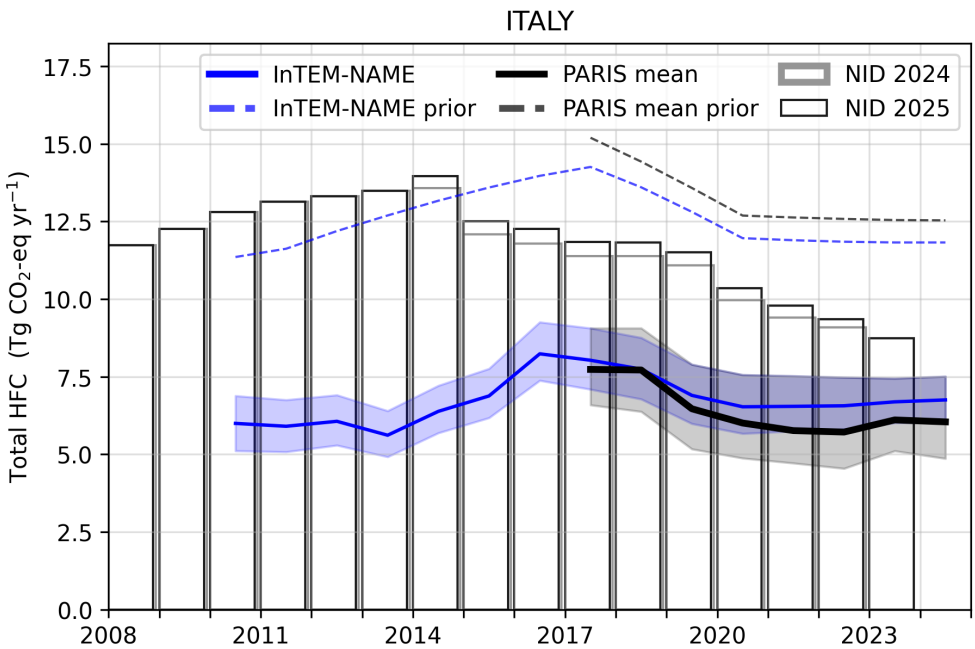

Table 2: Emissions estimation for HFCs according to the National Inventory Document (NID) 2025 and the inversions done in the PARIS project. For the PARIS estimation, the mean of all models is displayed, along with a range of uncertainty estimated via the half distance between the maximum and minimum uncertainties of the different models.

		2020	2021	2022	2023	2024
HFC-125	NID 2025	3.4	3.3	3.4	3.1	
$\left(\mathrm{TgCO_2\text{-}eq \cdot yr^{-1}}\right)$	PARIS mean	2.0 ± 0.6	2.0 ± 0.6	2.0 ± 0.5	2.1 ± 0.4	2.1 ± 0.5
HFC-134a	NID 2025	3.0	2.7	2.4	2.2	
$\left(\mathrm{TgCO_2\text{-}eq \cdot yr^{-1}}\right)$	PARIS mean	1.7 ± 0.4	1.6 ± 0.5	1.6 ± 0.5	1.8 ± 0.5	1.8 ± 0.5
HFC-143a	NID 2025	1.6	1.3	1.1	0.9	
$\left(\mathrm{TgCO_2\text{-}eq \cdot yr^{-1}}\right)$	PARIS mean	1.4 ± 0.5	1.2 ± 0.6	1.2 ± 0.6	1.2 ± 0.5	1.2 ± 0.5
HFC-23	NID 2025	0.30	0.29	0.29	0.28	
$\left(\mathrm{TgCO_2\text{-}eq \cdot yr^{-1}}\right)$	PARIS mean	0.56 ± 0.78	0.48 ± 0.68	0.44 ± 0.61	0.40 ± 0.47	0.43 ± 0.53
HFC-32	NID 2025	0.49	0.53	0.60	0.60	
$\left(\mathrm{TgCO_2\text{-}eq \cdot yr^{-1}}\right)$	PARIS mean	0.33 ± 0.09	0.37 ± 0.07	0.39 ± 0.09	0.46 ± 0.09	0.46 ± 0.10
HFC-227ea	NID 2025	1.4	1.4	1.4	1.4	
$\left(\mathrm{TgCO_2\text{-}eq \cdot yr^{-1}}\right)$	PARIS mean	0.0 ± 0.1	0.0 ± 0.1	0.0 ± 0.1	0.0 ± 0.1	0.0 ± 0.1
HFC-365mfc	NID 2025	0	0	0	0	
$\left(\mathrm{GgCO_2\text{-}eq \cdot yr^{-1}}\right)$	PARIS mean	34 ± 34	36 ± 41	37 ± 38	32 ± 31	22 ± 19
HFC-245fa	NID 2025	0.22	0.21	0.20	0.17	
$\left(\mathrm{TgCO_2\text{-}eq \cdot yr^{-1}}\right)$	PARIS mean	0.03 ± 0.05	0.02 ± 0.05	0.02 ± 0.03	0.01 ± 0.02	0.01 ± 0.01
HFC-236fa	NID 2025	0	0	0	0	
$\left(\mathrm{GgCO_2\text{-}eq \cdot yr^{-1}}\right)$	PARIS mean	12 ± 23	11 ± 23	10 ± 23	10 ± 21	9 ± 20
HFC-4310mee	NID 2025	0.0	0.0	0.0	0.0	
$\left(\mathrm{GgCO_2\text{-}eq \cdot yr^{-1}}\right)$	PARIS mean	8.5 ± 19.9	5.7 ± 17.2	5.7 ± 15.2	5.3 ± 11.6	5.3 ± 10.6
HFC-152a	NID 2025	0.0	0.0	0.0	0.0	
$\left(\mathrm{GgCO_2\text{-}eq \cdot yr^{-1}}\right)$	PARIS mean	5.3 ± 12.1	4.8 ± 13.9	4.2 ± 14.0	3.7 ± 10.8	3.0 ± 7.7

7 Perfluorocarbons (PFCs)

7.1 PFC-14

Figure 7.1.1: Verification of the Italian emissions inventory estimates for PFC-14. Modelled annual emissions are given as the mean from all models (black line) and the individual result from InTEM-NAME (blue line). The shaded blue area is the 68 % confidence interval (CI) of InTEM-NAME and the shaded grey area encompasses the 68 % CI from all models. National inventory annual totals from 2024 and 2025 are given as grey and black bars, respectively.

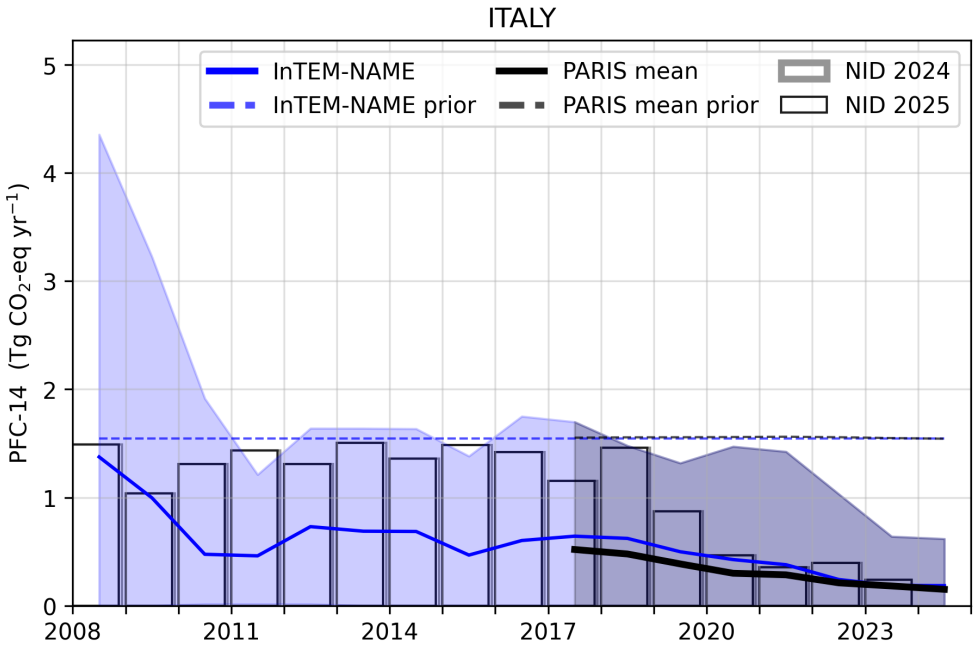

7.2 PFC-116

Figure 7.2.1: Verification of the Italian emissions inventory estimates for PFC-116. Modelled annual emissions are given as the mean from all models (black line) and the individual result from InTEM-NAME (blue line). The shaded blue area is the 68 % confidence interval (CI) of InTEM-NAME and the shaded grey area encompasses the 68 % CI from all models. National inventory annual totals from 2024 and 2025 are given as grey and black bars, respectively.

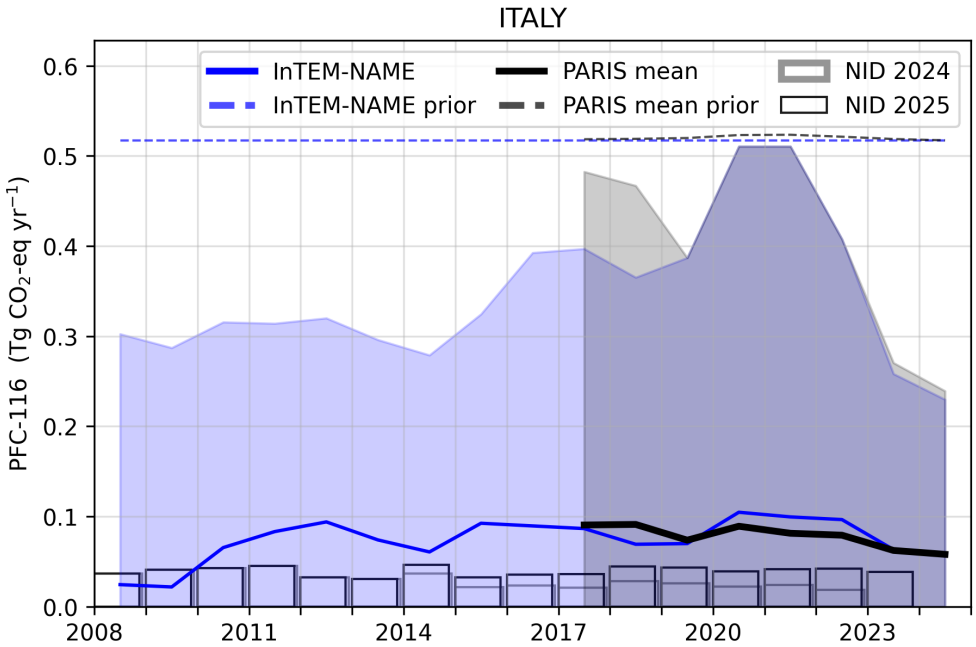

7.3 PFC-218

Figure 7.3.1: Verification of the Italian emissions inventory estimates for PFC-218. Modelled annual emissions are given as the mean from all models (black line) and the individual result from InTEM-NAME (blue line). The shaded blue area is the 68 % confidence interval (CI) of InTEM-NAME and the shaded grey area encompasses the 68 % CI from all models. National inventory annual totals from 2024 and 2025 are given as grey and black bars, respectively.

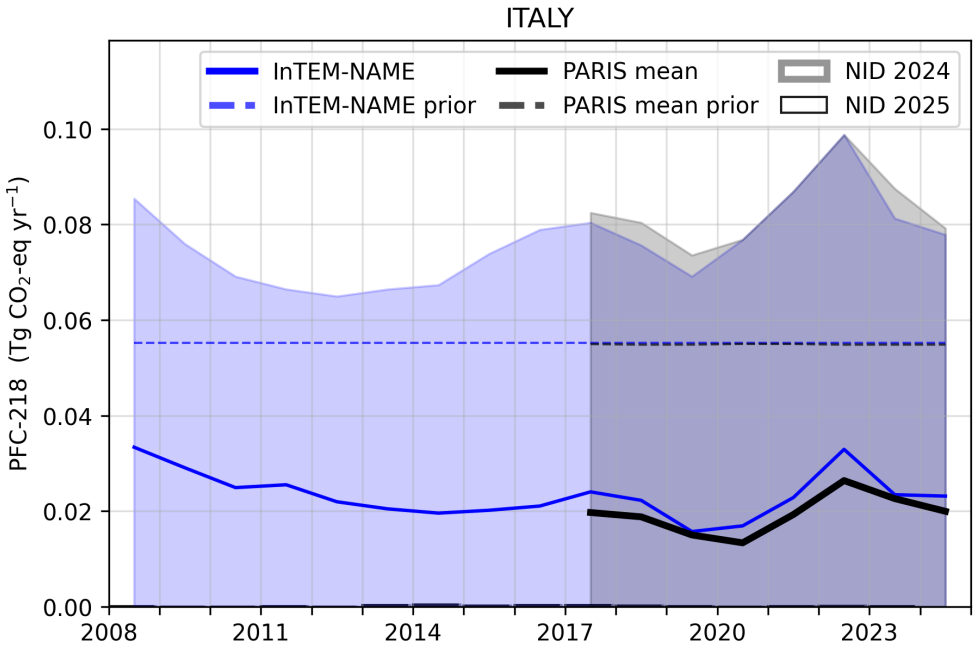

7.4 PFC-318

Figure 7.4.1: Verification of the Italian emissions inventory estimates for PFC-318. Modelled annual emissions are given as the mean from all models (black line) and the individual result from InTEM-NAME (blue line). The shaded blue area is the 68 % confidence interval (CI) of InTEM-NAME and the shaded grey area encompasses the 68 % CI from all models. National inventory annual totals from 2024 and 2025 are given as grey and black bars, respectively.

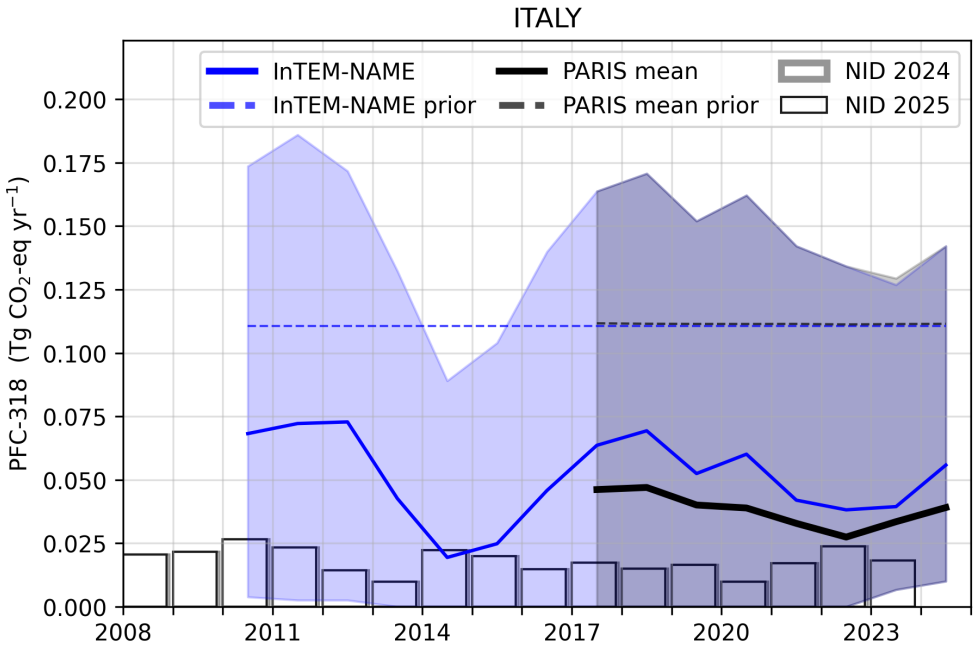

7.5 Total PFCs

Figure 7.5.1: Verification of the Italian emissions inventory estimates for total PFCs. Modelled annual emissions are given as the mean from all models (black line) and the individual result from InTEM-NAME (blue line). The shaded blue area is the 68 % confidence interval (CI) of InTEM-NAME and the shaded grey area encompasses the 68 % CI from all models. National inventory annual totals from 2024 and 2025 are given as grey and black bars, respectively.

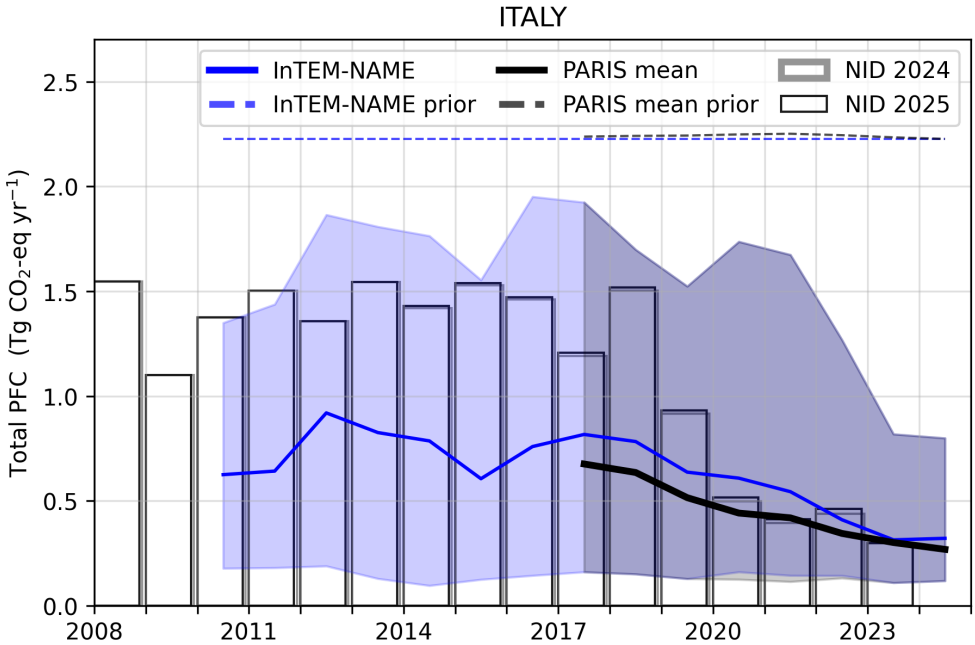

Table 3: Emissions estimation for PFCs according to the National Inventory Document (NID) 2025 and the inversions done in the PARIS project. For the PARIS estimation, the mean of all models is displayed, along with a range of uncertainty estimated via the half distance between the maximum and minimum uncertainties of the different models.

		2020	2021	2022	2023	2024
PFC-14	NID 2025	0.47	0.35	0.40	0.24	
$(\mathrm{TgCO_2\text{-}eq \cdot yr^{-1}})$	PARIS mean	0.30 ± 0.74	0.29 ± 0.71	0.21 ± 0.52	0.18 ± 0.32	0.15 ± 0.31
PFC-116	NID 2025	39	42	42	39	
$(\mathrm{GgCO_2\text{-}eq \cdot yr^{-1}})$	PARIS mean	89 ± 255	81 ± 255	79 ± 204	62 ± 135	58 ± 120
PFC-318	NID 2025	10	17	24	18	
$(\mathrm{GgCO_2\text{-}eq \cdot yr^{-1}})$	PARIS mean	39 ± 81	33 ± 71	27 ± 67	33 ± 61	39 ± 66
PFC-218	NID 2025	0	0	0	0	
$(\mathrm{GgCO_2\text{-}eq \cdot yr^{-1}})$	PARIS mean	13 ± 38	19 ± 43	26 ± 49	23 ± 44	20 ± 40

8 Carbon Dioxide (CO_2)

Measurements of CO_2 at ICOS sites and related observatories are influenced by a complex combination of sources and sinks. Fossil fuel combustion for transport, heating, energy generation, and other applications produce CO_2, along with other anthropogenic activities such as cement production. The terrestrial and oceanic biosphere produces CO_2 through animal and plant respiration and takes up CO_2 through photosynthesis. Furthermore, CO_2 is exchanged with the ocean through physical and chemical processes.

When considering high-frequency (∼hourly) CO_2 mole fraction deviations from baseline values—used to infer national emissions in regional inverse modelling studies—the influence of biospheric fluxes can be

comparable to, or larger than, those of anthropogenic sources (e.g. White et al., 2019). Therefore, research is under way to develop new tracers that can determine fossil fuel CO_2 fluxes independent of biosphere sources and sinks.

Ongoing Horizon Europe projects PARIS and CORSO are examining methods for estimating fossil fuel CO_2 fluxes based on simultaneous measurements of CO_2 and O_2 (Figure 8.0.1). The method relies on the fact that CO_2 and O_2 are inter-converted during combustion and terrestrial biosphere exchange, but with different ratios for the two processes. A quantity can be constructed from these measurements, known as Atmospheric Potential Oxygen (APO), which is insensitive to biosphere fluxes, and may therefore be useful for isolating fossil fuel signals (Pickers et al., 2022).

High-frequency ($\sim$hourly) timeseries of APO are available from Weybourne (WAO, 2010 – present) and Heathfield (HFD, 2021 - present) in the UK (Figure 8.0.1; Pickers, Adcock, and Manning, 2024), and new sites are being established at Cabauw and Zweth in the Netherlands. Preliminary analyses of the WAO data have revealed regional APO trends consistent with the drop in fossil fuel CO_2 emissions during the COVID lockdowns in the UK (Pickers et al., 2022). However, quantification of absolute regional fossil fuel CO_2 emissions remains an area of active research. Recent studies have derived fossil fuel CO_2 emissions for the UK that are highly uncertain (Rigby et al., 2025). Potential confounding factors were identified in Chawner et al. (2024), such as highly uncertain APO fluxes from the ocean, and a poorly constrained regional APO background. These factors are the subject of ongoing research using atmospheric models and new APO measurements from PARIS, CORSO and ICOS.

An alternative method for top-down fossil fuel CO_2 emissions evaluation uses measurements of radiocarbon isotopologues ($^{14}CO_2$, compared to the dominant $^{12}CO_2$). Fossil fuels do not contain ^{14}C, and therefore, their combustion tends to decrease the atmospheric $^{14}CO_2/^{12}CO_2$ ratio. Currently, radiocarbon measurements can only be made at low frequency using flask sampling. However, a relatively intensive flask sampling campaign was carried out across Europe during 2024 as part of CORSO, and the results of this study will be reported on soon.

Figure 8.0.1: Carbon dioxide (top, red) and oxygen (bottom, blue) measurements from Weybourne Atmospheric Observatory in the UK, available from the ICOS Carbon Portal (Adcock et al., 2024).

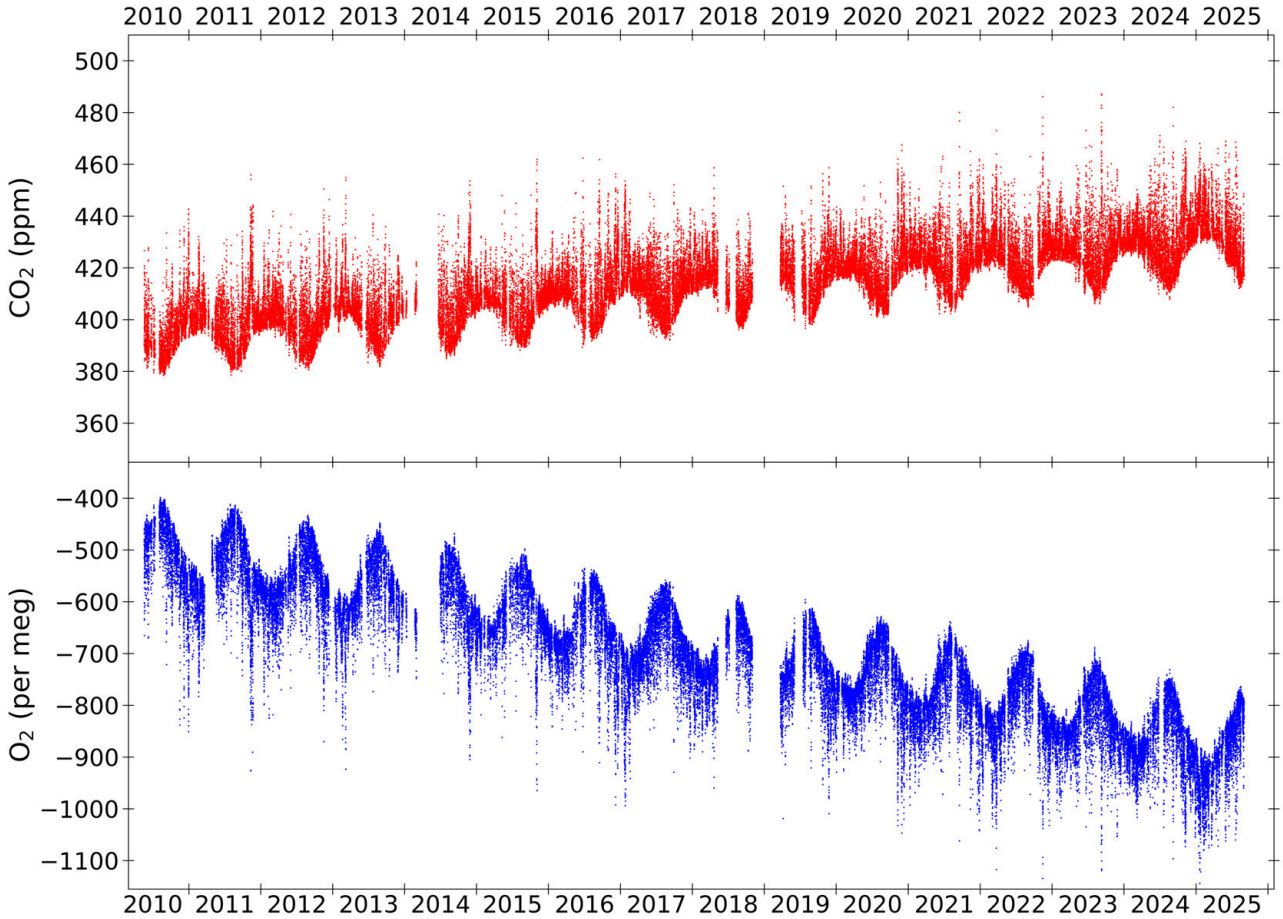

9 Impact of Capo Granitola

The impact on derived emissions by including observations from additional European stations, as developed partly within the PARIS project, can be assessed by running two sets of inversions, with (expanded network) and without (7-site network) these additional stations. Additional stations are Zugspitze, Germany (ZSF), Capo Granitola, Italy (CGR), Hegyhátsál, Hungary (HUN), Birkenes, Norway (BIR), whereas the seven core sites are Mace Head, Ireland (MHD), Tacolneston, UK (TAC), Jungfraujoch, Switzerland (JFJ), Monte Cimone, Italy (CMN), Zeppelin, Spitsbergen (ZEP), Taunus observatory, Germany (TOB), and Cabauw, Netherlands (CBW). Of special interest for estimating Italian emissions are the new measurements made at Capo Granitola in 2024. These measurements were made in high frequency on a GC-MS system installed at the station, and include HFC-134a, HFC-143a, HFC-152a, HFC-23, HFC-227ea, HFC-236fa, HFC-245fa, HFC-365mfc, HFC-4310mee, PFC-218, and PFC-318.

For all gases, observations from CGR help to constrain emissions from Sicily and the west coast of southern Italy.

Figure 9.0.1: 2024 HFC-134a emissions derived using (left) an expanded network, (middle) the base network, and (left) their difference. Measurement stations are shown in circles.

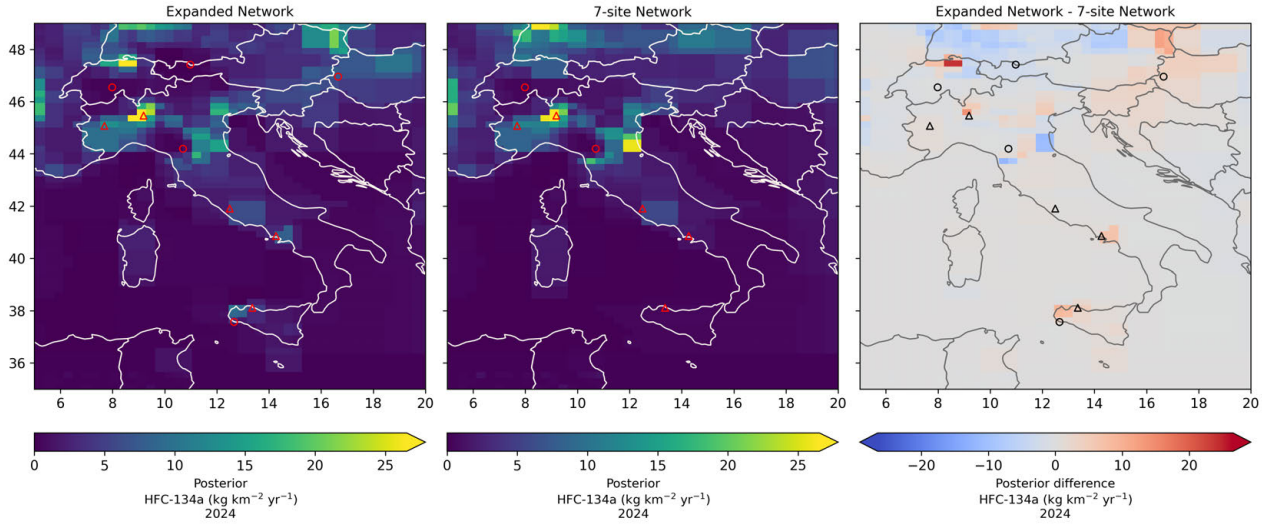

Figure 9.0.2: 2024 HFC-143a emissions derived using (left) an expanded network, (middle) the base network, and (left) their difference. Measurement stations are shown in circles.

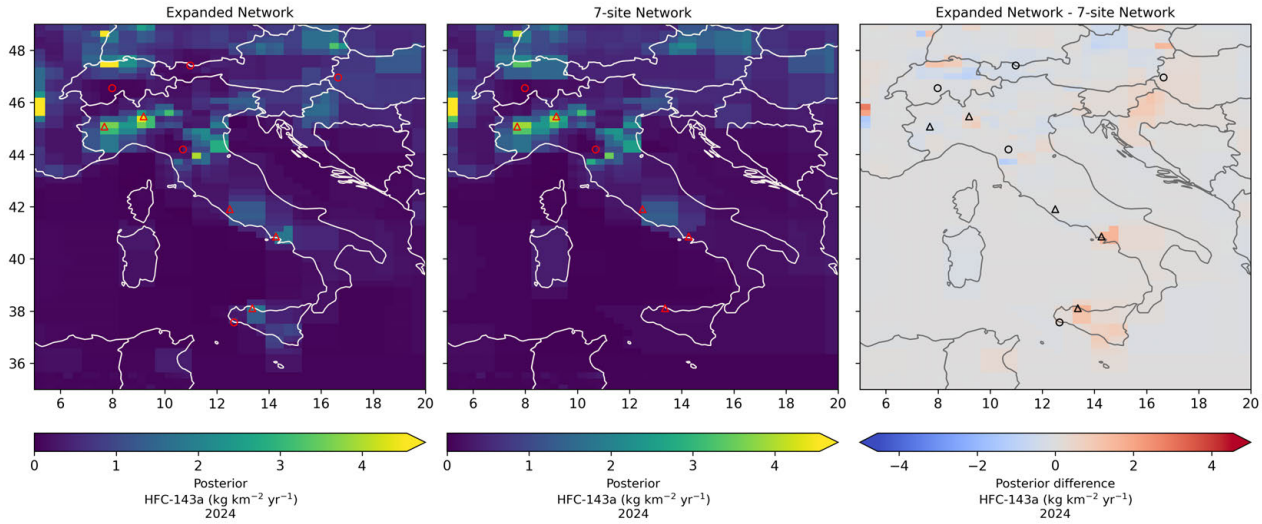

Figure 9.0.3: 2024 HFC-152a emissions derived using (left) an expanded network, (middle) the base network, and (left) their difference. Measurement stations are shown in circles.

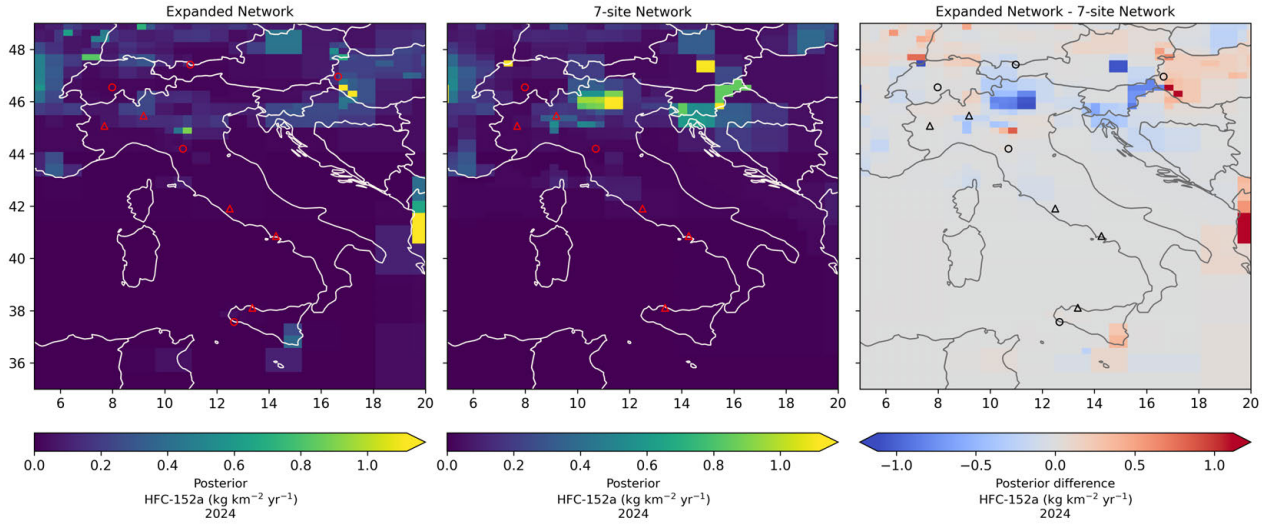

Figure 9.0.4: 2024 HFC-365mfc emissions derived using (left) an expanded network, (middle) the base network, and (left) their difference. Measurement stations are shown in circles.

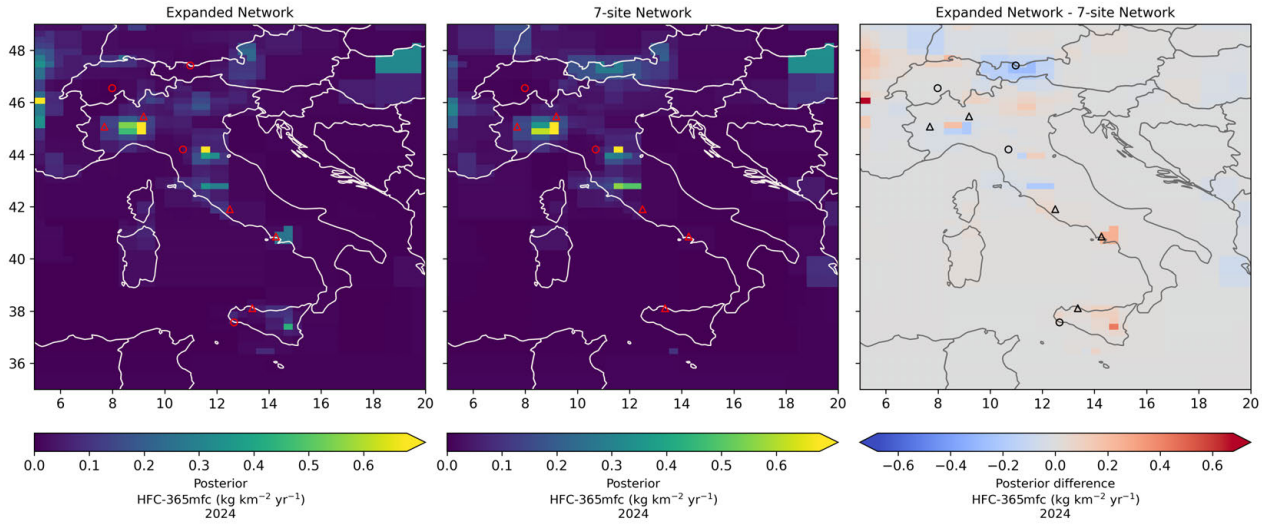

References

Adcock, Karina et al. (2024). *Atmospheric GHG data product (o2, o2_stdev, co2, co2_stdev) from Weybourne (10.0 m), 2010-05-19–2023-12-31*. URL: https://hdl.handle.net/11676/j4LzdHQiq3fPgfNeXHruC0Bb.

Chawner, Hannah et al. (Apr. 2024). "Atmospheric oxygen as a tracer for fossil fuel carbon dioxide: a sensitivity study in the UK". en. In: *Atmospheric Chemistry and Physics* 24.7, pp. 4231–4252. ISSN: 1680-7324. DOI: 10.5194/acp-24-4231-2024. URL: https://acp.copernicus.org/articles/24/4231/2024/ (visited on 04/10/2024).

European Commission: Joint Research, Centre et al. (2023). *GHG emissions of all world countries – 2023*. Publications Office of the European Union. DOI: 10.2760/953322.

Ganesan, A. L. et al. (2014). "Characterization of uncertainties in atmospheric trace gas inversions using hierarchical Bayesian methods". In: *Atmospheric Chemistry and Physics* 14.8, pp. 3855–3864. DOI: 10.5194/acp-14-3855-2014. URL: http://www.atmos-chem-phys.net/14/3855/2014/http://www.atmos-chem-phys.net/14/3855/2014/acp-14-3855-2014.pdf.

Ganesan, A. L. et al. (2015). "Quantifying methane and nitrous oxide emissions from the UK and Ireland using a national-scale monitoring network". In: *Atmos. Chem. Phys.* 15.11, pp. 6393–6406. DOI: 10.5194/acp-15-6393-2015. URL: https://www.atmos-chem-phys.net/15/6393/2015/https://www.atmos-chem-phys.net/15/6393/2015/acp-15-6393-2015.pdf.

Henne, S. et al. (2016). "Validation of the Swiss methane emission inventory by atmospheric observations and inverse modelling". In: *Atmospheric Chemistry and Physics* 16.6, pp. 3683–3710. DOI: 10.5194/acp-16-3683-2016. URL: http://www.atmos-chem-phys.net/16/3683/2016/.

Jones, A.R. et al. (2007). "The U.K. Met Office's next-generation atmospheric dispersion model, NAME III, in Borrego C. and Norman A.-L. (Eds)". In: *Air Pollution Modeling and its Application XVII (Proceedings of the 27th NATO/CCMS International Technical Meeting on Air Pollution Modelling and its Application), Springer*, pp. 580–589.

Katharopoulos, I. et al. (2023). "Impact of transport model resolution and a priori assumptions on inverse modeling of Swiss F-gas emissions". In: *Atmos. Chem. Phys.* 23.22, pp. 14159–14186. DOI: 10.5194/acp-23-14159-2023. URL: https://acp.copernicus.org/articles/23/14159/2023/.

Manning, A. J. et al. (2021). "Evidence of a recent decline in UK emissions of hydrofluorocarbons determined by the InTEM inverse model and atmospheric measurements". In: *Atmospheric Chemistry and Physics* 21.16, pp. 12739–12755. DOI: 10.5194/acp-21-12739-2021. URL: https://acp.copernicus.org/articles/21/12739/2021/.

Pickers, P., K. Adcock, and A. Manning (Feb. 2024). *Atmospheric oxygen and carbon dioxide observations from Weybourne Atmospheric Observatory, Norfolk, UK uploaded to public archives*. Tech. rep. Process Attribution of Regional Emissions (PARIS). URL: https://horizoneurope-paris.eu/wp-content/uploads/sites/914/2024/07/PARIS-deliverables-D6.1-High-frequency-APO-data-uploaded-final.pdf.

Pickers, Penelope A. et al. (Apr. 2022). "Novel quantification of regional fossil fuel CO2 reductions during COVID-19 lockdowns using atmospheric oxygen measurements". en. In: *Science Advances* 8.16, eabl9250. ISSN: 2375-2548. DOI: 10.1126/sciadv.abl9250. URL: https://www.science.org/doi/10.1126/sciadv.abl9250 (visited on 12/01/2023).

Rigby, M. et al. (2019). "Increase in CFC-11 emissions from eastern China based on atmospheric observations". In: *Nature* 569, pp. 546–550. DOI: 10.1038/s41586-019-1193-4. URL: https://doi.org/10.1038/s41586-019-1193-4.

Rigby, M. et al. (Apr. 2025). *Inverse estimates of fossil fuel CO2 emission*. Tech. rep. Process Attribution of Regional Emissions (PARIS). URL: https://horizoneurope-paris.eu/wp-content/uploads/sites/914/2025/01/PARIS-M24-Inverse-estimates-of-fossil-fuel-CO2-emissions-final.pdf.

Stohl, A. et al. (2005). "Technical note: The Lagrangian particle dispersion model FLEXPART version 6.2". In: *Atmospheric Chemistry and Physics* 5, pp. 2461–2474. DOI: 10.5194/acp-5-2461-2005. URL: <GotoISI>://000231983600002.

White, Emily D. et al. (Apr. 2019). "Quantifying the UK's carbon dioxide flux: an atmospheric inverse modelling approach using a regional measurement network". en. In: *Atmospheric Chemistry and Physics*

19.7, pp. 4345–4365. ISSN: 1680-7324. DOI: 10.5194/acp-19-4345-2019. URL: https://www.atmos-chem-phys.net/19/4345/2019/ (visited on 04/05/2019).

Draft Inventory Annex Netherlands 2025

30th October, 2025

1 Introduction

In this document, global concentration trends and national emissions estimates derived from atmospheric observations ("inverse estimates") are presented for most reported gases. Comparing the emissions submitted in national inventories with those calculated using atmospheric observations allows for emissions to be assessed using two fundamentally different approaches. Substantial differences can highlight areas that could warrant further investigation.

Global concentration trends for each gas are first shown using annual average concentrations from Mace Head, Ireland (Northern Hemisphere) and Kennaook/Cape Grim, Tasmania, Australia (Southern Hemisphere). Data from these stations were selected to exclude regionally-polluted air masses and therefore represents northern and southern hemispheric concentration trends. Mace Head observations were supported by the National Aeronautics and Space Administration (NASA) and the UK Department of Energy, Security and Net Zero (DESNZ), and Kennaook/Cape Grim observations by NASA and the Australian Bureau of Meteorology.

Observations of European concentrations of greenhouse gases used to derive national inverse emission estimates were collected from many different networks and providers. Methane and nitrous oxide concentrations originated from the European ICOS (Integrated Carbon Observation System) network, the UK DECC (Deriving Emissions related to Climate Change) network and other national or individual initiatives. F-gas observations were made by affiliates of the AGAGE (Advanced Global Atmospheric Gases Experiment) network. Observations from additional stations across Europe were supported by the Horizon-EU PARIS (Process Attribution of Regional Emissions) project. The observation stations used to derive emissions for each gas are shown in the corresponding sections of this document.

An atmospheric transport model provides the link between surface fluxes and concentrations measured at the observing stations. If not otherwise mentioned, inversion-based emissions estimates were derived using two atmospheric transport models combined with three inverse models, yielding a total of six inversions. This ensemble of six inversions allows us to better quantify the uncertainties associated with inverse modelling.

The two atmospheric transport models used are the Numerical Atmospheric dispersion Modelling Environment (NAME, Jones et al., 2007), and the FLEXible PARTicle dispersion model (FLEXPART, Stohl et al., 2005). Both models are backwards-running Lagrangian Particle Dispersion Models (LPDMs) that simulate the recent transport of air to each observing station. The two LPDMs have been widely used in the estimation of greenhouse gas emissions (Ganesan et al., 2015; Rigby et al., 2019; Manning et al., 2021; Henne et al., 2016).

The three inverse methods used are InTEM (Inversion Technique for Emission Modelling, Manning et al., 2021), ELRIS (Empa Lagrangian Regional Inversion System, Henne et al., 2016; Katharopoulos et al., 2023), and RHIME (Regional Hierarchical Inverse Modelling Environment, Ganesan et al., 2014). All three inverse methods estimate emissions within Europe along with boundary conditions that account for the concentration of the air entering Europe. All three systems started from the same set of a priori emissions that were either derived from the global EDGAR emission inventory (version 8, European Commission: Joint Research et al., 2023) or a uniform land-based emission, depending on the gas. A natural emission component, from the WETCHARTS product, was included in the methane prior. The same observational dataset was used by each inverse model, but data selection (i.e., filtering datasets for specific conditions) and treatment of uncertainties were chosen separately and hence differ. The three methods also differ in their statistical approaches for estimating emissions.

Emission estimates are presented for the period 2008-2024. Emissions for the full 2008-2024 period were derived with the InTEM-NAME inversion only, while emissions from 2017-2024 are presented as the mean of the six inversions (denoted the "PARIS mean"). The uncertainty shown is the minimum/maximum of the uncertainties in the ensemble.

All inversions employed a resolution of one month for CH_4 and N_2O and 1-year for the fluorinated gases. The inversion results used to compare with the inventories are a one-year calendar average for CH_4 and N_2O and the yearly value derived from a 3-year moving average for the fluorinated gases. For the 2008-2024

InTEM-NAME results, a 3-year moving average was also applied to the annualised CH_4 and N_2O results due to lack of observational coverage in the earlier years.

2 Global Concentration Trends

2.1 Methane (CH_4)

Figure 2.1.1: Background Northern Hemisphere monthly concentrations of CH_4 estimated from MHD, Ireland observations are shown in red, and background Southern Hemisphere monthly concentrations from CGO, Tasmania are shown in blue. Grey shading represents provisional data.

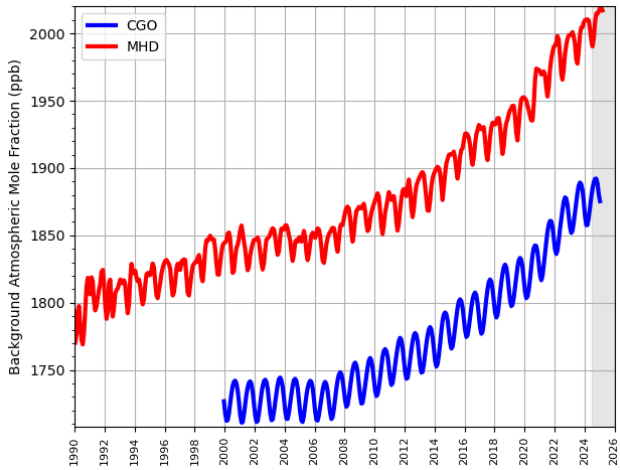

2.2 Nitrous Oxide (N_2O)

Figure 2.2.1: Background Northern Hemisphere monthly concentrations of N_2O estimated from MHD, Ireland observations are shown in red, and background Southern Hemisphere monthly concentrations from CGO, Tasmania are shown in blue. Grey shading represents provisional data.

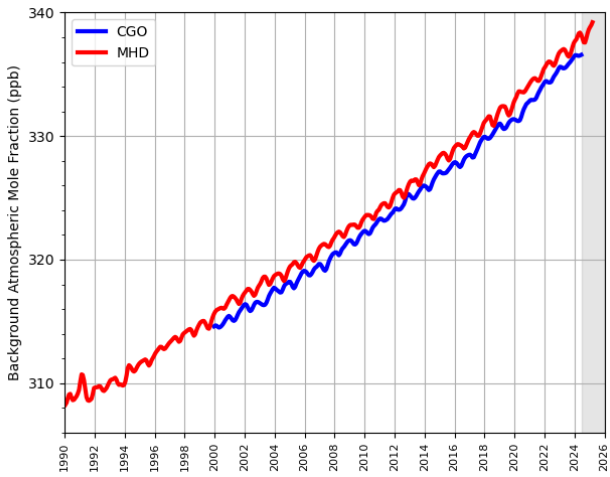

2.3 Hydrofluorocarbons (HFCs)

Figure 2.3.1: Background Northern Hemisphere monthly concentrations of six HFCs estimated from MHD, Ireland observations are shown in red, and background Southern Hemisphere monthly concentrations from CGO, Tasmania are shown in blue. Grey shading represents provisional data.

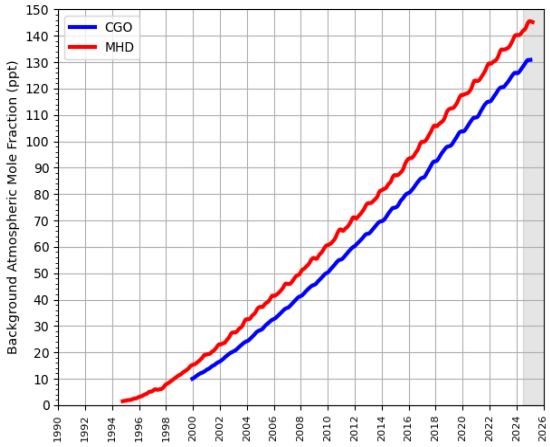

(a) HFC-134a

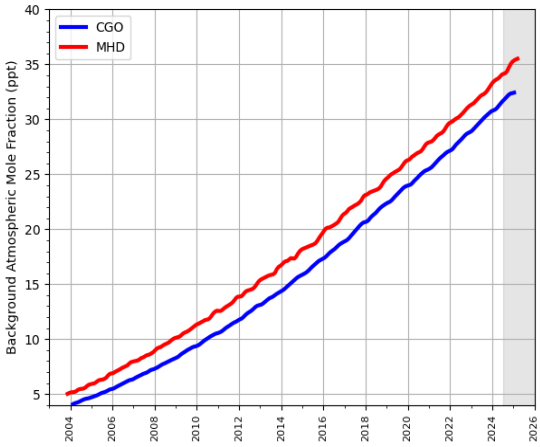

(b) HFC-143a

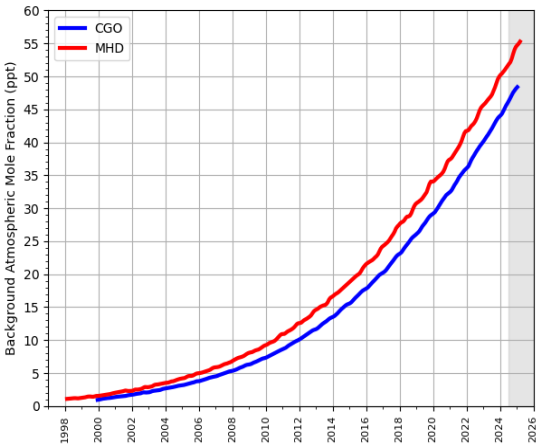

(c) HFC-125

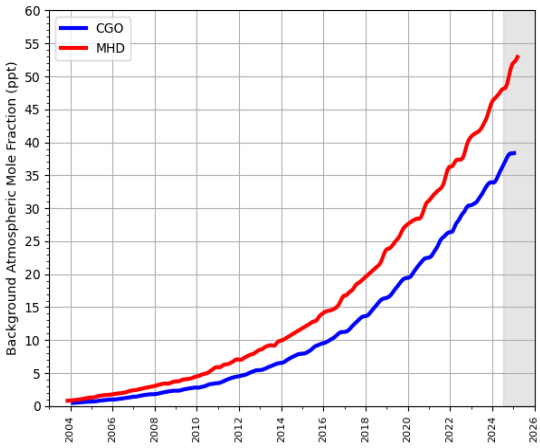

(d) HFC-32

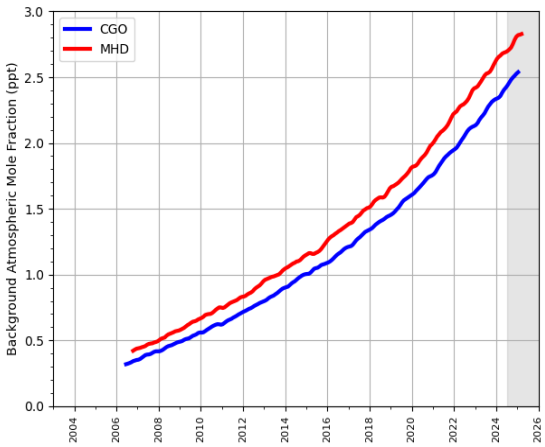

(e) HFC-227ea

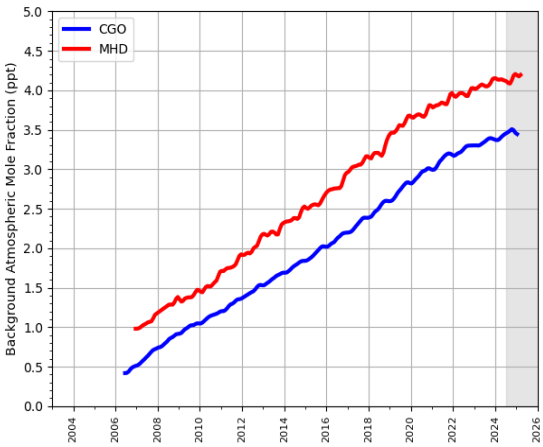

(f) HFC-245fa

Figure 2.3.2: Background Northern Hemisphere monthly concentrations of four HFCs estimated from MHD, Ireland observations are shown in red, and background Southern Hemisphere monthly concentrations from CGO, Tasmania are shown in blue. Grey shading represents provisional data.

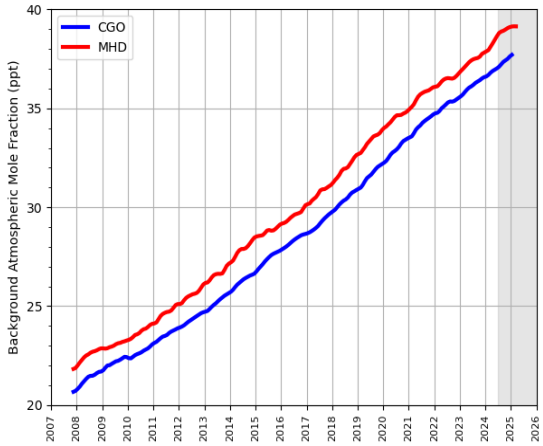

(a) HFC-23

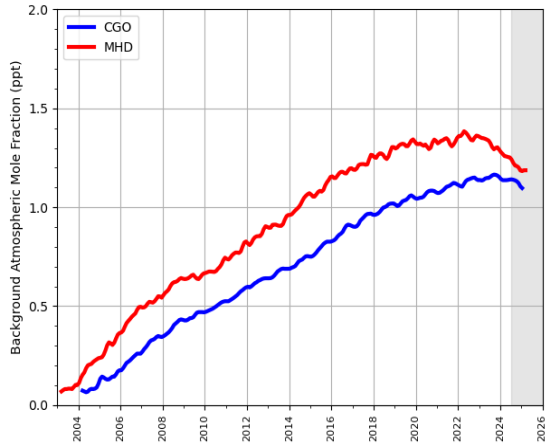

(b) HFC-365mfc

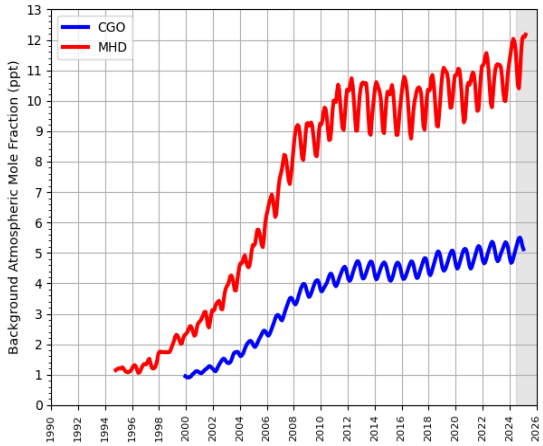

(c) HFC-152a

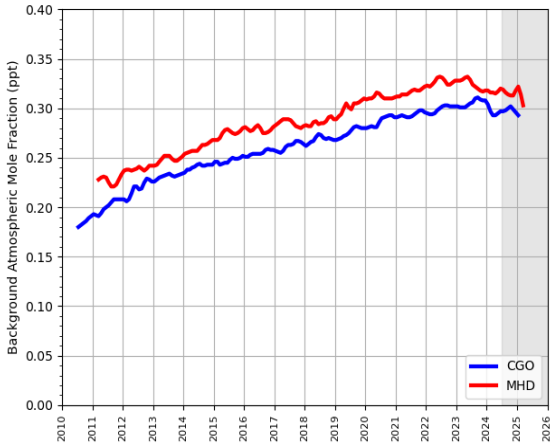

(d) HFC-43-10-mee

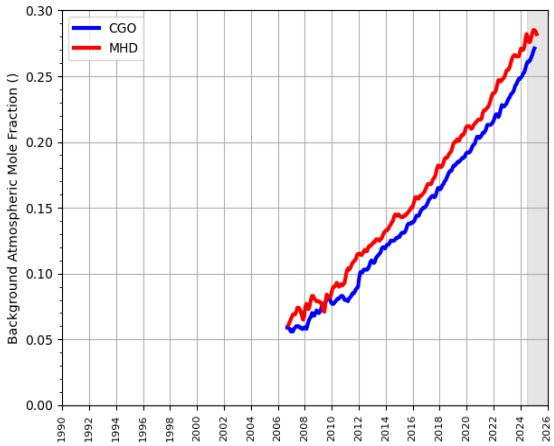

(e) HFC-236fa

2.4 Perfluorocarbons (PFCs)

Figure 2.4.1: Background Northern Hemisphere monthly concentrations of four PFCs estimated from MHD, Ireland observations are shown in red, and background Southern Hemisphere monthly concentrations from CGO, Tasmania are shown in blue. Grey shading represents provisional data.

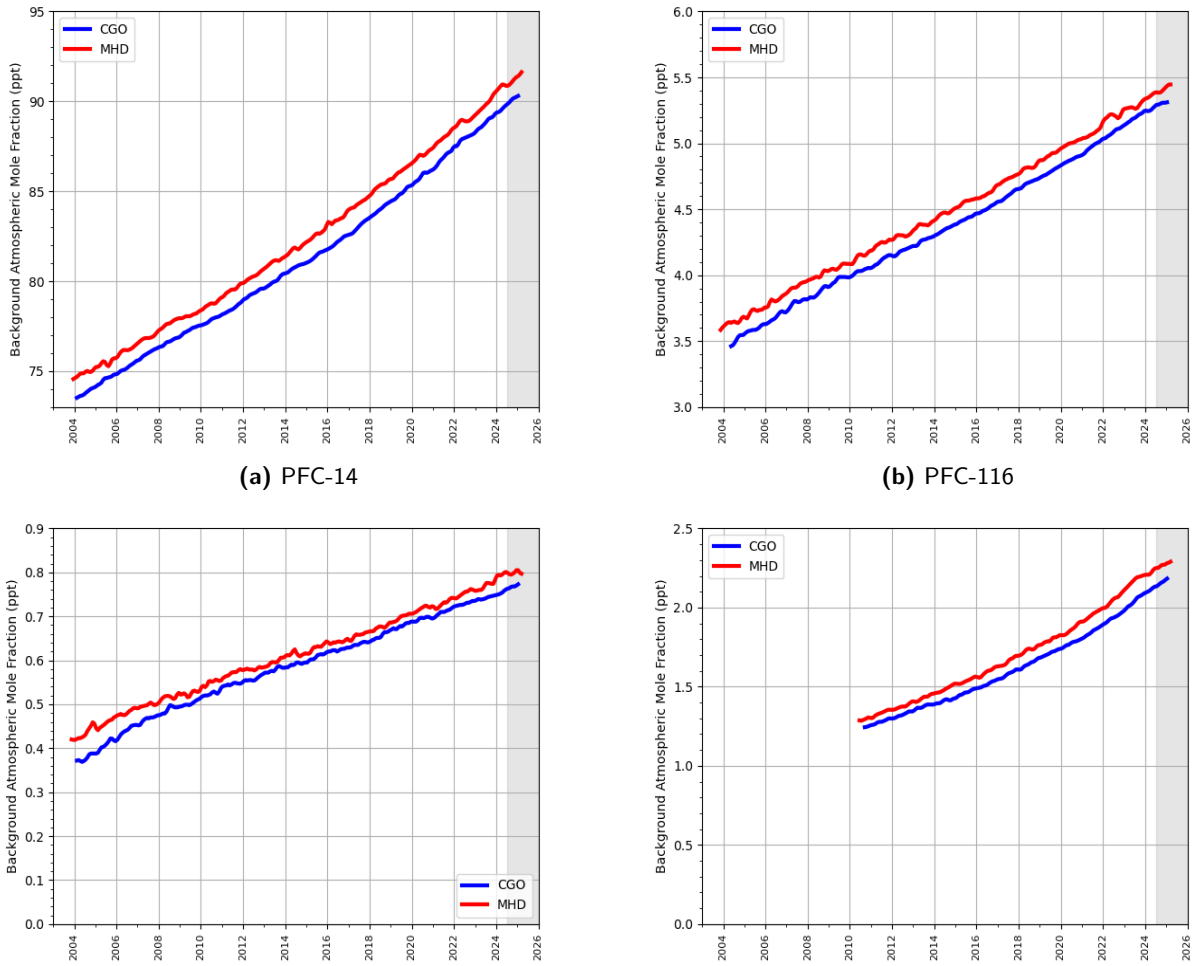

(a) PFC-14 **(b)** PFC-116 **(c)** PFC-218 **(d)** PFC-318

2.5 Sulphur Hexafluoride (SF_6) and Nitrogen Trifluoride (NF_3)

Figure 2.5.1: Background Northern Hemisphere monthly concentrations of SF_6 and NF_3 estimated from MHD, Ireland observations are shown in red, and background Southern Hemisphere monthly concentrations from CGO, Tasmania are shown in blue. Grey shading represents provisional data.

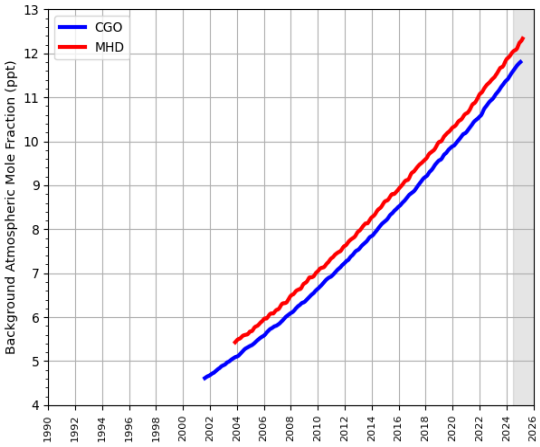

(a) SF_6

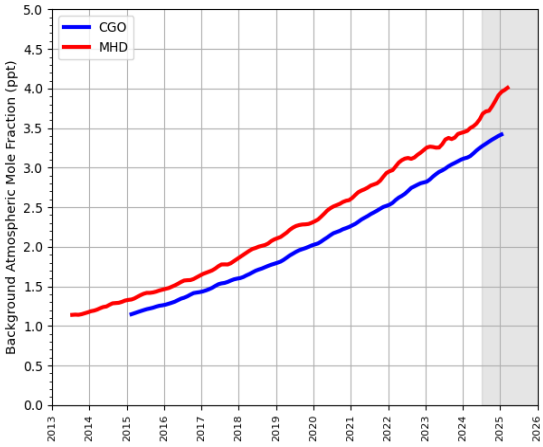

(b) NF_3

2.6 Carbon Dioxide (CO_2)

Figure 2.6.1: Background Northern Hemisphere monthly concentrations of CO_2 estimated from MHD, Ireland observations are shown in red, and background Southern Hemisphere monthly concentrations from CGO, Tasmania are shown in blue. Grey shading represents provisional data.

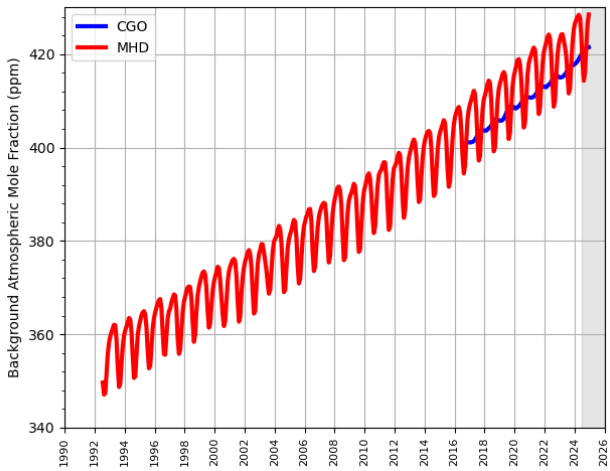

3 Key findings

- Methane (CH_4): The mean inversion results are around 40 % higher than the inventory estimates, although with significant spread. The inclusion of the observations from LUT does not appear to have a strong impact on the model results. LUT has high pollution events and the inverse models have a poor fit to the observations. In most years the inverse models estimate a seasonal cycle in emissions with the maximum in winter.
- Nitrous oxide (N_2O): Inversion results are around 25-35 % higher than the inventory estimates, though with significant spread. In all years the inverse models estimate a pronounced seasonal cycle in emissions with the maximum in late spring or early summer.
- Hydrofluorocarbons (HFCs): The inverse models generally estimate significantly higher emissions than those reported in the inventory, especially for HFC-32 where the inversion result is increasing sharply in contrast with the inventory. The decline in recent years in the total HFC inventory is not seen in the inverse results which remain flat, although the inverse model uncertainties are relatively high. The inverse model emissions are concentrated to the SW of the Netherlands.
- Perfluorocarbons (PFCs): The inverse model estimates are higher than those reported in the inventory although the uncertainties are very high.
- Sulphur hexafluoride (SF_6): The inverse model estimates reveal a significant source in the SW of the Netherlands or western Germany close to the border, given the resolution of the models it is not possible, currently, to be more precise. The trend estimated by the inversions is too uncertain to be reliable at the moment, data from future years will make this clearer.
- The resolutions of the inverse models mean that it is difficult for them to correctly allocate emissions precisely. This means for smaller countries like the Netherlands with close, highly populated neighbouring areas it is difficult to precisely allocate emissions to a specific country.

Table 1: Emissions estimation for the main greenhouse gases of focus according to the National Inventory Document (NID) 2025 and the inversions done in the PARIS project. For the PARIS estimation, the mean of all models is displayed, along with a range of uncertainty estimated via the half distance between the maximum and minimum uncertainties of the different models. For SF_6, the PARIS mean is the average of all InTEM and ELRIS inversions only.

		2020	2021	2022	2023	2024
CH_4	NID 2025	19.5	19.2	18.6	18.4	
$(\mathrm{TgCO_2\text{-}eq \cdot yr^{-1}})$	PARIS mean	27.3 ± 5.3	27.4 ± 5.6	28.1 ± 6.0	27.4 ± 5.3	27.4 ± 5.1
N_2O	NID 2025	7.5	7.2	6.7	6.6	
$(\mathrm{TgCO_2\text{-}eq \cdot yr^{-1}})$	PARIS mean	10.7 ± 2.0	10.6 ± 2.2	9.6 ± 1.9	9.2 ± 2.0	9.8 ± 2.4
Total HFC	NID 2025	0.9	0.7	0.6	0.5	
$(\mathrm{TgCO_2\text{-}eq \cdot yr^{-1}})$	PARIS mean	2.2 ± 0.6	2.2 ± 0.7	2.5 ± 0.6	2.4 ± 0.6	2.4 ± 0.5
SF_6	NID 2025	0.13	0.12	0.13	0.11	
$(\mathrm{TgCO_2\text{-}eq \cdot yr^{-1}})$	PARIS mean	0.08 ± 0.10	0.10 ± 0.09	0.15 ± 0.09	0.14 ± 0.10	0.15 ± 0.10
Total PFC	NID 2025	0.02	0.01	0.00	0.00	
$(\mathrm{TgCO_2\text{-}eq \cdot yr^{-1}})$	PARIS mean	0.13 ± 0.13	0.12 ± 0.14	0.13 ± 0.14	0.11 ± 0.11	0.10 ± 0.09
NF_3	NID 2025	0	0	0	0	
$(\mathrm{GgCO_2\text{-}eq \cdot yr^{-1}})$	PARIS mean	3 ± 22	5 ± 21	10 ± 27	15 ± 31	20 ± 38

4 Methane (CH_4)

Figure 4.0.1: Average monthly total source sensitivity of CH_4 observing sites as calculated by the FLEXPART transport model for the year 2018 (left) and 2024 (right) and used in the inversions. Observing stations active in each year are marked with red dots. Areas with visible land surface represent regions for which emissions can be observed well from the network. Shaded or dark areas represent regions for which limited emission information can be obtained from the network.

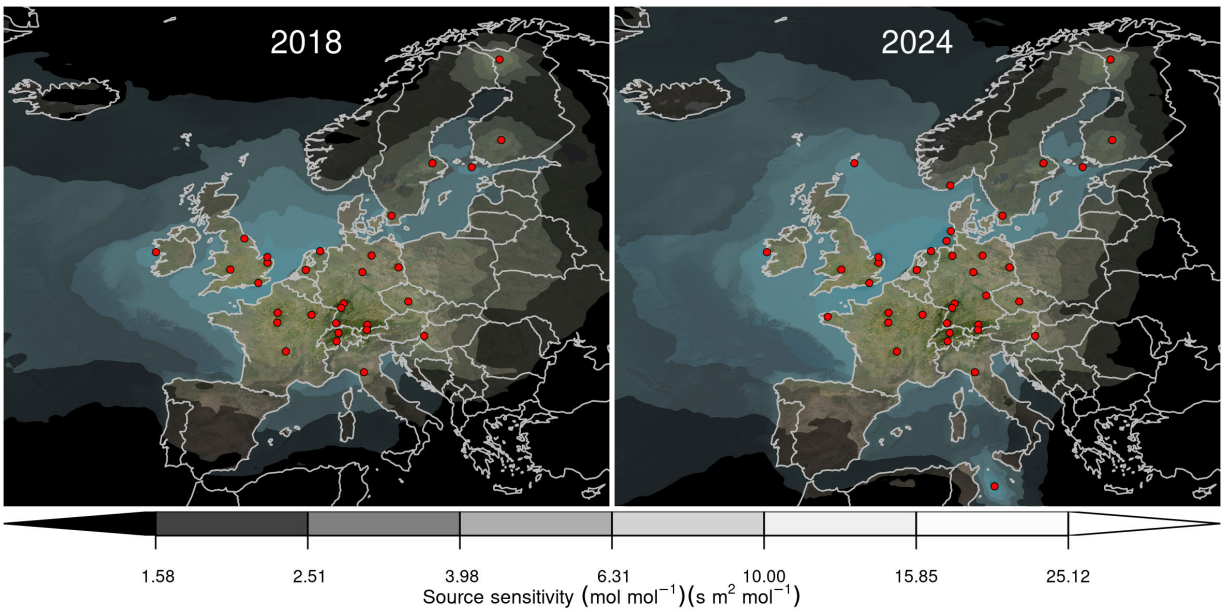

Figure 4.0.2: Verification of the Dutch emissions inventory estimates for CH_4. Modelled annual emissions are given as the mean from all models (black line) and the individual result from InTEM-NAME (blue line). The shaded blue area is the 68 % confidence interval (CI) of InTEM-NAME and the shaded grey area encompasses the 68 % CI from all models. National inventory annual totals from 2024 and 2025 are given as grey and black bars, respectively.

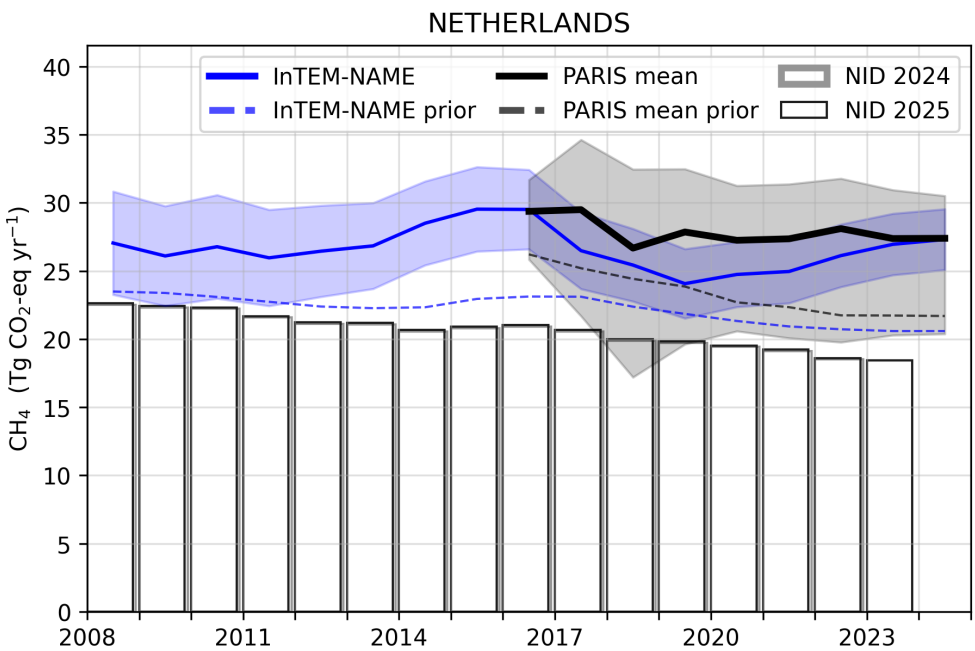

Figure 4.0.3: Verification of the Dutch emissions inventory estimates for CH_4 (zoom in to 2018-2024). Modelled annual emissions are given as the mean from all models (black line) and the individual result from InTEM-NAME (blue line). The shaded blue area is the 68 % confidence interval (CI) of InTEM-NAME and the shaded grey area encompasses the 68 % CI from all models. National inventory annual totals from 2024 and 2025 are given as grey and black bars, respectively.

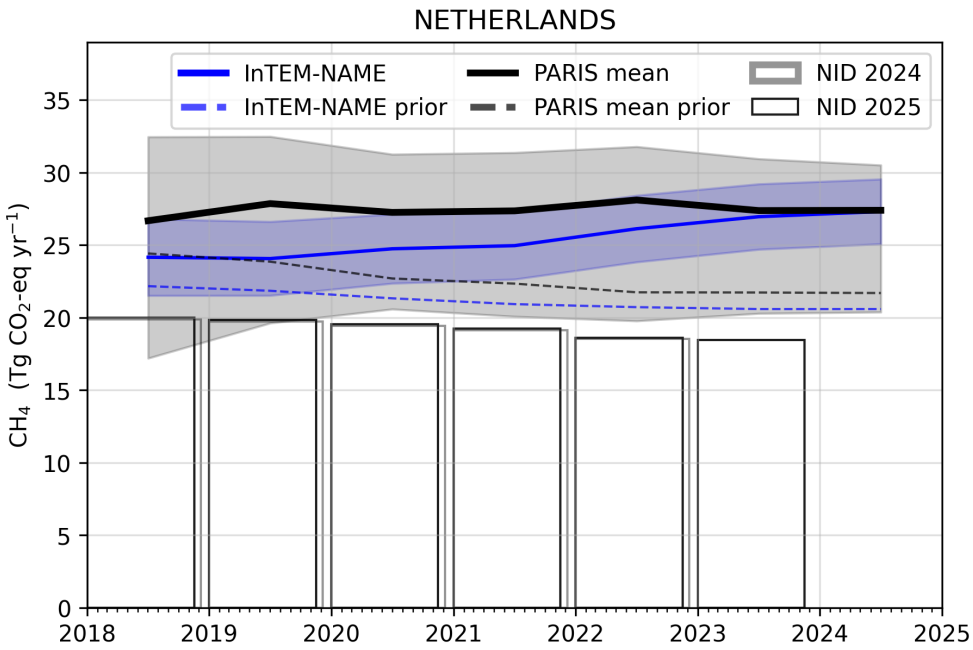

Figure 4.0.4: Verification of the Dutch emissions inventory estimates for CH_4 (zoom in to 2018-2024). Modelled monthly emissions are given as the mean from all models (black line) and the individual result from InTEM-NAME (blue line). The shaded blue area is the 68 % confidence interval (CI) of InTEM-NAME and the shaded grey area encompasses the 68 % CI from all models. National inventory annual totals from 2024 and 2025 are given as grey and black bars, respectively.

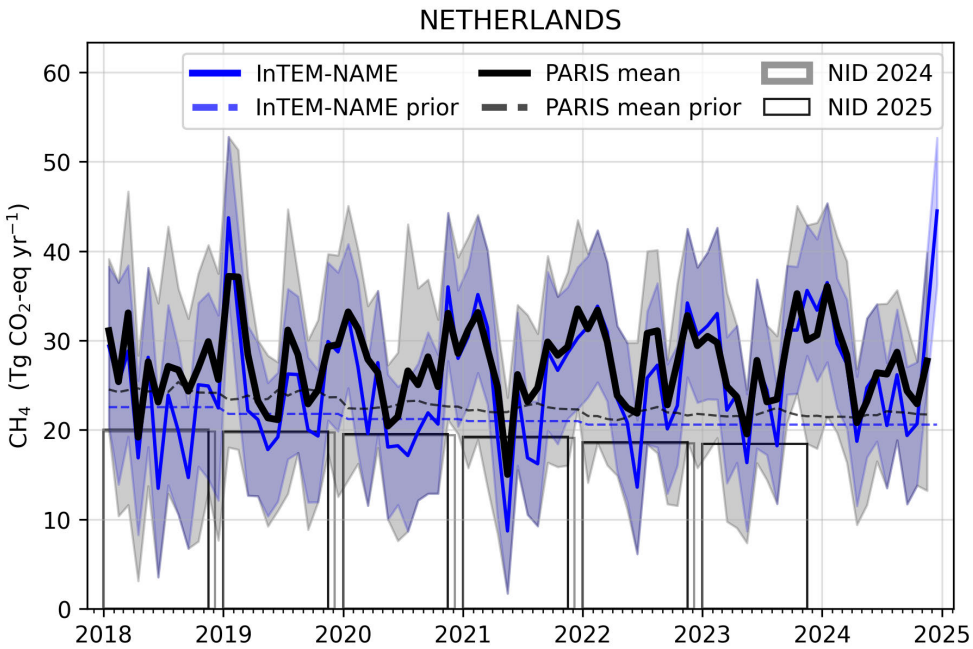

Figure 4.0.5: Spatial distribution of the Dutch average modelled emissions of CH_4 during the period of 2020-2024 (mean from all models). Observing stations are marked with red circles and highly-populated cities are marked with red triangles.

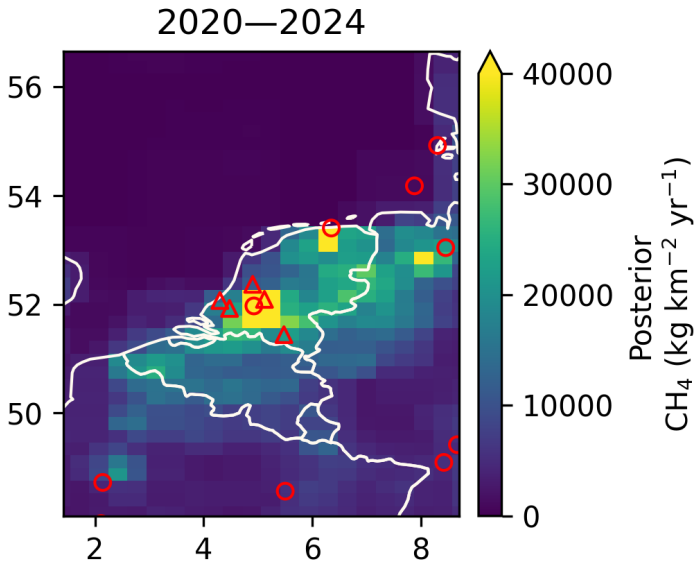

Figure 4.0.6: Spatial distribution of the seasonal deviation from the mean. The deviation is defined as the modelled Dutch seasonally averaged CH_4 emissions over 2020-2024 minus the average over the whole period. The mean across all models is shown. Observing stations are marked with black circles and highly-populated cities are marked with black triangles.

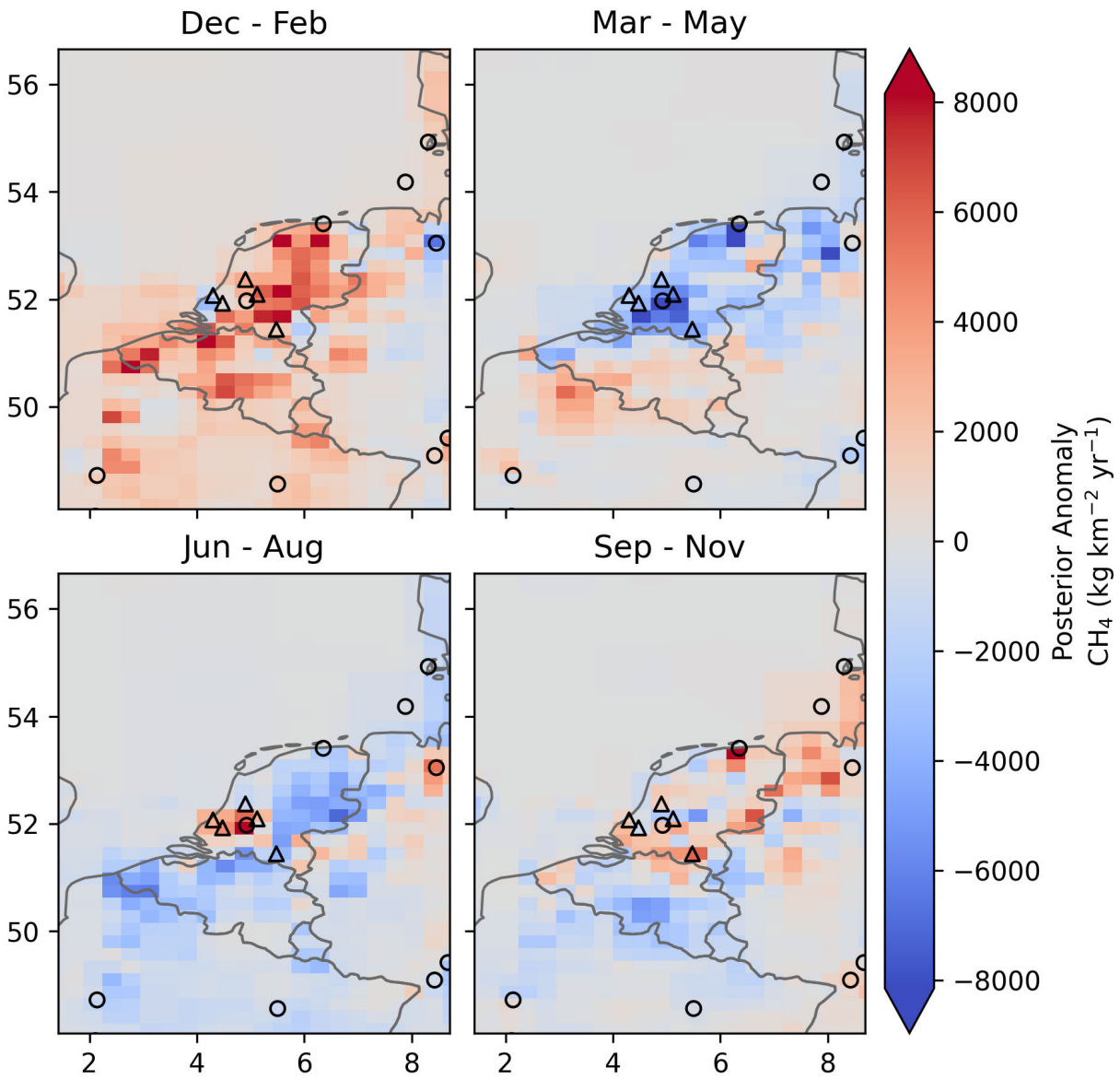

5 Nitrous Oxide (N_2O)

Figure 5.0.1: Average monthly total source sensitivity of N_2O observing sites as calculated by the FLEXPART transport model for the year 2018 (left) and 2024 (right) and used in the inversions. Observing stations active in each year are marked with red dots. Areas with visible land surface represent regions for which emissions can be observed well from the network. Shaded or dark areas represent regions for which limited emission information can be obtained from the network.

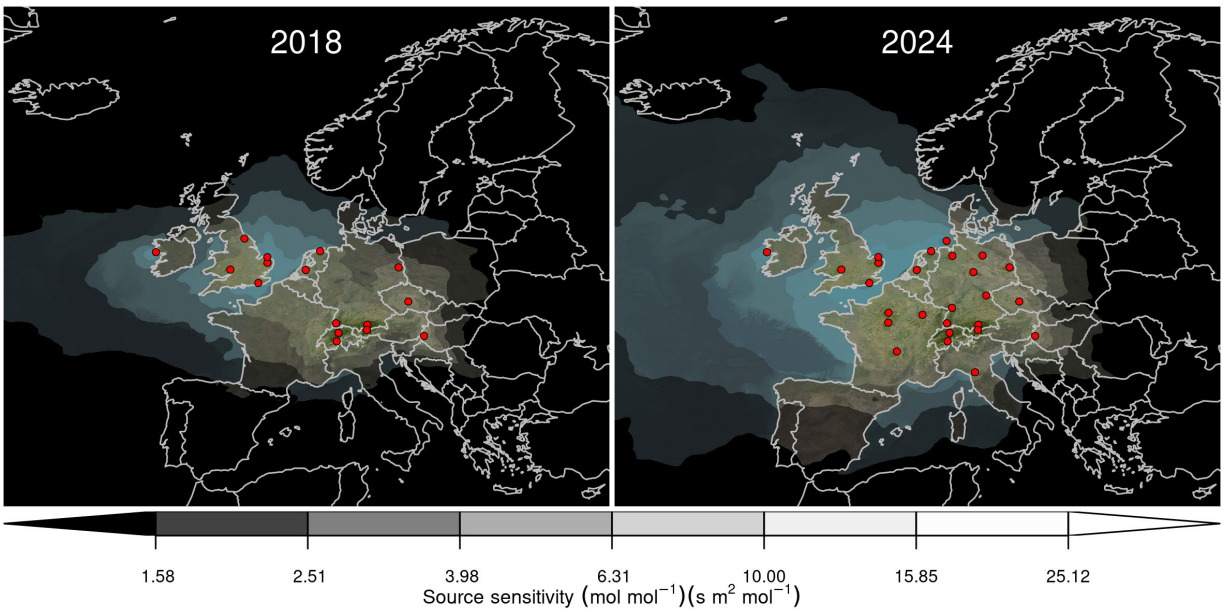

Figure 5.0.2: Verification of the Dutch emissions inventory estimates for N_2O. Modelled annual emissions are given as the mean from all models (black line) and the individual result from InTEM-NAME (blue line). The shaded blue area is the 68 % confidence interval (CI) of InTEM-NAME and the shaded grey area encompasses the 68 % CI from all models. National inventory annual totals from 2024 and 2025 are given as grey and black bars, respectively.

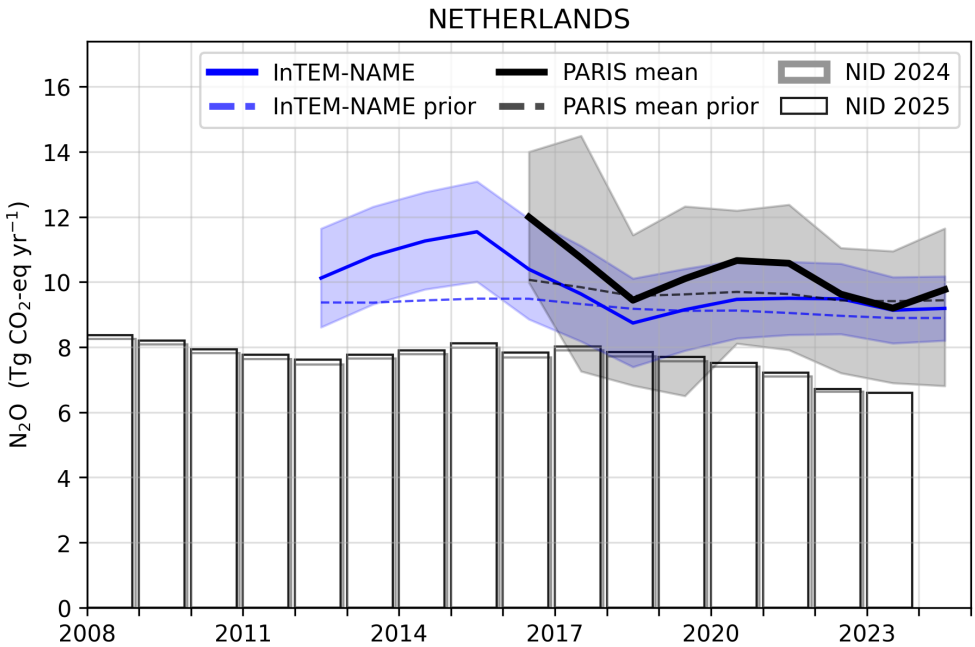

Figure 5.0.3: Verification of the Dutch emissions inventory estimates for N_2O (zoom in to 2018-2024). Modelled annual emissions are given as the mean from all models (black line) and the individual result from InTEM-NAME (blue line). The shaded blue area is the 68 % confidence interval (CI) of InTEM-NAME and the shaded grey area encompasses the 68 % CI from all models. National inventory annual totals from 2024 and 2025 are given as grey and black bars, respectively.

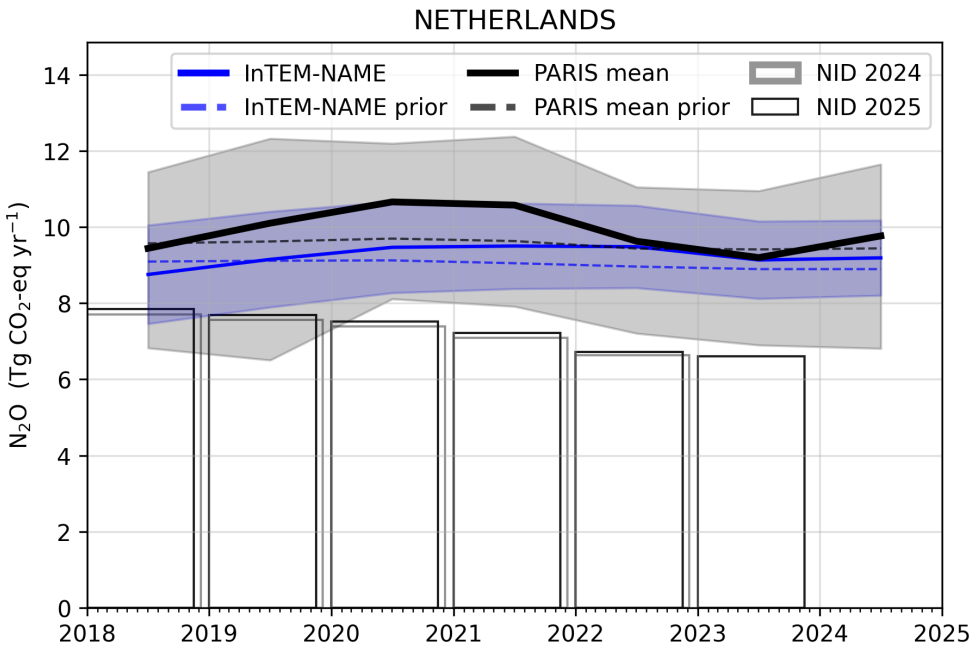

Figure 5.0.4: Verification of the Dutch emissions inventory estimates for N_2O (zoom in to 2018-2024). Modelled monthly emissions are given as the mean from all models (black line) and the individual result from InTEM-NAME (blue line). The shaded blue area is the 68 % confidence interval (CI) of InTEM-NAME and the shaded grey area encompasses the 68 % CI from all models. National inventory annual totals from 2024 and 2025 are given as grey and black bars, respectively.

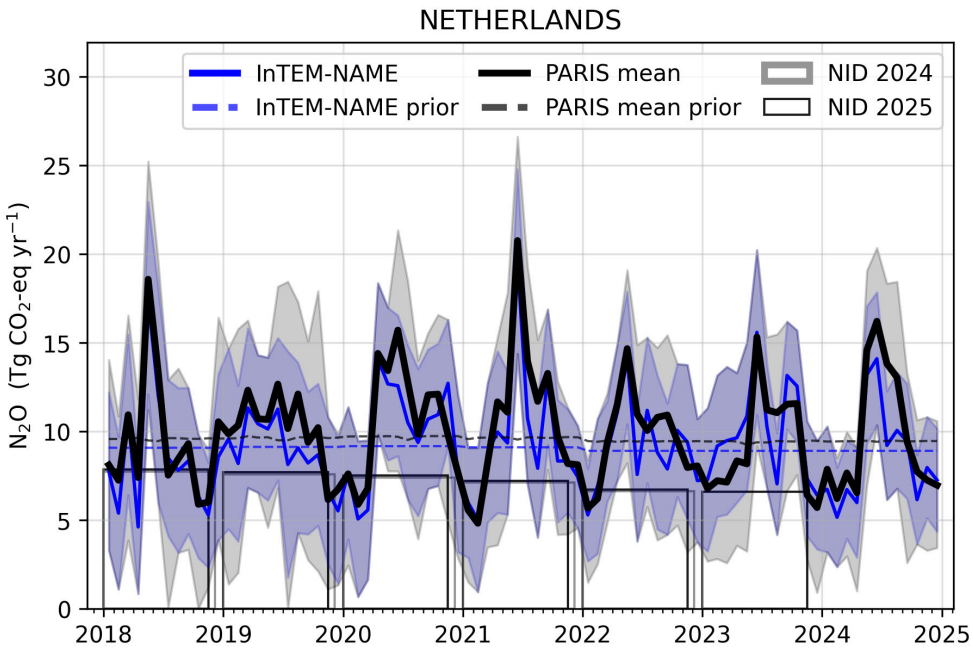

Figure 5.0.5: Spatial distribution of the Dutch average modelled emissions of N_2O during the period of 2020-2024 (mean from all models). Observing stations are marked with red circles and highly-populated cities are marked with red triangles.

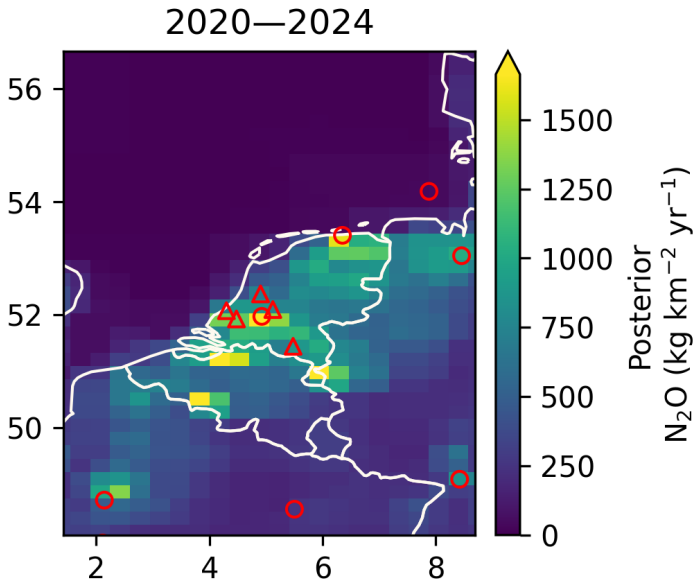

Figure 5.0.6: Spatial distribution of the seasonal deviation from the mean. The deviation is defined as the modelled Dutch seasonally averaged N_2O emissions over 2020-2024 minus the average over the whole period. The mean across all models is shown. Observing stations are marked with black circles and highly-populated cities are marked with black triangles.

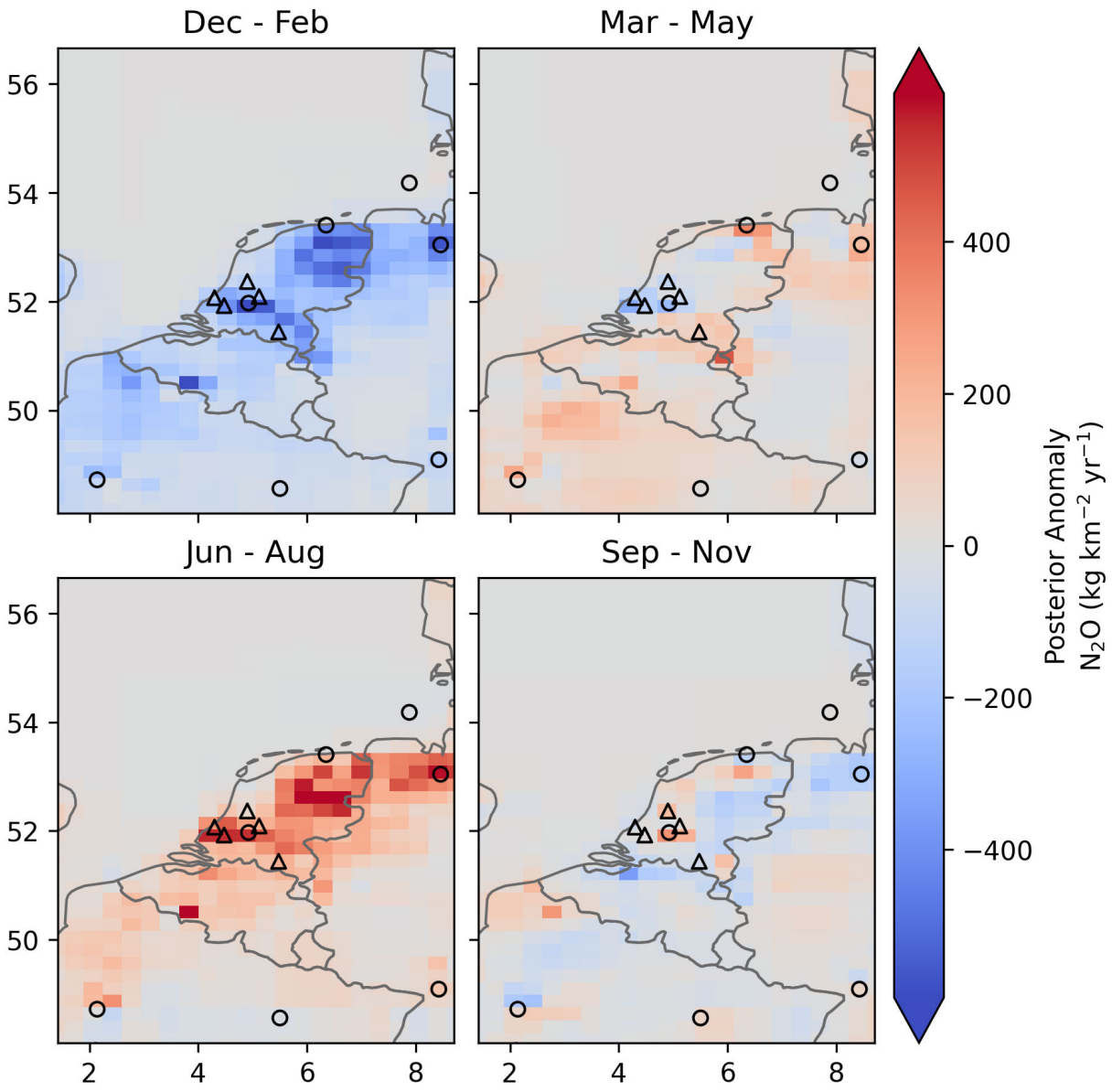

6 Hydrofluorocarbons (HFCs)

Figure 6.0.1: Total source sensitivity of HFCs/PFCs observing sites as calculated by the FLEXPART transport model for the year 2018 (left) and 2024 (right) and used in the inversions. Observing stations active in each year are marked with red dots. Areas with visible land surface represent regions for which emissions can be observed well from the network. Shaded or dark areas represent regions for which limited emission information can be obtained from the network.

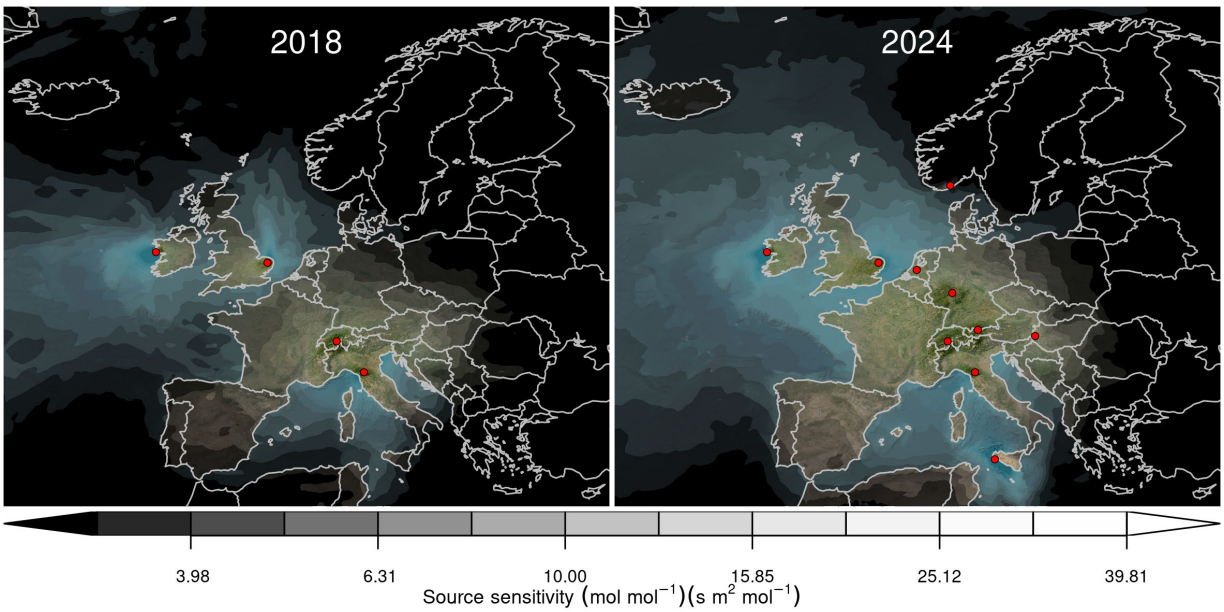

6.1 HFC-125

Figure 6.1.1: Verification of the Dutch emissions inventory estimates for HFC-125. Modelled annual emissions are given as the mean from all models (black line) and the individual result from InTEM-NAME (blue line). The shaded blue area is the 68 % confidence interval (CI) of InTEM-NAME and the shaded grey area encompasses the 68 % CI from all models. National inventory annual totals from 2024 and 2025 are given as grey and black bars, respectively.

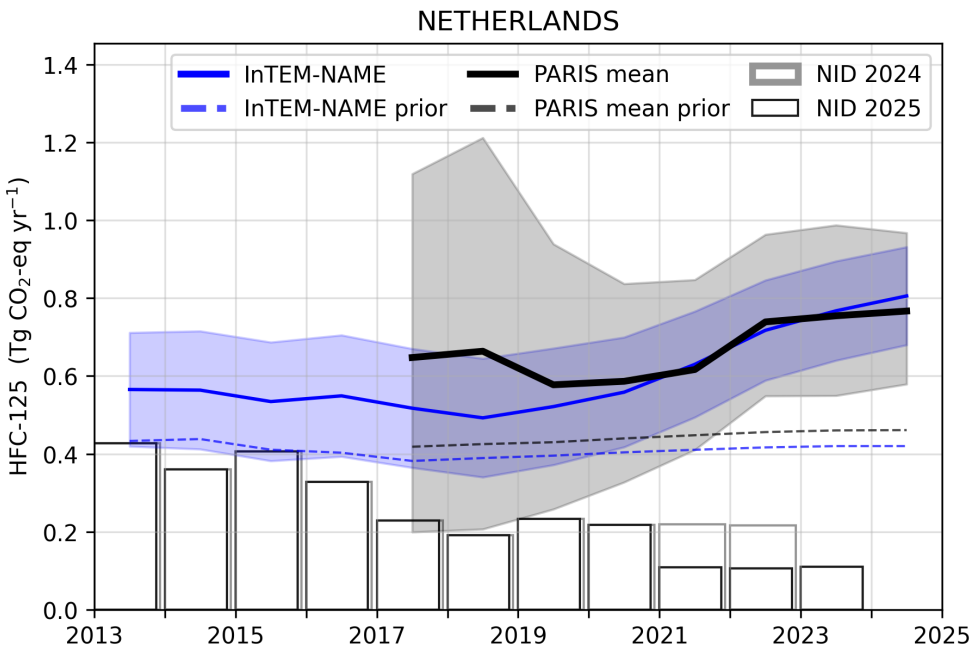

Figure 6.1.2: Spatial distribution of the Dutch average modelled emissions of HFC-125 during the period of 2020-2024 (mean from all models). Observing stations are marked with red circles and highly-populated cities are marked with red triangles.

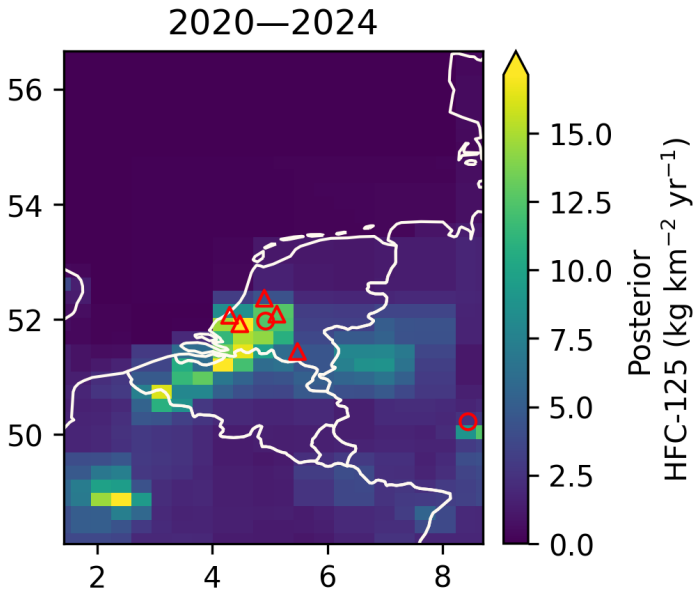

6.2 HFC-134a

Figure 6.2.1: Verification of the Dutch emissions inventory estimates for HFC-134a. Modelled annual emissions are given as the mean from all models (black line) and the individual result from InTEM-NAME (blue line). The shaded blue area is the 68 % confidence interval (CI) of InTEM-NAME and the shaded grey area encompasses the 68 % CI from all models. National inventory annual totals from 2024 and 2025 are given as grey and black bars, respectively.

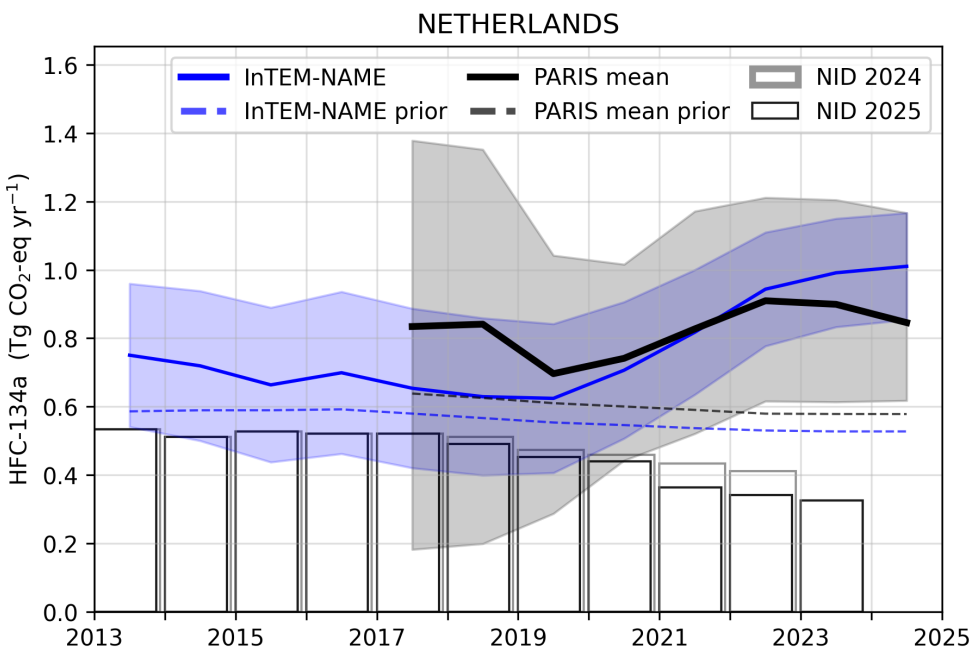

Figure 6.2.2: Spatial distribution of the Dutch average modelled emissions of HFC-134a during the period of 2020-2024 (mean from all models). Observing stations are marked with red circles and highly-populated cities are marked with red triangles.

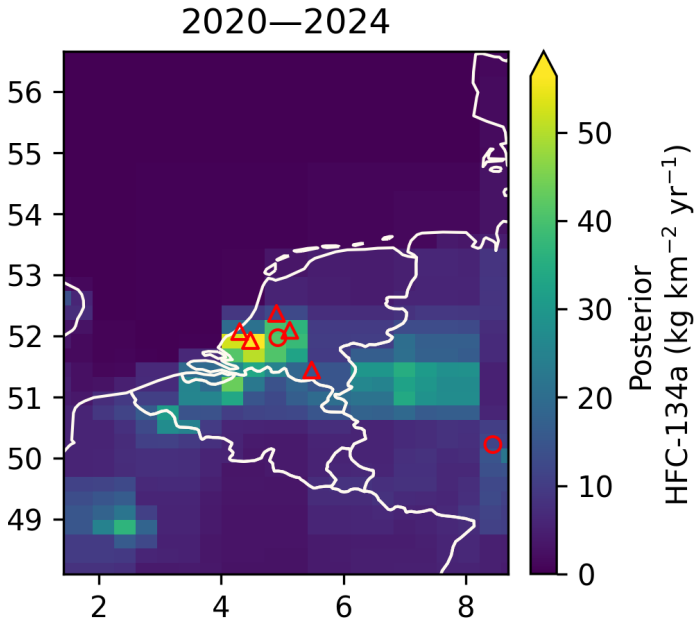

6.3 HFC-143a

Figure 6.3.1: Verification of the Dutch emissions inventory estimates for HFC-143a. Modelled annual emissions are given as the mean from all models (black line) and the individual result from InTEM-NAME (blue line). The shaded blue area is the 68 % confidence interval (CI) of InTEM-NAME and the shaded grey area encompasses the 68 % CI from all models. National inventory annual totals from 2024 and 2025 are given as grey and black bars, respectively.

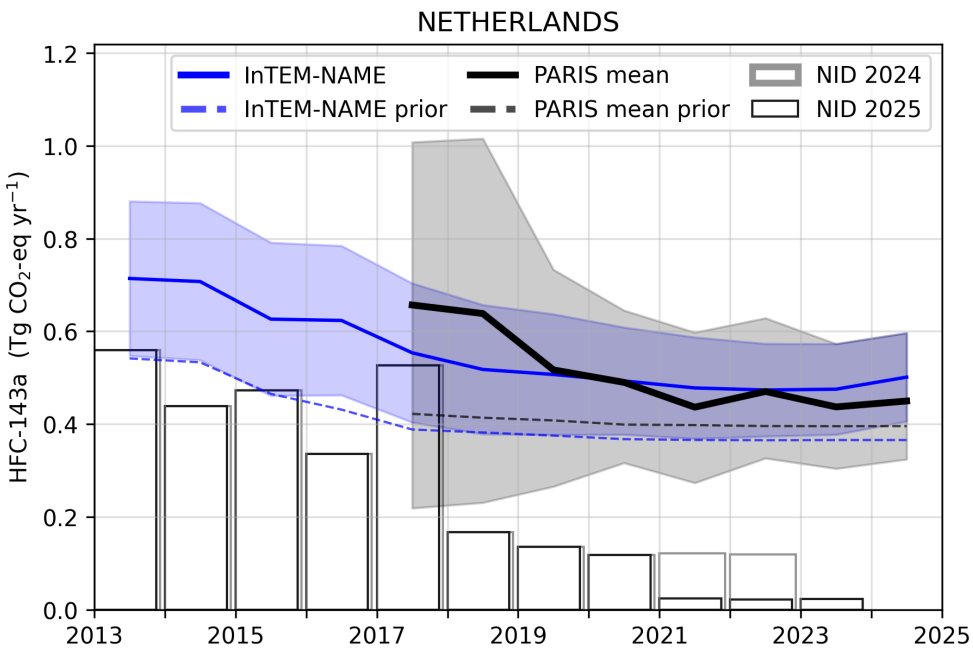

Figure 6.3.2: Spatial distribution of the Dutch average modelled emissions of HFC-143a during the period of 2020-2024 (mean from all models). Observing stations are marked with red circles and highly-populated cities are marked with red triangles.

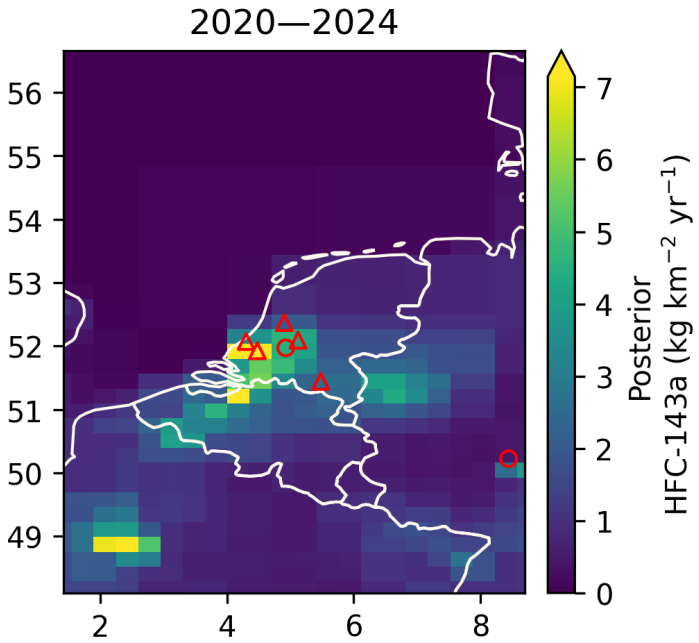

6.4 HFC-152a

Figure 6.4.1: Verification of the Dutch emissions inventory estimates for HFC-152a. Modelled annual emissions are given as the mean from all models (black line) and the individual result from InTEM-NAME (blue line). The shaded blue area is the 68 % confidence interval (CI) of InTEM-NAME and the shaded grey area encompasses the 68 % CI from all models. National inventory annual totals from 2024 and 2025 are given as grey and black bars, respectively.

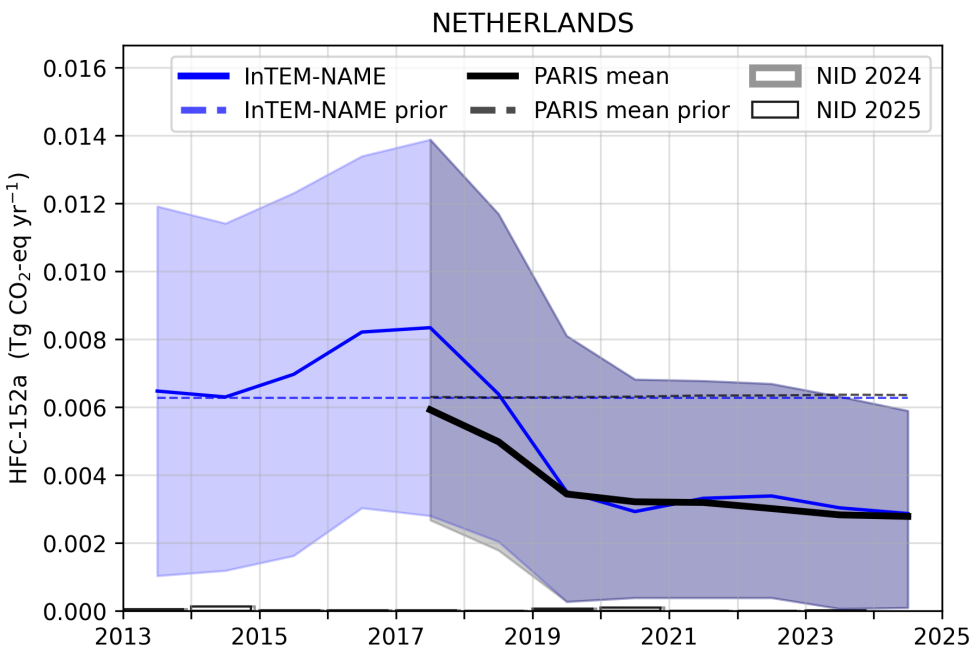

Figure 6.4.2: Spatial distribution of the Dutch average modelled emissions of HFC-152a during the period of 2020-2024 (mean from all models). Observing stations are marked with red circles and highly-populated cities are marked with red triangles.

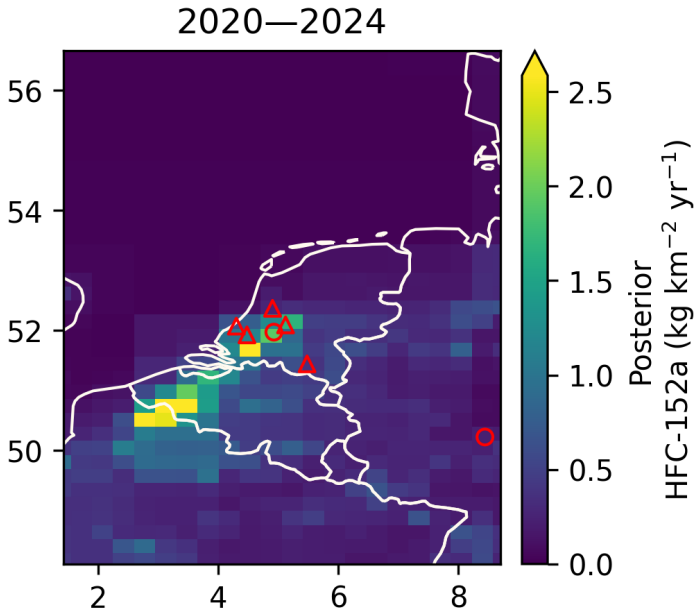

6.5 HFC-227ea

Figure 6.5.1: Verification of the Dutch emissions inventory estimates for HFC-227ea. Modelled annual emissions are given as the mean from all models (black line) and the individual result from InTEM-NAME (blue line). The shaded blue area is the 68 % confidence interval (CI) of InTEM-NAME and the shaded grey area encompasses the 68 % CI from all models. National inventory annual totals from 2024 and 2025 are given as grey and black bars, respectively.

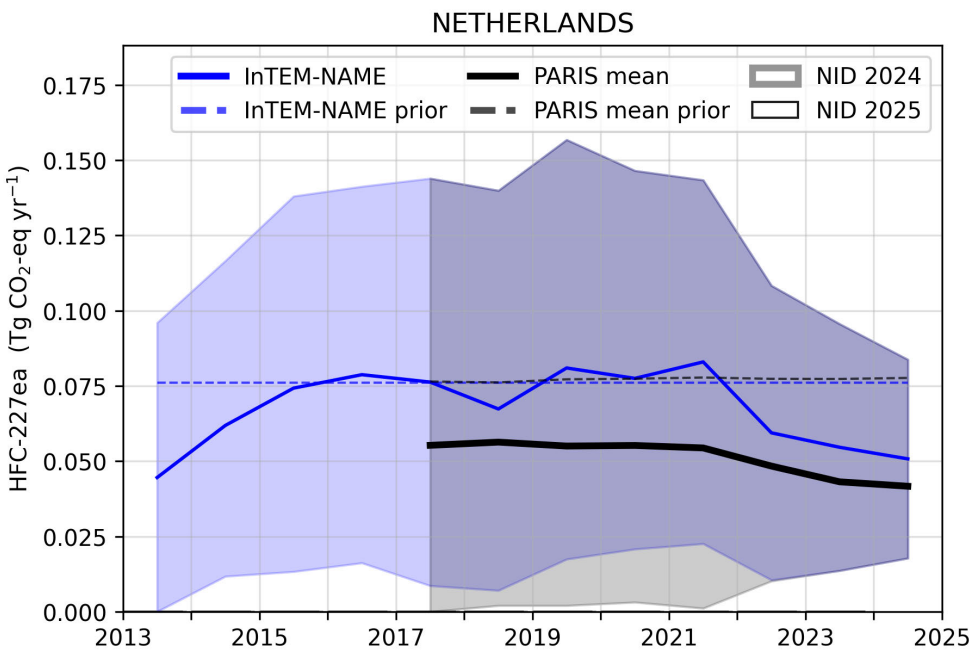

Figure 6.5.2: Spatial distribution of the Dutch average modelled emissions of HFC-227ea during the period of 2020-2024 (mean from all models). Observing stations are marked with red circles and highly-populated cities are marked with red triangles.

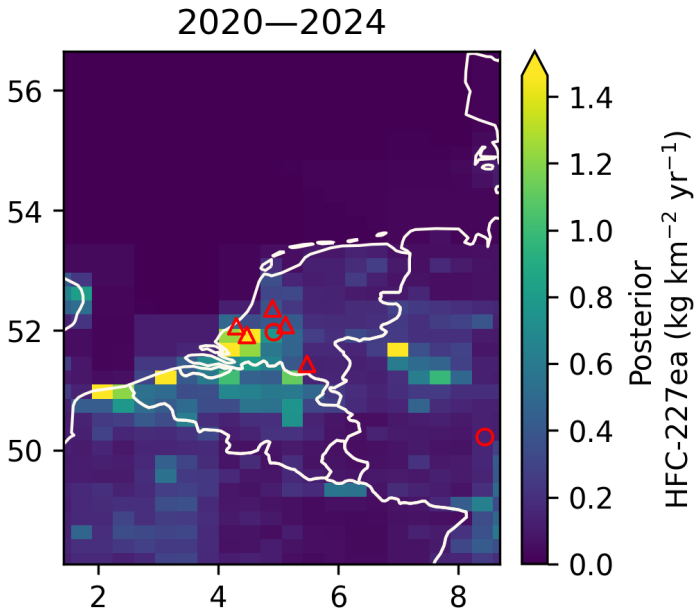

6.6 HFC-32

Figure 6.6.1: Verification of the Dutch emissions inventory estimates for HFC-32. Modelled annual emissions are given as the mean from all models (black line) and the individual result from InTEM-NAME (blue line). The shaded blue area is the 68 % confidence interval (CI) of InTEM-NAME and the shaded grey area encompasses the 68 % CI from all models. National inventory annual totals from 2024 and 2025 are given as grey and black bars, respectively.

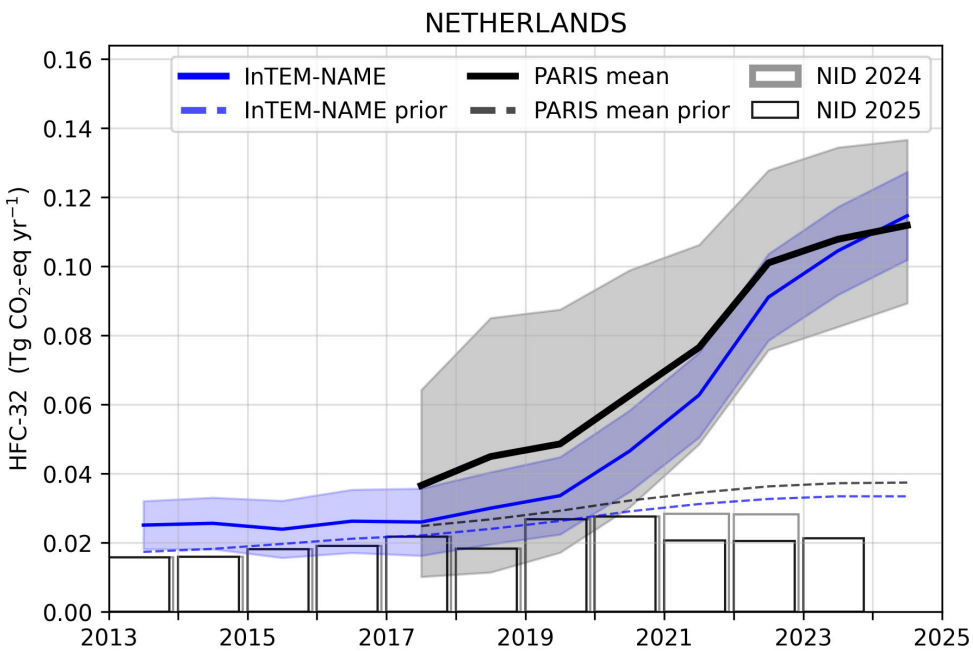

Figure 6.6.2: Spatial distribution of the Dutch average modelled emissions of HFC-32 during the period of 2020-2024 (mean from all models). Observing stations are marked with red circles and highly-populated cities are marked with red triangles.

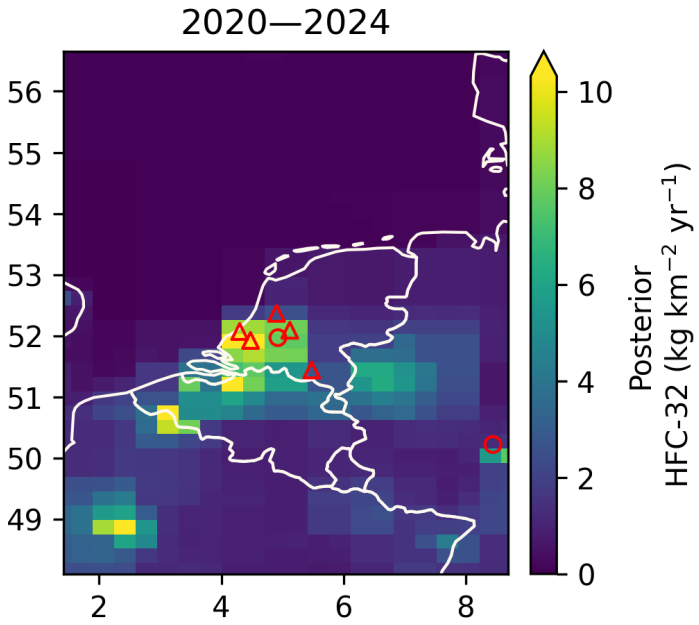

6.7 Total HFCs

Figure 6.7.1: Verification of the Dutch emissions inventory estimates for total HFCs. Modelled annual emissions are given as the mean from all models (black line) and the individual result from InTEM-NAME (blue line). The shaded blue area is the 68 % confidence interval (CI) of InTEM-NAME and the shaded grey area encompasses the 68 % CI from all models. National inventory annual totals from 2024 and 2025 are given as grey and black bars, respectively.

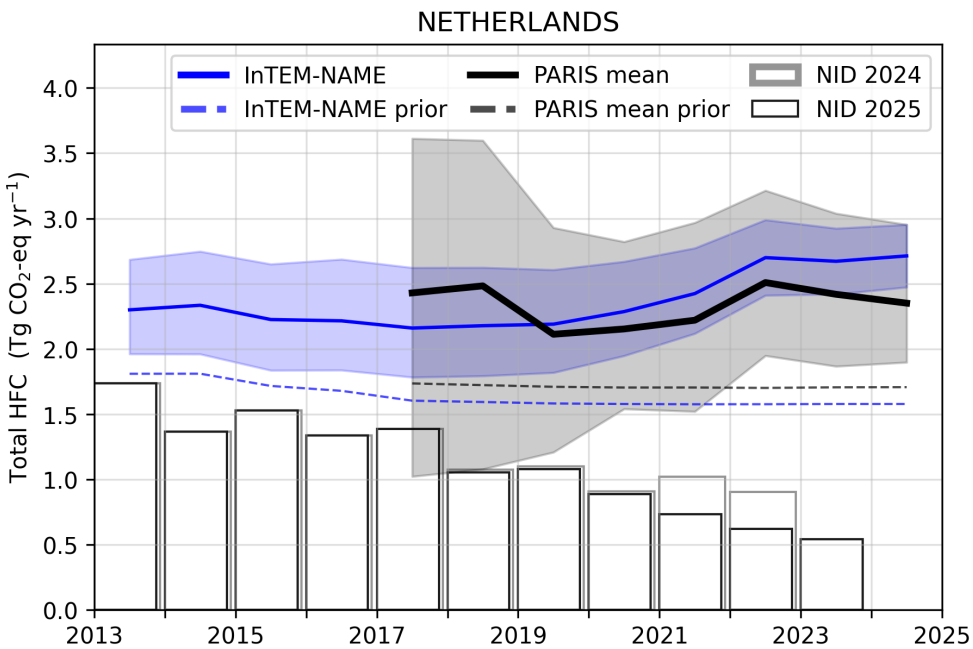

Table 2: Emissions estimation for HFCs according to the National Inventory Document (NID) 2025 and the inversions done in the PARIS project. For the PARIS estimation, the mean of all models is displayed, along with a range of uncertainty estimated via the half distance between the maximum and minimum uncertainties of the different models.

		2020	2021	2022	2023	2024
HFC-134a	NID 2025	0.44	0.36	0.34	0.33	
$(\mathrm{TgCO_2\text{-}eq \cdot yr^{-1}})$	PARIS mean	0.74 ± 0.29	0.83 ± 0.33	0.91 ± 0.30	0.90 ± 0.30	0.85 ± 0.27
HFC-125	NID 2025	0.22	0.11	0.11	0.11	
$(\mathrm{TgCO_2\text{-}eq \cdot yr^{-1}})$	PARIS mean	0.59 ± 0.25	0.62 ± 0.22	0.74 ± 0.21	0.75 ± 0.22	0.77 ± 0.19
HFC-143a	NID 2025	0.12	0.02	0.02	0.02	
$(\mathrm{TgCO_2\text{-}eq \cdot yr^{-1}})$	PARIS mean	0.49 ± 0.16	0.44 ± 0.16	0.47 ± 0.15	0.44 ± 0.13	0.45 ± 0.14
HFC-23	NID 2025	0.08	0.22	0.13	0.06	
$(\mathrm{TgCO_2\text{-}eq \cdot yr^{-1}})$	PARIS mean	0.16 ± 0.29	0.16 ± 0.24	0.20 ± 0.23	0.14 ± 0.15	0.10 ± 0.12
HFC-32	NID 2025	0.03	0.02	0.02	0.02	
$(\mathrm{TgCO_2\text{-}eq \cdot yr^{-1}})$	PARIS mean	0.06 ± 0.03	0.08 ± 0.03	0.10 ± 0.03	0.11 ± 0.03	0.11 ± 0.02
HFC-227ea	NID 2025	0	0	0	0	
$(\mathrm{GgCO_2\text{-}eq \cdot yr^{-1}})$	PARIS mean	55 ± 72	54 ± 71	48 ± 49	43 ± 41	42 ± 33
HFC-365mfc	NID 2025	0	0	0	0	
$(\mathrm{GgCO_2\text{-}eq \cdot yr^{-1}})$	PARIS mean	22 ± 19	20 ± 17	20 ± 15	16 ± 12	13 ± 11
HFC-245fa	NID 2025	0	0	0	0	
$(\mathrm{GgCO_2\text{-}eq \cdot yr^{-1}})$	PARIS mean	20 ± 15	18 ± 12	15 ± 10	12 ± 9	11 ± 8
HFC-236fa	NID 2025	0.0	0.0	0.0	0.0	
$(\mathrm{GgCO_2\text{-}eq \cdot yr^{-1}})$	PARIS mean	6.7 ± 13.6	5.4 ± 12.1	3.4 ± 7.7	2.3 ± 4.4	1.9 ± 3.2
HFC-152a	NID 2025	0.1	0.0	0.0	0.0	
$(\mathrm{GgCO_2\text{-}eq \cdot yr^{-1}})$	PARIS mean	3.2 ± 3.2	3.2 ± 3.2	3.0 ± 3.2	2.8 ± 3.1	2.8 ± 2.9
HFC-4310mee	NID 2025	0.0	0.0	0.0	0.0	
$(\mathrm{GgCO_2\text{-}eq \cdot yr^{-1}})$	PARIS mean	2.4 ± 5.1	2.1 ± 4.2	2.5 ± 4.5	2.0 ± 3.9	1.5 ± 3.4

7 Perfluorocarbons (PFCs)

7.1 PFC-14

Figure 7.1.1: Verification of the Dutch emissions inventory estimates for PFC-14. Modelled annual emissions are given as the mean from all models (black line) and the individual result from InTEM-NAME (blue line). The shaded blue area is the 68 % confidence interval (CI) of InTEM-NAME and the shaded grey area encompasses the 68 % CI from all models. National inventory annual totals from 2024 and 2025 are given as grey and black bars, respectively.

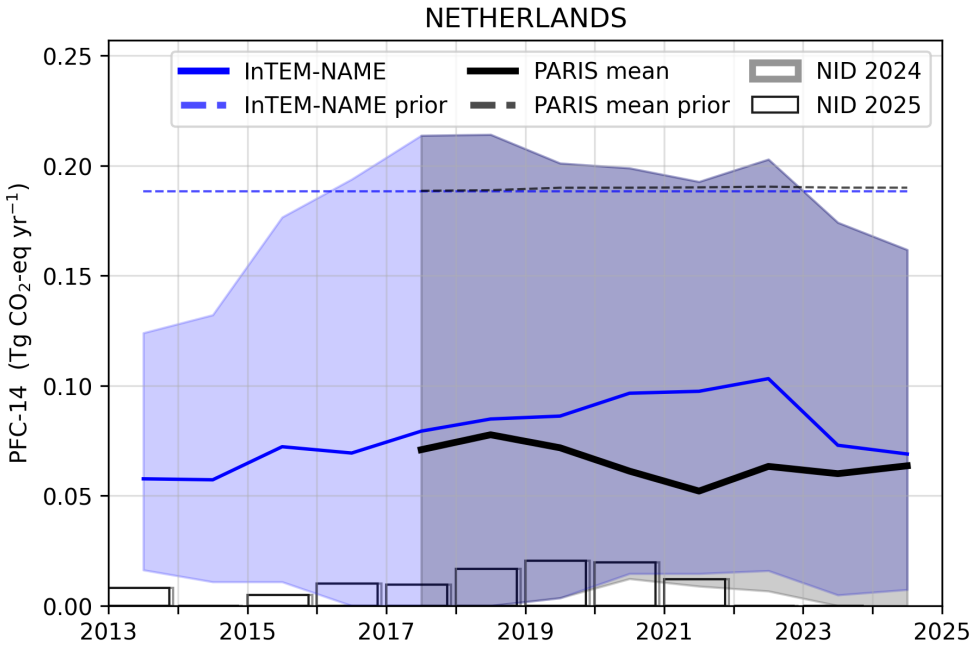

Figure 7.1.2: Spatial distribution of the Dutch average modelled emissions of PFC-14 during the period of 2020-2024 (mean from all models). Observing stations are marked with red circles and highly-populated cities are marked with red triangles.

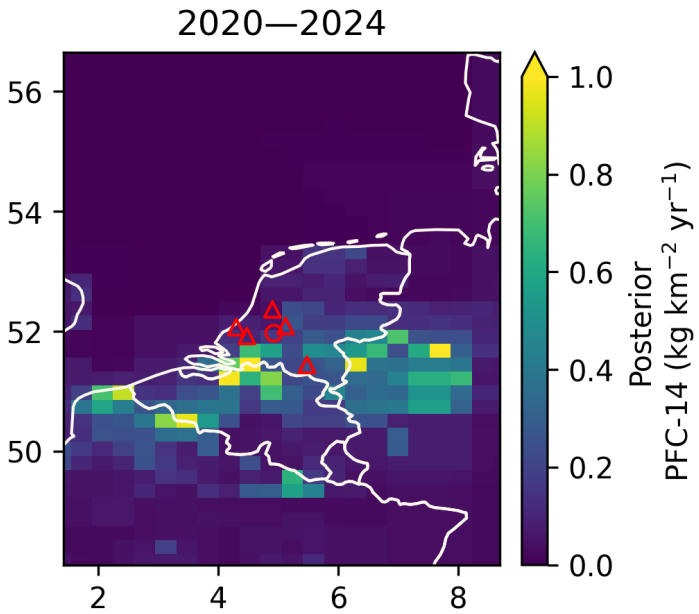

7.2 PFC-116

Figure 7.2.1: Verification of the Dutch emissions inventory estimates for PFC-116. Modelled annual emissions are given as the mean from all models (black line) and the individual result from InTEM-NAME (blue line). The shaded blue area is the 68 % confidence interval (CI) of InTEM-NAME and the shaded grey area encompasses the 68 % CI from all models. National inventory annual totals from 2024 and 2025 are given as grey and black bars, respectively.

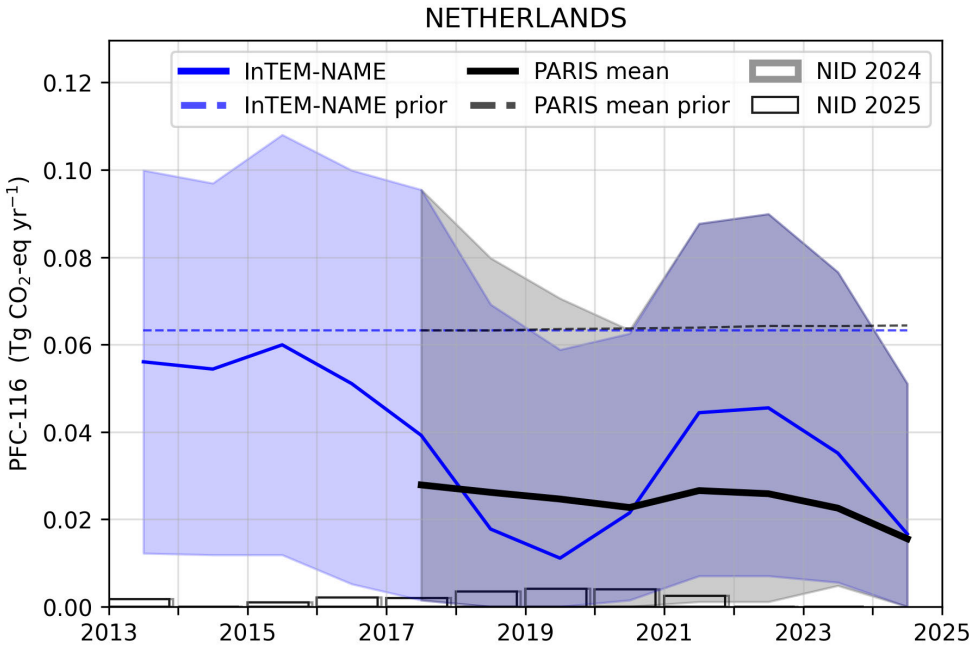

Figure 7.2.2: Spatial distribution of the Dutch average modelled emissions of PFC-116 during the period of 2020-2024 (mean from all models). Observing stations are marked with red circles and highly-populated cities are marked with red triangles.

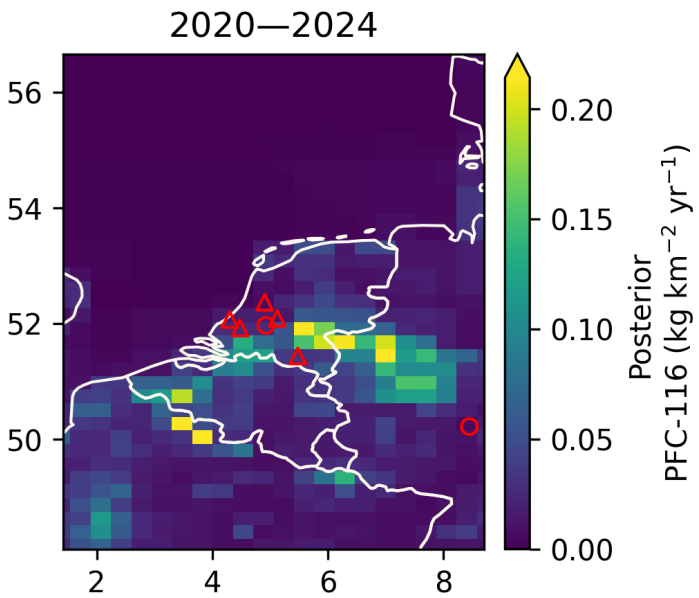

7.3 PFC-218

Figure 7.3.1: Verification of the Dutch emissions inventory estimates for PFC-218. Modelled annual emissions are given as the mean from all models (black line) and the individual result from InTEM-NAME (blue line). The shaded blue area is the 68 % confidence interval (CI) of InTEM-NAME and the shaded grey area encompasses the 68 % CI from all models. National inventory annual totals from 2024 and 2025 are given as grey and black bars, respectively.

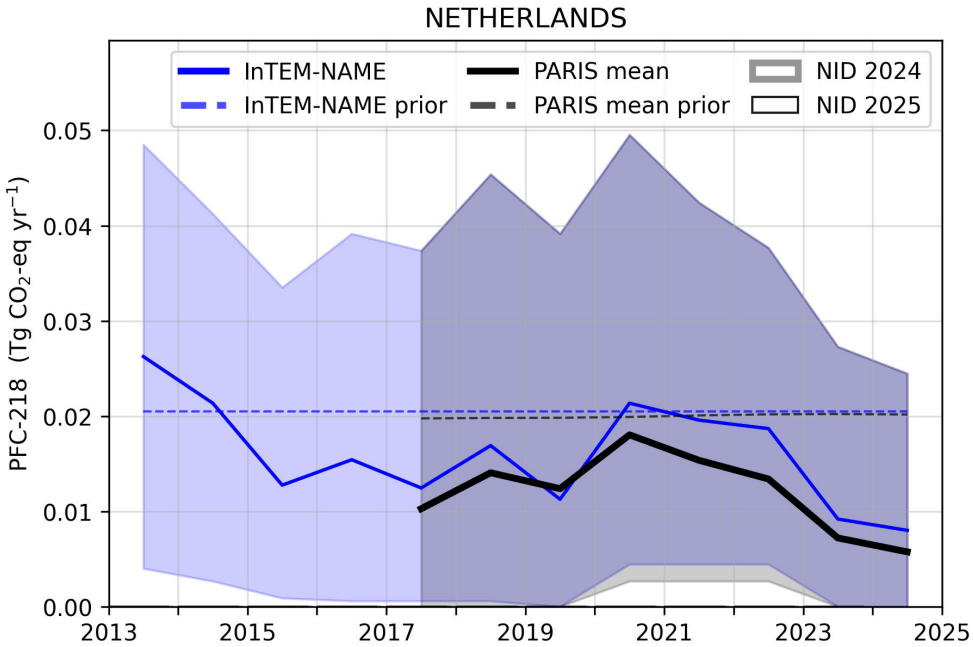

Figure 7.3.2: Spatial distribution of the Dutch average modelled emissions of PFC-218 during the period of 2020-2024 (mean from all models). Observing stations are marked with red circles and highly-populated cities are marked with red triangles.

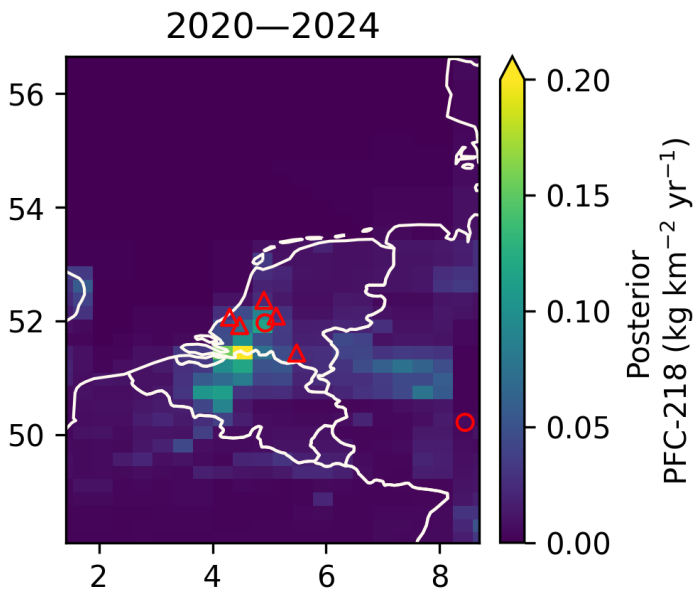

7.4 PFC-318

Figure 7.4.1: Verification of the Dutch emissions inventory estimates for PFC-318. Modelled annual emissions are given as the mean from all models (black line) and the individual result from InTEM-NAME (blue line). The shaded blue area is the 68 % confidence interval (CI) of InTEM-NAME and the shaded grey area encompasses the 68 % CI from all models. National inventory annual totals from 2024 and 2025 are given as grey and black bars, respectively.

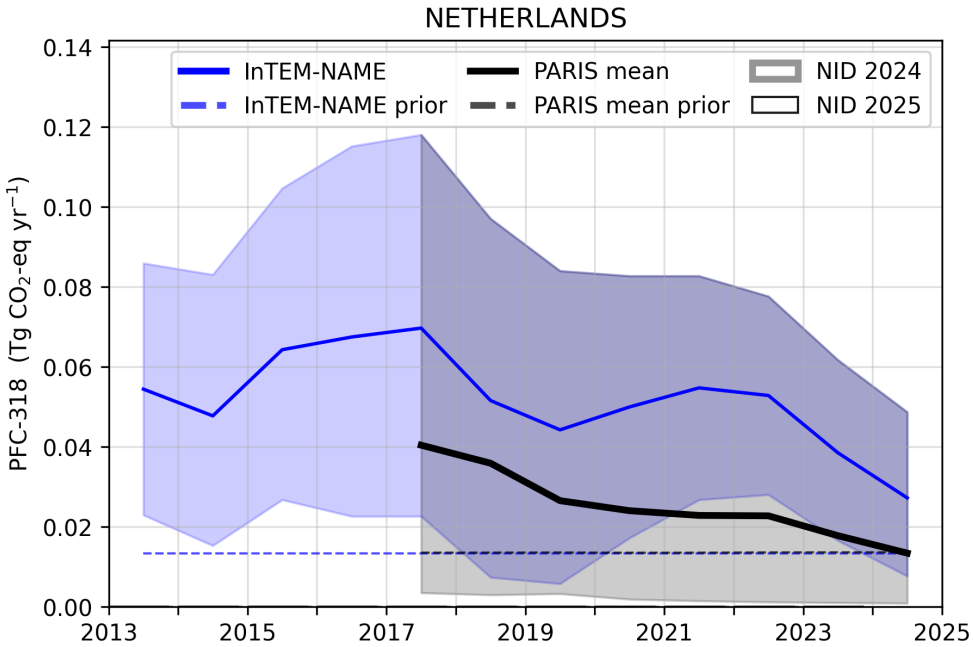

Figure 7.4.2: Spatial distribution of the Dutch average modelled emissions of PFC-318 during the period of 2020-2024 (mean from all models). Observing stations are marked with red circles and highly-populated cities are marked with red triangles.

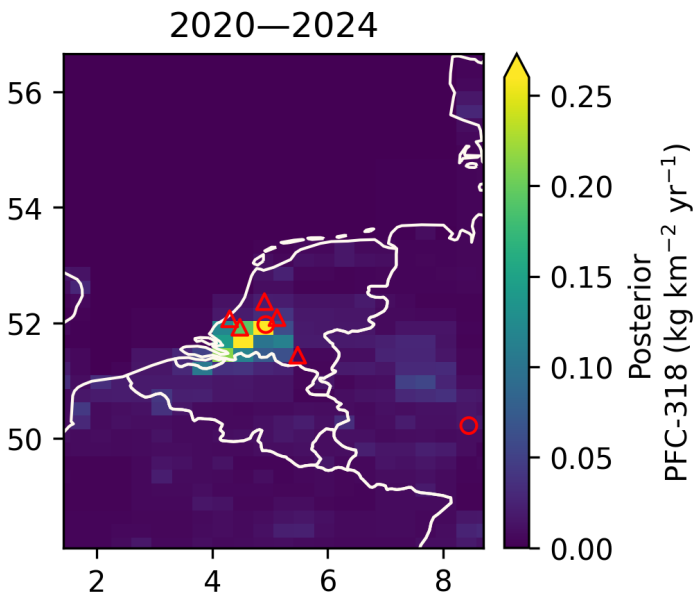

7.5 Total PFCs

Figure 7.5.1: Verification of the Dutch emissions inventory estimates for total PFCs. Modelled annual emissions are given as the mean from all models (black line) and the individual result from InTEM-NAME (blue line). The shaded blue area is the 68 % confidence interval (CI) of InTEM-NAME and the shaded grey area encompasses the 68 % CI from all models. National inventory annual totals from 2024 and 2025 are given as grey and black bars, respectively.

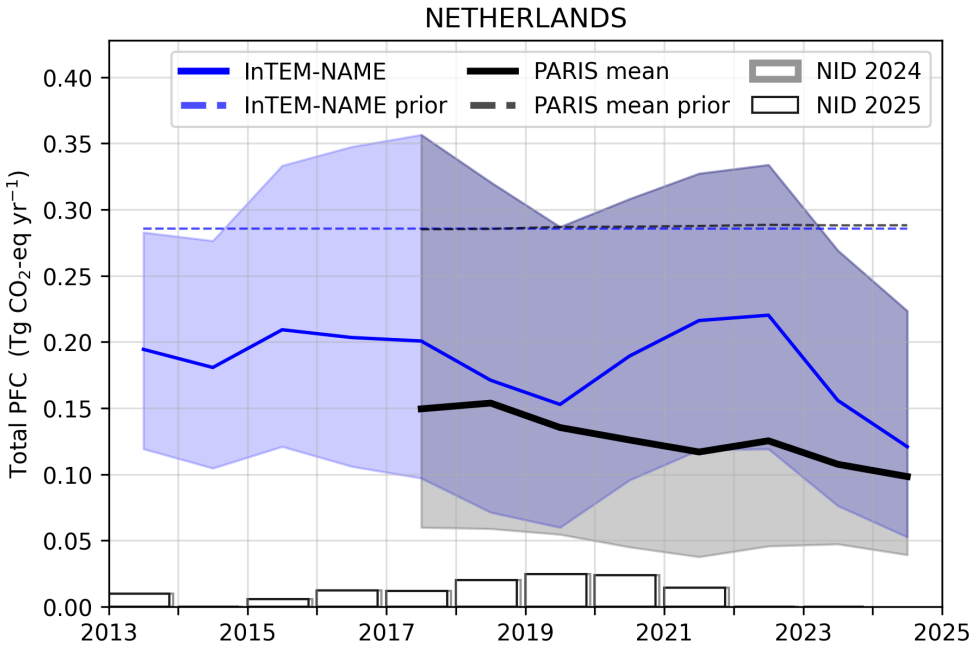

Table 3: Emissions estimation for PFCs according to the National Inventory Document (NID) 2025 and the inversions done in the PARIS project. For the PARIS estimation, the mean of all models is displayed, along with a range of uncertainty estimated via the half distance between the maximum and minimum uncertainties of the different models.

		2020	2021	2022	2023	2024
PFC-14	NID 2025	20	12	0	0	
$(\mathrm{GgCO_2\text{-}eq} \cdot \mathrm{yr}^{-1})$	PARIS mean	61 ± 93	52 ± 92	63 ± 98	60 ± 87	64 ± 81
PFC-116	NID 2025	4	2	0	0	
$(\mathrm{GgCO_2\text{-}eq} \cdot \mathrm{yr}^{-1})$	PARIS mean	23 ± 32	27 ± 43	26 ± 44	23 ± 36	16 ± 26
PFC-318	NID 2025	0	0	0	0	
$(\mathrm{GgCO_2\text{-}eq} \cdot \mathrm{yr}^{-1})$	PARIS mean	24 ± 40	23 ± 41	23 ± 38	18 ± 30	13 ± 24
PFC-218	NID 2025	0	0	0	0	
$(\mathrm{GgCO_2\text{-}eq} \cdot \mathrm{yr}^{-1})$	PARIS mean	18 ± 23	15 ± 20	13 ± 18	7 ± 14	6 ± 12

8 Sulphur hexafluoride (SF_6)

Figure 8.0.1: Total source sensitivity of SF_6 observing sites as calculated by the FLEXPART transport model for the year 2018 (left) and 2024 (right) and used in the inversions. Observing stations active in each year are marked with red dots. Areas with visible land surface represent regions for which emissions can be observed well from the network. Shaded or dark areas represent regions for which limited emission information can be obtained from the network.

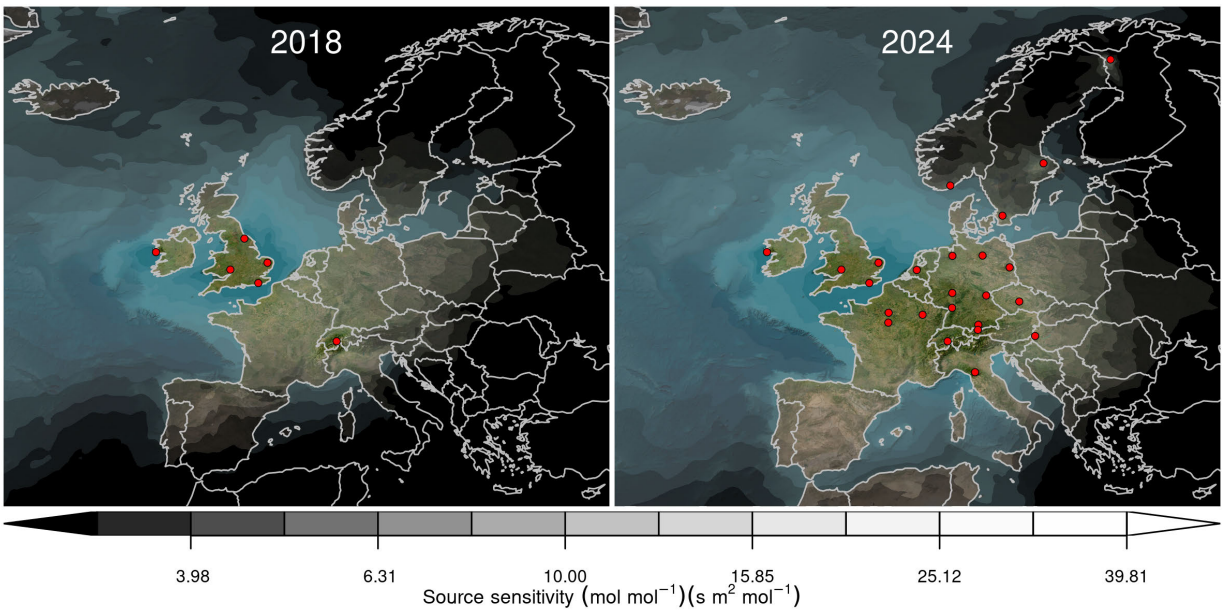

Figure 8.0.2: Verification of the Dutch emissions inventory estimates for SF_6. Modelled annual emissions are given as the mean from all InTEM and ELRIS inversions (black line) and the individual result from InTEM-NAME (blue line). The shaded blue area is the 68 % confidence interval (CI) of InTEM-NAME and the shaded grey area encompasses the 68 % CI from all models. National inventory annual totals from 2024 and 2025 are given as grey and black bars, respectively.

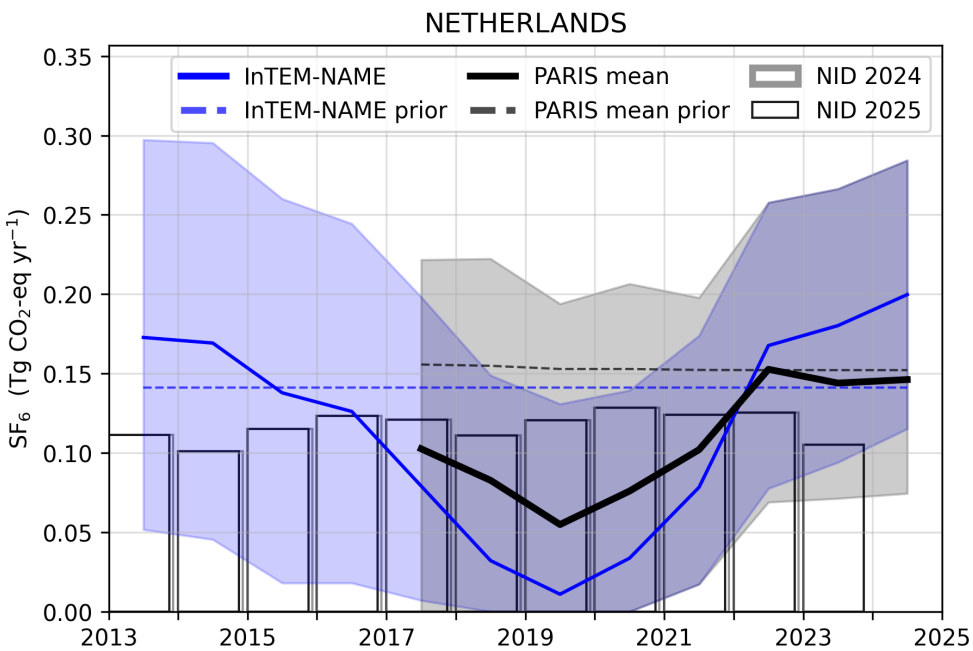

Figure 8.0.3: Spatial distribution of the Dutch average modelled emissions of SF_6 during the period of 2020-2024 (mean from all InTEM and ELRIS inversions). Observing stations are marked with red circles and highly-populated cities are marked with red triangles.

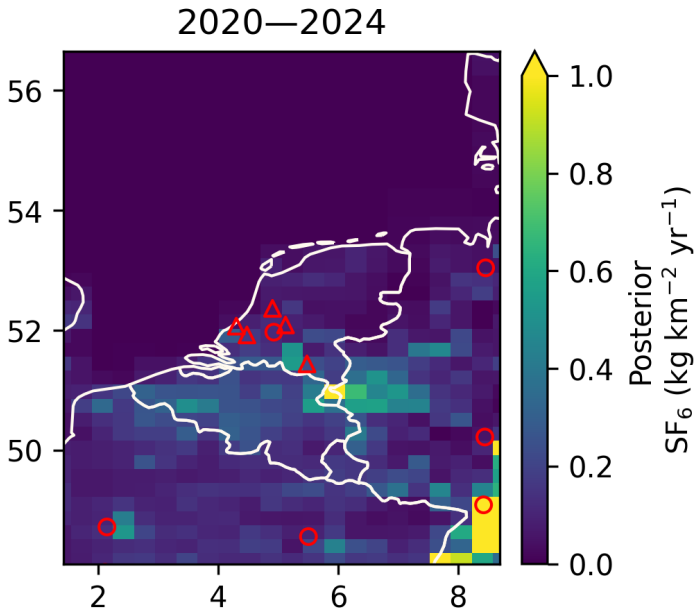

9 Nitrogen Trifluoride (NF_3)

Figure 9.0.1: Verification of the Dutch emissions inventory estimates for NF_3. Modelled annual emissions are given as the mean from all models (black line) and the individual result from InTEM-NAME (blue line). The shaded blue area is the 68 % confidence interval (CI) of InTEM-NAME and the shaded grey area encompasses the 68 % CI from all models. National inventory annual totals from 2024 and 2025 are given as grey and black bars, respectively.

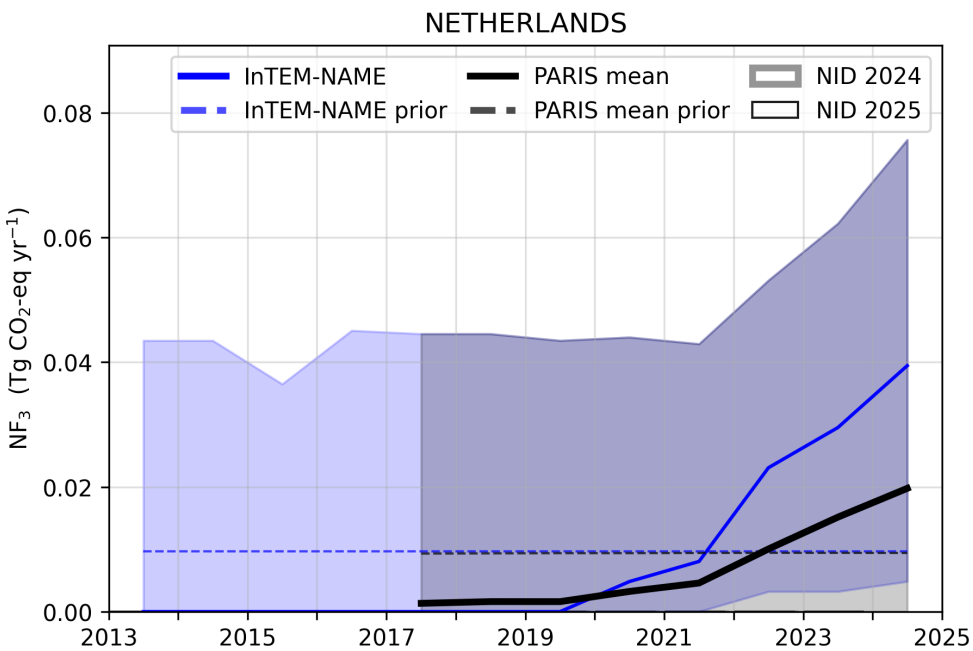

Figure 9.0.2: Spatial distribution of the Dutch average modelled emissions of NF_3 during the period of 2020-2024 (mean from all models). Observing stations are marked with red circles and highly-populated cities are marked with red triangles.

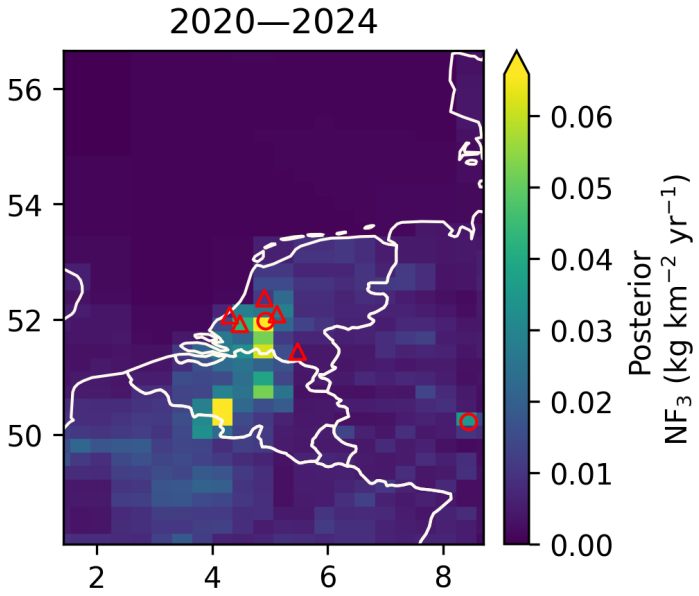

10 Carbon Dioxide (CO_2)

Measurements of CO_2 at ICOS sites and related observatories are influenced by a complex combination of sources and sinks. Fossil fuel combustion for transport, heating, energy generation, and other applications produce CO_2, along with other anthropogenic activities such as cement production. The terrestrial and oceanic biosphere produces CO_2 through animal and plant respiration and takes up CO_2 through photosynthesis. Furthermore, CO_2 is exchanged with the ocean through physical and chemical processes.

When considering high-frequency (∼hourly) CO_2 mole fraction deviations from baseline values—used to infer national emissions in regional inverse modelling studies—the influence of biospheric fluxes can be comparable to, or larger than, those of anthropogenic sources (e.g. White et al., 2019). Therefore, research is under way to develop new tracers that can determine fossil fuel CO_2 fluxes independent of biosphere sources and sinks.

Ongoing Horizon Europe projects PARIS and CORSO are examining methods for estimating fossil fuel CO_2 fluxes based on simultaneous measurements of CO_2 and O_2 (Figure 10.0.1). The method relies on the fact that CO_2 and O_2 are inter-converted during combustion and terrestrial biosphere exchange, but with different ratios for the two processes. A quantity can be constructed from these measurements, known as Atmospheric Potential Oxygen (APO), which is insensitive to biosphere fluxes, and may therefore be useful for isolating fossil fuel signals (Pickers et al., 2022).

High-frequency (∼hourly) timeseries of APO are available from Weybourne (WAO, 2010 – present) and Heathfield (HFD, 2021 - present) in the UK (Figure 10.0.1; Pickers, Adcock, and Manning, 2024), and new sites are being established at Cabauw and Zweth in the Netherlands. Preliminary analyses of the WAO data have revealed regional APO trends consistent with the drop in fossil fuel CO_2 emissions during the COVID lockdowns in the UK (Pickers et al., 2022). However, quantification of absolute regional fossil fuel CO_2 emissions remains an area of active research. Recent studies have derived fossil fuel CO_2 emissions for the UK that are highly uncertain (Rigby et al., 2025). Potential confounding factors were identified in Chawner et al. (2024), such as highly uncertain APO fluxes from the ocean, and a poorly constrained regional APO background. These factors are the subject of ongoing research using atmospheric models and new APO measurements from PARIS, CORSO and ICOS.

An alternative method for top-down fossil fuel CO_2 emissions evaluation uses measurements of radiocarbon isotopologues ($^{14}CO_2$, compared to the dominant $^{12}CO_2$). Fossil fuels do not contain ^{14}C, and therefore, their combustion tends to decrease the atmospheric $^{14}CO_2/^{12}CO_2$ ratio. Currently, radiocarbon measurements can only be made at low frequency using flask sampling. However, a relatively intensive flask sampling campaign was carried out across Europe during 2024 as part of CORSO, and the results of this study will be reported on soon.

Figure 10.0.1: Carbon dioxide (top, red) and oxygen (bottom, blue) measurements from Weybourne Atmospheric Observatory in the UK, available from the ICOS Carbon Portal (Adcock et al., 2024).

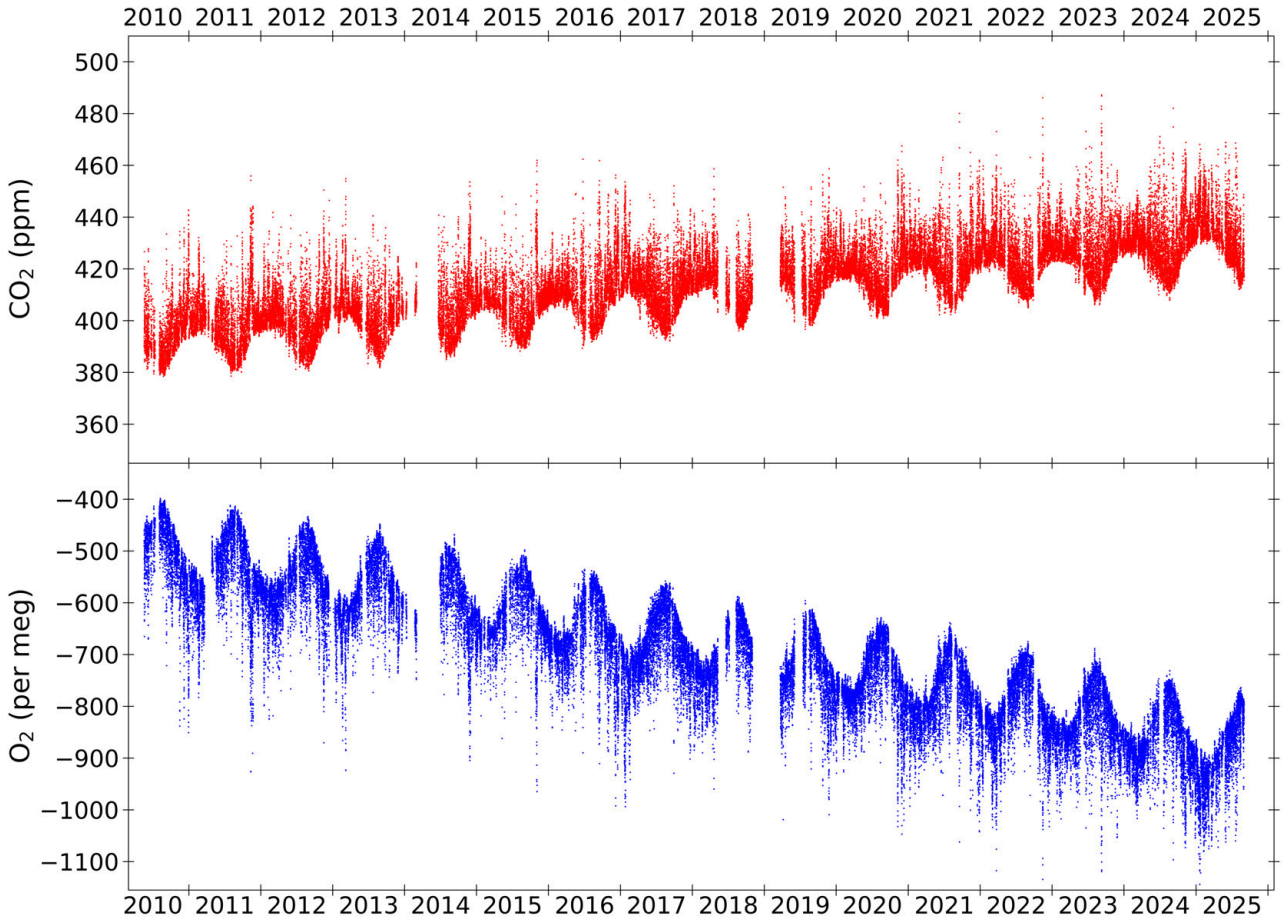

References

Adcock, Karina et al. (2024). *Atmospheric GHG data product (o2, o2_stdev, co2, co2_stdev) from Weybourne (10.0 m), 2010-05-19–2023-12-31*. URL: https://hdl.handle.net/11676/j4LzdHQiq3fPgfNeXHruC0Bb.

Chawner, Hannah et al. (Apr. 2024). "Atmospheric oxygen as a tracer for fossil fuel carbon dioxide: a sensitivity study in the UK". en. In: *Atmospheric Chemistry and Physics* 24.7, pp. 4231–4252. ISSN: 1680-7324. DOI: 10.5194/acp-24-4231-2024. URL: https://acp.copernicus.org/articles/24/4231/2024/ (visited on 04/10/2024).

European Commission: Joint Research, Centre et al. (2023). *GHG emissions of all world countries – 2023*. Publications Office of the European Union. DOI: 10.2760/953322.

Ganesan, A. L. et al. (2014). "Characterization of uncertainties in atmospheric trace gas inversions using hierarchical Bayesian methods". In: *Atmospheric Chemistry and Physics* 14.8, pp. 3855–3864. DOI: 10.5194/acp-14-3855-2014. URL: http://www.atmos-chem-phys.net/14/3855/2014/http://www.atmos-chem-phys.net/14/3855/2014/acp-14-3855-2014.pdf.

Ganesan, A. L. et al. (2015). "Quantifying methane and nitrous oxide emissions from the UK and Ireland using a national-scale monitoring network". In: *Atmos. Chem. Phys.* 15.11, pp. 6393–6406. DOI: 10.5194/acp-15-6393-2015. URL: https://www.atmos-chem-phys.net/15/6393/2015/https://www.atmos-chem-phys.net/15/6393/2015/acp-15-6393-2015.pdf.

Henne, S. et al. (2016). "Validation of the Swiss methane emission inventory by atmospheric observations and inverse modelling". In: *Atmospheric Chemistry and Physics* 16.6, pp. 3683–3710. DOI: 10.5194/acp-16-3683-2016. URL: http://www.atmos-chem-phys.net/16/3683/2016/.

Jones, A.R. et al. (2007). "The U.K. Met Office's next-generation atmospheric dispersion model, NAME III, in Borrego C. and Norman A.-L. (Eds)". In: *Air Pollution Modeling and its Application XVII (Proceedings of the 27th NATO/CCMS International Technical Meeting on Air Pollution Modelling and its Application), Springer*, pp. 580–589.

Katharopoulos, I. et al. (2023). "Impact of transport model resolution and a priori assumptions on inverse modeling of Swiss F-gas emissions". In: *Atmos. Chem. Phys.* 23.22, pp. 14159–14186. DOI: 10.5194/acp-23-14159-2023. URL: https://acp.copernicus.org/articles/23/14159/2023/.

Manning, A. J. et al. (2021). "Evidence of a recent decline in UK emissions of hydrofluorocarbons determined by the InTEM inverse model and atmospheric measurements". In: *Atmospheric Chemistry and Physics* 21.16, pp. 12739–12755. DOI: 10.5194/acp-21-12739-2021. URL: https://acp.copernicus.org/articles/21/12739/2021/.

Pickers, P., K. Adcock, and A. Manning (Feb. 2024). *Atmospheric oxygen and carbon dioxide observations from Weybourne Atmospheric Observatory, Norfolk, UK uploaded to public archives*. Tech. rep. Process Attribution of Regional Emissions (PARIS). URL: https://horizoneurope-paris.eu/wp-content/uploads/sites/914/2024/07/PARIS-deliverables-D6.1-High-frequency-APO-data-uploaded-final.pdf.

Pickers, Penelope A. et al. (Apr. 2022). "Novel quantification of regional fossil fuel CO2 reductions during COVID-19 lockdowns using atmospheric oxygen measurements". en. In: *Science Advances* 8.16, eabl9250. ISSN: 2375-2548. DOI: 10.1126/sciadv.abl9250. URL: https://www.science.org/doi/10.1126/sciadv.abl9250 (visited on 12/01/2023).

Rigby, M. et al. (2019). "Increase in CFC-11 emissions from eastern China based on atmospheric observations". In: *Nature* 569, pp. 546–550. DOI: 10.1038/s41586-019-1193-4. URL: https://doi.org/10.1038/s41586-019-1193-4.

Rigby, M. et al. (Apr. 2025). *Inverse estimates of fossil fuel CO2 emission*. Tech. rep. Process Attribution of Regional Emissions (PARIS). URL: https://horizoneurope-paris.eu/wp-content/uploads/sites/914/2025/01/PARIS-M24-Inverse-estimates-of-fossil-fuel-CO2-emissions-final.pdf.

Stohl, A. et al. (2005). "Technical note: The Lagrangian particle dispersion model FLEXPART version 6.2". In: *Atmospheric Chemistry and Physics* 5, pp. 2461–2474. DOI: 10.5194/acp-5-2461-2005. URL: <GotoISI>://000231983600002.

White, Emily D. et al. (Apr. 2019). "Quantifying the UK's carbon dioxide flux: an atmospheric inverse modelling approach using a regional measurement network". en. In: *Atmospheric Chemistry and Physics*

19.7, pp. 4345–4365. ISSN: 1680-7324. DOI: 10.5194/acp-19-4345-2019. URL: https://www.atmos-chem-phys.net/19/4345/2019/ (visited on 04/05/2019).

Draft Inventory Annex
Norway 2025

30th October, 2025

1 Introduction

In this document, global concentration trends and national emissions estimates derived from atmospheric observations ("inverse estimates") are presented for most reported gases. Comparing the emissions submitted in national inventories with those calculated using atmospheric observations allows for emissions to be assessed using two fundamentally different approaches. Substantial differences can highlight areas that could warrant further investigation.

Global concentration trends for each gas are first shown using annual average concentrations from Mace Head, Ireland (Northern Hemisphere) and Kennaook/Cape Grim, Tasmania, Australia (Southern Hemisphere). Data from these stations were selected to exclude regionally-polluted air masses and therefore represents northern and southern hemispheric concentration trends. Mace Head observations were supported by the National Aeronautics and Space Administration (NASA) and the UK Department of Energy, Security and Net Zero (DESNZ), and Kennaook/Cape Grim observations by NASA and the Australian Bureau of Meteorology.

Observations of European concentrations of greenhouse gases used to derive national inverse emission estimates were collected from many different networks and providers. Methane and nitrous oxide concentrations originated from the European ICOS (Integrated Carbon Observation System) network, the UK DECC (Deriving Emissions related to Climate Change) network and other national or individual initiatives. F-gas observations were made by affiliates of the AGAGE (Advanced Global Atmospheric Gases Experiment) network. Observations from additional stations across Europe were supported by the Horizon-EU PARIS (Process Attribution of Regional Emissions) project. The observation stations used to derive emissions for each gas are shown in the corresponding sections of this document.

An atmospheric transport model provides the link between surface fluxes and concentrations measured at the observing stations. If not otherwise mentioned, inversion-based emissions estimates were derived using two atmospheric transport models combined with three inverse models, yielding a total of six inversions. This ensemble of six inversions allows us to better quantify the uncertainties associated with inverse modelling.

The two atmospheric transport models used are the Numerical Atmospheric dispersion Modelling Environment (NAME, Jones et al., 2007), and the FLEXible PARTicle dispersion model (FLEXPART, Stohl et al., 2005). Both models are backwards-running Lagrangian Particle Dispersion Models (LPDMs) that simulate the recent transport of air to each observing station. The two LPDMs have been widely used in the estimation of greenhouse gas emissions (Ganesan et al., 2015; Rigby et al., 2019; Manning et al., 2021; Henne et al., 2016).

The three inverse methods used are InTEM (Inversion Technique for Emission Modelling, Manning et al., 2021), ELRIS (Empa Lagrangian Regional Inversion System, Henne et al., 2016; Katharopoulos et al., 2023), and RHIME (Regional Hierarchical Inverse Modelling Environment, Ganesan et al., 2014). All three inverse methods estimate emissions within Europe along with boundary conditions that account for the concentration of the air entering Europe. All three systems started from the same set of a priori emissions that were either derived from the global EDGAR emission inventory (version 8, European Commission: Joint Research et al., 2023) or a uniform land-based emission, depending on the gas. A natural emission component, from the WETCHARTS product, was included in the methane prior. The same observational dataset was used by each inverse model, but data selection (i.e., filtering datasets for specific conditions) and treatment of uncertainties were chosen separately and hence differ. The three methods also differ in their statistical approaches for estimating emissions.

Emission estimates are presented for the period 2008-2024. Emissions for the full 2008-2024 period were derived with the InTEM-NAME inversion only, while emissions from 2017-2024 are presented as the mean of the six inversions (denoted the "PARIS mean"). The uncertainty shown is the minimum/maximum of the uncertainties in the ensemble.

All inversions employed a resolution of one month for CH_4 and N_2O and 1-year for the fluorinated gases. The inversion results used to compare with the inventories are a one-year calendar average for CH_4 and N_2O and the yearly value derived from a 3-year moving average for the fluorinated gases. For the 2008-2024

InTEM-NAME results, a 3-year moving average was also applied to the annualised CH_4 and N_2O results due to lack of observational coverage in the earlier years.

2 Global Concentration Trends

2.1 Methane (CH_4)

Figure 2.1.1: Background Northern Hemisphere monthly concentrations of CH_4 estimated from MHD, Ireland observations are shown in red, and background Southern Hemisphere monthly concentrations from CGO, Tasmania are shown in blue. Grey shading represents provisional data.

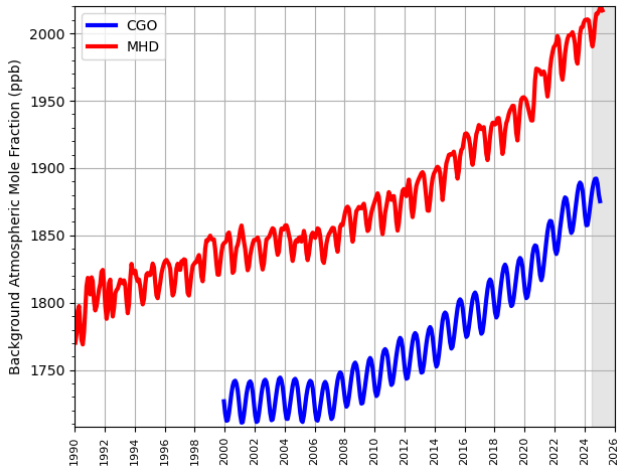

2.2 Nitrous Oxide (N_2O)

Figure 2.2.1: Background Northern Hemisphere monthly concentrations of N_2O estimated from MHD, Ireland observations are shown in red, and background Southern Hemisphere monthly concentrations from CGO, Tasmania are shown in blue. Grey shading represents provisional data.

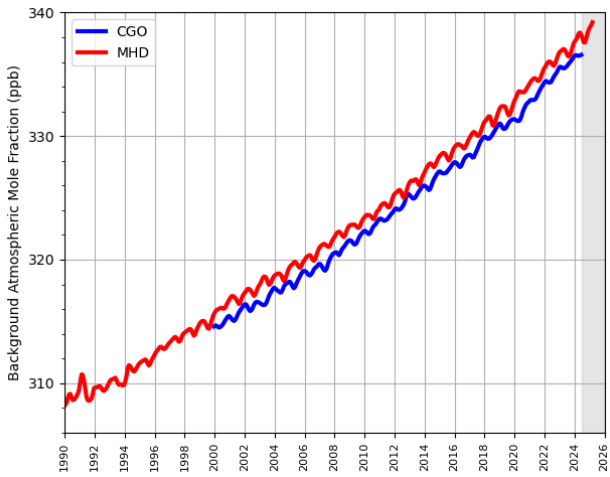

2.3 Hydrofluorocarbons (HFCs)

Figure 2.3.1: Background Northern Hemisphere monthly concentrations of six HFCs estimated from MHD, Ireland observations are shown in red, and background Southern Hemisphere monthly concentrations from CGO, Tasmania are shown in blue. Grey shading represents provisional data.

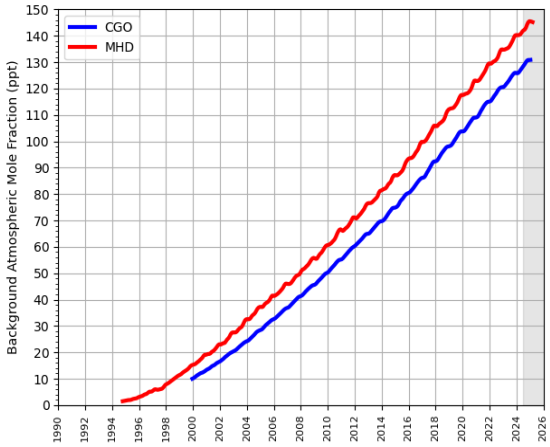

(a) HFC-134a

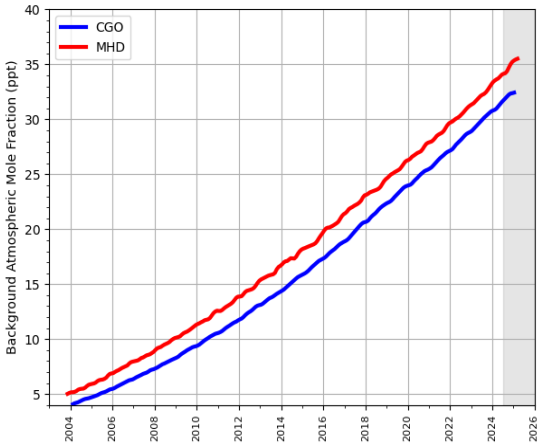

(b) HFC-143a

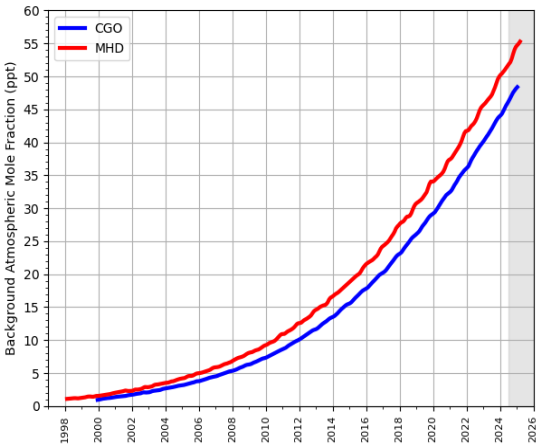

(c) HFC-125

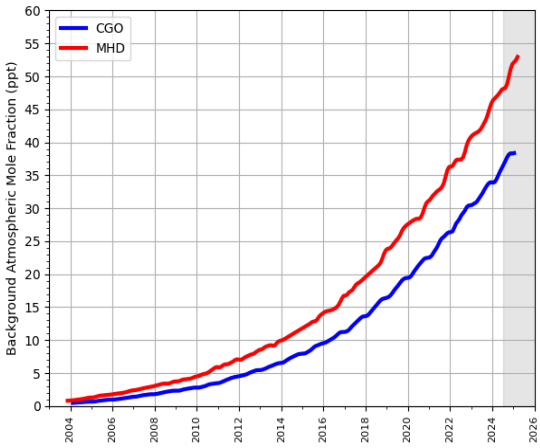

(d) HFC-32

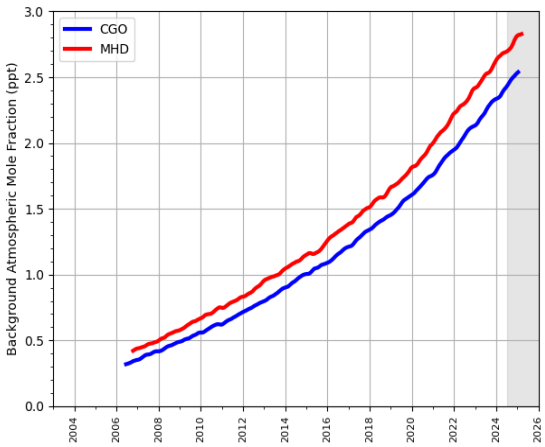

(e) HFC-227ea

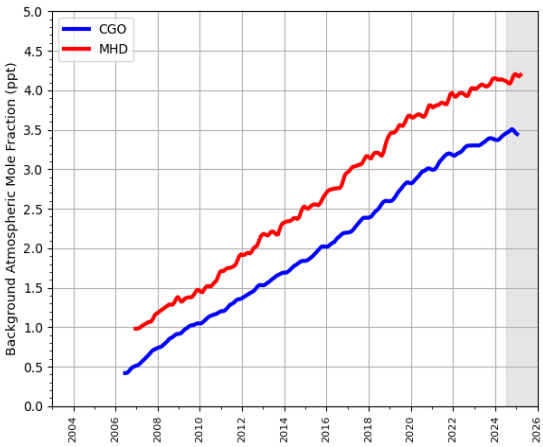

(f) HFC-245fa

Figure 2.3.2: Background Northern Hemisphere monthly concentrations of four HFCs estimated from MHD, Ireland observations are shown in red, and background Southern Hemisphere monthly concentrations from CGO, Tasmania are shown in blue. Grey shading represents provisional data.

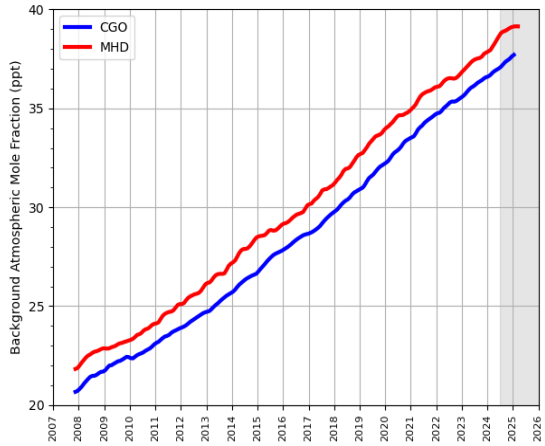

(a) HFC-23

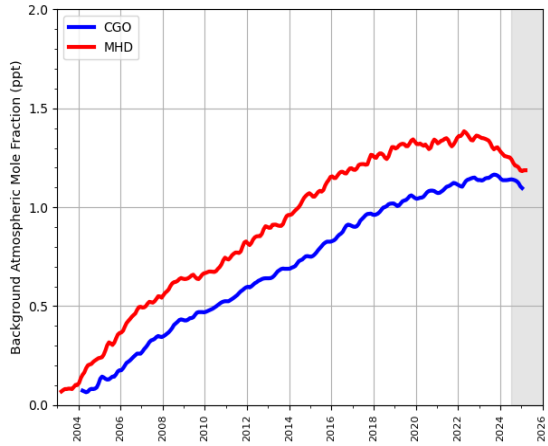

(b) HFC-365mfc

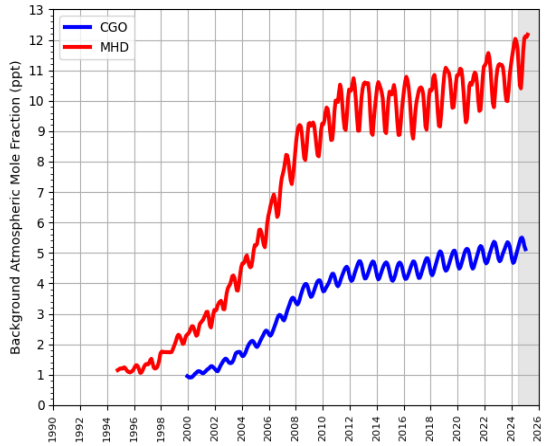

(c) HFC-152a

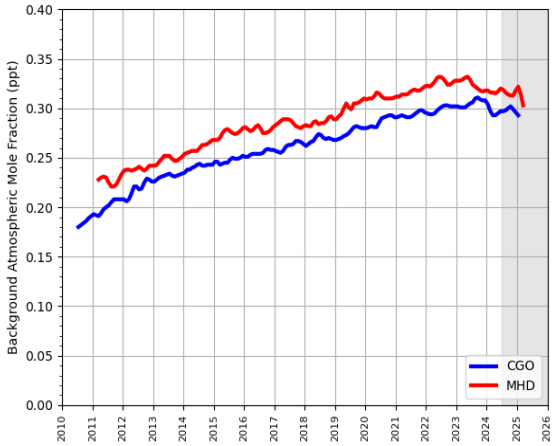

(d) HFC-43-10-mee

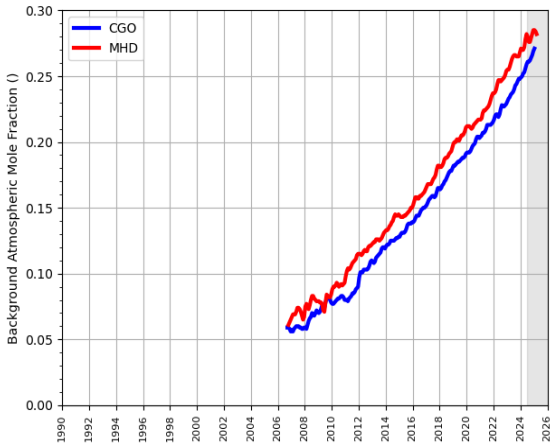

(e) HFC-236fa

2.4 Perfluorocarbons (PFCs)

Figure 2.4.1: Background Northern Hemisphere monthly concentrations of four PFCs estimated from MHD, Ireland observations are shown in red, and background Southern Hemisphere monthly concentrations from CGO, Tasmania are shown in blue. Grey shading represents provisional data.

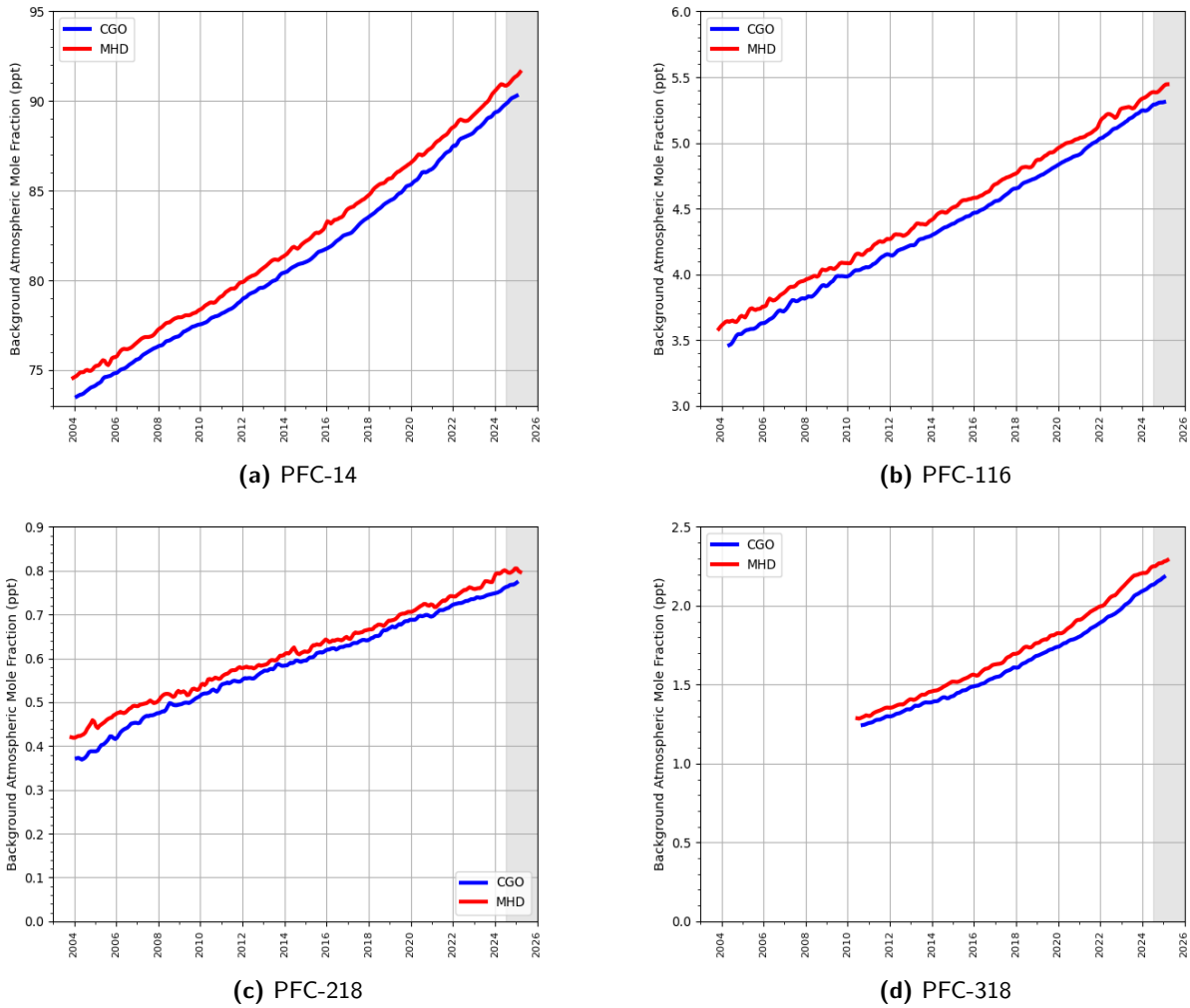

(a) PFC-14 **(b)** PFC-116 **(c)** PFC-218 **(d)** PFC-318

2.5 Sulphur Hexafluoride (SF_6) and Nitrogen Trifluoride (NF_3)

Figure 2.5.1: Background Northern Hemisphere monthly concentrations of SF_6 and NF_3 estimated from MHD, Ireland observations are shown in red, and background Southern Hemisphere monthly concentrations from CGO, Tasmania are shown in blue. Grey shading represents provisional data.

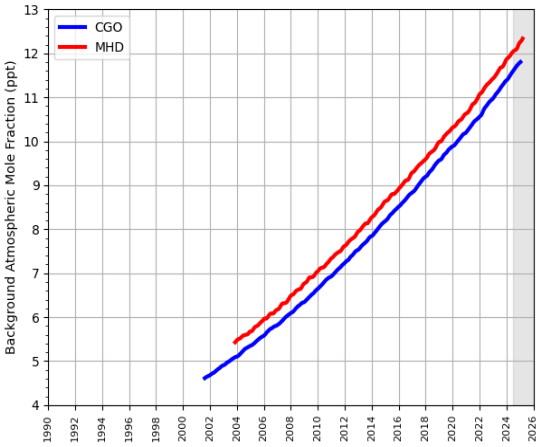

(a) SF_6

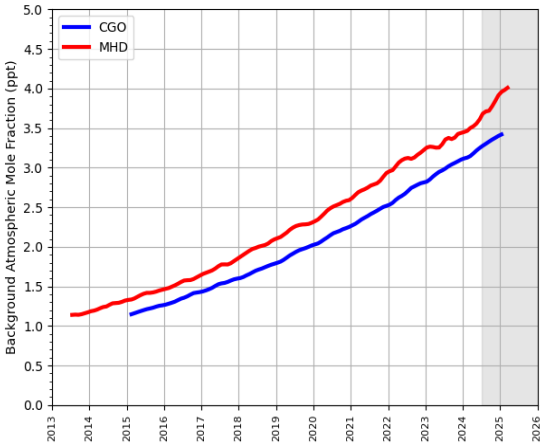

(b) NF_3

2.6 Carbon Dioxide (CO_2)

Figure 2.6.1: Background Northern Hemisphere monthly concentrations of CO_2 estimated from MHD, Ireland observations are shown in red, and background Southern Hemisphere monthly concentrations from CGO, Tasmania are shown in blue. Grey shading represents provisional data.

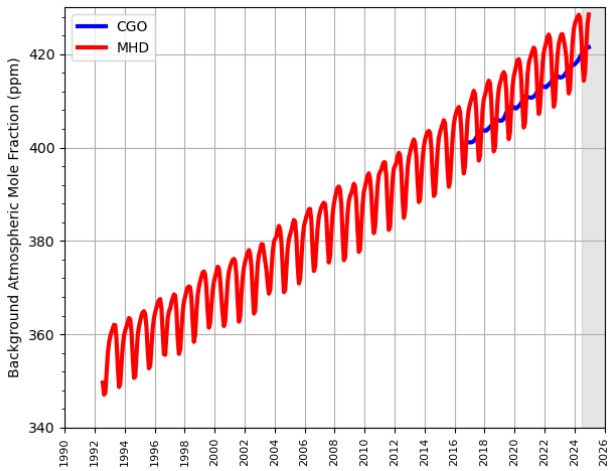

3 Key findings

- Methane (CH_4): Inverse results are potentially marginally higher than the reported inventory estimates between 2018 and 2024. However the inverse results include all sources, both natural and anthropogenic, and the contribution from the natural sources is very uncertain. It is therefore difficult to glean much additional information. The EDGAR V8, plus natural components from WETCHARTS, prior emission distribution used in the inversions was significantly reduced by more than a factor of two.
- Hydrofluorocarbons (HFCs), perfluorocarbons (PFCs) and sulphur hexafluoride (SF_6): Due to the limited observational constraint very large uncertainties remain in the Norwegian emissions estimates obtained from inverse modelling for these gases. These estimates stay relatively close to the a priori values. Incorporating the new flask observations from Birkenes from late 2024 onward will improve the estimates in future years.
- It is unlikely, given the current observational coverage, that inverse estimates from nitrous oxide (N_2O) will be viable.

Table 1: Emissions estimation for CH_4 according to the National Inventory Document (NID) 2025 and the inversions done in the PARIS project. For the PARIS estimation, the mean of all models is displayed, along with a range of uncertainty estimated via the half distance between the maximum and minimum uncertainties of the different models.

		2020	2021	2022	2023	2024
CH_4	NID 2025	5.23	5.22	5.19	5.01	
$(\mathrm{TgCO_2\text{-}eq} \cdot \mathrm{yr}^{-1})$	PARIS mean	5.93 ± 6.77	7.46 ± 9.09	6.23 ± 8.23	6.58 ± 6.40	6.01 ± 6.45

4 Methane (CH_4)

Figure 4.0.1: Average monthly total source sensitivity of CH_4 observing sites as calculated by the FLEXPART transport model for the year 2018 (left) and 2024 (right) and used in the inversions. Observing stations active in each year are marked with red dots. Areas with visible land surface represent regions for which emissions can be observed well from the network. Shaded or dark areas represent regions for which limited emission information can be obtained from the network.

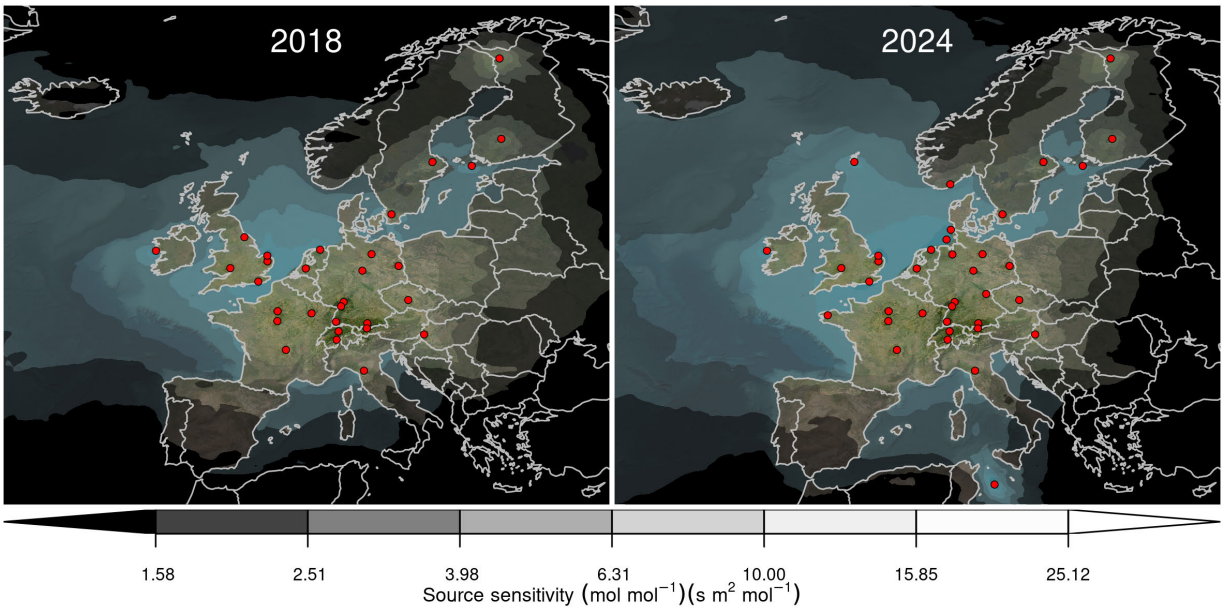

Figure 4.0.2: Verification of the Norwegian emissions inventory estimates for CH_4 (zoom in to 2018-2024). Modelled annual emissions are given as the mean from all models (black line) and the individual result from InTEM-NAME (blue line). The shaded blue area is the 68 % confidence interval (CI) of InTEM-NAME and the shaded grey area encompasses the 68 % CI from all models. National inventory annual totals from 2024 and 2025 are given as grey and black bars, respectively.

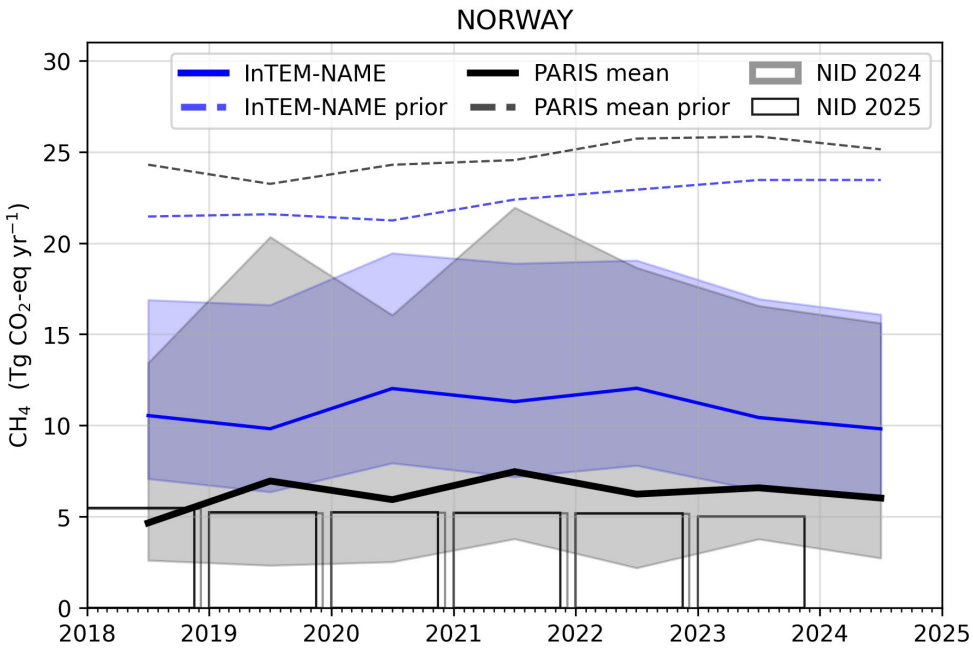

Figure 4.0.3: Verification of the Norwegian emissions inventory estimates for CH_4 (zoom in to 2018-2024). Modelled monthly emissions are given as the mean from all models (black line) and the individual result from InTEM-NAME (blue line). The shaded blue area is the 68 % confidence interval (CI) of InTEM-NAME and the shaded grey area encompasses the 68 % CI from all models. National inventory annual totals from 2024 and 2025 are given as grey and black bars, respectively.

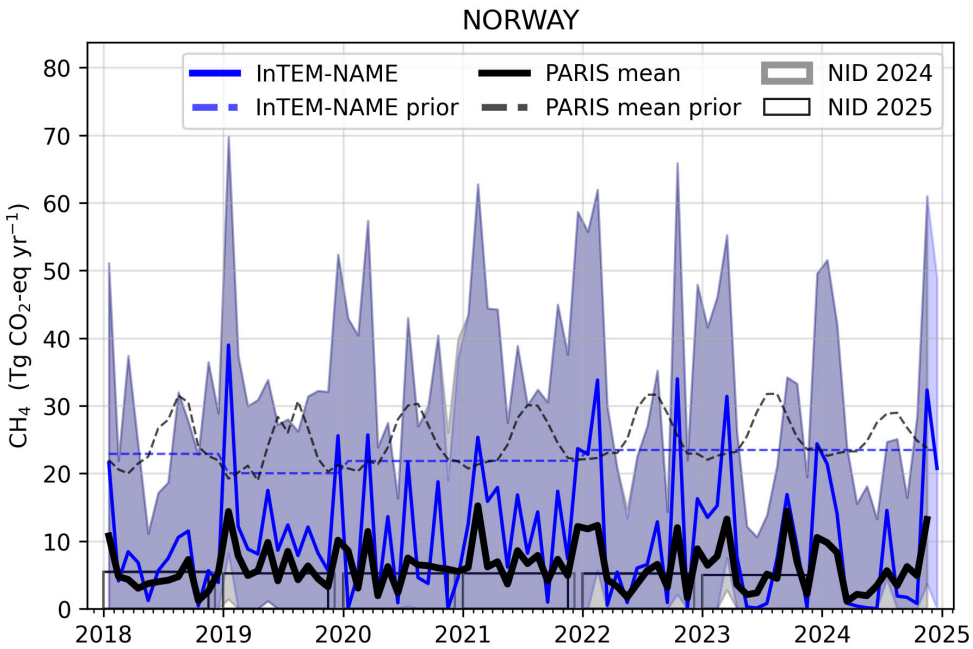

Figure 4.0.4: Spatial distribution of the Norwegian average modelled emissions of CH_4 during the period of 2020-2024 (mean from all models). Observing stations are marked with red circles and highly-populated cities are marked with red triangles.

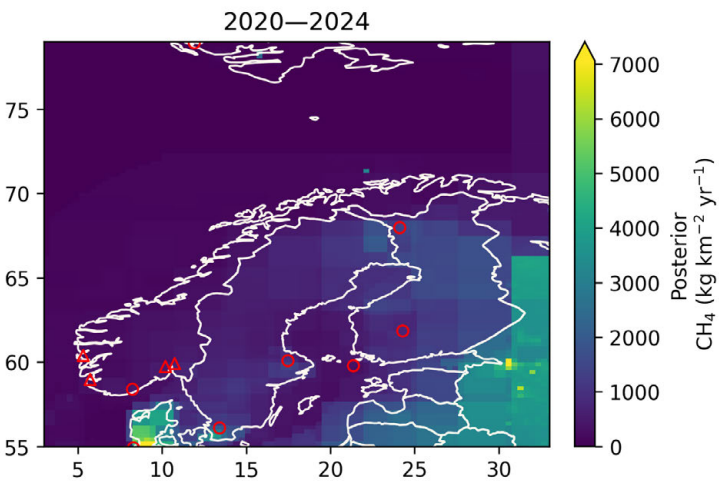

Figure 4.0.5: Spatial distribution of the seasonal deviation from the mean. The deviation is defined as the modelled Norwegian seasonally averaged CH_4 emissions over 2020-2024 minus the average over the whole period. The mean across all models is shown. Observing stations are marked with black circles and highly-populated cities are marked with black triangles.

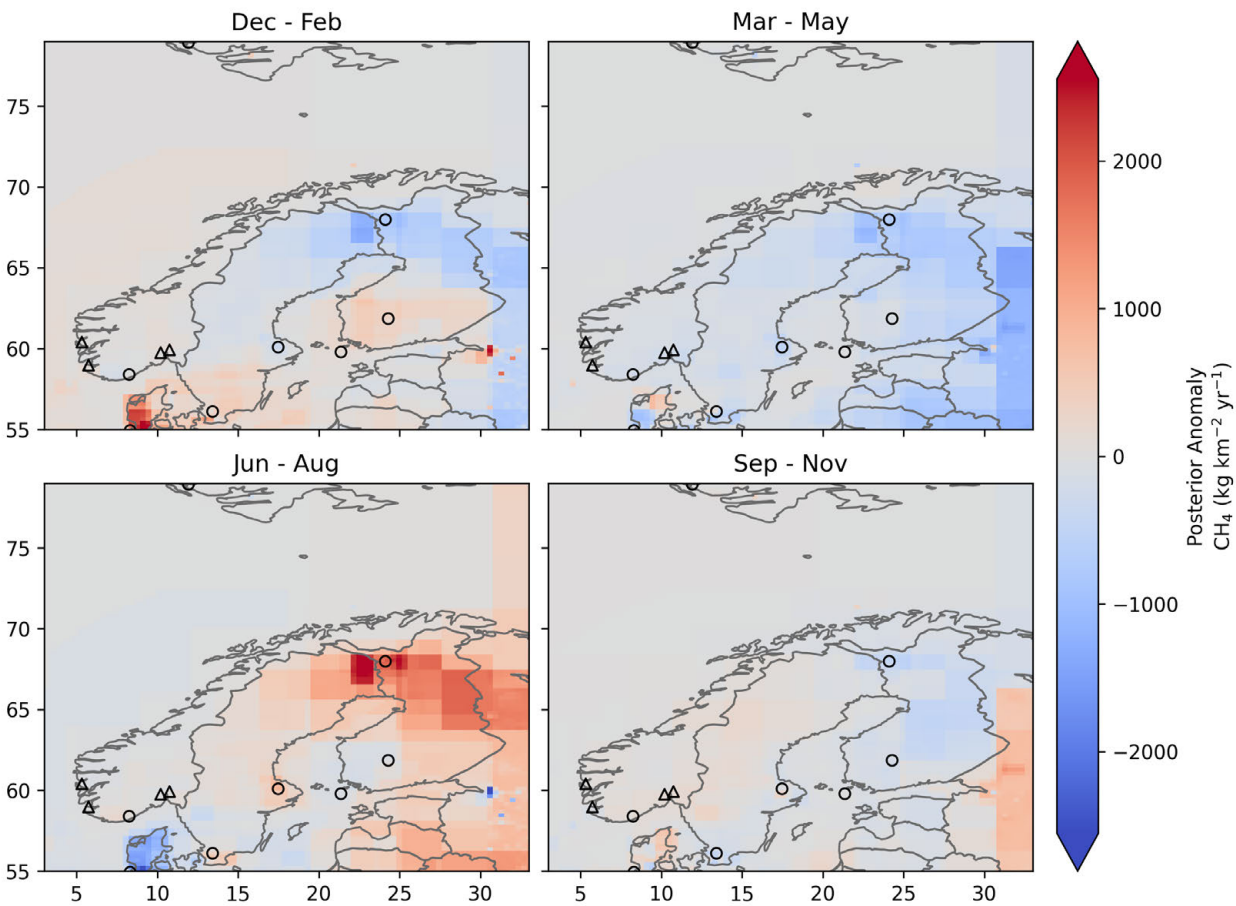

5 Nitrous Oxide (N_2O)

Figure 5.0.1: Average monthly total source sensitivity of N_2O observing sites as calculated by the FLEXPART transport model for the year 2018 (left) and 2024 (right) and used in the inversions. Observing stations active in each year are marked with red dots. Areas with visible land surface represent regions for which emissions can be observed well from the network. Shaded or dark areas represent regions for which limited emission information can be obtained from the network.

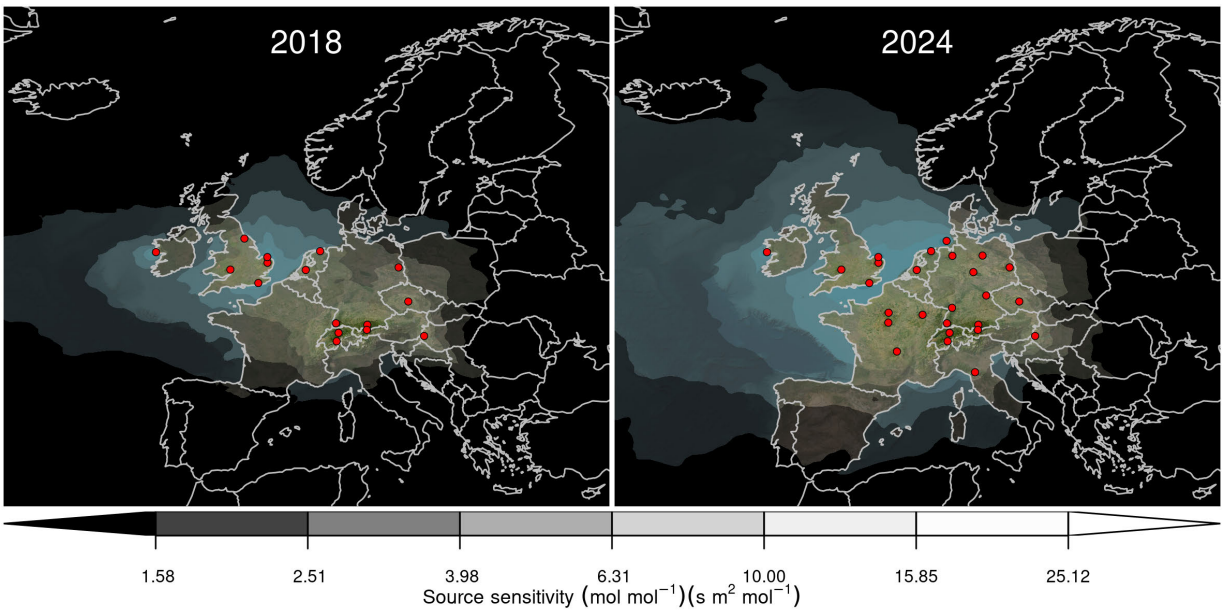

6 Hydrofluorocarbons (HFCs) and Perfluorocarbons (PFCs)

Figure 6.0.1: Total source sensitivity of HFCs/PFCs observing sites as calculated by the FLEXPART transport model for the year 2018 (left) and 2024 (right) and used in the inversions. Observing stations active in each year are marked with red dots. Areas with visible land surface represent regions for which emissions can be observed well from the network. Shaded or dark areas represent regions for which limited emission information can be obtained from the network.

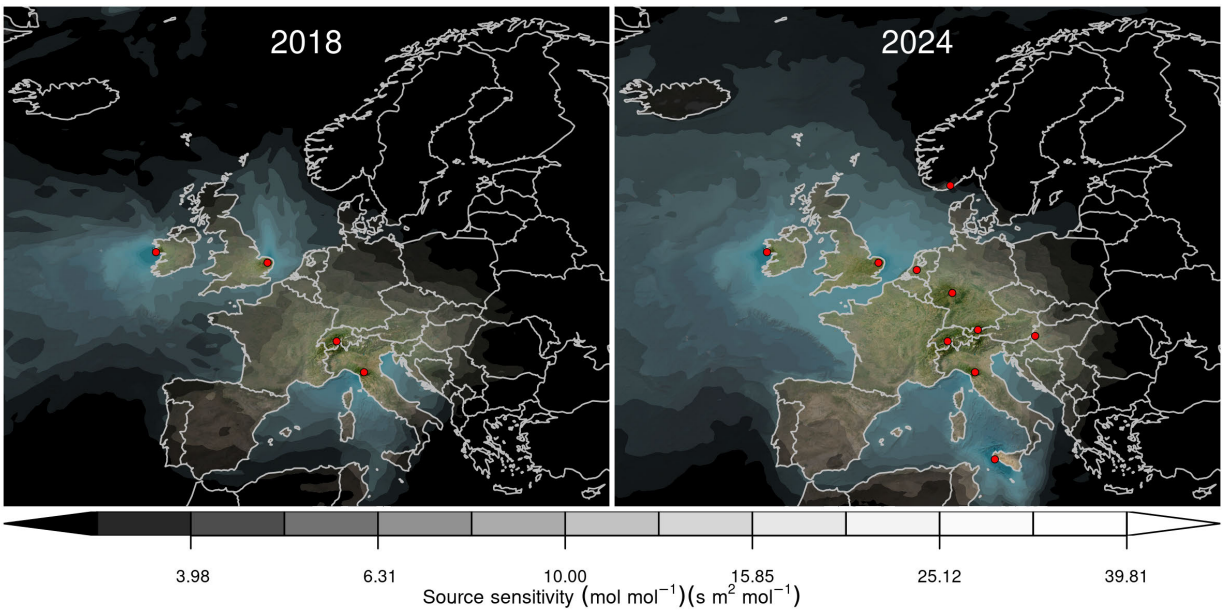

7 Sulphur hexafluoride (SF_6)

Figure 7.0.1: Total source sensitivity of SF_6 observing sites as calculated by the FLEXPART transport model for the year 2018 (left) and 2024 (right) and used in the inversions. Observing stations active in each year are marked with red dots. Areas with visible land surface represent regions for which emissions can be observed well from the network. Shaded or dark areas represent regions for which limited emission information can be obtained from the network.

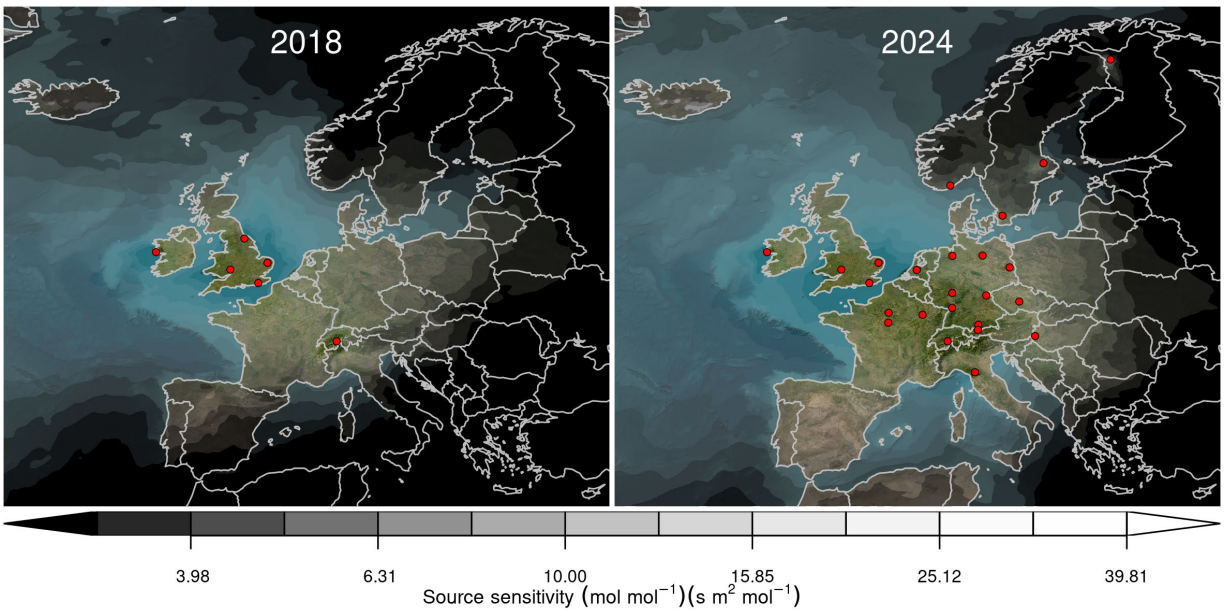

8 Carbon Dioxide (CO_2)

Measurements of CO_2 at ICOS sites and related observatories are influenced by a complex combination of sources and sinks. Fossil fuel combustion for transport, heating, energy generation, and other applications produce CO_2, along with other anthropogenic activities such as cement production. The terrestrial and oceanic biosphere produces CO_2 through animal and plant respiration and takes up CO_2 through photosynthesis. Furthermore, CO_2 is exchanged with the ocean through physical and chemical processes.

When considering high-frequency (∼hourly) CO_2 mole fraction deviations from baseline values—used to infer national emissions in regional inverse modelling studies—the influence of biospheric fluxes can be comparable to, or larger than, those of anthropogenic sources (e.g. White et al., 2019). Therefore, research is under way to develop new tracers that can determine fossil fuel CO_2 fluxes independent of biosphere sources and sinks.

Ongoing Horizon Europe projects PARIS and CORSO are examining methods for estimating fossil fuel CO_2 fluxes based on simultaneous measurements of CO_2 and O_2 (Figure 8.0.1). The method relies on the fact that CO_2 and O_2 are inter-converted during combustion and terrestrial biosphere exchange, but with different ratios for the two processes. A quantity can be constructed from these measurements, known as Atmospheric Potential Oxygen (APO), which is insensitive to biosphere fluxes, and may therefore be useful for isolating fossil fuel signals (Pickers et al., 2022).

High-frequency (∼hourly) timeseries of APO are available from Weybourne (WAO, 2010 – present) and Heathfield (HFD, 2021 - present) in the UK (Figure 8.0.1; Pickers, Adcock, and Manning, 2024), and new sites are being established at Cabauw and Zweth in the Netherlands. Preliminary analyses of the WAO data have revealed regional APO trends consistent with the drop in fossil fuel CO_2 emissions during the COVID lockdowns in the UK (Pickers et al., 2022). However, quantification of absolute regional fossil fuel CO_2 emissions remains an area of active research. Recent studies have derived fossil fuel CO_2 emissions for the UK that are highly uncertain (Rigby et al., 2025). Potential confounding factors were identified in Chawner et al. (2024), such as highly uncertain APO fluxes from the ocean, and a poorly constrained

regional APO background. These factors are the subject of ongoing research using atmospheric models and new APO measurements from PARIS, CORSO and ICOS.

An alternative method for top-down fossil fuel CO_2 emissions evaluation uses measurements of radiocarbon isotopologues ($^{14}CO_2$, compared to the dominant $^{12}CO_2$). Fossil fuels do not contain ^{14}C, and therefore, their combustion tends to decrease the atmospheric $^{14}CO_2/^{12}CO_2$ ratio. Currently, radiocarbon measurements can only be made at low frequency using flask sampling. However, a relatively intensive flask sampling campaign was carried out across Europe during 2024 as part of CORSO, and the results of this study will be reported on soon.

Figure 8.0.1: Carbon dioxide (top, red) and oxygen (bottom, blue) measurements from Weybourne Atmospheric Observatory in the UK, available from the ICOS Carbon Portal (Adcock et al., 2024).

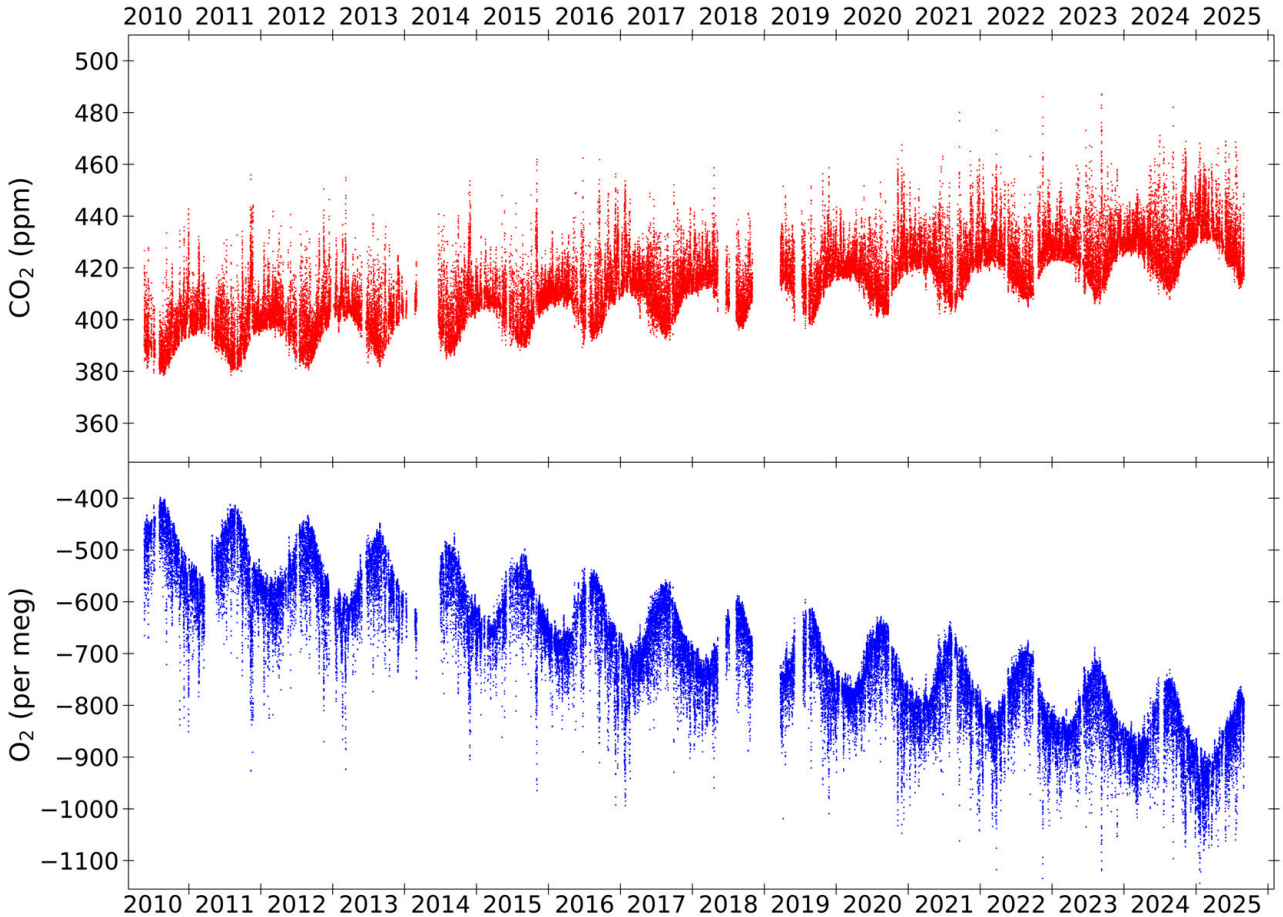

References

Adcock, Karina et al. (2024). *Atmospheric GHG data product (o2, o2_stdev, co2, co2_stdev) from Weybourne (10.0 m), 2010-05-19–2023-12-31*. URL: https://hdl.handle.net/11676/j4LzdHQiq3fPgfNeXHruC0Bb.

Chawner, Hannah et al. (Apr. 2024). "Atmospheric oxygen as a tracer for fossil fuel carbon dioxide: a sensitivity study in the UK". en. In: *Atmospheric Chemistry and Physics* 24.7, pp. 4231–4252. ISSN: 1680-7324. DOI: 10.5194/acp-24-4231-2024. URL: https://acp.copernicus.org/articles/24/4231/2024/ (visited on 04/10/2024).

European Commission: Joint Research, Centre et al. (2023). *GHG emissions of all world countries – 2023*. Publications Office of the European Union. DOI: 10.2760/953322.

Ganesan, A. L. et al. (2014). "Characterization of uncertainties in atmospheric trace gas inversions using hierarchical Bayesian methods". In: *Atmospheric Chemistry and Physics* 14.8, pp. 3855–3864. DOI: 10.5194/acp-14-3855-2014. URL: http://www.atmos-chem-phys.net/14/3855/2014/http://www.atmos-chem-phys.net/14/3855/2014/acp-14-3855-2014.pdf.

Ganesan, A. L. et al. (2015). "Quantifying methane and nitrous oxide emissions from the UK and Ireland using a national-scale monitoring network". In: *Atmos. Chem. Phys.* 15.11, pp. 6393–6406. DOI: 10.5194/acp-15-6393-2015. URL: https://www.atmos-chem-phys.net/15/6393/2015/https://www.atmos-chem-phys.net/15/6393/2015/acp-15-6393-2015.pdf.

Henne, S. et al. (2016). "Validation of the Swiss methane emission inventory by atmospheric observations and inverse modelling". In: *Atmospheric Chemistry and Physics* 16.6, pp. 3683–3710. DOI: 10.5194/acp-16-3683-2016. URL: http://www.atmos-chem-phys.net/16/3683/2016/.

Jones, A.R. et al. (2007). "The U.K. Met Office's next-generation atmospheric dispersion model, NAME III, in Borrego C. and Norman A.-L. (Eds)". In: *Air Pollution Modeling and its Application XVII (Proceedings of the 27th NATO/CCMS International Technical Meeting on Air Pollution Modelling and its Application), Springer*, pp. 580–589.

Katharopoulos, I. et al. (2023). "Impact of transport model resolution and a priori assumptions on inverse modeling of Swiss F-gas emissions". In: *Atmos. Chem. Phys.* 23.22, pp. 14159–14186. DOI: 10.5194/acp-23-14159-2023. URL: https://acp.copernicus.org/articles/23/14159/2023/.

Manning, A. J. et al. (2021). "Evidence of a recent decline in UK emissions of hydrofluorocarbons determined by the InTEM inverse model and atmospheric measurements". In: *Atmospheric Chemistry and Physics* 21.16, pp. 12739–12755. DOI: 10.5194/acp-21-12739-2021. URL: https://acp.copernicus.org/articles/21/12739/2021/.

Pickers, P., K. Adcock, and A. Manning (Feb. 2024). *Atmospheric oxygen and carbon dioxide observations from Weybourne Atmospheric Observatory, Norfolk, UK uploaded to public archives*. Tech. rep. Process Attribution of Regional Emissions (PARIS). URL: https://horizoneurope-paris.eu/wp-content/uploads/sites/914/2024/07/PARIS-deliverables-D6.1-High-frequency-APO-data-uploaded-final.pdf.

Pickers, Penelope A. et al. (Apr. 2022). "Novel quantification of regional fossil fuel CO2 reductions during COVID-19 lockdowns using atmospheric oxygen measurements". en. In: *Science Advances* 8.16, eabl9250. ISSN: 2375-2548. DOI: 10.1126/sciadv.abl9250. URL: https://www.science.org/doi/10.1126/sciadv.abl9250 (visited on 12/01/2023).

Rigby, M. et al. (2019). "Increase in CFC-11 emissions from eastern China based on atmospheric observations". In: *Nature* 569, pp. 546–550. DOI: 10.1038/s41586-019-1193-4. URL: https://doi.org/10.1038/s41586-019-1193-4.

Rigby, M. et al. (Apr. 2025). *Inverse estimates of fossil fuel CO2 emission*. Tech. rep. Process Attribution of Regional Emissions (PARIS). URL: https://horizoneurope-paris.eu/wp-content/uploads/sites/914/2025/01/PARIS-M24-Inverse-estimates-of-fossil-fuel-CO2-emissions-final.pdf.

Stohl, A. et al. (2005). "Technical note: The Lagrangian particle dispersion model FLEXPART version 6.2". In: *Atmospheric Chemistry and Physics* 5, pp. 2461–2474. DOI: 10.5194/acp-5-2461-2005. URL: <GotoISI>://000231983600002.

White, Emily D. et al. (Apr. 2019). "Quantifying the UK's carbon dioxide flux: an atmospheric inverse modelling approach using a regional measurement network". en. In: *Atmospheric Chemistry and Physics*

19.7, pp. 4345–4365. ISSN: 1680-7324. DOI: 10.5194/acp-19-4345-2019. URL: https://www.atmos-chem-phys.net/19/4345/2019/ (visited on 04/05/2019).

Draft Inventory Annex
Switzerland 2025

30th October, 2025

1 Introduction

In this document, global concentration trends and national emissions estimates derived from atmospheric observations ("inverse estimates") are presented for most reported gases. Comparing the emissions submitted in national inventories with those calculated using atmospheric observations allows for emissions to be assessed using two fundamentally different approaches. Substantial differences can highlight areas that could warrant further investigation.

Global concentration trends for each gas are first shown using annual average concentrations from Mace Head, Ireland (Northern Hemisphere) and Kennaook/Cape Grim, Tasmania, Australia (Southern Hemisphere). Data from these stations were selected to exclude regionally-polluted air masses and therefore represents northern and southern hemispheric concentration trends. Mace Head observations were supported by the National Aeronautics and Space Administration (NASA) and the UK Department of Energy, Security and Net Zero (DESNZ), and Kennaook/Cape Grim observations by NASA and the Australian Bureau of Meteorology.

Observations of European concentrations of greenhouse gases used to derive national inverse emission estimates were collected from many different networks and providers. Methane and nitrous oxide concentrations originated from the European ICOS (Integrated Carbon Observation System) network, the UK DECC (Deriving Emissions related to Climate Change) network and other national or individual initiatives. F-gas observations were made by affiliates of the AGAGE (Advanced Global Atmospheric Gases Experiment) network. Observations from additional stations across Europe were supported by the Horizon-EU PARIS (Process Attribution of Regional Emissions) project. The observation stations used to derive emissions for each gas are shown in the corresponding sections of this document.

An atmospheric transport model provides the link between surface fluxes and concentrations measured at the observing stations. If not otherwise mentioned, inversion-based emissions estimates were derived using two atmospheric transport models combined with three inverse models, yielding a total of six inversions. This ensemble of six inversions allows us to better quantify the uncertainties associated with inverse modelling.

The two atmospheric transport models used are the Numerical Atmospheric dispersion Modelling Environment (NAME, Jones et al., 2007), and the FLEXible PARTicle dispersion model (FLEXPART, Stohl et al., 2005). Both models are backwards-running Lagrangian Particle Dispersion Models (LPDMs) that simulate the recent transport of air to each observing station. The two LPDMs have been widely used in the estimation of greenhouse gas emissions (Ganesan et al., 2015; Rigby et al., 2019; Manning et al., 2021; Henne et al., 2016).

The three inverse methods used are InTEM (Inversion Technique for Emission Modelling, Manning et al., 2021), ELRIS (Empa Lagrangian Regional Inversion System, Henne et al., 2016; Katharopoulos et al., 2023), and RHIME (Regional Hierarchical Inverse Modelling Environment, Ganesan et al., 2014). All three inverse methods estimate emissions within Europe along with boundary conditions that account for the concentration of the air entering Europe. All three systems started from the same set of a priori emissions that were either derived from the global EDGAR emission inventory (version 8, European Commission: Joint Research et al., 2023) or a uniform land-based emission, depending on the gas. A natural emission component, from the WETCHARTS product, was included in the methane prior. The same observational dataset was used by each inverse model, but data selection (i.e., filtering datasets for specific conditions) and treatment of uncertainties were chosen separately and hence differ. The three methods also differ in their statistical approaches for estimating emissions.

Emission estimates are presented for the period 2008-2024. Emissions for the full 2008-2024 period were derived with the InTEM-NAME inversion only, while emissions from 2017-2024 are presented as the mean of the six inversions (denoted the "PARIS mean"). The uncertainty shown is the minimum/maximum of the uncertainties in the ensemble.

All inversions employed a resolution of one month for CH_4 and N_2O and 1-year for the fluorinated gases. The inversion results used to compare with the inventories are a one-year calendar average for CH_4 and N_2O and the yearly value derived from a 3-year moving average for the fluorinated gases. For the 2008-2024

InTEM-NAME results, a 3-year moving average was also applied to the annualised CH_4 and N_2O results due to lack of observational coverage in the earlier years.

2 Global Concentration Trends

2.1 Methane (CH_4)

Figure 2.1.1: Background Northern Hemisphere monthly concentrations of CH_4 estimated from MHD, Ireland observations are shown in red, and background Southern Hemisphere monthly concentrations from CGO, Tasmania are shown in blue. Grey shading represents provisional data.

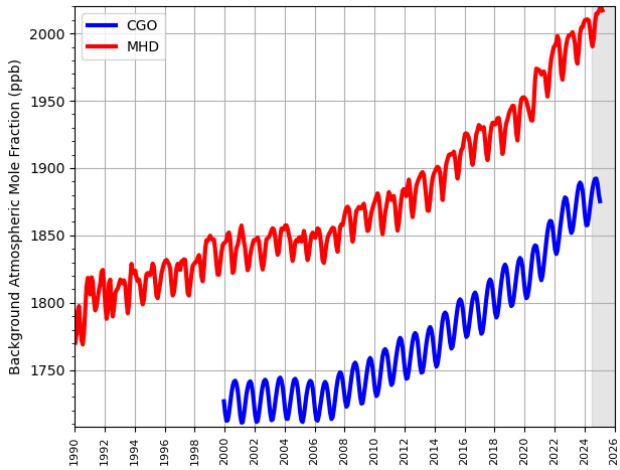

2.2 Nitrous Oxide (N_2O)

Figure 2.2.1: Background Northern Hemisphere monthly concentrations of N_2O estimated from MHD, Ireland observations are shown in red, and background Southern Hemisphere monthly concentrations from CGO, Tasmania are shown in blue. Grey shading represents provisional data.

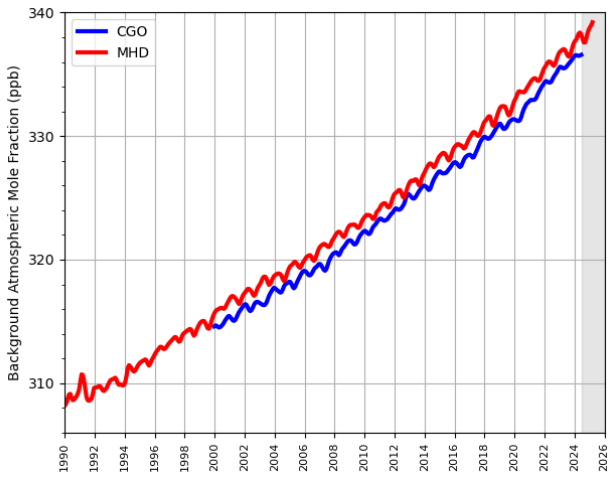

2.3 Hydrofluorocarbons (HFCs)

Figure 2.3.1: Background Northern Hemisphere monthly concentrations of six HFCs estimated from MHD, Ireland observations are shown in red, and background Southern Hemisphere monthly concentrations from CGO, Tasmania are shown in blue. Grey shading represents provisional data.

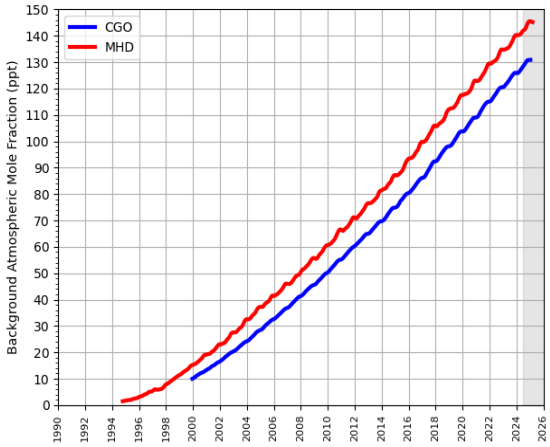

(a) HFC-134a

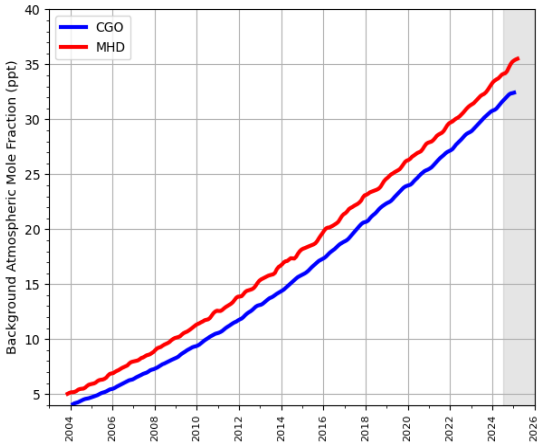

(b) HFC-143a

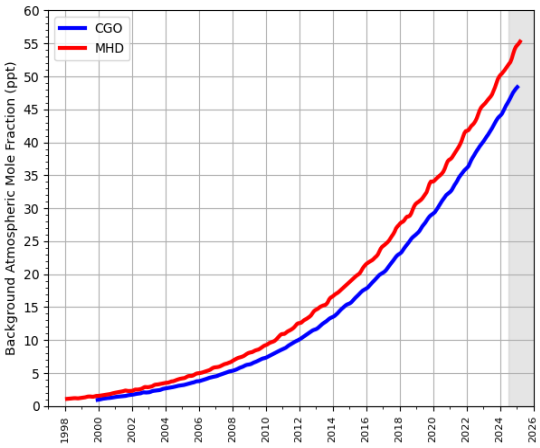

(c) HFC-125

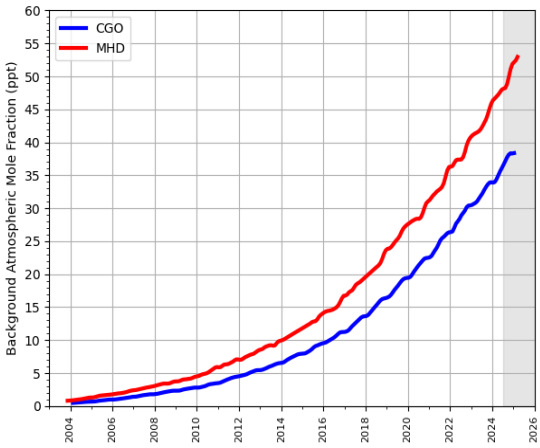

(d) HFC-32

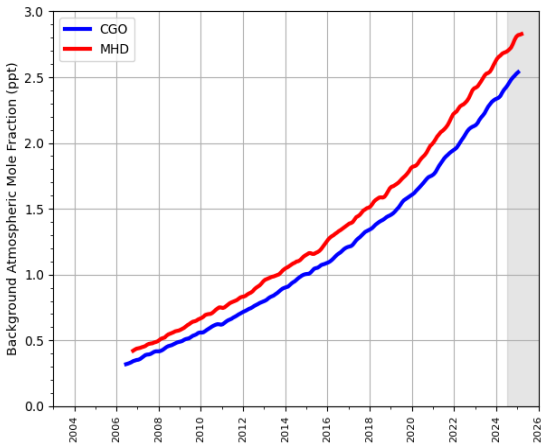

(e) HFC-227ea

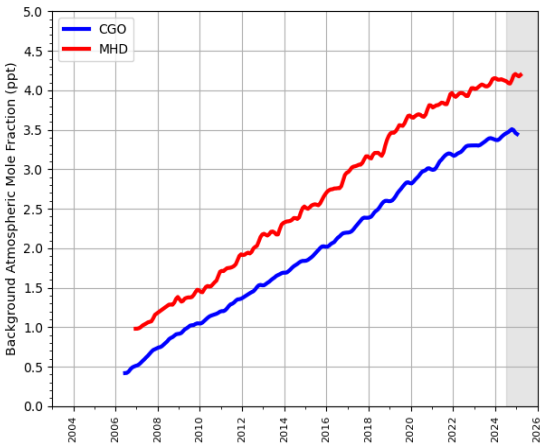

(f) HFC-245fa

Figure 2.3.2: Background Northern Hemisphere monthly concentrations of four HFCs estimated from MHD, Ireland observations are shown in red, and background Southern Hemisphere monthly concentrations from CGO, Tasmania are shown in blue. Grey shading represents provisional data.

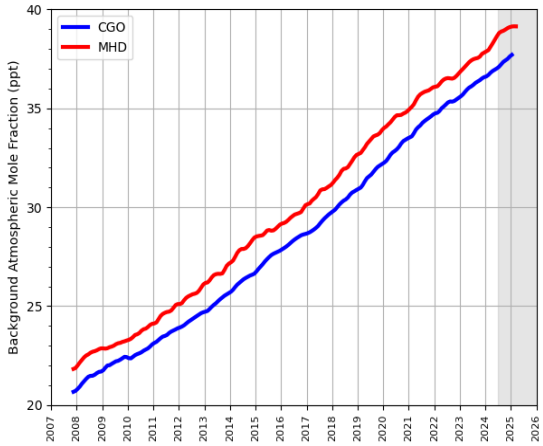

(a) HFC-23

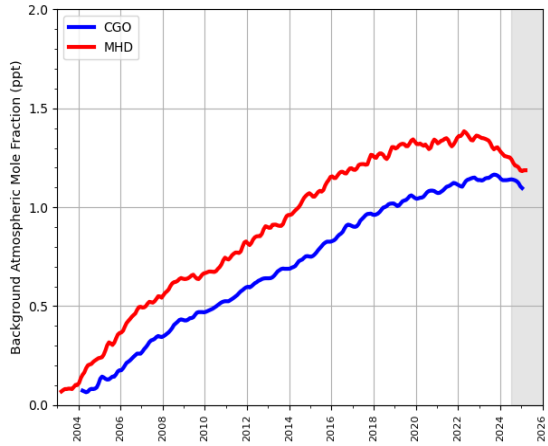

(b) HFC-365mfc

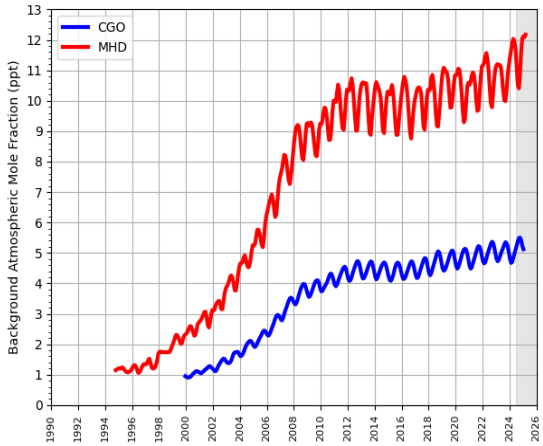

(c) HFC-152a

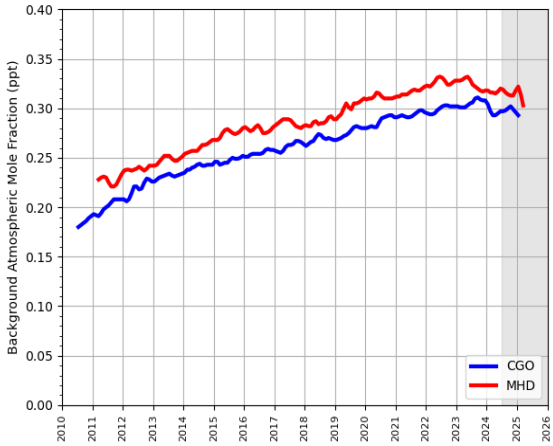

(d) HFC-43-10-mee

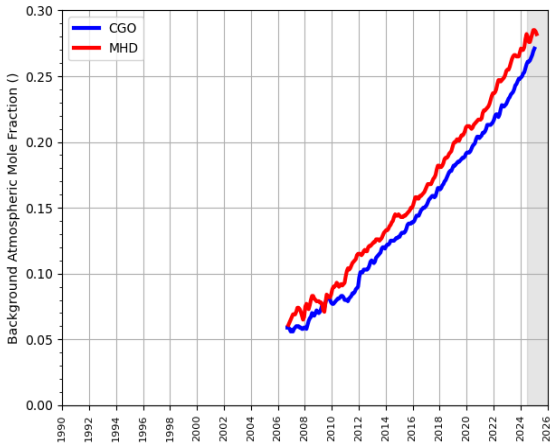

(e) HFC-236fa

2.4 Perfluorocarbons (PFCs)

Figure 2.4.1: Background Northern Hemisphere monthly concentrations of four PFCs estimated from MHD, Ireland observations are shown in red, and background Southern Hemisphere monthly concentrations from CGO, Tasmania are shown in blue. Grey shading represents provisional data.

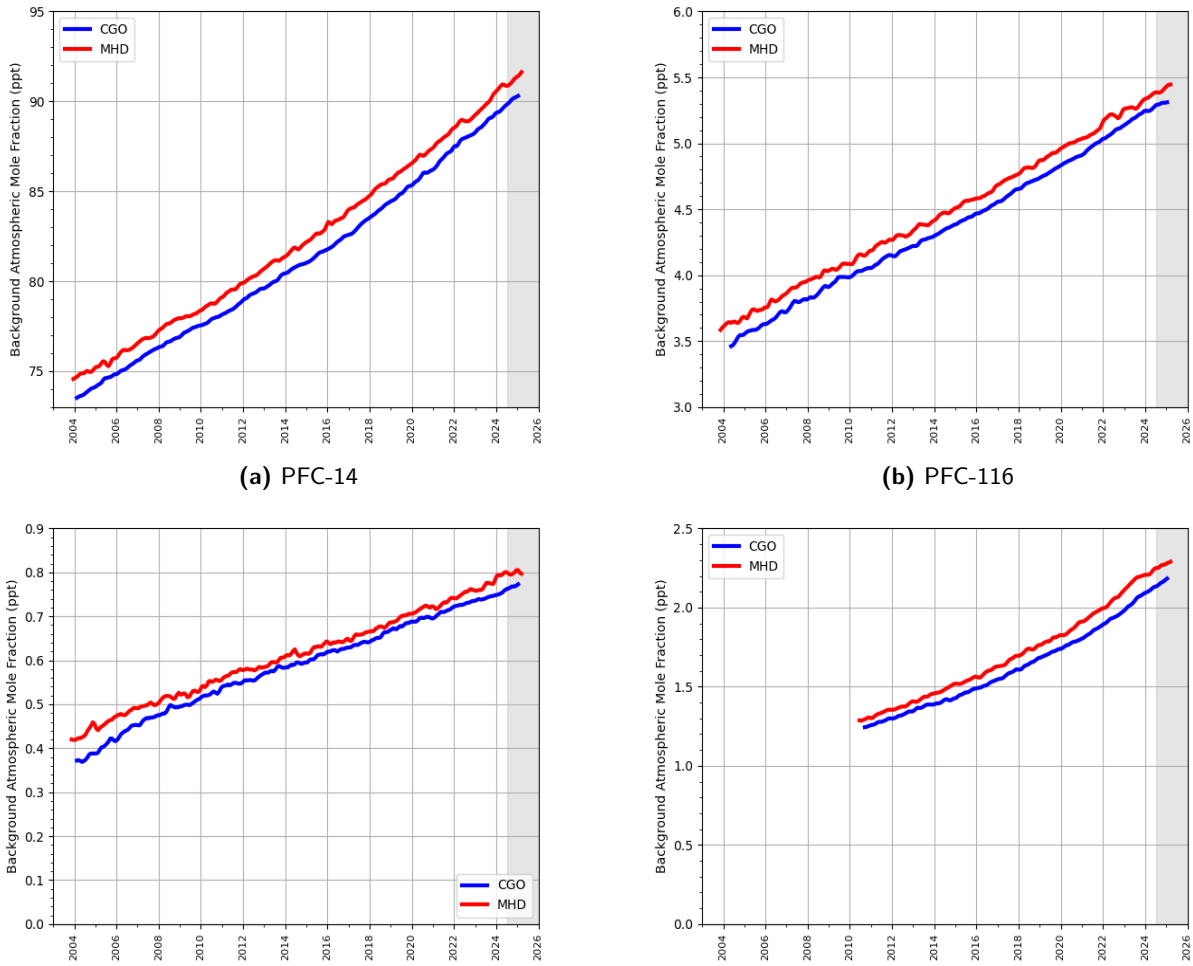

(a) PFC-14 **(b)** PFC-116 **(c)** PFC-218 **(d)** PFC-318

2.5 Sulphur Hexafluoride (SF_6) and Nitrogen Trifluoride (NF_3)

Figure 2.5.1: Background Northern Hemisphere monthly concentrations of SF_6 and NF_3 estimated from MHD, Ireland observations are shown in red, and background Southern Hemisphere monthly concentrations from CGO, Tasmania are shown in blue. Grey shading represents provisional data.

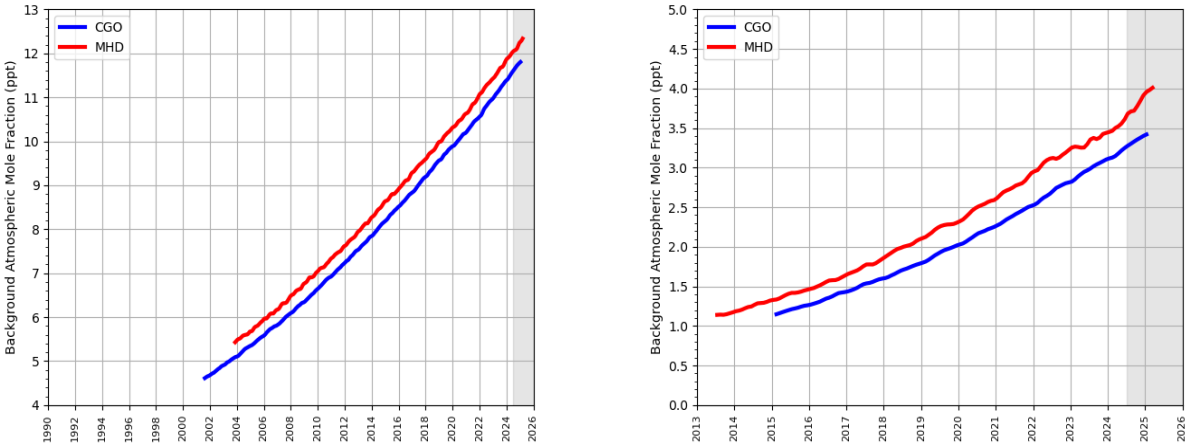

(a) SF_6 **(b)** NF_3

2.6 Carbon Dioxide (CO_2)

Figure 2.6.1: Background Northern Hemisphere monthly concentrations of CO_2 estimated from MHD, Ireland observations are shown in red, and background Southern Hemisphere monthly concentrations from CGO, Tasmania are shown in blue. Grey shading represents provisional data.

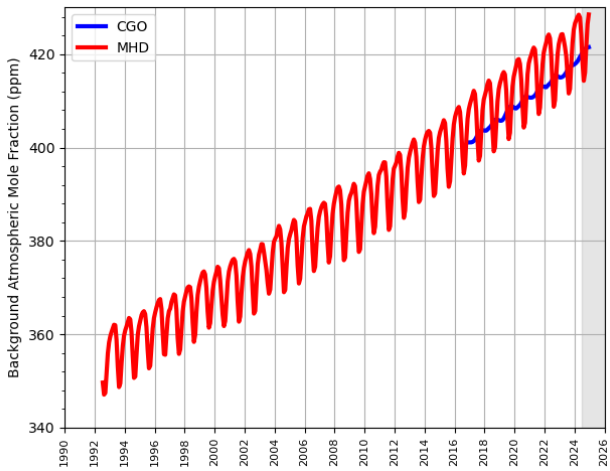

3 Key findings

- General note: Currently, the presented inverse modelling estimates of Swiss emissions are limited by several factors. First, the applied transport model is not ideal for the complex topography of Switzerland and with an approximate horizontal resolution of 12 km much coarser than what is used in the national atmospheric support effort of the inventory reporting. Second, for a relatively small country like Switzerland, the applied inversion grids with a maximal horizontal resolution of about 25 km may cause mis-attribution of emissions from neighbouring countries. Third, observations from the Swiss Plateau (Beromünster tall tower) are only available for CH_4 and N_2O but not for fluorinated compounds. Hence, observational constraint in Switzerland for these gases mainly originates from the high-altitude site Jungfraujoch and from sites in neighbouring countries.
- Methane (CH_4): Inverse results are in fairly good agreement with the inventory between 2018 and 2024 (Figure 4.0.2). However, the uncertainty estimate on the a posteriori inversion results is relatively large. Highest emissions are obtained along the Swiss Plateau, where agriculture is most intense (Figure 4.0.4). The inverse results indicate pronounced month-to-month variability with some inversions (NAME-based) tending more towards a robust seasonality in the methane emissions, with increased emissions during the winter (Figures 4.0.3 and 4.0.5). However, seasonality shows spatially variable patterns in Switzerland even containing areas with maximal summer-time emissions.
- Nitrous oxide (N_2O): Inverse results are significantly smaller, about half, than inventory estimates between 2018 and 2023 (Figure 5.0.2). As for CH_4, highest emissions are obtained along the eastern Swiss Plateau with very little spatial distinctness (Figure 5.0.4). The inverse results indicate a pronounced seasonality in the nitrous oxide emissions with a maximum in summer and autumn (Figures 5.0.3 and 5.0.5). This is somewhat in contrast to previous studies and the expectation of an earlier emission maximum in spring and summer due to fertiliser application and enhanced soil microbial activity.
- Hydrofluorocarbons (HFCs): From the current inverse modelling results, very little can be concluded about the Swiss HFC emissions. Both the coarse resolution of the transport model and the lack of observations in the Swiss atmospheric boundary layer make the inverse estimates very uncertain and hinder a direct comparison with the inventory. Absolute emission levels of total HFCs are about a factor of two lower in the inversions than in the inventory (Figure 6.7.1). No downward trend is visible in the inversion results for recent years. Of the individual compounds, only the positive trend in HFC-32 is observed in both inventory and inversion results. However, inversion results are about a factor of two lower than the inventory (Figure 6.6.1).
- Perfluorocarbons (PFCs): From the current inverse modelling results very little can be concluded about the Swiss PFC emissions. Both the coarse resolution of the transport model and the lack of observations in the Swiss atmospheric boundary layer make the inverse estimates very uncertain and hinder a direct comparison with the inventory.
- Sulphur hexafluoride (SF_6): Similar to HFCs and PFCs, no observations are available from the Swiss boundary layer. However, for recent years additional flask samples of SF_6 were taken at some of the ICOS sites in Southern Germany that provide some constraint on Switzerland and have let to somewhat reduced a posteriori uncertainties after 2021 (Figure 8.0.2). However, a positive emission trend is obtained by the inversions, whereas the inventory contains quickly declining emissions after 2015. One additional problem in the SF_6 inversions is the presence of a large emission source in southwestern Germany. Large a posteriori emissions in the area of Basel may actually be misattributed because of the presence of the point source further north.

Table 1: Emissions estimation for the main greenhouse gases of focus according to the National Inventory Document (NID) 2025 and the inversions done in the PARIS project. For the PARIS estimation, the mean of all models is displayed, along with a range of uncertainty estimated via the half distance between the maximum and minimum uncertainties of the different models. For SF_6, the PARIS mean is the average of all InTEM and ELRIS inversions only.

		2020	2021	2022	2023	2024
CH_4	NID 2025	4.96	4.96	4.93	4.88	
$(\mathrm{TgCO_2\text{-}eq \cdot yr^{-1}})$	PARIS mean	4.67 ± 1.70	4.61 ± 1.78	4.63 ± 2.30	4.45 ± 1.70	4.00 ± 1.64
N_2O	NID 2025	3.26	3.15	2.66	2.64	
$(\mathrm{TgCO_2\text{-}eq \cdot yr^{-1}})$	PARIS mean	1.85 ± 0.61	1.82 ± 1.10	1.65 ± 0.75	1.42 ± 0.77	1.54 ± 0.76
Total HFC	NID 2025	1.3	1.2	1.2	1.2	
$(\mathrm{TgCO_2\text{-}eq \cdot yr^{-1}})$	PARIS mean	0.6 ± 0.3	0.6 ± 0.3	0.6 ± 0.3	0.5 ± 0.3	0.6 ± 0.3
SF_6	NID 2025	0.16	0.13	0.06	0.06	
$(\mathrm{TgCO_2\text{-}eq \cdot yr^{-1}})$	PARIS mean	0.09 ± 0.09	0.09 ± 0.10	0.09 ± 0.09	0.10 ± 0.08	0.12 ± 0.08
Total PFC	NID 2025	21	12	12	13	
$(\mathrm{GgCO_2\text{-}eq \cdot yr^{-1}})$	PARIS mean	31 ± 43	34 ± 47	36 ± 57	42 ± 61	48 ± 63

4 Methane (CH_4)

Figure 4.0.1: Average monthly total source sensitivity of CH_4 observing sites as calculated by the FLEXPART transport model for the year 2018 (left) and 2024 (right) and used in the inversions. Observing stations active in each year are marked with red dots. Areas with visible land surface represent regions for which emissions can be observed well from the network. Shaded or dark areas represent regions for which limited emission information can be obtained from the network.

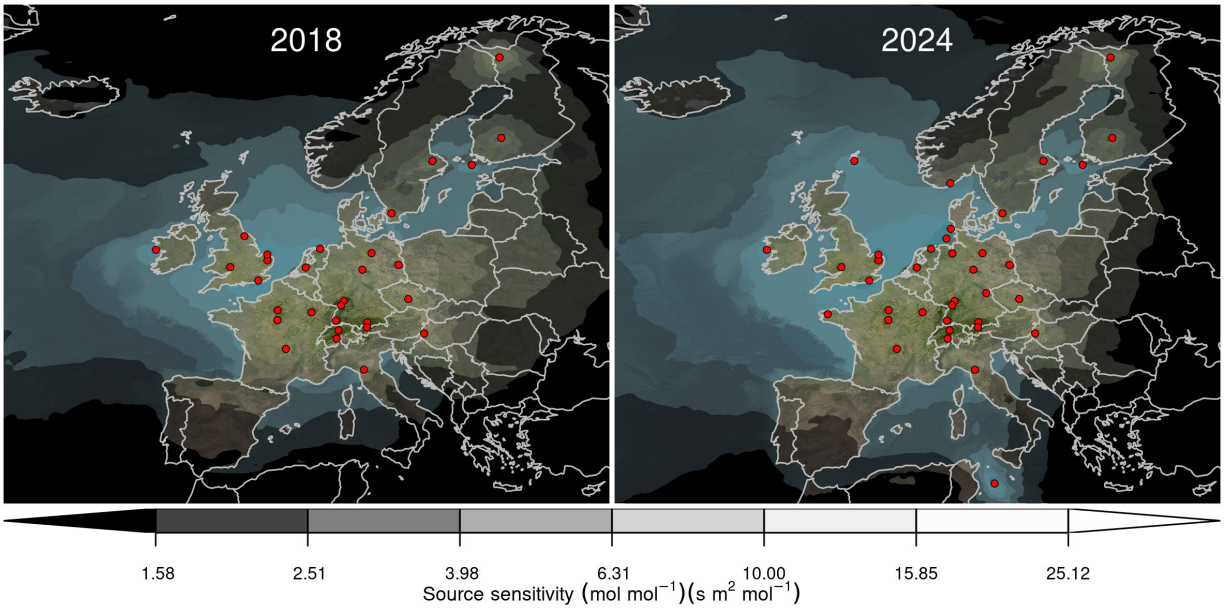

Figure 4.0.2: Verification of the Swiss emissions inventory estimates for CH_4 (zoom in to 2018-2024). Modelled annual emissions are given as the mean from all models (black line) and the individual result from InTEM-NAME (blue line). The shaded blue area is the 68 % confidence interval (CI) of InTEM-NAME and the shaded grey area encompasses the 68 % CI from all models. National inventory annual totals from 2024 and 2025 are given as grey and black bars, respectively.

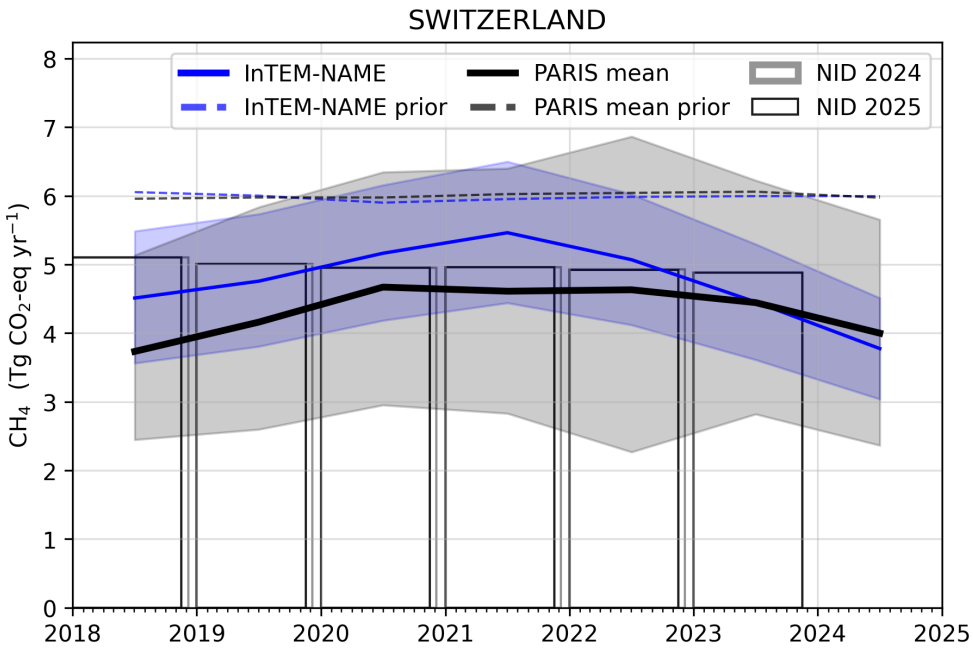

Figure 4.0.3: Verification of the Swiss emissions inventory estimates for CH_4 (zoom in to 2018-2024). Modelled monthly emissions are given as the mean from all models (black line) and the individual result from InTEM-NAME (blue line). The shaded blue area is the 68 % confidence interval (CI) of InTEM-NAME and the shaded grey area encompasses the 68 % CI from all models. National inventory annual totals from 2024 and 2025 are given as grey and black bars, respectively.

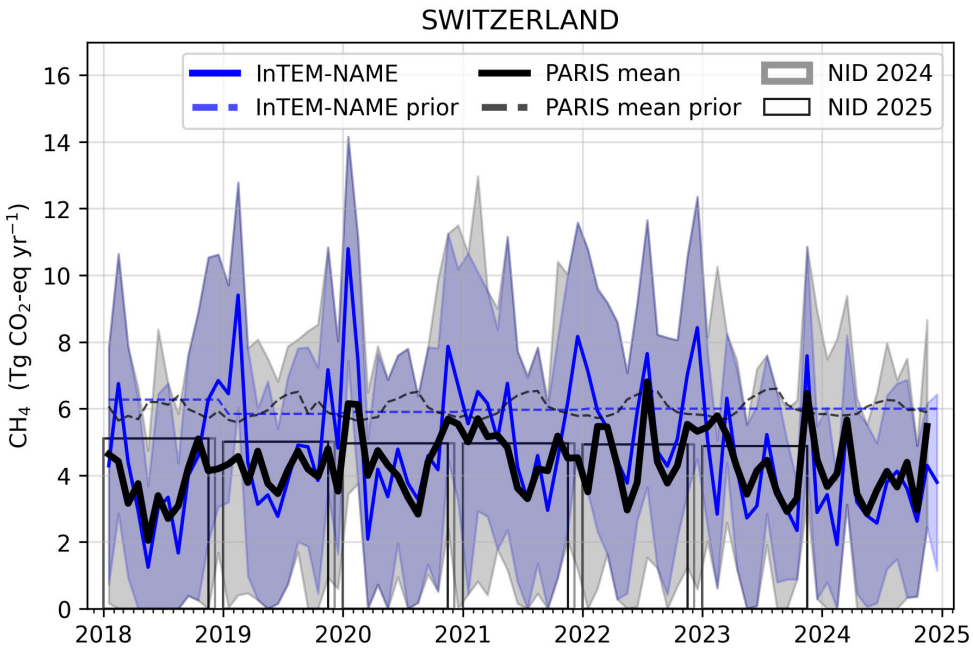

Figure 4.0.4: Spatial distribution of the Swiss average modelled emissions of CH_4 during the period of 2020-2024 (mean from all models). Observing stations are marked with red circles and highly-populated cities are marked with red triangles.

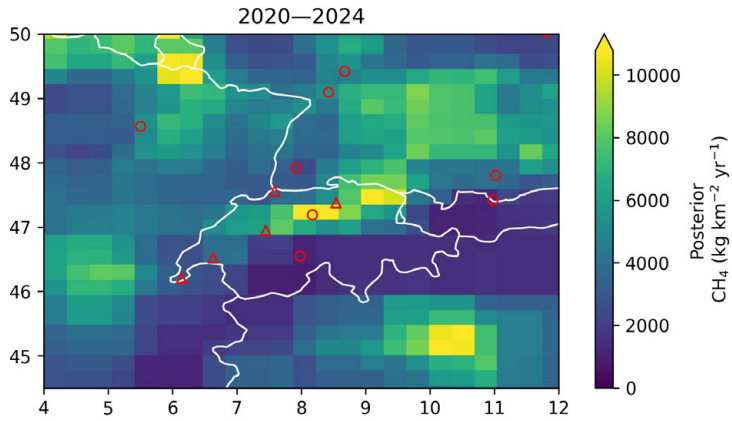

Figure 4.0.5: Spatial distribution of the seasonal deviation from the mean. The deviation is defined as the modelled Swiss seasonally averaged CH_4 emissions over 2020-2024 minus the average over the whole period. The mean across all models is shown. Observing stations are marked with black circles and highly-populated cities are marked with black triangles.

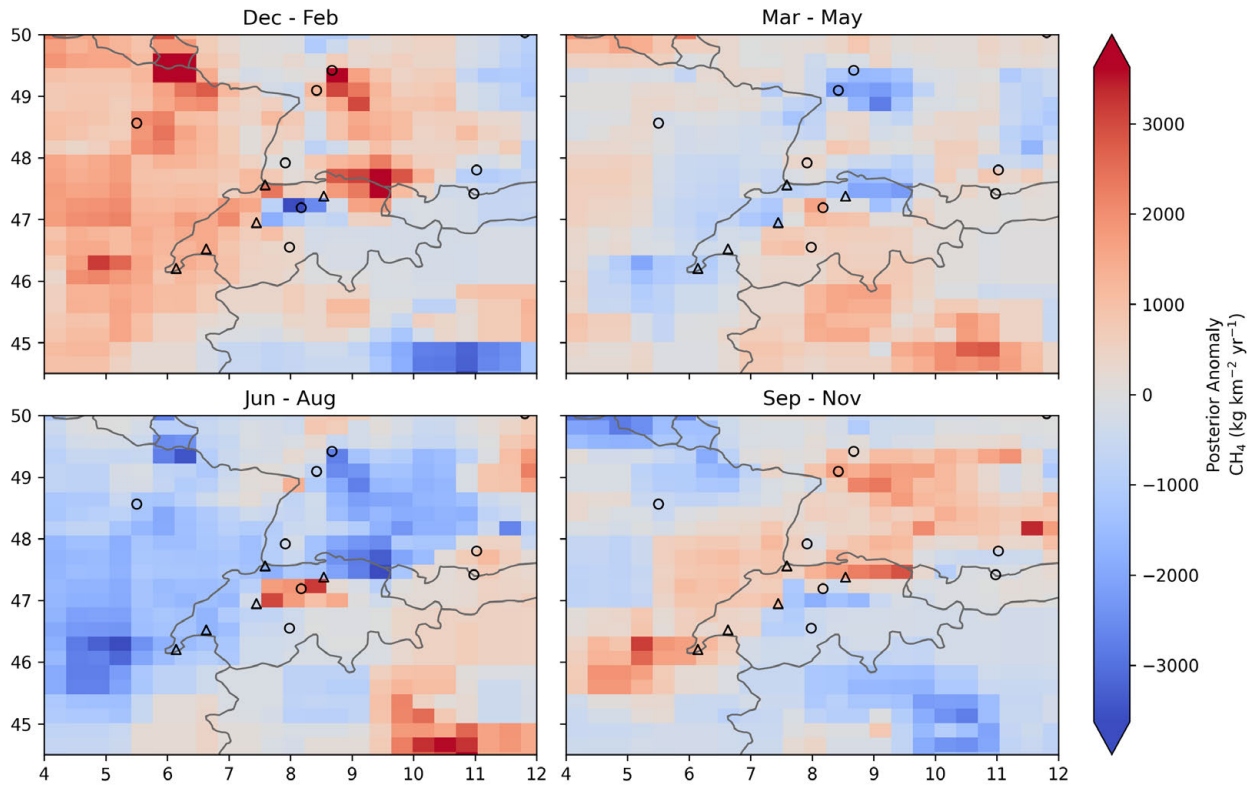

5 Nitrous Oxide (N_2O)

Figure 5.0.1: Average monthly total source sensitivity of N_2O observing sites as calculated by the FLEXPART transport model for the year 2018 (left) and 2024 (right) and used in the inversions. Observing stations active in each year are marked with red dots. Areas with visible land surface represent regions for which emissions can be observed well from the network. Shaded or dark areas represent regions for which limited emission information can be obtained from the network.

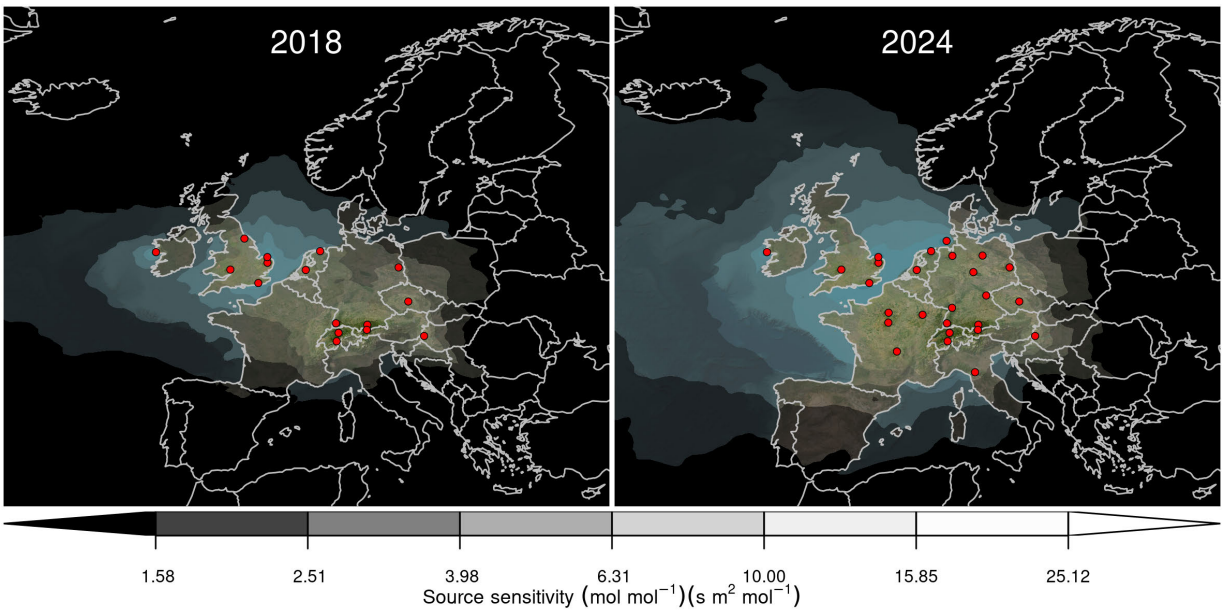

Figure 5.0.2: Verification of the Swiss emissions inventory estimates for N_2O (zoom in to 2018-2024). Modelled annual emissions are given as the mean from all models (black line) and the individual result from InTEM-NAME (blue line). The shaded blue area is the 68 % confidence interval (CI) of InTEM-NAME and the shaded grey area encompasses the 68 % CI from all models. National inventory annual totals from 2024 and 2025 are given as grey and black bars, respectively.

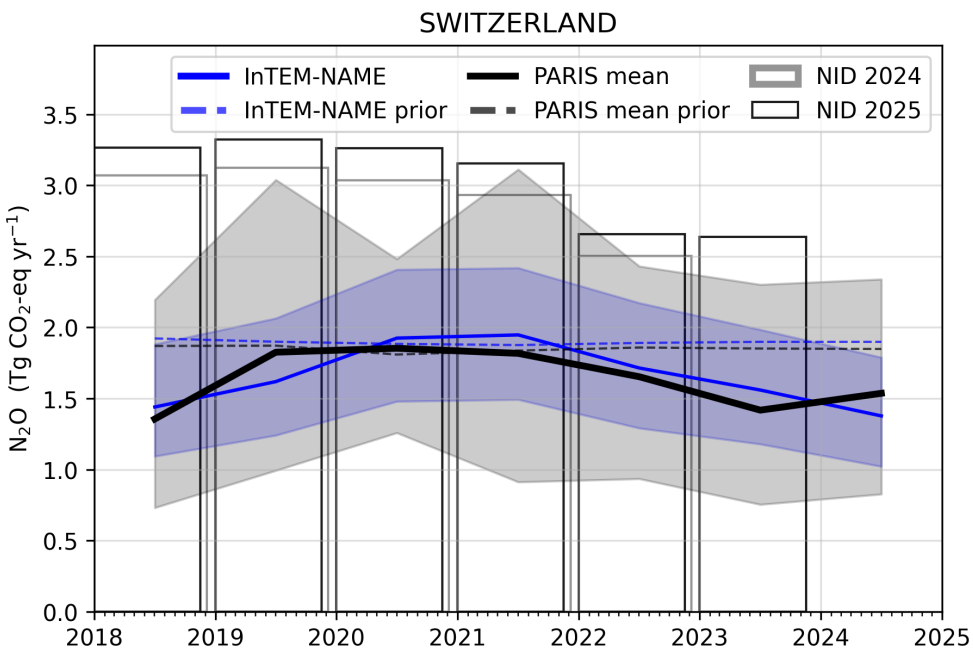

Figure 5.0.3: Verification of the Swiss emissions inventory estimates for N_2O (zoom in to 2018-2024). Modelled monthly emissions are given as the mean from all models (black line) and the individual result from InTEM-NAME (blue line). The shaded blue area is the 68 % confidence interval (CI) of InTEM-NAME and the shaded grey area encompasses the 68 % CI from all models. National inventory annual totals from 2024 and 2025 are given as grey and black bars, respectively.

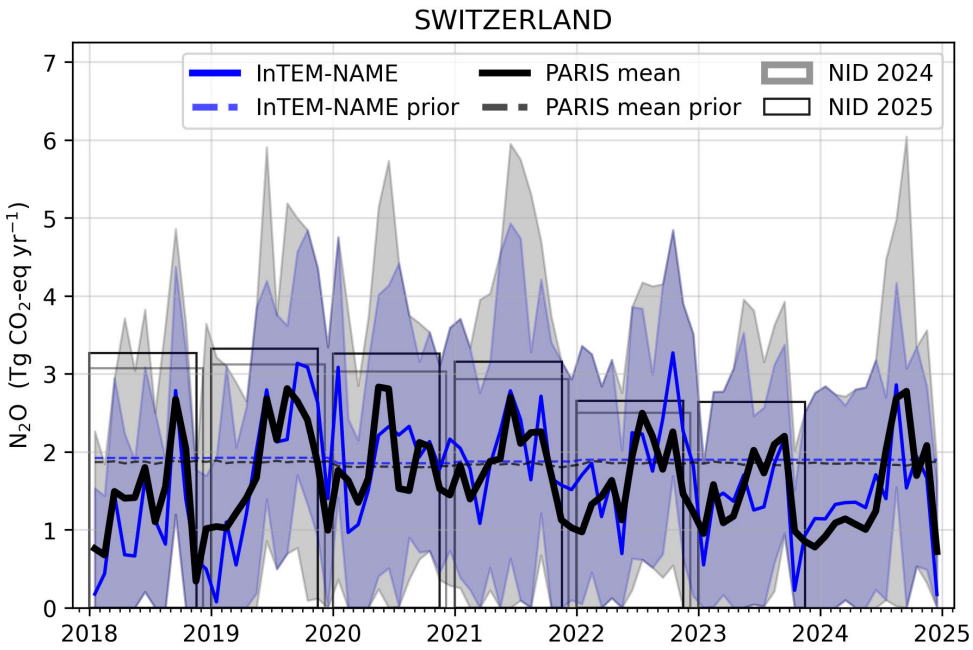

Figure 5.0.4: Spatial distribution of the Swiss average modelled emissions of N_2O during the period of 2020-2024 (mean from all models). Observing stations are marked with red circles and highly-populated cities are marked with red triangles.

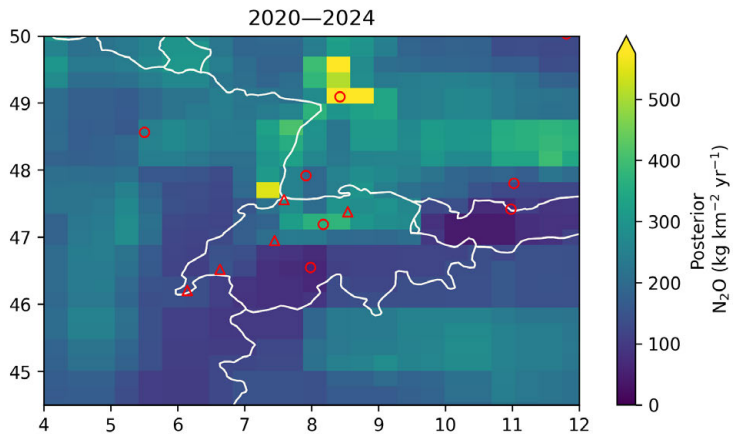

Figure 5.0.5: Spatial distribution of the seasonal deviation from the mean. The deviation is defined as the modelled Swiss seasonally averaged N_2O emissions over 2020-2024 minus the average over the whole period. The mean across all models is shown. Observing stations are marked with black circles and highly-populated cities are marked with black triangles.

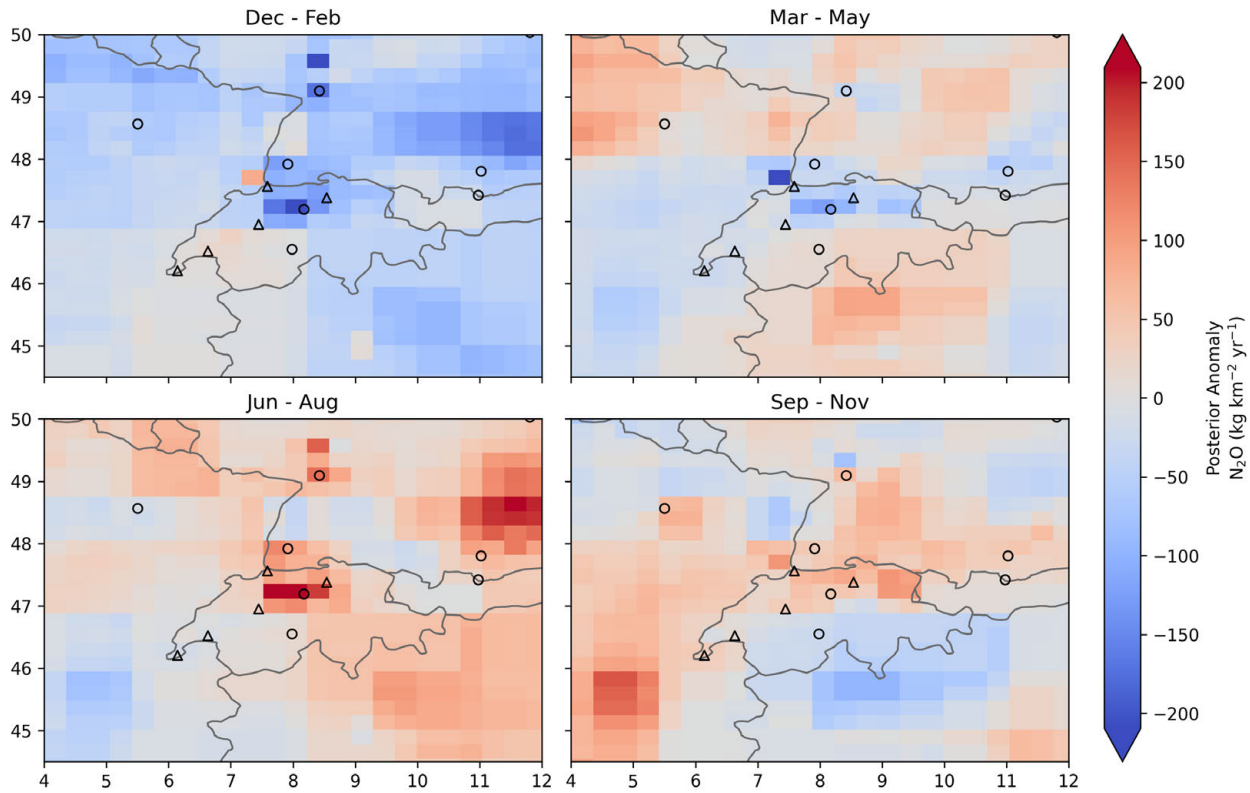

6 Hydrofluorocarbons (HFCs)

Figure 6.0.1: Total source sensitivity of HFCs/PFCs observing sites as calculated by the FLEXPART transport model for the year 2018 (left) and 2024 (right) and used in the inversions. Observing stations active in each year are marked with red dots. Areas with visible land surface represent regions for which emissions can be observed well from the network. Shaded or dark areas represent regions for which limited emission information can be obtained from the network.

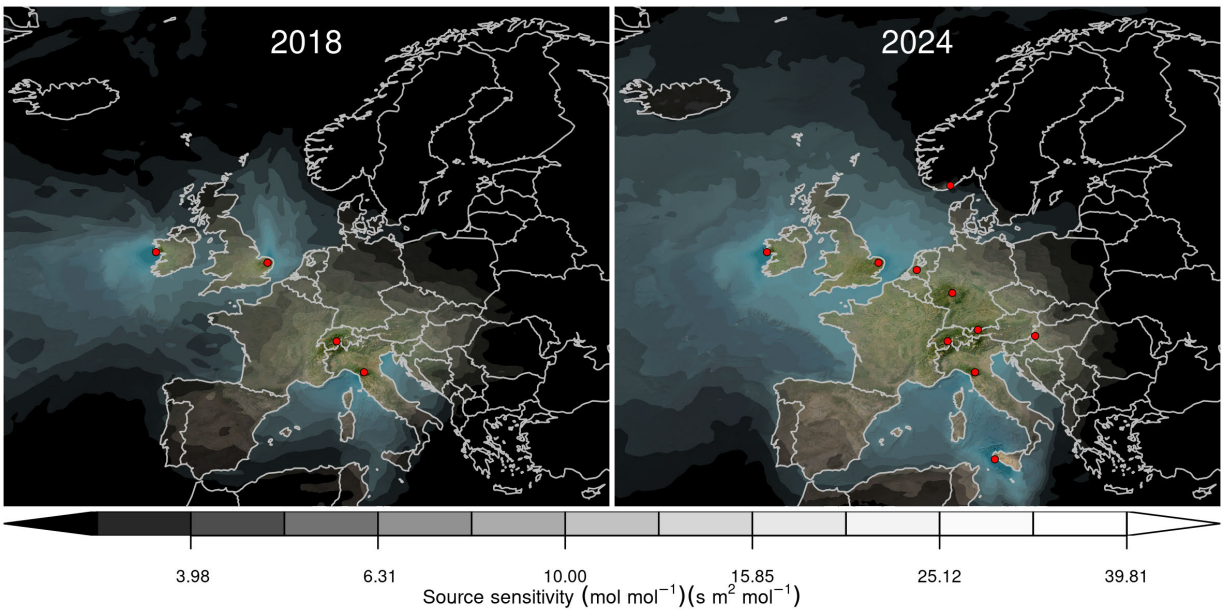

6.1 HFC-125

Figure 6.1.1: Verification of the Swiss emissions inventory estimates for HFC-125. Modelled annual emissions are given as the mean from all models (black line) and the individual result from InTEM-NAME (blue line). The shaded blue area is the 68 % confidence interval (CI) of InTEM-NAME and the shaded grey area encompasses the 68 % CI from all models. National inventory annual totals from 2024 and 2025 are given as grey and black bars, respectively.

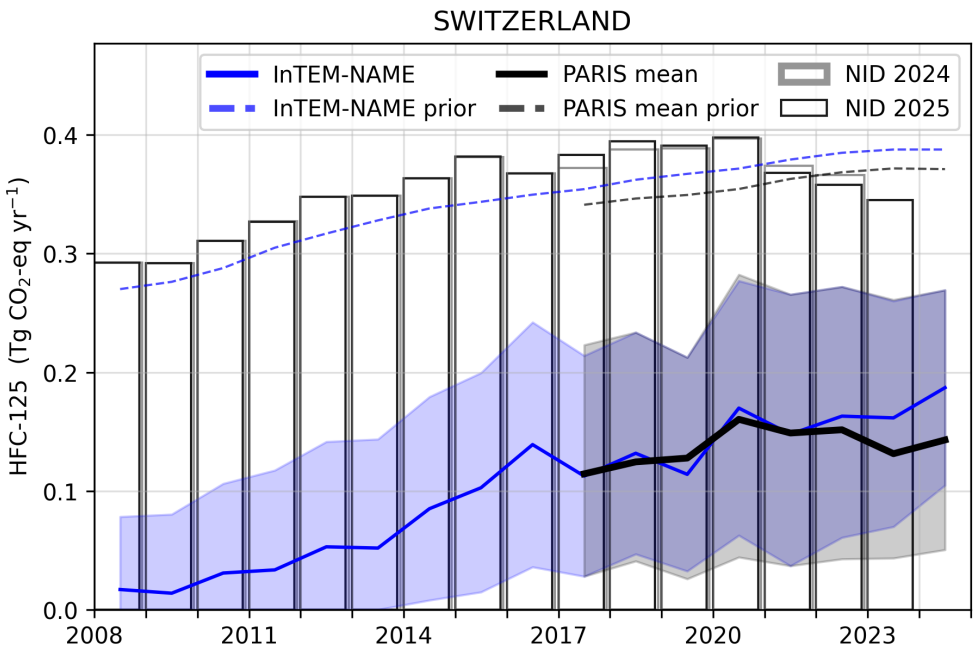

Figure 6.1.2: Spatial distribution of the Swiss average modelled emissions of HFC-125 during the period of 2020-2024 (mean from all models). Observing stations are marked with red circles and highly-populated cities are marked with red triangles.

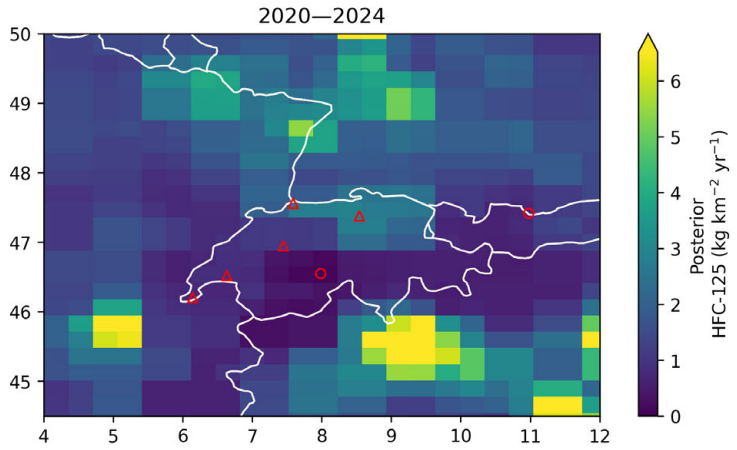

6.2 HFC-134a

Figure 6.2.1: Verification of the Swiss emissions inventory estimates for HFC-134a. Modelled annual emissions are given as the mean from all models (black line) and the individual result from InTEM-NAME (blue line). The shaded blue area is the 68 % confidence interval (CI) of InTEM-NAME and the shaded grey area encompasses the 68 % CI from all models. National inventory annual totals from 2024 and 2025 are given as grey and black bars, respectively.

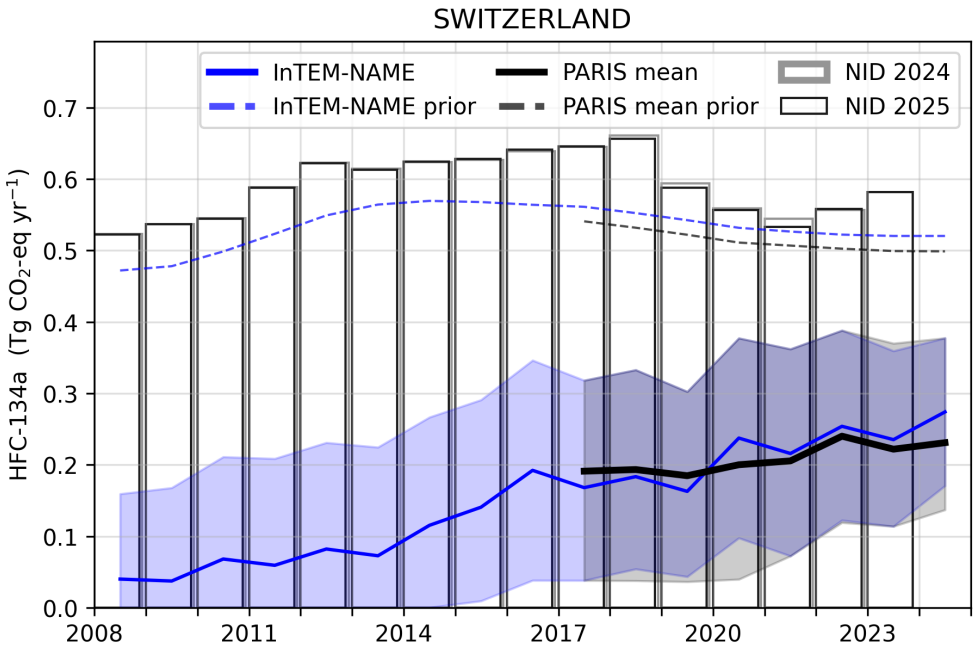

Figure 6.2.2: Spatial distribution of the Swiss average modelled emissions of HFC-134a during the period of 2020-2024 (mean from all models). Observing stations are marked with red circles and highly-populated cities are marked with red triangles.

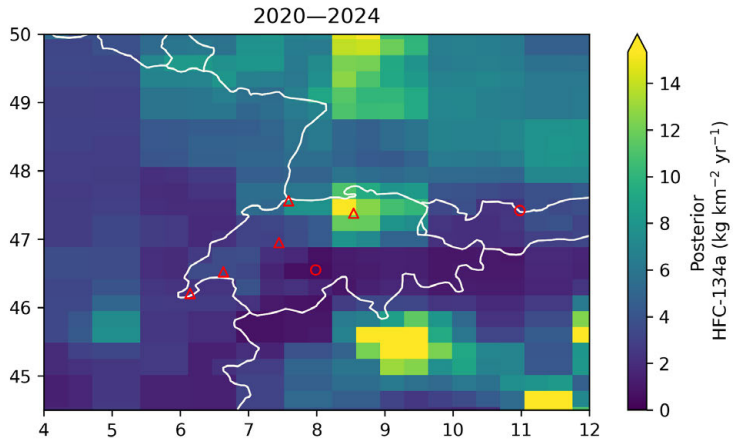

6.3 HFC-143a

Figure 6.3.1: Verification of the Swiss emissions inventory estimates for HFC-143a. Modelled annual emissions are given as the mean from all models (black line) and the individual result from InTEM-NAME (blue line). The shaded blue area is the 68 % confidence interval (CI) of InTEM-NAME and the shaded grey area encompasses the 68 % CI from all models. National inventory annual totals from 2024 and 2025 are given as grey and black bars, respectively.

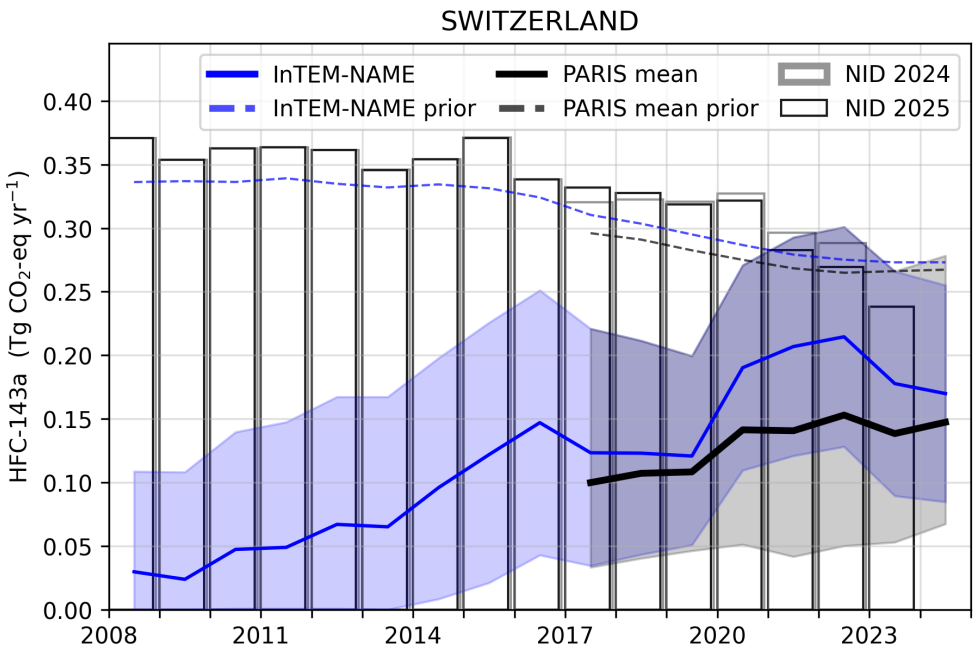

Figure 6.3.2: Spatial distribution of the Swiss average modelled emissions of HFC-143a during the period of 2020-2024 (mean from all models). Observing stations are marked with red circles and highly-populated cities are marked with red triangles.

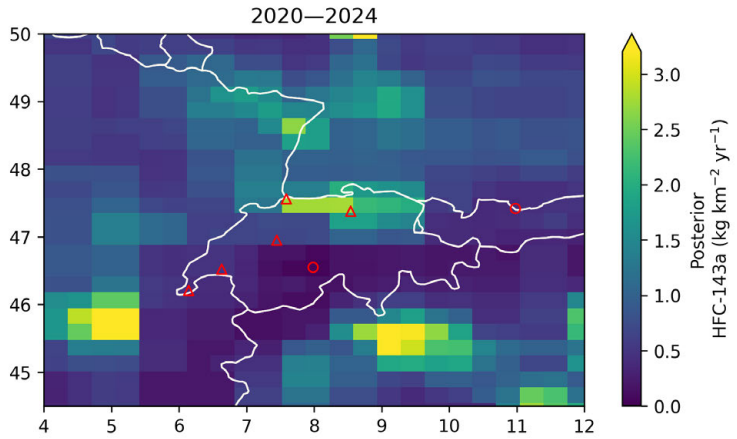

6.4 HFC-152a

Figure 6.4.1: Verification of the Swiss emissions inventory estimates for HFC-152a. Modelled annual emissions are given as the mean from all models (black line) and the individual result from InTEM-NAME (blue line). The shaded blue area is the 68 % confidence interval (CI) of InTEM-NAME and the shaded grey area encompasses the 68 % CI from all models. National inventory annual totals from 2024 and 2025 are given as grey and black bars, respectively.

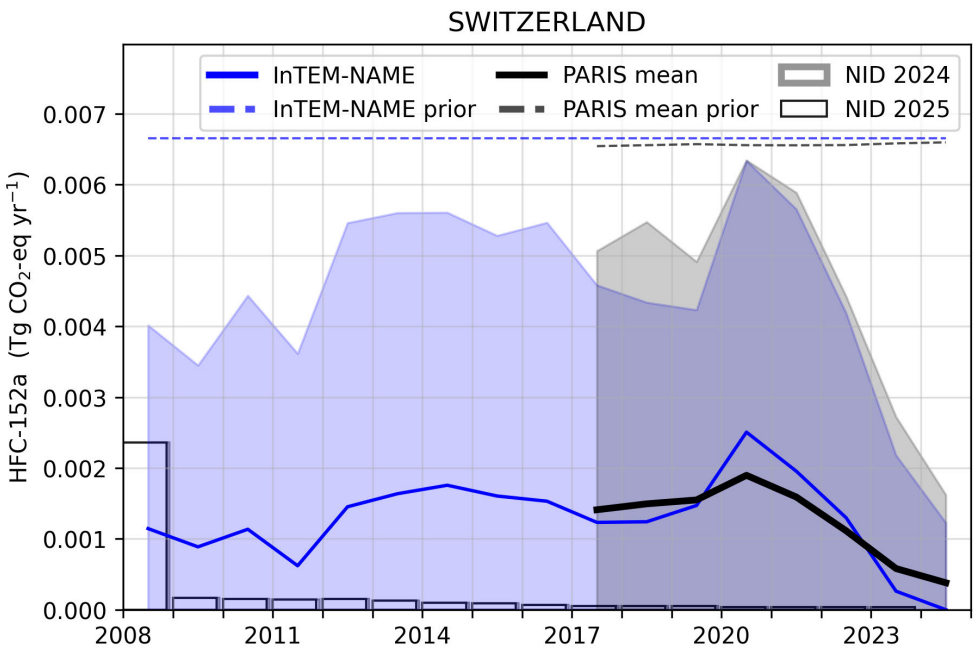

Figure 6.4.2: Spatial distribution of the Swiss average modelled emissions of HFC-152a during the period of 2020-2024 (mean from all models). Observing stations are marked with red circles and highly-populated cities are marked with red triangles.

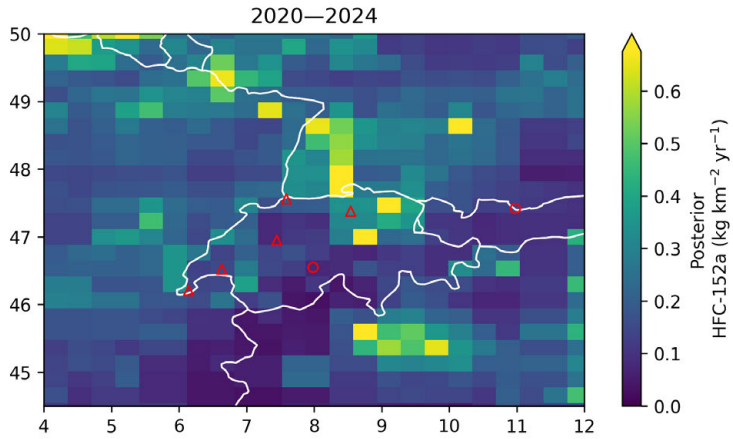

6.5 HFC-227ea

Figure 6.5.1: Verification of the Swiss emissions inventory estimates for HFC-227ea. Modelled annual emissions are given as the mean from all models (black line) and the individual result from InTEM-NAME (blue line). The shaded blue area is the 68 % confidence interval (CI) of InTEM-NAME and the shaded grey area encompasses the 68 % CI from all models. National inventory annual totals from 2024 and 2025 are given as grey and black bars, respectively.

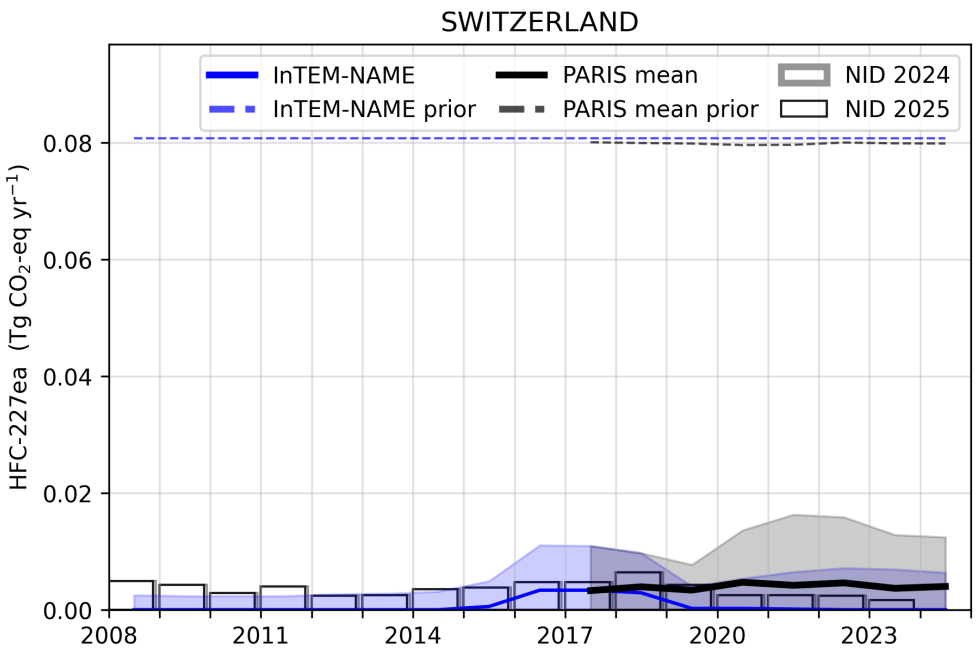

Figure 6.5.2: Spatial distribution of the Swiss average modelled emissions of HFC-227ea during the period of 2020-2024 (mean from all models). Observing stations are marked with red circles and highly-populated cities are marked with red triangles.

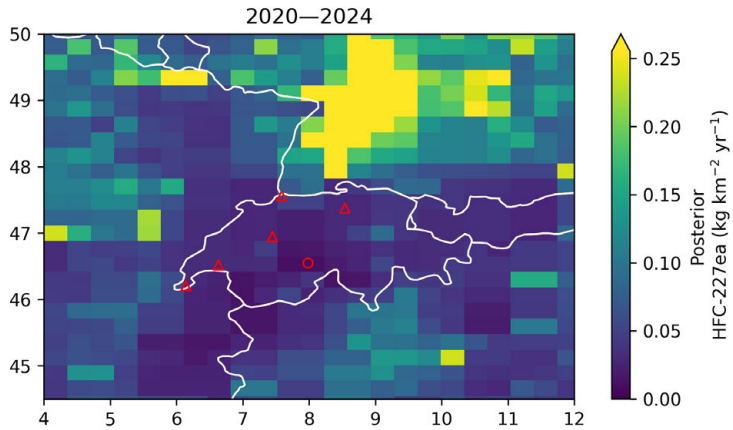

6.6 HFC-32

Figure 6.6.1: Verification of the Swiss emissions inventory estimates for HFC-32. Modelled annual emissions are given as the mean from all models (black line) and the individual result from InTEM-NAME (blue line). The shaded blue area is the 68 % confidence interval (CI) of InTEM-NAME and the shaded grey area encompasses the 68 % CI from all models. National inventory annual totals from 2024 and 2025 are given as grey and black bars, respectively.

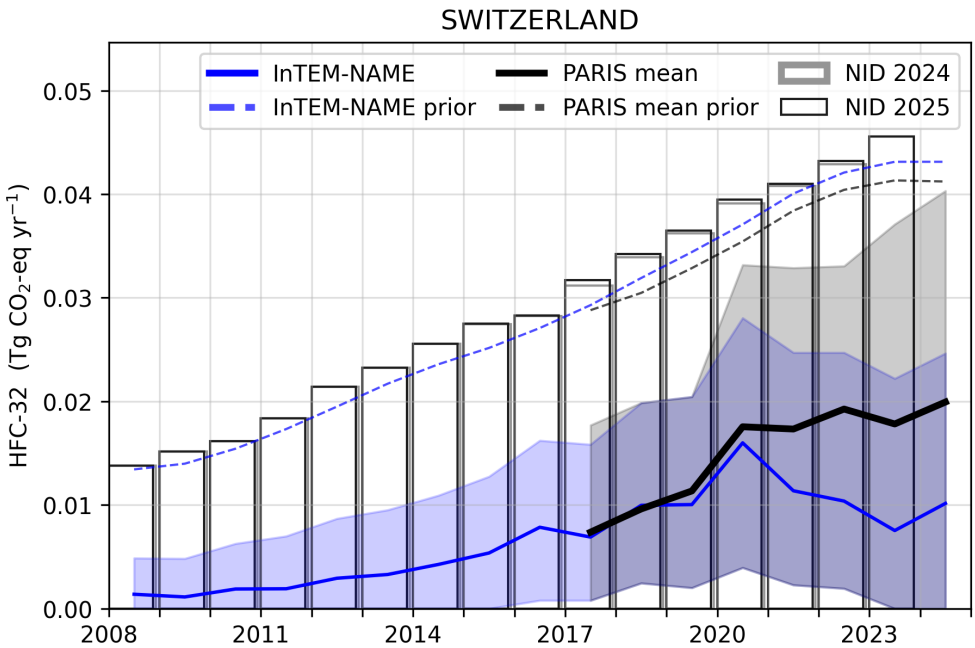

Figure 6.6.2: Spatial distribution of the Swiss average modelled emissions of HFC-32 during the period of 2020-2024 (mean from all models). Observing stations are marked with red circles and highly-populated cities are marked with red triangles.

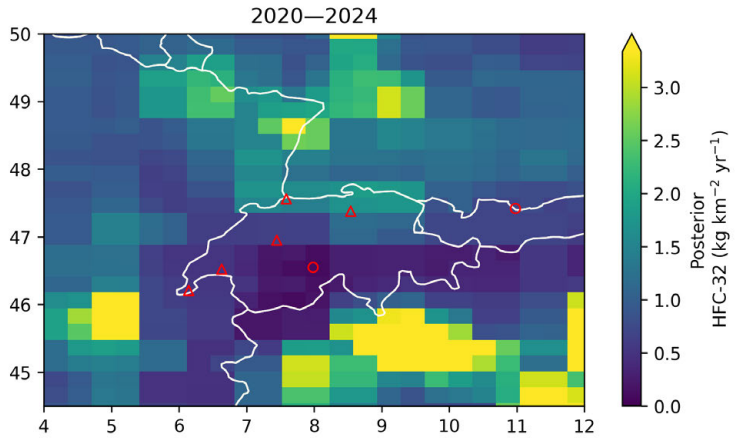

6.7 Total HFCs

Figure 6.7.1: Verification of the Swiss emissions inventory estimates for total HFCs. Modelled annual emissions are given as the mean from all models (black line) and the individual result from InTEM-NAME (blue line). The shaded blue area is the 68 % confidence interval (CI) of InTEM-NAME and the shaded grey area encompasses the 68 % CI from all models. National inventory annual totals from 2024 and 2025 are given as grey and black bars, respectively.

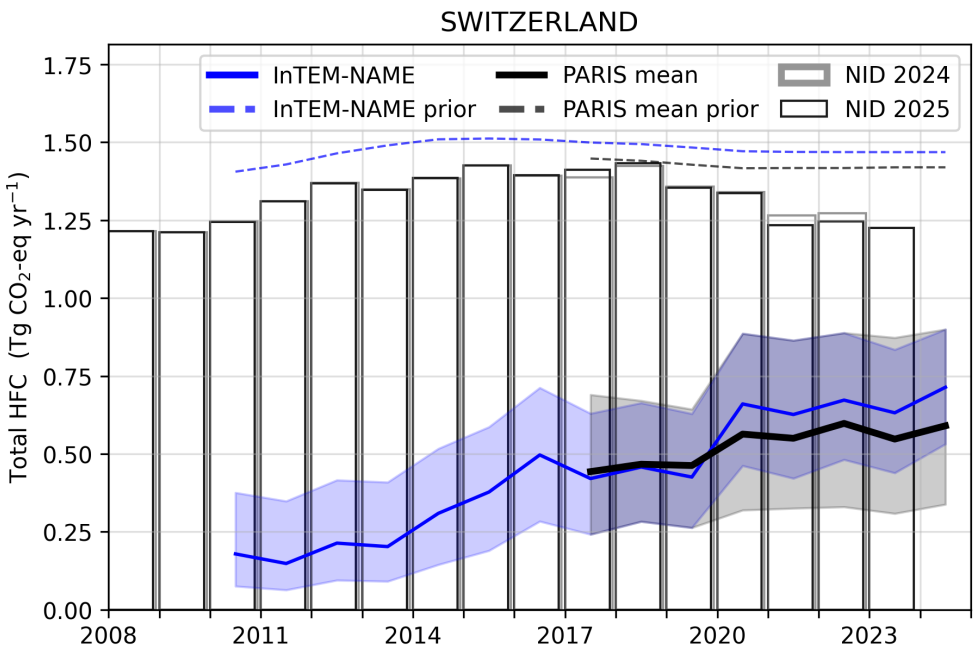

Table 2: Emissions estimation for HFCs according to the National Inventory Document (NID) 2025 and the inversions done in the PARIS project. For the PARIS estimation, the mean of all models is displayed, along with a range of uncertainty estimated via the half distance between the maximum and minimum uncertainties of the different models.

		2020	2021	2022	2023	2024
HFC-134a	NID 2025	0.56	0.53	0.56	0.58	
$(\mathrm{TgCO_2\text{-}eq \cdot yr^{-1}})$	PARIS mean	0.20 ± 0.17	0.21 ± 0.14	0.24 ± 0.13	0.22 ± 0.13	0.23 ± 0.12
HFC-125	NID 2025	0.40	0.37	0.36	0.35	
$(\mathrm{TgCO_2\text{-}eq \cdot yr^{-1}})$	PARIS mean	0.16 ± 0.12	0.15 ± 0.11	0.15 ± 0.11	0.13 ± 0.11	0.14 ± 0.11
HFC-143a	NID 2025	0.32	0.28	0.27	0.24	
$(\mathrm{TgCO_2\text{-}eq \cdot yr^{-1}})$	PARIS mean	0.14 ± 0.11	0.14 ± 0.13	0.15 ± 0.13	0.14 ± 0.11	0.15 ± 0.11
HFC-23	NID 2025	13	3	3	4	
$(\mathrm{GgCO_2\text{-}eq \cdot yr^{-1}})$	PARIS mean	29 ± 70	24 ± 68	21 ± 52	29 ± 61	40 ± 81
HFC-32	NID 2025	39	41	43	46	
$(\mathrm{GgCO_2\text{-}eq \cdot yr^{-1}})$	PARIS mean	18 ± 15	17 ± 15	19 ± 16	18 ± 19	20 ± 20
HFC-227ea	NID 2025	2.5	2.5	2.4	1.7	
$(\mathrm{GgCO_2\text{-}eq \cdot yr^{-1}})$	PARIS mean	4.7 ± 6.8	4.2 ± 8.2	4.6 ± 7.9	3.7 ± 6.4	4.0 ± 6.2
HFC-365mfc	NID 2025	5	4	11	8	
$(\mathrm{GgCO_2\text{-}eq \cdot yr^{-1}})$	PARIS mean	4 ± 7	3 ± 6	3 ± 5	1 ± 3	1 ± 2
HFC-4310mee	NID 2025	0.2	0.0	0.0	0.0	
$(\mathrm{GgCO_2\text{-}eq \cdot yr^{-1}})$	PARIS mean	1.8 ± 3.5	1.6 ± 3.5	1.4 ± 3.2	1.2 ± 2.8	1.2 ± 2.4
HFC-245fa	NID 2025	0.2	0.2	0.2	0.2	
$(\mathrm{GgCO_2\text{-}eq \cdot yr^{-1}})$	PARIS mean	2.1 ± 4.8	1.5 ± 3.4	1.5 ± 3.3	1.0 ± 1.7	1.1 ± 1.9
HFC-236fa	NID 2025	11	1	1	1	
$(\mathrm{GgCO_2\text{-}eq \cdot yr^{-1}})$	PARIS mean	2 ± 4	1 ± 3	1 ± 3	1 ± 3	1 ± 2
HFC-152a	NID 2025	0.0	0.0	0.0	0.0	
$(\mathrm{GgCO_2\text{-}eq \cdot yr^{-1}})$	PARIS mean	1.9 ± 3.2	1.6 ± 2.9	1.1 ± 2.2	0.6 ± 1.4	0.4 ± 0.8

7 Perfluorocarbons (PFCs)

7.1 PFC-14

Figure 7.1.1: Verification of the Swiss emissions inventory estimates for PFC-14. Modelled annual emissions are given as the mean from all models (black line) and the individual result from InTEM-NAME (blue line). The shaded blue area is the 68 % confidence interval (CI) of InTEM-NAME and the shaded grey area encompasses the 68 % CI from all models. National inventory annual totals from 2024 and 2025 are given as grey and black bars, respectively.

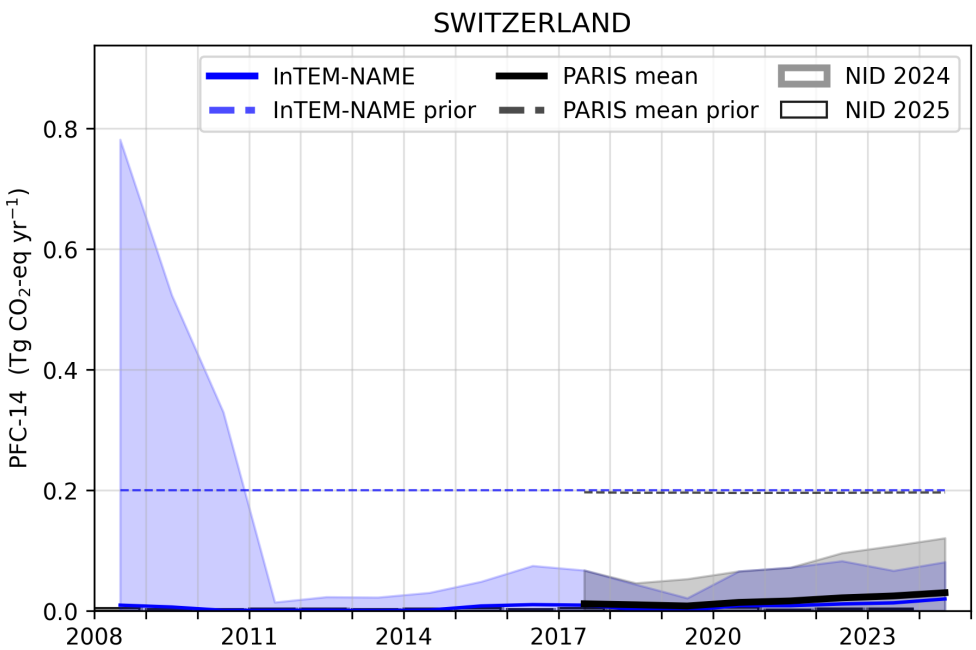

Figure 7.1.2: Spatial distribution of the Swiss average modelled emissions of PFC-14 during the period of 2020-2024 (mean from all models). Observing stations are marked with red circles and highly-populated cities are marked with red triangles.

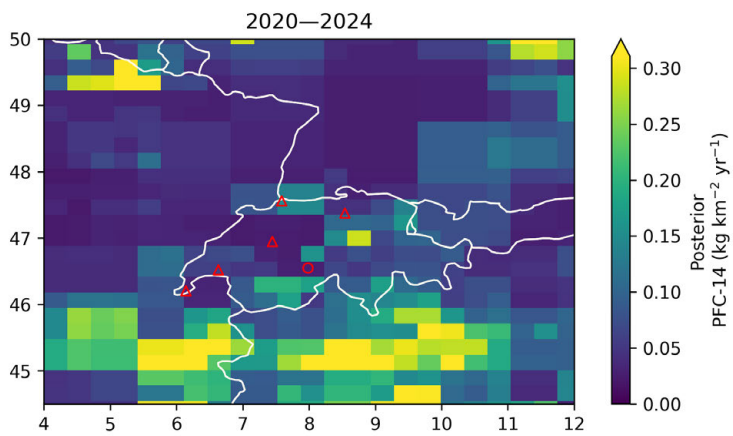

7.2 PFC-116

Figure 7.2.1: Verification of the Swiss emissions inventory estimates for PFC-116. Modelled annual emissions are given as the mean from all models (black line) and the individual result from InTEM-NAME (blue line). The shaded blue area is the 68 % confidence interval (CI) of InTEM-NAME and the shaded grey area encompasses the 68 % CI from all models. National inventory annual totals from 2024 and 2025 are given as grey and black bars, respectively.

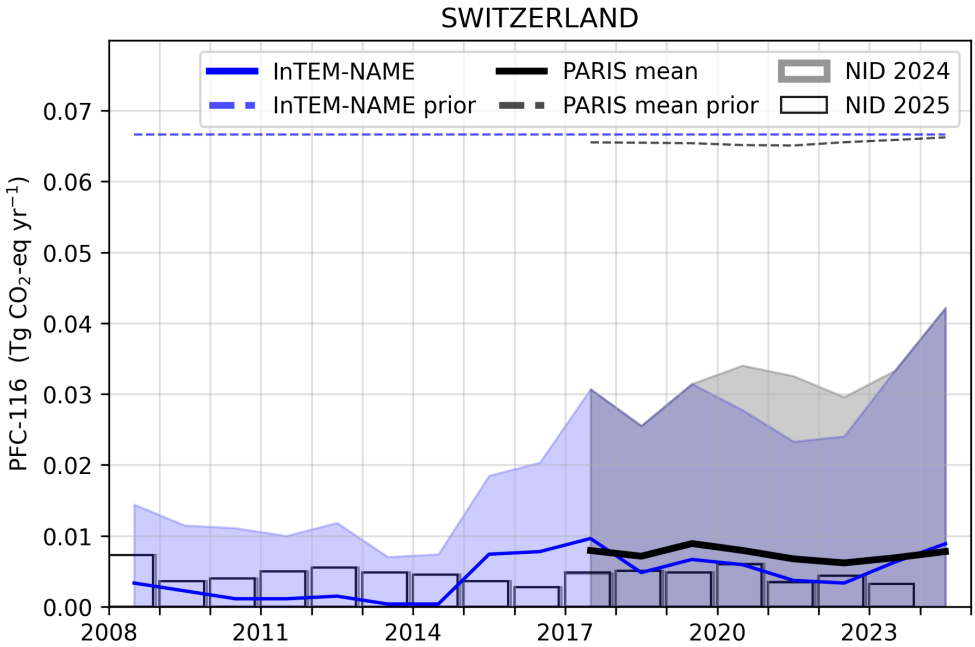

Figure 7.2.2: Spatial distribution of the Swiss average modelled emissions of PFC-116 during the period of 2020-2024 (mean from all models). Observing stations are marked with red circles and highly-populated cities are marked with red triangles.

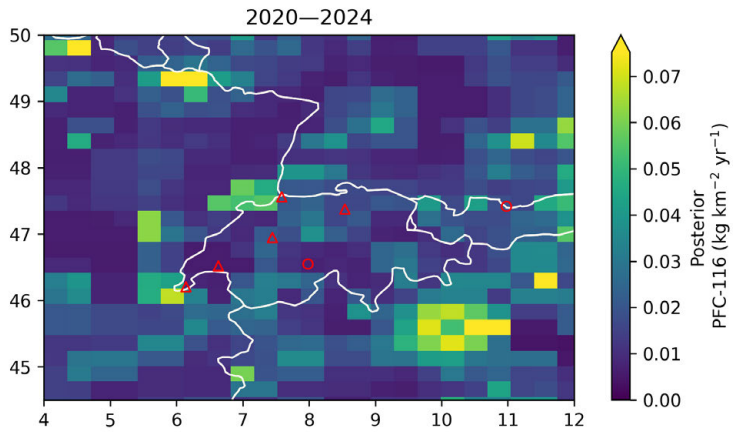

7.3 PFC-218

Figure 7.3.1: Verification of the Swiss emissions inventory estimates for PFC-218. Modelled annual emissions are given as the mean from all models (black line) and the individual result from InTEM-NAME (blue line). The shaded blue area is the 68 % confidence interval (CI) of InTEM-NAME and the shaded grey area encompasses the 68 % CI from all models. National inventory annual totals from 2024 and 2025 are given as grey and black bars, respectively.

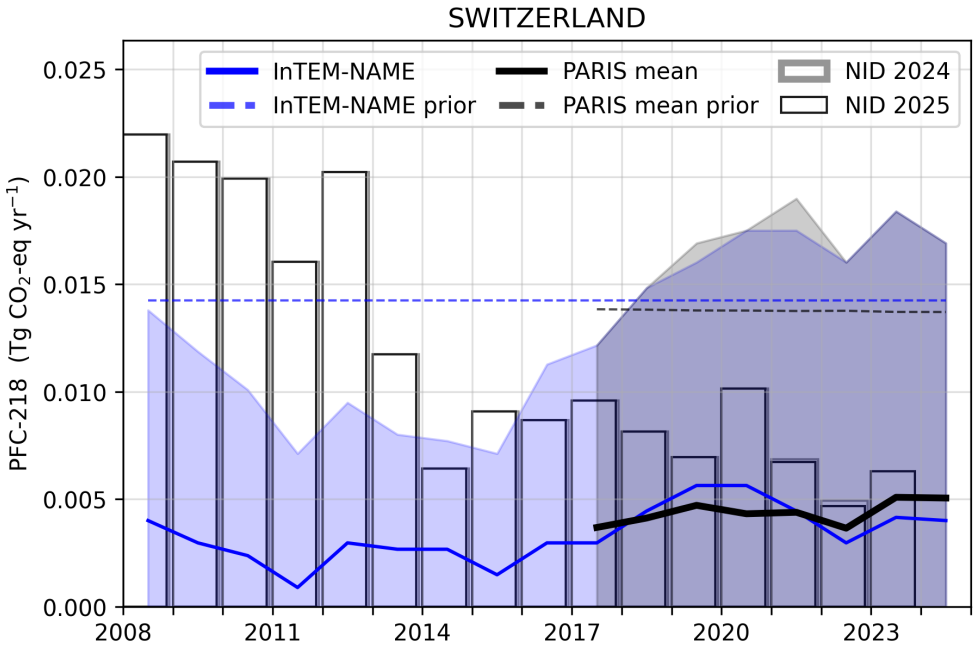

Figure 7.3.2: Spatial distribution of the Swiss average modelled emissions of PFC-218 during the period of 2020-2024 (mean from all models). Observing stations are marked with red circles and highly-populated cities are marked with red triangles.

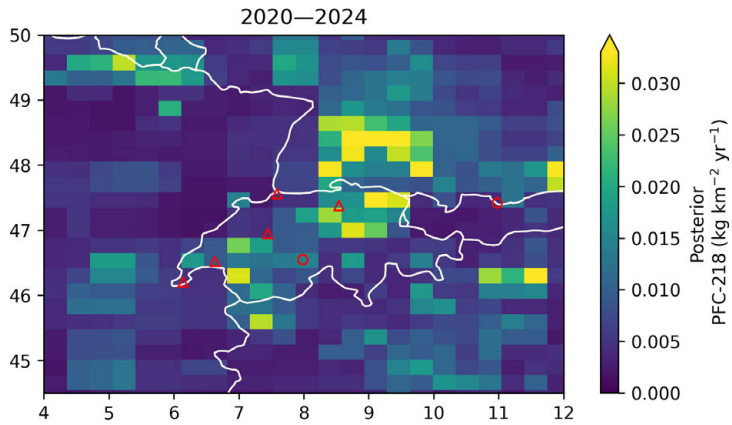

7.4 PFC-318

Figure 7.4.1: Verification of the Swiss emissions inventory estimates for PFC-318. Modelled annual emissions are given as the mean from all models (black line) and the individual result from InTEM-NAME (blue line). The shaded blue area is the 68 % confidence interval (CI) of InTEM-NAME and the shaded grey area encompasses the 68 % CI from all models. National inventory annual totals from 2024 and 2025 are given as grey and black bars, respectively.

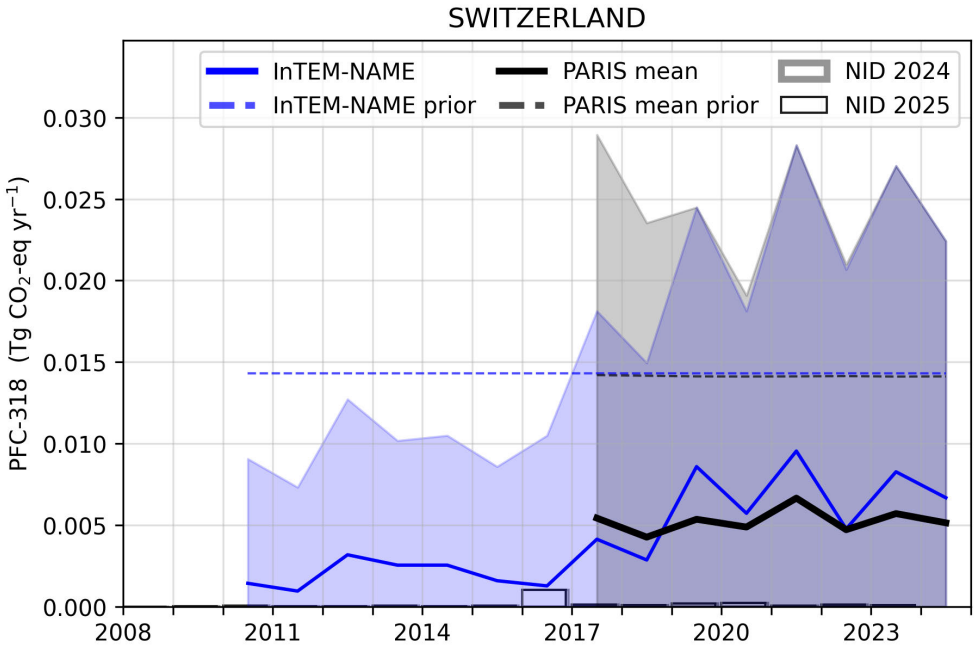

Figure 7.4.2: Spatial distribution of the Swiss average modelled emissions of PFC-318 during the period of 2020-2024 (mean from all models). Observing stations are marked with red circles and highly-populated cities are marked with red triangles.

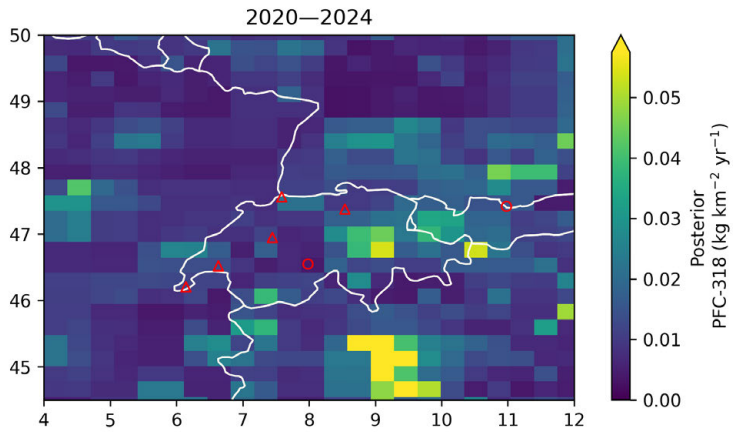

7.5 Total PFCs

Figure 7.5.1: Verification of the Swiss emissions inventory estimates for total PFCs. Modelled annual emissions are given as the mean from all models (black line) and the individual result from InTEM-NAME (blue line). The shaded blue area is the 68 % confidence interval (CI) of InTEM-NAME and the shaded grey area encompasses the 68 % CI from all models. National inventory annual totals from 2024 and 2025 are given as grey and black bars, respectively.

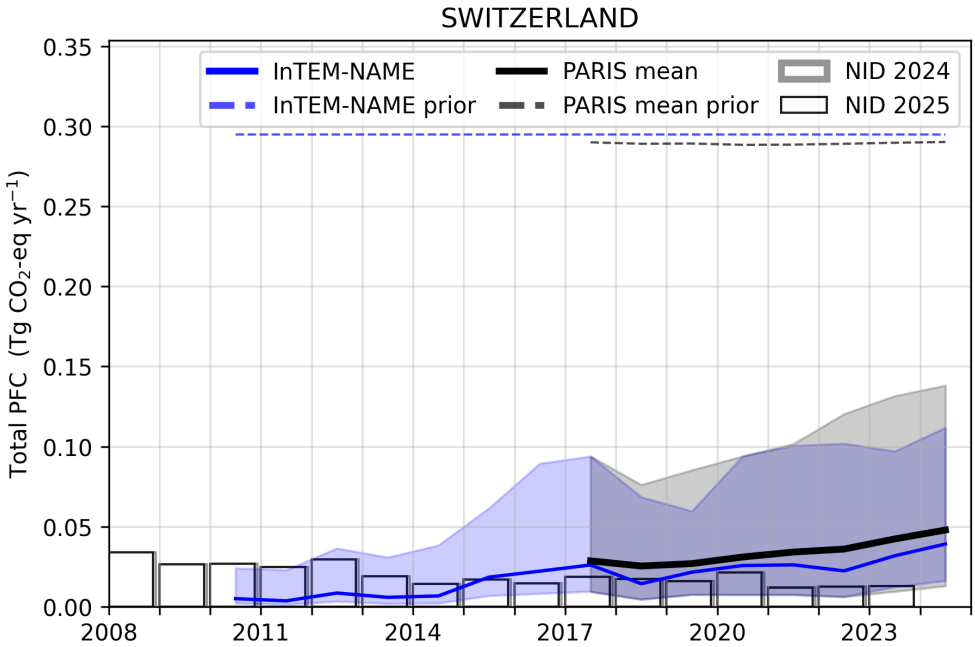

Table 3: Emissions estimation for PFCs according to the National Inventory Document (NID) 2025 and the inversions done in the PARIS project. For the PARIS estimation, the mean of all models is displayed, along with a range of uncertainty estimated via the half distance between the maximum and minimum uncertainties of the different models.

		2020	2021	2022	2023	2024
PFC-14	NID 2025	5	2	3	3	
$(\mathrm{GgCO_2\text{-}eq} \cdot \mathrm{yr}^{-1})$	PARIS mean	14 ± 33	16 ± 36	21 ± 48	25 ± 54	30 ± 60
PFC-116	NID 2025	6.0	3.5	4.3	3.2	
$(\mathrm{GgCO_2\text{-}eq} \cdot \mathrm{yr}^{-1})$	PARIS mean	7.9 ± 17.0	6.7 ± 16.3	6.2 ± 14.8	6.9 ± 16.7	7.8 ± 21.1
PFC-318	NID 2025	0.2	0.1	0.1	0.1	
$(\mathrm{GgCO_2\text{-}eq} \cdot \mathrm{yr}^{-1})$	PARIS mean	4.9 ± 9.5	6.7 ± 14.2	4.7 ± 10.5	5.7 ± 13.5	5.1 ± 11.2
PFC-218	NID 2025	10	7	5	6	
$(\mathrm{GgCO_2\text{-}eq} \cdot \mathrm{yr}^{-1})$	PARIS mean	4 ± 9	4 ± 9	4 ± 8	5 ± 9	5 ± 8

8 Sulphur hexafluoride (SF_6)

Figure 8.0.1: Total source sensitivity of SF_6 observing sites as calculated by the FLEXPART transport model for the year 2018 (left) and 2024 (right) and used in the inversions. Observing stations active in each year are marked with red dots. Areas with visible land surface represent regions for which emissions can be observed well from the network. Shaded or dark areas represent regions for which limited emission information can be obtained from the network.

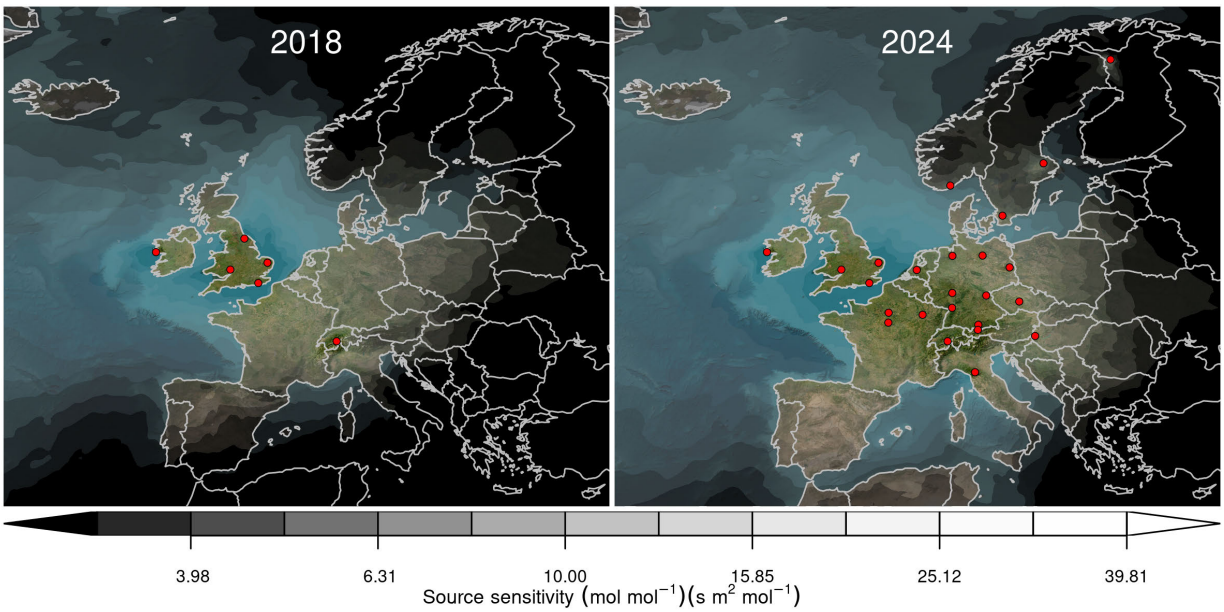

Figure 8.0.2: Verification of the Swiss emissions inventory estimates for SF_6. Modelled annual emissions are given as the mean from all InTEM and ELRIS inversions (black line) and the individual result from InTEM-NAME (blue line). The shaded blue area is the 68 % confidence interval (CI) of InTEM-NAME and the shaded grey area encompasses the 68 % CI from all models. National inventory annual totals from 2024 and 2025 are given as grey and black bars, respectively.

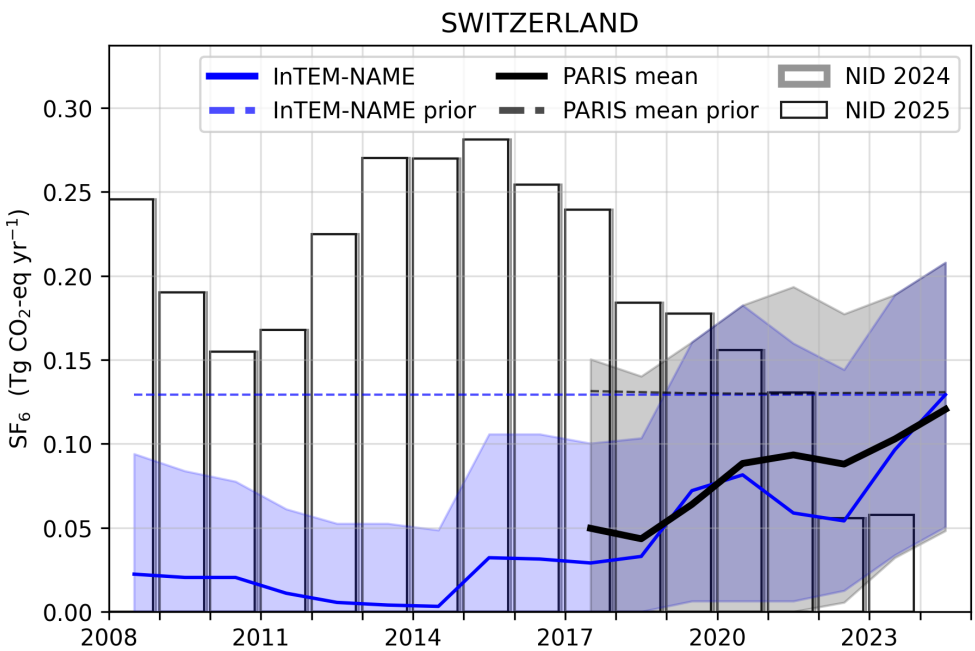

Figure 8.0.3: Spatial distribution of the Swiss average modelled emissions of SF_6 during the period of 2020-2024 (mean from all InTEM and ELRIS inversions). Observing stations are marked with red circles and highly-populated cities are marked with red triangles.

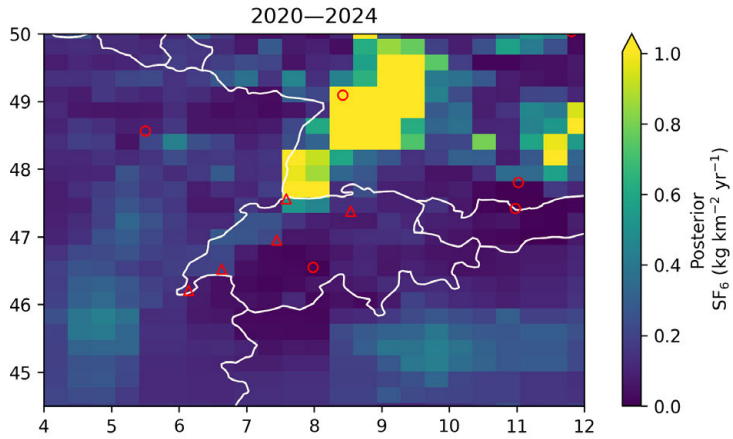

9 Carbon Dioxide (CO_2)

Measurements of CO_2 at ICOS sites and related observatories are influenced by a complex combination of sources and sinks. Fossil fuel combustion for transport, heating, energy generation, and other applications produce CO_2, along with other anthropogenic activities such as cement production. The terrestrial and oceanic biosphere produces CO_2 through animal and plant respiration and takes up CO_2 through photosynthesis. Furthermore, CO_2 is exchanged with the ocean through physical and chemical processes.

When considering high-frequency (∼hourly) CO_2 mole fraction deviations from baseline values—used to infer national emissions in regional inverse modelling studies—the influence of biospheric fluxes can be comparable to, or larger than, those of anthropogenic sources (e.g. White et al., 2019). Therefore, research is under way to develop new tracers that can determine fossil fuel CO_2 fluxes independent of biosphere sources and sinks.

Ongoing Horizon Europe projects PARIS and CORSO are examining methods for estimating fossil fuel CO_2 fluxes based on simultaneous measurements of CO_2 and O_2 (Figure 9.0.1). The method relies on the fact that CO_2 and O_2 are inter-converted during combustion and terrestrial biosphere exchange, but with different ratios for the two processes. A quantity can be constructed from these measurements, known as Atmospheric Potential Oxygen (APO), which is insensitive to biosphere fluxes, and may therefore be useful for isolating fossil fuel signals (Pickers et al., 2022).

High-frequency (∼hourly) timeseries of APO are available from Weybourne (WAO, 2010 – present) and Heathfield (HFD, 2021 - present) in the UK (Figure 9.0.1; Pickers, Adcock, and Manning, 2024), and new sites are being established at Cabauw and Zweth in the Netherlands. Preliminary analyses of the WAO data have revealed regional APO trends consistent with the drop in fossil fuel CO_2 emissions during the COVID lockdowns in the UK (Pickers et al., 2022). However, quantification of absolute regional fossil fuel CO_2 emissions remains an area of active research. Recent studies have derived fossil fuel CO_2 emissions for the UK that are highly uncertain (Rigby et al., 2025). Potential confounding factors were identified in Chawner et al. (2024), such as highly uncertain APO fluxes from the ocean, and a poorly constrained regional APO background. These factors are the subject of ongoing research using atmospheric models and new APO measurements from PARIS, CORSO and ICOS.

An alternative method for top-down fossil fuel CO_2 emissions evaluation uses measurements of radiocarbon isotopologues ($^{14}CO_2$, compared to the dominant $^{12}CO_2$). Fossil fuels do not contain ^{14}C, and therefore, their combustion tends to decrease the atmospheric $^{14}CO_2/^{12}CO_2$ ratio. Currently, radiocarbon measurements can only be made at low frequency using flask sampling. However, a relatively intensive flask sampling campaign was carried out across Europe during 2024 as part of CORSO, and the results of this

study will be reported on soon.

Figure 9.0.1: Carbon dioxide (top, red) and oxygen (bottom, blue) measurements from Weybourne Atmospheric Observatory in the UK, available from the ICOS Carbon Portal (Adcock et al., 2024).

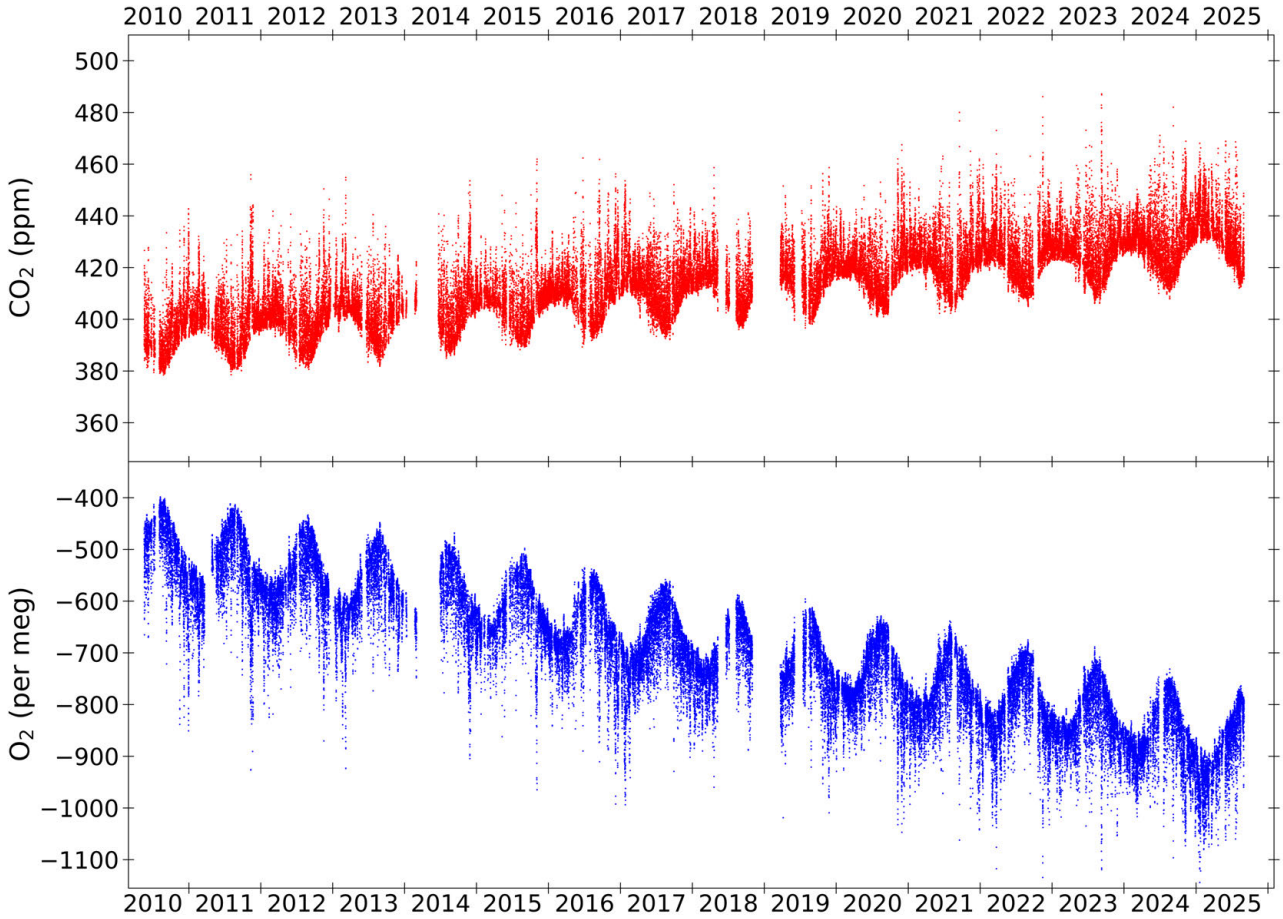

References

Adcock, Karina et al. (2024). *Atmospheric GHG data product (o2, o2_stdev, co2, co2_stdev) from Weybourne (10.0 m), 2010-05-19–2023-12-31*. URL: https://hdl.handle.net/11676/j4LzdHQiq3fPgfNeXHruC0Bb.

Chawner, Hannah et al. (Apr. 2024). "Atmospheric oxygen as a tracer for fossil fuel carbon dioxide: a sensitivity study in the UK". en. In: *Atmospheric Chemistry and Physics* 24.7, pp. 4231–4252. ISSN: 1680-7324. DOI: 10.5194/acp-24-4231-2024. URL: https://acp.copernicus.org/articles/24/4231/2024/ (visited on 04/10/2024).

European Commission: Joint Research, Centre et al. (2023). *GHG emissions of all world countries – 2023*. Publications Office of the European Union. DOI: 10.2760/953322.

Ganesan, A. L. et al. (2014). "Characterization of uncertainties in atmospheric trace gas inversions using hierarchical Bayesian methods". In: *Atmospheric Chemistry and Physics* 14.8, pp. 3855–3864. DOI: 10.5194/acp-14-3855-2014. URL: http://www.atmos-chem-phys.net/14/3855/2014/http://www.atmos-chem-phys.net/14/3855/2014/acp-14-3855-2014.pdf.

Ganesan, A. L. et al. (2015). "Quantifying methane and nitrous oxide emissions from the UK and Ireland using a national-scale monitoring network". In: *Atmos. Chem. Phys.* 15.11, pp. 6393–6406. DOI: 10.5194/acp-15-6393-2015. URL: https://www.atmos-chem-phys.net/15/6393/2015/https://www.atmos-chem-phys.net/15/6393/2015/acp-15-6393-2015.pdf.

Henne, S. et al. (2016). "Validation of the Swiss methane emission inventory by atmospheric observations and inverse modelling". In: *Atmospheric Chemistry and Physics* 16.6, pp. 3683–3710. DOI: 10.5194/acp-16-3683-2016. URL: http://www.atmos-chem-phys.net/16/3683/2016/.

Jones, A.R. et al. (2007). "The U.K. Met Office's next-generation atmospheric dispersion model, NAME III, in Borrego C. and Norman A.-L. (Eds)". In: *Air Pollution Modeling and its Application XVII (Proceedings of the 27th NATO/CCMS International Technical Meeting on Air Pollution Modelling and its Application), Springer*, pp. 580–589.

Katharopoulos, I. et al. (2023). "Impact of transport model resolution and a priori assumptions on inverse modeling of Swiss F-gas emissions". In: *Atmos. Chem. Phys.* 23.22, pp. 14159–14186. DOI: 10.5194/acp-23-14159-2023. URL: https://acp.copernicus.org/articles/23/14159/2023/.

Manning, A. J. et al. (2021). "Evidence of a recent decline in UK emissions of hydrofluorocarbons determined by the InTEM inverse model and atmospheric measurements". In: *Atmospheric Chemistry and Physics* 21.16, pp. 12739–12755. DOI: 10.5194/acp-21-12739-2021. URL: https://acp.copernicus.org/articles/21/12739/2021/.

Pickers, P., K. Adcock, and A. Manning (Feb. 2024). *Atmospheric oxygen and carbon dioxide observations from Weybourne Atmospheric Observatory, Norfolk, UK uploaded to public archives*. Tech. rep. Process Attribution of Regional Emissions (PARIS). URL: https://horizoneurope-paris.eu/wp-content/uploads/sites/914/2024/07/PARIS-deliverables-D6.1-High-frequency-APO-data-uploaded-final.pdf.

Pickers, Penelope A. et al. (Apr. 2022). "Novel quantification of regional fossil fuel CO2 reductions during COVID-19 lockdowns using atmospheric oxygen measurements". en. In: *Science Advances* 8.16, eabl9250. ISSN: 2375-2548. DOI: 10.1126/sciadv.abl9250. URL: https://www.science.org/doi/10.1126/sciadv.abl9250 (visited on 12/01/2023).

Rigby, M. et al. (2019). "Increase in CFC-11 emissions from eastern China based on atmospheric observations". In: *Nature* 569, pp. 546–550. DOI: 10.1038/s41586-019-1193-4. URL: https://doi.org/10.1038/s41586-019-1193-4.

Rigby, M. et al. (Apr. 2025). *Inverse estimates of fossil fuel CO2 emission*. Tech. rep. Process Attribution of Regional Emissions (PARIS). URL: https://horizoneurope-paris.eu/wp-content/uploads/sites/914/2025/01/PARIS-M24-Inverse-estimates-of-fossil-fuel-CO2-emissions-final.pdf.

Stohl, A. et al. (2005). "Technical note: The Lagrangian particle dispersion model FLEXPART version 6.2". In: *Atmospheric Chemistry and Physics* 5, pp. 2461–2474. DOI: 10.5194/acp-5-2461-2005. URL: <GotoISI>://000231983600002.

White, Emily D. et al. (Apr. 2019). "Quantifying the UK's carbon dioxide flux: an atmospheric inverse modelling approach using a regional measurement network". en. In: *Atmospheric Chemistry and Physics*

19.7, pp. 4345–4365. ISSN: 1680-7324. DOI: 10.5194/acp-19-4345-2019. URL: https://www.atmos-chem-phys.net/19/4345/2019/ (visited on 04/05/2019).

Draft Inventory Annex
UK 2025

30th October, 2025

1 Introduction

In this document, global concentration trends and national emissions estimates derived from atmospheric observations ("inverse estimates") are presented for most reported gases. Comparing the emissions submitted in national inventories with those calculated using atmospheric observations allows for emissions to be assessed using two fundamentally different approaches. Substantial differences can highlight areas that could warrant further investigation.

Global concentration trends for each gas are first shown using annual average concentrations from Mace Head, Ireland (Northern Hemisphere) and Kennaook/Cape Grim, Tasmania, Australia (Southern Hemisphere). Data from these stations were selected to exclude regionally-polluted air masses and therefore represents northern and southern hemispheric concentration trends. Mace Head observations were supported by the National Aeronautics and Space Administration (NASA) and the UK Department of Energy, Security and Net Zero (DESNZ), and Kennaook/Cape Grim observations by NASA and the Australian Bureau of Meteorology.

Observations of European concentrations of greenhouse gases used to derive national inverse emission estimates were collected from many different networks and providers. Methane and nitrous oxide concentrations originated from the European ICOS (Integrated Carbon Observation System) network, the UK DECC (Deriving Emissions related to Climate Change) network and other national or individual initiatives. F-gas observations were made by affiliates of the AGAGE (Advanced Global Atmospheric Gases Experiment) network. Observations from additional stations across Europe were supported by the Horizon-EU PARIS (Process Attribution of Regional Emissions) project. The observation stations used to derive emissions for each gas are shown in the corresponding sections of this document.

An atmospheric transport model provides the link between surface fluxes and concentrations measured at the observing stations. If not otherwise mentioned, inversion-based emissions estimates were derived using two atmospheric transport models combined with three inverse models, yielding a total of six inversions. This ensemble of six inversions allows us to better quantify the uncertainties associated with inverse modelling.

The two atmospheric transport models used are the Numerical Atmospheric dispersion Modelling Environment (NAME, Jones et al., 2007), and the FLEXible PARTicle dispersion model (FLEXPART, Stohl et al., 2005). Both models are backwards-running Lagrangian Particle Dispersion Models (LPDMs) that simulate the recent transport of air to each observing station. The two LPDMs have been widely used in the estimation of greenhouse gas emissions (Ganesan et al., 2015; Rigby et al., 2019; Manning et al., 2021; Henne et al., 2016).

The three inverse methods used are InTEM (Inversion Technique for Emission Modelling, Manning et al., 2021), ELRIS (Empa Lagrangian Regional Inversion System, Henne et al., 2016; Katharopoulos et al., 2023), and RHIME (Regional Hierarchical Inverse Modelling Environment, Ganesan et al., 2014). All three inverse methods estimate emissions within Europe along with boundary conditions that account for the concentration of the air entering Europe. All three systems started from the same set of a priori emissions that were either derived from the global EDGAR emission inventory (version 8, European Commission: Joint Research et al., 2023) or a uniform land-based emission, depending on the gas. A natural emission component, from the WETCHARTS product, was included in the methane prior. The same observational dataset was used by each inverse model, but data selection (i.e., filtering datasets for specific conditions) and treatment of uncertainties were chosen separately and hence differ. The three methods also differ in their statistical approaches for estimating emissions.

Emission estimates are presented for the period 2008-2024. Emissions for the full 2008-2024 period were derived with the InTEM-NAME inversion only, while emissions from 2017-2024 are presented as the mean of the six inversions (denoted the "PARIS mean"). The uncertainty shown is the minimum/maximum of the uncertainties in the ensemble.

All inversions employed a resolution of one month for CH_4 and N_2O and 1-year for the fluorinated gases. The inversion results used to compare with the inventories are a one-year calendar average for CH_4 and N_2O and the yearly value derived from a 3-year moving average for the fluorinated gases. For the 2008-2024

InTEM-NAME results, a 3-year moving average was also applied to the annualised CH_4 and N_2O results due to lack of observational coverage in the earlier years.

2 Global Concentration Trends

2.1 Methane (CH_4)

Figure 2.1.1: Background Northern Hemisphere monthly concentrations of CH_4 estimated from MHD, Ireland observations are shown in red, and background Southern Hemisphere monthly concentrations from CGO, Tasmania are shown in blue. Grey shading represents provisional data.

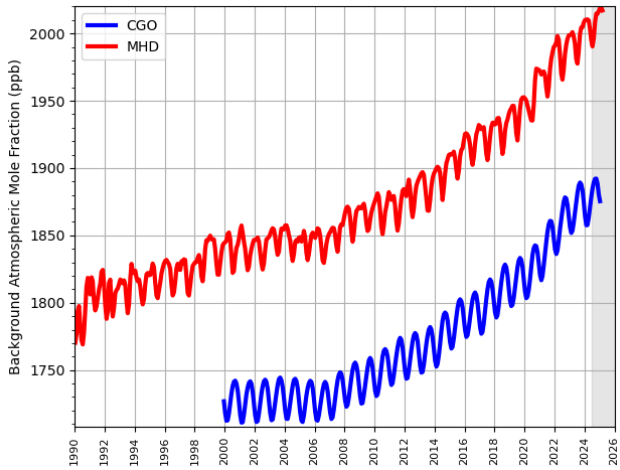

2.2 Nitrous Oxide (N_2O)

Figure 2.2.1: Background Northern Hemisphere monthly concentrations of N_2O estimated from MHD, Ireland observations are shown in red, and background Southern Hemisphere monthly concentrations from CGO, Tasmania are shown in blue. Grey shading represents provisional data.

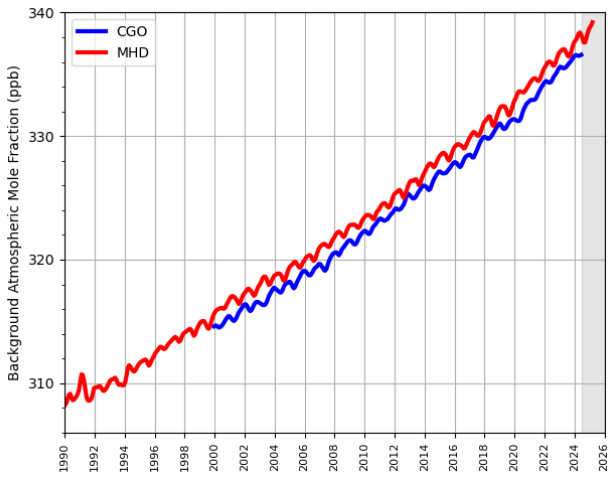

2.3 Hydrofluorocarbons (HFCs)

Figure 2.3.1: Background Northern Hemisphere monthly concentrations of six HFCs estimated from MHD, Ireland observations are shown in red, and background Southern Hemisphere monthly concentrations from CGO, Tasmania are shown in blue. Grey shading represents provisional data.

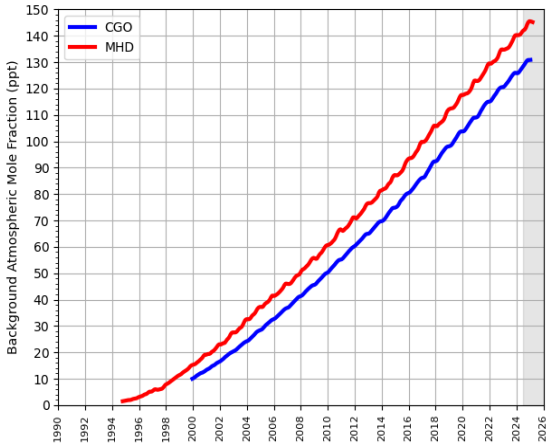

(a) HFC-134a

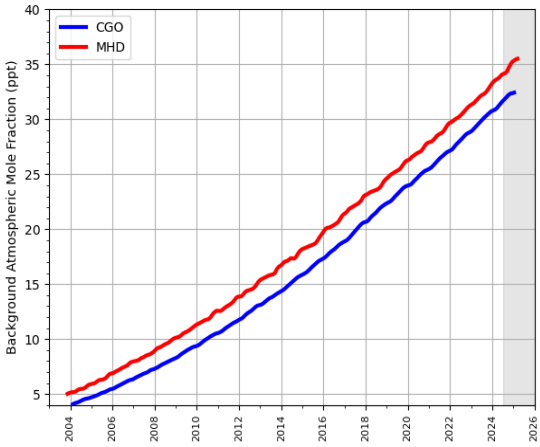

(b) HFC-143a

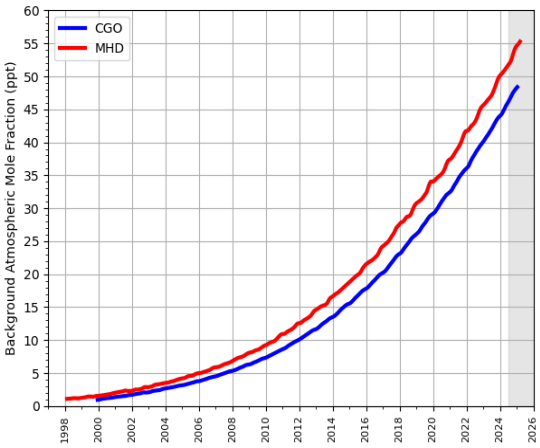

(c) HFC-125

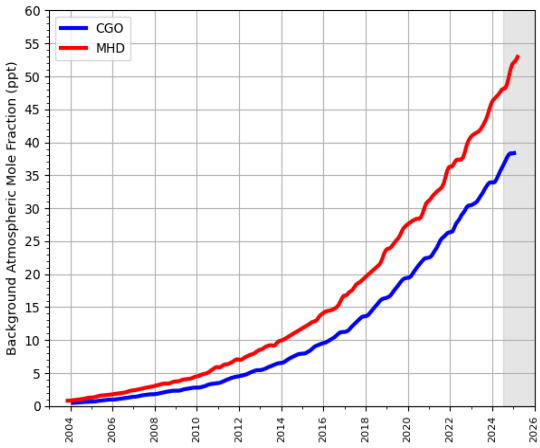

(d) HFC-32

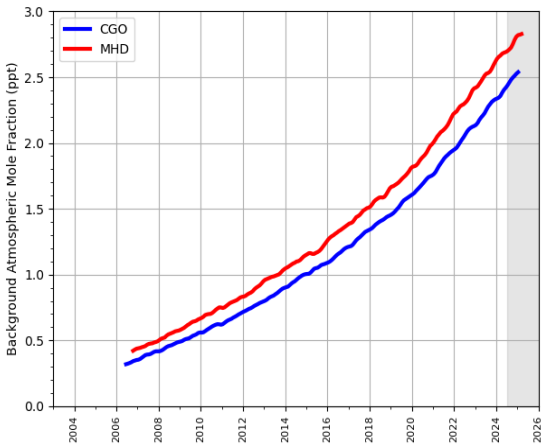

(e) HFC-227ea

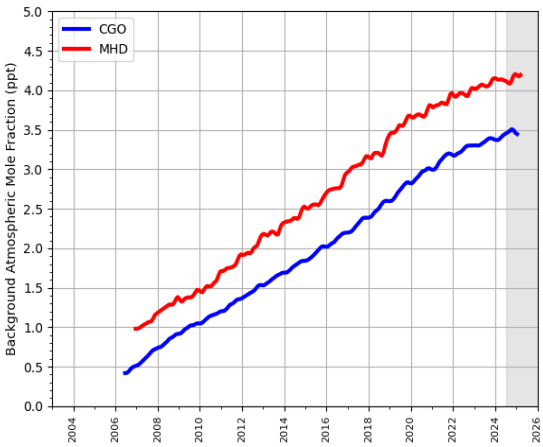

(f) HFC-245fa

Figure 2.3.2: Background Northern Hemisphere monthly concentrations of four HFCs estimated from MHD, Ireland observations are shown in red, and background Southern Hemisphere monthly concentrations from CGO, Tasmania are shown in blue. Grey shading represents provisional data.

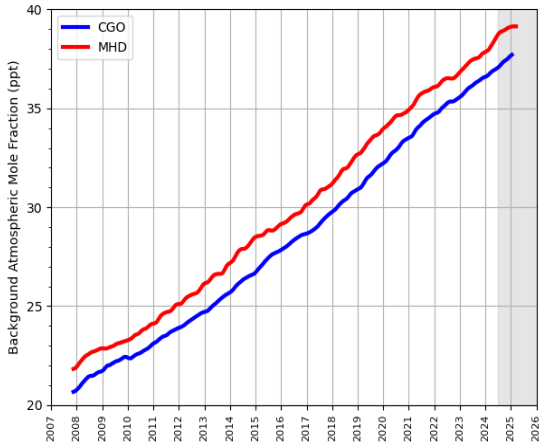

(a) HFC-23

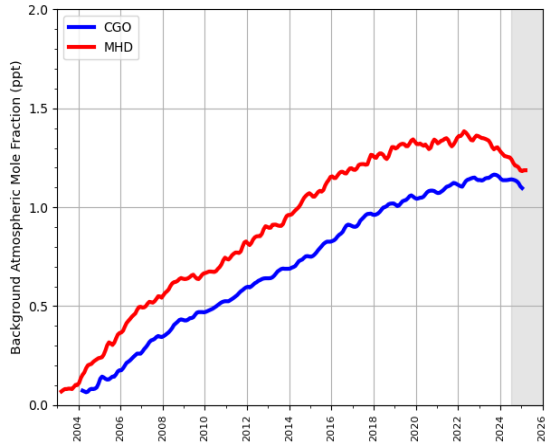

(b) HFC-365mfc

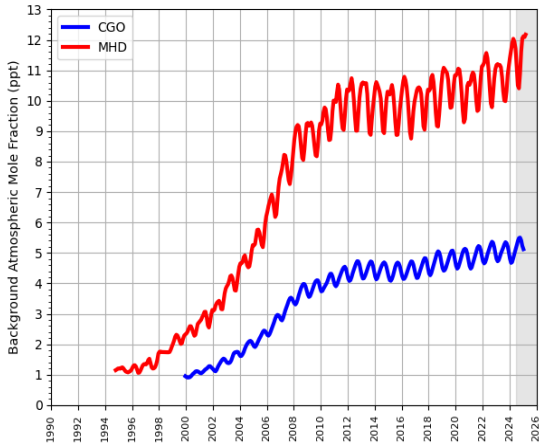

(c) HFC-152a

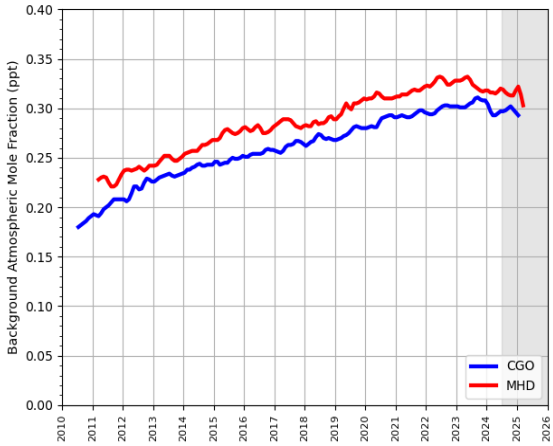

(d) HFC-43-10-mee

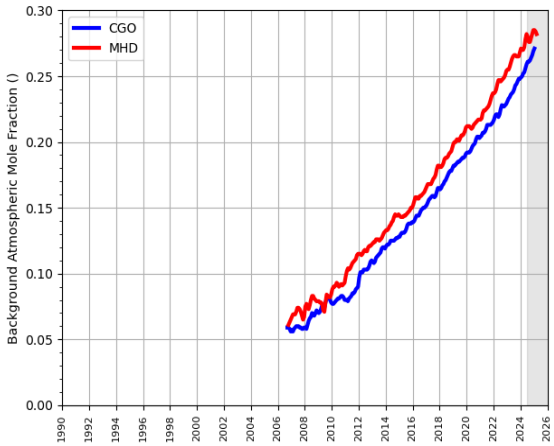

(e) HFC-236fa

2.4 Perfluorocarbons (PFCs)

Figure 2.4.1: Background Northern Hemisphere monthly concentrations of four PFCs estimated from MHD, Ireland observations are shown in red, and background Southern Hemisphere monthly concentrations from CGO, Tasmania are shown in blue. Grey shading represents provisional data.

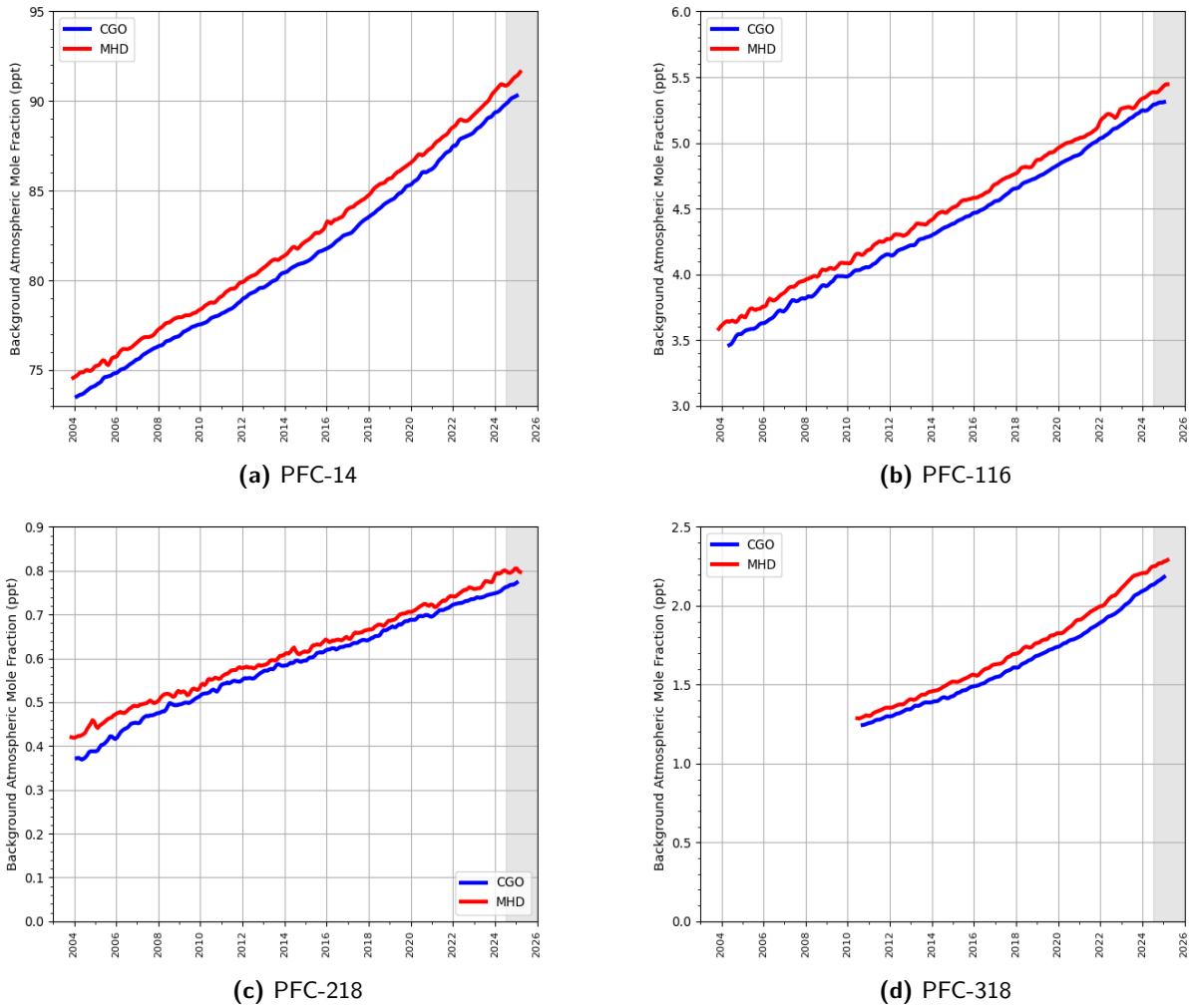

(a) PFC-14 **(b)** PFC-116 **(c)** PFC-218 **(d)** PFC-318

2.5 Sulphur Hexafluoride (SF_6) and Nitrogen Trifluoride (NF_3)

Figure 2.5.1: Background Northern Hemisphere monthly concentrations of SF_6 and NF_3 estimated from MHD, Ireland observations are shown in red, and background Southern Hemisphere monthly concentrations from CGO, Tasmania are shown in blue. Grey shading represents provisional data.

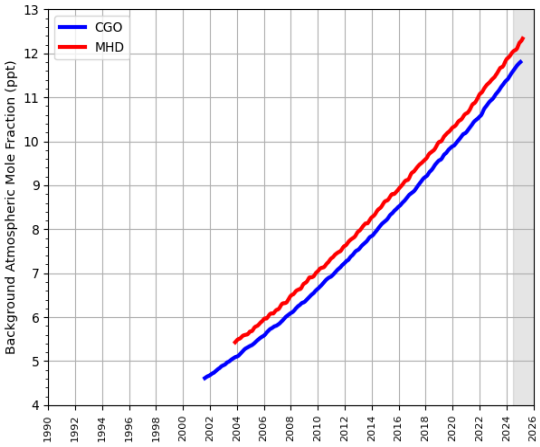

(a) SF_6

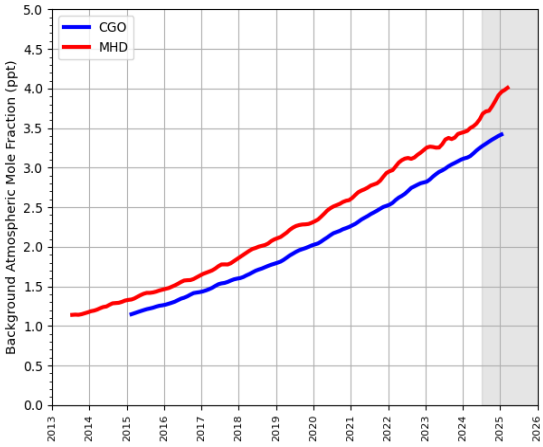

(b) NF_3

2.6 Carbon Dioxide (CO_2)

Figure 2.6.1: Background Northern Hemisphere monthly concentrations of CO_2 estimated from MHD, Ireland observations are shown in red, and background Southern Hemisphere monthly concentrations from CGO, Tasmania are shown in blue. Grey shading represents provisional data.

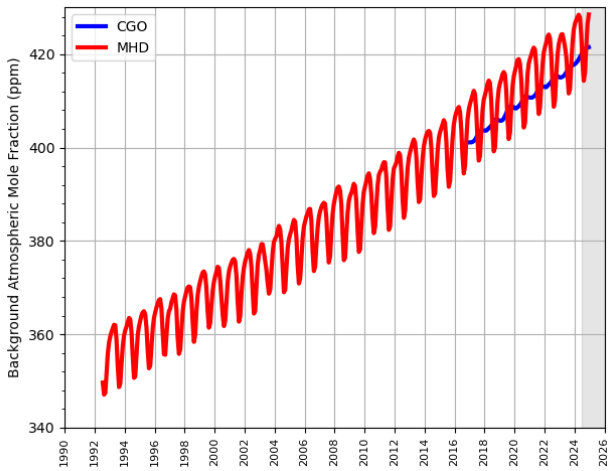

3 Key findings

- Methane (CH_4): Inversion results are around 15-25% lower than the inventory estimates between 2016 and 2023. The inclusion of additional observational data from 2017 has had an impact on the UK estimates even though no additional observational data were added close to the UK. This impact requires further investigation. There is a moderate seasonal cycle with a maximum in winter.
- Nitrous oxide (N_2O): The PARIS mean results are around 10% higher than the inventory estimates, though the uncertainty overlaps from 2019. The NAME InTEM estimates are 20% higher but in this case the uncertainties do not overlap with the inventory. In all years the inverse models estimate a pronounced seasonal cycle in emissions with the maximum in late spring or early summer.
- Hydrofluorocarbons (HFCs): The total HFC emission estimates from the inverse models follow the declining trend of the inventory from 2017, with the PARIS mean emissions being 10-20% lower than those reported in the inventory.
- Perfluorocarbons (PFCs): The inverse results reveal a notable area of emission in NW of England for PFC-14, PFC-116 and PFC-218. The inverse model estimates are higher than those reported in the inventory although the uncertainties are high.
- Sulphur hexafluoride (SF_6): The trend and magnitude estimated by the inversions are consistent with what are reported in the inventory 2018-2023. In earlier years, 2008-2015, the InTEM estimates are somewhat higher. The spatial distribution appears to be largely population-based.
- The observational coverage of the UK is generally very good. Scotland is the least well constrained area, especially for HFCs and PFCs.
- The model results using FLEXPART for all three inverse systems have a tendency to estimate lower emissions. This has lowered the PARIS mean and broadened the overall uncertainty.

Table 1: Emissions estimation for the main greenhouse gases of focus according to the National Inventory Document (NID) 2025 and the inversions done in the PARIS project. For the PARIS estimation, the mean of all models is displayed, along with a range of uncertainty estimated via the half distance between the maximum and minimum uncertainties of the different models. For SF_6, the PARIS mean is the average of all InTEM and ELRIS inversions only.

		2020	2021	2022	2023	2024
CH_4	NID 2025	60.4	59.1	58.5	57.3	
$(\mathrm{TgCO_2\text{-}eq \cdot yr^{-1}})$	PARIS mean	43.0 ± 7.7	44.5 ± 7.6	44.0 ± 6.0	42.7 ± 7.1	50.0 ± 6.8
N_2O	NID 2025	18.9	19.3	18.4	18.2	
$(\mathrm{TgCO_2\text{-}eq \cdot yr^{-1}})$	PARIS mean	20.6 ± 3.2	21.7 ± 3.3	19.2 ± 4.0	20.9 ± 3.5	21.5 ± 2.9
Total HFC	NID 2025	8.5	7.9	7.4	6.9	
$(\mathrm{TgCO_2\text{-}eq \cdot yr^{-1}})$	PARIS mean	6.9 ± 1.3	6.7 ± 1.0	6.7 ± 0.9	6.4 ± 0.9	6.3 ± 1.0
SF_6	NID 2025	0.43	0.39	0.33	0.30	
$(\mathrm{TgCO_2\text{-}eq \cdot yr^{-1}})$	PARIS mean	0.46 ± 0.19	0.40 ± 0.19	0.42 ± 0.20	0.43 ± 0.19	0.46 ± 0.18
Total PFC	NID 2025	0.16	0.19	0.15	0.14	
$(\mathrm{TgCO_2\text{-}eq \cdot yr^{-1}})$	PARIS mean	0.36 ± 0.13	0.41 ± 0.15	0.45 ± 0.17	0.45 ± 0.18	0.42 ± 0.16
NF_3	NID 2025	0	0	0	0	
$(\mathrm{GgCO_2\text{-}eq \cdot yr^{-1}})$	PARIS mean	20 ± 28	21 ± 40	33 ± 63	48 ± 81	53 ± 85

4 Methane (CH_4)

Figure 4.0.1: Average monthly total source sensitivity of CH_4 observing sites as calculated by the FLEXPART transport model for the year 2018 (left) and 2024 (right) and used in the inversions. Observing stations active in each year are marked with red dots. Areas with visible land surface represent regions for which emissions can be observed well from the network. Shaded or dark areas represent regions for which limited emission information can be obtained from the network.

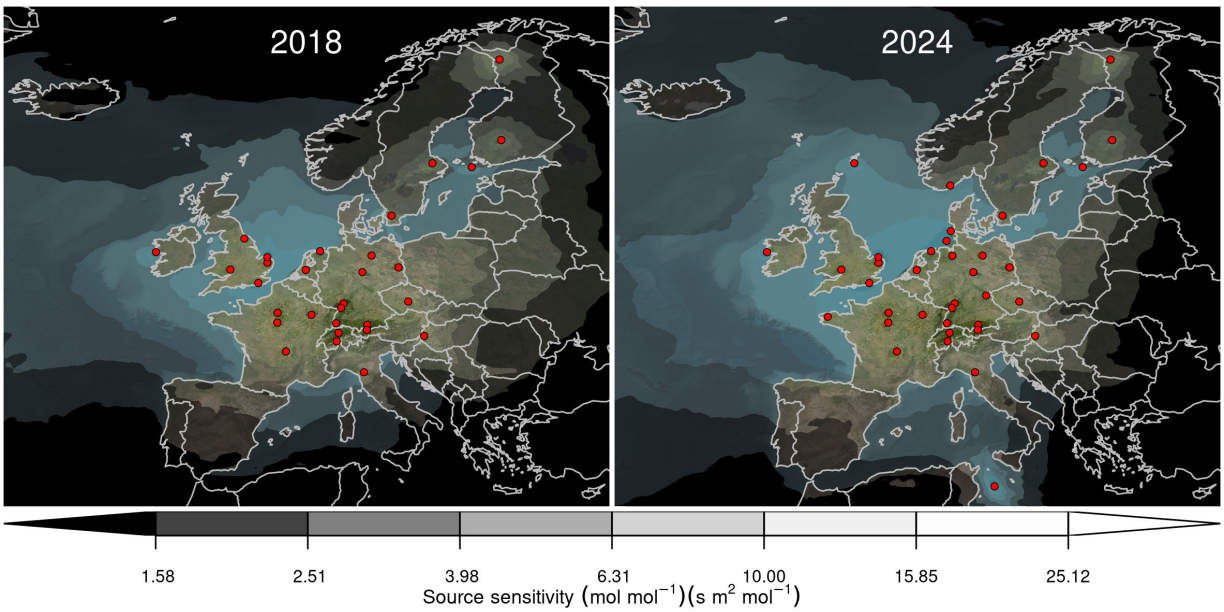

Figure 4.0.2: Verification of the UK emissions inventory estimates for CH_4. Modelled annual emissions are given as the mean from all models (black line) and the individual result from InTEM-NAME (blue line). The shaded blue area is the 68 % confidence interval (CI) of InTEM-NAME and the shaded grey area encompasses the 68 % CI from all models. National inventory annual totals from 2024 and 2025 are given as grey and black bars, respectively.

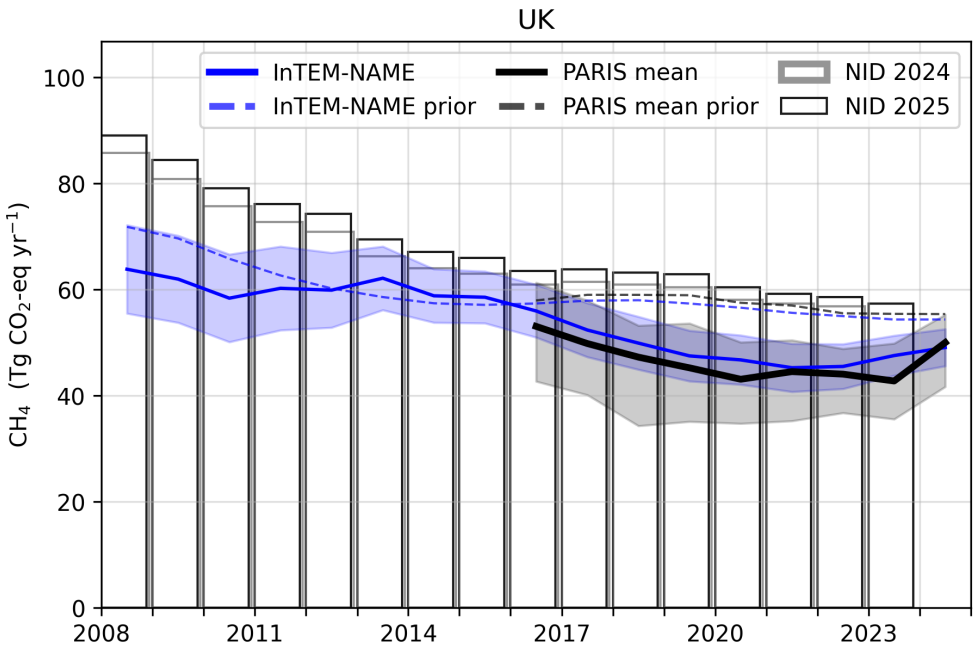

Figure 4.0.3: Verification of the UK emissions inventory estimates for CH_4 (zoom in to 2018-2024). Modelled annual emissions are given as the mean from all models (black line) and the individual result from InTEM-NAME (blue line). The shaded blue area is the 68 % confidence interval (CI) of InTEM-NAME and the shaded grey area encompasses the 68 % CI from all models. National inventory annual totals from 2024 and 2025 are given as grey and black bars, respectively.

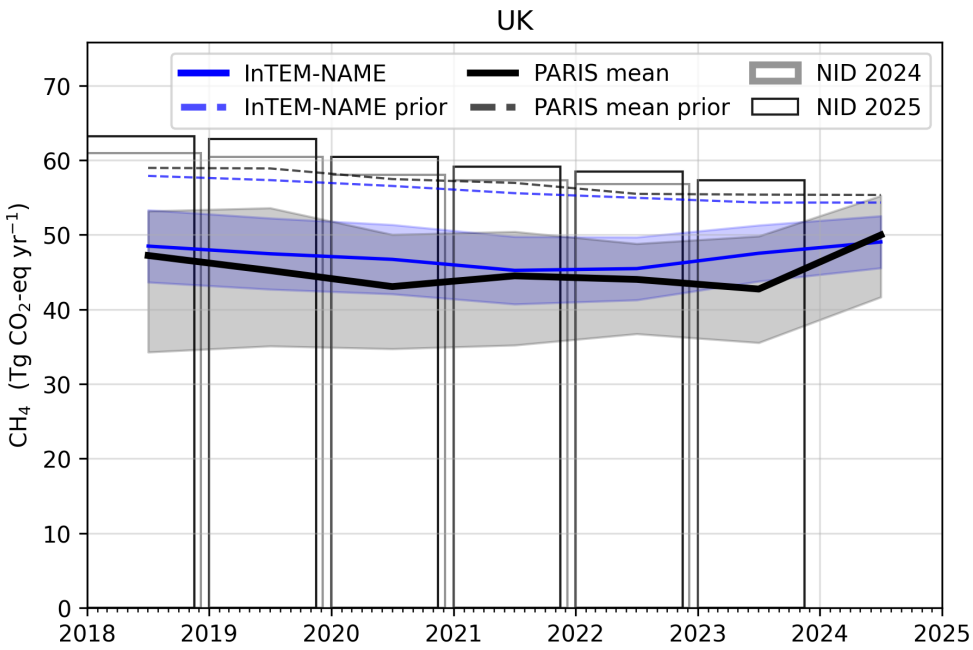

Figure 4.0.4: Verification of the UK emissions inventory estimates for CH_4 (zoom in to 2018-2024). Modelled monthly emissions are given as the mean from all models (black line) and the individual result from InTEM-NAME (blue line). The shaded blue area is the 68 % confidence interval (CI) of InTEM-NAME and the shaded grey area encompasses the 68 % CI from all models. National inventory annual totals from 2024 and 2025 are given as grey and black bars, respectively.

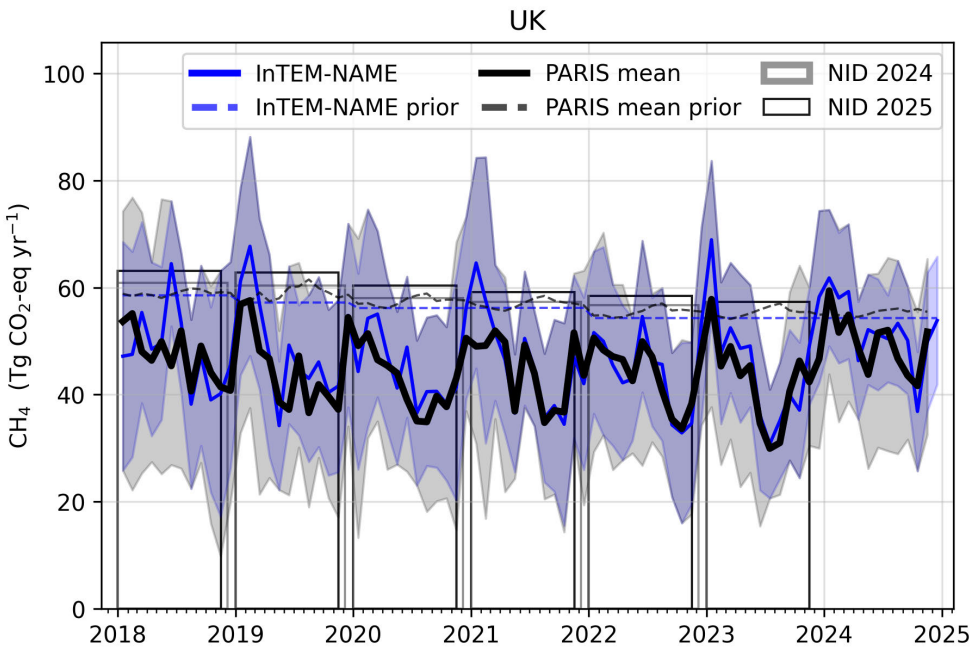

Figure 4.0.5: Spatial distribution of the UK average modelled emissions of CH_4 during the period of 2020-2024 (mean from all models). Observing stations are marked with red circles and highly-populated cities are marked with red triangles.

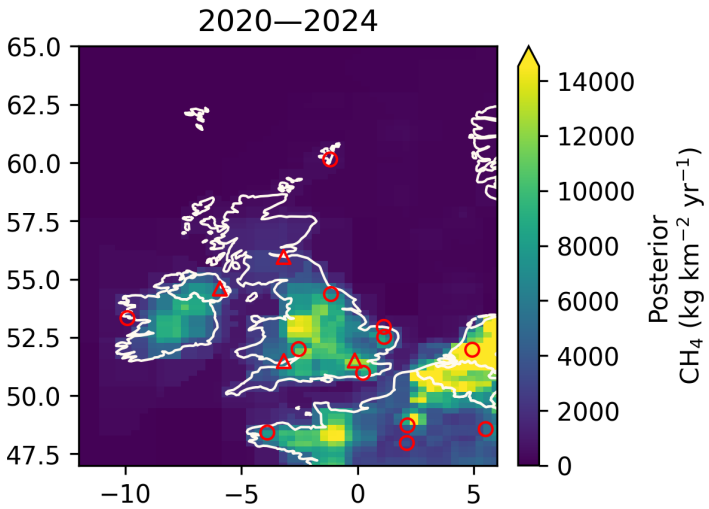

Figure 4.0.6: Spatial distribution of the seasonal deviation from the mean. The deviation is defined as the modelled UK seasonally averaged CH_4 emissions over 2020-2024 minus the average over the whole period. The mean across all models is shown. Observing stations are marked with black circles and highly-populated cities are marked with black triangles.

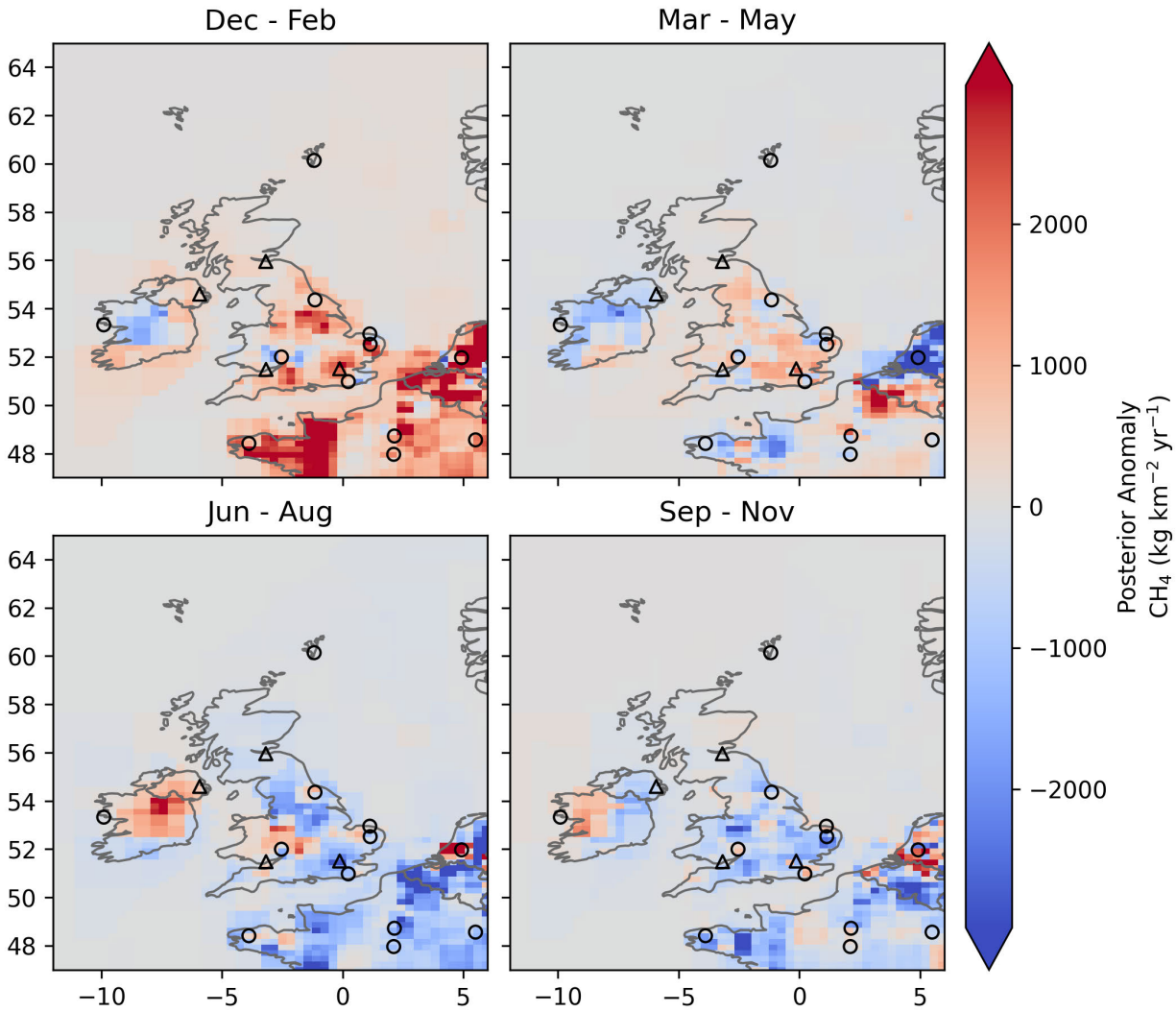

5 Nitrous Oxide (N_2O)

Figure 5.0.1: Average monthly total source sensitivity of N_2O observing sites as calculated by the FLEXPART transport model for the year 2018 (left) and 2024 (right) and used in the inversions. Observing stations active in each year are marked with red dots. Areas with visible land surface represent regions for which emissions can be observed well from the network. Shaded or dark areas represent regions for which limited emission information can be obtained from the network.

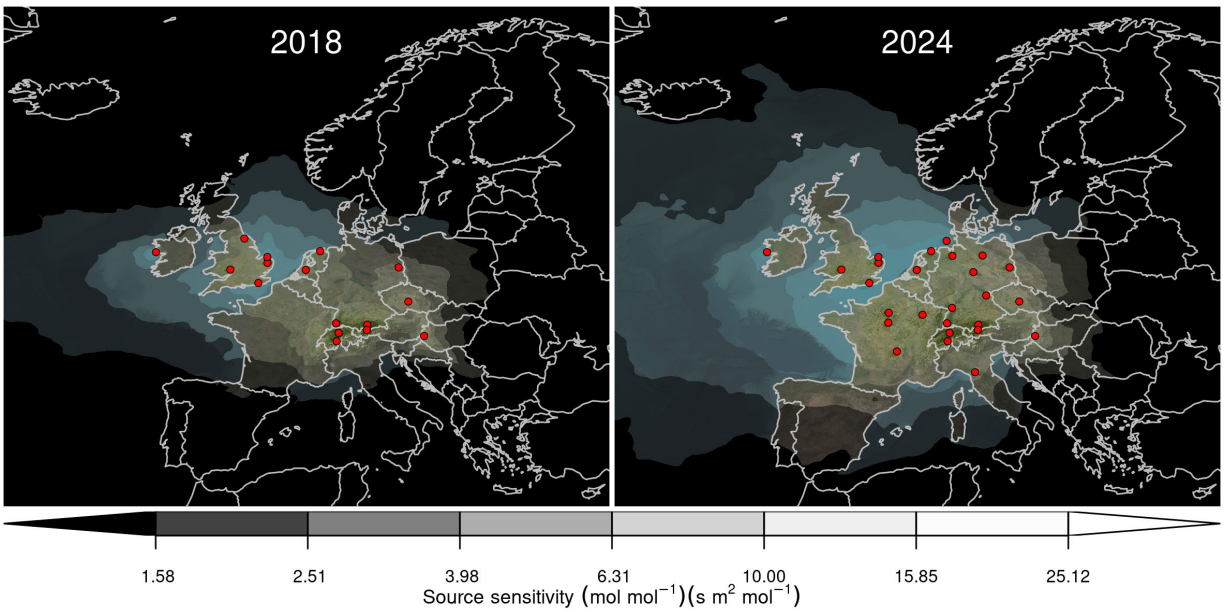

Figure 5.0.2: Verification of the UK emissions inventory estimates for N_2O. Modelled annual emissions are given as the mean from all models (black line) and the individual result from InTEM-NAME (blue line). The shaded blue area is the 68 % confidence interval (CI) of InTEM-NAME and the shaded grey area encompasses the 68 % CI from all models. National inventory annual totals from 2024 and 2025 are given as grey and black bars, respectively.

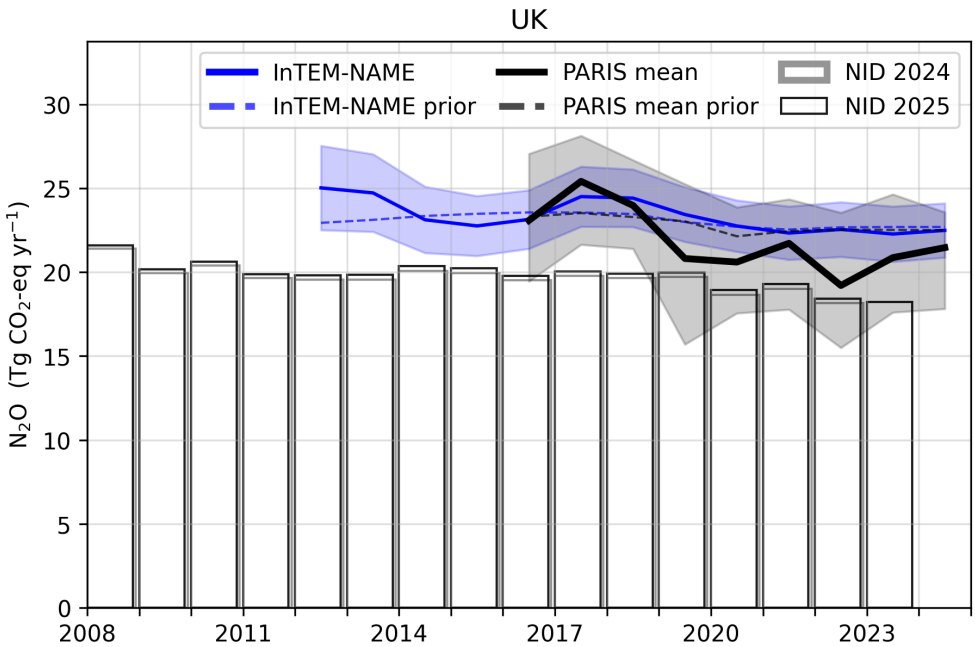

Figure 5.0.3: Verification of the UK emissions inventory estimates for N_2O (zoom in to 2018-2024). Modelled annual emissions are given as the mean from all models (black line) and the individual result from InTEM-NAME (blue line). The shaded blue area is the 68 % confidence interval (CI) of InTEM-NAME and the shaded grey area encompasses the 68 % CI from all models. National inventory annual totals from 2024 and 2025 are given as grey and black bars, respectively.

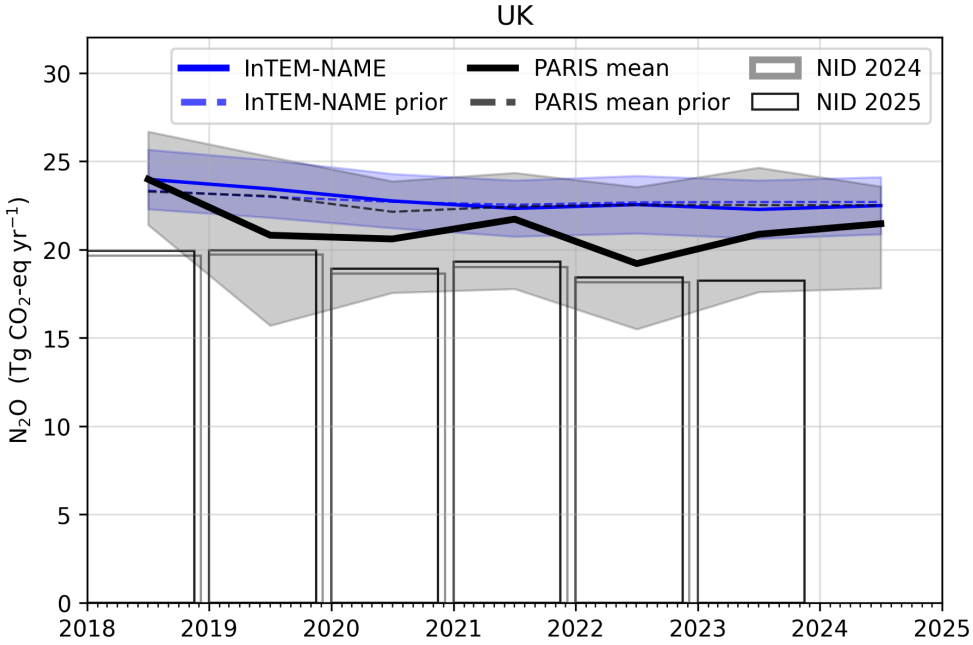

Figure 5.0.4: Verification of the UK emissions inventory estimates for N_2O (zoom in to 2018-2024). Modelled monthly emissions are given as the mean from all models (black line) and the individual result from InTEM-NAME (blue line). The shaded blue area is the 68 % confidence interval (CI) of InTEM-NAME and the shaded grey area encompasses the 68 % CI from all models. National inventory annual totals from 2024 and 2025 are given as grey and black bars, respectively.

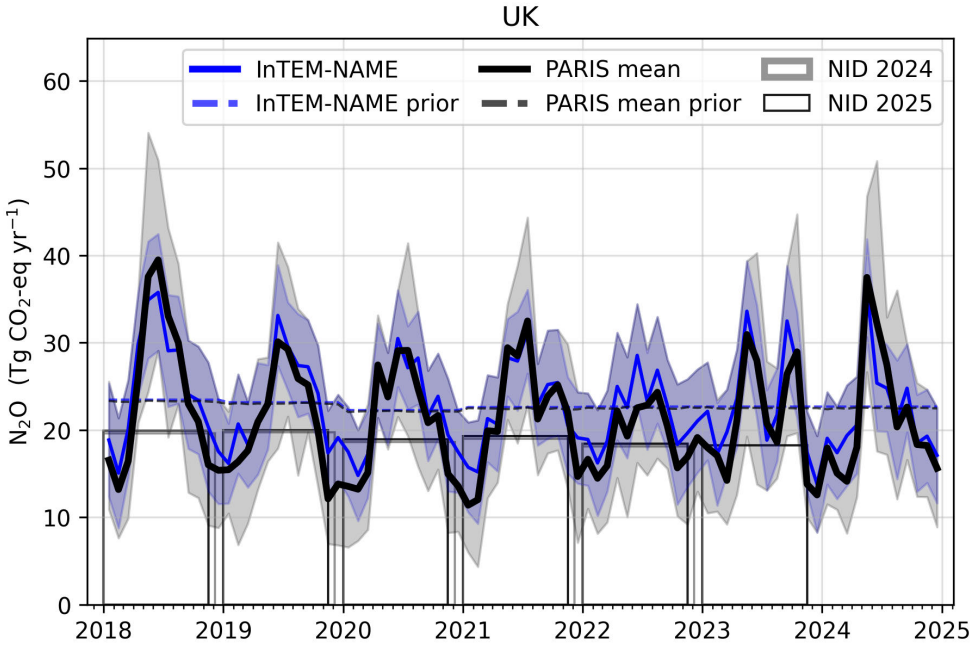

Figure 5.0.5: Spatial distribution of the UK average modelled emissions of N_2O during the period of 2020-2024 (mean from all models). Observing stations are marked with red circles and highly-populated cities are marked with red triangles.

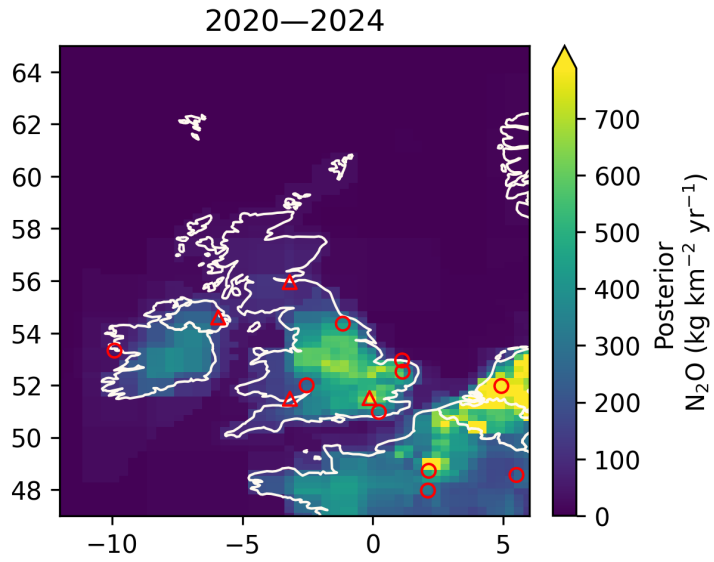

Figure 5.0.6: Spatial distribution of the seasonal deviation from the mean. The deviation is defined as the modelled UK seasonally averaged N_2O emissions over 2020-2024 minus the average over the whole period. The mean across all models is shown. Observing stations are marked with black circles and highly-populated cities are marked with black triangles.

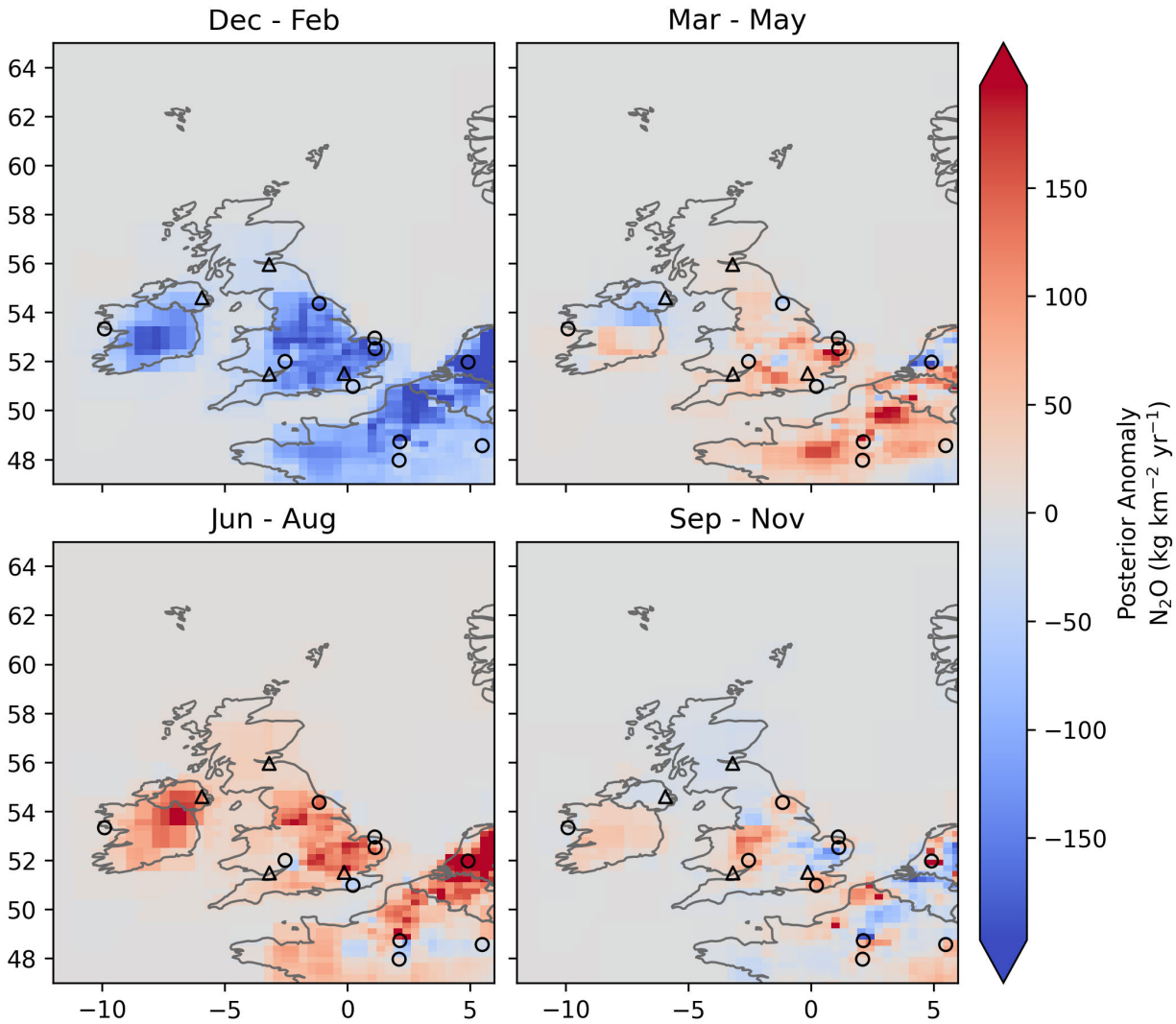

6 Hydrofluorocarbons (HFCs)

Figure 6.0.1: Total source sensitivity of HFCs/PFCs observing sites as calculated by the FLEXPART transport model for the year 2018 (left) and 2024 (right) and used in the inversions. Observing stations active in each year are marked with red dots. Areas with visible land surface represent regions for which emissions can be observed well from the network. Shaded or dark areas represent regions for which limited emission information can be obtained from the network.

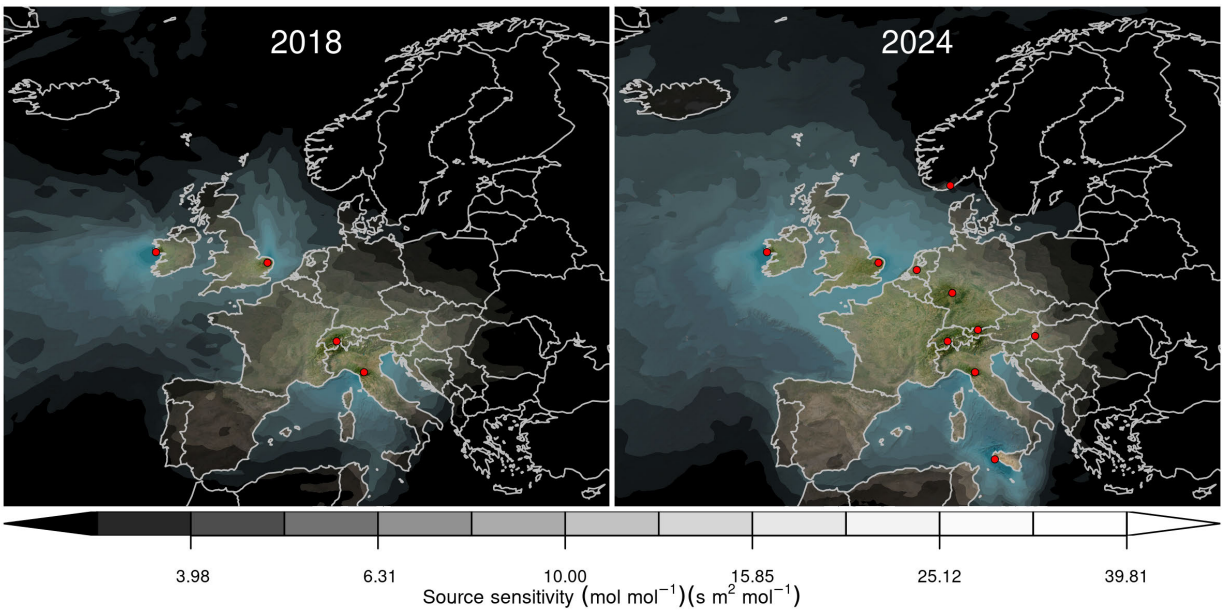

6.1 HFC-125

Figure 6.1.1: Verification of the UK emissions inventory estimates for HFC-125. Modelled annual emissions are given as the mean from all models (black line) and the individual result from InTEM-NAME (blue line). The shaded blue area is the 68 % confidence interval (CI) of InTEM-NAME and the shaded grey area encompasses the 68 % CI from all models. National inventory annual totals from 2024 and 2025 are given as grey and black bars, respectively.

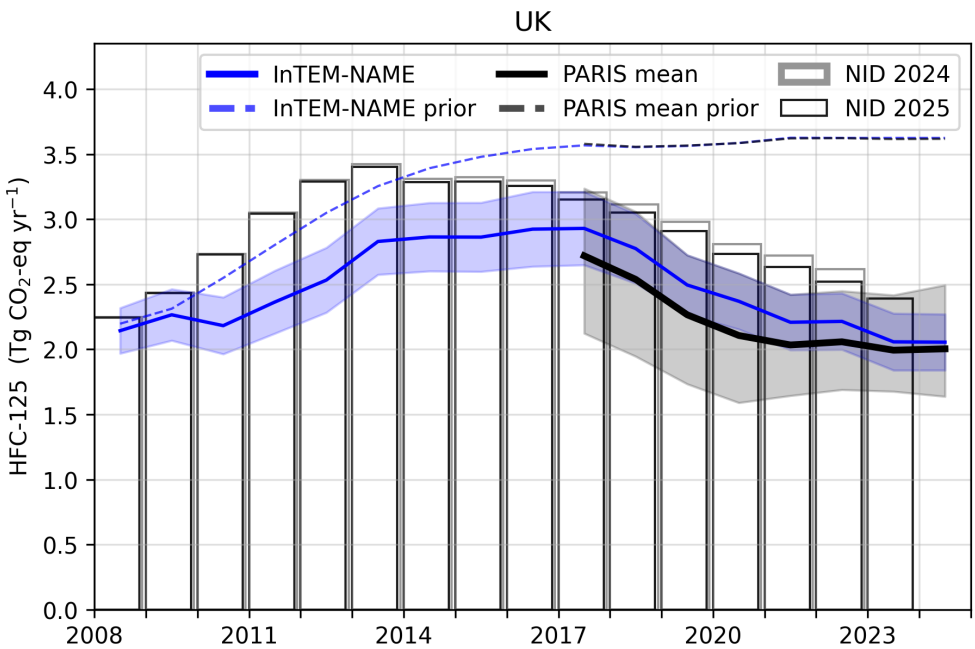

Figure 6.1.2: Spatial distribution of the UK average modelled emissions of HFC-125 during the period of 2020-2024 (mean from all models). Observing stations are marked with red circles and highly-populated cities are marked with red triangles.

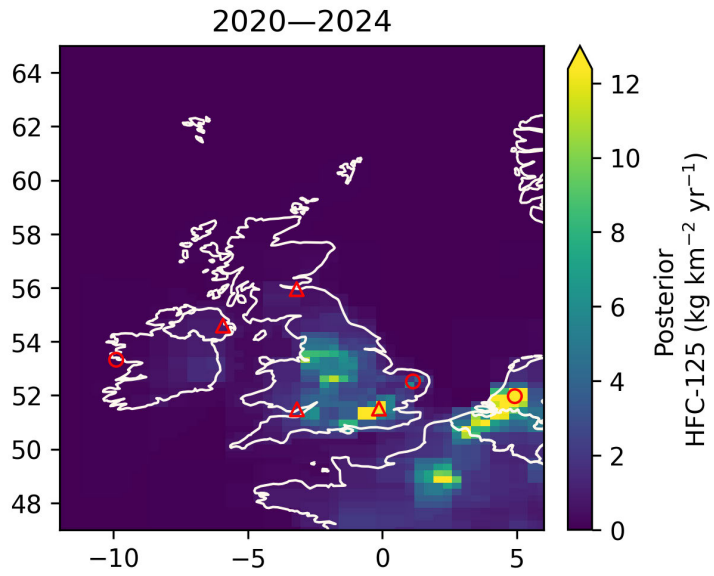

6.2 HFC-134a

Figure 6.2.1: Verification of the UK emissions inventory estimates for HFC-134a. Modelled annual emissions are given as the mean from all models (black line) and the individual result from InTEM-NAME (blue line). The shaded blue area is the 68 % confidence interval (CI) of InTEM-NAME and the shaded grey area encompasses the 68 % CI from all models. National inventory annual totals from 2024 and 2025 are given as grey and black bars, respectively.

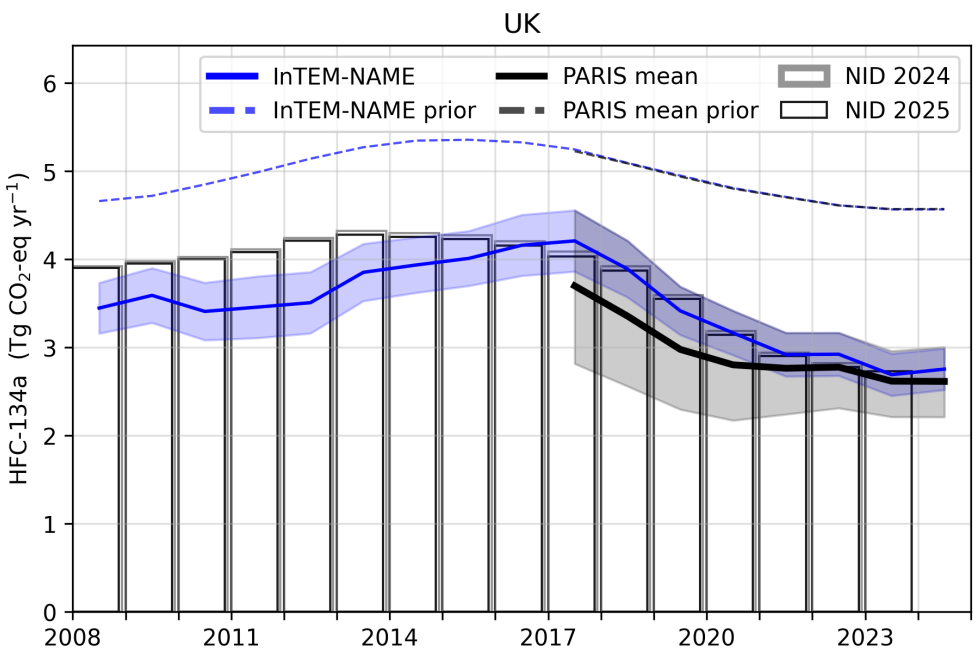

Figure 6.2.2: Spatial distribution of the UK average modelled emissions of HFC-134a during the period of 2020-2024 (mean from all models). Observing stations are marked with red circles and highly-populated cities are marked with red triangles.

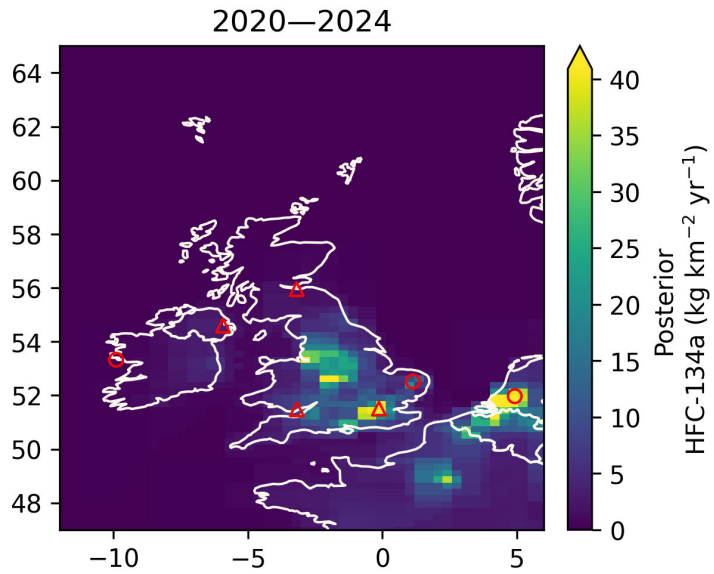

6.3 HFC-143a

Figure 6.3.1: Verification of the UK emissions inventory estimates for HFC-143a. Modelled annual emissions are given as the mean from all models (black line) and the individual result from InTEM-NAME (blue line). The shaded blue area is the 68 % confidence interval (CI) of InTEM-NAME and the shaded grey area encompasses the 68 % CI from all models. National inventory annual totals from 2024 and 2025 are given as grey and black bars, respectively.

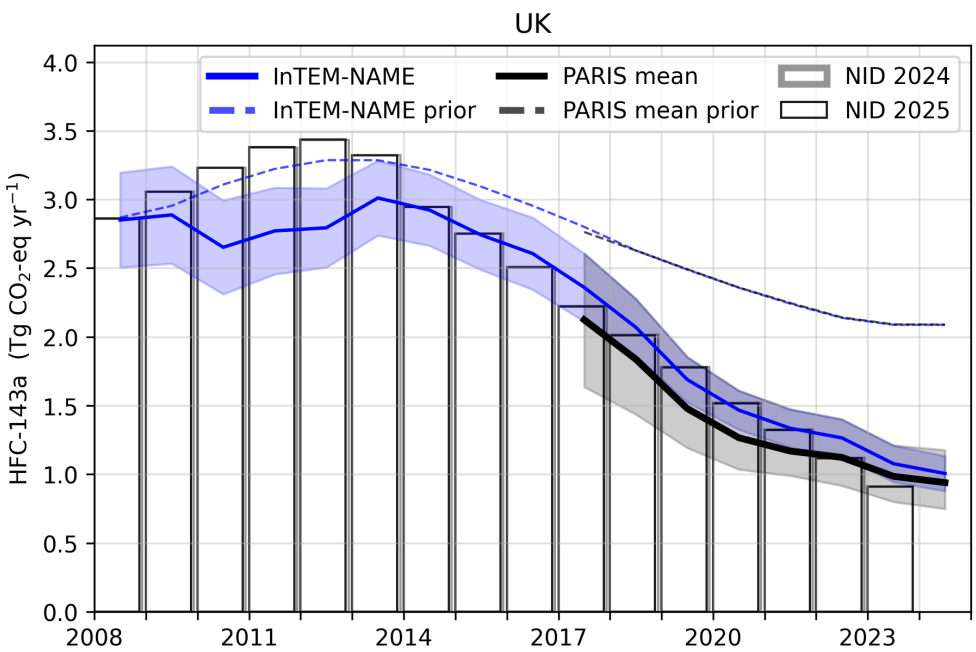

Figure 6.3.2: Spatial distribution of the UK average modelled emissions of HFC-143a during the period of 2020-2024 (mean from all models). Observing stations are marked with red circles and highly-populated cities are marked with red triangles.

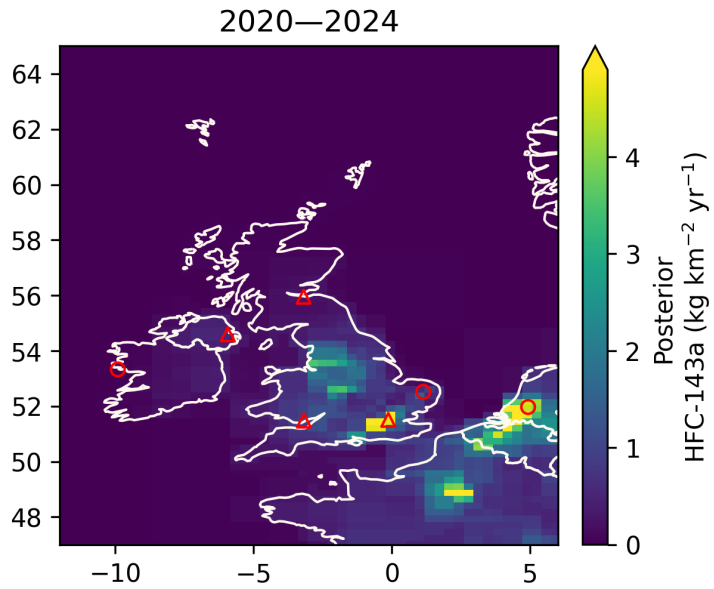

6.4 HFC-152a

Figure 6.4.1: Verification of the UK emissions inventory estimates for HFC-152a. Modelled annual emissions are given as the mean from all models (black line) and the individual result from InTEM-NAME (blue line). The shaded blue area is the 68 % confidence interval (CI) of InTEM-NAME and the shaded grey area encompasses the 68 % CI from all models. National inventory annual totals from 2024 and 2025 are given as grey and black bars, respectively.

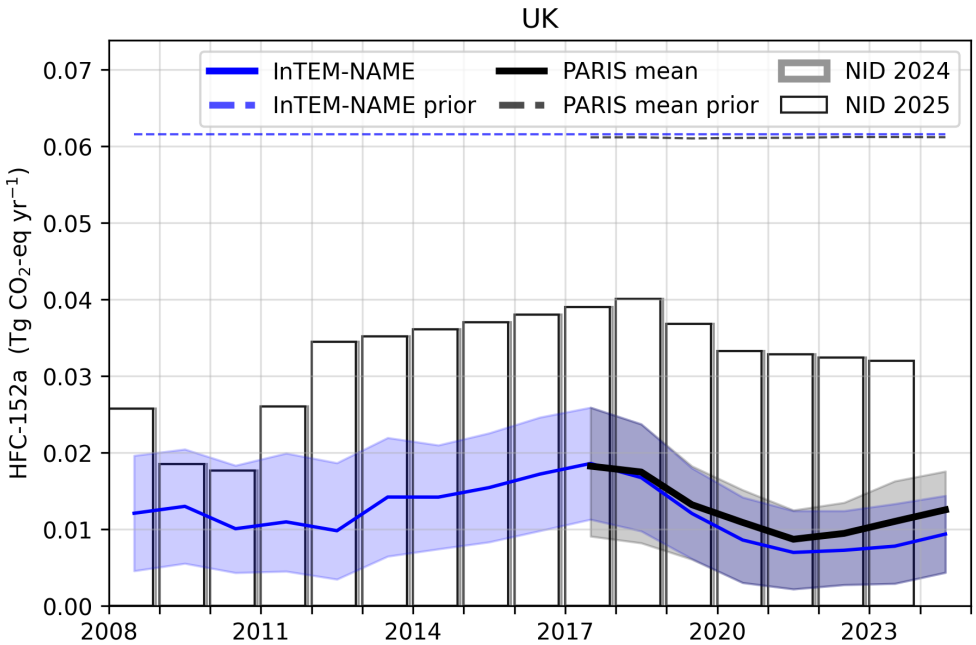

Figure 6.4.2: Spatial distribution of the UK average modelled emissions of HFC-152a during the period of 2020-2024 (mean from all models). Observing stations are marked with red circles and highly-populated cities are marked with red triangles.

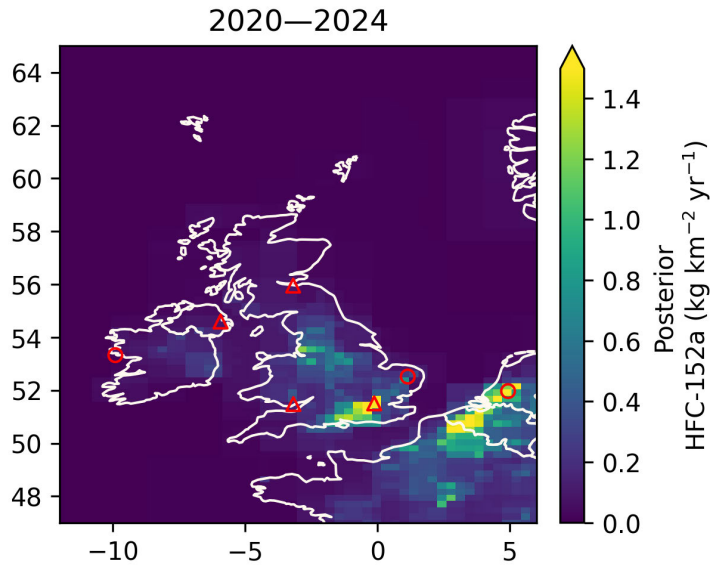

6.5 HFC-227ea

Figure 6.5.1: Verification of the UK emissions inventory estimates for HFC-227ea. Modelled annual emissions are given as the mean from all models (black line) and the individual result from InTEM-NAME (blue line). The shaded blue area is the 68 % confidence interval (CI) of InTEM-NAME and the shaded grey area encompasses the 68 % CI from all models. National inventory annual totals from 2024 and 2025 are given as grey and black bars, respectively.

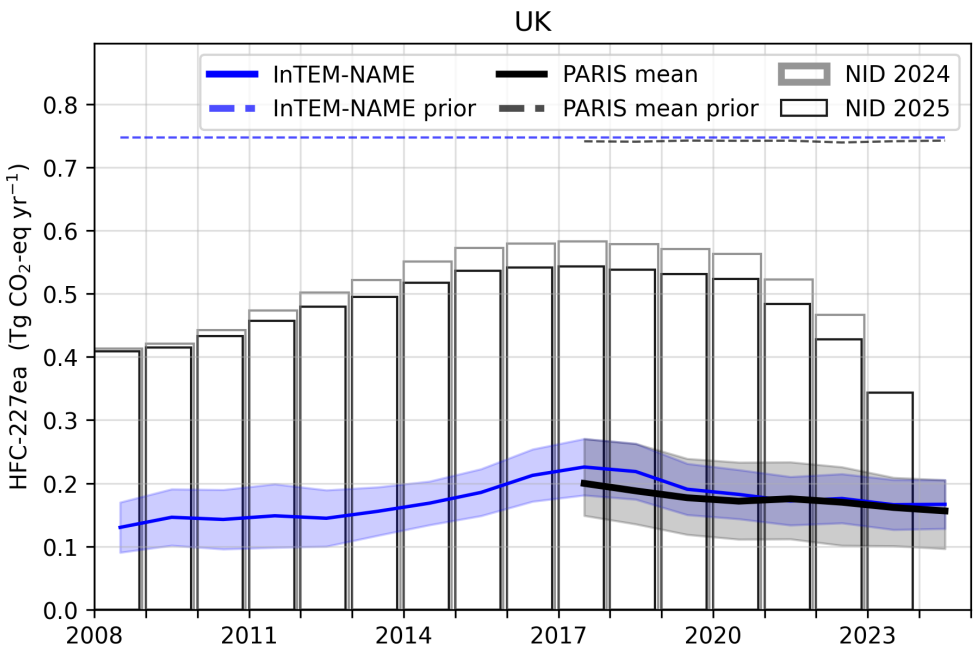

Figure 6.5.2: Spatial distribution of the UK average modelled emissions of HFC-227ea during the period of 2020-2024 (mean from all models). Observing stations are marked with red circles and highly-populated cities are marked with red triangles.

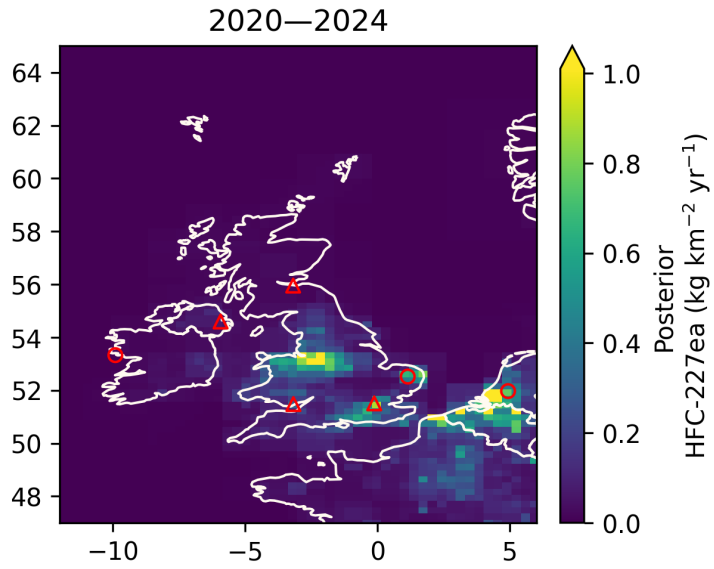

6.6 HFC-32

Figure 6.6.1: Verification of the UK emissions inventory estimates for HFC-32. Modelled annual emissions are given as the mean from all models (black line) and the individual result from InTEM-NAME (blue line). The shaded blue area is the 68 % confidence interval (CI) of InTEM-NAME and the shaded grey area encompasses the 68 % CI from all models. National inventory annual totals from 2024 and 2025 are given as grey and black bars, respectively.

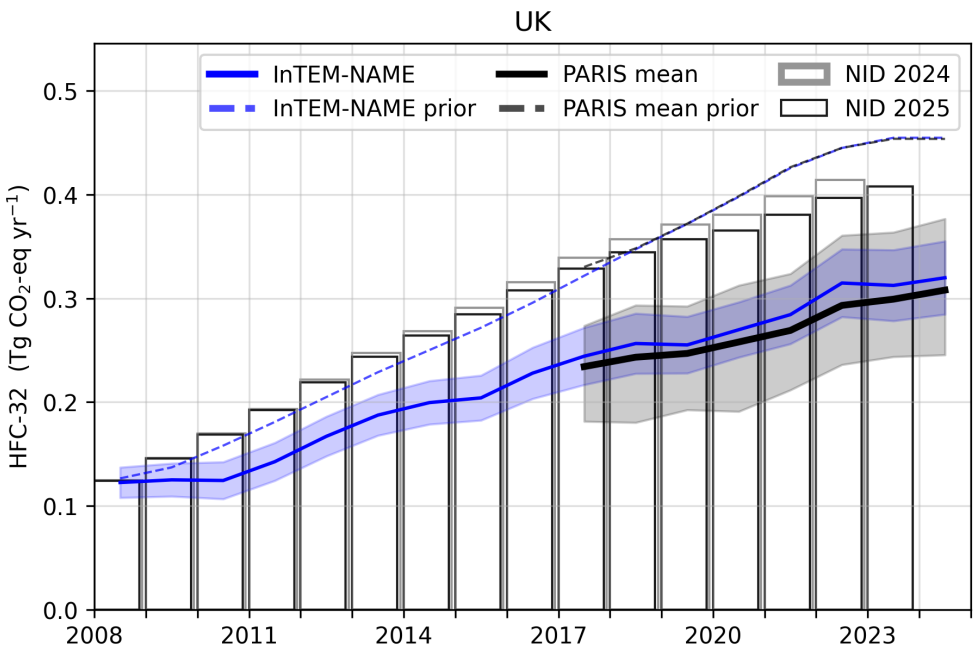

Figure 6.6.2: Spatial distribution of the UK average modelled emissions of HFC-32 during the period of 2020-2024 (mean from all models). Observing stations are marked with red circles and highly-populated cities are marked with red triangles.

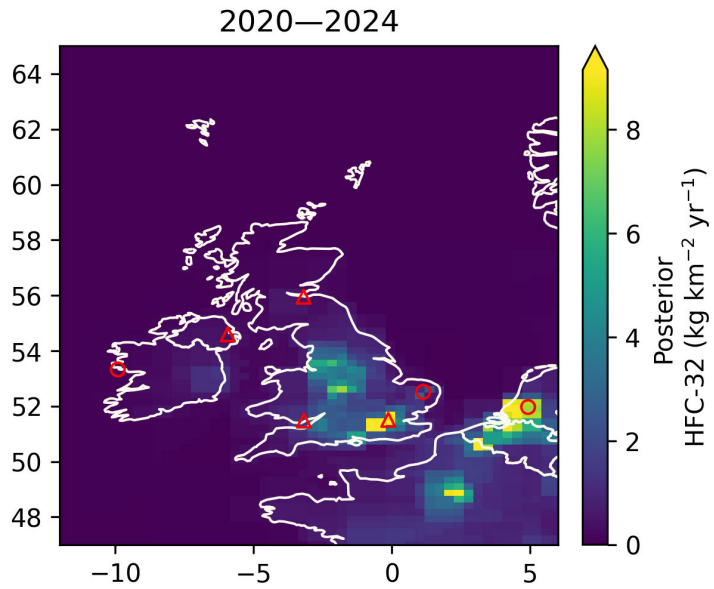

6.7 Total HFCs

Figure 6.7.1: Verification of the UK emissions inventory estimates for total HFCs. Modelled annual emissions are given as the mean from all models (black line) and the individual result from InTEM-NAME (blue line). The shaded blue area is the 68 % confidence interval (CI) of InTEM-NAME and the shaded grey area encompasses the 68 % CI from all models. National inventory annual totals from 2024 and 2025 are given as grey and black bars, respectively.

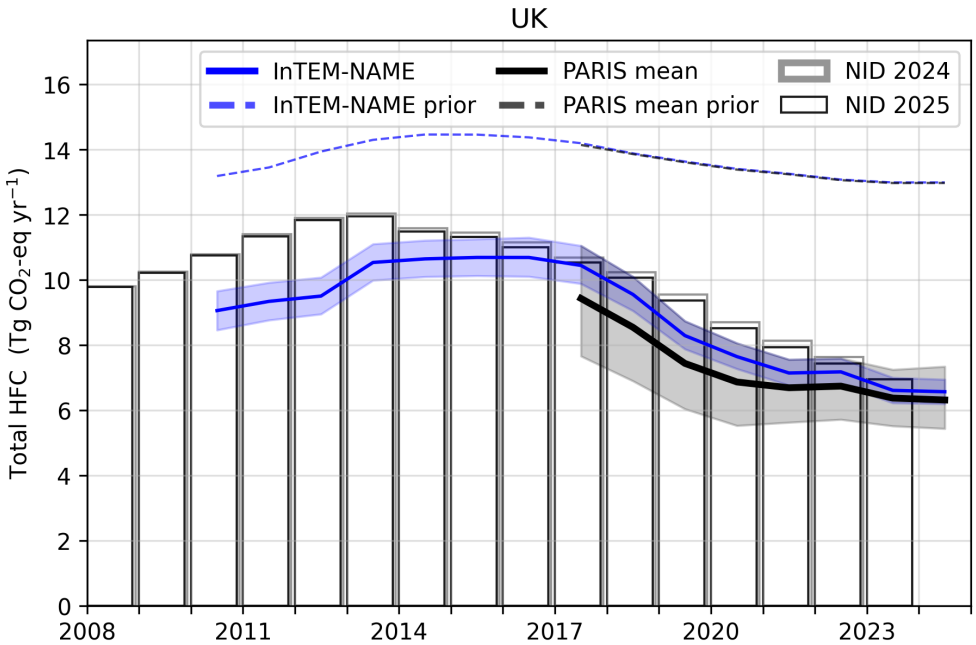

Table 2: Emissions estimation for HFCs according to the National Inventory Document (NID) 2025 and the inversions done in the PARIS project. For the PARIS estimation, the mean of all models is displayed, along with a range of uncertainty estimated via the half distance between the maximum and minimum uncertainties of the different models.

		2020	2021	2022	2023	2024
HFC-134a	NID 2025	3.1	2.9	2.8	2.7	
$\left(\mathrm{TgCO_2\text{-}eq \cdot yr^{-1}}\right)$	PARIS mean	2.8 ± 0.6	2.8 ± 0.5	2.8 ± 0.4	2.6 ± 0.4	2.6 ± 0.4
HFC-125	NID 2025	2.7	2.6	2.5	2.4	
$\left(\mathrm{TgCO_2\text{-}eq \cdot yr^{-1}}\right)$	PARIS mean	2.1 ± 0.5	2.0 ± 0.4	2.1 ± 0.4	2.0 ± 0.4	2.0 ± 0.4
HFC-143a	NID 2025	1.5	1.3	1.1	0.9	
$\left(\mathrm{TgCO_2\text{-}eq \cdot yr^{-1}}\right)$	PARIS mean	1.3 ± 0.3	1.2 ± 0.2	1.1 ± 0.2	1.0 ± 0.2	0.9 ± 0.2
HFC-32	NID 2025	0.37	0.38	0.40	0.41	
$\left(\mathrm{TgCO_2\text{-}eq \cdot yr^{-1}}\right)$	PARIS mean	0.26 ± 0.06	0.27 ± 0.06	0.29 ± 0.06	0.30 ± 0.06	0.31 ± 0.07
HFC-23	NID 2025	0.01	0.01	0.01	0.01	
$\left(\mathrm{TgCO_2\text{-}eq \cdot yr^{-1}}\right)$	PARIS mean	0.13 ± 0.18	0.16 ± 0.22	0.21 ± 0.24	0.22 ± 0.21	0.20 ± 0.17
HFC-227ea	NID 2025	0.52	0.48	0.43	0.34	
$\left(\mathrm{TgCO_2\text{-}eq \cdot yr^{-1}}\right)$	PARIS mean	0.17 ± 0.06	0.18 ± 0.06	0.17 ± 0.06	0.16 ± 0.05	0.16 ± 0.05
HFC-365mfc	NID 2025	0.11	0.10	0.08	0.07	
$\left(\mathrm{TgCO_2\text{-}eq \cdot yr^{-1}}\right)$	PARIS mean	0.05 ± 0.02	0.04 ± 0.01	0.04 ± 0.01	0.03 ± 0.01	0.03 ± 0.01
HFC-245fa	NID 2025	82	75	63	52	
$\left(\mathrm{GgCO_2\text{-}eq \cdot yr^{-1}}\right)$	PARIS mean	45 ± 15	41 ± 15	36 ± 13	30 ± 12	27 ± 11
HFC-236fa	NID 2025	0	0	0	0	
$\left(\mathrm{GgCO_2\text{-}eq \cdot yr^{-1}}\right)$	PARIS mean	22 ± 16	21 ± 15	22 ± 15	21 ± 17	19 ± 18
HFC-152a	NID 2025	33	33	32	32	
$\left(\mathrm{GgCO_2\text{-}eq \cdot yr^{-1}}\right)$	PARIS mean	11 ± 6	9 ± 5	9 ± 5	11 ± 7	13 ± 7
HFC-4310mee	NID 2025	13	13	13	13	
$\left(\mathrm{GgCO_2\text{-}eq \cdot yr^{-1}}\right)$	PARIS mean	9 ± 7	9 ± 7	9 ± 8	9 ± 8	9 ± 9

7 Perfluorocarbons (PFCs)

7.1 PFC-14

Figure 7.1.1: Verification of the UK emissions inventory estimates for PFC-14. Modelled annual emissions are given as the mean from all models (black line) and the individual result from InTEM-NAME (blue line). The shaded blue area is the 68 % confidence interval (CI) of InTEM-NAME and the shaded grey area encompasses the 68 % CI from all models. National inventory annual totals from 2024 and 2025 are given as grey and black bars, respectively.

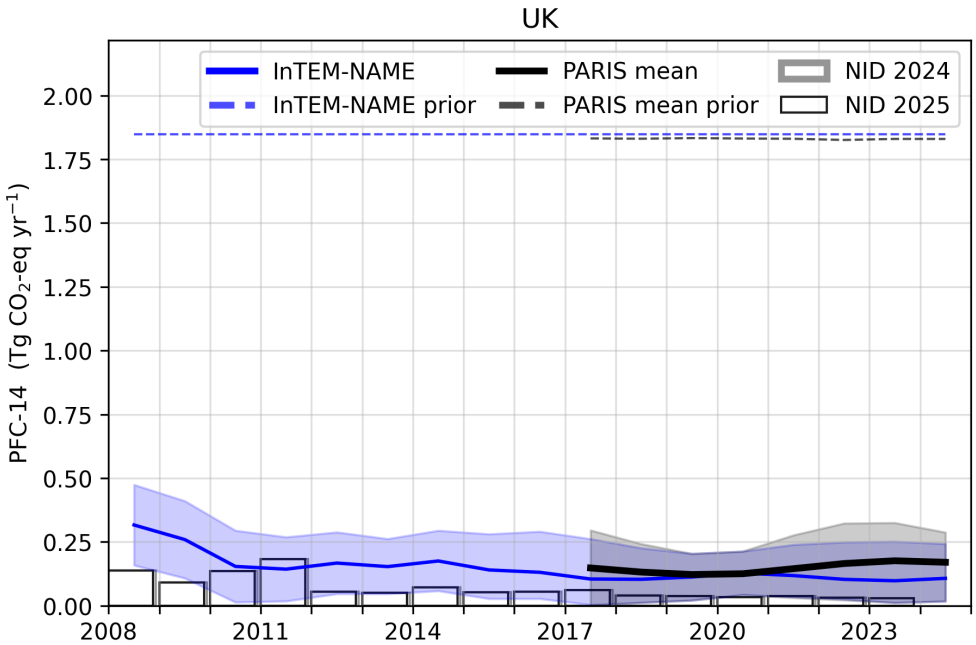

Figure 7.1.2: Spatial distribution of the UK average modelled emissions of PFC-14 during the period of 2020-2024 (mean from all models). Observing stations are marked with red circles and highly-populated cities are marked with red triangles.

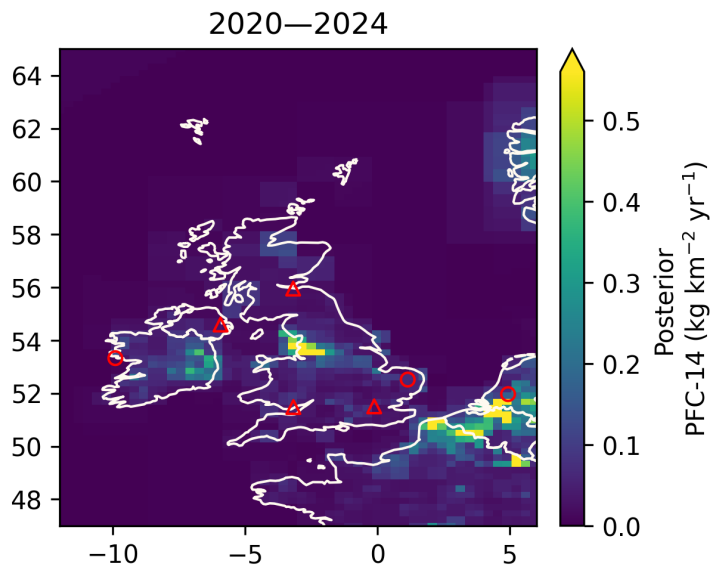

7.2 PFC-116

Figure 7.2.1: Verification of the UK emissions inventory estimates for PFC-116. Modelled annual emissions are given as the mean from all models (black line) and the individual result from InTEM-NAME (blue line). The shaded blue area is the 68 % confidence interval (CI) of InTEM-NAME and the shaded grey area encompasses the 68 % CI from all models. National inventory annual totals from 2024 and 2025 are given as grey and black bars, respectively.

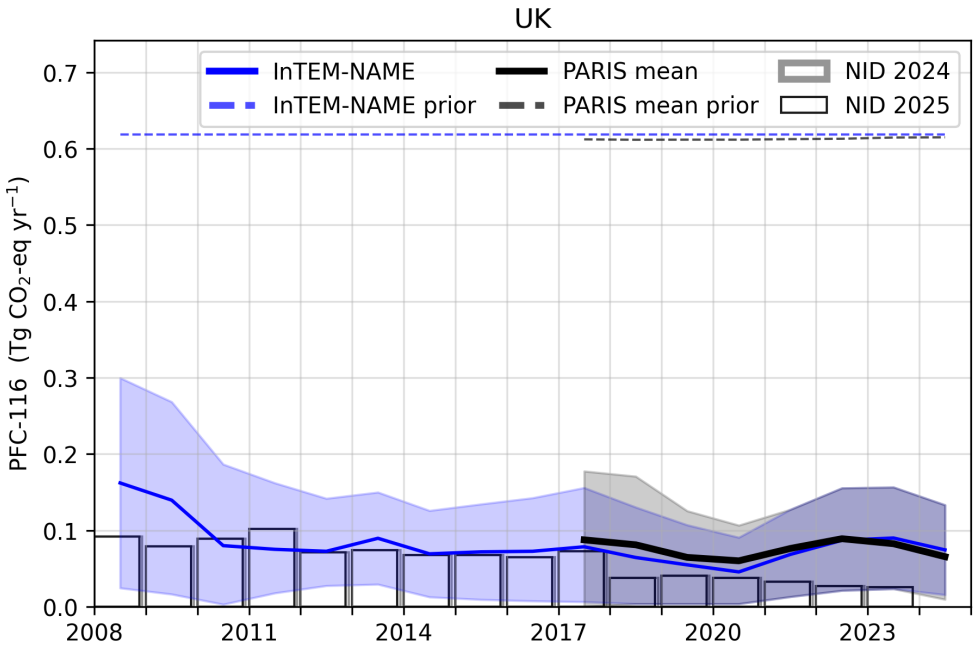

Figure 7.2.2: Spatial distribution of the UK average modelled emissions of PFC-116 during the period of 2020-2024 (mean from all models). Observing stations are marked with red circles and highly-populated cities are marked with red triangles.

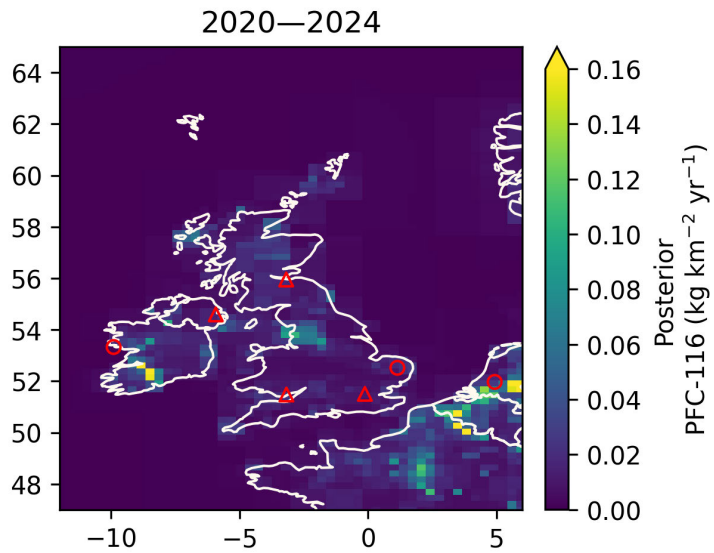

7.3 PFC-218

Figure 7.3.1: Verification of the UK emissions inventory estimates for PFC-218. Modelled annual emissions are given as the mean from all models (black line) and the individual result from InTEM-NAME (blue line). The shaded blue area is the 68 % confidence interval (CI) of InTEM-NAME and the shaded grey area encompasses the 68 % CI from all models. National inventory annual totals from 2024 and 2025 are given as grey and black bars, respectively.

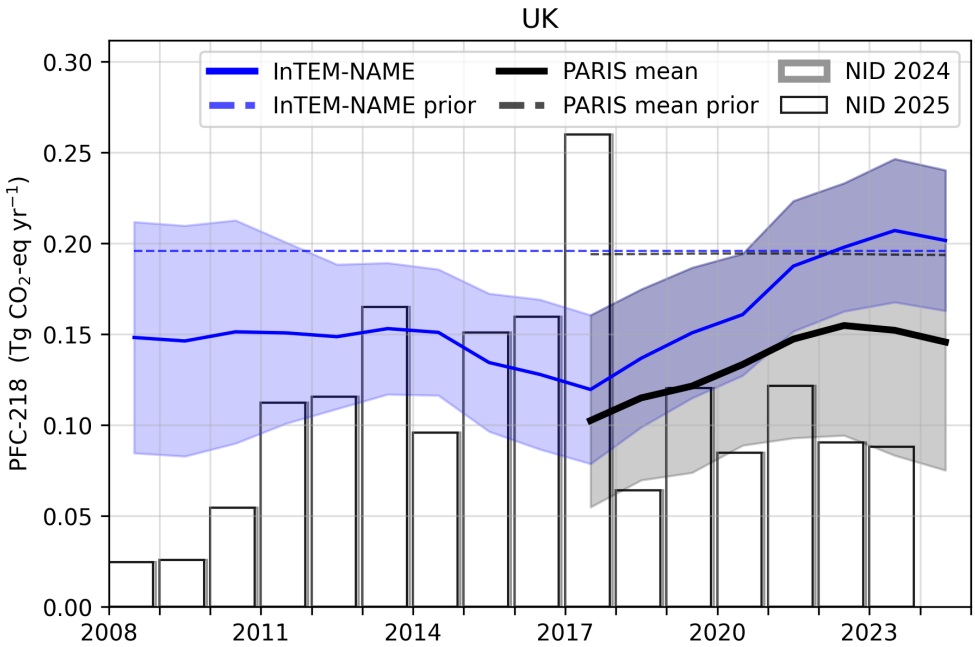

Figure 7.3.2: Spatial distribution of the UK average modelled emissions of PFC-218 during the period of 2020-2024 (mean from all models). Observing stations are marked with red circles and highly-populated cities are marked with red triangles.

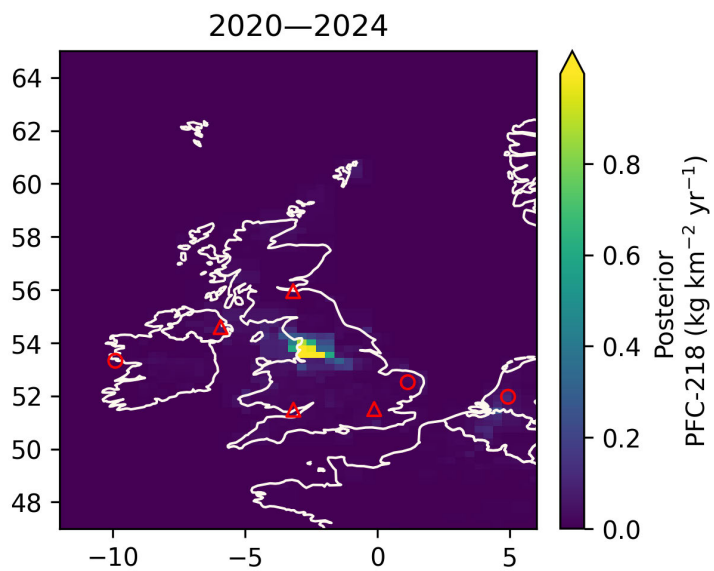

7.4 PFC-318

Figure 7.4.1: Verification of the UK emissions inventory estimates for PFC-318. Modelled annual emissions are given as the mean from all models (black line) and the individual result from InTEM-NAME (blue line). The shaded blue area is the 68 % confidence interval (CI) of InTEM-NAME and the shaded grey area encompasses the 68 % CI from all models. National inventory annual totals from 2024 and 2025 are given as grey and black bars, respectively.

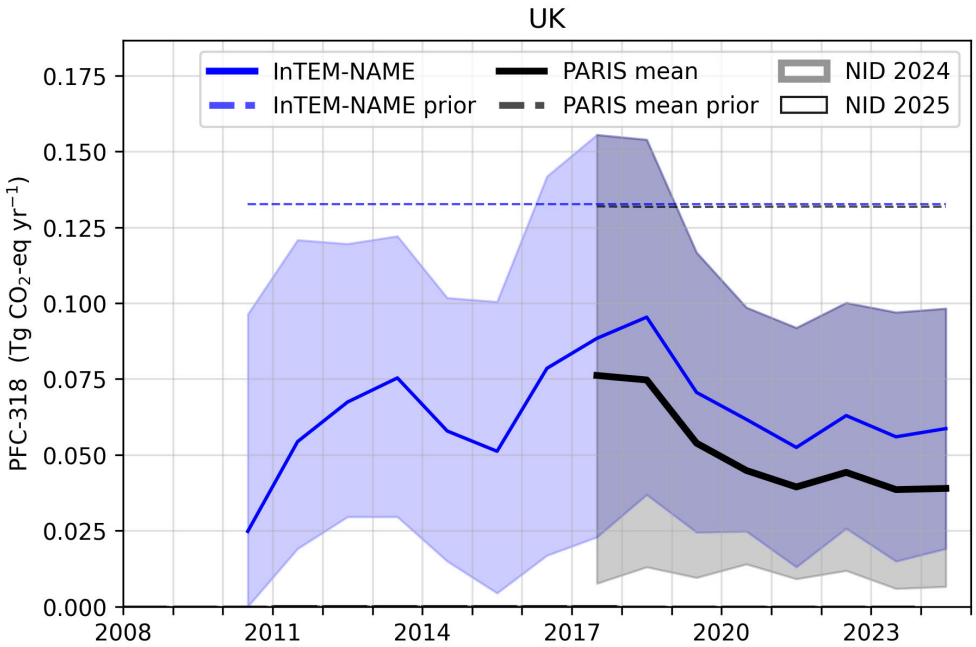

Figure 7.4.2: Spatial distribution of the UK average modelled emissions of PFC-318 during the period of 2020-2024 (mean from all models). Observing stations are marked with red circles and highly-populated cities are marked with red triangles.

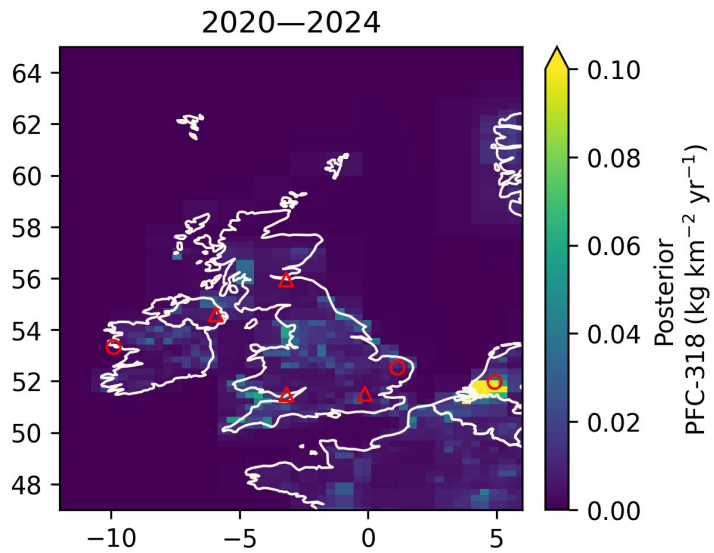

7.5 Total PFCs

Figure 7.5.1: Verification of the UK emissions inventory estimates for total PFCs. Modelled annual emissions are given as the mean from all models (black line) and the individual result from InTEM-NAME (blue line). The shaded blue area is the 68 % confidence interval (CI) of InTEM-NAME and the shaded grey area encompasses the 68 % CI from all models. National inventory annual totals from 2024 and 2025 are given as grey and black bars, respectively.

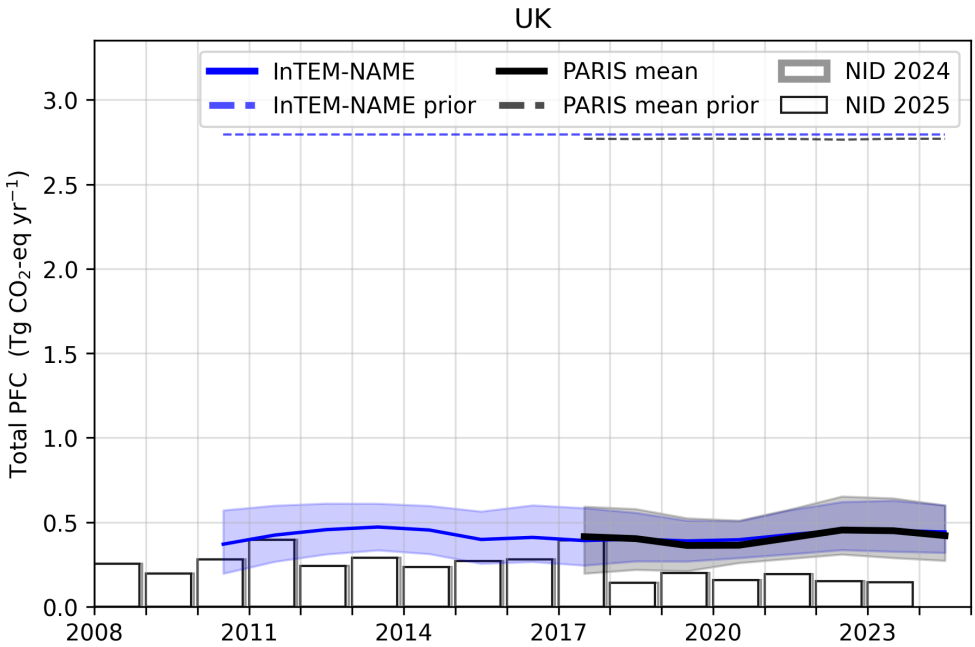

Table 3: Emissions estimation for PFCs according to the National Inventory Document (NID) 2025 and the inversions done in the PARIS project. For the PARIS estimation, the mean of all models is displayed, along with a range of uncertainty estimated via the half distance between the maximum and minimum uncertainties of the different models.

		2020	2021	2022	2023	2024
PFC-14	NID 2025	0.03	0.04	0.03	0.03	
$(\mathrm{TgCO_2\text{-}eq \cdot yr^{-1}})$	PARIS mean	0.13 ± 0.09	0.15 ± 0.12	0.17 ± 0.15	0.18 ± 0.16	0.17 ± 0.14
PFC-218	NID 2025	0.08	0.12	0.09	0.09	
$(\mathrm{TgCO_2\text{-}eq \cdot yr^{-1}})$	PARIS mean	0.13 ± 0.05	0.15 ± 0.07	0.15 ± 0.07	0.15 ± 0.08	0.15 ± 0.08
PFC-116	NID 2025	38	33	27	25	
$(\mathrm{GgCO_2\text{-}eq \cdot yr^{-1}})$	PARIS mean	60 ± 51	76 ± 57	89 ± 67	82 ± 67	65 ± 62
PFC-318	NID 2025	0	0	0	0	
$(\mathrm{GgCO_2\text{-}eq \cdot yr^{-1}})$	PARIS mean	45 ± 42	39 ± 41	44 ± 44	39 ± 46	39 ± 46

8 Sulphur hexafluoride (SF_6)

Figure 8.0.1: Total source sensitivity of SF_6 observing sites as calculated by the FLEXPART transport model for the year 2018 (left) and 2024 (right) and used in the inversions. Observing stations active in each year are marked with red dots. Areas with visible land surface represent regions for which emissions can be observed well from the network. Shaded or dark areas represent regions for which limited emission information can be obtained from the network.

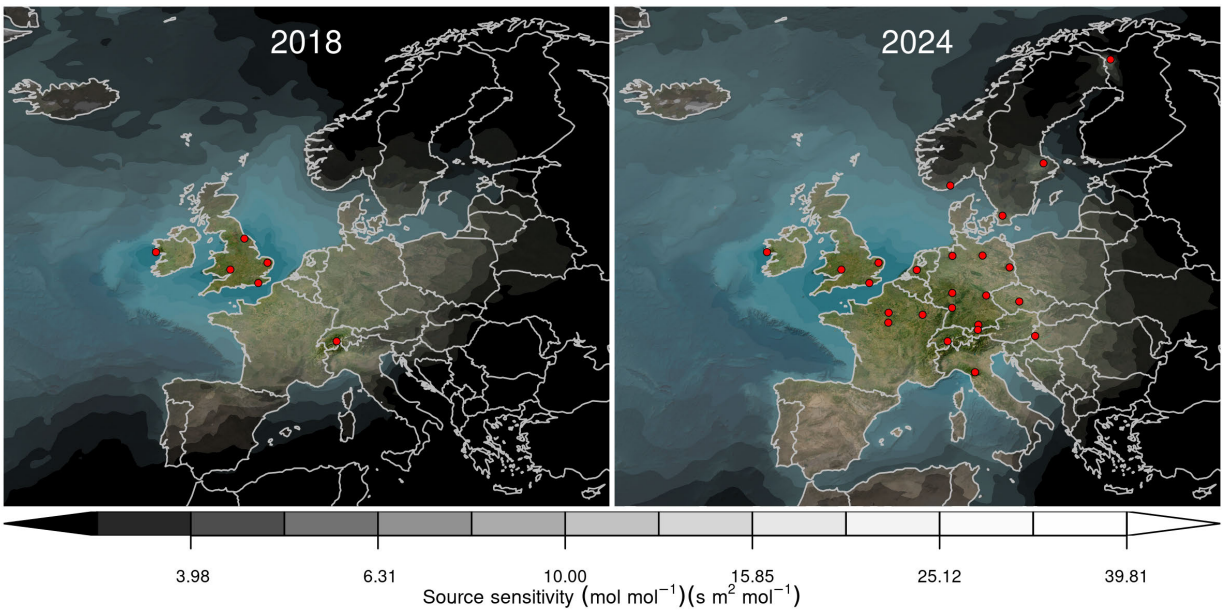

Figure 8.0.2: Verification of the UK emissions inventory estimates for SF_6. Modelled annual emissions are given as the mean from all InTEM and ELRIS inversions (black line) and the individual result from InTEM-NAME (blue line). The shaded blue area is the 68 % confidence interval (CI) of InTEM-NAME and the shaded grey area encompasses the 68 % CI from all models. National inventory annual totals from 2024 and 2025 are given as grey and black bars, respectively.

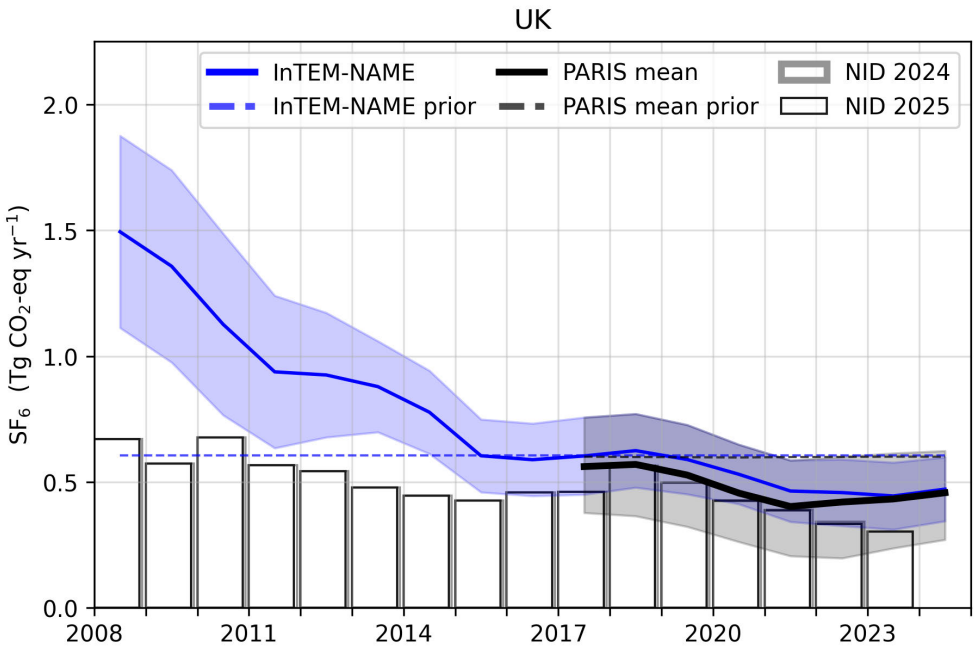

Figure 8.0.3: Spatial distribution of the UK average modelled emissions of SF_6 during the period of 2020-2024 (mean from all InTEM and ELRIS inversions). Observing stations are marked with red circles and highly-populated cities are marked with red triangles.

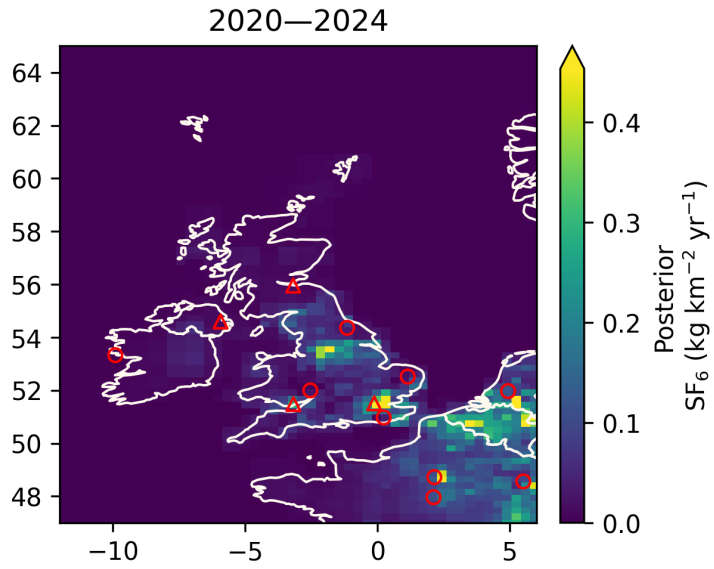

9 Nitrogen Trifluoride (NF_3)

Figure 9.0.1: Verification of the UK emissions inventory estimates for NF_3. Modelled annual emissions are given as the mean from all models (black line) and the individual result from InTEM-NAME (blue line). The shaded blue area is the 68 % confidence interval (CI) of InTEM-NAME and the shaded grey area encompasses the 68 % CI from all models. National inventory annual totals from 2024 and 2025 are given as grey and black bars, respectively.

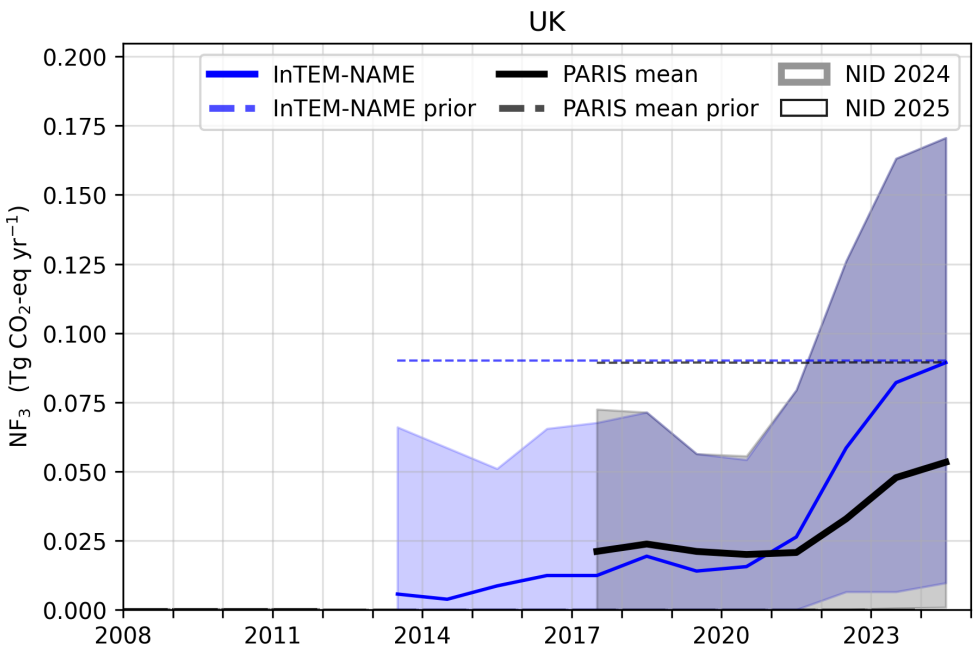

Figure 9.0.2: Spatial distribution of the UK average modelled emissions of NF_3 during the period of 2020-2024 (mean from all models). Observing stations are marked with red circles and highly-populated cities are marked with red triangles.

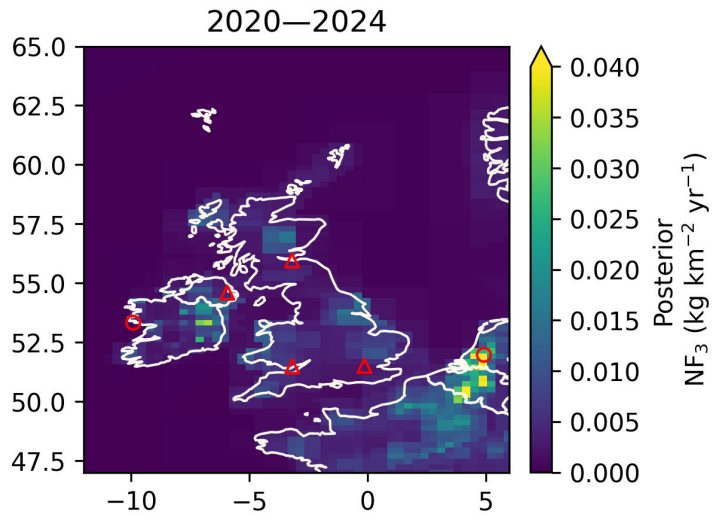

10 Carbon Dioxide (CO_2)

Measurements of CO_2 at ICOS sites and related observatories are influenced by a complex combination of sources and sinks. Fossil fuel combustion for transport, heating, energy generation, and other applications produce CO_2, along with other anthropogenic activities such as cement production. The terrestrial and oceanic biosphere produces CO_2 through animal and plant respiration and takes up CO_2 through photosynthesis. Furthermore, CO_2 is exchanged with the ocean through physical and chemical processes.

When considering high-frequency (∼hourly) CO_2 mole fraction deviations from baseline values—used to infer national emissions in regional inverse modelling studies—the influence of biospheric fluxes can be comparable to, or larger than, those of anthropogenic sources (e.g. White et al., 2019). Therefore, research is under way to develop new tracers that can determine fossil fuel CO_2 fluxes independent of biosphere sources and sinks.

Ongoing Horizon Europe projects PARIS and CORSO are examining methods for estimating fossil fuel CO_2 fluxes based on simultaneous measurements of CO_2 and O_2 (Figure 10.0.1). The method relies on the fact that CO_2 and O_2 are inter-converted during combustion and terrestrial biosphere exchange, but with different ratios for the two processes. A quantity can be constructed from these measurements, known as Atmospheric Potential Oxygen (APO), which is insensitive to biosphere fluxes, and may therefore be useful for isolating fossil fuel signals (Pickers et al., 2022).

High-frequency (∼hourly) timeseries of APO are available from Weybourne (WAO, 2010 – present) and Heathfield (HFD, 2021 - present) in the UK (Figure 10.0.1; Pickers, Adcock, and Manning, 2024), and new sites are being established at Cabauw and Zweth in the Netherlands. Preliminary analyses of the WAO data have revealed regional APO trends consistent with the drop in fossil fuel CO_2 emissions during the COVID lockdowns in the UK (Pickers et al., 2022). However, quantification of absolute regional fossil fuel CO_2 emissions remains an area of active research. Recent studies have derived fossil fuel CO_2 emissions for the UK that are highly uncertain (Rigby et al., 2025). Potential confounding factors were identified in Chawner et al. (2024), such as highly uncertain APO fluxes from the ocean, and a poorly constrained regional APO background. These factors are the subject of ongoing research using atmospheric models and new APO measurements from PARIS, CORSO and ICOS.

An alternative method for top-down fossil fuel CO_2 emissions evaluation uses measurements of radiocarbon isotopologues ($^{14}CO_2$, compared to the dominant $^{12}CO_2$). Fossil fuels do not contain ^{14}C, and therefore, their combustion tends to decrease the atmospheric $^{14}CO_2/^{12}CO_2$ ratio. Currently, radiocarbon mea-

surements can only be made at low frequency using flask sampling. However, a relatively intensive flask sampling campaign was carried out across Europe during 2024 as part of CORSO, and the results of this study will be reported on soon.

Figure 10.0.1: Carbon dioxide (top, red) and oxygen (bottom, blue) measurements from Weybourne Atmospheric Observatory in the UK, available from the ICOS Carbon Portal (Adcock et al., 2024).

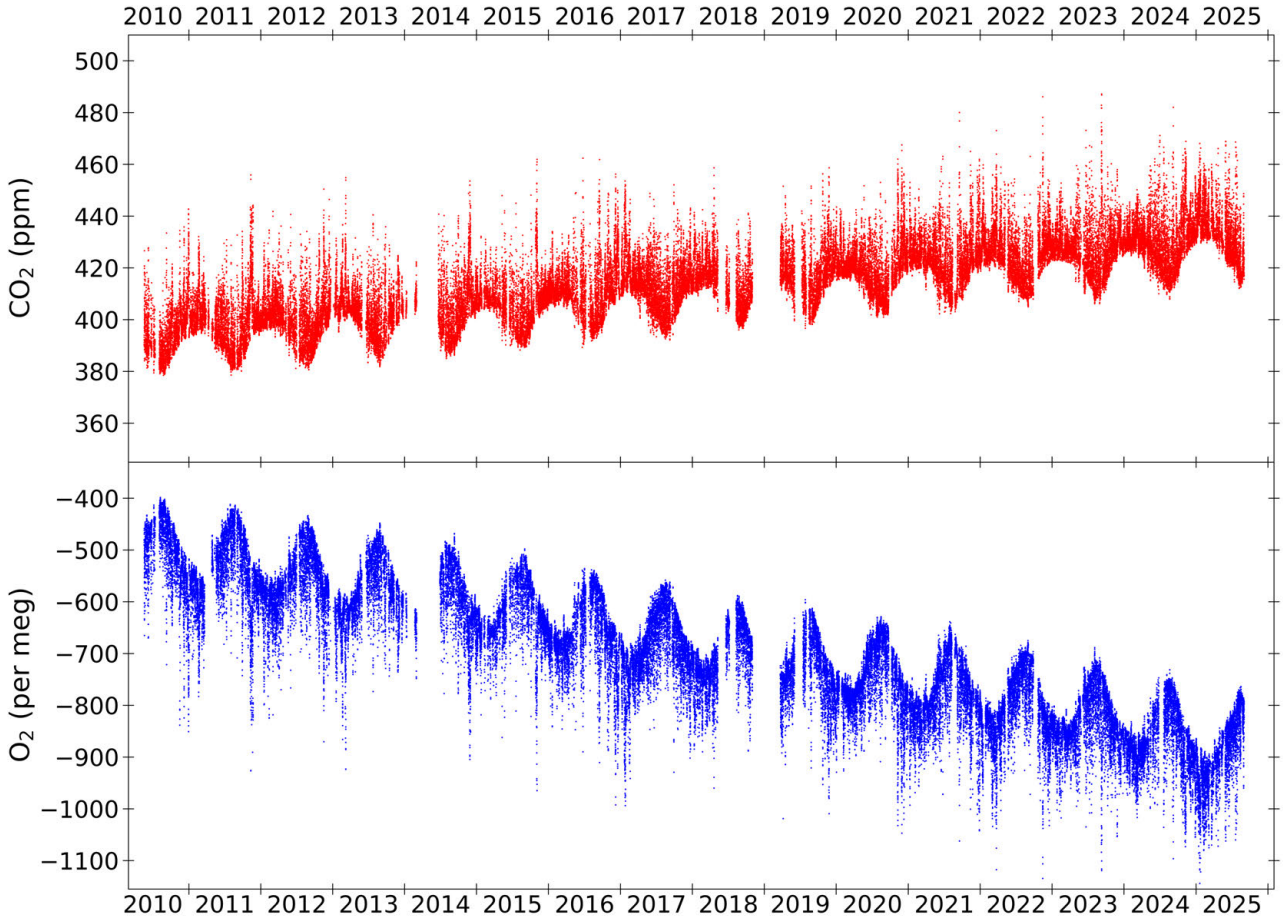

References

Adcock, Karina et al. (2024). *Atmospheric GHG data product (o2, o2_stdev, co2, co2_stdev) from Weybourne (10.0 m), 2010-05-19–2023-12-31*. URL: https://hdl.handle.net/11676/j4LzdHQiq3fPgfNeXHruC0Bb.

Chawner, Hannah et al. (Apr. 2024). "Atmospheric oxygen as a tracer for fossil fuel carbon dioxide: a sensitivity study in the UK". en. In: *Atmospheric Chemistry and Physics* 24.7, pp. 4231–4252. ISSN: 1680-7324. DOI: 10.5194/acp-24-4231-2024. URL: https://acp.copernicus.org/articles/24/4231/2024/ (visited on 04/10/2024).

European Commission: Joint Research, Centre et al. (2023). *GHG emissions of all world countries – 2023*. Publications Office of the European Union. DOI: 10.2760/953322.

Ganesan, A. L. et al. (2014). "Characterization of uncertainties in atmospheric trace gas inversions using hierarchical Bayesian methods". In: *Atmospheric Chemistry and Physics* 14.8, pp. 3855–3864. DOI: 10.5194/acp-14-3855-2014. URL: http://www.atmos-chem-phys.net/14/3855/2014/http://www.atmos-chem-phys.net/14/3855/2014/acp-14-3855-2014.pdf.

Ganesan, A. L. et al. (2015). "Quantifying methane and nitrous oxide emissions from the UK and Ireland using a national-scale monitoring network". In: *Atmos. Chem. Phys.* 15.11, pp. 6393–6406. DOI: 10.5194/acp-15-6393-2015. URL: https://www.atmos-chem-phys.net/15/6393/2015/https://www.atmos-chem-phys.net/15/6393/2015/acp-15-6393-2015.pdf.

Henne, S. et al. (2016). "Validation of the Swiss methane emission inventory by atmospheric observations and inverse modelling". In: *Atmospheric Chemistry and Physics* 16.6, pp. 3683–3710. DOI: 10.5194/acp-16-3683-2016. URL: http://www.atmos-chem-phys.net/16/3683/2016/.

Jones, A.R. et al. (2007). "The U.K. Met Office's next-generation atmospheric dispersion model, NAME III, in Borrego C. and Norman A.-L. (Eds)". In: *Air Pollution Modeling and its Application XVII (Proceedings of the 27th NATO/CCMS International Technical Meeting on Air Pollution Modelling and its Application), Springer*, pp. 580–589.

Katharopoulos, I. et al. (2023). "Impact of transport model resolution and a priori assumptions on inverse modeling of Swiss F-gas emissions". In: *Atmos. Chem. Phys.* 23.22, pp. 14159–14186. DOI: 10.5194/acp-23-14159-2023. URL: https://acp.copernicus.org/articles/23/14159/2023/.

Manning, A. J. et al. (2021). "Evidence of a recent decline in UK emissions of hydrofluorocarbons determined by the InTEM inverse model and atmospheric measurements". In: *Atmospheric Chemistry and Physics* 21.16, pp. 12739–12755. DOI: 10.5194/acp-21-12739-2021. URL: https://acp.copernicus.org/articles/21/12739/2021/.

Pickers, P., K. Adcock, and A. Manning (Feb. 2024). *Atmospheric oxygen and carbon dioxide observations from Weybourne Atmospheric Observatory, Norfolk, UK uploaded to public archives*. Tech. rep. Process Attribution of Regional Emissions (PARIS). URL: https://horizoneurope-paris.eu/wp-content/uploads/sites/914/2024/07/PARIS-deliverables-D6.1-High-frequency-APO-data-uploaded-final.pdf.

Pickers, Penelope A. et al. (Apr. 2022). "Novel quantification of regional fossil fuel CO2 reductions during COVID-19 lockdowns using atmospheric oxygen measurements". en. In: *Science Advances* 8.16, eabl9250. ISSN: 2375-2548. DOI: 10.1126/sciadv.abl9250. URL: https://www.science.org/doi/10.1126/sciadv.abl9250 (visited on 12/01/2023).

Rigby, M. et al. (2019). "Increase in CFC-11 emissions from eastern China based on atmospheric observations". In: *Nature* 569, pp. 546–550. DOI: 10.1038/s41586-019-1193-4. URL: https://doi.org/10.1038/s41586-019-1193-4.

Rigby, M. et al. (Apr. 2025). *Inverse estimates of fossil fuel CO2 emission*. Tech. rep. Process Attribution of Regional Emissions (PARIS). URL: https://horizoneurope-paris.eu/wp-content/uploads/sites/914/2025/01/PARIS-M24-Inverse-estimates-of-fossil-fuel-CO2-emissions-final.pdf.

Stohl, A. et al. (2005). "Technical note: The Lagrangian particle dispersion model FLEXPART version 6.2". In: *Atmospheric Chemistry and Physics* 5, pp. 2461–2474. DOI: 10.5194/acp-5-2461-2005. URL: <GotoISI>://000231983600002.

White, Emily D. et al. (Apr. 2019). "Quantifying the UK's carbon dioxide flux: an atmospheric inverse modelling approach using a regional measurement network". en. In: *Atmospheric Chemistry and Physics*

19.7, pp. 4345–4365. ISSN: 1680-7324. DOI: 10.5194/acp-19-4345-2019. URL: https://www.atmos-chem-phys.net/19/4345/2019/ (visited on 04/05/2019).

Draft Inventory Annex
Ireland 2025

30th October, 2025

1 Introduction

In this document, global concentration trends and national emissions estimates derived from atmospheric observations ("inverse estimates") are presented for most reported gases. Comparing the emissions submitted in national inventories with those calculated using atmospheric observations allows for emissions to be assessed using two fundamentally different approaches. Substantial differences can highlight areas that could warrant further investigation.

Global concentration trends for each gas are first shown using annual average concentrations from Mace Head, Ireland (Northern Hemisphere) and Kennaook/Cape Grim, Tasmania, Australia (Southern Hemisphere). Data from these stations were selected to exclude regionally-polluted air masses and therefore represents northern and southern hemispheric concentration trends. Mace Head observations were supported by the National Aeronautics and Space Administration (NASA) and the UK Department of Energy, Security and Net Zero (DESNZ), and Kennaook/Cape Grim observations by NASA and the Australian Bureau of Meteorology.

Observations of European concentrations of greenhouse gases used to derive national inverse emission estimates were collected from many different networks and providers. Methane and nitrous oxide concentrations originated from the European ICOS (Integrated Carbon Observation System) network, the UK DECC (Deriving Emissions related to Climate Change) network and other national or individual initiatives. F-gas observations were made by affiliates of the AGAGE (Advanced Global Atmospheric Gases Experiment) network. Observations from additional stations across Europe were supported by the Horizon-EU PARIS (Process Attribution of Regional Emissions) project. The observation stations used to derive emissions for each gas are shown in the corresponding sections of this document.

An atmospheric transport model provides the link between surface fluxes and concentrations measured at the observing stations. If not otherwise mentioned, inversion-based emissions estimates were derived using two atmospheric transport models combined with three inverse models, yielding a total of six inversions. This ensemble of six inversions allows us to better quantify the uncertainties associated with inverse modelling.

The two atmospheric transport models used are the Numerical Atmospheric dispersion Modelling Environment (NAME, Jones et al., 2007), and the FLEXible PARTicle dispersion model (FLEXPART, Stohl et al., 2005). Both models are backwards-running Lagrangian Particle Dispersion Models (LPDMs) that simulate the recent transport of air to each observing station. The two LPDMs have been widely used in the estimation of greenhouse gas emissions (Ganesan et al., 2015; Rigby et al., 2019; Manning et al., 2021; Henne et al., 2016).

The three inverse methods used are InTEM (Inversion Technique for Emission Modelling, Manning et al., 2021), ELRIS (Empa Lagrangian Regional Inversion System, Henne et al., 2016; Katharopoulos et al., 2023), and RHIME (Regional Hierarchical Inverse Modelling Environment, Ganesan et al., 2014). All three inverse methods estimate emissions within Europe along with boundary conditions that account for the concentration of the air entering Europe. All three systems started from the same set of a priori emissions that were either derived from the global EDGAR emission inventory (version 8, European Commission: Joint Research et al., 2023) or a uniform land-based emission, depending on the gas. A natural emission component, from the WETCHARTS product, was included in the methane prior. The same observational dataset was used by each inverse model, but data selection (i.e., filtering datasets for specific conditions) and treatment of uncertainties were chosen separately and hence differ. The three methods also differ in their statistical approaches for estimating emissions.

Emission estimates are presented for the period 2008-2024. Emissions for the full 2008-2024 period were derived with the InTEM-NAME inversion only, while emissions from 2017-2024 are presented as the mean of the six inversions (denoted the "PARIS mean"). The uncertainty shown is the minimum/maximum of the uncertainties in the ensemble.

All inversions employed a resolution of one month for CH_4 and N_2O and 1-year for the fluorinated gases. The inversion results used to compare with the inventories are a one-year calendar average for CH_4 and N_2O and the yearly value derived from a 3-year moving average for the fluorinated gases. For the 2008-2024

InTEM-NAME results, a 3-year moving average was also applied to the annualised CH_4 and N_2O results due to lack of observational coverage in the earlier years.

2 Global Concentration Trends

2.1 Methane (CH_4)

Figure 2.1.1: Background Northern Hemisphere monthly concentrations of CH_4 estimated from MHD, Ireland observations are shown in red, and background Southern Hemisphere monthly concentrations from CGO, Tasmania are shown in blue. Grey shading represents provisional data.

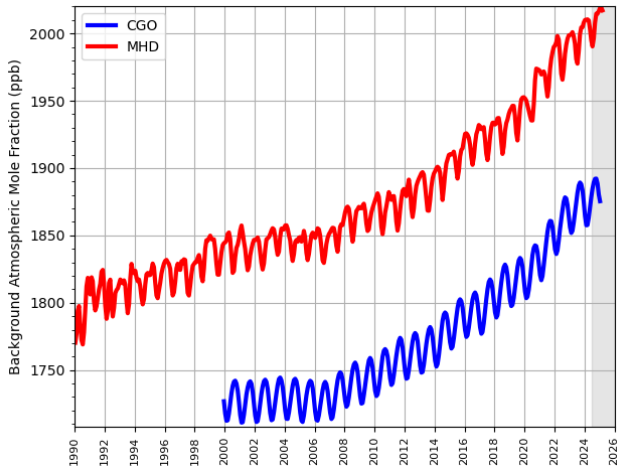

2.2 Nitrous Oxide (N_2O)

Figure 2.2.1: Background Northern Hemisphere monthly concentrations of N_2O estimated from MHD, Ireland observations are shown in red, and background Southern Hemisphere monthly concentrations from CGO, Tasmania are shown in blue. Grey shading represents provisional data.

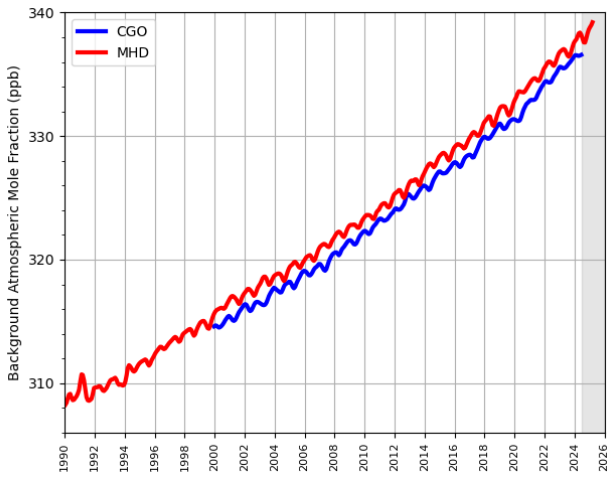

2.3 Hydrofluorocarbons (HFCs)

Figure 2.3.1: Background Northern Hemisphere monthly concentrations of six HFCs estimated from MHD, Ireland observations are shown in red, and background Southern Hemisphere monthly concentrations from CGO, Tasmania are shown in blue. Grey shading represents provisional data.

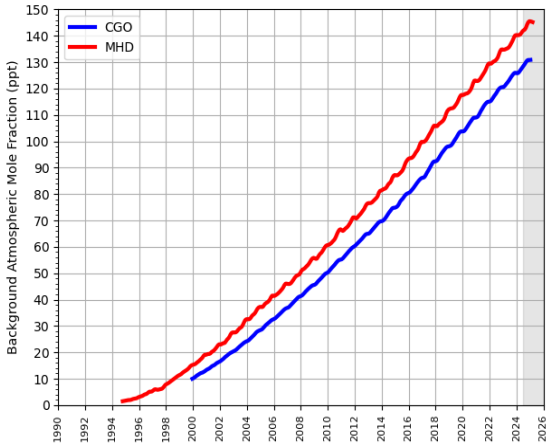

(a) HFC-134a

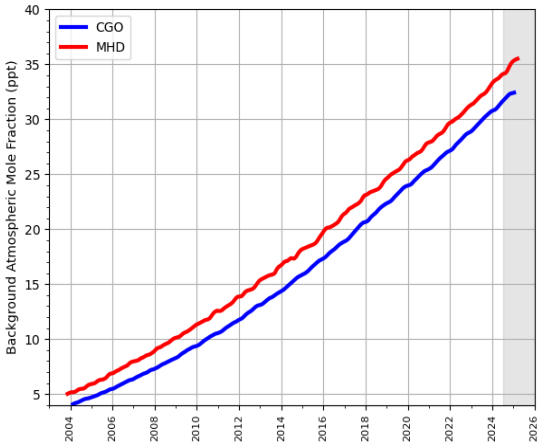

(b) HFC-143a

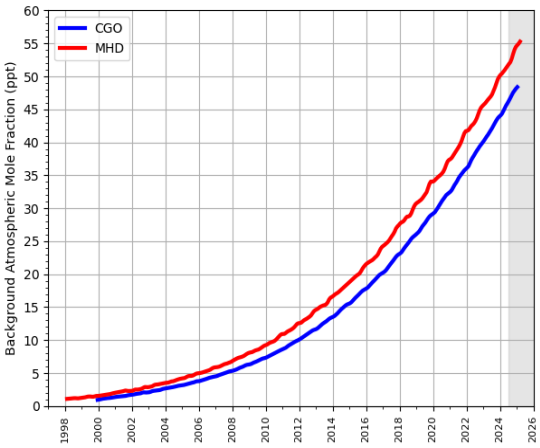

(c) HFC-125

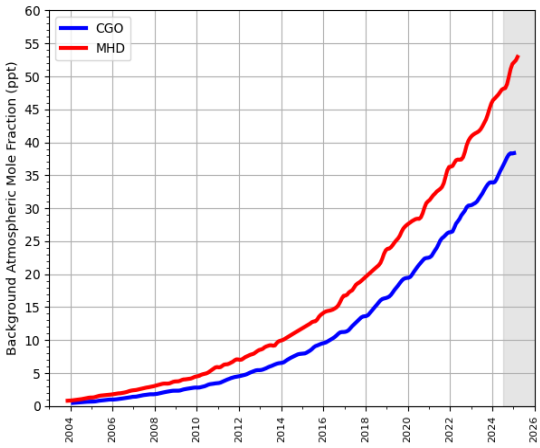

(d) HFC-32

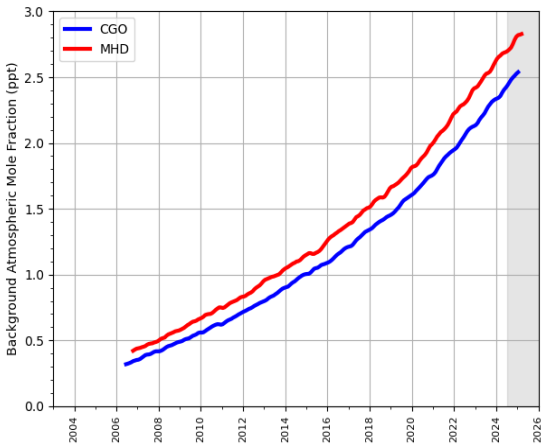

(e) HFC-227ea

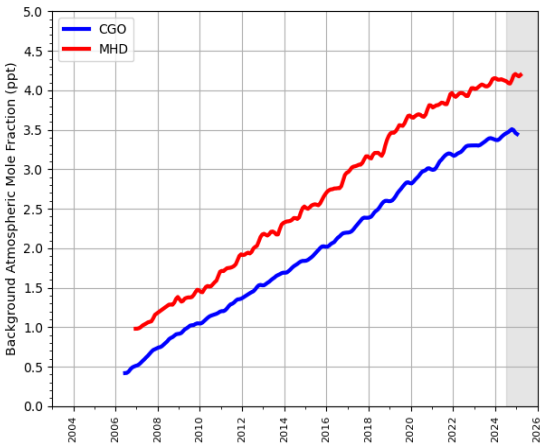

(f) HFC-245fa

Figure 2.3.2: Background Northern Hemisphere monthly concentrations of four HFCs estimated from MHD, Ireland observations are shown in red, and background Southern Hemisphere monthly concentrations from CGO, Tasmania are shown in blue. Grey shading represents provisional data.

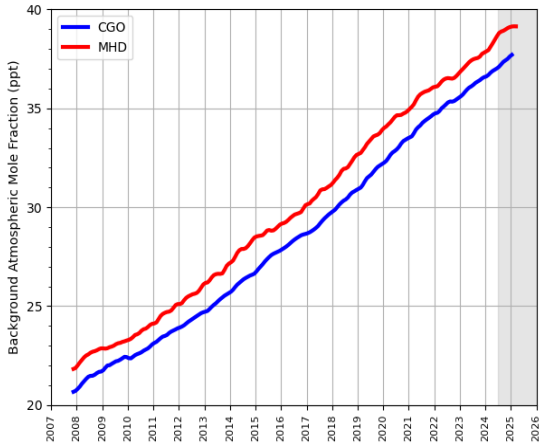

(a) HFC-23

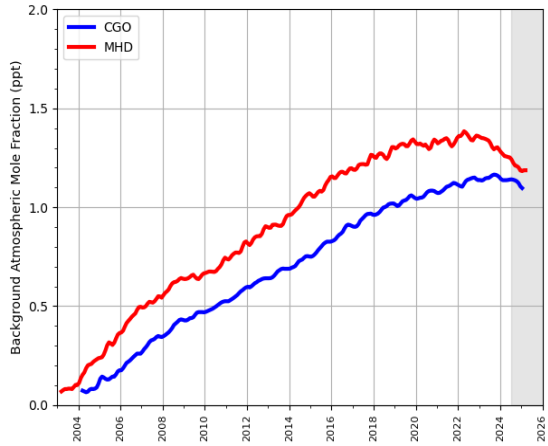

(b) HFC-365mfc

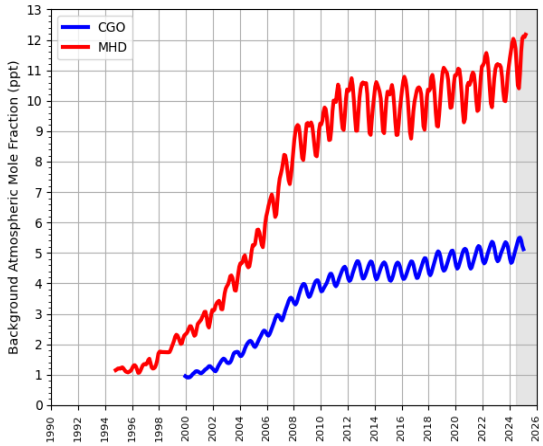

(c) HFC-152a

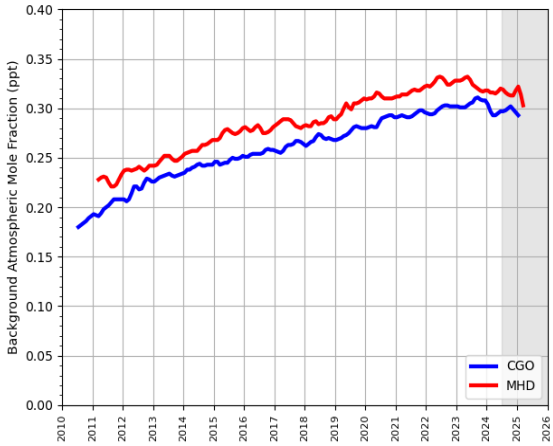

(d) HFC-43-10-mee

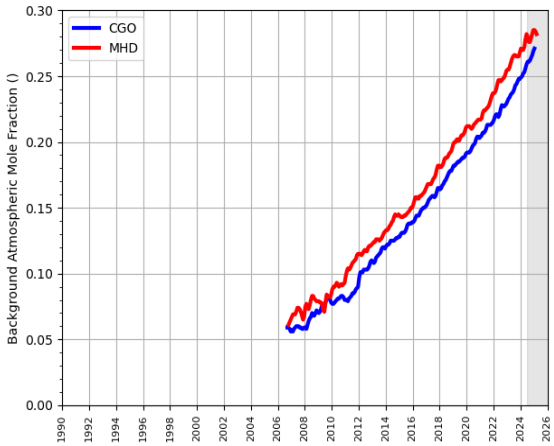

(e) HFC-236fa

2.4 Perfluorocarbons (PFCs)

Figure 2.4.1: Background Northern Hemisphere monthly concentrations of four PFCs estimated from MHD, Ireland observations are shown in red, and background Southern Hemisphere monthly concentrations from CGO, Tasmania are shown in blue. Grey shading represents provisional data.

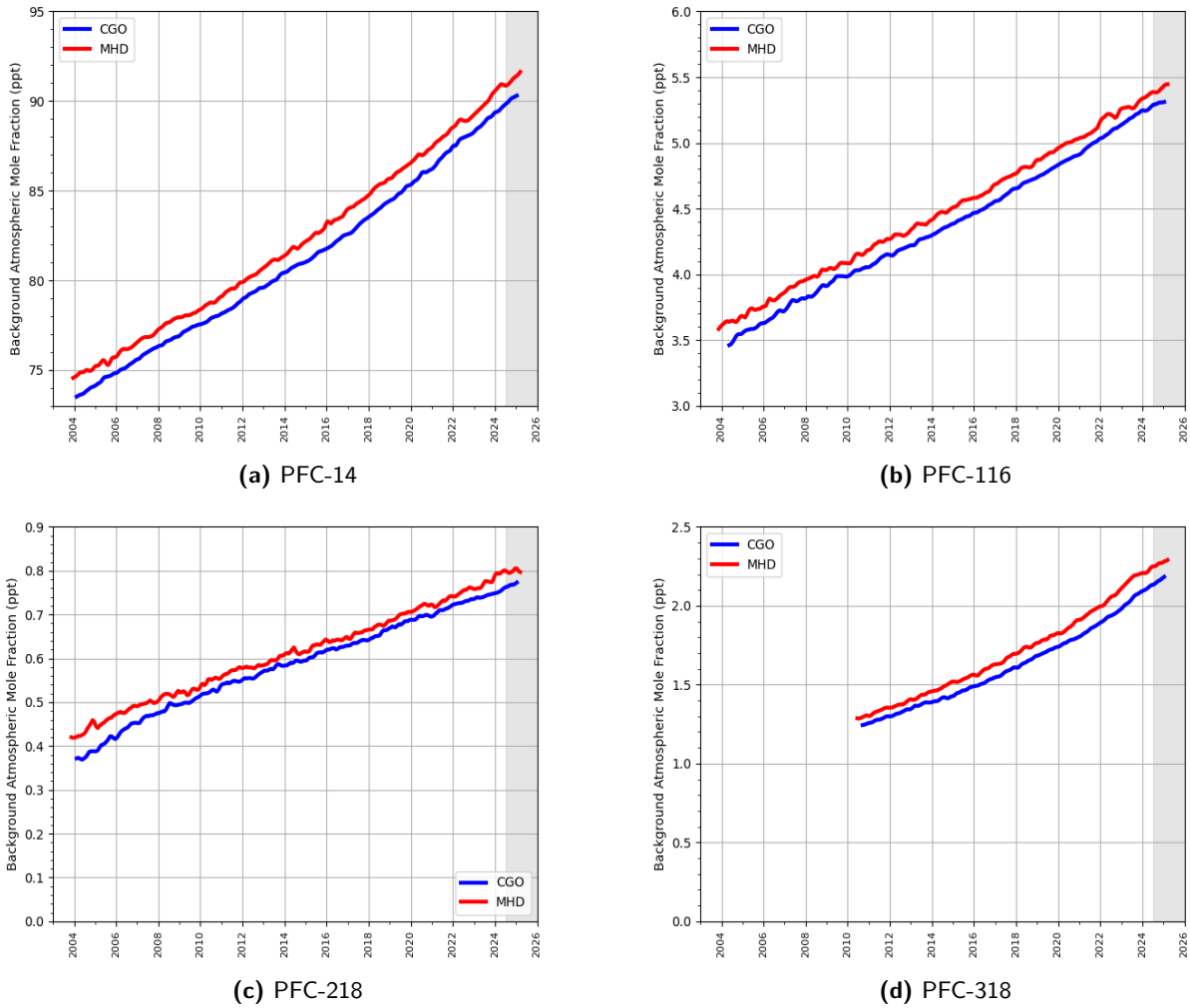

(a) PFC-14 **(b)** PFC-116 **(c)** PFC-218 **(d)** PFC-318

2.5 Sulphur Hexafluoride (SF_6) and Nitrogen Trifluoride (NF_3)

Figure 2.5.1: Background Northern Hemisphere monthly concentrations of SF_6 and NF_3 estimated from MHD, Ireland observations are shown in red, and background Southern Hemisphere monthly concentrations from CGO, Tasmania are shown in blue. Grey shading represents provisional data.

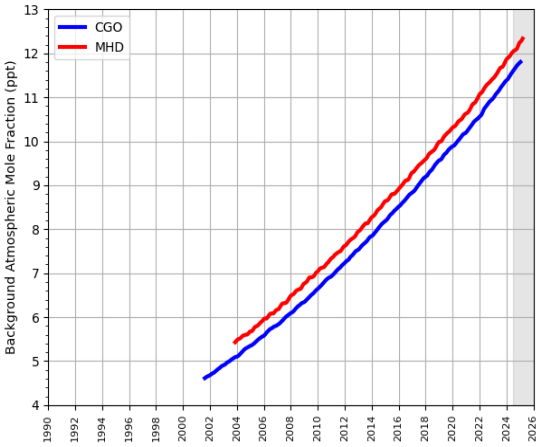

(a) SF_6

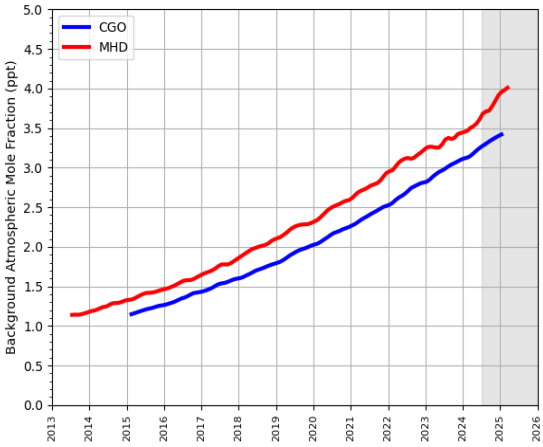

(b) NF_3

2.6 Carbon Dioxide (CO_2)

Figure 2.6.1: Background Northern Hemisphere monthly concentrations of CO_2 estimated from MHD, Ireland observations are shown in red, and background Southern Hemisphere monthly concentrations from CGO, Tasmania are shown in blue. Grey shading represents provisional data.

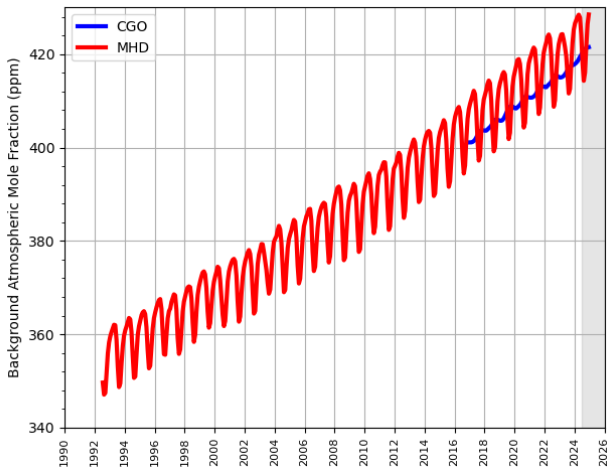

3 Key findings

- Methane (CH_4): Inversion results are around 20% lower than the inventory estimates from 2018. The inclusion of additional observational data, from sites remote from Ireland from 2017, has had an impact on the inverse estimates. This impact requires further investigation. There does not appear to be a strong seasonal cycle in the emissions.
- Nitrous oxide (N_2O): Inversion results are around 15% higher than the inventory estimates. Over the last eight years the inverse results show a declining trend. A decline is seen in the inventory from 2021. In all years the inverse models estimate a pronounced seasonal cycle in emissions with the maximum in late spring or early summer.
- Hydrofluorocarbons (HFCs): The emission estimates from the inverse models generally agree, within the uncertainties, with those reported in the inventory. The very sharp drop in the inventory emissions in 2018 for HFC-143a is not seen in the inversions, they have a more steady decline.
- Perfluorocarbons (PFCs): The inverse results reveal some notable areas of emission, near Dublin for PFC-14 and near Cork for PFC-116. The inverse model estimates are very low and uncertain for PFC-218 and PFC-318. The total estimate is dominated by PFC-14 and the inversions indicate a growth in emissions although the uncertainties are large, in contrast the inventory has been flat or declining since 2019.
- Sulphur hexafluoride (SF_6): The trend estimated by the inversions is approximately consistent with that reported in the inventory, although the inverse results are generally higher, albeit with high uncertainty.
- The observational coverage of Ireland is acceptable.
- The model results using FLEXPART for all three inverse systems have a tendency to estimate lower emissions. This has generally lowered the PARIS mean and broadened the overall uncertainty.

Table 1: Emissions estimation for the main greenhouse gases of focus according to the National Inventory Document (NID) 2025 and the inversions done in the PARIS project. For the PARIS estimation, the mean of all models is displayed, along with a range of uncertainty estimated via the half distance between the maximum and minimum uncertainties of the different models. For SF_6, the PARIS mean is the average of all InTEM and ELRIS inversions only.

		2020	2021	2022	2023	2024
CH_4	NID 2025	19.8	19.9	19.9	19.5	
$(\mathrm{TgCO_2\text{-}eq \cdot yr^{-1}})$	PARIS mean	13.4 ± 4.1	16.1 ± 3.6	16.8 ± 3.5	16.4 ± 3.5	17.1 ± 4.5
N_2O	NID 2025	5.82	5.97	5.55	5.10	
$(\mathrm{TgCO_2\text{-}eq \cdot yr^{-1}})$	PARIS mean	6.84 ± 2.06	7.30 ± 1.85	6.06 ± 2.50	5.73 ± 2.31	6.21 ± 1.48
Total HFC	NID 2025	0.62	0.67	0.63	0.61	
$(\mathrm{TgCO_2\text{-}eq \cdot yr^{-1}})$	PARIS mean	0.78 ± 0.24	0.69 ± 0.22	0.59 ± 0.19	0.59 ± 0.17	0.56 ± 0.17
Total PFC	NID 2025	0.06	0.06	0.05	0.03	
$(\mathrm{TgCO_2\text{-}eq \cdot yr^{-1}})$	PARIS mean	0.07 ± 0.05	0.08 ± 0.06	0.10 ± 0.09	0.11 ± 0.09	0.12 ± 0.10
SF_6	NID 2025	17	25	30	31	
$(\mathrm{GgCO_2\text{-}eq \cdot yr^{-1}})$	PARIS mean	53 ± 41	37 ± 33	21 ± 36	20 ± 31	26 ± 37
NF_3	NID 2025	10	9	9	8	
$(\mathrm{GgCO_2\text{-}eq \cdot yr^{-1}})$	PARIS mean	6 ± 10	8 ± 18	8 ± 20	11 ± 27	11 ± 25

4 Methane (CH_4)

Figure 4.0.1: Average monthly total source sensitivity of CH_4 observing sites as calculated by the FLEXPART transport model for the year 2018 (left) and 2024 (right) and used in the inversions. Observing stations active in each year are marked with red dots. Areas with visible land surface represent regions for which emissions can be observed well from the network. Shaded or dark areas represent regions for which limited emission information can be obtained from the network.

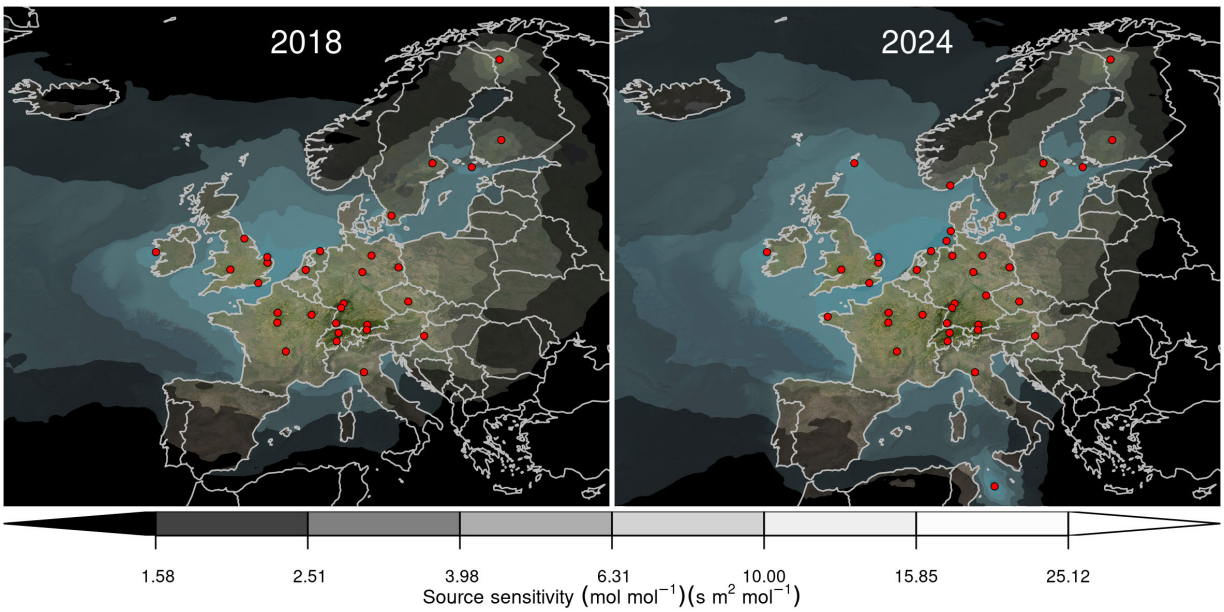

Figure 4.0.2: Verification of the Irish emissions inventory estimates for CH_4. Modelled annual emissions are given as the mean from all models (black line) and the individual result from InTEM-NAME (blue line). The shaded blue area is the 68 % confidence interval (CI) of InTEM-NAME and the shaded grey area encompasses the 68 % CI from all models. National inventory annual totals from 2024 and 2025 are given as grey and black bars, respectively.

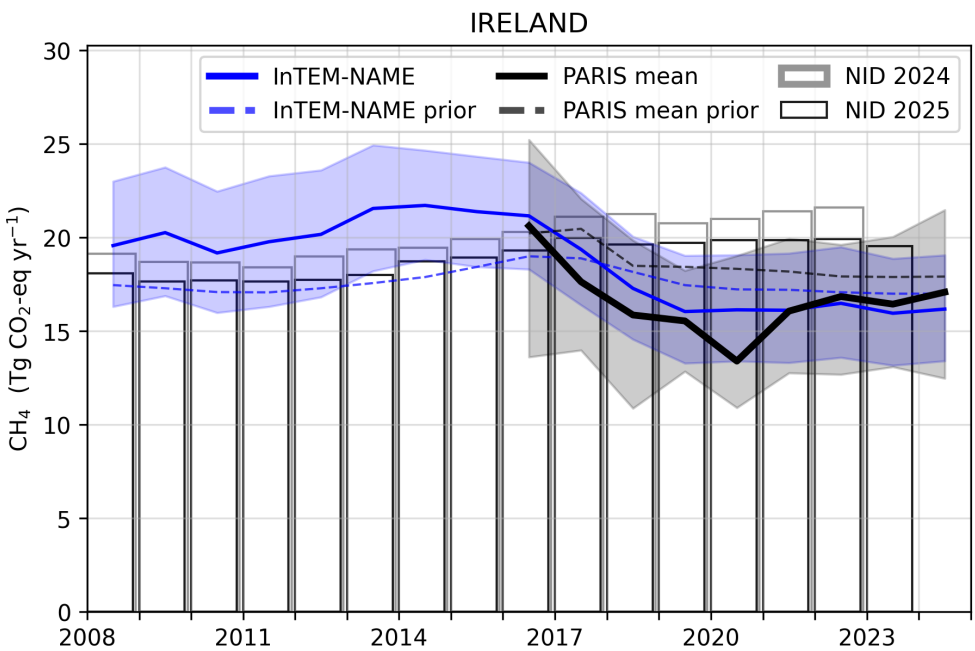

Figure 4.0.3: Verification of the Irish emissions inventory estimates for CH_4 (zoom in to 2018-2024). Modelled annual emissions are given as the mean from all models (black line) and the individual result from InTEM-NAME (blue line). The shaded blue area is the 68 % confidence interval (CI) of InTEM-NAME and the shaded grey area encompasses the 68 % CI from all models. National inventory annual totals from 2024 and 2025 are given as grey and black bars, respectively.

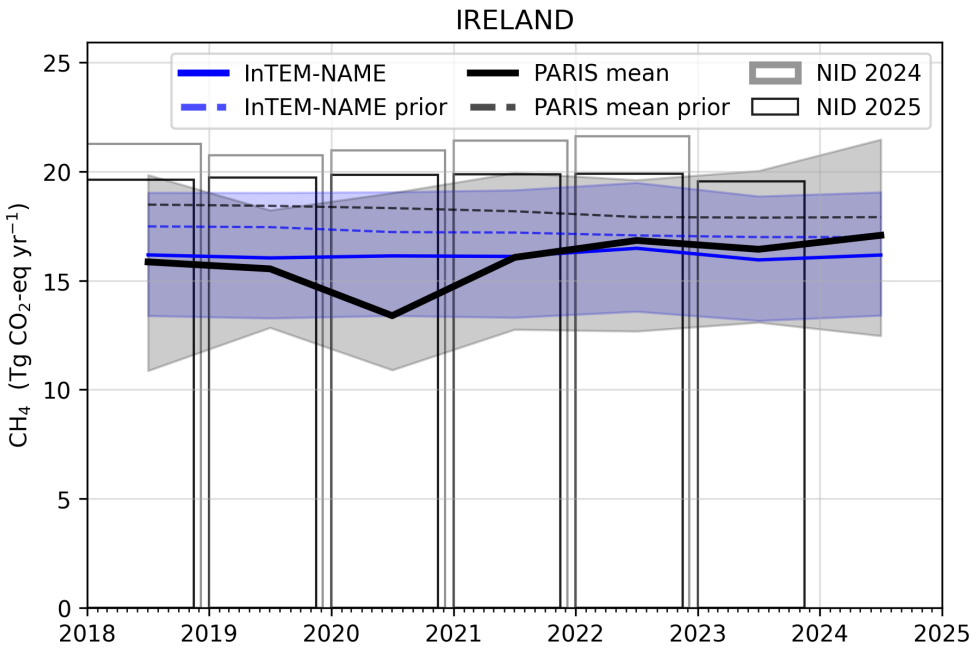

Figure 4.0.4: Verification of the Irish emissions inventory estimates for CH_4 (zoom in to 2018-2024). Modelled monthly emissions are given as the mean from all models (black line) and the individual result from InTEM-NAME (blue line). The shaded blue area is the 68 % confidence interval (CI) of InTEM-NAME and the shaded grey area encompasses the 68 % CI from all models. National inventory annual totals from 2024 and 2025 are given as grey and black bars, respectively.

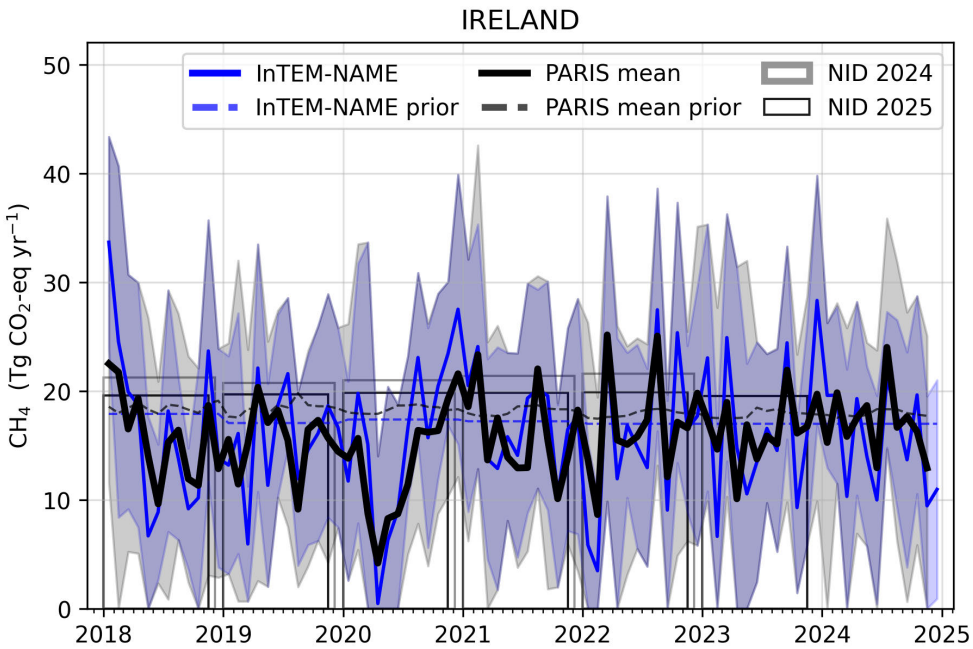

Figure 4.0.5: Spatial distribution of the Irish average modelled emissions of CH_4 during the period of 2020-2024 (mean from all models). Observing stations are marked with red circles and highly-populated cities are marked with red triangles.

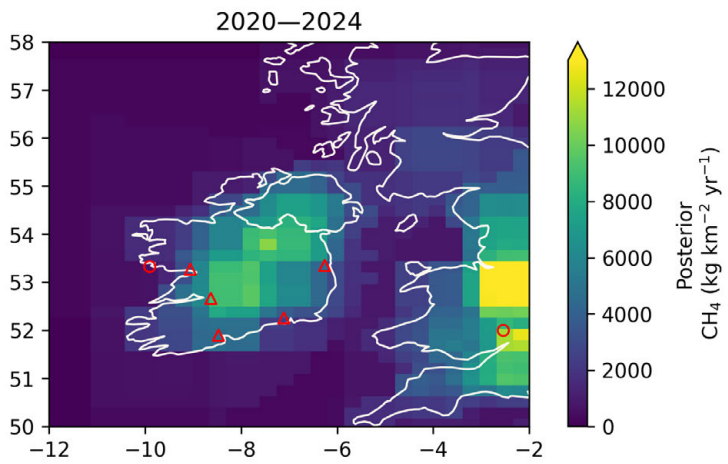

Figure 4.0.6: Spatial distribution of the seasonal deviation from the mean. The deviation is defined as the modelled Irish seasonally averaged CH_4 emissions over 2020-2024 minus the average over the whole period. The mean across all models is shown. Observing stations are marked with black circles and highly-populated cities are marked with black triangles.

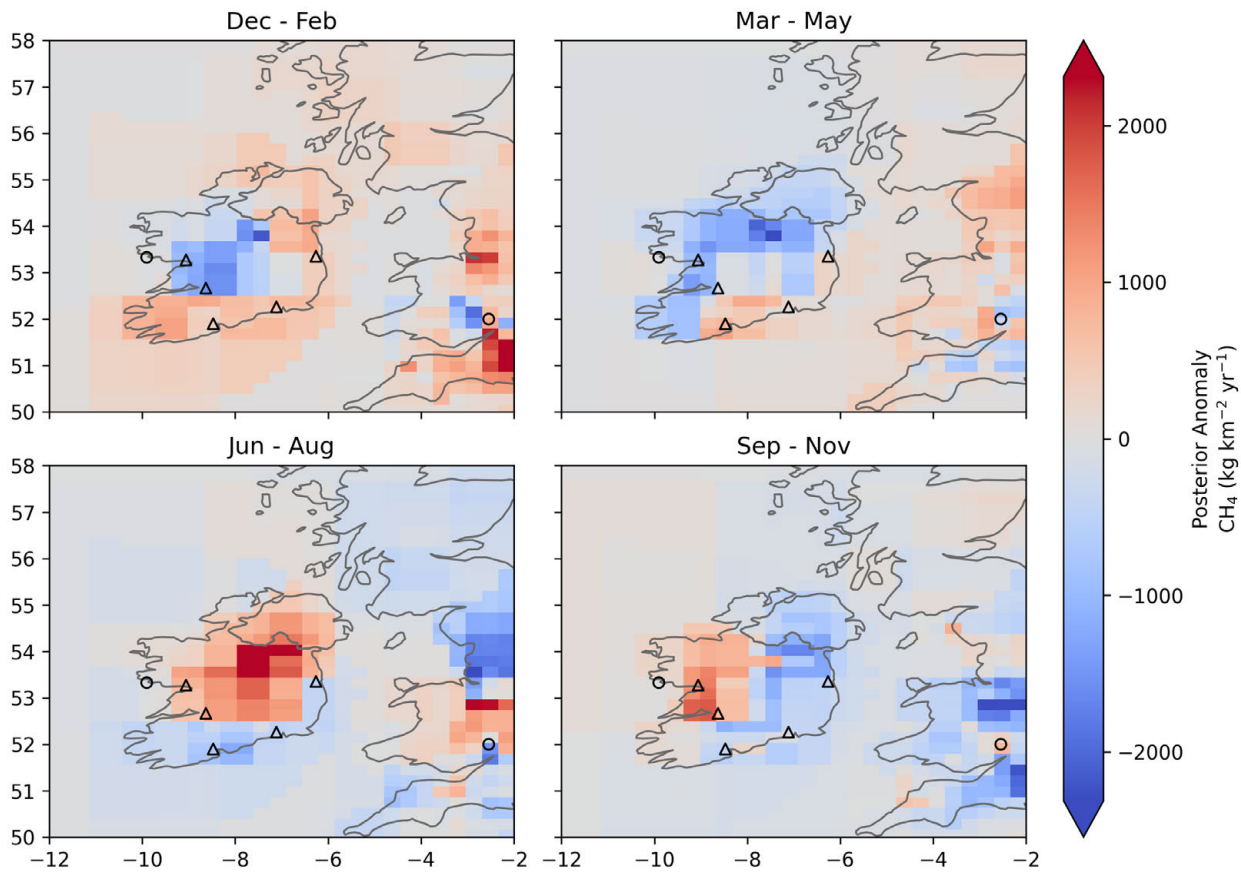

5 Nitrous Oxide (N_2O)

Figure 5.0.1: Average monthly total source sensitivity of N_2O observing sites as calculated by the FLEXPART transport model for the year 2018 (left) and 2024 (right) and used in the inversions. Observing stations active in each year are marked with red dots. Areas with visible land surface represent regions for which emissions can be observed well from the network. Shaded or dark areas represent regions for which limited emission information can be obtained from the network.

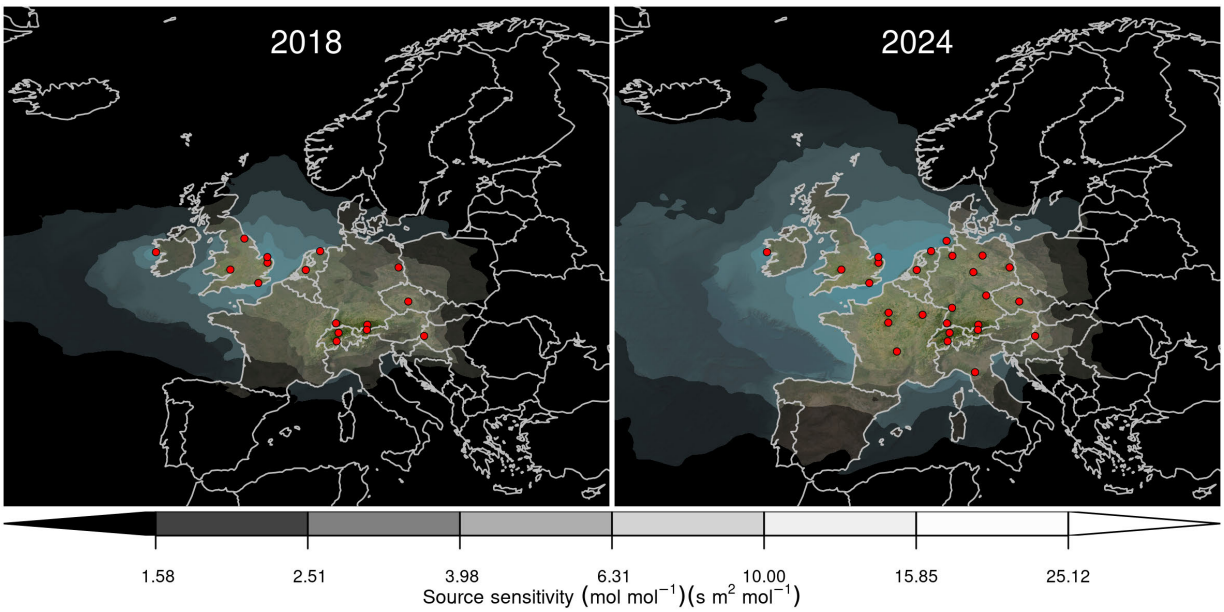

Figure 5.0.2: Verification of the Irish emissions inventory estimates for N_2O. Modelled annual emissions are given as the mean from all models (black line) and the individual result from InTEM-NAME (blue line). The shaded blue area is the 68 % confidence interval (CI) of InTEM-NAME and the shaded grey area encompasses the 68 % CI from all models. National inventory annual totals from 2024 and 2025 are given as grey and black bars, respectively.

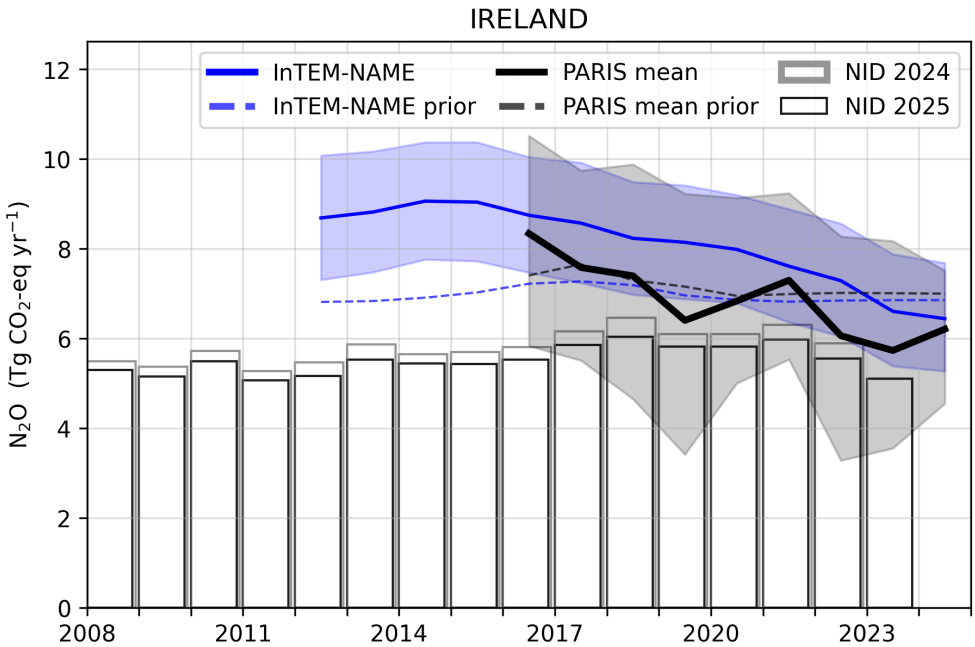

Figure 5.0.3: Verification of the Irish emissions inventory estimates for N_2O (zoom in to 2018-2024). Modelled annual emissions are given as the mean from all models (black line) and the individual result from InTEM-NAME (blue line). The shaded blue area is the 68 % confidence interval (CI) of InTEM-NAME and the shaded grey area encompasses the 68 % CI from all models. National inventory annual totals from 2024 and 2025 are given as grey and black bars, respectively.

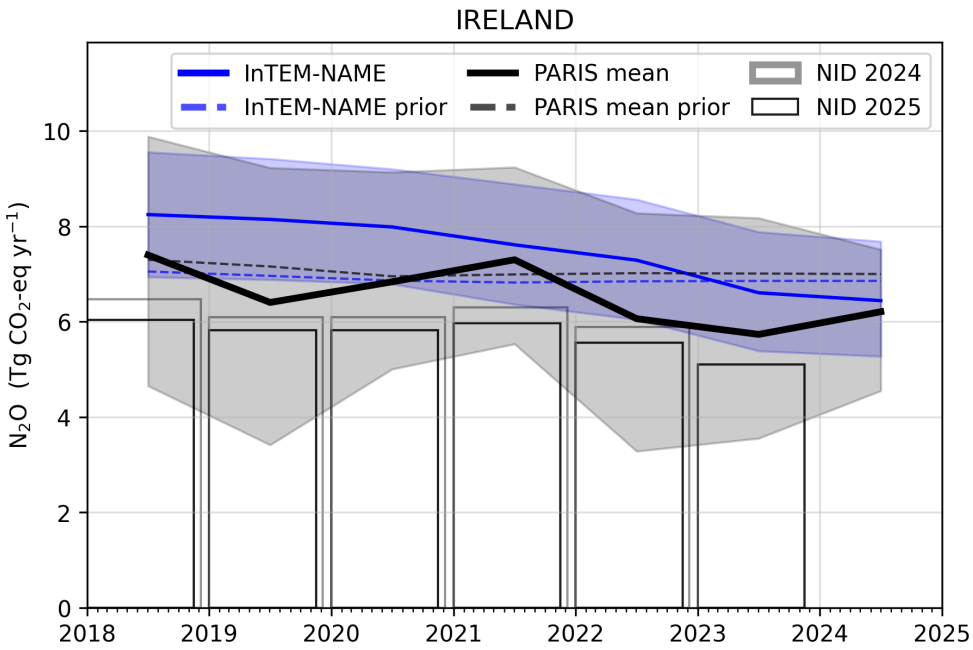

Figure 5.0.4: Verification of the Irish emissions inventory estimates for N_2O (zoom in to 2018-2024). Modelled monthly emissions are given as the mean from all models (black line) and the individual result from InTEM-NAME (blue line). The shaded blue area is the 68 % confidence interval (CI) of InTEM-NAME and the shaded grey area encompasses the 68 % CI from all models. National inventory annual totals from 2024 and 2025 are given as grey and black bars, respectively.

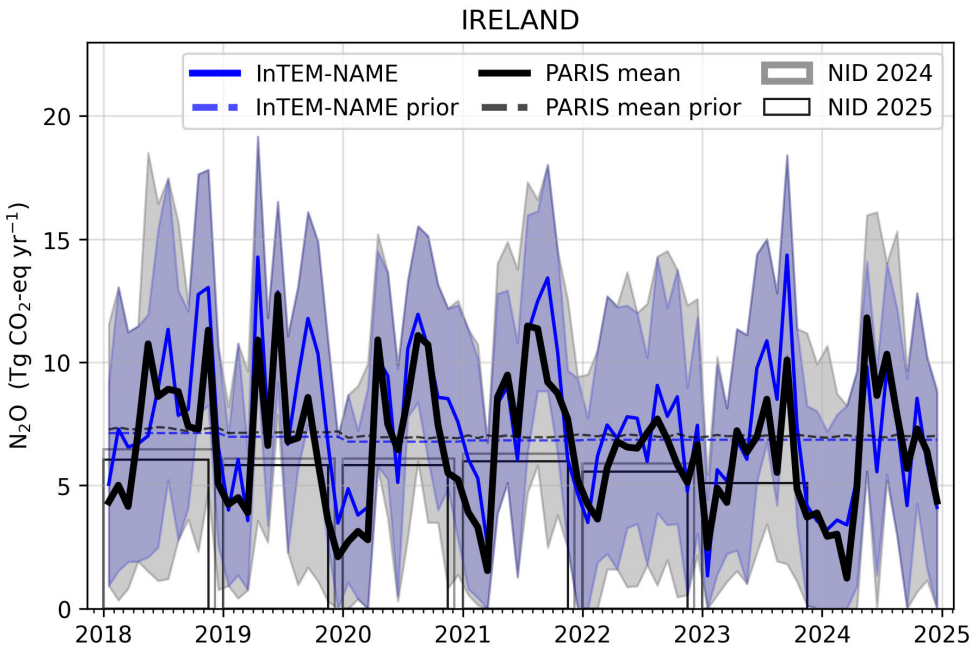

Figure 5.0.5: Spatial distribution of the Irish average modelled emissions of N_2O during the period of 2020-2024 (mean from all models). Observing stations are marked with red circles and highly-populated cities are marked with red triangles.

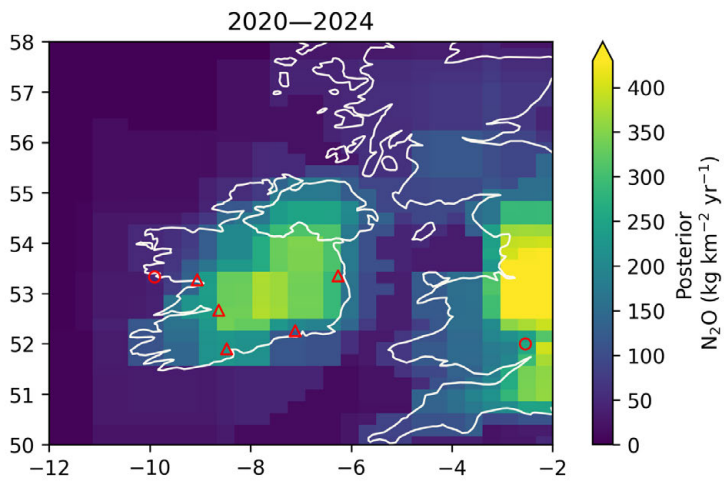

Figure 5.0.6: Spatial distribution of the seasonal deviation from the mean. The deviation is defined as the modelled Irish seasonally averaged N_2O emissions over 2020-2024 minus the average over the whole period. The mean across all models is shown. Observing stations are marked with black circles and highly-populated cities are marked with black triangles.

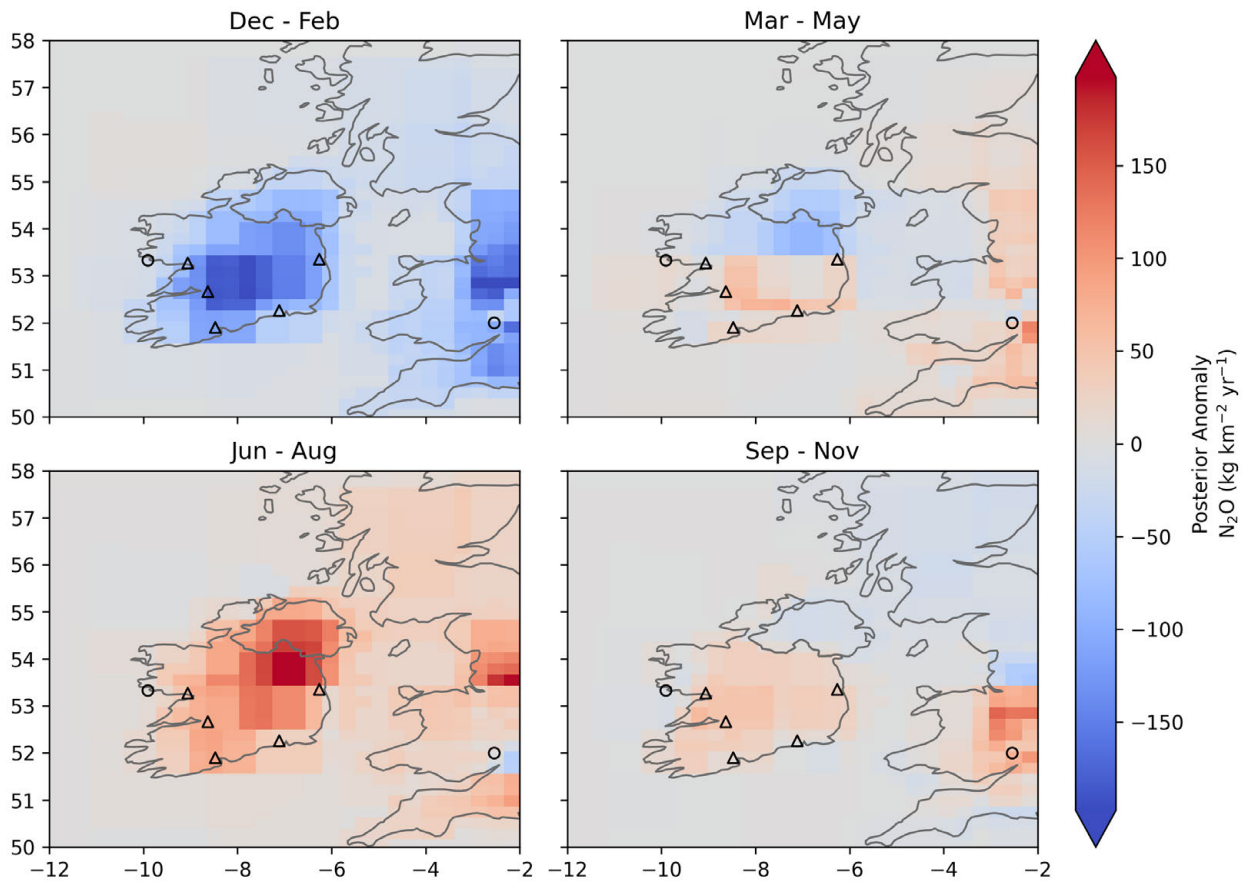

6 Hydrofluorocarbons (HFCs)

Figure 6.0.1: Total source sensitivity of HFCs/PFCs observing sites as calculated by the FLEXPART transport model for the year 2018 (left) and 2024 (right) and used in the inversions. Observing stations active in each year are marked with red dots. Areas with visible land surface represent regions for which emissions can be observed well from the network. Shaded or dark areas represent regions for which limited emission information can be obtained from the network.

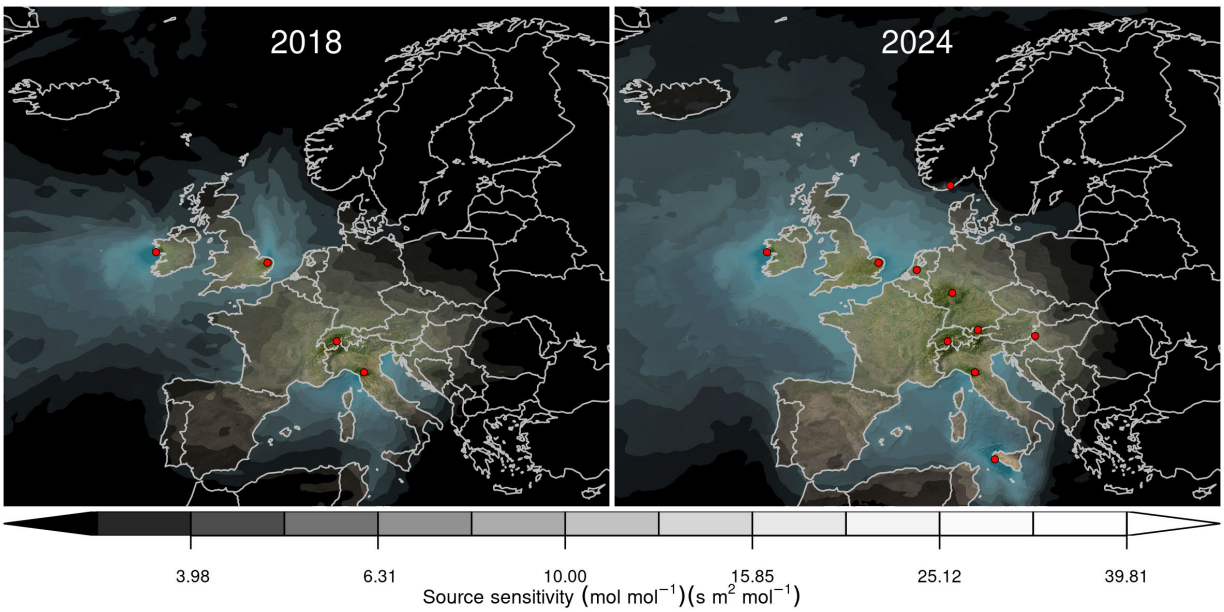

6.1 HFC-125

Figure 6.1.1: Verification of the Irish emissions inventory estimates for HFC-125. Modelled annual emissions are given as the mean from all models (black line) and the individual result from InTEM-NAME (blue line). The shaded blue area is the 68 % confidence interval (CI) of InTEM-NAME and the shaded grey area encompasses the 68 % CI from all models. National inventory annual totals from 2024 and 2025 are given as grey and black bars, respectively.

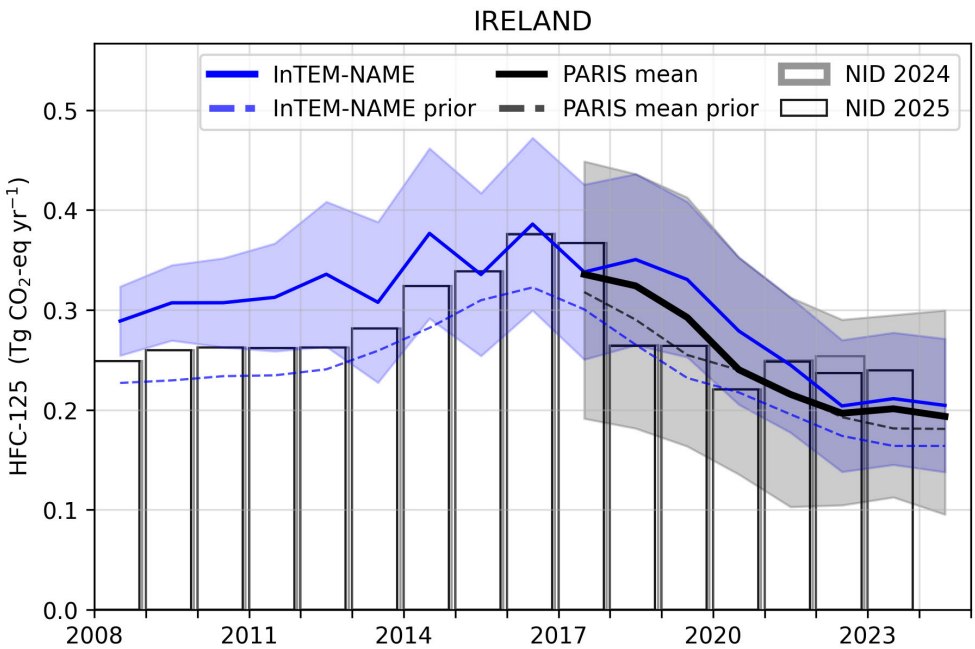

Figure 6.1.2: Spatial distribution of the Irish average modelled emissions of HFC-125 during the period of 2020-2024 (mean from all models). Observing stations are marked with red circles and highly-populated cities are marked with red triangles.

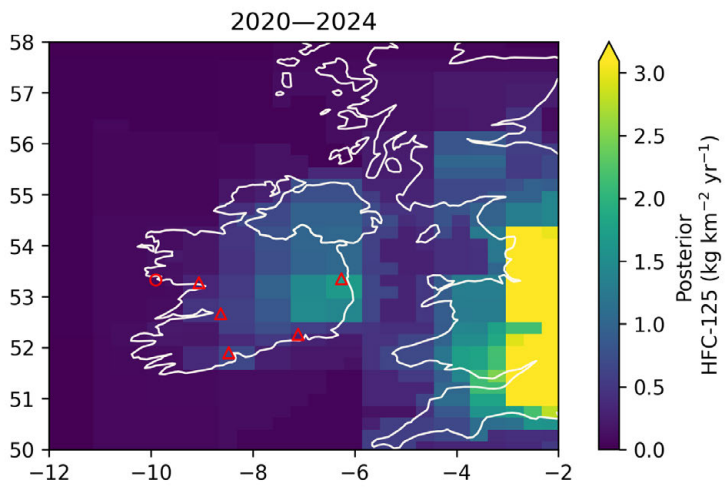

6.2 HFC-134a

Figure 6.2.1: Verification of the Irish emissions inventory estimates for HFC-134a. Modelled annual emissions are given as the mean from all models (black line) and the individual result from InTEM-NAME (blue line). The shaded blue area is the 68 % confidence interval (CI) of InTEM-NAME and the shaded grey area encompasses the 68 % CI from all models. National inventory annual totals from 2024 and 2025 are given as grey and black bars, respectively.

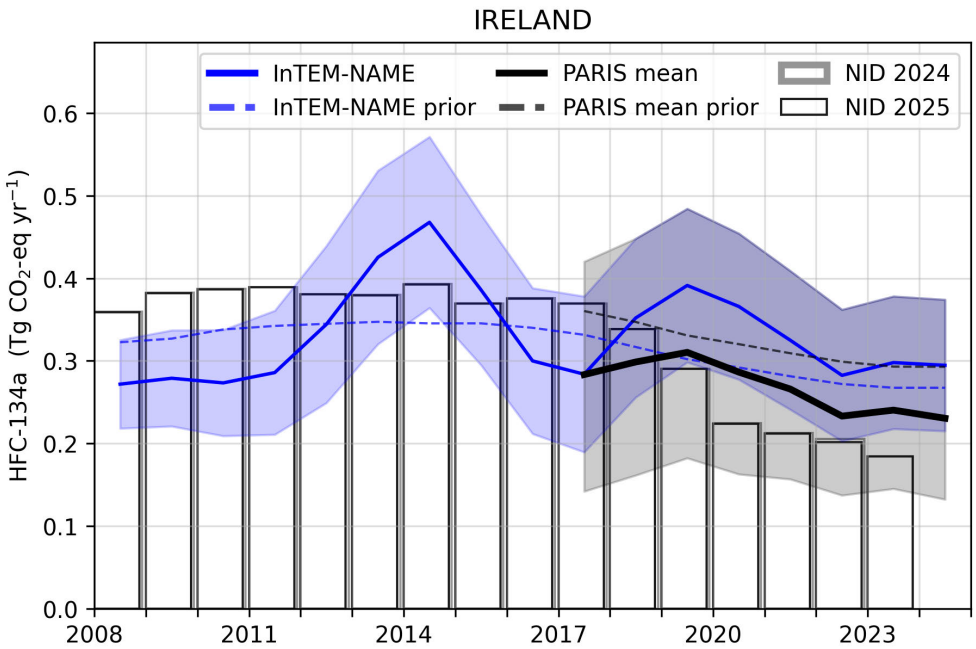

Figure 6.2.2: Spatial distribution of the Irish average modelled emissions of HFC-134a during the period of 2020-2024 (mean from all models). Observing stations are marked with red circles and highly-populated cities are marked with red triangles.

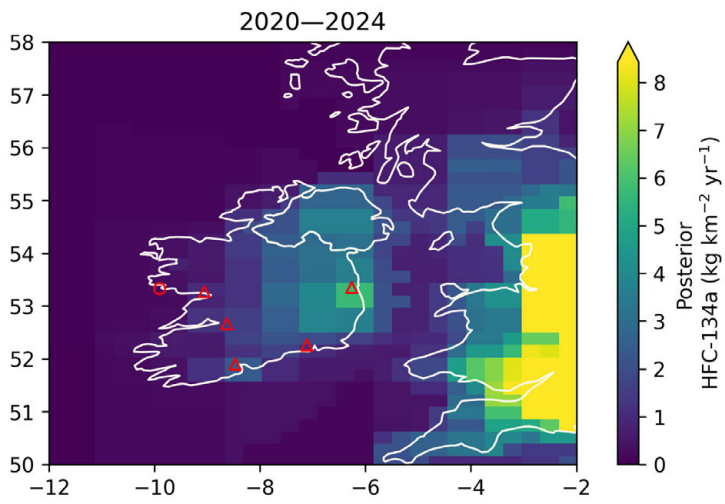

6.3 HFC-143a

Figure 6.3.1: Verification of the Irish emissions inventory estimates for HFC-143a. Modelled annual emissions are given as the mean from all models (black line) and the individual result from InTEM-NAME (blue line). The shaded blue area is the 68 % confidence interval (CI) of InTEM-NAME and the shaded grey area encompasses the 68 % CI from all models. National inventory annual totals from 2024 and 2025 are given as grey and black bars, respectively.

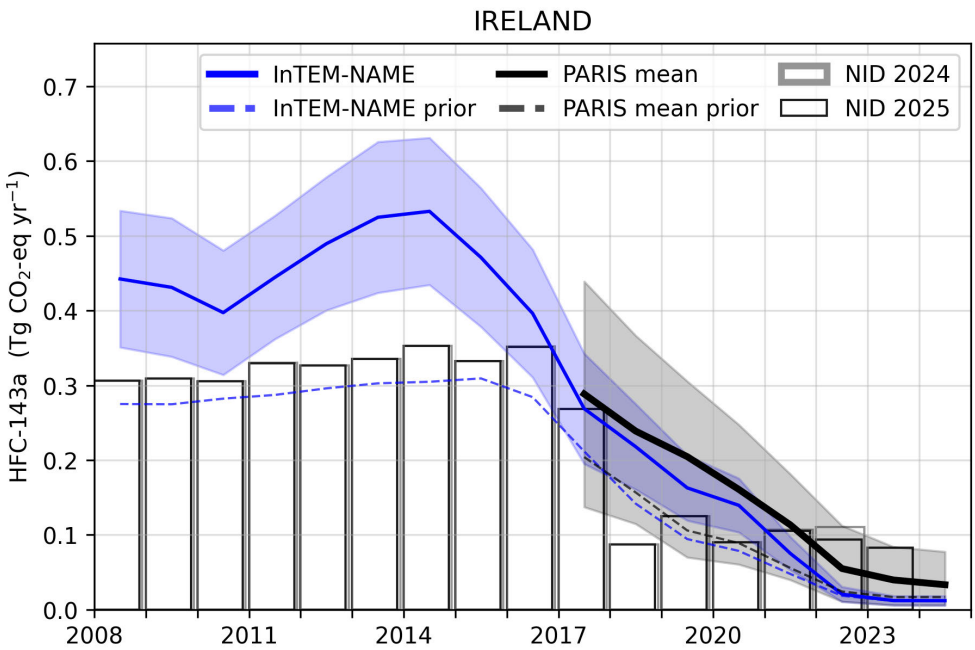

Figure 6.3.2: Spatial distribution of the Irish average modelled emissions of HFC-143a during the period of 2020-2024 (mean from all models). Observing stations are marked with red circles and highly-populated cities are marked with red triangles.

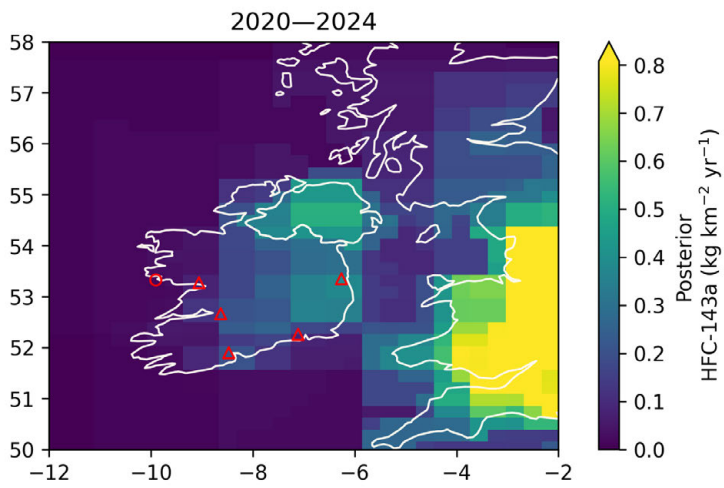

6.4 HFC-152a

Figure 6.4.1: Verification of the Irish emissions inventory estimates for HFC-152a. Modelled annual emissions are given as the mean from all models (black line) and the individual result from InTEM-NAME (blue line). The shaded blue area is the 68 % confidence interval (CI) of InTEM-NAME and the shaded grey area encompasses the 68 % CI from all models. National inventory annual totals from 2024 and 2025 are given as grey and black bars, respectively.

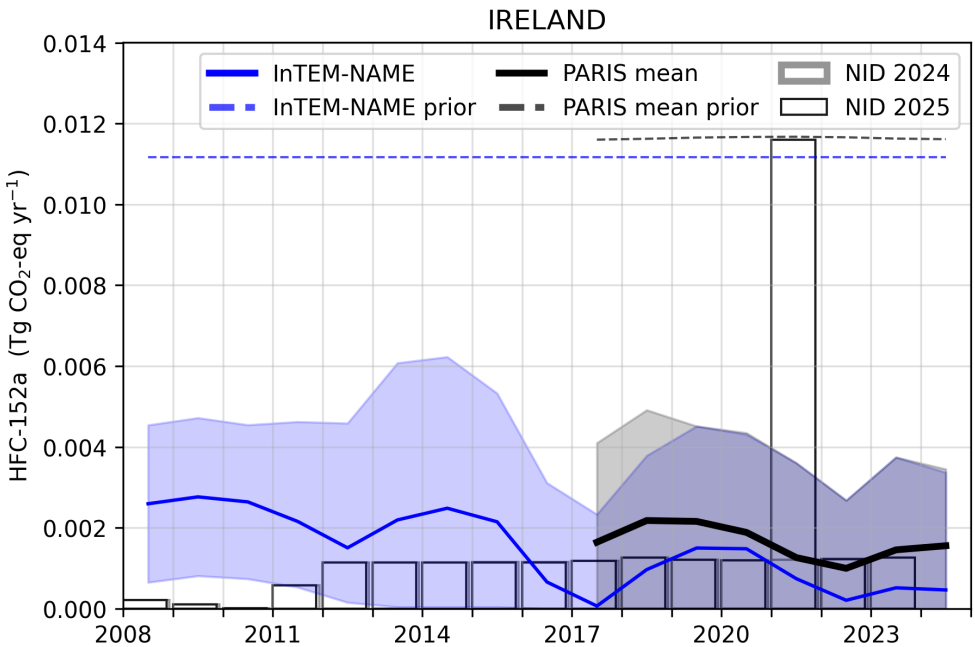

Figure 6.4.2: Spatial distribution of the Irish average modelled emissions of HFC-152a during the period of 2020-2024 (mean from all models). Observing stations are marked with red circles and highly-populated cities are marked with red triangles.

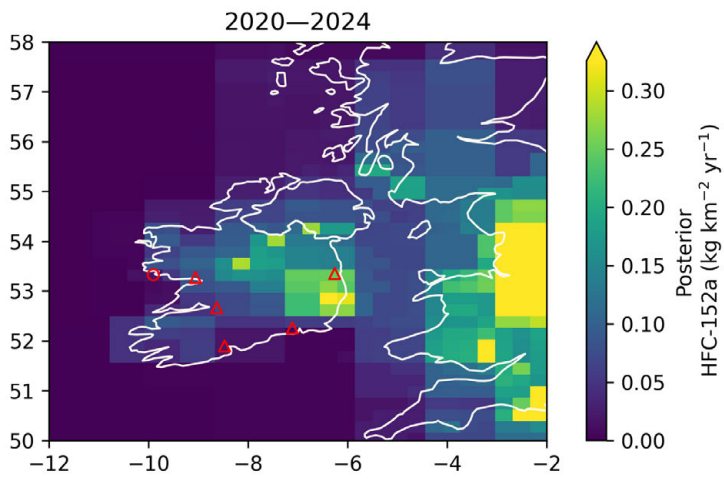

6.5 HFC-227ea

Figure 6.5.1: Verification of the Irish emissions inventory estimates for HFC-227ea. Modelled annual emissions are given as the mean from all models (black line) and the individual result from InTEM-NAME (blue line). The shaded blue area is the 68 % confidence interval (CI) of InTEM-NAME and the shaded grey area encompasses the 68 % CI from all models. National inventory annual totals from 2024 and 2025 are given as grey and black bars, respectively.

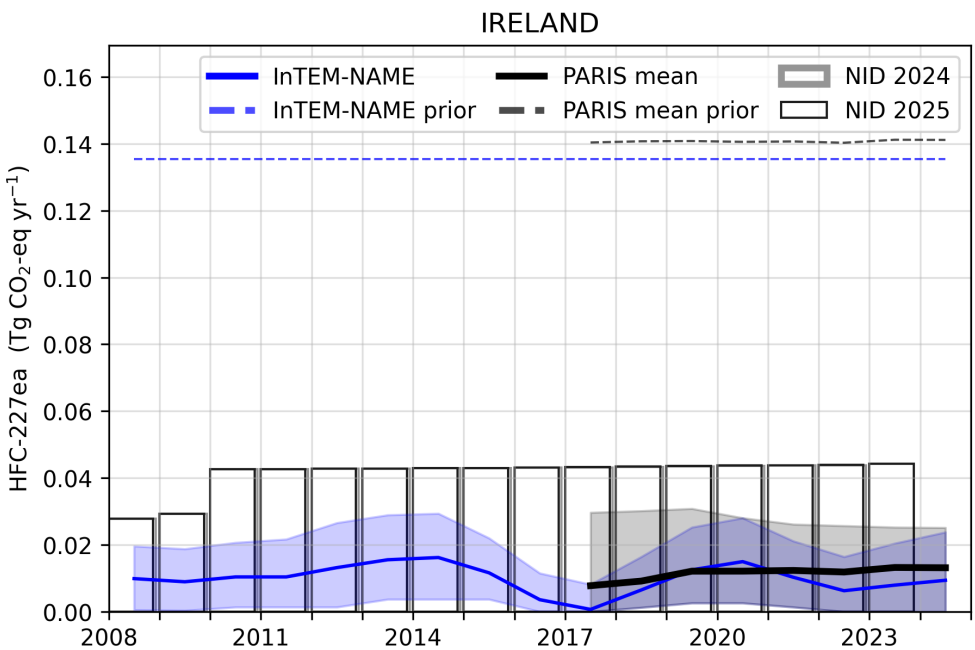

Figure 6.5.2: Spatial distribution of the Irish average modelled emissions of HFC-227ea during the period of 2020-2024 (mean from all models). Observing stations are marked with red circles and highly-populated cities are marked with red triangles.

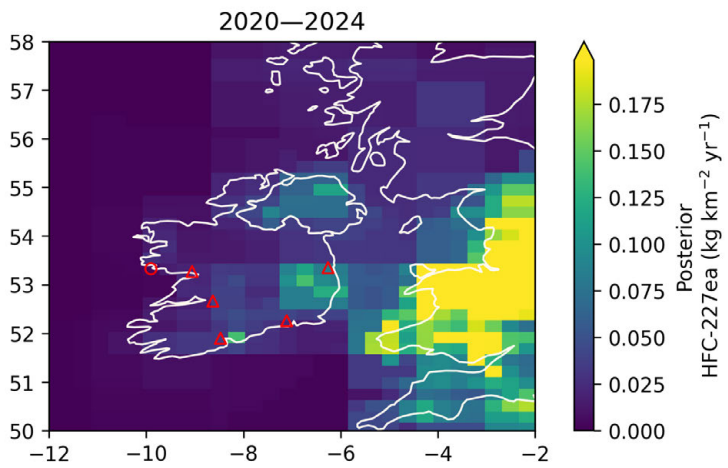

6.6 HFC-32

Figure 6.6.1: Verification of the Irish emissions inventory estimates for HFC-32. Modelled annual emissions are given as the mean from all models (black line) and the individual result from InTEM-NAME (blue line). The shaded blue area is the 68 % confidence interval (CI) of InTEM-NAME and the shaded grey area encompasses the 68 % CI from all models. National inventory annual totals from 2024 and 2025 are given as grey and black bars, respectively.

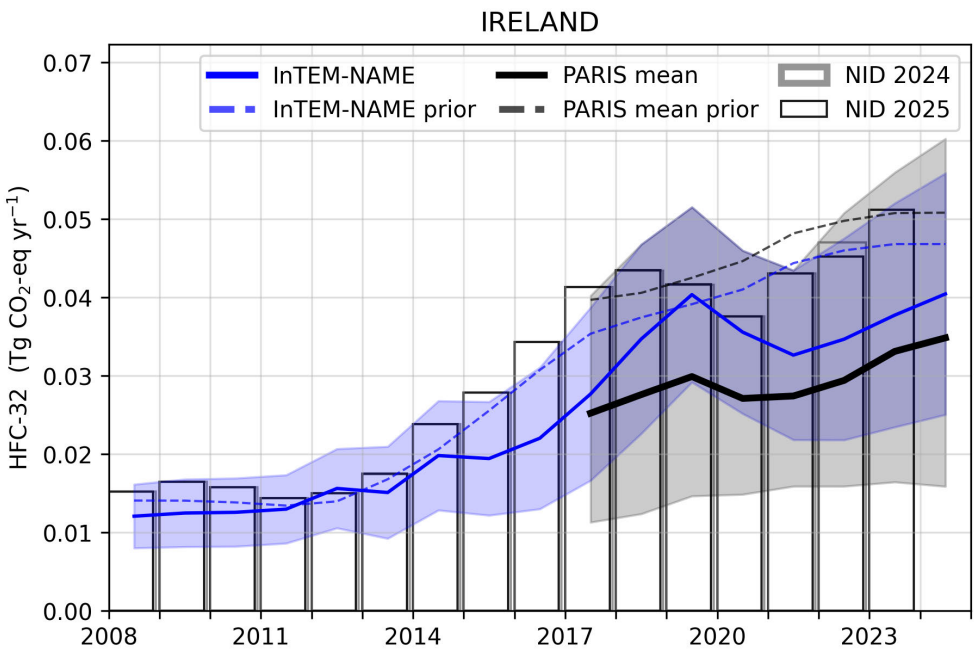

Figure 6.6.2: Spatial distribution of the Irish average modelled emissions of HFC-32 during the period of 2020-2024 (mean from all models). Observing stations are marked with red circles and highly-populated cities are marked with red triangles.

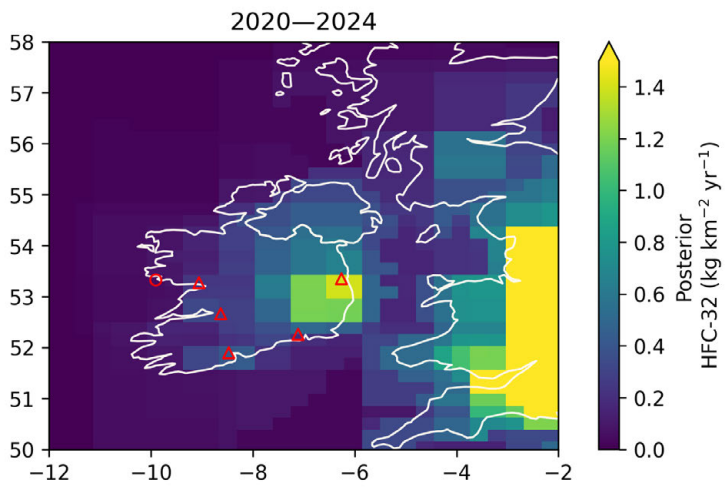

6.7 Total HFCs

Figure 6.7.1: Verification of the Irish emissions inventory estimates for total HFCs. Modelled annual emissions are given as the mean from all models (black line) and the individual result from InTEM-NAME (blue line). The shaded blue area is the 68 % confidence interval (CI) of InTEM-NAME and the shaded grey area encompasses the 68 % CI from all models. National inventory annual totals from 2024 and 2025 are given as grey and black bars, respectively.

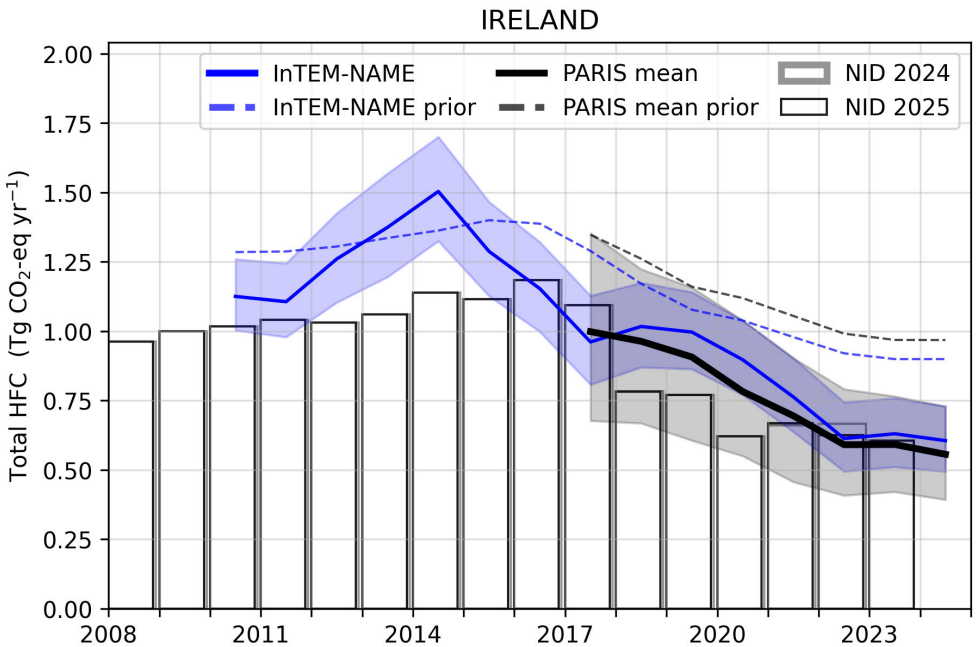

Table 2: Emissions estimation for HFCs according to the National Inventory Document (NID) 2025 and the inversions done in the PARIS project. For the PARIS estimation, the mean of all models is displayed, along with a range of uncertainty estimated via the half distance between the maximum and minimum uncertainties of the different models.

		2020	2021	2022	2023	2024
HFC-134a	NID 2025	0.22	0.21	0.20	0.18	
$(\mathrm{TgCO_2\text{-}eq \cdot yr^{-1}})$	PARIS mean	0.29 ± 0.15	0.27 ± 0.13	0.23 ± 0.11	0.24 ± 0.12	0.23 ± 0.12
HFC-125	NID 2025	0.22	0.25	0.24	0.24	
$(\mathrm{TgCO_2\text{-}eq \cdot yr^{-1}})$	PARIS mean	0.24 ± 0.11	0.22 ± 0.10	0.20 ± 0.09	0.20 ± 0.09	0.19 ± 0.10
HFC-143a	NID 2025	0.09	0.11	0.09	0.08	
$(\mathrm{TgCO_2\text{-}eq \cdot yr^{-1}})$	PARIS mean	0.16 ± 0.09	0.11 ± 0.07	0.05 ± 0.05	0.04 ± 0.04	0.03 ± 0.04
HFC-23	NID 2025	4	5	4	2	
$(\mathrm{GgCO_2\text{-}eq \cdot yr^{-1}})$	PARIS mean	35 ± 49	43 ± 67	51 ± 67	51 ± 67	39 ± 58
HFC-32	NID 2025	38	43	45	51	
$(\mathrm{GgCO_2\text{-}eq \cdot yr^{-1}})$	PARIS mean	27 ± 16	27 ± 14	29 ± 17	33 ± 20	35 ± 22
HFC-227ea	NID 2025	44	44	44	44	
$(\mathrm{GgCO_2\text{-}eq \cdot yr^{-1}})$	PARIS mean	12 ± 13	12 ± 12	12 ± 13	13 ± 13	13 ± 13
HFC-365mfc	NID 2025	0.0	0.0	0.0	0.0	
$(\mathrm{GgCO_2\text{-}eq \cdot yr^{-1}})$	PARIS mean	8.6 ± 7.0	8.0 ± 6.5	5.7 ± 4.9	4.5 ± 4.5	3.5 ± 3.6
HFC-245fa	NID 2025	0.0	0.0	0.0	0.0	
$(\mathrm{GgCO_2\text{-}eq \cdot yr^{-1}})$	PARIS mean	5.8 ± 8.4	4.2 ± 6.4	3.1 ± 5.5	2.5 ± 4.6	2.6 ± 4.7
HFC-236fa	NID 2025	0.0	0.0	0.0	0.0	
$(\mathrm{GgCO_2\text{-}eq \cdot yr^{-1}})$	PARIS mean	3.2 ± 5.6	2.9 ± 4.6	2.5 ± 3.6	3.2 ± 4.6	3.3 ± 4.6
HFC-152a	NID 2025	1	12	1	1	
$(\mathrm{GgCO_2\text{-}eq \cdot yr^{-1}})$	PARIS mean	2 ± 2	1 ± 2	1 ± 1	1 ± 2	2 ± 2
HFC-4310mee	NID 2025	0.0	0.0	0.0	0.0	
$(\mathrm{GgCO_2\text{-}eq \cdot yr^{-1}})$	PARIS mean	1.6 ± 3.8	1.5 ± 3.5	1.2 ± 2.5	0.9 ± 1.9	0.8 ± 1.7

7 Perfluorocarbons (PFCs)

7.1 PFC-14

Figure 7.1.1: Verification of the Irish emissions inventory estimates for PFC-14. Modelled annual emissions are given as the mean from all models (black line) and the individual result from InTEM-NAME (blue line). The shaded blue area is the 68 % confidence interval (CI) of InTEM-NAME and the shaded grey area encompasses the 68 % CI from all models. National inventory annual totals from 2024 and 2025 are given as grey and black bars, respectively.

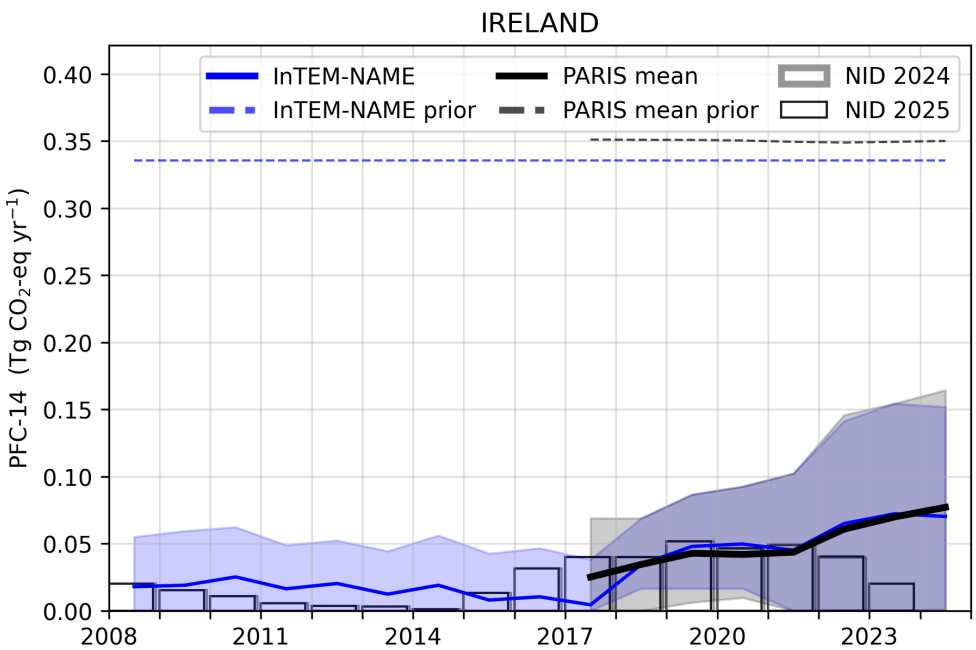

Figure 7.1.2: Spatial distribution of the Irish average modelled emissions of PFC-14 during the period of 2020-2024 (mean from all models). Observing stations are marked with red circles and highly-populated cities are marked with red triangles.

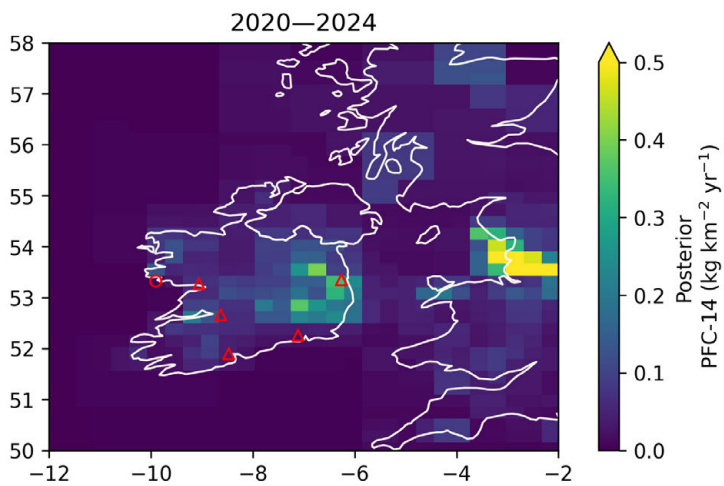

7.2 PFC-116

Figure 7.2.1: Verification of the Irish emissions inventory estimates for PFC-116. Modelled annual emissions are given as the mean from all models (black line) and the individual result from InTEM-NAME (blue line). The shaded blue area is the 68 % confidence interval (CI) of InTEM-NAME and the shaded grey area encompasses the 68 % CI from all models. National inventory annual totals from 2024 and 2025 are given as grey and black bars, respectively.

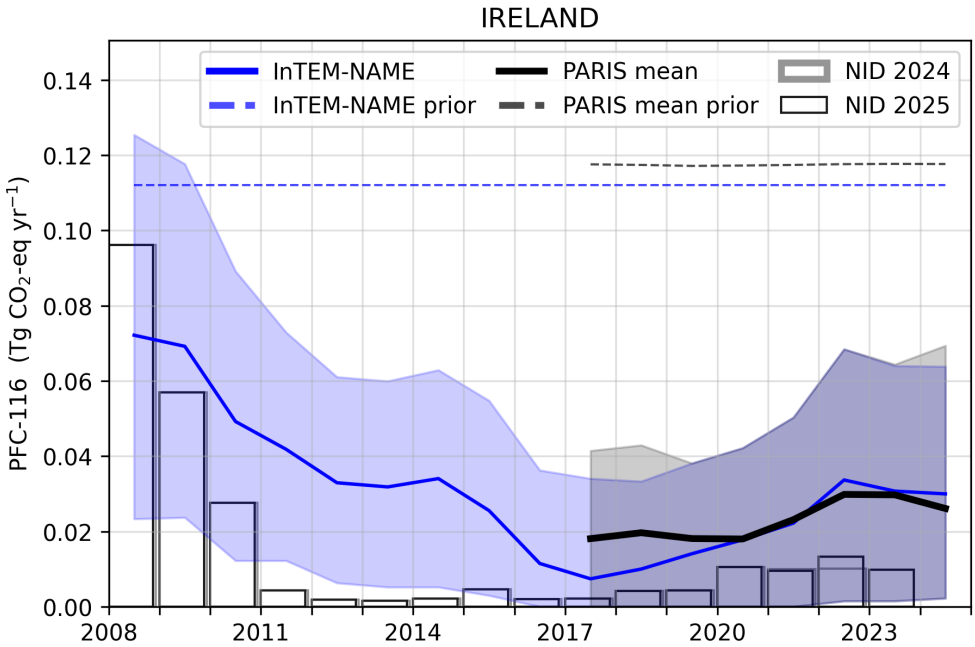

Figure 7.2.2: Spatial distribution of the Irish average modelled emissions of PFC-116 during the period of 2020-2024 (mean from all models). Observing stations are marked with red circles and highly-populated cities are marked with red triangles.

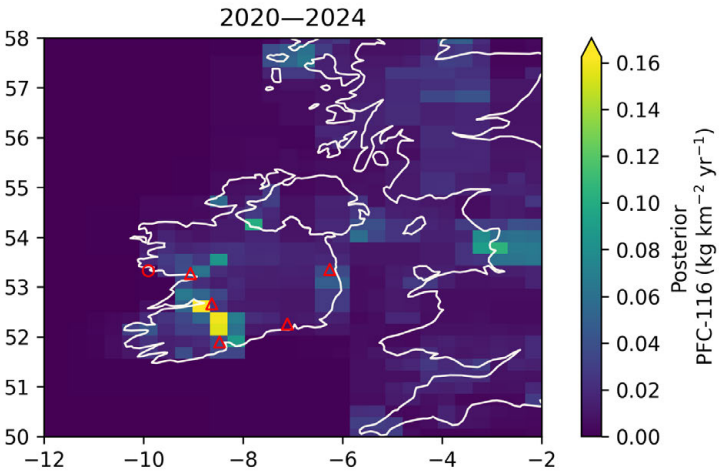

7.3 PFC-218

Figure 7.3.1: Verification of the Irish emissions inventory estimates for PFC-218. Modelled annual emissions are given as the mean from all models (black line) and the individual result from InTEM-NAME (blue line). The shaded blue area is the 68 % confidence interval (CI) of InTEM-NAME and the shaded grey area encompasses the 68 % CI from all models. National inventory annual totals from 2024 and 2025 are given as grey and black bars, respectively.

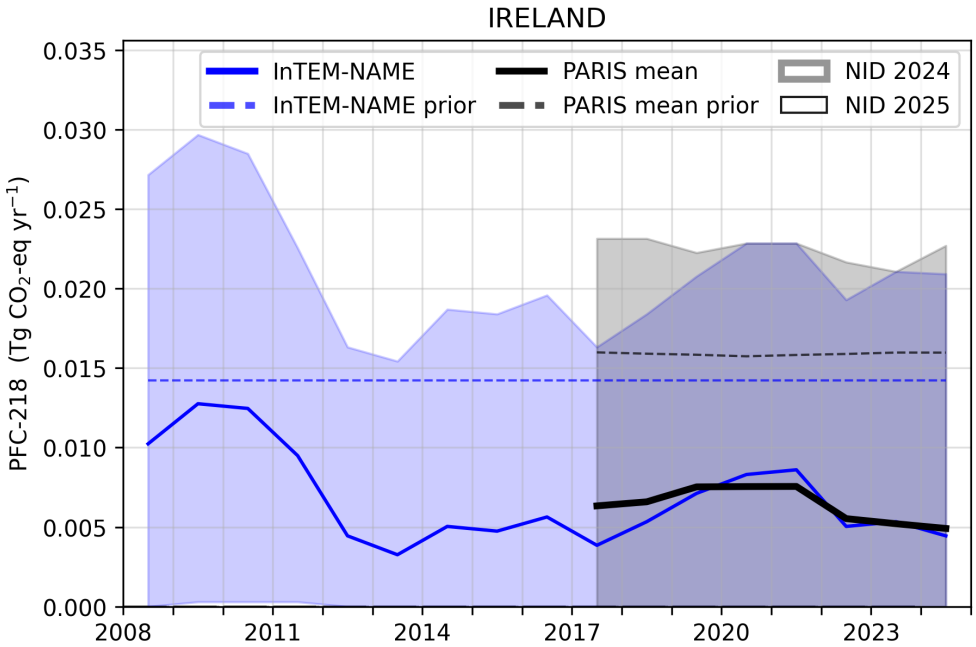

Figure 7.3.2: Spatial distribution of the Irish average modelled emissions of PFC-218 during the period of 2020-2024 (mean from all models). Observing stations are marked with red circles and highly-populated cities are marked with red triangles.

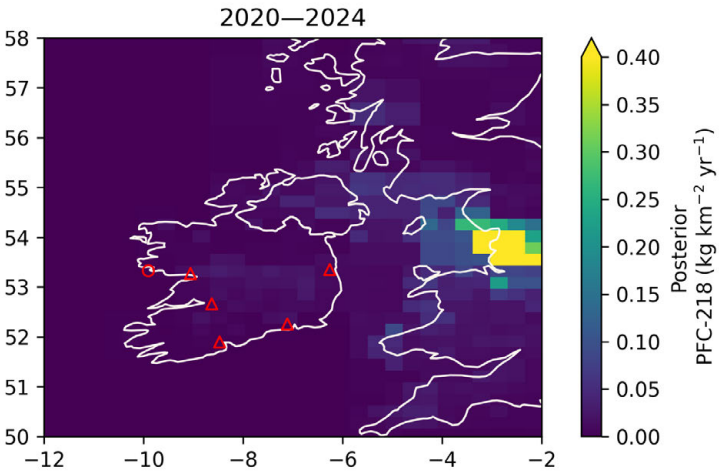

7.4 PFC-318

Figure 7.4.1: Verification of the Irish emissions inventory estimates for PFC-318. Modelled annual emissions are given as the mean from all models (black line) and the individual result from InTEM-NAME (blue line). The shaded blue area is the 68 % confidence interval (CI) of InTEM-NAME and the shaded grey area encompasses the 68 % CI from all models. National inventory annual totals from 2024 and 2025 are given as grey and black bars, respectively.

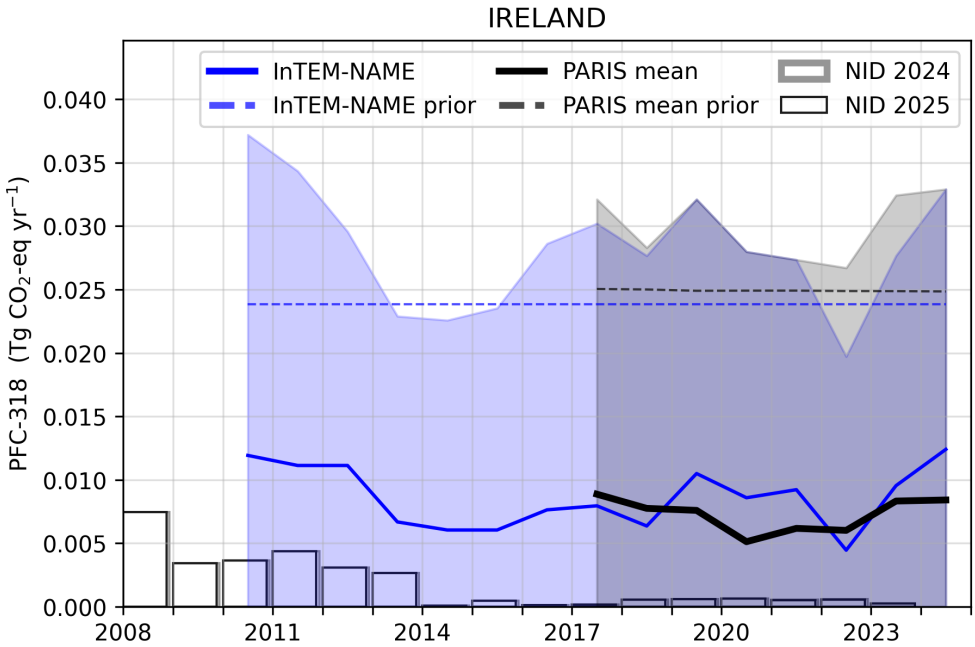

Figure 7.4.2: Spatial distribution of the Irish average modelled emissions of PFC-318 during the period of 2020-2024 (mean from all models). Observing stations are marked with red circles and highly-populated cities are marked with red triangles.

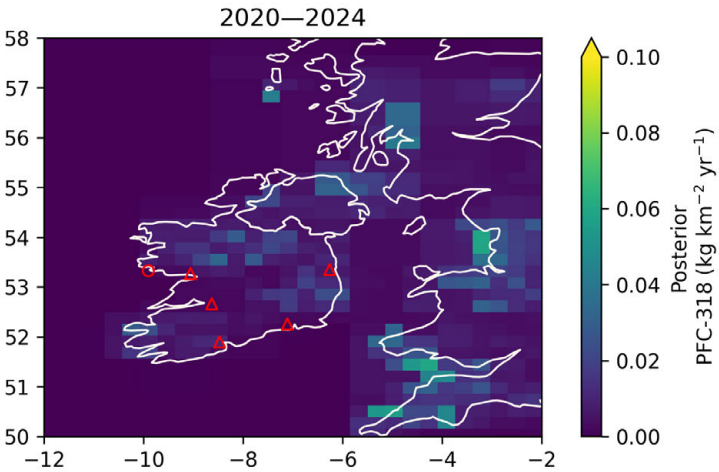

7.5 Total PFCs

Figure 7.5.1: Verification of the Irish emissions inventory estimates for total PFCs. Modelled annual emissions are given as the mean from all models (black line) and the individual result from InTEM-NAME (blue line). The shaded blue area is the 68 % confidence interval (CI) of InTEM-NAME and the shaded grey area encompasses the 68 % CI from all models. National inventory annual totals from 2024 and 2025 are given as grey and black bars, respectively.

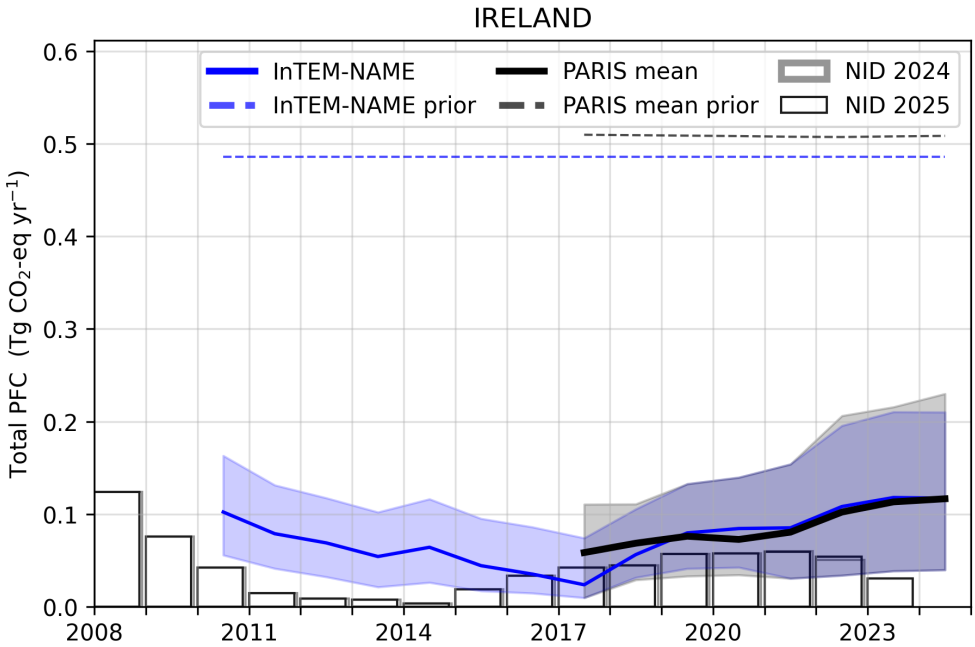

Table 3: Emissions estimation for PFCs according to the National Inventory Document (NID) 2025 and the inversions done in the PARIS project. For the PARIS estimation, the mean of all models is displayed, along with a range of uncertainty estimated via the half distance between the maximum and minimum uncertainties of the different models.

		2020	2021	2022	2023	2024
PFC-14	NID 2025	47	49	40	20	
$(\mathrm{GgCO_2\text{-}eq} \cdot \mathrm{yr}^{-1})$	PARIS mean	42 ± 41	44 ± 51	61 ± 73	70 ± 77	77 ± 82
PFC-116	NID 2025	11	9	13	10	
$(\mathrm{GgCO_2\text{-}eq} \cdot \mathrm{yr}^{-1})$	PARIS mean	18 ± 21	23 ± 25	30 ± 33	30 ± 31	26 ± 34
PFC-318	NID 2025	0.6	0.5	0.5	0.2	
$(\mathrm{GgCO_2\text{-}eq} \cdot \mathrm{yr}^{-1})$	PARIS mean	5.1 ± 14.0	6.2 ± 13.7	6.0 ± 13.4	8.3 ± 16.2	8.4 ± 16.5
PFC-218	NID 2025	0.0	0.0	0.0	0.0	
$(\mathrm{GgCO_2\text{-}eq} \cdot \mathrm{yr}^{-1})$	PARIS mean	7.5 ± 11.4	7.6 ± 11.4	5.5 ± 10.8	5.2 ± 10.5	4.9 ± 11.3

8 Sulphur hexafluoride (SF_6)

Figure 8.0.1: Total source sensitivity of SF_6 observing sites as calculated by the FLEXPART transport model for the year 2018 (left) and 2024 (right) and used in the inversions. Observing stations active in each year are marked with red dots. Areas with visible land surface represent regions for which emissions can be observed well from the network. Shaded or dark areas represent regions for which limited emission information can be obtained from the network.

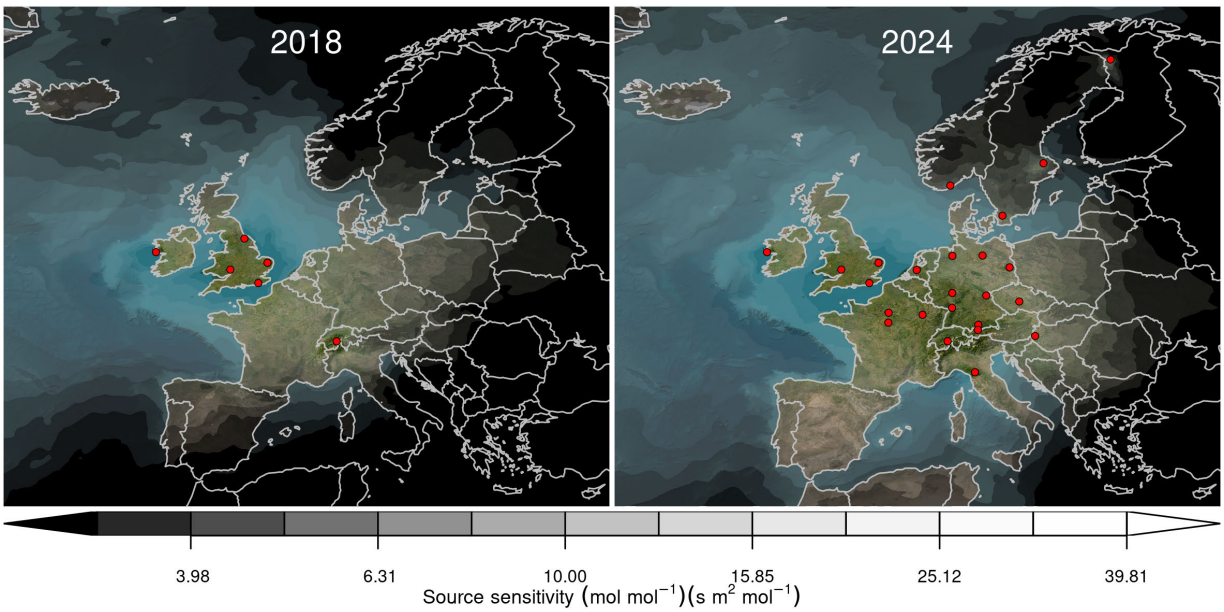

Figure 8.0.2: Verification of the Irish emissions inventory estimates for SF_6. Modelled annual emissions are given as the mean from all InTEM and ELRIS inversions (black line) and the individual result from InTEM-NAME (blue line). The shaded blue area is the 68 % confidence interval (CI) of InTEM-NAME and the shaded grey area encompasses the 68 % CI from all models. National inventory annual totals from 2024 and 2025 are given as grey and black bars, respectively.

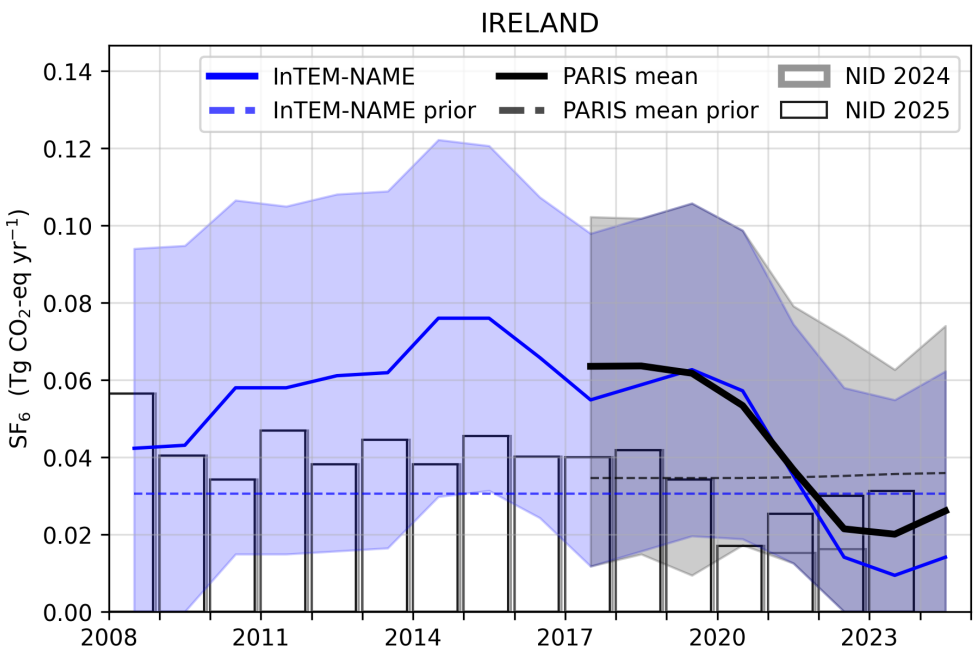

Figure 8.0.3: Spatial distribution of the Irish average modelled emissions of SF_6 during the period of 2020-2024 (mean from all InTEM and ELRIS inversions). Observing stations are marked with red circles and highly-populated cities are marked with red triangles.

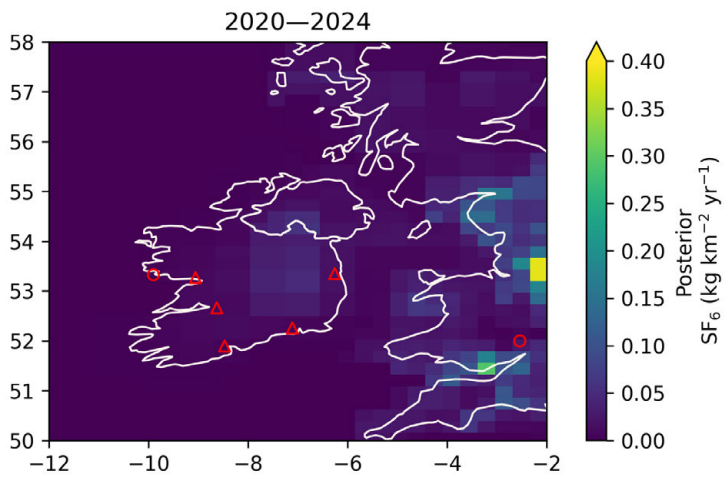

9 Nitrogen Trifluoride (NF_3)

Figure 9.0.1: Verification of the Irish emissions inventory estimates for NF_3. Modelled annual emissions are given as the mean from all models (black line) and the individual result from InTEM-NAME (blue line). The shaded blue area is the 68 % confidence interval (CI) of InTEM-NAME and the shaded grey area encompasses the 68 % CI from all models. National inventory annual totals from 2024 and 2025 are given as grey and black bars, respectively.

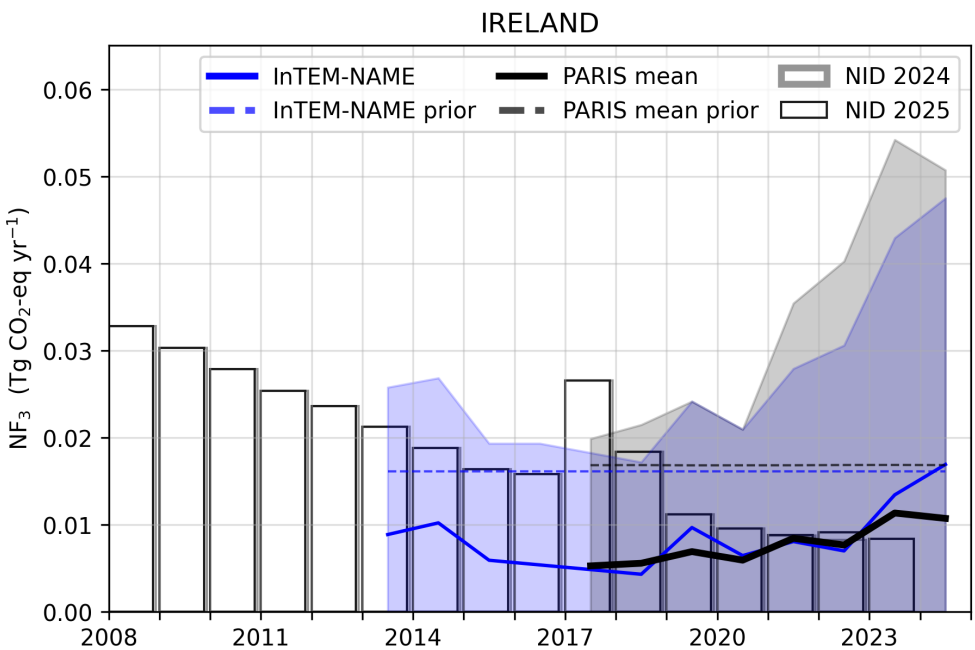

Figure 9.0.2: Spatial distribution of the Irish average modelled emissions of NF_3 during the period of 2020-2024 (mean from all models). Observing stations are marked with red circles and highly-populated cities are marked with red triangles.

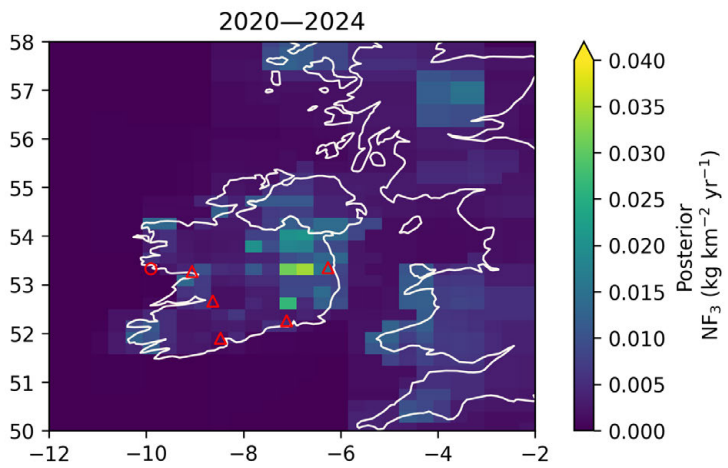

10 Carbon Dioxide (CO_2)

Measurements of CO_2 at ICOS sites and related observatories are influenced by a complex combination of sources and sinks. Fossil fuel combustion for transport, heating, energy generation, and other applications produce CO_2, along with other anthropogenic activities such as cement production. The terrestrial and oceanic biosphere produces CO_2 through animal and plant respiration and takes up CO_2 through photosynthesis. Furthermore, CO_2 is exchanged with the ocean through physical and chemical processes.

When considering high-frequency (∼hourly) CO_2 mole fraction deviations from baseline values—used to infer national emissions in regional inverse modelling studies—the influence of biospheric fluxes can be comparable to, or larger than, those of anthropogenic sources (e.g. White et al., 2019). Therefore, research is under way to develop new tracers that can determine fossil fuel CO_2 fluxes independent of biosphere sources and sinks.

Ongoing Horizon Europe projects PARIS and CORSO are examining methods for estimating fossil fuel CO_2 fluxes based on simultaneous measurements of CO_2 and O_2 (Figure 10.0.1). The method relies on the fact that CO_2 and O_2 are inter-converted during combustion and terrestrial biosphere exchange, but with different ratios for the two processes. A quantity can be constructed from these measurements, known as Atmospheric Potential Oxygen (APO), which is insensitive to biosphere fluxes, and may therefore be useful for isolating fossil fuel signals (Pickers et al., 2022).

High-frequency (∼hourly) timeseries of APO are available from Weybourne (WAO, 2010 – present) and Heathfield (HFD, 2021 - present) in the UK (Figure 10.0.1; Pickers, Adcock, and Manning, 2024), and new sites are being established at Cabauw and Zweth in the Netherlands. Preliminary analyses of the WAO data have revealed regional APO trends consistent with the drop in fossil fuel CO_2 emissions during the COVID lockdowns in the UK (Pickers et al., 2022). However, quantification of absolute regional fossil fuel CO_2 emissions remains an area of active research. Recent studies have derived fossil fuel CO_2 emissions for the UK that are highly uncertain (Rigby et al., 2025). Potential confounding factors were identified in Chawner et al. (2024), such as highly uncertain APO fluxes from the ocean, and a poorly constrained regional APO background. These factors are the subject of ongoing research using atmospheric models and new APO measurements from PARIS, CORSO and ICOS.

An alternative method for top-down fossil fuel CO_2 emissions evaluation uses measurements of radiocarbon isotopologues ($^{14}CO_2$, compared to the dominant $^{12}CO_2$). Fossil fuels do not contain ^{14}C, and therefore, their combustion tends to decrease the atmospheric $^{14}CO_2/^{12}CO_2$ ratio. Currently, radiocarbon measurements can only be made at low frequency using flask sampling. However, a relatively intensive flask

sampling campaign was carried out across Europe during 2024 as part of CORSO, and the results of this study will be reported on soon.

Figure 10.0.1: Carbon dioxide (top, red) and oxygen (bottom, blue) measurements from Weybourne Atmospheric Observatory in the UK, available from the ICOS Carbon Portal (Adcock et al., 2024).

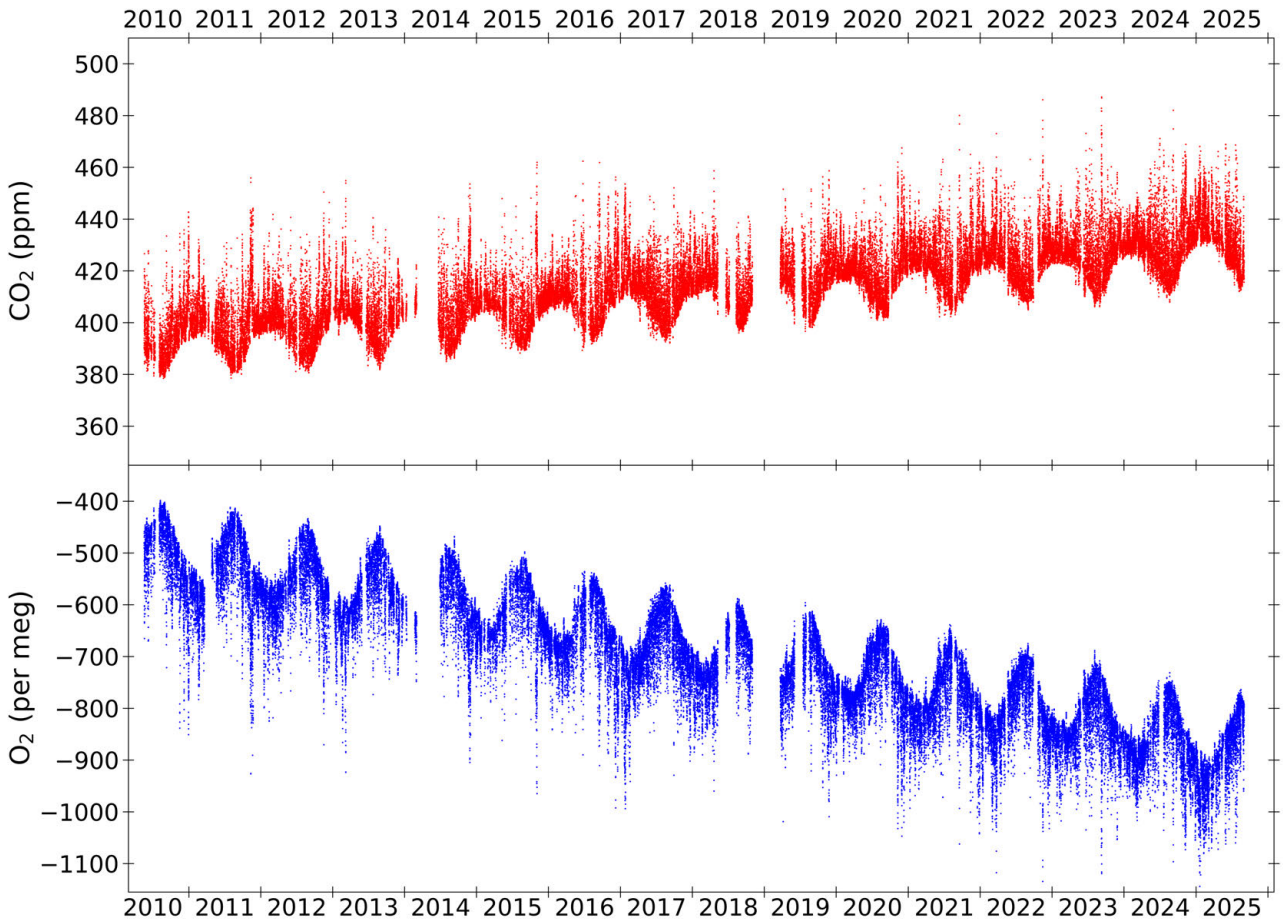

References

Adcock, Karina et al. (2024). *Atmospheric GHG data product (o2, o2_stdev, co2, co2_stdev) from Weybourne (10.0 m), 2010-05-19–2023-12-31*. URL: https://hdl.handle.net/11676/j4LzdHQiq3fPgfNeXHruC0Bb.

Chawner, Hannah et al. (Apr. 2024). "Atmospheric oxygen as a tracer for fossil fuel carbon dioxide: a sensitivity study in the UK". en. In: *Atmospheric Chemistry and Physics* 24.7, pp. 4231–4252. ISSN: 1680-7324. DOI: 10.5194/acp-24-4231-2024. URL: https://acp.copernicus.org/articles/24/4231/2024/ (visited on 04/10/2024).

European Commission: Joint Research, Centre et al. (2023). *GHG emissions of all world countries – 2023*. Publications Office of the European Union. DOI: 10.2760/953322.

Ganesan, A. L. et al. (2014). "Characterization of uncertainties in atmospheric trace gas inversions using hierarchical Bayesian methods". In: *Atmospheric Chemistry and Physics* 14.8, pp. 3855–3864. DOI: 10.5194/acp-14-3855-2014. URL: http://www.atmos-chem-phys.net/14/3855/2014/http://www.atmos-chem-phys.net/14/3855/2014/acp-14-3855-2014.pdf.

Ganesan, A. L. et al. (2015). "Quantifying methane and nitrous oxide emissions from the UK and Ireland using a national-scale monitoring network". In: *Atmos. Chem. Phys.* 15.11, pp. 6393–6406. DOI: 10.5194/acp-15-6393-2015. URL: https://www.atmos-chem-phys.net/15/6393/2015/https://www.atmos-chem-phys.net/15/6393/2015/acp-15-6393-2015.pdf.

Henne, S. et al. (2016). "Validation of the Swiss methane emission inventory by atmospheric observations and inverse modelling". In: *Atmospheric Chemistry and Physics* 16.6, pp. 3683–3710. DOI: 10.5194/acp-16-3683-2016. URL: http://www.atmos-chem-phys.net/16/3683/2016/.

Jones, A.R. et al. (2007). "The U.K. Met Office's next-generation atmospheric dispersion model, NAME III, in Borrego C. and Norman A.-L. (Eds)". In: *Air Pollution Modeling and its Application XVII (Proceedings of the 27th NATO/CCMS International Technical Meeting on Air Pollution Modelling and its Application), Springer*, pp. 580–589.

Katharopoulos, I. et al. (2023). "Impact of transport model resolution and a priori assumptions on inverse modeling of Swiss F-gas emissions". In: *Atmos. Chem. Phys.* 23.22, pp. 14159–14186. DOI: 10.5194/acp-23-14159-2023. URL: https://acp.copernicus.org/articles/23/14159/2023/.

Manning, A. J. et al. (2021). "Evidence of a recent decline in UK emissions of hydrofluorocarbons determined by the InTEM inverse model and atmospheric measurements". In: *Atmospheric Chemistry and Physics* 21.16, pp. 12739–12755. DOI: 10.5194/acp-21-12739-2021. URL: https://acp.copernicus.org/articles/21/12739/2021/.

Pickers, P., K. Adcock, and A. Manning (Feb. 2024). *Atmospheric oxygen and carbon dioxide observations from Weybourne Atmospheric Observatory, Norfolk, UK uploaded to public archives*. Tech. rep. Process Attribution of Regional Emissions (PARIS). URL: https://horizoneurope-paris.eu/wp-content/uploads/sites/914/2024/07/PARIS-deliverables-D6.1-High-frequency-APO-data-uploaded-final.pdf.

Pickers, Penelope A. et al. (Apr. 2022). "Novel quantification of regional fossil fuel CO2 reductions during COVID-19 lockdowns using atmospheric oxygen measurements". en. In: *Science Advances* 8.16, eabl9250. ISSN: 2375-2548. DOI: 10.1126/sciadv.abl9250. URL: https://www.science.org/doi/10.1126/sciadv.abl9250 (visited on 12/01/2023).

Rigby, M. et al. (2019). "Increase in CFC-11 emissions from eastern China based on atmospheric observations". In: *Nature* 569, pp. 546–550. DOI: 10.1038/s41586-019-1193-4. URL: https://doi.org/10.1038/s41586-019-1193-4.

Rigby, M. et al. (Apr. 2025). *Inverse estimates of fossil fuel CO2 emission*. Tech. rep. Process Attribution of Regional Emissions (PARIS). URL: https://horizoneurope-paris.eu/wp-content/uploads/sites/914/2025/01/PARIS-M24-Inverse-estimates-of-fossil-fuel-CO2-emissions-final.pdf.

Stohl, A. et al. (2005). "Technical note: The Lagrangian particle dispersion model FLEXPART version 6.2". In: *Atmospheric Chemistry and Physics* 5, pp. 2461–2474. DOI: 10.5194/acp-5-2461-2005. URL: <GotoISI>://000231983600002.

White, Emily D. et al. (Apr. 2019). "Quantifying the UK's carbon dioxide flux: an atmospheric inverse modelling approach using a regional measurement network". en. In: *Atmospheric Chemistry and Physics*

19.7, pp. 4345–4365. ISSN: 1680-7324. DOI: 10.5194/acp-19-4345-2019. URL: https://www.atmos-chem-phys.net/19/4345/2019/ (visited on 04/05/2019).